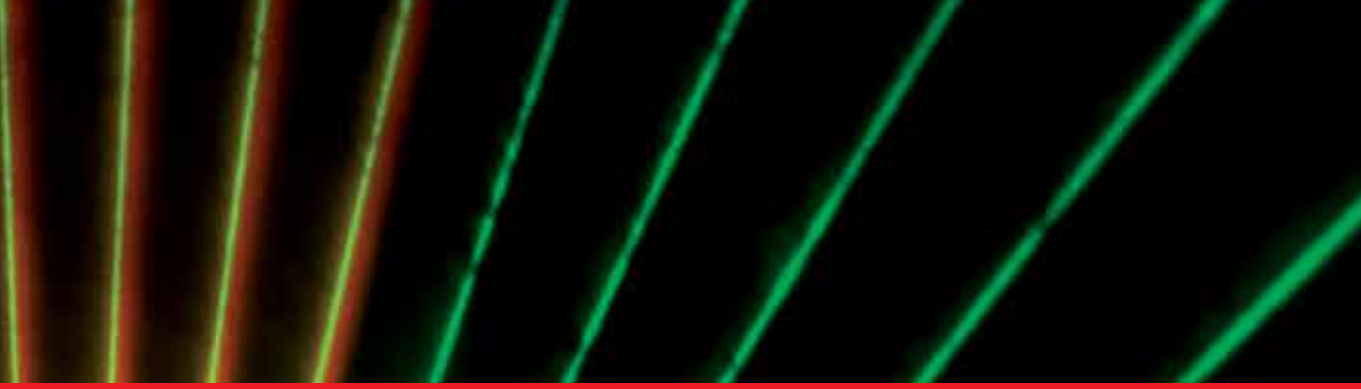

IntechOpen

Raman Spectroscopy and Applications

Edited by Khan Maaz

RAMAN SPECTROSCOPY AND APPLICATIONS

Edited by **Khan Maaz**

Raman Spectroscopy and Applications
http://dx.doi.org/10.5772/62717
Edited by Khan Maaz

Contributors

Søren Hassing, Cedric Pardanaud, Celine Martin, Pascale Roubin, Ujjal Kumar Sur, Frédéric Foucher, Guillaume Guimbretière, Nicolas Bost, Frances Westall, Lei Ouyang, Lihua Zhu, Ariel Flores-Rosas, Cristina Coman, Paulo De Tarso Freire, Felipe Barboza, José Lima Jr., Francisco Melo, Josué Mendes Filho, Piter Miedema, Raffaele Tommasi, Jonathan Birchall, Jason Skinner, Michael Barlow, Boyd Goodson, Nicholas Whiting, Zhixun Luo, Jiannian Yao, Ilaria Zardo, Marta De Luca, Zhenqiang Ma, Hongyi Mi, Jams. P Blanchard, Ming Zhang, Nicoleta Elena Dina, Alia Colnita

Notice

First published in Croatia, 2017 by INTECH d.o.o.
eBook (PDF) Published by IN TECH d.o.o.
Place and year of publication of eBook (PDF): Rijeka, 2019.
IntechOpen is the global imprint of IN TECH d.o.o.
Printed in Croatia

Legal deposit, Croatia: National and University Library in Zagreb

Additional hard and PDF copies can be obtained from orders@intechopen.com

Raman Spectroscopy and Applications
Edited by Khan Maaz
p. cm.
Print ISBN 978-953-51-2907-3
Online ISBN 978-953-51-2908-0
eBook (PDF) ISBN 978-953-51-4112-9

Meet the editor

Dr. Maaz Khan is working as principal scientist in Pakistan Institute of Nuclear Science and Technology (PINSTECH). He has done his PhD from Quaid-i-Azam University, Pakistan, and postdoctorates from South Korea and China. His research interests include fabrication of nanomaterials by different chemical and electrochemical techniques. He is working on structural, magnetic, optical, and electrical characterization of various materials. He has authored more than 60 research articles in peer-reviewed journals, and he is the author and editor of many books. Dr. Maaz is working as editor in chief of *Journal of Materials, Processing and Design* and executive editor of *International Journal of Nano Studies and Technology* and is among the editorial board members of many journals including *World Journal of Condensed Matter Physics*, *International Journal of Materials Science and Applications*, *Frontiers in Physics*, and *Advances in Alloys and Compounds*.

Contents

Preface

Raman spectroscopy is a spectroscopic technique based on inelastic scattering of monochromatic light, usually from a laser source. Photons of the laser light are absorbed by the sample and then reemitted, and their frequency is shifted either up or down as compared to the original monochromatic frequency, which is called Raman effect. The frequency shift provides useful information about the vibrational, rotational, and other low-frequency transitions in molecules. This technique has a variety of applications in material science, nanotechnology, and medicine for structural characterization of the samples. This book presents the background and implementation of the techniques that have allowed true imaging and chemical analysis at the atomic scale.

The book is divided mainly into two parts. The first part comprises works that deal with Raman spectroscopy and its applications in various fields and how to utilize this technique for analysis of the samples. The second part comprises surface-enhanced Raman spectroscopy (SERS), which is an important part of the Raman spectroscopy. Surface-enhanced Raman spectroscopy is a Raman spectroscopic technique that provides greatly enhanced Raman signals from Raman-active analyte molecules that have been adsorbed onto certain specially prepared metal surfaces (rough metal surfaces or by the nanostructures).

The chapters are focused on experimental aspects of nanotechnology as well as on theoretical explanations. All the contributors are active researchers in their fields of specialization, and thus this book provides an up-to-date knowledge about the Raman spectroscopy and its applications. Various topics in this book are developed to a level appropriate for most modern materials research using Raman spectroscopy. The content of this book provides the fundamental preparation needed for further study of advanced topics in Raman microscopy. Moreover, at the end of each chapter, proper references have been included that can lead the readers to the best sources in the literature and help them to go into more details about Raman spectroscopy.

I am grateful to all the authors who are experts in their fields for helping me to complete this project and also to the entire InTech's publishing team for making this project possible. I am also thankful to the Publishing Process Manager Ms. Romina Skomersic for her cooperative attitude during the publishing process. I hope that this book will help the readers in a more efficient way to characterize their materials using Raman spectroscopy and will provide an opportunity to strengthen their knowledge and research capabilities in the field of material science and nanotechnology using Raman spectroscopy.

Dr. Khan Maaz
Pakistan Institute of Nuclear Science and Technology
Nilore, Islamabad
Pakistan

Section 1

Raman Spectroscopy

Chapter 1

Raman Microscopy: A Suitable Tool for Characterizing Surfaces in Interaction with Plasmas in the Field of Nuclear Fusion

Cedric Pardanaud, Celine Martin and
Pascale Roubin

Additional information is available at the end of the chapter

http://dx.doi.org/10.5772/65649

Abstract

Raman microscopy, which is sensitive to chemical bonds, defects, structure, is a suitable tool that can give information on how a material can be modified by interacting with ions. We will first give concrete examples on how it can be used to characterize with a micrometric resolution samples extracted from tokamaks. We will then give concrete examples on what information can be obtained by doing a study on laboratory synthesized materials, benchmarking Raman microscopy with quantitative techniques. The first part of the chapter is focused on carbon-based material analysis. We will show how Raman spectra are sensitive to the presence of hydrogen, a major safety issue in the field. The second part of the chapter will be focused on beryllium- and tungsten-based material analysis. We will show that hydrogen can be stored as an hydride after ion implantation and that it can be released easily in tungsten oxide.

Keywords: plasma wall interaction, hydrogen isotope implantation, carbon, beryllium, tungsten

1. Introduction

Raman microscopy, which is sensitive to chemical bonds, defects, and structure, is a suitable tool that can give information on how a material can be modified by interacting with ions. We first gave concrete examples on how it can be used to characterize with a micrometric resolution samples extracted from tokamaks. We then gave concrete examples on what information can be obtained by doing a study on laboratory-synthesized materials, comparing

Raman microscopy with quantitative techniques. The first part of the chapter is focused on carbon-based material analysis. We showed how Raman spectra are sensitive to the presence of hydrogen, a major safety issue in the field. The second part of the chapter is focused on beryllium- and tungsten-based material analysis. We showed that hydrogen can be stored as a hydride after ion implantation and that it can be released easily in tungsten oxide.

1.1. Plasma-wall interactions in tokamaks

Tokamaks are machines made to study the possibility to make energy from nuclear fusion reactions by confining hot plasma (1–100 keV ions) magnetically. The future international reactor *ITER*[1] (International Thermonuclear Experimental Reactor), now in construction at Cadarache (south of France), is one of them. One of its aims is to produce, with the help of the D+T nuclear reaction, 500 MW by injecting 50 MW. The D+T nuclear reaction has been chosen because it has the highest cross section in the relevant domain of energy (one to two orders of magnitudes higher than the D+D reactions). The D+T reaction will produce 14-MeV neutrons and 3.52-MeV He nuclei, which will maintain the temperature of the D+T reacting plasma to an equilibrium state. Magnetic field lines are however connected to the inner walls of the ITER torus, which leads to the existence of cold edge plasma (composed of He, D, T, impurities such as oxygen or eroded metals) interacting with them. The heat produced by the hot plasma is received mainly on a part of the wall called a *divertor*. The material that will compose this part will have to work with heat loads in the range 10–20 MW/m^2.

Then, in tokamaks, understanding and being able to predict the evolution of the plasma-facing components (PFCs) that interact with both heat loads and the cold edge plasma is one of the keystones to make nuclear fusion a way of producing energy in the future [2]. The material chosen for the *divertor* is tungsten as it drives well the heat to the underlying cooling loops present in the PFCs, it is difficult to erode, and its melting/fusion temperatures are very high, and hence creating bonding with hydrogen isotope is supposed to be difficult. The other parts of the PFCs are composed of beryllium [3]. Some tokamaks are already working nowadays in an ITER-like wall (ILW) configuration to prepare the ITER project, such as the Joint European Torus/JET tokamak, with some PFCs composed of tungsten-coated carbon tiles [4–6], carbon tiles, mounted on *limiters* and/or *neutralizers*, being used in the ancient carbon area of tokamaks, now abandoned, because of tritium retention (tritium being radioactive and being easily trapped in carbon) [7, 8]. In that framework, the surface composition and morphology modifications under operation will lead to changes in the material properties that can address safety issues. These changes will have to be measured and then understood. In more details, the migration [9] and/or melting of elements in the machine [10, 11], the production of dust, the hydrogen isotope retention [12, 13], the impurity contamination (traces of carbon and/or oxygen, nitrogen seeding [14], etc.) leading to formation of new mixed materials/phases (such as oxides or alloys) and the complex surface erosion will all influence the lifetime of these PFCs and their fuel retention properties. Surface characterization techniques are then necessary to measure the elemental changes in JET and in ITER PFCs erosion zones and deposits.

[1]To give an idea of the size of the project and the machine: the tokamak alone will stay in a room which is 60 m high, all the site will be sprayed on a surface which is 420,000 m2 and the machine itself weighed 23,000 tons [1].

http://dx.doi.org/10.5772/65649

1.2. Raman microscopy as a technique to probe the top of deposits

In this field of research, due to their isotope selectivity, ion beam analyses (IBA) play a prominent role in this characterization, as discussed in Refs. [15, 16]. Thermal desorption spectroscopy (TDS) also plays a key role as it can give access to the characterization of D or T trap energies in metals such as Be [17–19] or W [20]. However, even if TDS and IBA techniques give quantitative information about hydrogen isotope concentration, they only give indirect information about chemical bonding. A direct way to probe that chemical bondings is to probe them spectroscopically by means of their vibrational spectrum using Raman microscopy.

Moreover, the in-depth resolution reached by IBA is not enough to describe properly the top layer of deposits called the *hydrogen isotope supersaturated layer*, which sizes in the range of tens of nanometers, and is composed of few atomic percent to few tens of atomic percent of hydrogen isotopes [13]. Depending on the material, Raman microscopy can be a well-suited technique adapted to that depth, as can be seen in **Figure 1**. In that figure, the transmittance coding the effectiveness of a material in transmitting incident light is plotted for λ_L = 514 nm and for Be, W, C (graphite and amorphous form). The depth at which the transmitted energy reaches 10% of the initial incident energy is 30, 35, 70 and 310 nm for, respectively, Be, W, C\graphite and amorphous carbon. The last value depends on the local organization of the amorphous structure, as detailed in Refs. [21–23]. Note that as the Raman measurements are generally done in back scattering geometry, one as to take into account an additional factor 2 in the argument of the exponential, as mentioned in [21, 22].

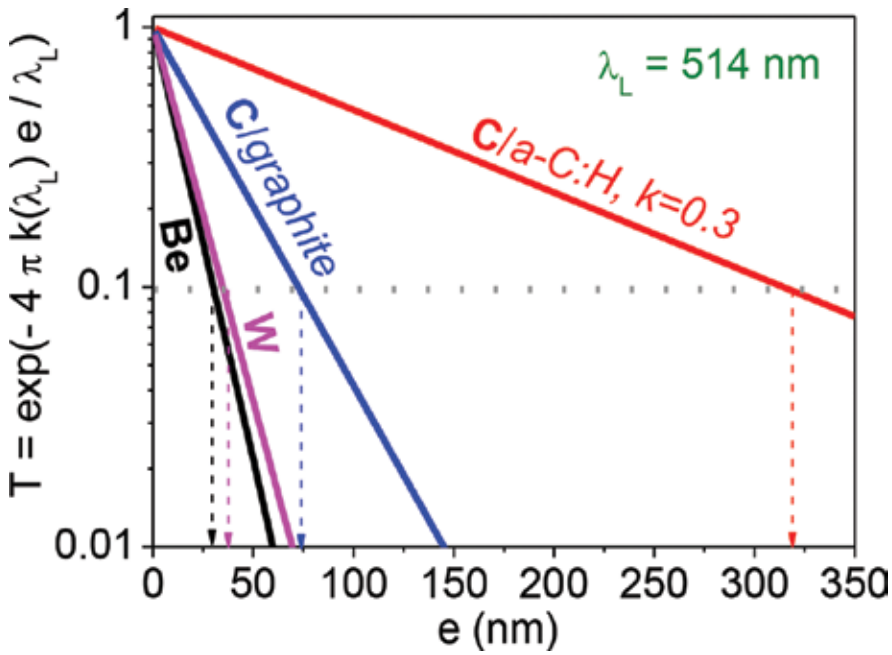

Figure 1. Transmittance in function of the depth for Be, W, C.

The aim of this chapter is to give concrete examples on how Raman microscopy can be used to characterize samples extracted from tokamaks, from the micrometric to the macroscopic scale of the machine. We then gave concrete examples on what information can be obtained by doing a study on laboratory-synthesized materials, benchmarking Raman microscopy with quantitative techniques such as TDS or IBA. The first part of the chapter is focused on carbon-based material analysis as all the previous tokamaks were using this element in the past. We showed how Raman spectra are sensitive to the presence of hydrogen, a major safety issue in the field. The second part of the chapter is focused on beryllium and tungsten based material analysis. We showed that hydrogen can be stored as a hydride after ion implantation, and that it can be released easily in tungsten oxide.

2. Carbon materials

2.1. Context

The Tore Supra tokamak had the ability to perform long plasma discharges with actively cooled PFC, which was a good opportunity to study fuel retention, a major concern in the plasma-wall interaction community. The study devoted to that was the Deuterium Inventory in Tore Supra (DITS) campaign. It was aimed at studying and linking the erosion of carbon PFCs and the fuel retention. The in-vessel D inventory was followed after the D loading campaign through particle balance [24], a part of the toroidal pump limiter (TPL), which was actively cooled during discharges, was dismantled for an extensive postmortem analysis of a few tens of carbon fiber composite tiles (CFC). The TPL was situated on top of a part of the machine called the neutralizer (NTR), which was also composed of CFC, but which was not actively cooled during discharges.

The *post-mortem* analyses used techniques devoted to the estimation of the D inventory [25, 26] and to structural and chemical characterizations [27], Raman microscopy being one of them [26, 28, 29]. Due to the different rates of erosion/deposition associated to the plasma footprint, the TPL surface exhibited a pattern which combined deposition-dominated zones (labeled thick and thin depending on the amount of matter found) and erosion-dominated zones. The shapes of these patterns were reproduced by simulating plasma wall interactions from the micrometric to the metric scale [30, 31].

Temperatures of the TPL were determined (with the help of thermographic measurements [24]) to be 500°C for gap surfaces of both thick deposit tiles and eroded tiles, 200°C for top surfaces of eroded tiles and 120°C for both gap and top surfaces of CFC tiles situated in the so-called thin deposit region. Temperature was estimated to vary in the range 500–900°C for the top surface of thick deposit tiles.

In **Figure 6**, we display Raman spectroscopic parameters of several samples, but before detailing the figure, we need to remember some well-known facts about the Raman

http://dx.doi.org/10.5772/65649

spectroscopy of disordered and amorphous carbons. They are briefly given below but are not detailed.

Raman microscopy is routinely used to characterize rapidly C-based materials, from nanocrystalline graphite (nc-G) to amorphous carbons, hydrogenated or not (a-C:H or a-C). It probes the structure [32] and is highly sensitive to bonding properties by interpreting the 1000–1800 cm^{-1} region, dominated by the G and D bands due to C(sp^2) hybridization of carbon atoms [33]. The G band, close to σ_G=1600 cm^{-1}, is assigned to the bond stretching of both aromatic and aliphatic C-C pairs, whereas the D band, close to 1350 cm^{-1} with a 514-nm laser (associated with a D′ band close to 1620 cm^{-1}) is assigned to the breathing mode of aromatic rings. The Raman analysis of graphite and nc-G clearly shows that this D band exists only when there is disorder [32]. Implanted graphite also displays this D band [34]. For a-C and a-C:H, the G bandwidth is related to disorder (sp^2 cluster size, cluster size distribution, chemical bonding) or stress [35] and presence of C(sp^3). For disordered multilayer graphene, the G bandwidth evolution can also be related to disorder [36].

Spectra of a-C and nc-G are clearly distinct [37] (spectrum 1 from **Figure 8(a)** belongs to a-C, whereas spectrum 3 belongs to nc-G, whereas spectrum 2 is in between): for example, G and D bands are much broader for a-C (width Γ_G ~80–200 cm^{-1}) than for nc-G (width ~15 to 40 cm^{-1}). Moreover, the intensity ratio (D over G band intensity) depends on the amount of disorder. Generally, to reproduce experimental nc-G spectra, bands at ~1500 cm^{-1} and at ~1200 cm^{-1} are very often needed, interpreted as sp^3 or out-of-plane defects, or as an additional amorphous contribution [38–43], see the discussions in Refs. [29, 43]. Raman spectra thus contain information on disorder [35] such as the size clusters, L_a, [32, 44], the C(sp^2)/C(sp^3) ratio, the hydrogen content [45–47], etc. All these information will help trying to understand the complex thermo/chemistry story of samples extracted from tokamaks.

2.2. Laboratory experiments

2.2.1. H-content determination in a-C:H layers

The Raman parameters generally used to probe the structure are the peak wavenumber and the width of the G and D bands, respectively, and the peak height ratio of these two bands, H_D/H_G [48]. An additional spectral feature has to be taken into account: a photoluminescence background which is superimposed to the Raman spectrum and is correlated to the H content [46]. The slope of this background, m, is calculated between 800 and 2000 cm^{-1}. The higher m, the higher is the photoluminescence intensity. **Figure 2** displays ultra-high vacuum heating effect on a 220-nm thick hard amorphous, hydrogenated carbon thin films (a-C:H) that were deposited on a Si [49]. The mass density of such typical hard a-C:H layers, with H/H+C ~ 30 at.% is ~1.9 g cm^{-3} are formed [50].

Figure 2 displays the thermal evolution of m/H_G and H_D/H_G compared to the H content determined by IBA and the H_2 release determined by TPD. σ_G is not shown here but it reaches a plateau for T > 600°C, meaning that the number of C(sp^3) neighboring C(sp^2) no longer changes.

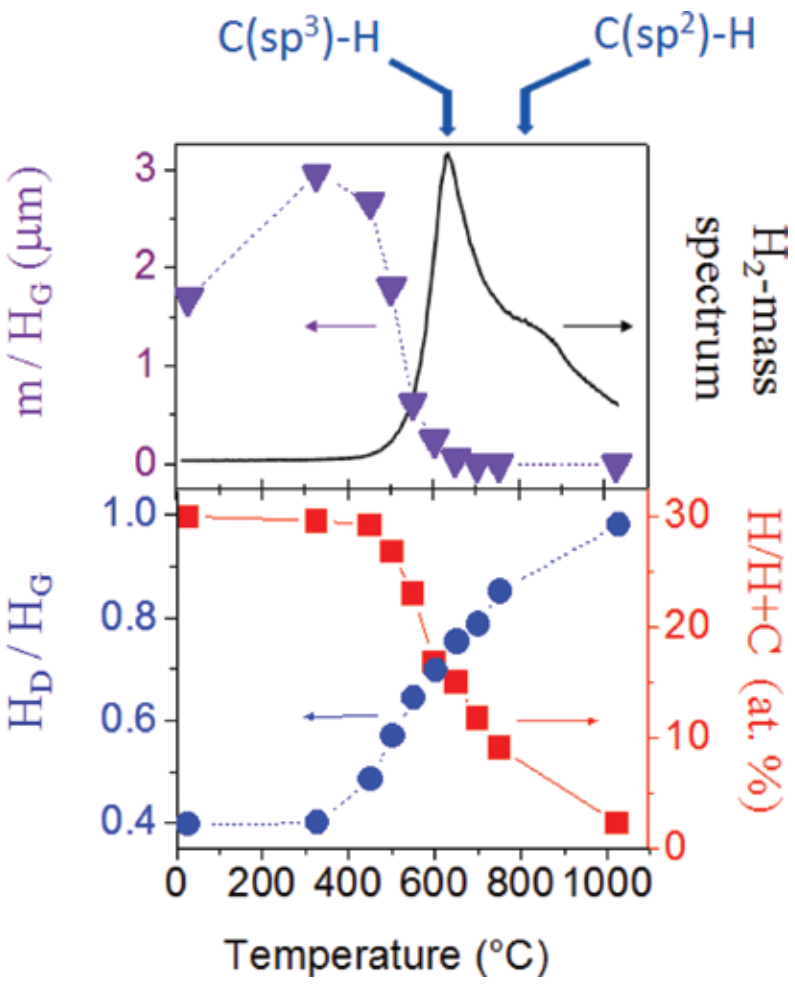

Figure 2. TDS, IBA and Raman microscopy measurements of a heated a-C:H sample.

We see that m/H_G increases by ~40% between room temperature and 300°C, decreasing between 300 and 600°C (at that point, m/H_G ~0.05). For $T > 600$°C, the slope is close to zero. If we compare to the H content, between RT and 300°C, it is constant (H/H+C ~ 30 at.%). Then, the increase of the m/H_G spectroscopic parameter is due to aromatization (and defect passivation) that leads to an increase of the photoluminescence background. As a consequence, m/H_G cannot be related easily to H/H+C in this thermal range. For higher temperatures, the H content decreases from 30 down to approximately 2%, without reaching a plateau.

The bottom part of **Figure 2** shows that H_D/H_G and H/H+C evolve in a remarkably symmetrical way. This suggests that the two parameters are correlated and that H_D/H_G could be used to probe the hydrogen content. The relation obtained that works with a 514 nm laser is (H/H+C = 0.54–0.53 H_D/H_G) in the range H/H+C = 2–30 at .%. Such a linear law, with the same slope, can be obtained for other wavelengths (407–633 nm has been tested), but with a different value at the origin.

http://dx.doi.org/10.5772/65649

2.2.2. Long-term hydrogen release revealed by in situ Raman spectroscopy

The thermal stability of six 200-nm-thick plasma enhanced chemical vapor deposited a-C, a-C:H and a-C:D layers ranging from soft to hard layers has been studied. The imaginary part of the refractive index at 633 nm and the corresponding H or D contents have been displayed together and compared to results from the literature [50], showing a good agreement with what is known: when the H content increases, the sample becomes more transparent, because of the diminution of aromatic C(sp^2) bonds. **Figure 3(b)** displays the thermal evolution of H_D/H_G for these six samples heated with a linear ramp (3°C min^{-1}) under a 1-bar argon atmosphere from room temperature to 600°C.Without entering into details, that can be found in [23], let us only focus on H data. One can see that the more hydrogen there is on the as deposited sample, at a lower temperature, the H_D/H_G ratio starts to increase. Because the evolution of H_D/H_G for a H-free amorphous carbon is small and because of what was shown in the previous part, most of the evolution in that thermal range is due to hydrogen release from C(sp3). This is consistent with what is known in the literature about the bad thermal stability of hydrogen-rich a-C [51–55].

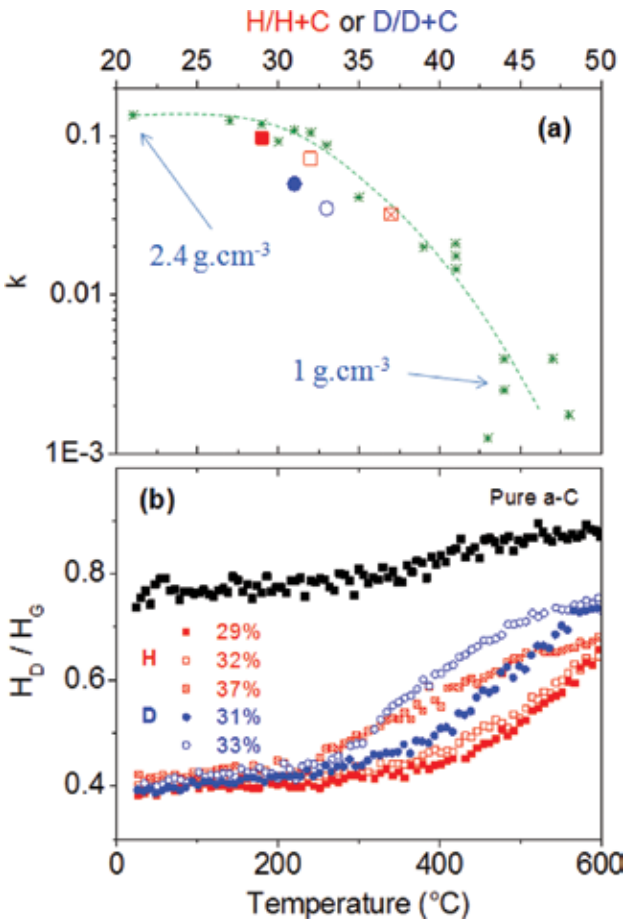

Figure 3. Thermal evolution of HD/HG for six a-C samples. (a) Optical constant in function of H content. (b) Comparative linear ramp study. Green stars in the top figure are from Ref. [50].

Figure 4 displays an example of isothermal evolution in function of time. This evolution cannot be due to the effect of the laser on the sample, accumulating heat with long times, as we compared two sets of data: one by switching off the laser between acquisitions and one with a continuous flux of heat. The position of the G band (not shown) no more evolves after 50 min, meaning there is no order increase due to an overestimated heat load by the probe laser. In Ref. [56], we studied that we had no power dependence in the range 0.01–1 mW/μm². Then, this technique allows to probe long-term hydrogen release. We will use it on tokamak samples in Section 2.3.

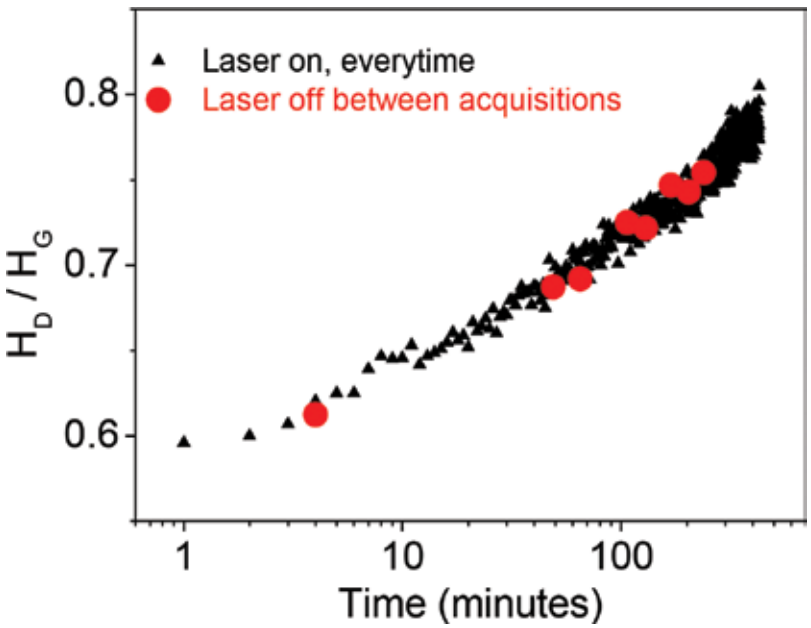

Figure 4. Example of in situ measurement isothermal annealing.

Then, to resume, we have shown that

- The m/H_G parameter, often used to estimate the H content in the literature, should be used with care, first because it is sensitive to various photoluminescence-quenching processes and second because it is not sensitive to H bonded to $C(sp^2)$.
- The H_D/H_G parameter is quasi-linear in the full range of H content and can thus be used to estimate the H content.
- H_D/H_G can be used in situ to retrieve the H content evolution under heating.

2.2.3. H, D and He implantation in graphite: Starting the amorphization regime

The modification by ion impact of graphite has been studied both theoretically and experimentally ([57–67] and references therein). Inside the sample, collision cascades are created by ions that knock on the surface and penetrate. It creates defects and vacancies, ions being implanted

after they slow down [68]. Protusions (height lower than 1 nm), called hillocks, are observed for low fluencies (<10^{14} ions cm^{-2}) [57, 58]. They are due to stress created by the first collision under the near surface region. More precisely, interstitial carbon clusters or coalescence of interstitials and vacancies are at the origin of these hillocks. At fluencies >10^{15} ions cm^{-2} [61, 62] and in the 400–800 K range, domes with a height one order of magnitude higher were observed.

We have exposed graphite to hydrogen deuterium and helium plasma (from 10^{16} to 10^{18} cm^{-2}) [43]. The energies were tuned from 40 to 800 eV. The ion incidence was parallel to the basal plane for CFC (carbon/carbon composite) and perpendicular for HOPG (highly oriented pyrolitic graphite). The changes of the material were studied by means of both Raman and atomic force microscopies.

We display the 400 eV/D implantation Raman spectra in **Figure 5** as an illustration. The main differences or common points between HOPG and CFC are

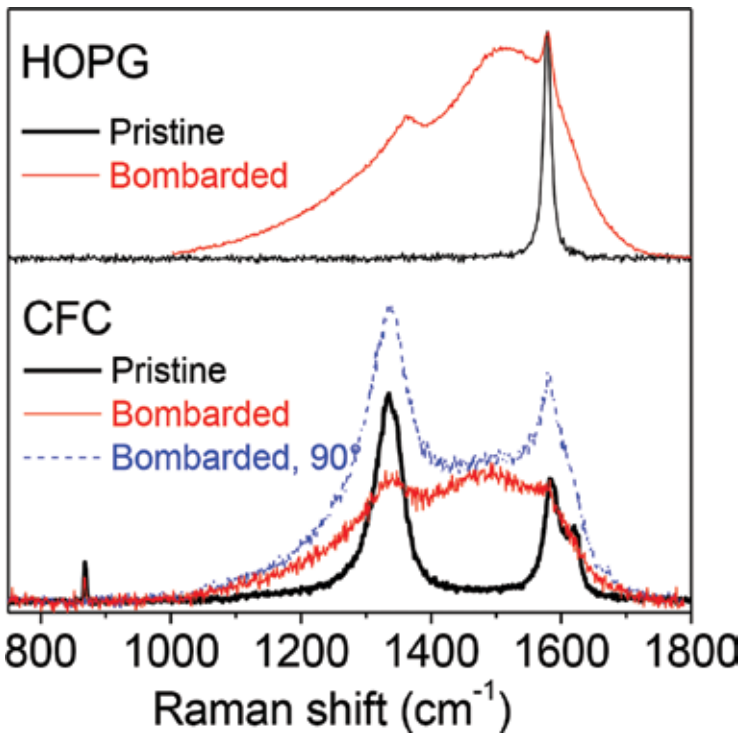

Figure 5. Raman spectra of bombarded HOPG and CFC.

- Pristine HOPG contains less defects than CFC (D band at 1350 cm^{-1} is close to zero for HOPG, whereas H_D/H_G is close to 2 for CFC, indicating nanometric crystal size domains)
- Implantation produces an amorphization for both materials (broad bands at 1500–1300 cm^{-1} appearing in the spectra, looking like the spectrum 1 in **Figure 8(a)**)

- The underlying pristine sample is visible can be seen in both cases. This is because the ions penetrate only 15–20 nm and the penetration depth of light is few tens of nanometer (see **Figure 1**).
- Both bombarded Raman spectra display two kind of environment: in-plane defects and out of plane defects (see Ref. [43] for details).
- No laser probe polarization effect of IPD and OPD on the HOPG sample, whereas there is one for IPD of the CFC.

When increasing the impinging ion energy, the growth of nanometric domes at the surface has been observed by atomic force microscopy (AFM) and the incident kinetic energy has been found as the parameter determining their height. The Raman study has also revealed that both the defect-defect distance in the IPD and OPD are typically 1 nm. When the number of vacancies created in the material increases, the number of in-plane defects decreases to the benefit of the out-of-plane defects.

2.3. Information retrieved from tokamak samples

2.3.1. Raman measurements inside the tokamak Tore Supra

Figure 6 displays the G band position, σ_G, in function of its width, Γ_G, for many samples collected in the Tokamak Tore Supra (deposition zones and erosion zones of the TPL, and on the NTR) and compared to pristine CFC and to heated laboratory deposited a-C:H (see Sect. 2.2 of this chapter for more information). The data points form a wide range of carbon materials from nc-G to a-C, all described in more details in [28, 69, 70]. Pristine CFC data points are all situated at Γ_Gv~ 25 cm^{-1} and $\sigma_G \sim 1580$ cm^{-1}. NTR deposits form a data point cloud continuously spread either along the positive slope straight line (Γ_G in the range 20–80 cm^{-1}, σ_G in the range 1580–1600 cm^{-1}) or along the negative slope straight line for the TPL deposited and eroded samples (Γ_G in the range 80–180 cm^{-1}, σ_G in the range 1600–1520 cm^{-1}). The deposited TPL points are very close to a-C:H data points, at slightly lower frequency. Note that the shift between heated a-C:H and the TPL deposits can be attributed to an isotopic effect as TS samples are deuterated samples, which downshifts the G band position. A proof of that can be found in Ref. [23] where both synthetic a-C:H and a-C:D were heated and compared. The a-C:H data were heated under vacuum from room temperature (right down corner up to 1000°C, left up corner). Then this line from right to left means that the carbons locally organize under heating. This is in agreement with the temperature measured in situ by thermography. The NTR deposits display lower Γ_G values, meaning they are more structured. This is in agreement with the fact that the NTR was not actively cooled, being able to reach temperatures higher than 1000°C. As it is know that the deuterium is released at these temperatures (see Section 2.2 of this chapter, below), one can say that the D is mainly trapped in deposits found on the TPL and not on the NTR. The eroded TPL samples are less spread than the others, meaning the structure of the implanted carbons is more homogeneous and more amorphous. It can retain more deuterium, relatively. However, the thickness of that layer was found to be few nanometers only [69], which is low compared to the hundreds of microns found for Tore Supra deposits, meaning the D is essentially trapped in these deposits or deeper in the porosities of the initial prisitine CFC. These points are investigated in a next subpart.

http://dx.doi.org/10.5772/65649

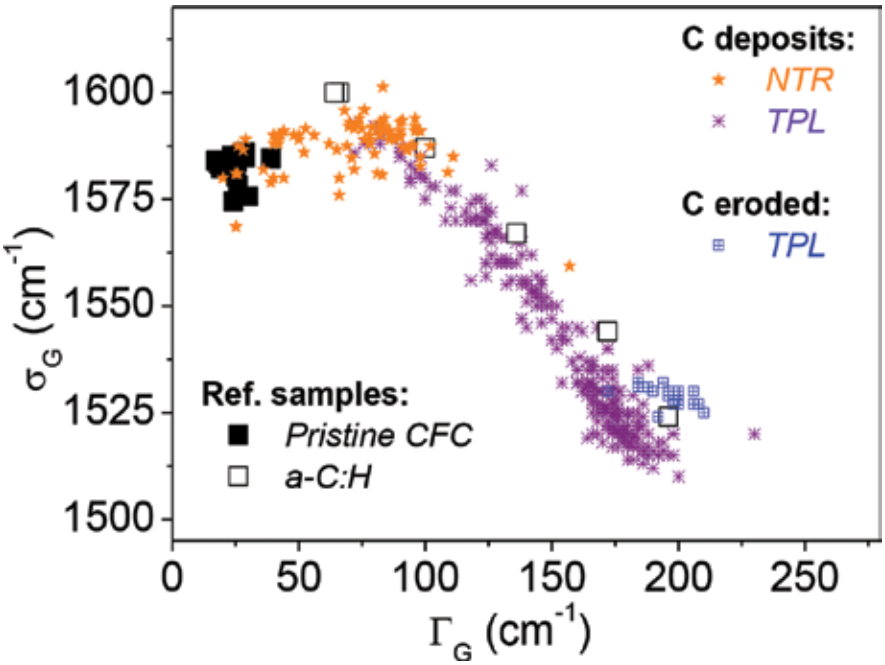

Figure 6. Carbon deposits spectroscopic parameters: G band position in function of its full width at half maximum.

2.3.2. Micrometric inhomogeneities and long-term release of H

In Ref. [23], we compared with Raman microscopy the thermal evolution of reference samples to samples extracted from the Tore Supra tokamak, as it was shown that a long-term mechanism [71] occurred even at low temperature (low means here 120°C, which correspond to the thermostat temperature of the PFC cooling loop, staying at this values for days and weeks even when the plasma is off) and as we wanted to distinguish the Raman signature of this heating. **Figure 7** displays the Raman data of the Tore Supra samples. **Figure 7(a)** and **(b)** is mappings of m/H_G and s_G, respectively, for an as received sample. One can see that the deposit is inhomogeneous, the sample being more organized in the upper right part. The high value of m/H_G does not mean here that there is more hydrogen there, as mentioned by discussing **Figure 2**. In fact, this is the opposite. The value of H_D/H_G in the blue and red regions (not shown here) give typically values of 28 down to 17%, using the linear relation mentioned in Sect. 2.1. The zone where hydrogen has been outgassed displays a higher value of σ_G which is in agreement with what we know about the thermal stability of a-C:H [23, 49, 56]. The histograms of a TS deposit heated isothermally at 120°C for three times (120, 300 and 640 h) and at 250°C allows to show that the sample still evolve under long time scales (the average value of m/H_G increases slightly with time). The problem is that we need to average spectra on large zones because of large inhomogeneities found at the micrometric scale. However, using the mapping mode allows to identify different kind of defects of chemical environments which is needed to better characterize the sample. The average value of H_D/H_G (not shown here) leads to a value of H close to 20 %.

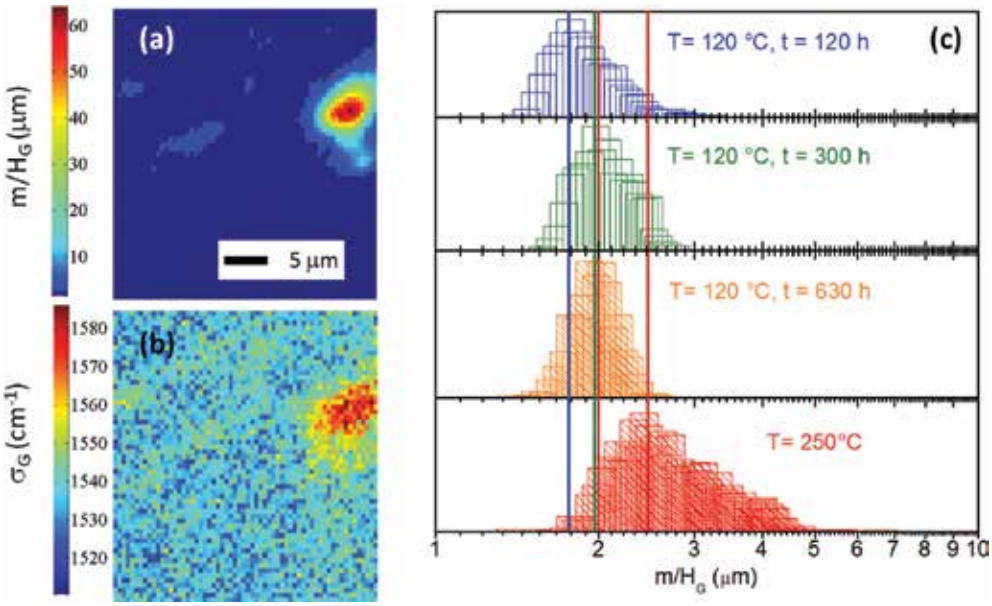

Figure 7. Raman spectroscopy imaging of a unheated Tore Supra (TS) deposit. (a) m/H_G mapping of this TS sample. (b) σ_G mapping. (c) Histograms of heated TS samples (120°C during 120, 300 and 630 h, and 250°C).

2.3.3. Hydrogen depth concentration and history of Tore Supra deposits

In Ref. [72], lock-in thermography, scanning electron microscopy and confocal microscopy were used to study the erosion and depositions on the TPL of the Tore Supra tokamak. Taking into account, all the methods allowed the authors to perform a complete mapping of the mass of carbon that has been eroded and deposited. The foundings were 520 g of deposits and 920 g of eroded carbon. It shows that more than a half of the carbon that is eroded is redeposited on the TPL. It was also found that the zones containing the highest deposits were found close to erosion zones.

Such things were simulated recently [31]. The gap deposition contribution is estimated at 23%, mostly from the erosion zones and with a main contribution from the low field side of the tile toroidal gap surfaces. This deuterium impoverishment in the deep layer has also been investigated more systematically in Ref. [73] where IBA and cross-section electron microscopy where done on 15 samples. The mean in-depth hydrogen isotope content is plotted in **Figure 8(b)** and scaled to the 120 μm of the deposit shown. The surface content has been divided by 2 in less than 20 μm. In parallel, σ_G is displayed for three lines of sight. Then on top of this deposit, the H content is close to 20%, whereas it decreases close to zero at the interface between the deposit and the top of the CFC. The diminution is rapid in the 20 first microns. Same trends are seen with the structure probed with Raman spectroscopy: carbon close to the surface is less organized (σ_G close to 1520 cm^{-1}), whereas σ_G increases (meaning an increase of order) and then reaches a plateau 20 μm deep in the deposit, at the value of σ_G = 1580 cm^{-1}. This deuterium impoverishment of the deep layers may be caused by long-term release mechanisms, as discussed in the previous part.

http://dx.doi.org/10.5772/65649

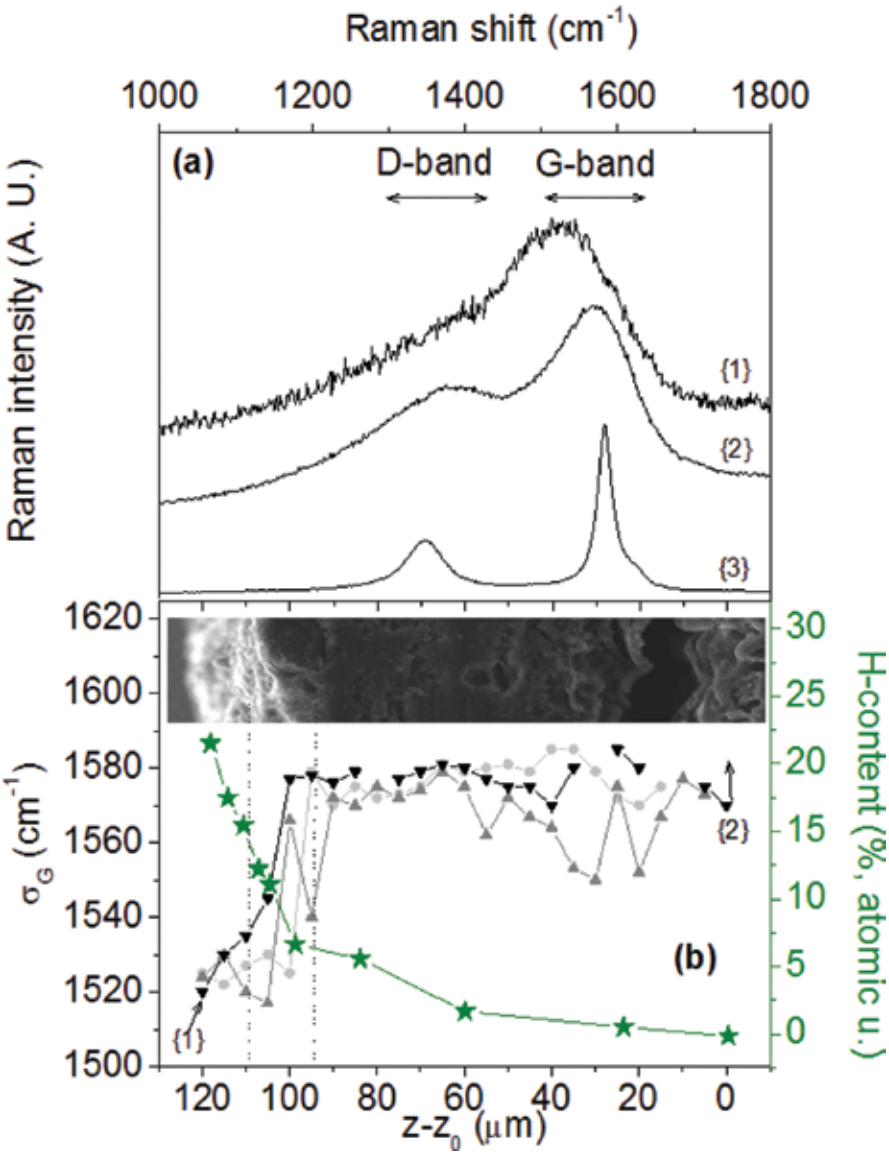

Figure 8. H-content impoverishment in deep deposits compared to ordering of the carbon. H content is extracted from Ref. [73].

3. Beryllium- and tungsten-based materials

3.1. Context

Tritium retention, occurring in a magnetically confined deuterium plus tritium plasma, can be obtained by erosion, retention, material modification, dust formation (and more generally plasma wall interactions). This is a big safety issue because of tritium radioactivity [7, 74].

Hydrogen isotope retention in beryllium can also play a role in the lifetime estimation of the ≈700 m^2 ITER's beryllium inner walls because of erosion [75]. This explains why several studies based on ion irradiation of Be samples have been devoted to D behavior to ensure that tritium retention will not be a limiting issue in ITER operations. Previous studies found D/Be ratio in the range 0.1–0.7 using energies in the range 0.6–20 keV/D and fluency in the range 10^{16}–10^{19} cm^{-2} [76–82].

At fluencies close to 2×10^{17} cm^{-2} (in the range 0.6-1 keV/D), the existence of the D-content saturation (D/Be close to 0.25) has been shown [13, 83–84]. For fluencies lower than 0.7×10^{17} cm^{-2} TDS display only one peak at 900 K, whereas for fluencies between 0.7 and 1×10^{17} cm^{-2}, a second peak lies at 750 K. For fluencies higher than 1.2×10^{17} cm^{-2}, two extra peak rise close to 500 K. These last peaks were explained by structural modification of the sample. Moreover, the role of crystal orientation and D diffusion along grain boundaries was investigated in [85]. The existence of BeH_2 was suggested in [17] but never observed before.

Raman microscopy is a nondestructive, noncontact and local (≈1 μm^2 lateral resolution [86]) technique that has been proved to be sensitive to Be stretching modes [87], beryllium oxide modes [88], bending and stretching tungsten oxide modes [89], Be_xW_y-mixed samples density of states [90], BeCW-irradiated samples [91] and give information when a pristine material is implanted by hydrogen ions [90, 92, 93]. First Raman analyses in ILW-tokamaks were performed on some molybdenum JET mirrors [90], showing that the technique is sensitive to thin ≈10 nm deposited layer composed of ≈33% Be, ≈33% C and ≈33% O and the underlying molybdenum oxidized mirror. C-O and C=O modes have been detected in that layer and defective or beryllium mixed with O and/or C have been found without possibility to identify the phases rigorously up to now, because of a poor benchmarking of the technique for these materials. Raman microscopy can also be able to give information about the hydrogen isotope behavior by combining IBA, Raman microscopy, atomic force microscopy (AFM) and with the help of DFT modeling. As an illustration of this complementarity, in Ref. [94], we identified on laboratory experiments the growth of BeD_2 with dendritic forms appearing subsequently to 2 keV ion implantation when the Be layer is saturated by implanted D ions. The width of the bands recorded by Raman microscopy suggested that this hydride has grown in a crystalline form which seems to be close to a body-centered orthorhombic structure with Ibam symmetry as the spectra look like to the ones reported in [95], who determined recently the structure by using additionally synchrotron X-ray diffraction. In [94], we showed that these dendrites appear when the amount of deuterium in the material is higher than $\approx 2 \times 10^{17}$ $D.cm^{-2}$, when the ≈40 nm under surface layer is saturated by D.

3.2. Laboratory experiments

3.2.1. Defect-induced bands in beryllium

Below, we compare defective Be samples that have been produced by Be deposits in an impurity atmosphere or by D implantation. In more details, the defective deposit sample has been produced by the thermionic vacuum (TVA) method (more details can be found in Ref. [96] and references therein). To introduce disorder, a partial pressure of N_2 (in the range from 10^{-2} to 10^{-3} Pa partial pressure) has been used during the deposit. The amount of N being ≈5 atomic %.

http://dx.doi.org/10.5772/65649

The D-implanted Be sample have been prepared with two impinging ion geometries, with 2 keV/D: normal incidence (90°) and 45° incidence. More details about the implantation of the 90° geometry can be found in [94].

Figure 9 displays Raman spectra of a deposited Be sample with a high content of defects for four laser wavelengths. Data were acquired with 633, 514, 488 and 325 nm lasers. The band associated to the E_{2G} Raman active mode is downshifted for the defective sample, but the shift depends on the wavelength. Γ_{E2G} for the reference sample is close to 8 cm^{-1}. For the defective sample, it is higher (27 cm^{-1}). The logarithmic scale used here allows to distinguish several additional broad bands (413, 544 and 616 cm^{-1}) that were first evidenced in Ref. [90] and called defect-induced bands. These bands are attributed to the phonon density of states (PDOS), as can be seen by comparing the Raman spectrum (where the E_{2G} band has been removed) to the PDOS of Be measured in the literature. Their intensity reaches values as high as 23% of the Raman active E_{2G} mode heights and they are related to the defect content, defect being a term which can be impurity, vacancy or other kind of defects.

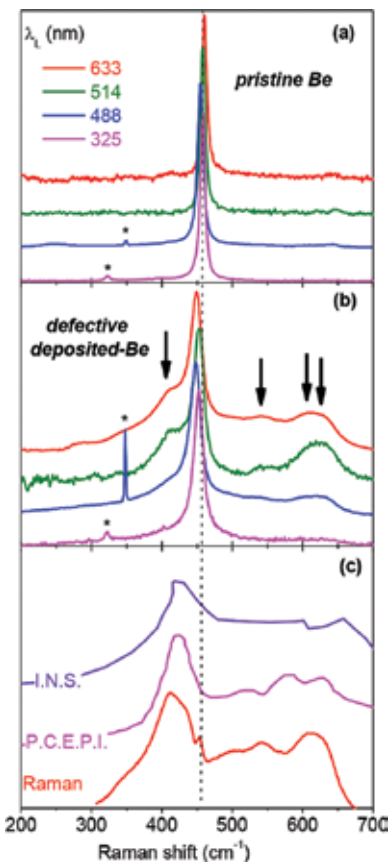

Figure 9. Normalized Raman spectra of a pristine (a) and defective (b) Be deposited sample, using four laser wavelength. (c) The 633 nm spectrum of the defective sample is displayed after removing the E_{2G} Raman active mode and is compared to the PDOS measured by INS and by PCEPI [97]. The bands marked by stars are due to other laser electronic transitions.

Changing the wavelength does not change the qualitative trends: the band related to the E_{2G} mode is more downshifted to low frequencies and broader. However, quantitative differences can also be seen, with some information. For example, the height of the PDOS diminishes monotonically with the decrease of the laser wavelength (from 23% with 633 nm down to 4% with 325 nm for the defective sample). σ_{E2G} does not display a monotonic evolution with the laser wavelength for the defective sample. The reference sample, oppositely, does not disperse in the range 325–633 nm. Shifts observed may then be due to stress [86] in the deposited layer, the nonmonotonic behavior being caused by two effects: stress gradients existing in the deposited layers and the penetration depth of the laser that is wavelength dependent.

In **Figure 10**, we compare 514 nm spectra of a pristine Be, a Be sample containing 2×10^{17} D cm^{-2} in the 90° geometry and 514 nm spectrum of Be sample in the 45° geometry. D implantation (**Figure 10(b)**) and vacancy creation profiles were evaluated for the 90° and 45° geometries

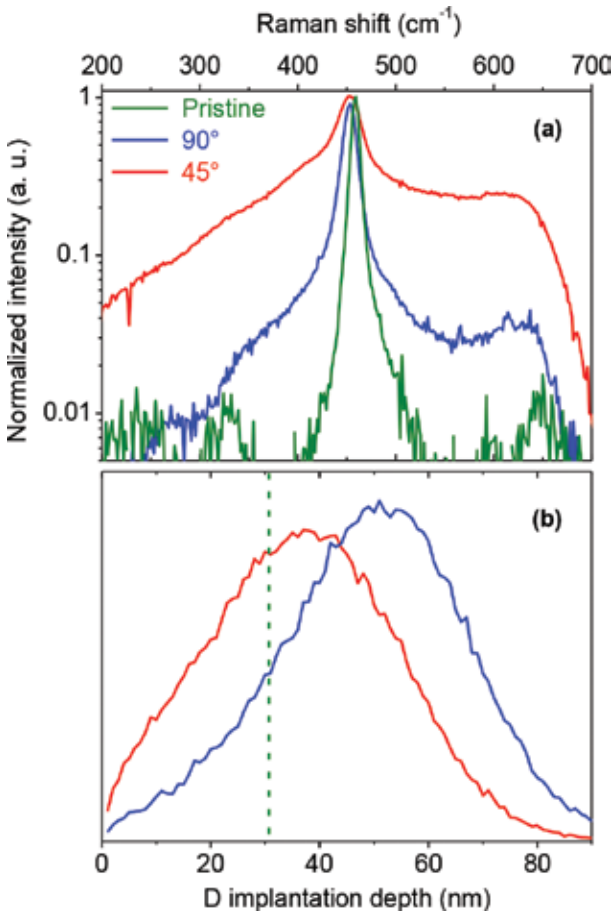

Figure 10. Varying the in-depth defects. (a) Normalized Raman spectra of D implanted Be samples. Geometry implantation (90° and 45°) are compared with the 514 nm laser wavelength.

http://dx.doi.org/10.5772/65649

using the stopping and range of ions in matter (SRIM) code[2] [68]. If we believe in SRIM calculations (which gives trends as many mechanisms and effects are not included), we can then estimate that 16% of the implanted deuterium atoms are implanted in the range 0–19 nm, 31% in the range 0–28 nm and 37% in the range 0–31 nm. For the corresponding ranges, the total amount of vacancies created are, respectively, 37, 59 and 65% of the total vacancies created. The lineal density of vacancies is the higher in the range 0–28 nm, being lower by 7.6% in the 0–19 nm range and by 0.4% in the 0–31 nm range.

We see that the Be implanted by D in the 90° geometry displays a Raman spectrum with a E_{2G} mode downshifted by 5 cm^{-1} and with an additional broadening of 6.5 cm^{-1} compared to the pristine sample. The PDOS is present, with a relative height ratio of H_{PDOS}/H_{Be}=3%. If we compare with the Be implanted by D in the 45° geometry, we see that the band corresponding to the E_{2G} mode is downshifted by 5 cm^{-1}, with an additional broadening of 30 cm^{-1} compared to the pristine sample. The PDOS is rising, with a relative height ratio H_{PDOS}/H_{Be} of 24%. The band position is the same in the two implantation geometries. However, the bandwidth Γ_{Be} is increased by a factor 2.7 and the PDOS relative height H_{PDOS}/H_{Be} is increased by a factor 11 from the 90° to the 45° geometry. How these differences can be interpreted? According to SRIMS calculations in the subsurface slab going from 0 down to 31 nm, there are more defects (implanted D and vacancy) created in the 45° geometry than in the 90° geometry. Then, it explains why H_{PDOS}/H_{Be} and Γ_{Be} are higher in the first case than in the second.

3.2.2. Characterization of Be nanometric hydrides

By using energetic ions, and with the help of nuclear reaction analysis (NRA), AFM, optical microscopy and quantum calculations compared to Raman spectroscopy, we were able to evidence the formation of crystalline BeD_2 [94]. The spectra are typically close to the one found for BeH_2 in Ref. [95] using high pressure to form them. It was shown previously that this latter technique is sensitive to the way hydrogen isotopes are bonded and organized in materials and thus that it can be relevant for fusion [92] and might be of interest for hydrogen storage by forming hydrides [98].

Figure 11 shows Raman imaging in the vicinity of a dendrite. In **Figure 11(c)**, the intensities of the band at 1397 cm^{-1} due to a Be-D mode are displayed. It is more intense on the dendrite and less intense off the dendrite. The corresponding spectra are displayed in **Figure 11(d)**. Details on how were obtained the spectra can be obtained in [94]. The bands marked by stars are due to Be-D bonds in BeD_2. The fact that their corresponding intensity are higher are more intense on dendrite allows to conclude that the dendrites are made of BeD_2. If the formation of such dendrites occurs in tokamaks, it could become a high fuel reservoir.

Figure 11(d) display the intensity of a mode found close to 1580 cm^{-1} and due to carbon contamination of the sample before it was bombarded (D and G bands in **Figure 11(e)**), and that has nothing to do with the experimental conditions.

[2]This code is widely used to investigate ion-surface interaction phenomena. It is a free access Monte-Carlo computer program based on the binary collision approximation that do not take into account crystal structure or vacancy diffusion (i.e. each single collision event is treated independently between two steps).

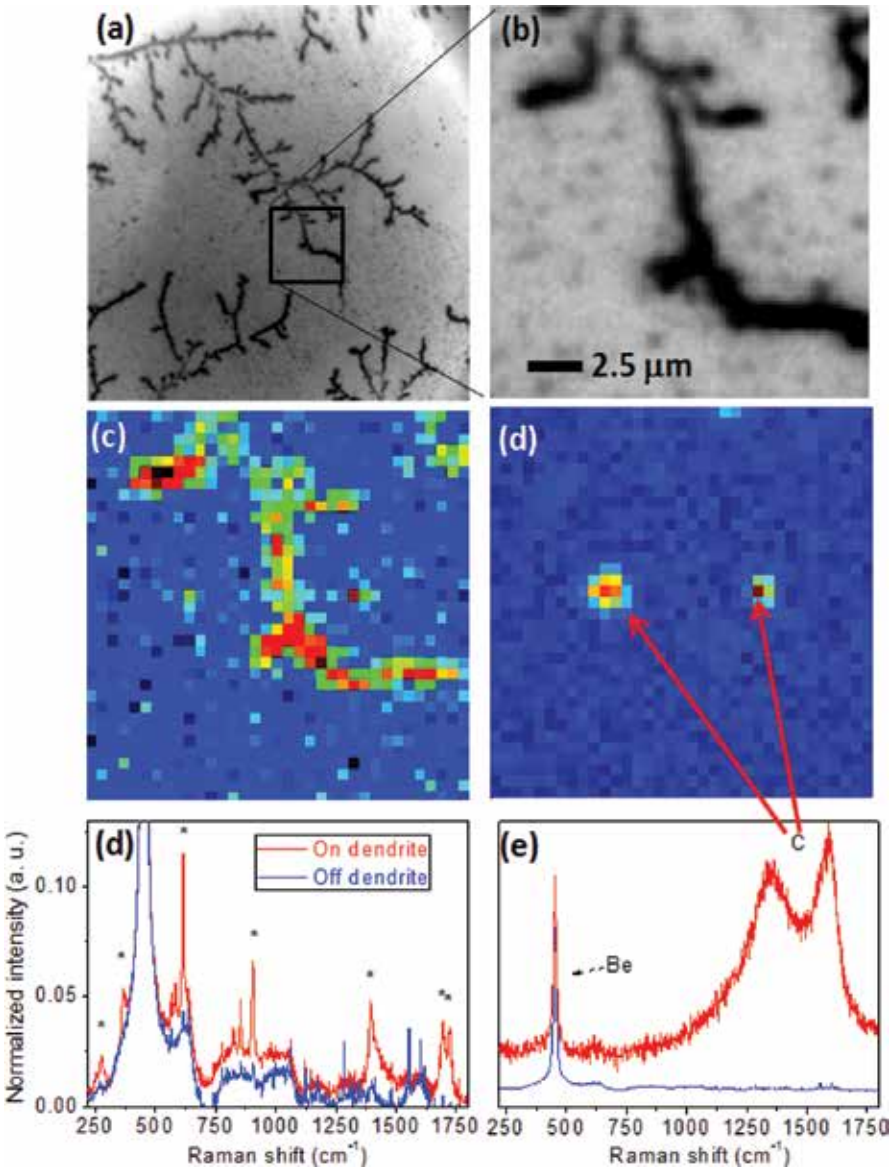

Figure 11. Beryllium hydride formation under ion implantation. (a) and (b) Optical microscopy. (c) Be-D bond intensity mapping. (d) Position of carbon impurities. (d) Comparison off/on dendrites. (e) Raman spectrum of carbon impurities.

3.2.3. Hydrogen behavior in tungsten oxide

Tungsten alone cannot be seen using standard Raman microscopy because there are no optical phonons that can be probed close to the center of the Brillouin zone. However, as oxygen is one of the impurities that can be found in tokamaks, and as the inner walls will be at temperatures ranging from few hundreds to 1000°C because of heat loads, it could be possible

that some oxide will be formed [99]. Then it would be of interest for the plasma-wall interaction community to take care of D and T behavior in tungsten oxides. Without entering into details, tungsten oxides can exist in various forms (dioxide, trioxide, in between stoichiometry), with many phase transitions that can be affected by nanosize effects [100] so that a systematic D implantation study could be helpful for the future. Today, only a few studies exist on the subject. In [93], we report on the formation of thin tungsten oxide layers that have been grown on W surfaces by thermal oxidation (thicknesses up to ~250 nm) and that have been exposed to low energy deuterium plasma (11 eV/D^+). Raman microscopy and X-ray diffraction show a nanocrystalline WO_3 monoclinic structure. We observed that the low-energy deuterium plasma exposure has induced a phase transition, a change in the sample color and the formation of tungsten bronze (D_xWO_3). After exposure under ambient conditions, a reversible deuterium retention, due to oxidation of the D_xWO_3 layer, has been observed. **Figure 12** displays the effect of D implantation. The spectral range of tungsten trioxides can be roughly distributed in two kind of spectral regions: the bending modes region, lower than 500 cm^{-1} and the stretching modes region at higher wavenumbers. Before exposure, we can see the characteristic peaks of the monoclinic structure at 703 and 805 cm^{-1} which are attributed to symmetric and antisymmetric (O-W-O) stretching modes, respectively (see references in Ref. [93]). The wing in the range 920–970 cm^{-1} is attributed to terminal oxygen bonding in case of nanocrystalline structures, but other interpretations can be found in the literature that we do not review here. Due to implantation, all the peaks are broadened, the bending modes display bands that are more intense than stretching modes, which can be the sign of some disorder, and two new bands appeared: one at 950 and the other at 388 cm^{-1}. These bands disappeared with time once put in air due to reoxydation.

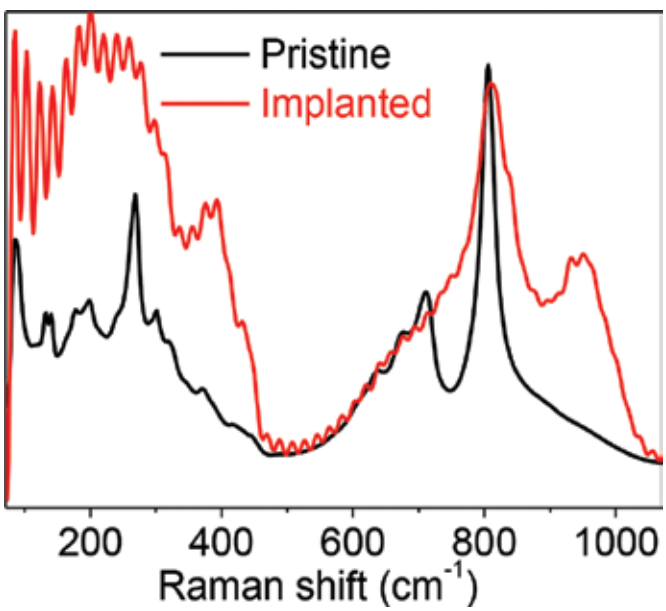

Figure 12. Raman spectra of bombarded WO_3.

4. Discussion/conclusion

Because of safety issue, it is important to understand how and where tritium will be stored in tokamaks due to plasma-wall interaction. In this chapter, we have demonstrated the ability of Rama microscopy to detect and characterize material changes subsequently to interaction with hydrogen, for both carbon-based tokamaks and for ITER-like wall materials (tungsten that is oxidized and beryllium). The comparison between well-controlled samples and sample extracted from tokamak has been used to better characterize some of the tokamaks' properties.

Among other findings, we report that by changing temperature on various carbon samples, extracted from tokamak (Tore Supra) or comparative reference laboratory samples (a-C:H) synthesized in controlled conditions, we have shown how Raman spectroscopic parameters can be used to characterize structural and H-content evolution/changes.

We also report that beryllium hydrides that can form high tritium reservoir in tokamaks can be formed and detected under ion implantation.

To conclude, next studies will have to use different laser wavelengths as they can be used to probe gradients of properties in the beryllium's depth due to the fact the depth probed is in the range of few tens of nanometer. This is the typical depth at which a high content of hydrogen isotope is found in modern tokamak samples like JET. Future studies have to be driven with this technique to better characterize the so-called supersaturated layer.

Author details

Cedric Pardanaud*, Celine Martin and Pascale Roubin

*Address all correspondence to: cedric.pardanaud@univ-amu.fr

Aix-Marseille Université/CNRS, Marseille, France

References

[1] I.w. site, https://www.iter.org/factsfigures, in. ITER.org web site

[2] R. Neu, A.U. Team, E.P. Taskforce, J.E. Contributors, Preparing the scientific basis for an all metal ITER, Plasma Physics and Controlled Fusion, 53 (2011) 124040.

[3] V. Philipps, Tungsten as material for plasma-facing components in fusion devices, Journal of Nuclear Materials, 415 (2011) S2–S9.

[4] F. Romanelli, I. Abel, V. Afanesyev, et al., Overview of the JET results with the ITER-like wall, Nuclear Fusion, 53 (2013) 104002.

[5] S. Brezinsek, J.-E. Contributors, Plasma-surface interaction in the Be/W environment: Conclusions drawn from the JET-ILW for ITER, Journal of Nuclear Materials, 463 (2015) 11–21.

[6] S. Brezinsek, A. Widdowson, M. Mayer, V. Philipps, P. Baron-Wiechec, J.W. Coenen, K. Heinola, A. Huber, J. Likonen, P. Petersson, M. Rubel, M.F. Stamp, D. Borodin, J.P. Coad, A.G. Carrasco, A. Kirschner, S. Krat, K. Krieger, B. Lipschultz, C. Linsmeier, G.F. Matthews, K. Schmid, J.E.T. Contributors, Beryllium migration in JET ITER-like wall plasmas, Nuclear Fusion, 55 (2015) 063021.

[7] J. Roth, E. Tsitrone, A. Loarte, et al., Recent analysis of key plasma wall interactions issues for ITER, Journal of Nuclear Materials, 390-91 (2009) 1–9.

[8] G.F. Matthews, J.E. Contributors, A.S.-U. Team, Plasma operation with an all metal first-wall: Comparison of an ITER-like wall with a carbon wall in JET, Journal of Nuclear Materials, 438 (2013) S2–S10.

[9] I. Bykov, H. Bergsaker, G. Possnert, et al., Studies of Be migration in the JET tokamak using AMS with Be-10 marker, Nuclear Instruments & Methods in Physics Research Section B-Beam Interactions with Materials and Atoms, 371 (2016) 370–375.

[10] K. Krieger, S. Brezinsek, M. Reinelt et al., Beryllium migration and evolution of first wall surface composition in the JET ILW configuration, Journal of Nuclear Materials, 438 (2013) S262–S266.

[11] K. Schmid, M. Reinelt, K. Krieger, An integrated model of impurity migration and wall composition dynamics for tokamaks, Journal of Nuclear Materials, 415 (2011) S284–S288.

[12] J. Likonen, K. Heinola, A. De Backer, S. Koivuranta, A. Hakola, C.F. Ayres, A. Baron-Wiechec, P. Coad, G.F. Matthews, M. Mayer, A. Widdowson, J. Contributors, Deuterium trapping and release in JET ITER-like wall divertor tiles, Physica Scripta, T167 (2016) 014074.

[13] K. Heinola, A. Widdowson, J. Likonen, E. Alves, A. Baron-Wiechec, N. Barradas, S. Brezinsek, N. Catarino, P. Coad, S. Koivuranta, Long-term fuel retention in JET ITER-like wall, Physica Scripta, T167 (2016) 014075.

[14] A. Kallenbach, M. Bernert, R. Dux, L. Casali, T. Eich, L. Giannone, A. Herrmann, R. McDermott, A. Mlynek, H.W. Mueller, F. Reimold, J. Schweinzer, M. Sertoli, G. Tardini, W. Treutterer, E. Viezzer, R. Wenninger, M. Wischmeier, A.U. Team, Impurity seeding for tokamak power exhaust: From present devices via ITER to DEMO, Plasma Physics and Controlled Fusion, 55 (2013) 124041.

[15] M. Rubel, P. Petersson, E. Alves, S. Brezinsek, J.P. Coad, K. Heinola, M. Mayer, A. Widdowson, J.E.T. Contributors, The role and application of ion beam analysis for studies of plasma-facing components in controlled fusion devices, Nuclear Instruments & Methods in Physics Research Section B-Beam Interactions with Materials and Atoms, 371 (2016) 4–11.

[16] P. Strom, P. Petersson, M. Rubel, A. Weckmann, S. Brezinsek, A. Kreter, S. Moeller, K. Rozniatowski, Characterisation of surface layers formed on plasma-facing components in controlled fusion devices: Role of heavy ion elastic recoil detection, Vacuum, 122 (2015) 260–267.

[17] M. Reinelt, A. Allouche, M. Oberkofler, C. Linsmeier, Retention mechanisms and binding states of deuterium implanted into beryllium, New Journal of Physics, 11 (2009) 043023.

[18] M. Reinelt, C. Linsmeier, Temperature programmed desorption of 1 keV deuterium implanted into clean beryllium, Physica Scripta, T128 (2007) 111–114.

[19] M. Reinelt, C. Linsmeier, Ion implanted deuterium retention and release from clean and oxidized beryllium, Journal of Nuclear Materials, 390–91 (2009) 568–571.

[20] R. Bisson, S. Markelj, O. Mourey, F. Ghiorghiu, K. Achkasov, J.M. Layet, P. Roubin, G. Cartry, C. Grisolia, T. Angot, Dynamic fuel retention in tokamak wall materials: An in situ laboratory study of deuterium release from polycrystalline tungsten at room temperature, Journal of Nuclear Materials, 467 (2015) 432–438.

[21] C. Pardanaud, E. Areou, C. Martin, R. Ruffe, T. Angot, P. Roubin, C. Hopf, T. Schwarz-Selinger, W. Jacob, Raman micro-spectroscopy as a tool to measure the absorption coefficient and the erosion rate of hydrogenated amorphous carbon films heat-treated under hydrogen bombardment, Diamond and Related Materials, 22 (2012) 92–95.

[22] T.W. Scharf, I.L. Singer, Thickness of diamond-like carbon coatings quantified with Raman spectroscopy, Thin Solid Films, 440 (2003) 138–144.

[23] C. Pardanaud, C. Martin, G. Giacometti, N. Mellet, B. Pegourie, P. Roubin, Thermal stability and long term hydrogen/deuterium release from soft to hard amorphous carbon layers analyzed using in-situ Raman spectroscopy. Comparison with Tore Supra deposits, Thin Solid Films, 581 (2015) 92–98.

[24] E. Tsitrone, C. Brosset, B. Pegourie, E. Gauthier, J. Bouvet, J. Bucalossi, S. Carpentier, Y. Corre, E. Delchambre, L. Desgranges, T. Dittmar, D. Douai, A. Ekedahl, A. Escarguel, P. Ghendrih, C. Grisolia, A. Grosman, J. Gunn, S.H. Hong, W. Jacob, F. Kazarian, M. Kocan, H. Khodja, F. Linez, T. Loarer, Y. Marandet, A. Martinez, M. Mayer, O. Meyer, P.M. Garbet, P. Moreau, J.Y. Pascal, B. Pasquet, F. Rimini, H. Roche, I. Roure, S. Rosanvallon, P. Roubin, J. Roth, F. Saint-Laurent, F. Samaille, S. Vartanian, Deuterium inventory in Tore Supra: Reconciling particle balance and post-mortem analysis, Nuclear Fusion, 49 (2009) 075011.

[25] T. Dittmar, P. Roubin, E. Tsitrone, E. Gauthier, A. Hakola, J. Likonen, F. Linez, C. Martin, M. Mayer, C. Pardanaud, J.Y. Pascal, B. Pasquet, B. Pégourié, J. Roth, I. Roure, R. Ruffe, Deuterium inventory in Tore Supra: Status of post-mortem analyses, Physica Scripta, T138 (2009) 014027.

[26] T. Dittmar, E. Tsitrone, B. Pegourie, I. Cadez, P. Pelicon, E. Gauthier, P. Languille, J. Likonen, A. Litnovsky, S. Markelj, C. Martin, M. Mayer, J.-Y. Pascal, C. Pardanaud, V. Philipps, J. Roth, P. Roubin, P. Vavpetic, Deuterium Inventory in Tore Supra (DITS):

2nd post-mortem analysis campaign and fuel retention in the gaps, Journal Of Nuclear Materials, 415 (2011) S757–S760.

[27] C. Martin, B. Pegourie, R. Ruffe, Y. Marandet, G. Giacometti, C. Pardanaud, P. Languille, S. Panayotis, E. Tsitrone, P. Roubin, Structural analysis of eroded carbon fiber composite tiles of Tore Supra: Insights on ion transport and erosion parameters, Physica Scripta, T145 (2011) 4.

[28] C. Pardanaud, G. Giacometti, C. Martin, R. Ruffe, T. Angot, E. Aréou, B. Pégourié, E. Tsitrone, T. Dittmar, C. Hopf, W. Jacob, T. Schwarz-Selinger, P. Roubin, Raman study of CFC tiles extracted from the toroidal pump limiter of Tore Supra, Journal of Nuclear Materials, 415 (2011) S254–S257.

[29] C. Pardanaud, C. Martin, P. Roubin, Multiwavelength Raman spectroscopy analysis of a large sampling of disordered carbons extracted from the Tore Supra tokamak, Vibrational Spectroscopy, 70 (2014) 187–192.

[30] N. Mellet, C. Martin, B. Pegourie, G. Giacometti, J.P. Gunn, G. Cartry, P. Languille, C. Pardanaud, S. Panayotis, G. Amiard, Y. Marandet, P. Roubin, Modelling of the micrometric erosion pattern observed on the Tore Supra limiter tiles, Nuclear Fusion, 54 (2014).

[31] S. Panayotis, B. Pegourie, D. Borodin, A. Kirschner, J. Gunn, Y. Marandet, N. Mellet, Modelling the erosion/deposition pattern of the Tore Supra toroidal pumped limiter, Journal of Nuclear Materials, 463 (2015) 827–831.

[32] F. Tuinstra, J.L. Koenig, Raman spectrum of graphite, Journal of Chemical Physics, 53 (1970) 1126.

[33] S. Piscanec, F. Mauri, A.C. Ferrari, M. Lazzeri, J. Robertson, Ab initio Raman spectra of diamond like carbons, Diamond and Related Materials, 14 (2005) 1078.

[34] M.M. Lucchese, F. Stavale, E.H.M. Ferreira, C. Vilani, M.V.O. Moutinho, R.B. Capaz, C.A. Achete, A. Jorio, Quantifying ion-induced defects and Raman relaxation length in graphene, Carbon, 48 (2010) 1592–1597.

[35] J. Schwan, S. Ulrich, V. Bathori, H. Erhardt, S.R.P. Silva, Raman spectroscopy on amorphous carbon films, Journal of Applied Physics, 80 (1996) 440–447.

[36] E.H.M. Ferreira, M.V.O. Moutinho, F. Stavale, M.M. Lucchese, R.B. Capaz, C.A. Achete, A. Jorio, Evolution of the Raman spectra from single-, few-, and many-layer graphene with increasing disorder, Physical Review B, 82 (2010) 9.

[37] A.C. Ferrari, J. Robertson, Resonant Raman spectroscopy of disordered, amorphous, and diamond like carbon, Physical Review B, 64 (2001) 075414.

[38] C. Beny-Bassez, J.N. Rouzaud, Characterization of carbonaceous materials by correlated electron and optical microscopy and Raman microspectroscopy, Scanning Electron Microscope, 1 (1985) 119–132.

[39] T. Jawhari, A. Roid, J. Casado, Raman spectroscopic characterization of some commercially available carbon black materials, Carbon, 33 (1995) 1561–1565.

[40] A. Sadezky, H. Muckenhuber, H. Grothe, R. Niessner, U. Pöschl, Raman micro spectroscopy of soot and related carbonaceous materials: Spectral analysis and structural information, Carbon, 43 (2005) 1731–1742.

[41] J.M. Vallerot, X. Bourrat, A. Mouchon, G. Chollon, Quantitative structural and textural assessment of laminar pyrocarbons through Raman spectroscopy, electron diffraction and few techniques, Carbon, 44 (2006) 1833–1844.

[42] J. Wagner, M. Ramsteiner, C.H. Wild, P. Koidl, Resonant Raman scattering of amorphous carbon and polycrystalline diamond films, Physical Review B, 40 (1989) 1817–1824.

[43] C. Pardanaud, C. Martin, G. Cartry, A. Ahmad, L. Schiesko, G. Giacometti, M. Carrere, P. Roubin, In-plane and out-of-plane defects of graphite bombarded by H, D and He investigated by atomic force and Raman microscopies, Journal of Raman Spectroscopy, 46 (2015) 256–265.

[44] A.C. Ferrari, J. Robertson, Interpretation of Raman spectra of disordered and amorphous carbon, Physical Review, B, 61 (2000) 14095.

[45] J.G. Buijnsters, R. Gago, I. Jiménez, M. Camero, F. Agullo-Rueda, C. Gomez-Aleixandre, Hydrogen quantification in hydrogenated amorphous carbon films by infrared, Raman, and X-ray absorption near edge spectroscopies, Journal of Applied Physics, 105 (2009) 093510.

[46] C. Casiraghi, A.C. Ferrari, J. Robertson, Raman spectroscopy of hydrogenated amorphous carbons, Physical Review B, 72 (2005) 085401.

[47] C. Pardanaud, C. Martin, P. Roubin, G. Giacometti, C. Hopf, T. Schwarz-Selinger, W. Jacob., Raman spectroscopy investigation of the H content of heated hard amorphous carbon layers, Diamond and Related Materials, 34 (2013) 100–104.

[48] A.C. Ferrari, J. Robertson, Interpretation of Raman spectra of disordered and amorphous carbon, Physical Review B, 61 (2000) 14095–14107.

[49] C. Pardanaud, C. Martin, P. Roubin, G. Giacometti, C. Hopf, T. Schwarz-Selinger, W. Jacob, Raman spectroscopy investigation of the H content of heated hard amorphous carbon layers, Diamond and Related Materials, 34 (2013) 100–104.

[50] T. Schwarz-Selinger, A. von Keudell, W. Jacob, Plasma chemical vapor deposition of hydrocarbon films: The influence of hydrocarbon source gas on the film properties, Journal of Applied Physics, 86 (1999) 3988–3996.

[51] C. Wild, P. Koidl, Thermal gas effusion from hydrogenated amorphous-carbon films, Applied Physics Letter, 51 (1987) 1506–1508.

[52] J. Ristein, R.T. Stief, L. Ley, W. Beyer, A comparative analysis of a-C : H by infrared spectroscopy and mass selected thermal effusion, Journal of Applied Physics, 84 (1998) 3836–3847.

[53] E. Salançon, T. Dürbeck, T. Schwarz-Selinger, F. Genoese, W. Jacob, Redeposition of amorphous hydrogenated carbon films during thermal decomposition, Journal of Nuclear Materials, 376 (2008) 160.

[54] H. Ito, K. Yamamoto, M. Masuko, Thermal stability of UBM sputtered DLC coatings with various hydrogen contents, Thin Solid Films, 517 (2008) 1115–1119.

[55] J.G. Buijnsters, R. Gago, A. Redondo-Cubero, I. Jimenez, Hydrogen stability in hydrogenated amorphous carbon films with polymer-like and diamond-like structure, Journal of Applied Physics, 112 (2012) 093502.

[56] C. Pardanaud, C. Martin, G. Giacometti, P. Roubin, B. Pegourie, C. Hopf, T. Schwarz-Selinger, W. Jacob, J.G. Buijnsters, Long-term H-release of hard and intermediate between hard and soft amorphous carbon evidenced by in situ Raman microscopy under isothermal heating, Diamond and Related Materials, 37 (2013) 92–96.

[57] R. Coratger, A. Claverie, A. Chahboun, V. Landry, F. Ajustron, J. Beauvillain, Effects of ion mass and energy on the damage induced by an ion beam on graphite surfaces: A scanning tunneling microscopy study, Surface Science, 262 (1992) 208–218.

[58] B. An, S. Fukuyama, K. Yokogawa, M. Yoshimura, Evolution of Ar+-damaged graphite surface during annealing as investigated by scanning probe microscopy, Journal of Applied Physics, 92 (2002) 2317–2322.

[59] V.F. Elesin, L.A. Openov, Clusters of interstitial carbon atoms near the graphite surface as a possible origin of dome-like features observed by scanning tunneling microscopy, Surface Science, 442 (1999) 131–140.

[60] B.S. Elman, M. Shayegan, M.S. Dresselhaus, H. Mazurek, G. Dresselhaus, Structural characterization of ion-implanted graphite, Physical Review B, 25 (1982) 4142.

[61] M. Kappel, J. Küppers, Ripening of subsurface amorphous C clusters formed by low energy He ion bombardment of graphite, Surface Science, 440 (1999) 387–397.

[62] M. Kappel, M. Steidl, J. Biener, J. Küppers, Surface topography of low energy He-ion-bombarded graphite by AFM: Temperature effects, Surface Science Letters, 387 (1997) L1062–L1067.

[63] T.L. Makarova, A.L. Shelankov, I.T. Serenkov, V.I. Sakharov, D.W. Boukhvalov, Anisotropic magnetism of graphite irradiated with medium-energy hydrogen and helium ions, Physical Review B, 83 (2011) 085417.

[64] K. Niwase, Irradiation-induced amorphisation of graphite, Physical Review B, 52 (1995) 15785–15798.

[65] K. Nordlund, J. Keinonen, T. Mattila, Formation of ion irradiation induced small-scale defects on graphite surfaces, Physical Review Letter, 77 (1996) 699.

[66] P.J. Zhai, Y.X. Xing, Y. Zhang, S.L. Feng, Y.X. Kang, X.W. Tang, Y.G. Wang, W.J. Zhao, S. Yan, Observation and study of latent tracks on the surface of HOPG induced by H+ ions, Radiation Measurements, 28 (1997) 97–100.

[67] H. Zhang, M. Zhao, X. Yang, H. Xia, X. Liu, Y. Xia, Diffusion and coalescence of vacancies and interstitials in graphite: A first-principles study, Diamond and Related Materials, 19 (2010) 1240–1244.

[68] J.F. Ziegler, J.P. Biersack, U. Littmark, The Stopping and Range of Ions in Matter, Pergamon, New York, 1995.

[69] C. Martin, R. Ruffe, C. Pardanaud, M. Cabié, C. Dominici, T. Dittmar, P. Languille, B. Pegourié, E. Tsitrone, P. Roubin, Structure of the carbon layers deposited on the toroidal pump limiter of Tore Supra, Journal of Nuclear Materials, 415 (2011) S258–S261.

[70] M. Richou, C. Martin, P. Delhaes, M. Couzi, W. Saikaly, C. Brosset, B. Pégourié, A. Litnovsky, V. Philipps, P. Wienhold, J. Dentzer, C. Vix-Guterl, P. Roubin, Physico-chemical characteristics of carbon deposits collected in TEXTOR and Tore Supra tokamaks, Carbon, 45 (2007) 2723–2731.

[71] S. Panayotis, B. Pegourie, E. Caprin, D. Douai, J.-C. Hatchressian, V. Negrier, J.-Y. Pascal, S. Vartanian, J. Bucalossi, P. Monier-Garbet, Deuterium inventory in Tore Supra: Contribution of carbon deposits outgassing, Journal of Nuclear Materials, 438 (2013) S1059–S1062.

[72] C. Martin, P. Languille, S. Panayotis, B. Pegourie, H. Roche, C. Pardanaud, G. Giacometti, R. Ruffe, E. Gauthier, X. Courtois, E. Tsitrone, P. Roubin, Erosion-deposition mapping of the toroidal pump limiter of Tore Supra, Journal of Nuclear Materials, 438 (2013) S771–S774.

[73] B. Pegourie, S. Panayotis, P. Languille, C. Martin, T. Dittmar, E. Gauthier, J.-C. Hatchressian, J.-Y. Pascal, P. Roubin, R.T. Ruffe, E., S. Vartanian, H. Wang, A. Beaute, J. Bouvet, C. Brosset, J. Bucalossi, M. Cabie, E. Caprin, X. Courtois, R. Dachicourt, E. Delchambre, C. Dominici, D. Douai, A. Ekedahl, J.P. Gunn, A. Hakola, W. Jacob, H. Khodja, J. Likonen, F. Linez, A. Litnovsky, Y. Marandet, S. Markelj, A. Martinez, M. Mayer, O. Meyer, P. Monier-Garbet, P. Moreau, V. Negrier, P. Oddon, C. Pardanaud, B. Pasquet, P. Pelicon, P. Petersson, V. Philipps, G. Possnert, D. Reiter, J. Roth, I. Roure, M. Rubel, F. St-Laurent, F. Samaille, P. Vavpetic, Deuterium inventory in Tore Supra: Coupled carbon-deuterium balance, Journal of Nuclear Materials, 438 (2013) S120–S125.

[74] J. Roth, E. Tsitrone, A. Loarte, Plasma-wall interaction: Important ion induced surface processes and strategy of the EU Task Force, Nuclear Instruments & Methods in Physics Research Section B-Beam Interactions with Materials and Atoms, 258 (2007) 253–263.

[75] D. Borodin, S. Brezinsek, J. Miettunen, M. Stamp, A. Kirschner, C. Bjorkas, M. Groth, S. Marsen, C. Silva, S.W. Lisgo, D. Matveev, M. Airila, V. Philipps, J.-E. Contributors, Determination of Be sputtering yields from spectroscopic observations at the JET ITER-like wall based on three-dimensional ERO modelling, Physica Scripta, T159 (2014) 014057.

[76] G. De Temmerman, M.J. Baldwin, R.P. Doerner, D. Nishijima, K. Schmid, An empirical scaling for deuterium retention in co-deposited beryllium layers, Nuclear Fusion, 48 (2008) 075008.

[77] G. De Temmerman, R.P. Doerner, Revised scaling equation for the prediction of tritium retention in beryllium co-deposited layers, Nuclear Fusion, 49 (2009) 042002.

[78] M. Mayer, R. Behrisch, H. Plank, J. Roth, G. Dollinger, C.M. Frey, Codeposition of hydrogen with beryllium, carbon and tungsten, Journal of Nuclear Materials, 230 (1996) 67–73.

[79] R.A. Causey, D.S. Walsh, Codeposition of deuterium with beryllium, Journal of Nuclear Materials, 254 (1998) 84–86.

[80] M.J. Baldwin, K. Schmid, R.P. Doerner, A. Wiltner, R. Seraydarian, C. Linsmeier, Composition and hydrogen isotope retention analysis of co-deposited C/Be layers, Journal of Nuclear Materials, 337 (2005) 590–594.

[81] J.T. Zhao, Q. Wang, T.S. Wang, X.X. Xu, S. Zhang, Y.S. Zhou, X.C. Guan, K.H. Fang, J. Kasagi, Dynamical saturated concentration of deuterium in a beryllium foil studied by low energy D(d,p)T reaction, Nuclear Instruments & Methods in Physics Research Section B-Beam Interactions with Materials and Atoms, 316 (2013) 13–16.

[82] V.K. Alimov, V.N. Chernikov, A.P. Zakharov, Depth distribution of deuterium atoms and molecules in beryllium implanted with D ions, Journal of Nuclear Materials, 241 (1997) 1047–1051.

[83] M. Oberkofler, C. Linsmeier, Deuterium release from implanted beryllium and beryllium oxide, Journal of Nuclear Materials, 415 (2011) S724–S727.

[84] A.A. Haasz, J.W. Davis, Deuterium retention in beryllium, molybdenum and tungsten at high fluences, Journal of Nuclear Materials, 241 (1997) 1076–1081.

[85] R. Piechoczek, M. Reinelt, M. Oberkofler, A. Allouche, C. Linsmeier, Deuterium trapping and release in Be(0001), Be(11-20) and polycrystalline beryllium, Journal of Nuclear Materials, 438 (2013) S1072–S1075.

[86] G. Gouadec, P. Colomban, Raman spectroscopy of nanomaterials: How spectra relate to disorder, particle size and mechanical properties, Progress in Crystal Growth and Characterization of Materials, 53 (2007) 1–56.

[87] W.J. Evans, M.J. Lipp, H. Cynn, C.S. Yoo, M. Somayazulu, D. Hausermann, G. Shen, V. Prakapenka, X-ray diffraction and Raman studies of beryllium: Static and elastic properties at high pressures, Physical Review B, 72 (2005).

[88] G. Morell, W. Perez, E. ChingPrado, R.S. Katiyar, An harmonic interactions in beryllium oxide, Physical Review B, 53 (1996) 5388–5395.

[89] M. Boulova, N. Rosman, P. Bouvier, G. Lucazeau, High-pressure Raman study of microcrystalline WO3 tungsten oxide, Journal of Physics-Condensed Matter, 14 (2002) 5849–5863.

[90] C. Pardanaud, M.I. Rusu, G. Giacometti, C. Martin, Y. Addab, P. Roubin, C.P. Lungu, C. Porosnicu, I. Jepu, P. Dinca, M. Lungu, O.G. Pompilian, R. Mateus, E. Alves, M. Rubel, J. contributors, Raman microscopy investigation of beryllium materials, Physica Scripta, T167 (2016) 014027.

[91] L. Avotina, A. Marcu, C. Porosnicu, M. Lungu, A. Stancalie, A.G. Ilie, P.C. Ganea, D. Savastru, J. Kalnacs, C.P. Lungu, G. Kizane, S. Antohe, Multi-wavelength laser irradiation of Be-C-W coatings, Digest Journal of Nanomaterials and Biostructures, 11 (2016) 293–302.

[92] C. Pardanaud, Y. Addab, C. Martin, P. Roubin, B. Pegourié, M. Oberkofler, M. Köppen, T. Dittmar, C. Linsmeier, Raman microscopy as a defect microprobe for hydrogen bonding characterization in materials used in fusion applications, Physica Status Solidi (c), 12 (2015) 98–101.

[93] Y. Addab, C. Martin, C. Pardanaud, J. Khayadjian, K. Achkasov, D. Kogut, G. Cartry, G. Giacometti, M. Cabié, J.L. Gardarein, Formation of thin tungsten oxide layers: Characterization and exposure to deuterium, Physica Scripta, T167 (2016) 014036.

[94] C. Pardanaud, M.I. Rusu, C. Martin, G. Giacometti, P. Roubin, Y. Ferro, A. Allouche, M. Oberkofler, M. Köppen, T. Dittmar, C. Linsmeier, Hydrogen retention in beryllium: Concentration effect and nanocrystalline growth, Journal of Physics: Condensed Matter, 27 (2015) 475401.

[95] C. Pépin, P. Loubeyre, Layered structure and re-entrant disproportionation observed in crystalline BeH2 under pressure, Physical Review B, 93 (2016) 224104.

[96] C.P. Lungu, C. Porosnicu, I. Jepu, M. Lungu, A. Marcu, C. Luculescu, C. Ticos, A. Marin, C.E.A. Grigorescu, The behavior of W, Be and C layers in interaction with plasma produced by terawatt laser beam pulses, Vacuum, 110 (2014) 207–212.

[97] A.V. Khotkevich, I.K. Yanson, Atlas of point contact spectra of electron-phonon interactions in metals, Springer, 1995 springer Science+Business Media, New York, 978-0-7923-9526-3, DOI:10.1007/978-1-4615-2265-2

[98] D. Reed, D. Book, Recent applications of Raman spectroscopy to the study of complex hydrides for hydrogen storage, Current Opinion in Solid State & Materials Science, 15 (2011) 62–72.

[99] A. Pezzoli, D. Dellasega, V. Russo, A. Gallo, P.A.Z. van Emmichoven, M. Passoni, Thermal annealing and exposure to divertor-like deuterium plasma of tailored tungsten oxide coatings, Journal of Nuclear Materials, 463 (2015) 1041–1044.

[100] T. Pagnier, M. Boulova, N. Sergent, P. Bouvier, G. Lucazeau, Nanopowders and nanostructured oxides: Phase transitions and surface reactivity, Journal of Raman Spectroscopy, 38 (2007) 756–761.

Chapter 2

Raman Investigations of Atomic/Molecular Clusters and Aggregates

Zhixun Luo and Jiannian Yao

Additional information is available at the end of the chapter

http://dx.doi.org/10.5772/66098

Abstract

Efforts to tune optic responses of molecular aggregates often alter the characteristics and performance of functional materials, revealing that chemical properties largely rely on molecular stacking and interactions. Although the intrinsic nature of materials is primarily determined by single-molecule structures, molecular aggregation behavior that determines material property resembles the architectural style of a building in which the bricks themselves could be less important. While the establishment of surface-enhanced Raman spectroscopy (SERS) inspired numerous research interest for trace analysis up to single-molecule level, Raman spectroscopy is also recognized for its importance in solving several issues relating to molecule aggregates owing to the capability of non-destructive detection and spectral fingerprints by which chemical structures and aggregation states can be identified. Raman spectroscopy is not only applied to identify chemicals at the gas phase, liquid phase and solid state and to monitor in-situ reactions of materials at reduced sizes but also to probe gas-to-particle conversion in aerosols, microcrystal magnetization and phase transition at aggregated states, which are believed to attract uprising research interest in the near future.

Keywords: molecular aggregates, clusters, Raman spectroscopy, SERS, aggregation-induced resonance

1. Introduction

Aggregation structures such as those of hydrophobic and hydrophilic surfactant molecules widely exist in aqueous solutions, micelles, liquid crystals, various membranes, and biological systems and are important for understanding physical and chemical properties and functions. Extensive investigations have demonstrated that optic responses of molecular aggregates

often determine the property and performance of optical functional materials [1–3]. Also found was that, selective controlling of excitonic states of molecular aggregates profits to engineer optical properties of promising photonic materials described in terms of the model of Frenkel excitons [4–6]. In poor solvents, self-assembly of organic molecules in the form of weakly coupled aggregates display significantly different spectroscopic behavior compared to their monomers [7]. From UV-vis spectral analysis based on Kasha exciton theory [8–10], typical aggregation behavior can be determined by checking out a tilt angle of molecular stacking [11–13]. In addition to UV-vis absorption, fluorescence of aggregates has also been meticulously investigated, where the fluorescence intensity of organic molecules often diminishes upon aggregation due to intermolecular interactions [14–18], but allowing for interesting exceptions such as those demonstrated as aggregation-induced emission enhancement (AIEE), revealing relationships between molecular structures/molecular arrangements and emission properties [2, 3, 19–21]. While numerous UV-vis and fluorescence investigations help determine the aggregation behavior, it is important to utilize vibrational spectroscopic fingerprints of molecular aggregates to identify the components and structures, phase transition, likely isomers, and conformation transition of chemicals at reduced sizes [22, 23].

Raman effect arises when light impinges upon a molecule or molecule aggregates and interacts with the electron cloud and chemical bonds. A fascinating world of Raman spectroscopy toward both bulk materials and single molecules has been fully demonstrated (i.e., the two ends), but for molecule aggregates, there are relatively less Raman spectroscopic studies in reported publications so far. A few Raman investigations have shed light on ionic surfactants [24–28] and photogenerating reactions [29–31] of organic molecule assemblies; and in-situ Raman techniques have been utilized to monitor real-time reactions and catalysis [32–36], as well as photo-induced polymerization and magnetization [37]. Recently, it was reported that small organic molecules could form uniform assembly with head-to-tail J-aggregation along the inner walls of the pores of an anodic aluminum oxide (AAO) template, giving rise to an interesting topic for surface-enhanced Raman spectroscopy [11, 13, 38]. Also, there were a few surface-enhanced Raman spectroscopy (SERS) investigations endeavoring to determine the plasmonic property of metal clusters and structural information of molecule aggregates. Raman spectroscopic studies of atomic/molecular clusters and aggregates are expected to become a significant solution to identify chemical structures at primary state of nucleation and growth of materials, gas-to-particle conversion mechanism of aerosols, as well as the aggregation states in liquid crystals, micelles, bilayers/monolayers, and biomembranes. These efforts also help understand the fundamentals in various fields such as catalysis, optics, magnetism, and medicine, etc.

2. Raman theory of aggregated molecules

According to the molecular exciton theory developed by Davydov [9] and Kasha [8, 10], the aggregation of molecules alters their absorption spectrum, reflecting hypsochromic (i.e., blue-shift) or bathochromic (i.e., red shift) absorption bands, corresponding to H-aggregate (face-to-face, or side-by-side) or J-aggregate (head-to-tail, or linear herring bone) absorptions,

http://dx.doi.org/10.5772/66098

respectively. Assuming that different accumulations of molecules have different tilt angles (defined as the angle between the transition dipole and the molecular axis of the aggregate), typical H-aggregates bear a tilt angle value greater than 54.7° and exhibit a broader, blue-shifted absorption band, while J-aggregates bear a tilt angle smaller than 54.7° characterized by a red-shift in the UV-vis spectrum relative to the monomer [11–13]. From UV-vis spectral analysis based on Kasha exciton theory [8–10], simply the approximate tilt angle for accumulation of N molecules can be calculated according to the following equation,

$$\Delta\nu = 2\frac{N-1}{N}\cdot\frac{<m^2>}{h\cdot r^3}(1-3\cos^2\alpha) \tag{1}$$

$$\left\langle \mathrm{m}^2 \right\rangle = 9.185\times10^{-39}\int_{\lambda_1}^{\lambda_2}\varepsilon(d\lambda/\lambda) \tag{2}$$

where $\Delta\nu$ is the spectral shift from the monomer absorption; h is the Planck's constant; r is the separation of centers; α is the tilt angle between the line of center and molecular long axes; $<m^2>$ refers to the transition dipole moment of monomer; ε aims at the molar extinction coefficient in $(\text{moles/L})^{-1}\,\text{cm}^{-1}$; λ is the wavelength; and λ_1 and λ_2 are the limits of a well-defined absorption band. This theory has been successfully applied to determine the J-aggregation of small organic molecules, such as perylene [11], assembled on pipe inner wall of AAO templates. This is further discussed below.

Further, in light of the molecular exciton theory, Akins [39] reported a study on Raman scattering enhancement theory for a finite aggregate structure consisting of N molecules, assuming the formation of molecular vibro-excitonic levels. The quantum mechanical Hamiltonian describing the internal system of the N molecules can mutually interact through a potential term V, which was given by [39],

$$\mathrm{H} = \sum_{n=1}^{N}\left(H_n + \sum_{m>n}V_{nm}\right) \tag{3}$$

where H is the Hamilton operator of kinetic energy; and V_{nm} refers to the interaction potential of molecules n and m (m is any of the other molecules taken together with molecule n). Thus for an individual molecule n, the vibronic wave function can be given by [39],

$$\varphi_{nj}(\rho, \mathrm{Q}) = \varphi_n(\rho,\ Q_0)x_{ni}(Q) \tag{4}$$

here n aims at the position of the probe molecule and j refers to a composite quantum number corresponding to the number of vibrational quanta of excitation. The character ρ is a composite spatial coordinate of the electrons, Q is the normal coordinate, and Q_0 represents the normal coordinates for the ground-state equilibrium configuration.The function φ refers to a multiple

electron wave function depending on the coordinates and spins of the electrons, while x corresponds to the vibrational wave function. Based on Born-Oppenheimer approximation, the normalized vibro-exciton wave function can be ascertained and thus the allowed energies. Further, according to the theory by Craig and Thirunamachandra [40], the Raman scattering intensity in a particular direction can be given by [39],

$$I(k') = \frac{\tilde{N} I_{k'}{}^4}{16\pi\varepsilon_0{}^2} \left| \sum_r \left\{ \frac{\left(\vec{\mu}^{mr} \cdot \vec{e}'\right)\left(\vec{\mu}^{r0} \cdot \vec{e}\right)}{E_{r0} - \hbar ck} + \frac{\left(\vec{\mu}^{mr} \cdot \vec{e}\right)\left(\vec{\mu}^{r0} \cdot \vec{e}'\right)}{E_{r0} + \hbar ck'} \right\} \right|^2 \tag{5}$$

where $\tilde{N}$ is the number of scattering centre; $\vec{\mu}$ is transition dipole moment vector; $\vec{e}$ is microscopic electric field strength vector; and E_{r0} shows the energy difference between the upper excited state r and the ground state 0. From first-order perturbation theory, the Raman scattering of aggregated molecules can be expressed as [39],

$$\lambda_{rs}(Q) = (\sum_\alpha h_{rs}{}^\alpha Q_\alpha)(\Delta E_{rs}{}^0)^{-1} \tag{6}$$

in which $h_{rs}{}^\alpha$ is a coupling term between electronic states r and s for the molecule with equilibrium ground-state configuration [39]. This theory has been successfully applied to dye molecules that form ground-state and excited-state aggregation structures, where an intrinsic enhancement was often gained on the formation of aggregates containing N monomers [39, 41].

3. Plasmon-free Raman scattering of molecule aggregates

Raman scattering of molecule aggregates, held together by dispersion and electrostatic forces, has been found different from that of non-aggregated monomers and bulk crystals. Moreover, the Raman bands observed for the aggregates could shift from those of the isolated monomers depending on the intermolecular interactions (i.e., strong or weak; covalent or non-covalently coupled interactions). This characteristic enables Raman spectroscopic studies of molecule aggregates to determine phase transition and photo-assisted polymerization. It is worth noting that, upon resonant excitation, the excited states often bring forth new Raman bands associated with lattice motions, e.g., typical motions in the aggregate formation direction. In this section, we emphasize on a few examples of normal Raman investigations of molecule aggregates.

3.1. To determine phase transition

It has been widely recognized that the assembly of target molecules can result in novel responses of Raman spectroscopy. For example, when examining Raman spectra of barium dialkyl phosphates at various chain lengths, Okabayashi et al. [42] found that the PO_2^-

symmetric stretching mode of dipentyl phosphate appears at 1106 cm^{-1} for the liquid crystal state formed at room temperature, which differs from that in the aqueous solution (ca. 1075 cm^{-1}). Also found was that, the relative intensities of the Raman spectral lines changed sharply at the phase-transition temperature but were found to be a constant below and above the transition point. By fully examining the Raman intensities and Raman shifts of the PO_2^- symmetric-stretching modes of dipentyl phosphate (1075 cm^{-1}), diester O-P-O and dibutyl phosphate (at 1090 and 1068 cm^{-1}), phase transition and the coexistence of two types of aggregation structures were determined. These Raman investigations illustrated how cation-phosphate interactions are important to form aggregation structures and affect the phase transition in liquid crystals of dialkyl phosphates.

3.2. Aggregation-enhanced Raman scattering (AERS)

A few meticulous investigations dealing with relative Raman intensities and selection rules for aggregates have demonstrated a concept termed "aggregation-enhanced Raman scattering" (AERS) [43], which was proposed to represent a concept solely for studies of aggregates, which differs from a mechanism based on SERS, resonance Raman scattering, and Mie scattering since these Raman effects ignore the impact of aggregation of molecules. The aggregation of molecules in their ground state may result in enhanced polarizability compared to monomeric species and hence intensified radiation according to the basic principle for a dipole moment $\mu = \alpha E$, where α is the polarizability and E is the coupled field. On the other hand, the aggregates could form molecular excitonic states allowing for a coupling effect (between excitonic states) which alters the cross-section of Raman scattering, because the participation of more energetic states readily gives rise to an enhanced response to incident radiation [43]. In this point, resonance Raman scattering, where the incident exciton overlaps a small number of exciton bands, is expected to result in further enhancement of vibrational bands. Akins have conducted numerous investigations relating to AERS [41, 44–54], as partly included in a recent review article [43].

3.3. Resonance Raman effect from aggregation

Resonant Raman spectroscopy (RRS) has been known as a main enhancement strategy to solve the sensitivity issue and to derive Raman labels for applications. For example, Zajac et al. [23] reported an interesting study on aggregation-induced resonance Raman optical activity (AIRROA) of astaxanthin (3,3′-dihydroxy-β,β-carotene-4,4′-dione, AXT), a chiral xanthophyll that was known to bear high antioxidant potency beneficial to cardiovascular, inflammatory, immune and neurodegenerative diseases. Along with striking differences of UV-vis spectra of the monomer and aggregates, Raman spectra (**Figure 1**) demonstrated spectral changes (e.g., 5 cm^{-1} blue-shift of the C═C stretching mode, and the appearance of a new band at ~280 cm^{-1}) due to J-aggregation of astaxanthin along with a quenched fluorescence background. Considering the fact of low sensitivity determined by the main limitation of Raman optical activity (c.a., approximately one photon in a billion), resonance effect and aggregation enhancement is important to further advances of AIRROA investigations.

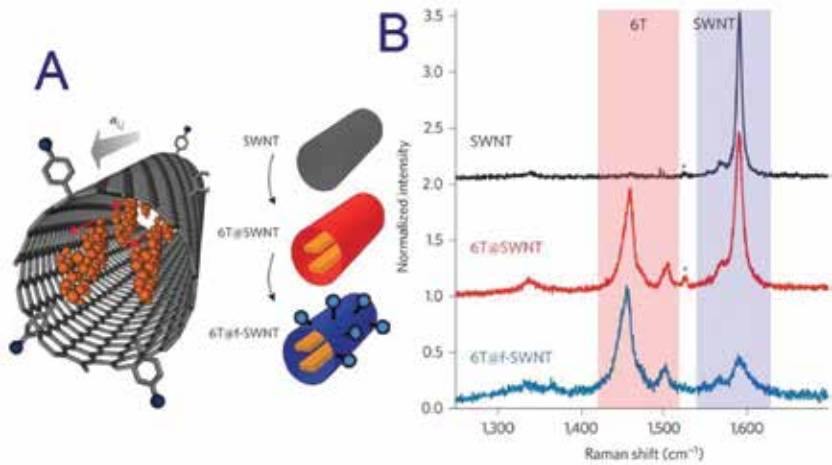

Figure 1. (A) A schematic representation of the 6T@f-SWNT with bromophenyl groups grafted onto its sidewall, and description of the encapsulation and chemical functionalization steps to prepare the α-sexithiophene encapsulated inside a covalently functionalized SWNT (6T@f-SWNT). (B) Raman spectra at λ = 532 nm excitation of an individual SWNT, α-sexithiophenes (6T) inside a SWNT (6T@SWNT) and after the covalent functionalization step (6T@f-SWNT). The polymer monoliths composed Ref. [55].

Recently, Gaufrès et al. [55] reported an interesting study on encapsulated and aggregated dye molecules inside single-walled carbon nanotubes [55], where giant Raman scattering effect was discovered. Raman measurements for the rod-like dyes (α-sexithiophene and β-carotene) assembled in single-walled carbon nanotubes exhibit highly-polarizable J-aggregates, as shown in **Figure 1**, giving an enhanced resonant Raman cross-section above that required for detecting individual aggregates. It was found that the shielding of carbon nanotube enables fluorescence-free background and photobleaching-free Raman signals, allowing the giant Raman effect used as functionalized nanoprobe labels for Raman imaging with robust detection using multispectral analysis. Beside this, there are also a few other interesting research papers dealing with Raman scattering by encapsulated molecules in carbon nanotubes, where the formation of aggregates give rise to well-resolved Raman spectra due to interaction and charge transfer within the carbon nanotubes [56, 57].

3.4. Magnetic field-trapped Raman scattering

The exploration of magnets and magnetism is associated with human history. Recently, Luo et al. [37] reported an interesting photo-assisted method to magnetize microcrystal fullerene C_{60} at room temperature by exciting C_{60} molecules to triplet states via proper laser radiation and then trapping the spin-polarized states under a strong magnetic field (**Figure 2**). Raman spectroscopy was found an operative probe due to its fingerprint spectra regarding energy levels and molecular states, and the crystalline form of C_{60} molecule aggregates is held together by van der Waals forces allowing the conversion to polymeric phase under proper laser radiation [58]. As results, novel changes on Raman scattering of micro-crystal solid C_{60} were discovered in the presence and absence of the magnetic field; also found was that the Raman

http://dx.doi.org/10.5772/66098

spectra exhibited "hysteresis" phenomenon when the external magnetic field was removed. Together with first-principles calculations which well reproduced the Raman activities of C_{60} on different states [37], as seen in **Figure 2**, photo-assisted magnetization (PAM) of the fullerenes and magnetic-field trapped Raman spectroscopy (MFTRS) were proposed [37]. The PAM strategy with MFTRS verification opens a new approach and, as a general protocol, enables the magnetization of common materials that consist of only light elements. The importance of spin-spin and spin-orbit interactions was also demonstrated in nano-graphene fragments [59]; Raman spectroscopy also plays an important role in identifying single- and few-layer graphene [60, 61].

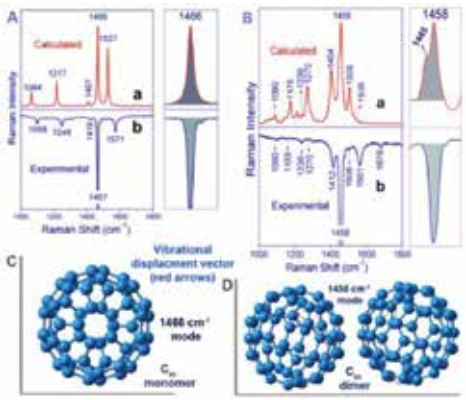

Figure 2. (A) Calculated Raman activity of a singlet-state C_{60} monomer (a), comparison of a normal FT-Raman spectrum of solid C_{60} (b); (B) calculated Raman spectrum of a quintet-state dimer C_{60} (a), compared with the 514.5-nm Raman of solid C_{60} in the presence of a B = 2.5 T magnetic field (b); (C and D) The strongest vibrational modes of a singlet-state C_{60} monomer (1466-cm^{-1}) and a quintet-state C_{60} dimer (1458-cm^{-1}). The displacement vectors are shown with red arrows.

3.5. Raman probes for aerosols

Raman spectroscopy is useful in characterizing atmospheric aerosols profiting from the development of portable Raman instrument in recent years [62–77]. For example, Aggarwal et al. [77] developed a Raman spectrometer using 532-nm continuous wave laser and used for detecting and identifying chemical aerosols of a low-concentration in atmospheric air. As results, they demonstrated the successful application of Raman for trace detection and analysis of iso-vanillin aerosols up to a mass concentration of 1.8 ng/cm^3 with the signal-to-noise ratio at about 19 in 30s for the 1116-cm^{-1} mode with a decent Raman cross section of 3.3×10^{-28} cm^2 at the use of 8-W double-pass laser power. Among others, Batonneau et al. [78] reported an interesting study on heterogeneous chemistry of aerosol particles utilizing Raman mapping and spectroscopic method, which was found in agreement with elemental images obtained by X-ray-mapping. An et al. [79] conducted a systematic study to identify a few typical organic compounds (isoprene, terpenoids, pinenes etc.) which are known as the main sources of organic aerosols (OAs) particle matter in air pollution. Raman and IR spectra of isoprene,

terpenoids, pinenes and their mixtures were examined showing distinguishable vibrational spectroscopic fingerprints of the three components respectively. It was noted that, in a certain case such as β-pinene, a dimer model reproduces the experimental results other than single molecule modeling, indicating nonneglectable intermolecular interactions and aggregation states for aerosols challenging the present mechanisms based on single molecule theory. Further, Raman spectra from an ambient sample can be analyzed using a hierarchical clustering method to check out whether the spectra of aerosols in consistence with relating organic compounds. In particular, analysis on time-resolved aerosol Raman spectra over the course of several hours, simply by checking the D-G bands of amorphous carbon plotted vs time (e.g., a half-hour intervals), enables to monitor and judge the increase/decrease of related pollution in atmosphere [78, 80, 81].

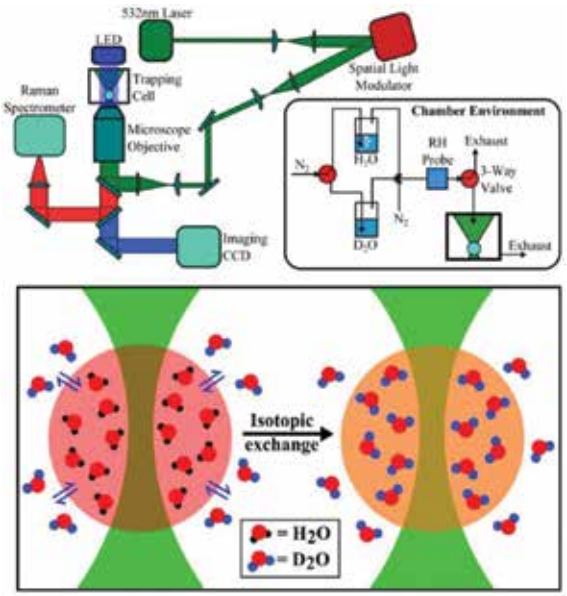

Figure 3. (Top) Standard optical tweezers (Biral AOT 100) arrangement. (Inset) Valve system used to initiate exchange between D_2O and H_2O. (Bottom) A sketch showing isotopic water diffusion in aerosol by the use of optical tweezers. Reproduced with permission from Ref. [71].

Recently, Davies and Wilson [71] employed an aerosol optical tweezer technique for contactless levitation of single droplets (e.g., 3–6 μm in radius) and then for Raman investigations, as shown in **Figure 3**. Flexible environmental control system allows for rapid exchange of the gas-phase humidity source between H_2O and D_2O (**Figure 3**) to monitor the progression of the droplet composition using Raman spectroscopy. Utilizing a model describing diffusion in a sphere (i.e., solution to Fick's second law), they analyzed the data by varying diffusion coefficients (D_w) in viscous media to achieve the best fit to both D_2O and H_2O data sets. This droplet-based isotopic tracer method takes a few advantages for measurement of diffusion coefficients. The resolution of gel formation suggests promising application to identify phase

behavior that leads to abrupt changes in water mobility (e.g., hydrophobic phase separation, aerosol formation and rapid growth), enabling to explore the changing role of water diffusion at chemical transformation thus valuable insights into the oxidative aging behavior in determining diffusive properties of atmospheric aerosol.

4. SERS systems involving molecule aggregates

Besides normal Raman, abundant SERS investigations have been undertaken by employing thin films of analytes on functional substrates, such as the extensive investigations of Raman and SERS from Langmuir-Blodgett (LB) films which are often associated with intermolecular interactions of aggregates [82–89]. One of the advantages is that the uniform sampling of thin films allows for better signal-to-noise of the SERS spectra from the analytes [82, 86]. Besides extensive investigations of such 2D assemblies of "analytes + nanoparticles" into thin films, previous publications also addressed 1D assemblies of molecular aggregates (analytes) and metal nanoparticles (signal amplifier).

4.1. Template-based uniform assembly

Considering that Raman/SERS measurements at different positions of the samples could take on diversity due to molecule orientation and disorder degree, location and/or "hot-spots" dependence, the uniformity of molecular aggregates or SERS substrate is largely desired in order to get a better averaged collection of Raman signal. Anodic aluminum oxide (AAO) membrane is widely utilized as a versatile template to prepare 1D rodding/tubing and 2D nanoarray ordered structures, [90–95] both of which have found applications to SERS investigations. On one hand, AAO templates are ideal sublayers to filtrate and support noble metal nanoparticles hence forming highly SERS-active systems [96–98]. For another, AAO templates were also utilized to assemble organic molecules (e.g., perylene) for SERS investigations [11], as shown in **Figure 4**(left), where highly-ordered arrays of core-shell nano-pillars of Ag-perylene were fabricated simply by preparing perylene nanotubes utilizing the versatile AAO template [13], and followed by an electrochemical deposition of Ag [11]. Well-resolved Raman spectra with very good signal-to-noise background were obtained for the perylene (originally a large fluorescence yield) at an UV-vis excitation, profiting from the uniform assembly of perylene molecules. Based on the aforementioned theory and Eqs. (1) and (2), it was estimated that the molecular tilt angle is less than 54.7° indicating a head-to-tail J-aggregation of the perylene molecules along the inner walls of the AAO pores [11]. Similarly, high-quality SERS spectra of fullerene C_{60}/C_{70} were also obtained from ordered arrays of core-shell nano-pillars of $Au@C_{60}/C_{70}$, as shown in **Figure 4**(right) [99]. These results evidenced that coincident and uniform assembly of fullerene molecules along the Au nano-rods leads to fluorescence quenching, and the ordered arrays of nano-pillars generate enhanced LSPR and hence remarkable SERS effect up to 10 times of signal amplification compared to the usual SERS results.

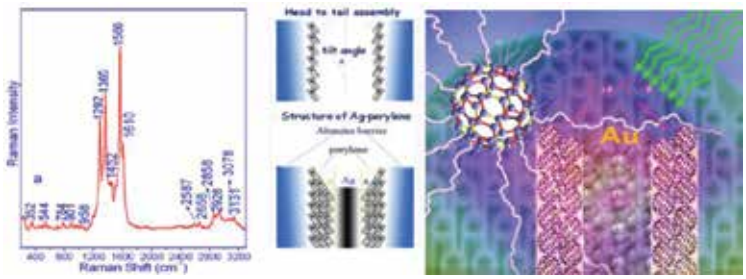

Figure 4. (Left) SERS spectrum of perylene from the standing Ag-perylene core-shell nano-pillars array; (middle) a sketch of the assembly of perylene molecules loaded with Ag as the core; (right) a sketch map showing the Au@C_{60}/C_{70} nanopillars.

4.2. Assemblies of "analytes + nanoparticles"

By utilizing porous polymer monoliths functionalized with Ag nanoparticles as media, Liu et al. [100] showed a SERS system with assembly of the analyte molecules, as shown in **Figure 5**. The polymer monoliths composed of porous 3D-structured organic materials were prepared from monomers with unsaturated vinyl groups [101]. The monoliths could have μm- to nm- sized tortuous fluidic channel networks which enable the convection flow for rapid mass transfer while shorten the characteristic diffusion length. Compared to usual colloidal SERS systems, the monolith was demonstrated to concentrate the embedded metal nanoparticles and present a tremendous amount of surface area and more interaction between the analyte and Ag nanoparticles [100].

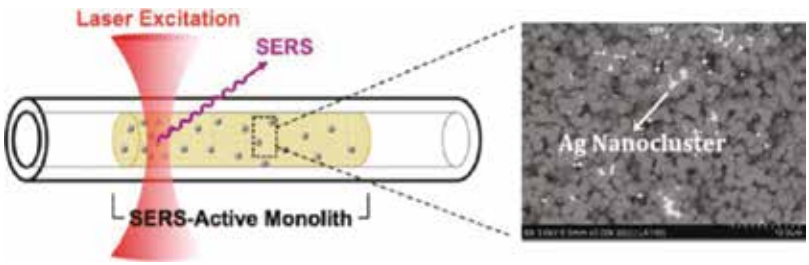

Figure 5. A sketch for the nanoparticle-functionalized porous polymer monolith detection elements for SERS investigations. Reproduced with permission from *Anal. Chem.* 2011 [100].

The one-dimensional assembly of "analytes + nanoparticles" may not need any supports or templates. For example, Z. Luo found that, micro-fiber assembly of organic molecules such as 2,2′-bipyridyl (22BPY) can be formed by directly injecting saturated solution of the target molecules into ice-cold Ag colloid [22]. This strategy was demonstrated to resemble a reprecipitation method (or named as microfluidic technique) which was widely used to prepare size-controlled organic nanostructures [102]. As shown in **Figure 6**, the high-quality spectrum

http://dx.doi.org/10.5772/66098

suggested that the microfiber assemblies of 22BPY combined with Ag nanoparticles are a highly SERS-active systems differing from SERS of individuals [22].

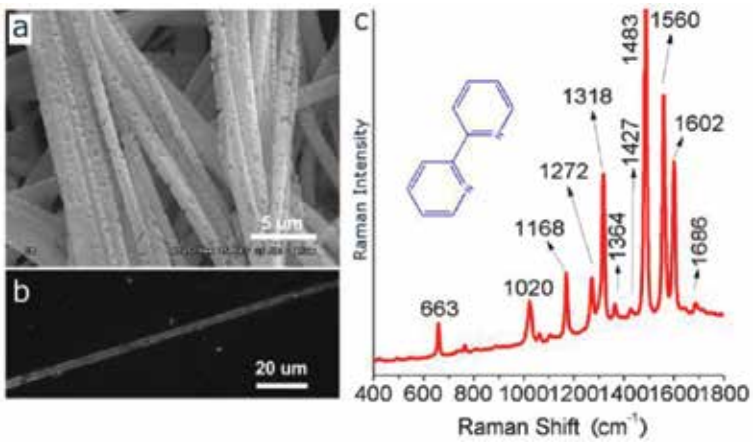

Figure 6. (a) A SEM image of 22BPY microfibers via reprecipitation method by injecting saturated 22BPY solution into ice-cold Ag colloid, (b) microscopy bright-field image of a single fiber, and (c) correlative micro-Raman spectrum measured from this microfiber of 22BPY.

4.3. On-the-specimen method

As a powerful technique for trace analysis and detection due to the extremely high sensitivity and rich structural information that it can offer, SERS has been extensively investigated not only on the primal three classes of SERS systems (i.e., metal colloids, electrodes, and island films), but also non-traditional substrates [103–105]. For example, SERS studies involving surface coatings of Ag/Au nanoparticles, as named *on-the-specimen* method, have been largely applied in identification for art conservation, especially cultural relics and archeology [38, 106]. In general, the colorant components comprised of inorganic salts can be identified using normal Raman spectroscopic measurements, but strong fluorescence of organic dyes often precludes Raman measurements. SERS fulfills the requirements of an ideal analytical technique to detect and identify colorants and organic dyes in artworks [107–109]. In a few typical investigations such as those by Brosseau et al. [110, 111] examination on the samples of actual historical textiles, pastels, and watercolors, etc. have been conducted revealing the unique advantages of SERS sensitivity and providing distinguishable information available for long term preservation. Recently utilizing bubbling gas strategy for laser ablation in liquid (LAL), Luo et al. [112] prepared chemically-pure gold clusters for a practical use of discrimination among different surfaces, as demonstrated the identification of various documents from different printers/copiers and written with different pen-inks, as shown in **Figure 7** [112]. These investigations pertaining to molecule aggregation states give important application of Raman/SERS spectroscopy within a minimally-invasive manner [112].

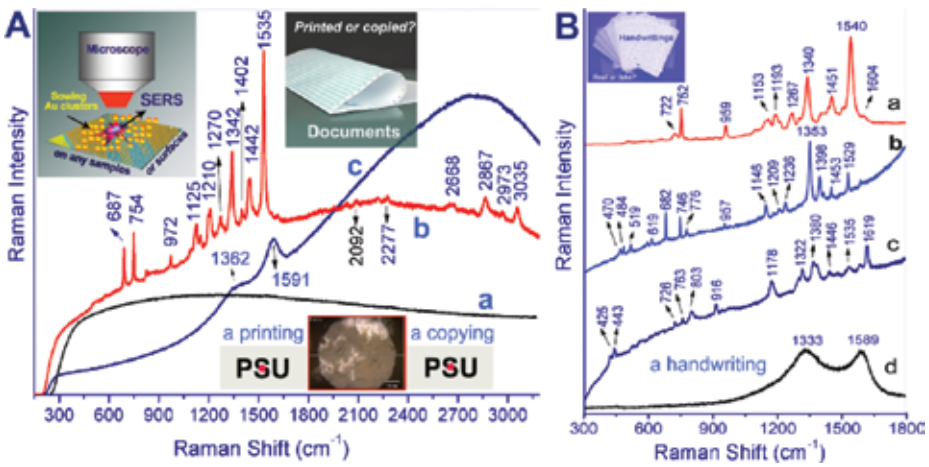

Figure 7. (A) Undistinguishable Raman of a "PSU" document from both a printer and a copier (a); SERS spectrum of the document from the printer (Xerox Phaser 8560DN PS, Genuine XEROX Solid Ink, black) (b), compared with that from a copier (RICOH, Aficio, MP 7001) (c). (B) SERS examination of four handwritten samples, by coating the gold clusters on the ink-area.

Recently, Tian et al. have further pullulated this method in help of shell-isolated nanoparticle-enhanced Raman scattering (SHINERS) technique [113, 114], as sketched in **Figure 8**. For a typical SHINERS system, Au nanoparticles were coated with ultrathin silica shells and sowing on probed surfaces, where the Au core provides SERS signal enhancement while the silica shell shields the metal core from direct contact with analyte molecules (i.e., prevents the contamination of the chemical system under study) [115], which differs from general SERS sampling method, simply by adding analytes onto SERS-active substrates or directly mixing the target solution with metal colloids [115–118]. The SHIERS 'smart dust' on the analyte surfaces was demonstrated of practical use in a few interdisciplinary research fields, such as inspecting pesticide residues on food and fruit, examining drug security and environment protection accurately and rapidly, and characterizing biological structures.

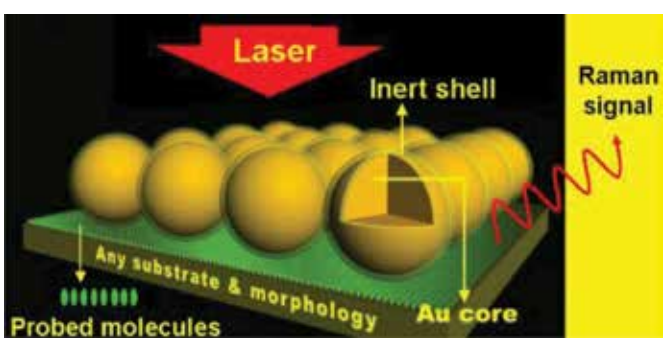

Figure 8. A sketch showing the in-situ probing of biological structures by SHINERS. Reproduced with permission from *Nature* 2010. [61, 62]

http://dx.doi.org/10.5772/66098

5. Raman investigations of cluster systems

5.1. Raman scattering of gas-phase clusters

Raman spectroscopy can also provide essential vibrational information of clusters, although only a few investigations have been published so far. For this study, coherent anti-Stokes Raman spectroscopy (CARS) takes advantages of its excellent sensitivity as applied to investigations of isolated water clusters [119–121], but the nonlinearity of CARS experiments remains a challenge to the assignment of cluster sizes and structure identification. It is worth mentioning that Raman activity of gas-phase clusters is associated with free-rotating especially at high temperature, thus the internal rotational motions could largely differ from that obtained by matrix-assisted vibrational spectroscopic measurements where the molecule/clusters could be partially or wholly clamped. Among others, Otto et al. [122] reported a study of cold water oligomers utilizing spontaneous Raman scattering (SRS) technique and revealed the vibrational dynamics of water molecules, as shown in **Figure 9**. Analysis of Raman and IR activities of the hydrogen bond-mediated water clusters seeded in rare-gas expansion molecule beam provides insights into the excitonic OH oscillator coupling, as well as vivid information of ultrafast intermolecular energy transfer (which was often suppressed in femtosecond experiments for the condensed phase due to isotopic dilution). Such investigations from gas-phase chemistry enable to determine weakened or intensified Fermi resonance between OH-stretching and OH-bending motion of hydroxide radicals.

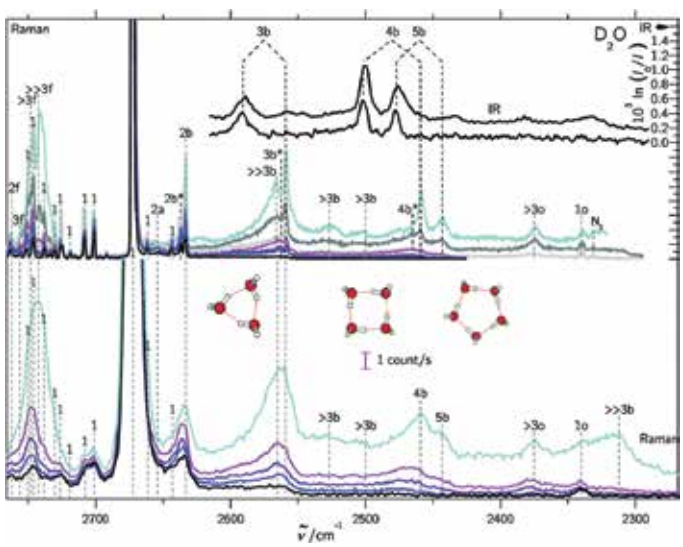

Figure 9. Raman and IR spectra of mixed D_2O/rare gas expansions. Raman spectra were scaled to the same monomer scattering intensity at the point of measurement in the respective blocks. Lower part: Raman spectra recorded using a 0.5 m monochromator. Basically, the clustering extent increases from bottom to top. Upper part: similar conditions but recorded using a 1 m monochromator. The clustering extent increases from bottom to top. Reproduced with permission from Ref. [122].

5.2. Raman scattering from monolayer-protected clusters

While expanded Raman investigations of gas-phase clusters remain a reasonable challenge, there are several publications addressing the Raman activities of monolayer-protected clusters (MPCs). Considering that the mid infrared region of the spectrum mainly reveals information about the ligand structures (e.g., C—H, N—H, O—H bond etc.) and their interactions with the metal core [123, 124], Raman spectroscopy actually has its advantages to identify low frequency vibrational modes such as S-Au-S stretching, wagging, scissoring, rocking, and twisting. These vibrations are expected to be weak in IR spectrum due to the low polarity (i.e., IR non-active) but likely prominent in the Raman spectrum (i.e., Raman active) [125, 126]. **Figure 10** presents a typical example of Au_{38} and Au_{25} MPCs, where the vibrations of two clusters containing monomeric (SR-Au-SR) and dimeric (SR-Au-SR-Au-SR) gold-thiolate staples in the metal-ligand interface are addressed. Raman activities of these clusters at different charge state with different protection ligands illustrated influences of cluster sizes and composition with respect to the monomeric and dimeric moieties [127].

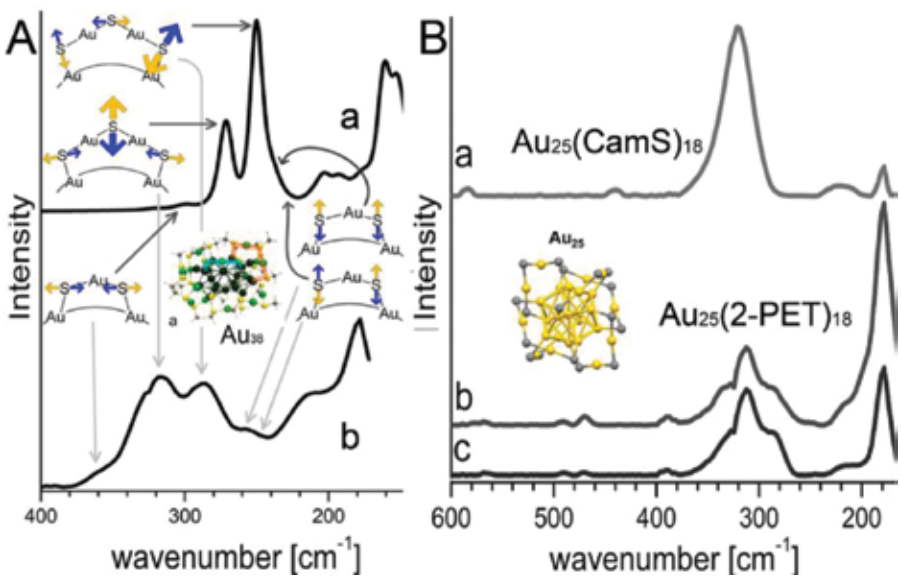

Figure 10. (A) Calculated (a) and experimental (b) Raman spectrum of the $Au_{38}(SCH_3)_{24}$ and $Au_{38}(2\text{-PET})_{24}$ cluster, respectively. The experimental spectrum is cut off at 170 cm^{-1}, the cutoff point of our optical filter. Radial and tangential Au–S modes of the staples are schematically represented. Radial vibrations of the long staples are responsible for bands with high intensity. Modes associated with the short staples (symmetric and antisymmetric stretching and tangential vibrations) have lower Raman intensity. (B) RCF-corrected Raman spectra of the low-frequency region of $Au_{25}(CamS)_{18}$ (a), $Au_{25}(2\text{-PET})_{18}^{0}$ (b), and $Au_{25}(2\text{-PET})_{18}^{-}$ (c). The clusters were measured coated on a rotating glass slide. Reproduced with permission from Ref. [127].

In addition to the small number of experimental Raman investigations of clusters, there are vast theoretical studies relating to cluster systems [128–136]. For example, utilizing time-dependent density functional theory (DFT) calculations, Chen et al. [137] conducted a detailed Raman study of pyridine adsorbed on $M@Au_{12}$ and $M@Ag_{12}$ (M = Mo, W) clusters. They found

http://dx.doi.org/10.5772/66098

that, the calculated Raman intensity of pyridine on $M@Ag_{12}$ at charge transfer (CT) transition excitations were twice as that for pyridine on $M@Au_{12}$, as shown in **Figure 11**, and the energies used for SERS excitations (in the region of 1.63–2.10 eV) were largely different from each other. Calculated interactions between the core and shell produced varying and strong CT transitions from the metal clusters to pyridine, which was demonstrated to be responsible for the altered optical properties. Also found was that, the complexes of pyridine on silver-caged clusters are largely tunable with the core compared to gold-caged clusters, providing insights to the silver and gold clusters even at the same sizes.

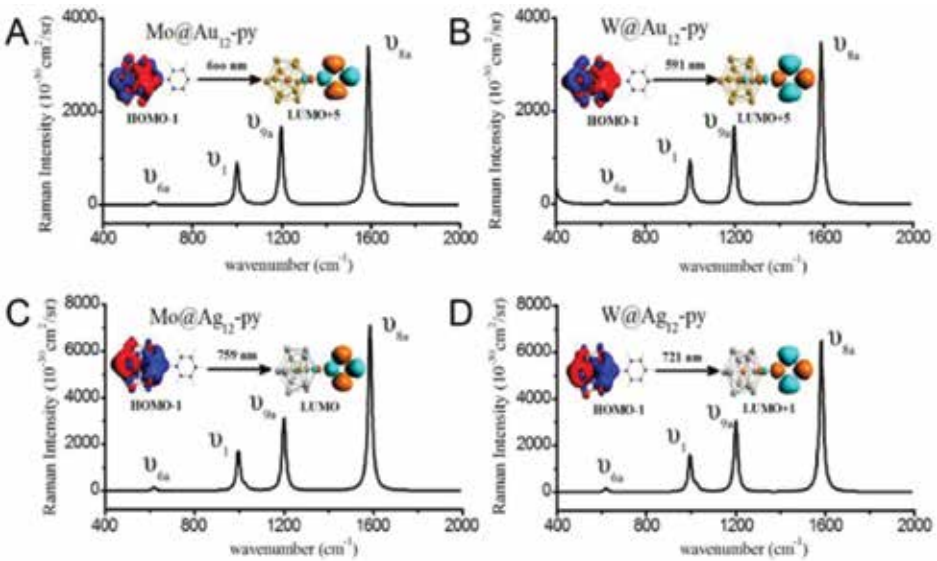

Figure 11. Raman spectra with CT excitation of the (A) $Mo@Au_{12}$-Py complex, (B) $W@Au_{12}$-Py complex, (C) $Mo@Ag_{12}$-Py complex, and (D) $W@Ag_{12}$-Py complex. Differential cross sections are in units of 10^{-30} cm^2/sr and wavenumbers are in cm^{-1}. Spectra have been broadened by a Lorentzian having a width of 20 cm^{-1}. Reproduced with permission from Ref. [137].

Regarding to the interesting CT of silver cluster with small organic molecules, recently Chen et al. [138] have given a study to the interactions between tetracyanoquinodimethane (TCNQ) and two typical silver clusters Ag_{13} and Ag_{20}, as shown in **Figure 12**. It was found that charge transfer from silver clusters to TCNQ molecules initiates the Ag—N bond formation at selective sites giving rise to different isomers of the Ag_{13}-TCNQ and Ag_{20}-TCNQ complexes. From a spectroscopic analysis for the two CT complexes mainly on Raman and infrared activities, vivid illustration of electron cloud interactions and the behavior of TCNQ adsorbed on silver clusters was comprehensively demonstrated, along with frontier molecular orbital (FMO) and natural bond orbital (NBO) patterns. The calculated Raman activity for a TCNQ molecule of Ag_{20} was found consistent with experimental Raman measurement of TCNQ molecules on single-crystal Ag(1 1 1) surface. Further efforts in this field regarding to clusters and complex molecular aggregates are expected to clarify the charge-transfer interactions within building blocks of granular materials [138–140].

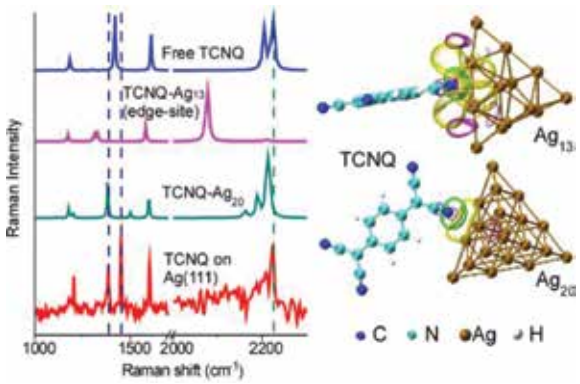

Figure 12. (Left) Raman spectra of TCNQ molecules. Calculated spectra of a free TCNQ molecule (blue, top) and surface-adsorbing Ag_{13}-TCNQ (purple) Ag_{20}-TCNQ (green) complexes; and experimental spectra of TCNQ on Ag(1 1 1) surface of silver single crystal (red).Interactions of tetracyanoquinodimethane with silver clusters Ag_{13} and Ag_{20} are demonstrated by first-principles calculations and Raman/IR spectroscopy. (Right) Natural bond orbital (NBO) donor-acceptor (overlap) interactions between N and Ag atoms in Ag (cluster)-TCNQ complexes.

6. Conclusions

In this chapter, Raman spectroscopy is demonstrated of importance in solving scientific issues relating to molecule aggregates and cluster systems profiting from its spectral fingerprints by which aggregation states, phase transition and cluster structures can be identified. Raman theory for aggregated molecules is simply introduced based on molecular exciton theory and Raman scattering enhancement at the formation of vibro-excitonic levels. Next, we summarize the research advances toward both plasmon-free Raman and SERS systems, such as aggregation-enhanced Raman scattering (AERS), resonance Raman (RR) effect from aggregation, magnetic-field trapped Raman scattering (MFTRS), shell-isolated nanoparticle-enhanced Raman scattering (SHINERS), and Raman probes for aerosols, etc. With the development of scientific instrumentation, the importance of Raman spectroscopy toward precise-sized molecule aggregates and cluster systems will be more clearly embodied, enabling to step toward interdisciplines of cluster science, molecular science, material science and surface science.

Author details

Zhixun Luo* and Jiannian Yao

*Address all correspondence to: zxluo@iccas.ac.cn

Institute of Chemistry, Chinese Academy of Sciences, Beijing, China

http://dx.doi.org/10.5772/66098

References

[1] Jayakannan, M. Probing the π-stacking induced molecular aggregation in π-conjugated polymers, oligomers, and their blends of -phenylenevinylenes. *J. Phys. Chem. B* 2008, *112*, 1119–1129.

[2] Hu, R.; Feng, J. A.; Hu, D. H.; Wang, S. Q.; Li, S. Y.; Li, Y.; Yang, G. Q. A rapid aqueous fluoride ion sensor with dual output modes. *Angew. Chem. Int. Ed.* 2010, *49*, 4915–4918.

[3] Chen, J. W.; Law, C. C. W.; Lam, J. W. Y.; Dong, Y. P.; Lo, S. M. F.; Williams, I. D.; Zhu, D. B.; Tang, B. Z. Synthesis, light emission, nanoaggregation, and restricted intramolecular rotation of 1,1-substituted 2,3,4,5-tetraphenylsiloles. *Chem. Mater.* 2003, *15*, 1535–1546.

[4] Knapp, E. W. Lineshapes of molecular aggregates, exchange narrowing and intersite correlation. *Chem. Phys.* 1984, *85*, 73–82.

[5] Fidder, H.; Knoester, J.; Wiersma, D. A. Optical properties of disordered molecular aggregates: numerical study. *J. Chem. Phys.* 1991, *95*, 7880.

[6] Davydov, A. S.: *Theory of molecular excitons*; Plenum Press: New York, 1971.

[7] Köhn, S.; Kolbe, H.; Korger, M.; Köpsel, C.; Mayer, B.; Auweter, H.; Lüddecke, E.; Bettermann, H.; Martin, H. D.: Aggregation and interface behaviour of carotenoids. In *Carotenoids: Volume 4: Natural Functions*; Britton, G., Liaaen-Jensen, S., Pfander, H., Eds.; Birkhäuser Basel: Basel, 2008; pp. 53–98.

[8] Kasha, M.; Rawls, H. R.; EI-Bayoumi, M. A. The exciton model in molecular spectroscopy. *Pure Appl. Chem.* 1965, *11*, 371–392.

[9] Davydov, A. S.: *Theory of molecular excitons*; McGraw-Hill: New York, 1962.

[10] Kasha, M. Relation between exciton bands and conduction bands in molecular lamellar systems. *Rev. Mod. Phys.* 1959, *31*, 162–169.

[11] Luo, Z.; Peng, A.; Fu, H.; Ma, Y.; Yao, J. N.; Loo, B. H. An application of AAO template: orderly assembled organic molecules for surface-enhanced Raman scattering. *J. Mater. Chem.* 2008, *18*, 133–138.

[12] Katoh, T.; Inagaki, Y.; Okazaki, R. Synthesis and properties of bismerocyanines linked by a 1,8-naphthylene skeleton. Novel solvatochromism based on change of intramolecular excitonic coupling mode. *J. Am. Chem. Soc.* 1998, *120*, 3623–3628.

[13] Zhao, L.; Yang, W.; Ma, Y.; Yao, J.; Li, Y.; Liu, H. Perylene nanotubes fabricated by the template method. *Chem. Commun.* 2003, 2442–2443.

[14] James, T. H.: *The theory of the photographic process*; Macmillan: New York, 1977.

[15] Infelta, P. P. Fluorescence quenching in micellar solutions and its application to the determination of aggregation numbers. *Chem. Phys. Lett.* 1979, *61*, 88–91.

[16] Almgren, M.; Lofroth, J. E. Determination of micelle aggregation numbers and micelle fluidities from time-resolved fluorescence quenching studies. *J. Colloid Interface Sci.* 1981, *81*, 486–499.

[17] Alargova, R. G.; Kochijashky, II; Sierra, M. L.; Zana, R. Micelle aggregation numbers of surfactants in aqueous solutions: a comparison between the results from steady-state and time-resolved fluorescence quenching. *Langmuir* 1998, *14*, 5412–5418.

[18] Ma, X.; Sun, R.; Cheng, J.; Liu, J.; Gou, F.; Xiang, H.; Zhou, X. Fluorescence aggregation-caused quenching versus aggregation-induced emission: a visual teaching technology for undergraduate chemistry students. *J. Chem. Educ.* 2016, *93*, 345–350.

[19] An, B. K.; Kwon, S. K.; Jung, S. D.; Park, S. Y. Enhanced emission and its switching in fluorescent organic nanoparticles. *J. Am. Chem. Soc.* 2002, *124*, 14410–14415.

[20] Li, S. Y.; He, L. M.; Xiong, F.; Li, Y.; Yang, G. Q. Enhanced fluorescent emission of organic nanoparticles of an intramolecular proton transfer compound and spontaneous formation of one-dimensional nanostructures. *J. Phys. Chem. B* 2004, *108*, 10887–10892.

[21] Luo, J. D.; Xie, Z. L.; Lam, J. W. Y.; Cheng, L.; Chen, H. Y.; Qiu, C. F.; Kwok, H. S.; Zhan, X. W.; Liu, Y. Q.; Zhu, D. B.; Tang, B. Z. Aggregation-induced emission of 1-methyl-1,2,3,4,5-pentaphenylsilole. *Chem. Commun.* 2001, 1740–1741.

[22] Luo, Z.; Loo, B. H.; Cao, X.; Peng, A.; Yao, J. Probing the conformational transition of 2,2′-bipyridyl under external field by surface-enhanced Raman spectroscopy. *J. Phys. Chem. C* 2012, *116*, 2884–2890.

[23] Zajac, G.; Kaczor, A.; Pallares Zazo, A.; Mlynarski, J.; Dudek, M.; Baranska, M. Aggregation-induced resonance Raman optical activity (AIRROA): a new mechanism for chirality enhancement. *J. Phys. Chem. B* 2016, *120*, 4028–4033.

[24] Pienpinijtham, P.; Han, X. X.; Ekgasit, S.; Ozaki, Y. An ionic surfactant-mediated Langmuir-Blodgett method to construct gold nanoparticle films for surface-enhanced Raman scattering. *Phys. Chem. Chem. Phys.* 2012, *14*, 10132–10139.

[25] Ostrovskii, D.; Kjoniksen, A. L.; Nystrom, B.; Torell, L. M. Association and thermal gelation in aqueous mixtures of ethyl(hydroxyethyl)cellulose and ionic surfactant: FTIR and Raman study. *Macromolecules* 1999, *32*, 1534–1540.

[26] Ma, C. X.; Harris, J. M. Surface-enhanced Raman spectroscopy detection of ionic solutes by surfactant-mediated adsorption to a hydrophobic surface. *Appl. Spectrosc.* 2013, *67*, 801–807.

[27] Gaufres, R.; Bribes, J. L.; Sportouch, S.; Ammour, J.; Maillols, J. Phase-transitions in non-ionic surfactant water-systems as studied by Raman spectrometry.2. A new methodology. *J. Raman Spectrosc.* 1988, *19*, 149–153.

[28] Cooney, R. P.; Barraclough, C. G.; Healy, T. W. Non-ionic surfactant structure in the liquid and micelle states—a Raman-spectroscopic study. *J. Phys. Chem.* 1983, *87*, 1868–1873.

[29] Wang, P.; Fu, L. M.; Zhang, J. P.; Kakitani, Y.; Ishii, H.; Nagae, H.; Koyama, Y. Strong carotenoid-to-peptide interaction immediately after triplet excitation triggering conformational changes in photo-reaction center-bound 15-cis-spheroidene as revealed by submicrosecond time-resolved Raman spectroscopy. *Chem. Phys. Lett.* 2008, *458*, 175–179.

[30] Okazaki, E.; Ito, A. Study on photo-reaction of maleimide derivatives using Raman spectroscopy. *Abstr. Pap. Am. Chem. Soc.* 2001, *222*, U312–U312.

[31] Ma, C. S.; Du, Y.; Kwok, W. M.; Phillips, D. L. Femtosecond transient absorption and nanosecond time-resolved resonance Raman study of the solvent-dependent photodeprotection reaction of benzoin diethyl phosphate. *Chem. Eur. J.* 2007, *13*, 2290–2305.

[32] Tireli, M.; Kulcsar, M. J.; Cindro, N.; Gracin, D.; Biliskov, N.; Borovina, M.; Curic, M.; Halasz, I.; Uzarevic, K. Mechanochemical reactions studied by in situ Raman spectroscopy: base catalysis in liquid-assisted grinding. *Chem. Commun. (Cambridge, U. K.)* 2015, *51*, 8058–8061.

[33] Oyama, S. T.; Zhang, W. True and spectator intermediates in catalysis: the case of ethanol oxidation on molybdenum oxide as observed by in situ laser Raman spectroscopy. *J. Am. Chem. Soc.* 1996, *118*, 7173–7177.

[34] Mazeikiene, R.; Niaura, G.; Malinauskas, A. In situ Raman spectroelectrochemical study of electrocatalytic processes at polyaniline modified electrodes: redox vs. metal-like catalysis. *Electrochem. Commun.* 2005, *7*, 1021–1026.

[35] Formo, E.; Wu, Z. L.; Mahurin, S.; Dai, S. In situ high temperature surface enhanced Raman spectroscopy study of catalysis. *Abstr. Pap. Am. Chem. Soc.* 2011, *241*.

[36] Dai, Z. G.; Xiao, X. H.; Zhang, Y. P.; Ren, F.; Wu, W.; Zhang, S. F.; Zhou, J.; Mei, F.; Jiang, C. Z. In situ Raman scattering study on a controllable plasmon-driven surface catalysis reaction on Ag nanoparticle arrays. *Nanotechnology* 2012, *23*, 335701.

[37] Luo, Z.; Cheng, X.; Luo, Y.; Loo, B. H.; Peng, A.; Yao, J. Photoassisted magnetization of fullerene C_{60} with magnetic-field trapped Raman scattering. *J. Am. Chem. Soc.* 2011, *134*, 1130–1135.

[38] Chen, J.; Ding, W.; Luo, Z.; Loo, B. H.; Yao, J. Probing single molecules and molecular aggregates: Raman spectroscopic advances. *J Raman Spectros.* 2015, n/a-n/a.

[39] Akins, D. L. Theory of Raman scattering by aggregated molecules. *J. Phys. Chem.* 1986, *90*, 1530–1534.

[40] Craig, D. P.; Thirunamachandran, R.: *Molecular quantum electrodynamics*; Academic: New York, 1984.

[41] Akins, D. L.; Akpabli, C. K.; Li, X. Surface potential dependence of enhanced Raman bands of aggregated cyanine dyes. *J. Phys. Chem.* 1989, *93*, 1977–1984.

[42] Okabayashi, H.; Yoshida, T.; Ikeda, T.; Matsuura, H.; Kitagawa, T. PO_2^- symmetric-stretching Raman line and molecular aggregation states of barium dialkyl phosphates. *J. Am. Chem. Soc.* 1982, *104*, 5399–5402.

[43] Akins L. Daniel Enhanced Raman scattering by molecular nanoaggregates. *Nanomater. Nanotechnol.* 2014, 1.

[44] Ren, B.; Tian, Z. Q.; Guo, C.; Akins, D. L. Confocal microprobe Raman spectroscopy for investigating the aggregation process at the liquid/air interface. *Chem. Phys. Lett.* 2000, *328*, 17–22.

[45] Guo, C.; Aydin, M.; Zhu, H. R.; Akins, D. L. Density functional theory used in structure determinations and Raman band assignments for pseudoisocyanine and its aggregate. *J. Phys. Chem. B* 2002, *106*, 5447–5454.

[46] Aydin, M.; Dede, O.; Akins, D. L. Density functional theory and Raman spectroscopy applied to structure and vibrational mode analysis of 1,1′,3,3′-tetraethyl-5,5′,6,6′-tetrachloro-benzimidazolocarbocyanine iodide and its aggregate. *J. Chem. Phys.* 2011, *134*.

[47] Akins, D. L.; Zhuang, Y. H.; Zhu, H. R.; Liu, J. Q. Raman excitation-spectra of exciton-phonon modes of aggregated 2,2′-cyanine using an internal Raman standard. *J. Phys. Chem.* 1994, *98*, 1068–1072.

[48] Akins, D. L.; Zhu, H. R.; Guo, C. Absorption and Raman-scattering by aggregated meso-tetrakis(p-sulfonatophenyl)porphine. *J. Phys. Chem.* 1994, *98*, 3612–3618.

[49] Akins, D. L.; Zhu, H. R.; Guo, C. Near-infrared-excited fourier-transform Raman-spectroscopic study of covalently-linked porphyrin viologen compounds. *J. Phys. Chem.* 1993, *97*, 8681–8684.

[50] Akins, D. L.; Zhu, H. R. Raman excitation-spectra of coupled intramolecular intermolecular vibronic modes of aggregated 4,4′-cyanine. *Langmuir* 1992, *8*, 546–550.

[51] Akins, D. L.; Ozcelik, S.; Zhu, H. R.; Guo, C. Aggregation-enhanced Raman scattering of a cyanine dye in homogeneous solution. *J. Phys. Chem. A* 1997, *101*, 3251–3259.

[52] Akins, D. L.; Macklin, J. W.; Parker, L. A.; Zhu, H. R. Raman excitation-spectra of aggregate modes of 2,2′-cyanine. *Chem. Phys. Lett.* 1990, *169*, 564–568.

[53] Akins, D. L.; Macklin, J. W. Dependence of Raman-scattering by aggregated 2,2′-cyanine on PH and excitation wavelength. *J. Phys. Chem.* 1989, *93*, 5999–6007.

[54] Akins, D. L.; Lombardi, J. R. Excitation wavelength dependence of enhanced Raman bands of aggregated molecules. *Chem. Phys. Lett.* 1987, *135*, 495–500.

[55] Gaufrès, E.; Tang, N. Y. W.; Lapointe, F.; Cabana, J.; Nadon, M. A.; Cottenye, N.; Raymond, F.; Szkopek, T.; Martel, R. Giant Raman scattering from J-aggregated dyes inside carbon nanotubes for multispectral imaging. *Nat. Photonics* 2013, *8*, 72–78.

[56] Kalbac, M.; Kavan, L.; Gorantla, S.; Gemming, T.; Dunsch, L. Sexithiophene encapsulated in a single-walled carbon nanotube: an in situ Raman spectroelectrochemical study of a peapod structure. *Chemistry* 2010, *16*, 11753–11759.

[57] Hasobe, T.; Fukuzumi, S.; Kamat, P. V. Ordered assembly of protonated porphyrin driven by single-wall carbon nanotubes. J- and H-aggregates to nanorods. *J. Am. Chem. Soc.* 2005, *127*, 11884–11885.

[58] Rao, A. M.; Zhou, P.; Wang, K. A.; Eklund, P. C. Photoinduced polymerization of solid C_{60} films. *Science* 1993, *259*, 952–955.

[59] Perumal, S.; Minaev, B.; Agren, H. Spin-spin and spin-orbit interactions in nanographene fragments: a quantum chemistry approach. *J. Chem. Phys.* 2012, *136*, 104702.

[60] Ferrari, A. C.; Meyer, J. C.; Scardaci, V.; Casiraghi, C.; Lazzeri, M.; Mauri, F.; Piscanec, S.; Jiang, D.; Novoselov, K. S.; Roth, S.; Geim, A. K. Raman spectrum of graphene and graphene layers. *Phys. Rev. Lett.* 2006, *97*, 187401.

[61] Graf, D.; Molitor, F.; Ensslin, K.; Stampfer, C.; Jungen, A.; Hierold, C.; Wirtz, L. Spatially resolved raman spectroscopy of single- and few-layer graphene. *Nano Lett.* 2007, *7*, 238–242.

[62] Zhou, Q.; Pang, S. F.; Wang, Y.; Ma, J. B.; Zhang, Y. H. Confocal Raman studies of the evolution of the physical state of mixed phthalic acid/ammonium sulfate aerosol droplets and the effect of substrates. *J. Phys. Chem. B* 2014, *118*, 6198–6205.

[63] Zhao, L. J.; Zeng, Q. X.; Zhang, Y. H. State of water in supersaturated nitrate aerosols disclosed by the Raman difference spectra. *J. Phys. Chem. A* 2009, *113*, 215–220.

[64] Zhao, L. J.; Wang, F.; Zhang, K.; Zeng, Q. X.; Zhang, Y. H. Deliquescence and efflorescence processes of aerosol particles studied by in situ FTIR and Raman spectroscopy. *Chin. J. Chem. Phys.* 2008, *21*, 1–11.

[65] Wang, F.; Zhang, Y. H.; Zhao, L. J.; Zhang, H.; Cheng, H.; Shou, J. J. Micro-Raman study on the conformation behavior of succinate in supersaturated sodium succinate aerosols. *Phys. Chem. Chem. Phys.* 2008, *10*, 4154–4158.

[66] Tang, M. J.; Camp, J. C. J.; Rkiouak, L.; McGregor, J.; Watson, I. M.; Cox, R. A.; Kalberer, M.; Ward, A. D.; Pope, F. D. Heterogeneous interaction of SiO_2 with N_2O_5: aerosol flow tube and single particle optical levitation-Raman spectroscopy studies. *J. Phys. Chem. A* 2014, *118*, 8817–8827.

[67] Symes, R.; Gilham, R. J. J.; Sayer, R. M.; Reid, J. P. An investigation of the factors influencing the detection sensitivity of cavity enhanced Raman scattering for probing aqueous binary aerosol droplets. *Phys. Chem. Chem. Phys.* 2005, *7*, 1414–1422.

[68] Schill, G. P.; Tolbert, M. A. Heterogeneous ice nucleation on simulated sea-spray aerosol using Raman microscopy. *J. Phys. Chem. C* 2014, *118*, 29234–29241.

[69] Gen, M.; Lenggoro, W. Probing a dip-coated layer of organic molecules by an aerosol nanoparticle sensor with sub-100 nm resolution based on surface-enhanced Raman scattering. *RSC Adv.* 2015, *5*, 5158–5163.

[70] Gaffney, J. S.; Marley, N. A.; Smith, K. J. Characterization of fine mode atmospheric aerosols by Raman microscopy and diffuse reflectance FTIR. *J. Phys. Chem. A* 2015, *119*, 4524–4532.

[71] Davies, J. F.; Wilson, K. R. Raman spectroscopy of isotopic water diffusion in ultraviscous, glassy, and gel states in aerosol by use of optical tweezers. *Anal. Chem.* 2016, *88*, 2361–2366.

[72] Craig, R. L.; Bondy, A. L.; Ault, A. P. Surface enhanced Raman spectroscopy enables observations of previously undetectable secondary organic aerosol components at the individual particle level. *Anal. Chem.* 2015, *87*, 7510–7514.

[73] Buajarern, J.; Mitchem, L.; Reid, J. P. Characterizing the formation of organic layers on the surface of inorganic/aqueous aerosols by Raman spectroscopy. *J. Phys. Chem. A* 2007, *111*, 11852–11859.

[74] Ault, A. P.; Zhao, D.; Ebben, C. J.; Tauber, M. J.; Geiger, F. M.; Prather, K. A.; Grassian, V. H. Raman microspectroscopy and vibrational sum frequency generation spectroscopy as probes of the bulk and surface compositions of size-resolved sea spray aerosol particles. *Phys. Chem. Chem. Phys.* 2013, *15*, 6206–6214.

[75] Arunagirinathan, M. A.; Roy, M.; Dua, A. K.; Manohar, C.; Bellare, J. R. Micro-Raman investigations of myelins in aerosol-OT/water system. *Langmuir* 2004, *20*, 4816–4822.

[76] Aker, P. M.; Zhang, J. X.; Nichols, W. Nitrate ion detection in aerosols using morphology-dependent stimulated Raman scattering. *J. Chem. Phys.* 1999, *110*, 2202–2207.

[77] Aggarwal, R. L.; Di Cecca, S.; Farrar, L. W.; Jeys, T. H. Chemical aerosol detection and identification using Raman scattering. *J. Raman Spectrosc.* 2014, *45*, 677–679.

[78] Batonneau, Y.; Sobanska, S.; Laureyns, J.; Bremard, C. Confocal microprobe Raman imaging of urban tropospheric aerosol particles. *Environ. Sci. Technol.* 2006, *40*, 1300–1306.

[79] An, P.; Yuan, C. Q.; Liu, X. H.; Xiao, D. B.; Luo, Z. X. Vibrational spectroscopic identification of isoprene, pinenes and their mixture. *Chin. Chem. Lett.* 2016, *27*, 527–534.

[80] King, M. D.; Thompson, K. C.; Ward, A. D. Laser tweezers Raman study of optically trapped aerosol droplets of Seawater and oleic acid reacting with ozone: implications for cloud-droplet properties. *J. Am. Chem. Soc.* 2004, *126*, 16710–16711.

[81] Buehler, M. F.; Allen, T. M.; Davis, E. J. Microparticle Raman-spectroscopy of multicomponent aerosols. *J. Colloid Interface Sci.* 1991, *146*, 79–89.

[82] Xu, G.; Fang, Y. Studies of surface-enhanced Raman scattering of C60 Langmuir–Blodgett film on a new substrate. *Spectrochim. Acta A* 2008, *70*, 104–108.

[83] Wu, L. X.; Xu, W. Q.; Qin, L. D.; Wang, C. S. Self-assembly and Langmuir-Blodgett (LB) film of a novel hydrogen-bonded complex: a surface enhanced Raman scattering (SERS) study. *Colloid Surf. A* 2002, *198-200*, 135–140.

[84] Wu, S. X.; Huang, J. G.; Li, C.; Liang, Y. Q. Fourier transform surface-enhanced Raman scattering of single-layer nucleolipid Langmuir-Blodgett films on silver island film substrates. *J. Colloid Interface Sci.* 2004, *270*, 309–314.

[85] Constantino, C. J. L.; Aroca, R. F.; Mendonca, C. R.; Mello, S. V.; Balogh, D. T.; Oliveira, O. N. Surface enhanced fluorescence and Raman imaging of Langmuir-Blodgett azopolymer films. *Spectrochim. Acta A* 2001, *57*, 281–289.

[86] Siu, G. G.; Yulong, L.; Shishen, X.; Jingmei, X.; Tiankai, L.; Linge, X. Surface-enhanced Raman spectroscopy of monolayer C_{60} Langmuir-Blodgett films. *Thin Solid Films* 1996, *274*, 147–149.

[87] Puggelli, M.; Ricceri, R.; Gabrielli, G. SERS and molecular orientation in Langmuir-Blodgett films deposited onto smooth copper surfaces. *Langmuir* 1996, *12*, 4417–4420.

[88] Urai, Y.; Itoh, K. Surface-enhanced photopolymerization of a diacetylene derivative in Langmuir-Blodgett films on a silver island film. *J. Phys. Chem. B* 1998, *102*, 3765–3772.

[89] Constantino, C. J. L.; Aroca, R. F. Surface-enhanced resonance Raman scattering imaging of Langmuir-Blodgett monolayers of bis(benzimidazo)perylene on silver island films. *J. Raman Spectrosc.* 2000, *31*, 887-890.

[90] Masuda, H.; Fukuda, K. Ordered metal nanohole arrays made by a 2-step replication of honeycomb structures of anodic alumina. *Science* 1995, *268*, 1466–1468.

[91] Masuda, H.; Asoh, H.; Watanabe, M.; Nishio, K.; Nakao, M.; Tamamura, T. Square and triangular nanohole array architectures in anodic alumina. *Adv. Mater.* 2001, *13*, 189–192.

[92] Han, F.; Meng, G.; Xu, Q.; Zhu, X.; Zhao, X.; Chen, B.; Li, X.; Yang, D.; Chu, Z.; Kong, M. Alumina-sheathed nanocables with cores consisting of various structures and materials. *Angew. Chem. Int. Ed.* 2011, *50*, 2036–2040.

[93] Luo, Z.; Liu, Y.; Kang, L.; Wang, Y.; Fu, H.; Ma, Y.; Yao, J.; Loo, B. H. Controllable nanonet assembly utilizing a pressure-difference method based on anodic aluminum oxide templates. *Angew. Chem. Int. Ed.* 2008, *47*, 8905–8908.

[94] Luo, Z.; Yang, W.; Peng, A.; Ma, Y.; Fu, H.; Yao, J. The fabrication of TiO_2 nanorods from TiO_2 nanoparticles by organic protection assisted template method. *Nanotechnology* 2009, *20*, 345601.

[95] Luo, Z.; Fang, Y. Structural influence on Raman scattering of a new C_{60} thin film prepared by AAO template with the method of pressure difference. *J. Comb. Chem.* 2006, *8*, 500–504.

[96] Luo, Z.; Fang, Y.; Zhang, P. Surface enhanced raman scattering of gold/c60 (/c70) nanoclusters deposited on AAO nano-sieve. *Vib. Spectrosc.* 2006, *41*, 37-41.

[97] Luo, Z.; Yang, W.; Peng, A.; Ma, Y.; Fu, H.; Yao, J. Net-like assembly of au nanoparticles as a highly-active substrate for surface enhanced Raman and infrared spectroscopy. *J. Phys. Chem. A* 2009, *113*, 2467–2472.

[98] Luo, Z.; Loo, B. H.; Yao, J.: Uniformly-assembled metal nanoparticles on anodic aluminum oxide (AAO) applied in surface-enhanced Raman spectroscopy. In *MRS Spring Meeting*: San Francisco, California, 2011.

[99] Luo, Z.; Zhao, Y.; Yang, W.; Peng, A.; Ma, Y.; Fu, H.; Yao, J. Core-shell nanopillars of fullerene C_{60}/C_{70} loading with colloidal Au nanoparticles:A Raman scattering investigation. *J. Phys. Chem. A* 2009, *113*, 9612–9616.

[100] Liu, J.; White, I.; DeVoe, D. L. Nanoparticle-functionalized porous polymer monolith detection elements for surface-enhanced Raman scattering. *Anal. Chem.* 2011, *83*, 2119–2124.

[101] Peters, E. C.; Svec, F.; Frechet, J. M. J. Rigid macroporous polymer monoliths. *Adv. Mater.* 1999, *11*, 1169–1181.

[102] Fu, H.; Xiao, D.; Yao, J.; Yang, G. Nanofibers of 1,3-diphenyl-2-pyrazoline induced by cetyltrimethylammonium bromide micelles. *Angew. Chem. Int. Ed.* 2003, *42*, 2883–2886.

[103] Tian, Z. Q.; Ren, B.; Li, J. F.; Yang, Z. L. Expanding generality of surface-enhanced Raman spectroscopy with borrowing SERS activity strategy. *Chem. Commun.* 2007, 3514–3534.

[104] Park, S.; Yang, P.; Corredor, P.; Weaver, M. J. Transition metal-coated nanoparticle films: vibrational characterization with surface-enhanced Raman scattering. *J. Am. Chem. Soc.* 2002, *124*, 2428–2429.

[105] Tian, Z. Q.; Ren, B. Adsorption and reaction at electrochemical interfaces as probed by surface-enhanced Raman spectroscopy. *Annu. Rev. Phys. Chem.* 2004, *55*, 197–229.

[106] Park, W. H.; Kim, Z. H. Charge transfer enhancement in the SERS of a single molecule. *Nano Lett.* 2010, *10*, 4040–4048.

[107] Chen, K.; Leona, M.; Vo-Dinh, T. Surface-enhanced Raman scattering for identification of organic pigments and dyes in works of art and cultural heritage material. *Sens. Rev.* 2007, *27*, 109–120.

[108] Chen, K.; Vo-Dinh, K. C.; Yan, F.; Wabuyele, M. B.; Vo-Dinh, T. Direct identification of alizarin and lac dye on painting fragments using surface-enhanced Raman scattering. *Anal. Chim. Acta* 2006, *569*, 234–237.

[109] Jurasekova, Z.; Domingo, C.; Garcia-Ramos, J. V.; Sanchez-Cortes, S. In situ detection of flavonoids in weld-dyed wool and silk textiles by surface-enhanced Raman scattering. *J. Raman Spectrosc.* 2008, *39*, 1309–1312.

[110] Brosseau, C. L.; Gambardella, A.; Casadio, F.; Van Duyne R. P.; Grzywacz, C. M.; Wouters, J. Ad-hoc surface-enhanced Raman spectroscopy methodologies for the detection of artist dyestuffs: thin layer chromatography-surface enhanced raman spectroscopy and in situ on the fiber analysis. *Anal. Chem.* 2009, *81*, 3056–3062.

[111] Wustholz, K. L.; Brosseau, C. L.; Casadio, F.; Van Duyne, R. P. Surface-enhanced Raman spectroscopy of dyes: from single molecules to the artists' canvas. *Phys. Chem. Chem. Phys.* 2009, *11*, 7350–7359.

[112] Luo, Z.; Smith, J. C.; Goff, T. M.; Adair, J. H.; Castleman, A. W., Jr. Gold cluster coatings enhancing Raman scattering from surfaces: ink analysis and document identification. *Chem. Phys.* 2013, *423*, 73–75.

[113] Anema, J. R.; Li, J. F.; Yang, Z. L.; Ren, B.; Tian, Z. Q.: Shell-isolated nanoparticle-enhanced raman spectroscopy: expanding the versatility of surface-enhanced Raman scattering. In *Annu. Rev. Anal. Chem.*; Cooks, R. G., Yeung, E. S., Eds.; Annual Review of Analytical Chemistry; Annual Reviews: Palo Alto, 2011; Vol. 4; pp. 129–150.

[114] Li, J. F.; Huang, Y. F.; Ding, Y.; Yang, Z. L.; Li, S. B.; Zhou, X. S.; Fan, F. R.; Zhang, W.; Zhou, Z. Y.; Wu, D. Y.; Ren, B.; Wang, Z. L.; Tian, Z. Q. Shell-isolated nanoparticle-enhanced Raman spectroscopy. *Nature* 2010, *464*, 392–395.

[115] Moskovits, M. Surface-enhanced spectroscopy. *Rev. Mod. Phys.* 1985, *57*, 783–826.

[116] Kneipp, K.; Moskovits, M.; Kneipp, H.: *Surface-enhanced Raman scattering: physics and applications*; Springer: Berlin & New York, 2006; Vol. 103.

[117] Wu, D. Y.; Li, J. F.; Ren, B.; Tian, Z. Q. Electrochemical surface-enhanced Raman spectroscopy of nanostructures. *Chem. Soc. Rev.* 2008, *37*, 1025–1041.

[118] Luo, Z.; Fang, Y. Progress in application of surface enhanced Raman scattering spectrum technique. *Spectrosc. Spectral Anal.* 2006, *26*, 358–364.

[119] Wuelfert, S.; Herren, D.; Leutwyler, S. Reply to "The intramolecular fundamentals of the water dimer". *J. Chem. Phys.* 1988, *88*, 52–56.

[120] Wuelfert, S.; Herren, D.; Leutwyler, S. Supersonic jet CARS spectra of small water clusters. *J. Chem. Phys.* 1987, *86*, 3751.

[121] Nelander, B. The intramolecular fundamentals of the water dimer. *J. Chem. Phys.* 1988, *88*, 5254.

[122] Otto, K. E.; Xue, Z.; Zielke, P.; Suhm, M. A. The Raman spectrum of isolated water clusters. *Phys. Chem. Chem. Phys.* 2014, *16*, 9849–9858.

[123] Farrag, M.; Tschurl, M.; Dass, A.; Heiz, U. Infra-red spectroscopy of size selected Au25, Au38 and Au144 ligand protected gold clusters. *Phys. Chem. Chem. Phys.* 2013, *15*, 12539–12542.

[124] Petroski, J.; Chou, M.; Creutz, C. The coordination chemistry of gold surfaces: formation and far-infrared spectra of alkanethiolate-capped gold nanoparticles. *J. Organomet. Chem.* 2009, *694*, 1138–1143.

[125] Levin, C. S.; Janesko, B. G.; Bardhan, R.; Scuseria, G. E.; Hartgerink, J. D.; Halas, N. J. Chain-length-dependent vibrational resonances in alkanethiol self-assembled monolayers observed on plasmonic nanoparticle substrates. *Nano Lett.* 2006, *6*, 2617–2621.

[126] Burgi, T. Properties of the gold-sulphur interface: from self-assembled monolayers to clusters. *Nanoscale* 2015, *7*, 15553–15567.

[127] Varnholt, B.; Oulevey, P.; Luber, S.; Kumara, C.; Dass, A.; Bürgi, T. Structural information on the Au–S interface of thiolate-protected gold clusters: a Raman spectroscopy study. *J. Phys. Chem. C* 2014, *118*, 9604–9611.

[128] Yasuike, T.; Nobusada, K. Raman enhancement by plasmonic excitation of structurally-characterized metal clusters: Au8, Ag8, and Cu8. *Phys. Chem. Chem. Phys.* 2013, *15*, 5424–5429.

[129] Tomas, M.; Tinti, A.; Bofill, R.; Capdevila, M.; Atrian, S.; Torreggiani, A. Comparative Raman study of four plant metallothionein isoforms: insights into their Zn(II) clusters and protein conformations. *J. Inorg. Biochem.* 2016, *156*, 55–63.

[130] Su, J. P.; Lee, Y. T.; Lu, S. Y.; Lin, J. S. Chemical mechanism of surface-enhanced Raman scattering spectrum of pyridine adsorbed on Ag cluster: ab initio molecular dynamics approach. *J. Comput. Chem.* 2013, *34*, 2806–2815.

[131] Siebert, E.; Rippers, Y.; Frielingsdorf, S.; Fritsch, J.; Schmidt, A.; Kalms, J.; Katz, S.; Lenz, O.; Scheerer, P.; Paasche, L.; Pelmenschikov, V.; Kuhlmann, U.; Mroginski, M. A.; Zebger, I.; Hildebrandt, P. Resonance Raman spectroscopic analysis of the [NiFe] active site and the proximal [4Fe-3S] cluster of an O_2-tolerant membrane-bound hydrogenase in the crystalline state. *J. Phys. Chem. B* 2015, *119*, 13785–13796.

[132] Schmidt, M.; Fernandez, J. M.; Faruk, N.; Nooijen, M.; Le Roy, R. J.; Morilla, J. H.; Tejeda, G.; Montero, S.; Roy, P. N. Raman vibrational shifts of small clusters of hydrogen isotopologues. *J. Phys. Chem. A* 2015, *119*, 12551–12561.

[133] Santos, J. J.; Ando, R. A.; Toma, S. H.; Corio, P.; Araki, K.; Toma, H. E. Surface enhanced Raman spectroelectrochemistry of a mu-oxo triruthenium acetate cluster: an experimental and theoretical approach. *Inorg. Chem.* 2015, *54*, 9656–9663.

[134] Rudolph, W. W.; Fischer, D.; Tomney, M. R.; Pye, C. C. Indium(III) hydration in aqueous solutions of perchlorate, nitrate and sulfate. Raman and infrared spectroscopic studies and ab-initio molecular orbital calculations of indium(III)-water clusters. *Phys. Chem. Chem. Phys.* 2004, *6*, 5145–5155.

[135] Pradhani, A.; Halder, O.; Nozaki, S.; Rath, S. Raman modes, dipole moment and chirality in periodically positioned Au8clusters. *RSC Adv.* 2015, *5*, 65208–65213.

http://dx.doi.org/10.5772/66098

[136] Faruk, N.; Schmidt, M.; Li, H.; Le Roy, R. J.; Roy, P. N. First-principles prediction of the Raman shifts in parahydrogen clusters. *J. Chem. Phys.* 2014, *141*, 014310.

[137] Chen, L.; Gao, Y.; Cheng, Y.; Su, Y.; Wang, Z.; Li, Z.; Zhang, R. Q. Strong core@shell dependence in surface-enhanced Raman scattering of pyridine on stable 13-atom silver-caged bimetallic clusters. *J. Phys. Chem. C* 2015, *119*, 17429–17437.

[138] Chen, J.; Zhang, H.; Liu, X.; Yuan, C.; Jia, M.; Luo, Z.; Yao, J. Charge-transfer interactions between TCNQ and silver clusters Ag_{20} and Ag_{13}. *Phys. Chem. Chem. Phys.* 2016, *18*, 7190–7196.

[139] Luo, Z.; Reber, A. C.; Jia, M.; Blades, W. H.; Khanna, S. N.; Castleman, A. W. What determines if a ligand activates or passivates a superatom cluster? *Chem. Sci.* 2016, *7*, 3067–3074.

[140] Chen, J.; Luo, Z.; Yao, J. Theoretical study of tetrahydrofuran-stabilized Al_{13} superatom cluster. *J. Phys. Chem. A* 2016, *120*, 3950–3957.

Chapter 3

Raman Mapping: Emerging Applications

Cristina Coman and Loredana Florina Leopold

Additional information is available at the end of the chapter

http://dx.doi.org/10.5772/66097

Abstract

Raman mapping is a noninvasive, label-free technique with high chemical specificity and high potential to become a leading method in biological and biomedical applications. As opposed to Raman spectroscopy, which provides discrete chemical information at distinct positions within the sample, Raman mapping provides chemical information coupled with spatial information. The laser spot scans the investigated sample area with a preset step size and acquires Raman spectra pixel by pixel. The Raman spectra are then discriminated from each other by chemometric analysis, and the end result is a false color map, an image of the sample that contains highly precise structural and chemical information. Raman imaging has been successfully used for label-free investigations at cellular and subcellular level. Cell compartments, cell responses to drugs and different stages of the cell cycle from the stem cell to the completely differentiated cell were successfully distinguished. This technique is also able to differentiate between healthy and cancer cells, indicating great potential for replacing conventional cancer detection tools with Raman detection in the future.

Keywords: Raman spectroscopy, Raman mapping, Raman imaging, cells, tissues, medical diagnosis, plants, algae

1. Introduction

1.1. Basic concept and working principle

Various techniques are being currently used for imaging of cells and tissues. Individually, each technique is able to address some aspects of the system under study. For example, optical microscopy is very often used for cell and tissue analysis; it is a cost-effective method which gives morphological information, but is unable to provide molecular and structural

information. Electron microscopy and atomic force microscopy are high spatial resolution techniques, able to image subcellular compartments; however, they lack chemical specificity. In most cases, fluorescence microscopy, for example, confocal scanning fluorescence microscopy, is used for cellular visualization. Fluorescence microscopy requires fluorescent labels specifically bound to the substrate under study. Subcellular structures can be visualized, but since each fluorescent label is excited by a different wavelength, the number of structures that can be visualized is limited. The need to introduce fluorophores and their limited stability and photo bleaching are drawbacks of using confocal microscopy. Nonetheless, the technique is largely used for cell imaging and imaging of cellular uptake of micro and nanoparticles. There is great need for techniques that provide chemically specific information coupled to spatial information for the visualization of, for example, cellular uptake and localization of biologically active molecules, cellular transport pathways, molecular changes in cancer vs healthy tissues, etc.

Raman mapping (Raman imaging, Raman scanning or Raman micro-spectroscopy) has recently become an emerging imaging technique in biological and biomedical research and applications. The Raman effect is based on inelastic scattering of photons when electromagnetic waves interact with atoms or molecules. The small fraction of incident photons scattered inelastically have different frequencies compared to the incident photons. The phenomenon is called Raman scattering, and the difference in frequency between the incident photons and scattered photons is the so-called Raman shift (cm^{-1}). The Raman shift is related to the vibrational levels of each specific molecule, being used as a fingerprint for molecular identification [1].

In contrast to Raman spectroscopy, which provides discrete chemical information at distinct positions within the sample, Raman mapping provides chemical information coupled with spatial information [2]. Raman mapping is a noninvasive, label-free technique, with high chemical specificity. In Raman mapping, the laser spot scans the investigated sample area with a preset step size and acquires Raman spectra at every set point. The Raman spectra are then discriminated from each other by chemometric analysis, and the end result is an image of the sample that contains highly precise structural and chemical information. Excitation wavelengths in the visible and near-infrared range give high spatial resolution (<1 μm), making Raman spectroscopy combined with microscopy an ideal tool for biological samples imaging, and especially for cell and tissue imaging. In this latter case, Raman mapping has important advantages over conventional biological assays: it is a rapid, noninvasive, label-free technique, which does not damage the cells if using suitable laser wavelengths and power.

1.2. Instrumentation and data analysis

The most important parameters to ensure the success of a Raman imaging measurement on biological samples are the wavelength and power of the laser, the resolution of the images, and the sample preparation and fixation. The intensity of the scattered radiation is proportional to the wavelength at the power of −4 ($\sim\lambda^{-4}$), meaning that shorter (blue) wavelengths are scattered more strongly than longer (red) wavelengths. Thus, shorter wavelengths generate more photons scattered inelastically, giving thus higher Raman intensities. However, shorter wavelengths typically lead to stronger auto-fluorescence from the samples, which can mask

http://dx.doi.org/10.5772/66097

the Raman signal arising from the molecules of interest. Therefore, a compromise is needed. Hamada et al. studied the influence of 488, 514.5, 532 and 632.8 nm laser excitation wavelengths on the Raman signal yield and background signal for the imaging of living cells [3]. The authors found that the 532 nm excitation is a good compromise between Raman signal intensity and auto-fluorescence background because it generates strong Raman scattering signals and suppresses auto-fluorescence. Photodamage caused by light absorption of the biological samples is another important parameter to be considered for choosing the appropriate laser excitation. Puppels et al. [4] found that a 660 nm laser induces no photodamage to cells and chromosomes compared to the 514.5 nm (visible) laser. Even though Raman scattering efficiency decreases with increasing wavelength, recent advances in the design of Raman spectrometers with high optical throughput and highly sensitive CCD (charge-coupled device) detectors allow measuring spectra and obtaining reasonably high signal strength. Notingher et al. used a 785 nm laser for their measurements on live cells and tissues [5–7]. In one study, they compared the 488, 514 and 785 nm lasers with respect to photodamage of cells and found that the 488 and 514 nm lasers induce photodegradation and reduce the number of living cells; with the 785 laser, cell degradation and auto-fluorescence were low and the signal intensity was reasonably high [8]. Even though going higher than 785 nm (e.g., 1064 nm) in the laser wavelength would decrease the photodamage of the cells, it would also dramatically decrease the Raman scattering efficiency. The recent literature mentions mostly the use of 785 and 532 nm lasers for cellular mapping [6, 9]. However, when using near-infrared (NIR) lasers for Raman excitation, cooled deep depletion back-illuminated CCD detectors are preferred [6] instead of standard back-illuminated, visible-optimized CCDs, because of their higher quantum efficiencies (QE) in the near-infrared (NIR) spectral region (up to 95% with the new Low Dark Current Deep-Depletion (LDC-DD) Technology.

In some cases, for samples that cannot be detected by regular Raman scattering, signal enhancement can be induced. In some situations, it is possible to obtain resonance Raman effects. Such effects take place when the laser excitation wavelength overlaps with the absorption band of the molecules due to electronic transitions, and this can lead to increase the Raman intensity by a factor of 103–105 [1]. The phenomenon is called resonant Raman scattering. Consequently, Raman imaging of a resonant molecule can be significantly improved by choosing an excitation laser wavelength in the absorption band region of the molecule. For example, cytochrome C absorbs light at around 520 nm and shows a strong resonance Raman effect when analyzed using a 532 nm laser. This property can be used to image its intracellular distribution. Other examples of molecules that can benefit from strong Raman resonance effects are the carotenoids, chlorophylls, vitamin B12 and heme proteins [3, 10].

Another way to obtain signal enhancement in Raman spectroscopy is to use surface-enhanced Raman spectroscopy (SERS) or coherent anti-Stokes Raman scattering (CARS). In SERS, it is possible to reach high enhancements of the Raman intensity (by a factor of 10^7 or more) when the molecule of interest is adsorbed onto or in the very close vicinity of plasmonic metallic nanostructures such as silver and gold [11]. This effect significantly lowers the detection limit of molecules. CARS is a nonlinear optical effect in which two lasers, a pump laser and a Stoke laser, are overlapped and strongly focused onto the sample to generate the CARS signal. When

the difference in frequency between the pump and the Stoke lasers is tuned to the exact value of a vibrational frequency within the sample, strong enhancements of the CARS signal can occur [1].

The instrumental resolution is very important for cell and tissue mapping, in order to be able to image cellular and subcellular structures. The lateral resolution is limited by the wavelength of the laser and the numerical aperture of the objective used for the experiment, while the axial resolution is given by the instrument aperture (slit or pinhole) and the refractive index of the immersion medium. Currently available Raman spectrometers can go down to 200 nm for the lateral resolution and 500 nm for the axial resolution [2].

Cells and tissues could be fixed on specific substrates for usage over longer periods of time. The most important requirements for a substrate suitable for Raman imaging are as follows: (a) transparency in the visible and near-infrared region of the light spectrum; (b) low background signal to avoid overlapping with the Raman signals from the sample; and (c) suitability for cell culture growth or tissue fixation. Calcium and magnesium fluoride (CaF_2 and MgF_2) and quartz are the preferred substrates for Raman imaging. Glass and plastic substrates are not recommended because of high background signals [2, 12]. Zinc selenide (ZnSe) has the disadvantage of weak cell adherence [12]. A variety of cell fixation methods has been so far reported can be used: paraformaldehyde, methanol, methanol:acetone, formalin, air-drying and cytocentrifugation [2, 6, 13]. For live cell imaging, special instrument setups, in which cells are confined in a sterile chamber and kept at 37°C and a 5% CO_2 atmosphere to ensure viability [14, 15], have been reported.

After taking the pixel-by-pixel Raman spectra, the raw dataset needs to be processed in order to identify the key molecules in the sample and based on their spectral fingerprint, to generate the false color Raman images. Since no label is used, the pixel-to-pixel spectral variations are small and multivariate methods of analysis need to be employed to get the Raman images from the dataset. Several approaches are currently used: principal component analysis (PCA), self-modeling curve resolution (SMCR), K-means cluster analysis (KMCA), hierarchical cluster analysis (HCA), divisive correlation cluster analysis (DCCA), vertex component analysis (VCA), fuzzy C-means cluster analysis (FCCA) and linear discriminant analysis (LDA) [6, 16–20].

Here we aim to highlight the recent advances of Raman mapping and provide an overview on its emerging applications, which range from single cell and tissue imaging to medical diagnosis, including cancer detection. Some applications that will be discussed include:

- Stem cell research, especially stem cell differentiation [6, 21–23]
- Single cell and microorganism imaging [2, 18, 24, 25], including evidentiation of subcellular compartments [23]
- Identification of cell cycle phase [26]
- Monitoring of cell death [27, 28]
- Cellular responses to drugs [9]

- Imaging of intracellular localization of bioactive molecules and drug carriers such as colloidal nanostructures, liposomes and polymeric particles [2, 29, 30]
- Imaging of tissue physiology [31, 32]
- Medical diagnosis, including cancer detection based on the capacity of Raman mapping to detect molecular changes in cells, tissues or biofluids, that are either the cause or the effect of diseases [7, 33, 34]
- Intraoperative detection of tumor margins [7, 35]
- Cancer detection based on the ability to discriminate between normal and cancer cells [36]

2. Raman mapping for cell imaging

Several Raman peaks are used as fingerprints for the intracellular identification of nucleic acids, proteins and lipid-rich structures. In terms of chemical information, the richest part in a Raman spectrum is the region below 1800 cm^{-1}, also called the fingerprint region. Some representative Raman bands from the fingerprint region, characteristic for nucleic acids, proteins and lipids, are given in **Table 1** [6, 37, 38]. The region between 1800 and 2800 cm^{-1} is the so-called silent region, since no Raman cellular vibrations arising from functional groups appear in this region, excepting triple-bond vibrations. Finally, the high-frequency region above 2800 cm^{-1} is dominated by C–H stretching vibrations (CH, CH_2, CH_3).

Stem cells are attractive to be studied in the biomedical field because they have the ability to differentiate into any cell phenotype, and they can proliferate indefinitely [39]. Differentiation of stem cells could be used in stem cell therapy and tissue engineering. The differentiation process of stem cells needs identification of specific markers; currently, this involves the use of immunolabeling or fluorescence. Both methods have the disadvantage of being invasive. In contrast, using Raman-specific intrinsic fingerprints would be advantageous, being noninvasive, nonlabeling approach, and able to provide accurate and highly specific information. The method would be suitable also for cells that lack specific markers for separation by conventional means [21] such as cardiomyocytes.

The intracellular distribution and concentration of nucleic acids were used by Ghita et al. [6] to distinguish between undifferentiated and differentiated stem cells, more precisely from undifferentiated neural stem cells and the glial cells derived from them. They manage to differentiate with 89.4% sensitivity and 96.4% specificity. The spectral fingerprint of the nucleic acid backbone was used to detect DNA- and RNA-rich regions. The Raman spectrum of β-DNA shows a strong band at 788 cm^{-1} and a shoulder at 835 cm^{-1}, characteristic to the symmetric O-P-O stretching vibrations of the phosphate groups and to the asymmetric O-P-O vibrations, respectively. In case of RNA, the symmetric O-P-O vibrations appear shifted to 813 cm^{-1}, while the shoulder corresponding to the asymmetric O-P-O stretching disappears. Based on the spectral differences between DNA and RNA, it was found that undifferentiated neural cells have higher concentration of nucleic acids compared to glial cells. The Ram-

Raman peak position (cm^{-1})	Assignments
	Nucleic acid bands
684	Guanine ring breathing
729	Adenine ring breathing
751	Thymine ring breathing
782	Uracil ring breathing
785	Cytosine ring breathing
788	Symmetric O-P-O stretching in β-strands DNA
835	Asymmetric O-P-O stretching in β-strands DNA
813	Symmetric O-P-O stretching in RNA and α-strands DNA
1095–1098	O-P-O vibrations (DNA, RNA)
	Protein bands
938	Backbone C=C stretching
1005	Phenylalanine symmetric ring breathing
1033	Phenylalanine in plane C–H vibrations
1200–1300	Amide III band (CH, NH deformations)
1655–1662	Amide I (C=O stretching)
	Lipid bands
980	=C–H bending
1093	C–C stretching
1257	=C–H bending
1450	C–H deformation
1658	C=C stretching

Table 1. Some of the most representative Raman peaks for nucleic acids, proteins and lipids in cells.

an band at 813 cm^{-1} was the indicator of the differentiation status, and this allowed distinguishing between the two cell types. Undifferentiated neural stem cells have high concentration of RNA in the cytoplasm (as high as 4 mg/ml), while below the instrument detection limit (<1 mg/ml) in the glial cells. Based on Raman mapping, it was possible to image RNA- and DNA-rich structures in the stem cells. The RNA-rich structures, representing the stem cells cytoplasm, were imaged using the 813 cm^{-1} Raman band, and the DNA-rich part related to the stem cells nucleus was imaged using the 788 cm^{-1} Raman band. Similar results were reported by the same research group regarding the differentiation status of embryonic stem cells [22]. The differentiated cells had 75% less RNA, as monitored by the decrease in intensity of the 813 cm^{-1} peak. Basically, most prominent Raman peaks of embryonic stem cells are the ones of proteins (amide I band at 1660 cm^{-1}, amide III at 1200–1300 cm^{-1}, 1005 cm^{-1} vibration of phenylalanine and C=C stretching at 938 cm^{-1}) and nucleic acids. Dental follicle mesenchymal stem cells were also imaged using Raman mapping; several compo-

http://dx.doi.org/10.5772/66097

nents, and especially a high concentration of cytoplasmic RNA, were found to be a good indicator to the undifferentiated status of the cells [40].

Raman mapping was also used inside a bioreactor culture system, where human embryonic stem cells were grown and differentiated into cardiomyocytes [41]. The purpose was to monitor the cardiac differentiation of the embryonic bodies. The Raman maps were compared with immunofluorescence imaging. A positive correlation was found between Raman bands at 1340, 1083, 937, 858, 577 and 482 cm^{-1} and the expression of the α-actinin protein in the differentiated cardiomyocytes. Konorov et al. [26] obtained information on the cell cycle phase of human embryonic stem cells. The 783 cm^{-1} DNA band from a large number of cell nuclei was used as indicator of the cell cycle phase. The results were corrected for the RNA contribution at 811 cm^{-1}. As such, the authors were able to get information on the state of division of the embryonic stem cells by quantifying the DNA and RNA peaks from the Raman spectra and obtained Raman intensities similar to the fluorescence intensities of flow cytometry.

In another study, Pascut et al. [42] obtained 97% specificity and 96% sensitivity in differentiating the cardiomyocytes derived from human embryonic stem cells. The main spectral features that allowed the discrimination of cardiomyocytes were attributed to glycogen and myofibrils. The results were correlated with the immunofluorescence staining, and a good correlation was observed. The same authors investigated the potential for developing Raman-activated cell sorting of individual cells [43]. Hashimoto et al. [44] got information on osteoblast differentiation and mineralization mechanisms by monitoring fluctuations in the cytochrome C concentration. The above preliminary studies suggest that Raman spectroscopy has a great potential to become a leading method for stem cells investigation.

Raman mapping can be used as a tool to obtain molecular fingerprint information from different subcellular compartments. Based on their distinct chemical features, nucleus and cytoplasm and also other cellular organelles can be imaged. For example, in their study on follicle mesenchymal stem cells, Leopold et al. [40] were able to image the cell nucleus based on the 785 cm^{-1} band characteristic for the DNA O-P-O vibrations. Lipid characteristic peaks, such as the 1446 cm^{-1} peak characteristic to CH_2 vibrations, made it possible to highlight the smooth endoplasmic reticulum in the Raman images, which is known to be the source of intracellular lipid synthesis. Based on characteristic Raman vibrational peaks of lipids, proteins and nucleic acids, Krafft et al. [45] were able to reconstruct the main cellular components: the nucleus, the contour of the cell and the organelles. They focused mostly on the 2800–3000 cm^{-1} region, where CH_2 and CH_3 vibrations from proteins, lipids and nucleic acids are present. In both studies, the cellular organelle identification was carried out based on the score plots obtained from the principal component analysis. From the score plots, false color Raman maps were generated, highlighting the subcellular compartments. Raman images of subcellular organelles were also reported by Krauß et al. [23]. The authors have also correlated well their results with fluorescence microscopy.

Cytochrome C, protein and lipid-rich structures were evidenced in different Raman images on HeLa cells [3] by irradiating the cells with 488, 514, 532 and 633 nm lasers. The HeLa cells gave Raman spectra with peaks at 1000 cm^{-1} (breathing of phenylalanine), 1451, 2850, 2885, 2935 cm^{-1} (CH_2 deformation, CH_2 and CH_3 stretching) and 1660 cm^{-1} (amide I bands mode of

peptide bonds). When irradiated with the 532 nm laser, resonant peaks at 753, 1127, 1314 and 1583, characteristic to cytochrome C, were obtained. Raman images highlighting the Cytochrome C, protein β-sheets and lipids were created using the 753 cm^{-1} peak (pyrrole ring of cytochrome C), the 1686 cm^{-1} peak (amide I vibration of peptide bond in protein) and the 2852 cm^{-1} peak (CH_2 stretching vibration of hydrocarbon chain of lipids). Since cytochrome C is essential for the electron transfer in mitochondria, the Raman images of cytochrome C should also point out the distribution of mitochondria in the cell. In addition, Raman spectra from the nuclei showed no resonance, being similar for all excitation wavelengths. Matthäus et al. [46] reported on obtaining Raman maps pointing out the location of different cellular structures in HeLa cells, with emphasis on mitochondria. They performed hierarchical cluster analysis and found localization of mitochondria in the perinuclear region, which was supported by correlation with fluorescence maps.

In some cases, Raman imaging requires the use of tags. This happens when molecules cannot be detected by regular Raman scattering, either because they are in very low amounts, or because their Raman signal overlaps with other compounds and cannot be distinguished clearly. There are two approaches for using tags for Raman imaging: (a) using surface-enhanced Raman scattering, which implies binding of tags onto the plasmonic nanoparticles surface that can be further used for intracellular identification of analytes [47–50], and (b) taking advantage of the silent region in the Raman spectra of cells between 1800 and 2800 cm^{-1}. In this region, most of the biologically active molecules show no Raman vibrations, so functional molecules with Raman fingerprint in this region could be useful as tags for detection of molecules, which do not give clearly distinguishable Raman peaks in the intracellular medium. This also has the advantage of avoiding the overlap with any endogeneous molecules. Tags suitable for the silent region detection are alkynes, azides, deuterium and nitrile. Palonpon et al. [10] utilized alkyne-tagged EdU (5-ethynil-2-deoxyuridine), for the detection of DNA accumulation and synthesis in cells. EdU is rapidly incorporated in the DNA during the replication process, accumulates in the nucleus and is thus suitable for acquiring information about DNA synthesis in cells.

Silver nanoparticles (AgNPs) prepared by reduction with hydroxylamine according to the Leopold and Lendl method [51] were used for mapping sub-membrane hemoglobin in erythrocytes (red blood cells) [52]. Erythrocytes contain cytosolic and sub-membrane hemoglobin. Although hemoglobin exhibits strong Raman scattering, Raman spectra of erythrocytes generally have mostly contribution from cytosolic hemoglobin, since the sub-membrane hemoglobin is negligible in amount. To trace this sub-membrane hemoglobin, the authors used SERS-active AgNPs that were internalized in the cells and accumulated in the cell membrane. SERS images showed the erythrocytes that come in contact with the AgNPs. Lee et al. [53] used SERS to detect different human breast cancer cell lines phenotypes and to quantify the proteins on the cell surface. For the purpose of SERS enhancement, silica-encapsulated hollow gold nanospheres conjugated with specific antibodies were used. The expression of epidermal growth factor (EGF), ErbB2 and insulin-like growth factor-1 (IGF-1) receptors was determined in the MDA-MB-468, KPL4 and SK-BR-3 cell lines by SERS mapping. Different distributions of growth factors were clearly identified and distinguished from their corresponding SERS

http://dx.doi.org/10.5772/66097

mapping images. Taking advantage on the characteristic wave number of the carbonyl group vibration that lies within the silent region of the Raman spectra, Kong et al. [54] developed osmium carbonyl clusters for cancer cell imaging. The clusters were conjugated with PEG-coated AuNPs and further functionalized with antibody for epidermal growth factor receptors (anti-EGFR). AuNPs were used for carbon monoxide Raman signal enhancement, while functionalization with antibody was needed since the EGFR is highly expressed in many cancer cell lines. Both EGFR-positive and EGFR-negative cancer cells were used. The nanoparticle conjugates were imaged after cellular uptake based on the CO absorption signal at 2030 cm^{-1}, and the results showed the specificity and efficient targeting of CO-nanoparticle conjugates to EGFR-positive cells.

For toxicology studies, it is important to be able to distinguish between healthy and apoptotic cells and also to gain information on the molecular changes associated with apoptosis. Zoladek et al. [28] used Raman imaging for understanding changes associated with apoptosis in the MDA-MB-231 human breast cancer cells. Cells were exposed to the apoptotic drug etoposide, and Raman spectra were recorded 2, 4 and 6 h after exposure. An 1.5-fold increase in the DNA content was observed after 6 h, and the change was assigned to DNA condensation. The most drastic change was in the lipid profile; a high concentration in membrane phospholipids and unsaturated non-membrane lipids was observed in apoptotic cells. The Raman images of the lipidic areas of the cells were generated based on the 1005 and 1659 cm^{-1} peaks ratio. The 1005 cm^{-1} peak with contribution from phenylalanine is not affected by etoposide exposure, while the 1659 cm^{-1} C=C stretching vibrations from lipids show strong increase upon etoposide exposure, indicating an increased degree of unsaturation of lipids for the apoptotic cells. Okada et al. [55] used resonant Raman scattering for imaging the intracellular distribution of cytochrome C and observing dynamic changes of its 750 cm^{-1} band associated with cell apoptosis.

The cellular uptake of nanoparticles and drugs and the cellular responses to drugs are important aspects to be investigated for molecular biomedical applications. Cellular uptake and localization of polyethylene glycol-coated gold nanoparticles in human prostate cancer cells (LNCaP Pro 5) were visualized based on their photoluminescence peak (180–1800 cm^{-1}). In the Raman images of LNCaP Pro 5 cells with AuNPs internalized, cell nucleus and nucleoli are visible, as well as spots generated from the photoluminescence peak of AuNPs. The nanoparticles are located at different positions inside the cells, depending on the time elapsed from exposure. Two hours after exposure, the AuNPs are located in the cell membrane, 12 h after they are located in the cytoplasm, and after 24 h, AuNPs are imaged in the perinuclear region [29].

3. Raman mapping for tissue imaging and medical diagnosis

There is clear indication that Raman spectroscopy could provide insights into drug targeting mechanisms and could be used for detection of metabolic interactions of drugs with cancer cells. In their attempt to detect physiologically relevant cellular responses to drugs, El-Mashtoly et al. [9] used Raman imaging to quantify the effect of the epidermal growth factor

inhibitor panitumumab on colon cancer cells expressing Kirsten-ras mutations (oncogenic and wild-type). It is known that oncogenic K-ras mutations block the response to anti-epidermal growth factor therapy such as panitumumab, while cells expressing wild-type mutations respond to the treatment; all these facts were nicely confirmed by the Raman mapping results. The authors used hierarchical cluster analysis on the 700–1800 cm^{-1} and 2800–3050 cm^{-1} regions for the identification of subcellular components such as cellular membrane, cytoplasm, nucleus and lipid droplets. They found that the oncogenic mutated K-ras cells showed no response to the drug, while the wild-type mutated cells have strong cellular responses to panitumumab treatment, as demonstrated by Raman intensity changes and wave number shifts. The panitumumab-induced changes are strongest on the lipid droplets, suggesting that lipid droplets might play a crucial role in anticancer therapy. The results were confirmed by fluorescence spectroscopy. In another work, El-Mashtoly et al. [30] were able to image the spatial distribution of the erlotinib, another inhibitor of the epidermal growth factor receptor, in colon adenocarcinoma cells upon 12 h of incubating the cells with 100 μM erlotinib solution. Normally, erlotinib cannot be detected by Raman spectroscopy at 100 μM concentrations, which basically implies that its intracellular level was higher due to most likely concentration of the drug in the cell. The authors used the C=C alkyne vibration from the silent region of the Raman spectrum (2085–2140 cm^{-1}) to image the erlotinib distribution and found that the drug was mostly concentrated at the cell borders.

Cells, tissues and bio-fluids can be imaged by Raman micro-spectroscopy. Based on the hypothesis that molecular changes associated with different diseases can be quantified by Raman spectroscopy, the method has been used in medical research and diagnosis during the last years. On one hand, *in vitro* and *in vivo* analysis of tissue is important to be able to distinguish between healthy and tumor cells, and on the other hand, in the medical diagnostics field, there is imperative need for research directed toward identifying noninvasive methods for tumor analysis and toward determining the exact tumor margins. There are several papers reporting the use of Raman spectroscopy and imaging in these directions. Present research still requires comparison with conventionally used staining methods used in histopathology. The gold standard method for tumor pathology and classification is the hematoxylin and eosin (H&E) staining. As opposed to the H&E which involves tissue staining and fixation, Raman micro-spectroscopy is a nondestructive, nonlabeling method. Also, histopathology cannot be used intraoperatively as it requires long incubation times. NIR and the visible 532 nm laser are reported for tissue imaging related to cancer research [7, 30].

The major drawback of Raman technique that limits its application in the medical field is the low efficiency of the inelastic scattering process. Different strategies have been developed to overcome this difficulty, based on, for example: (a) using nonlinear imaging modes such as CARS; (b) acquiring selective sampling of the analyzed probe (e.g., tissue auto-fluorescence can be used to determine the characteristics of the tissue sample and to further use the information to prioritize the sampling points for Raman spectroscopy); (c) multimodal integration of Raman with other techniques such as auto-fluorescence; (d) use of fiber-optic probes for hand held instruments; and (e) use of plasmonic metallic nanoparticles suitable for surface-enhanced Raman scattering.

http://dx.doi.org/10.5772/66097

In vivo and *in vitro* cancer diagnosis based on Raman imaging was so far focused on brain, breast, lung, skin, prostate, colorectal, esophagus and bone cancer [33]. The group of Notingher et al. are pioneers in using Raman imaging for tumor diagnosis, in particular for detecting tumor margins. Multimodal spectral imaging, combining auto-fluorescence imaging and Raman micro-spectroscopy, was used [34, 35, 56] to distinguish between healthy and cancer cells in different carcinoma tissues during intraoperative or postoperative evaluations, for the purpose of accurately detecting the tumor margins. Multimodal spectral imaging is required to reduce the acquisition times needed for raster scanning. Instead of raster scanning the sample, selective sampling is achieved based on integrating collagen auto-fluorescence imaging with Raman imaging. First auto-fluorescence images are used to determine the features of the tissue, and then, the information is used to prioritize and decide the sampling points for Raman spectroscopy. The tissue areas with auto-fluorescence are those containing collagen and are thus identified as healthy dermis and excluded from the Raman measurements. In this way, a dramatic decrease in the acquisition time is achieved: autofluorescence Raman typically requires ~100-fold fewer Raman spectra compared to raster scanning [35]. The high speed of fluorescence imaging relies on the capability to image large tissue area, in contrast to Raman imaging, which requires a pixel-by-pixel readout. For example, an integrated system based on Raman scattering and auto-fluorescence imaging was used by Kong et al. [35] to diagnose basal cell carcinoma tumor margins during tissue-conserving surgery. The major challenge in tissue-conserving surgery is to completely remove the tumor, with minimal loss of healthy tissue. Auto-fluorescence images were necessary in order to prioritize the sampling points for Raman. By using k-means cluster analysis and comparing the images obtained from clustering with the histopathology images, it was possible to diagnose the tumor with 100% sensitivity and 92% specificity. As such, it was possible to assign tissue areas corresponding to the tumor, epidermis, dermis, fat, inflamed dermis, sebaceous gland and muscles. The tumor areas show more intense DNA peaks at 788 and 1098 cm^{-1} compared to healthy tissue. The spectra of the dermis were characterized by collagen-specific peaks at 851 and 950 cm^{-1}. It was possible to achieve shorter diagnosis times than those required by histopathology.

Selective sampling for intraoperative diagnosis during the breast cancer conserving surgery leads to a diagnosis of mammary ductal carcinoma with 95.6% sensitivity and 96.2% specificity [56]. As in the study above, discrimination between healthy and tumor areas was based on increased concentrations of nucleic acids (bands at 788, 1098 cm^{-1}) and decreased levels of collagen and fats (851 and 950 cm^{-1} bands) in the tumor regions. Tissues from 60 patients were deposited on MgF_2 plates; 20 μm tissue sections were sampled and analyzed by Raman micro-spectroscopy, and adjacent sections of 70 μm were stained with H&E. To reduce acquisition times needed for raster scanning, selective sampling was achieved based on integrated auto-fluorescence imaging and Raman. This procedure is also known as multimodal spectral histopathology. By comparing the Raman images obtained from the k-means cluster analysis with the ones obtained from H&E staining, the tumor *vs* healthy breast tissue assignment was successfully carried out. The images from the tumor regions showed large number of cells with enlarged nuclei. Compared to regular raster scanning Raman that would require 10,000 spectra/mm^2 and 5 h analysis time, the multimodal spectral imaging drastically reduces the

analysis time by reducing the number of Raman spectra acquired to 20 spectra/mm^2, which needs 17 min for reaching diagnosis. In a recent study [7], the same group reported on face and neck basal cell carcinoma analysis by selective sampling Raman with 95.3% sensitivity and 94.6% specificity. The results are promising; the method can significantly decrease the diagnosis time. However, it requires strong computing power for the calculations needed after measurement of each Raman spectrum, and this can still be considered a drawback.

Cancer and pre-cancer cells, erythrocytes and lymphocytes were successfully assigned to colon cancer tissue sections by combining Raman imaging with histopathology (H&E staining) and with immunohistochemistry [13]. Hierarchical cluster analysis was used in the spectral region 700–1800 cm^{-1} and 2600–3100 cm^{-1}. The tumor protein p53 is normally highly expressed in cancer and pre-cancer cells because it is a tumor suppresser. The possibility of obtaining Raman imaging of tumor and pre-tumor cells by highlighting p53 active areas was confirmed. By comparing the obtained false color Raman maps with the images given by the anti-p53 immunohistochemical stained image, it was found that the sample auto-fluorescence matches the fluorescence from the anti-p53 stained tissue, proving that the Raman imaging can be used for assigning the p53 active areas of the tissues. The p53 active areas represent more specifically the cancer cell nuclei.

Using SERS-active nanoparticles for intraoperative detection of tumor margins is another promising direction of research in Raman imaging. With this purpose in mind, Wang et al. [48] developed multi-receptor-targeted SERS-active nanoparticles that are topically applied at the surface of tissues excised during breast cancer lumpectomy and that enable quantitative molecular phenotyping at the tumor surface for the purpose of diagnosis. The nanoparticles are tagged with multiple antibodies to achieve as high accuracy as possible and to be able to eliminate influence of nonspecific binding of the nanoparticles. Bovin serum albumin (BSA) was also used to limit nonspecific accumulation of nanoparticles within cells. Antibodies for the epidermal growth factor receptor (EGFR) or the human epidermal growth factor receptor 2 (HER2) and a negative control antibody were conjugated to the nanoparticle surface; a fluorophore was also used to conduct flow cytometry for result confirmation. By targeting the SERS-active nanoparticles to various tumor biomarkers simultaneously and recording the SERS spectra, followed by computational demultiplexing to determine the relative concentrations of the individual SERS nanoparticles, it is possible to detect residual tumors at the surgical margins. The results of the study demonstrated the ability to perform successful Raman imaging on the tissues and to accurately quantify relative tumor biomarker expression levels (high levels of HER2 expression were found, characteristic for breast tumors), in less than 15 min.

4. Raman mapping in plant and algae research

There is a growing interest in getting a more comprehensive understanding of the chemical composition of various plant tissues. Investigations on structural aspects of plant cell wall components, on the chemistry of plant metabolites and relevant plant molecules, are feasible

http://dx.doi.org/10.5772/66097

using Raman mapping. NIR-FT Raman is suitable for imaging of large plant structures such as leaves, seeds and fruits, while the higher resolution visible lasers allow investigation of smaller plant structures.

For example, using the 633 nm laser, it was possible to image the distribution of cell wall components such as cellulose and lignin in a 55-year-old black spruce wood (*Picea mariana*) [57]. Raman images of cellulose and lignin were accurately generated. Cellulose gives three distinct peaks at 380, 1098 and 2900 cm^{-1}, whereas lignin has two overlapping bands at 1600 and 1650 cm^{-1}. The distribution of lignin was generated using both the 1600 and 1650 cm^{-1} bands, while the cellulose distribution maps were found to be most reliable when generated using the 2900 cm^{-1} band which has contribution from lignin alone, without other chemical interferences. Lignin-to-cellulose ratio was also determined, and it was found to differ in different areas of the plant cell wall. Because the 1650 cm^{-1} line had as well contribution from coniferaldehyde and coniferalcohol, it was possible to also image the coniferaldehyde and coniferalcohol distribution, which followed that of lignin. Sun et al. [58] have also used Raman mapping to get information on the lignin and cellulose polymers distribution and composition in *Eucalyptus globulus* and corn stover. They have imaged the lignin and cellulose within different areas on the plant cell walls, from the epidermis to the pith area. Based on the Raman spectral fingerprints, significant compositional differences between *Eucalyptus globulus* and corn stover were observed, but also between different types of cells within the same plant. Schmidt et al. [59] acquired sub-micrometer lateral resolution Raman images of *Arabidopsis thaliana* stem cross sections using the visible 532 nm laser and obtained information on the spatial distributions of cell wall polymers. As such, the distribution of carbohydrates (mainly cellulose) and lignin was obtained. The spatial distribution of polymers was obtained by integrating the C–H intensities between 2820–2935 cm^{-1} for cellulose and 1550–1700 cm^{-1} for lignin. Intense cellulose signals were identified within the secondary walls, whereas lignin was mainly found in the cell corners and in very little amounts in the secondary walls. However, since lignin distribution was not homogeneous, some secondary walls were strongly lignified (ensuring waterproofing). Richter et al. [60] took images from different tissues at different positions within the leaf of *Phormium tenax* and managed to visualize (using the 532 nm laser line) pectin and lignin distribution and to determine the cellulose microfibril angle on the cell walls.

Carotenoids are another promising class of compounds that can be analyzed and imaged through Raman mapping. They are organic pigments, conjugated double bond chains found in plants and other photosynthetic organisms, including bacteria and fungi. Carotenoids have important physiological roles, making them important molecules in plant biology, food science and pharmacology. In plants and algae, carotenoids protect from photodamage and absorb energy to be used in photosynthesis, whereas in human body they are potent antioxidants, and some of them are vitamin A precursors. The human body is unable to synthesize carotenoids, so they must be introduced through the diet, from carotenoid-rich foods (e.g., carrots, tomato, maize, kiwi, cucumber, spinach, broccoli, etc). Information about carotenoid distribution in different plants and plant tissues is limited. Brackmann et al. [61] used coherent anti-Stokes Raman scattering (CARS) to gain information on β-carotene distribution in sweet

potato, carrot and mango. The β-carotene distribution was probed using the C=C vibrational peaks at 1520 cm^{-1}, characteristic for β-carotene. Heterogeneous rod-shaped bodies with high carotenoid density were identified in sweet potato and carrot, while in mango carotenoid-filled lipid droplets were identified as homogeneous aggregates. Raman imaging would also be suitable for other types of carotenoids such as lutein and lycopene, since they all have similar vibrational Raman bands at 1500–1535 cm^{-1} (C=C stretching), at 1145–1165 cm^{-1} (C–C stretching) and at 1000–1010 cm^{-1} (C–CH_3 deformation) [62, 63]. The Raman bands are similar to all carotenoids, but shifted in position according to the number of conjugated bonds, the side groups and to the interaction of carotenoids to other plant constituents. Raman mapping was proved to be useful in evaluating the individual distribution of 7-, 8- and 9-double bond conjugated carotenoids in the intact tissues of *Calendula officinalis* [63]. The Raman images were generated based on the peak at round C=C stretching vibration at 1520 cm^{-1}. This band was shifted at 1536, 1530 and 1524 cm^{-1} for the 7-, 8- and 9-conjugated double bond carotenoids, respectively.

Roots of different carrot cultivars were screened for their individual carotenoid distribution. The β-carotene signal at 1520 cm^{-1} was used for integration. The level of β-carotene was heterogeneous across root sections of orange, yellow, red and purple carrots. In the secondary phloem, the level of β-carotene increased gradually from periderm toward the core, but declined fast in cells close to the vascular cambium. Lutein and α-carotene were deposited in younger cells, while lycopene in red carrots accumulated throughout the whole secondary phloem at the same level [64]. Raman mapping was also applied for studies of *Pelargonium hortorum* to illustrate the heterogeneous distribution of the individual carotenoids in the leaves [65].

Plant polyacetylenes are another class of compounds that can be identified based on their C=C stretching vibration in the 2100–2300 cm^{-1} range. Using the Raman peaks at 2258 and 2252 cm^{-1} characteristic to the most common polyacetylenes falcarinol and falcarindiol, Baranska et al. [66] showed that polyacetylenes are mainly located in the outer section of the carrot roots.

Algae species are important candidates for industrial lipid and biofuel production. Sharma et al. [67] used Raman mapping for lipid analysis of microalgae. Characterization of lipid contents in cells obtained by mutagenesis showed that they managed to obtain mutants with increased lipid content. They have generated Raman images of the lipid-rich, carotenoid-rich and protein-rich areas on the *Chlamydomonas reinhardtii* microalgae based on the characteristic peaks at 1003 cm^{-1} (proteins), 1445 cm^{-1} (lipids) and 1520 cm^{-1} (carotenoids).

Apart from mutations, the growth media can also induce generation of different metabolites. *Chlorella sorokiniana* and *Neochloris oleoabundans* represent two good candidates for biofuel production. The species were Raman mapped at 532 nm for identification of carotenoid and triglyceride production, and in consequence, the maps were generated based on the signal intensity in the 1505–1535 cm^{-1} for carotenoids and 2800–3000 cm^{-1} for triglycerides (CH_2 stretching) [68]. Both healthy algae and nitrogen-starved algae were examined. Only carotenoids could be mapped in the healthy cells. The maps showed distinct locations where the carotenoids are concentrated as they are normally located in the chloroplasts. Triglyceride production was observed under nitrogen-starvation conditions, and it was possible to image

the lipid-rich regions within the starved algae. He et al. [69] reported similar results of triglyceride accumulation upon nitrogen starvation of *Coccomyxa* sp. algae. The triglycerides were imaged through the Raman lipid characteristic peaks at 1440, 1650 and 2840–2950 cm^{-1} (alkyl C–H bending, C=C stretching and CH_2 stretching, respectively).

Some algae are able to produce large amounts of carotenoids when irradiated with light under specific conditions (e.g., *Hematoccocus pluvialis* which produces large amounts of zeaxanthin). Grudzinski et al. [70] analyzed two algal strains, *Chlorella protothecoides* and *Chlorella vulgaris,* with respect to carotenoid production upon light-induced yellowing. They found the yellow coloration to be associated with xanthophyll formation, especially zeaxanthin. Under strong light exposure conditions, newly formed carotenoids were identified as a cell nucleus. It was possible to determine that zeaxanthin is the major carotenoid by performing Raman mapping both at 488 and at 514 nm. Both wavelengths are in resonance with xanthophyll pigments, but 514 nm is in resonance with zeaxanthin only. The cell nuclei give particularly high signal assigned to carotenoids when imaged under the 514 nm laser and low signal when imaged under the 488 nm laser, proving that zeaxanthin is the major synthesized carotenoid.

5. Conclusions

Raman mapping is a powerful technique for label-free, noninvasive investigations of tissues, cells and microorganisms. The resulted Raman maps contain not only spatial information but also valuable structural and chemical information on the analyzed samples. Raman imaging has been successfully used for investigations at cellular and subcellular level, including identification of nucleus, nucleoli, mitochondria and lipid-rich structures. Cell responses to drugs and different stages of the cell cycle from the stem cell to the completely differentiated cell were as well distinguished. In addition, Raman mapping has a great potential for becoming a leading method in a wide range of biomedical applications, owing to its high chemical specificity, good resolution and to the fact that it is a noninvasive to tissues and cells. It is possible to achieve accurate detection of healthy and cancer tissues. At the moment, for the purpose of medical diagnosis, the results of Raman imaging need most often to be compared with currently used diagnosis tools (PCR, histopathology and immunohistopathology). But since it has already been proved that Raman images are sensitive indicators for cancer detection, there is strong indication of the possibility to replace the conventional tools with Raman detection in the future.

Acknowledgements

We thank the Romanian National Authority for Scientific Research, CNCS—UEFISCDI, for funding through project number PN-II-RU-TE-2014-4-2211.

Author details

Cristina Coman* and Loredana Florina Leopold

*Address all correspondence to: cristina.coman@usamvcluj.ro

Faculty of Food Science and Technology, University of Agricultural Sciences and Veterinary Medicine, Cluj-Napoca, Romania

References

[1] Lasch P, Kneipp J. Biomedical vibrational spectroscopy. John Wiley and Sons, New York, 2007.

[2] Kann B, Offerhaus HL, Windbergs M, Otto C. Raman microscopy for cellular investigations—from single cell imaging to drug carrier uptake visualization. Advanced Drug Delivery Reviews 2015;89:71–90.

[3] Hamada K, Fujita K, Smith NI, Kobayashi M, Inouye Y, Kawata S. Raman microscopy for dynamic molecular imaging of living cells. Journal of Biomedical Optics 2008;13:044027.

[4] Puppels GJ, Olminkhof JHF, Segers-Nolten GMJ, Otto C, de Mul FFM, Greve J. Laser irradiation and Raman spectroscopy of single living cells and chromosomes: sample degradation occurs with 514.5 nm but not with 660 nm laser light. Experimental Cell Research 1991;195:361–367.

[5] Notingher I, Boccaccini AR, Jones J, Maquet V, Hench LL. Application of Raman microspectroscopy to the characterisation of bioactive materials. Materials Characterization 2002;49:255–260.

[6] Ghita A, Pascut FC, Mather M, Sottile V, Notingher I. Cytoplasmic RNA in undifferentiated neural stem cells: a potential label-free Raman spectral marker for assessing the undifferentiated status. Analytical Chemistry 2012;84:3155–3162.

[7] Kong K, Rowlands CJ, Varma S, et al. Increasing the speed of tumour diagnosis during surgery with selective scanning Raman microscopy. Journal of Molecular Structure 2014;1073:58–65.

[8] Notingher I, Verrier S, Romanska H, Bishop AE, Polak JM, Hench LL. In situ characterisation of living cells by Raman spectroscopy. Spectroscopy 2002;16:43–51.

[9] El-Mashtoly SF, Yosef HK, Petersen D, et al. Label-free Raman spectroscopic imaging monitors the integral physiologically relevant drug responses in cancer cells. Analytical Chemistry 2015;87:7297–7304.

[10] Palonpon AF, Ando J, Yamakoshi H, et al. Raman and SERS microscopy for molecular imaging of live cells. Nature Protocols 2013;8:677–692.

[11] Schlücker S. Surface-enhanced raman spectroscopy: concepts and chemical applications. Angewandte Chemie International Edition 2014;53:4756–4795.

[12] Draux F, Jeannesson P, Beljebbar A, et al. Raman spectral imaging of single living cancer cells: a preliminary study. Analyst 2009;134:542–548.

[13] Mavarani L, Petersen D, El-Mashtoly SF, et al. Spectral histopathology of colon cancer tissue sections by Raman imaging with 532 nm excitation provides label free annotation of lymphocytes, erythrocytes and proliferating nuclei of cancer cells. Analyst 2013;138:4035–4039.

[14] Ghita A, Pascut FC, Sottile V, Denning C, Notingher I. Applications of Raman microspectroscopy to stem cell technology: label-free molecular discrimination and monitoring cell differentiation. EPJ Techniques and Instrumentation 2015;2:6.

[15] Notingher I, Hench LL. Raman microspectroscopy: a noninvasive tool for studies of individual living cells in vitro. Expert Review of Medical Devices 2006;3:215–234.

[16] Miljković M, Chernenko T, Romeo MJ, Bird B, Matthäus C, Diem M. Label-free imaging of human cells: algorithms for image reconstruction of Raman hyperspectral datasets. Analyst 2010;135:2002–2013.

[17] Hedegaard M, Matthäus C, Hassing S, Krafft C, Diem M, Popp J. Spectral unmixing and clustering algorithms for assessment of single cells by Raman microscopic imaging. Theoretical Chemistry Accounts 2011;130:1249–1260.

[18] Schie IW, Huser T. Methods and applications of Raman microspectroscopy to single-cell analysis. Applied Spectroscopy 2013;67:813–828.

[19] Swain RJ, Jell G, Stevens MM. Non-invasive analysis of cell cycle dynamics in single living cells with Raman micro-spectroscopy. Journal of Cellular Biochemistry 2008;104:1427–1438.

[20] Shinzawa H, Awa K, Kanematsu W, Ozaki Y. Multivariate data analysis for Raman spectroscopic imaging. Journal of Raman Spectroscopy 2009;40:1720–1725.

[21] Chan JW, Lieu DK, Huser T, Li RA. Label-free separation of human embryonic stem cells and their cardiac derivatives using Raman spectroscopy. Analytical Chemistry 2009;81:1324–1331.

[22] Notingher I, Jell G, Lohbauer U, Salih V, Hench LL. In situ non-invasive spectral discrimination between bone cell phenotypes used in tissue engineering. Journal of Cellular Biochemistry 2004;92:1180–1192.

[23] Krauß SD, Petersen D, Niedieker D, et al. Colocalization of fluorescence and Raman microscopic images for the identification of subcellular compartments: a validation study. Analyst 2015;140:2360–2368.

[24] Notingher I, Jell G, Notingher PL, et al. Multivariate analysis of Raman spectra for in vitro non-invasive studies of living cells. Journal of Molecular Structure 2005;744–747:179–185.

[25] Palonpon AF, Sodeoka M, Fujita K. Molecular imaging of live cells by Raman microscopy. Current Opinion in Chemical Biology 2013;17:708–715.

[26] Konorov SO, Schulze HG, Piret JM, Blades MW, Turner RFB. Label-free determination of the cell cycle phase in human embryonic stem cells by Raman microspectroscopy. Analytical Chemistry 2013;85:8996–9002.

[27] Verrier S, Zoladek A, Notingher I. Raman micro-spectroscopy as a non-invasive cell viability test. In: Stoddart MJ, ed. Mammalian cell viability: methods and protocols. Hatfield:Springer; 2011. pp. 179–189.

[28] Zoladek A, Pascut FC, Patel P, Notingher I. Non-invasive time-course imaging of apoptotic cells by confocal Raman micro-spectroscopy. Journal of Raman Spectroscopy 2011;42:251–258.

[29] Shah NB, Dong J, Bischof JC. Cellular uptake and nanoscale localization of gold nanoparticles in cancer using label-free confocal Raman microscopy. Molecular Pharmaceutics 2011;8:176–184.

[30] El-Mashtoly SF, Petersen D, Yosef HK, et al. Label-free imaging of drug distribution and metabolism in colon cancer cells by Raman microscopy. Analyst 2014;139:1155–1161.

[31] Huser T, Chan J. Raman spectroscopy for physiological investigations of tissues and cells. Advanced Drug Delivery Reviews 2015;89:57–70.

[32] Rowlands CJ, Varma S, Perkins W, Leach I, Williams H, Notingher I. Rapid acquisition of Raman spectral maps through minimal sampling: applications in tissue imaging. Journal of Biophotonics 2012;5:220–229.

[33] Kong K, Kendall C, Stone N, Notingher I. Raman spectroscopy for medical diagnostics —from in-vitro biofluid assays to in-vivo cancer detection. Advanced Drug Delivery Reviews 2015;89:121–134.

[34] Takamori S, Kong K, Varma S, Leach I, Williams HC, Notingher I. Optimization of multimodal spectral imaging for assessment of resection margins during Mohs micrographic surgery for basal cell carcinoma. Biomedical Optics Express 2015;6:98–111.

[35] Kong K, Rowlands CJ, Varma S, et al. Diagnosis of tumors during tissue-conserving surgery with integrated autofluorescence and Raman scattering microscopy. Proceedings of the National Academy of Sciences of the United States of America 2013;110:15189–15194.

[36] Eberhardt K, Stiebing C, Matthaüs C, Schmitt M, Popp J. Advantages and limitations of Raman spectroscopy for molecular diagnostics: an update. Expert Review of Molecular Diagnostics 2015;15:773–787.

[37] Tan Y, Konorov SO, Schulze HG, Piret JM, Blades MW, Turner RFB. Comparative study using Raman microspectroscopy reveals spectral signatures of human induced pluripotent cells more closely resemble those from human embryonic stem cells than those from differentiated cells. Analyst 2012;137:4509–4515.

[38] Tu T. Raman spectroscopy in biology: principles and applications. Wiley, New York, 1982.

[39] Notingher I, Bisson I, Polak JM, Hench LL. In situ spectroscopic study of nucleic acids in differentiating embryonic stem cells. Vibrational Spectroscopy 2004;35:199–203.

[40] Leopold LF, Coman C, Todor IS, et al. Raman imaging of dental follicle mesenchymal stem cells. Studia UBB Physica 2015;60:69–76.

[41] Pascut FC, Kalra S, George V, Welch N, Denning C, Notingher I. Non-invasive label-free monitoring the cardiac differentiation of human embryonic stem cells in-vitro by Raman spectroscopy. Biochimica et Biophysica Acta General Subjects 2013;1830:3517–3524.

[42] Pascut FC, Goh HT, Welch N, Buttery LD, Denning C, Notingher I. Noninvasive detection and imaging of molecular markers in live cardiomyocytes derived from human embryonic stem cells. Biophysical Journal 2011;100:251–259.

[43] Pascut FC, Goh HT, George V, Denning C, Notingher I. Toward label-free Raman-activated cell sorting of cardiomyocytes derived from human embryonic stem cells. Journal of Biomedical Optics 2011;16:045002.

[44] Hashimoto A, Yamaguchi Y, Chiu LD, et al. Time-lapse Raman imaging of osteoblast differentiation. Scientific Reports 2015;5:12529.

[45] Krafft C, Cervellati C, Paetz C, Schneider B, Popp J. Distribution of amygdalin in apricot (*Prunus armeniaca*) seeds studied by Raman microscopic imaging. Applied Spectroscopy 2012;66:644–649.

[46] Matthäus C, Chernenko T, Newmark JA, Warner CM, Diem M. Label-free detection of mitochondrial distribution in cells by nonresonant Raman microspectroscopy. Biophysical Journal 2007;93:668–673.

[47] Fabris L. SERS tags: the next promising tool for personalized cancer detection? ChemNanoMat 2016;2:249–258.

[48] Wang Y, Kang S, Khan A, et al. Quantitative molecular phenotyping with topically applied SERS nanoparticles for intraoperative guidance of breast cancer lumpectomy. Scientific Reports 2016;6:21242.

[49] Coman C, Leopold LF, Rugina OD, et al. Green synthesis of gold nanoparticles by *Allium sativum* extract and their assessment as SERS substrate. Journal of Nanoparticle Research 2013;16:2158.

[50] Leopold N, Chis V, Mircescu NE, et al. One step synthesis of SERS active colloidal gold nanoparticles by reduction with polyethylene glycol. Colloids and Surfaces A Physicochemical and Engineering Aspects 2013;436:133–138.

[51] Leopold N, Lendl B. A new method for fast preparation of highly surface-enhanced raman scattering (SERS) active silver colloids at room temperature by reduction of silver nitrate with hydroxylamine hydrochloride. Journal of Physical Chemistry B 2003;107:5723–5727.

[52] Brazhe NA, Parshina EY, Khabatova VV, et al. Tuning SERS for living erythrocytes: Focus on nanoparticle size and plasmon resonance position. Journal of Raman Spectroscopy 2013;44:686–694.

[53] Lee S, Chon H, Lee J, et al. Rapid and sensitive phenotypic marker detection on breast cancer cells using surface-enhanced Raman scattering (SERS) imaging. Biosensors and Bioelectronics 2014;51:238–243.

[54] Kong KV, Lam Z, Goh WD, Leong WK, Olivo M. Metal carbonyl-gold nanoparticle conjugates for live-cell SERS imaging. Angewandte Chemie International Edition 2012;51:9796–9799.

[55] Okada M, Smith NI, Palonpon AF, et al. Label-free Raman observation of cytochrome c dynamics during apoptosis. Proceedings of the National Academy of Sciences of the United States of America 2012;109:28–32.

[56] Kong K, Zaabar F, Rakha E, Ellis I, Koloydenko A, Notingher I. Towards intra-operative diagnosis of tumours during breast conserving surgery by selective-sampling Raman micro-spectroscopy. Physics in Medicine and Biology 2014;59:6141–6152.

[57] Agarwal UP. Raman imaging to investigate ultrastructure and composition of plant cell walls: distribution of lignin and cellulose in black spruce wood (*Picea mariana*). Planta 2006;224:1141–1153.

[58] Sun L, Simmons BA, Singh S. Understanding tissue specific compositions of bioenergy feedstocks through hyperspectral Raman imaging. Biotechnology and Bioengineering 2011;108:286–295.

[59] Schmidt M, Schwartzberg AM, Carroll A, Chaibang A, Adams PD, Schuck PJ. Raman imaging of cell wall polymers in *Arabidopsis thaliana*. Biochemical and Biophysical Research Communications 2010;395:521–523.

[60] Richter S, Müssig J, Gierlinger N. Functional plant cell wall design revealed by the Raman imaging approach. Planta 2011;233:763–772.

[61] Brackmann C, Bengtsson A, Alminger ML, Svanberg U, Enejder A. Visualization of β-carotene and starch granules in plant cells using CARS and SHG microscopy. Journal of Raman Spectroscopy 2011;42:586–592.

[62] Thomas DB, McGoverin CM. The analytical niche for Raman spectroscopy in biological pigment research. Spectroscopy Europe 2016;28:6–9.

[63] Schulz H, Baranska M, Baranski R. Potential of NIR-FT-Raman spectroscopy in natural carotenoid analysis. Biopolymers 2005;77:212–221.

[64] Baranska M, Baranski R, Schulz H, Nothnagel T. Tissue-specific accumulation of carotenoids in carrot roots. Planta 2006;224:1028–1037.

[65] Baranski R, Baranska M, Schulz H. Changes in carotenoid content and distribution in living plant tissue can be observed and mapped in situ using NIR-FT-Raman spectroscopy. Planta 2005;222:448–457.

[66] Baranska M, Schulz H, Baranski R, Nothnagel T, Christensen LP. In situ simultaneous analysis of polyacetylenes, carotenoids and polysaccharides in carrot roots. Journal of Agricultural and Food Chemistry 2005;53:6565–6571.

[67] Sharma SK, Nelson DR, Abdrabu R, et al. An integrative Raman microscopy-based workflow for rapid in situ analysis of microalgal lipid bodies. Biotechnology for Biofuels 2015;8:164.

[68] Huang YY, Beal CM, Cai WW, Ruoff RS, Terentjev EM. Micro-Raman spectroscopy of algae: composition analysis and fluorescence background behavior. Biotechnology and Bioengineering 2010;105:889–898.

[69] He XN, Allen J, Black PN, et al. Coherent anti-stokes Raman scattering and spontaneous Raman spectroscopy and microscopy of microalgae with nitrogen depletion. Biomedical Optics Express 2012;3:2896–2906.

[70] Grudzinski W, Krzeminska I, Luchowski R, Nosalewicz A, Gruszecki WI. Strong-light-induced yellowing of green microalgae Chlorella: a study on molecular mechanisms of the acclimation response. Algal Research 2016;16:245–254.

Chapter 4

Semiconductor Nanowires: Raman Spectroscopy Studies

Marta De Luca and Ilaria Zardo

Additional information is available at the end of the chapter

http://dx.doi.org/10.5772/65113

Abstract

Nanowires (NWs) are filamentary crystals with diameters of tens of nanometers and lengths of few microns. Semiconductor NWs have recently attracted a great interest, because they are emerging as building blocks for novel nanoscale devices. Since physical properties are size dependent, NWs display novel properties with respect to their bulk counterparts. Raman scattering is a nondestructive inelastic light scattering technique enabling the assessment of fundamental properties of NWs, such as crystal phase, electronic band structure, composition, and strain field. Here, we summarize the basic principles of Raman spectroscopy and measurement setup, with focus on the scattering geometries typically used for NWs. We show that changing experimental conditions, such as light polarization, excitation energy, and pressure, allows gaining information on specific NW properties, even in a spatially resolved manner along the NW length. As examples, we discuss Ge and GaAs NWs to highlight some differences between Raman spectra of NWs and the bulk, GaAs NWs to show how Raman permits to establish the crystal phase, and InGaAs/GaAs core/shell nanoneedles to explain how compositional homogeneity and strain field can be addressed by Raman spectroscopy. Finally, we discuss resonant Raman experiments on wurtzite InAs NWs that allowed the determination of their electronic band structure.

Keywords: inelastic light scattering, semiconductor nanowires, crystal phases, compositional disorder, strain, resonant Raman spectroscopy

1. Introduction: the world of nanowires

Semiconductor nanowires (NWs) are promising structures in the field of nanoscience. The name nanowire derives from the filamentary shape of these nanostructures. Indeed, they

have two dimensions in the range of few to tens of nanometers, while the third dimension is much longer, in the micrometer range. Typical NWs with a filamentary shape are shown in **Figure 1(a)**. The gold nanoparticles, which act as catalyzers during the growth, are clearly visible.

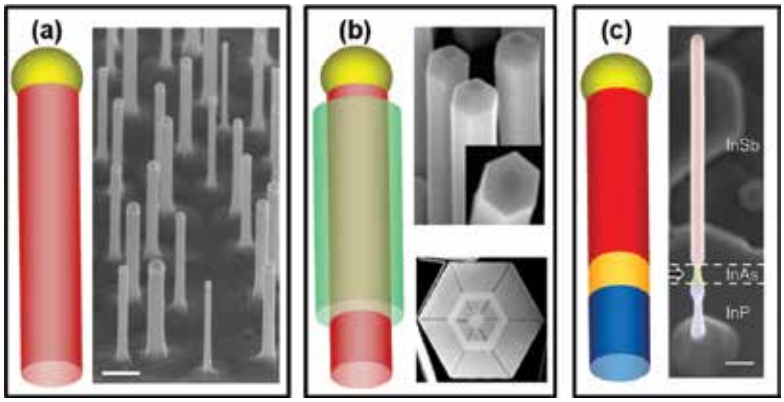

Figure 1. (a) Schematic and SEM image of gold-catalyzed InAs NWs. Scale bar is 200 nm. Courtesy of Dr. L. Sorba, NEST (Pisa, Italy). (b) Schematic of a radial heterostructure, with top-view SEM image of InAs-GaSb core-shell NWs (upper panel) and cross-sectional TEM image of core-multishell GaAs/AlGaAs NW heterostructures (lower panel). Courtesy of Dr. L. Sorba, NEST (Pisa, Italy) and Dr. G. Koblmuller, Walter Schottky Institut and Physik Department (Munchen, Germany), respectively. (c) Sketch of an axial NW heterostructure, together with a SEM image of an InP-InAs-InSb NW. Scale bar is 200 nm. Reproduced with permission from Ref. [3]. © 2012, American Chemical Society.

In 1991, K. Hiruma et al. accidentally grew InAs nanowires on GaAs substrates [1]. Since the time, when the word "nanowire" first appeared in a paper, NWs have attracted interest from a large number of scientists around the world owing to the extraordinary opportunities that they enable. In fact, NWs are smaller than bulk crystals and larger than nanocrystals, thus providing a natural bridge between macroscopic and microscopic worlds in both research and technology fields. Moreover, due to the anisotropic shape of NWs and their high surface-to-volume ratio, finite-size and surface/interface effects are more important than the (more known) quantum confinement effects, a circumstance that renders NWs an ideal platform for the discovery of a variety of novel phenomena.

Semiconductor NWs can exist in many different chemical compositions, structures, and shapes. Regarding the chemical composition, NWs can be made by elemental semiconductors like Si and Ge, or by III–V compounds (e.g., GaAs), II–VI compounds (e.g., CdSe), III–V alloys (e.g., InGaAs), III-nitrides (e.g., GaN), oxides (e.g., ZnO), etc. Not only homogeneously composed NWs exist, but also different materials can be mixed together in the same NW to form heterostructured NWs. Heterostructures are typically prepared in two ways [2]. In radial structures, one or more materials are grown around a NW, in a so-called core-shell or core-multishell arrangement. **Figure 1(b)** shows a schematic of this kind of structures along with a scanning electron microscope image (SEM) of an InAs-GaSb core-shell NW and a cross-section transmission electron microscopy (TEM) image of a core-multishell GaAs/AlGaAs NW. In axial structures, the NW composition is varied along the NW main axis, as depicted in **Figure 1(c)**,

http://dx.doi.org/10.5772/65113

whereas an SEM image of an InP/InAs/InSb axial heterostructure is also displayed [3]. In the NW form, highly mismatched materials can grow on top of each other without misfit dislocations, due to the NW capability to accommodate strain by a coherent expansion of the lattice outward.

Regarding the shape, NWs have been grown in many different, sometimes funny, shapes that could add functionalities to nanoscale devices [4]. For instance, NWs were grown in branched or flower-like morphologies [5], where an increased surface area ensures higher power-conversion efficiency compared to straight and vertical NWs.

NWs are the nanomaterial system in which pivotal key parameters, such as composition, structure, morphology, and doping, have been best controlled to date. At the heart of this control is the development of successful methods for NW growth. In the top-down technology, lithographic techniques allow to carve the nanowire structure out of a bulk material. This kind of approach ensures fine control over the position of the NWs, but the crystal quality of the NWs is not excellent (due to the surface damage produced by etching processes), and large-area production is problematic and expensive. Therefore, bottom-up NW fabrication is the most diffused. Since one-dimensional growth on a substrate is not energetically favored with respect to a two-dimensional growth, a change of the initial surface/interface is required to activate the NW growth. This change can be done by creating holes in the substrate (selective area growth) or by using metal particles, such as gold, to induce the crystal growth (particle-assisted growth) via the so-called "vapor-liquid-solid" (VLS) mechanism that was first invoked in the 1960s to explain the growth of Si whiskers [6]. In both cases, epitaxial techniques are employed to fabricate NWs. In **Figure 2**, the main steps of a typical VLS growth process leading

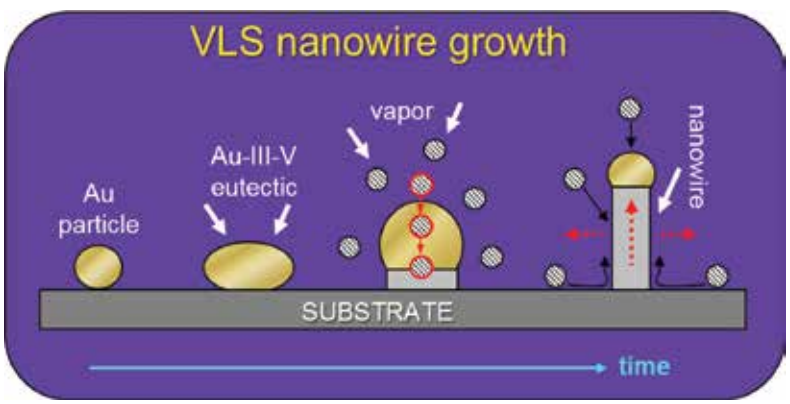

Figure 2. Main steps of the VLS growth process of III–V nanowire grown by metal-organic vapor phase epitaxy (MOVPE). First, a gold particle (with diameter <100 nm) is deposited/formed on a substrate made by III–V crystal. Then, the particle is heated until it melts. The liquid droplet often consists of a molten eutectic alloy between Au and the substrate. Afterwards, group-III and group-V precursors in the vapor phase are introduced. They do not decompose on the solid substrate, as typically the temperature used during growth is too low. Decomposition only occurs at the droplet interface due to the catalytic effect of the metal. The red path represents absorption, diffusion in the liquid droplet, and precipitation of adatoms at the base of the droplet. The precipitation is due to the continued incorporation into the liquid droplet leading to a supersaturation. Finally, axial and radial growth of the NW occurs as soon as additional material precipitates on the growth interface. The three possible diffusion paths of adatoms before adsorption are sketched by black arrows.

to free-standing III–V NWs are explained, since this is the most widely used technique to grow high-quality nanowires. Each gold droplet represents the nucleation site of a NW, so there are approximately as many NWs as the droplets are. The gold droplets can be directly deposited on the substrate or result from the annealing of an Au thin film. To achieve a perfect control on the NW position, an array of gold particles can be even prepared by using lithography techniques.

Thanks to the high degree of control reached on the NW growth process, nowadays most of NW properties can be finely tuned, to such an extent that the creation of NWs tailor fit to specific applications is close to be achieved. Due to the several technological applications enabled by NWs, the interest of the scientific community on them is rapidly growing, as testified by the exponentially growing number of papers published on NWs in the last two decades. The field where the peculiar shape and dimensions of NWs have revealed to have great potential in enabling new functions and/or simply enhancing performances of existing devices is very broad, as it includes electronics, photonics, biosensing, energy conversion, and storage [7]. Therefore, we will pick few examples taken from such a huge variety. For instance, the capability to controllably dope NWs is routinely exploited in field effect transistors [8] while the low mass peculiar to NWs renders them ideal to be used in cantilever force sensors [9] and the NW flexibility makes them easily integrable in devices like flexible displays and artificial skin [10]. Moreover, the NW diameter, smaller than the light wavelength in the visible range, allows NWs to confine electromagnetic waves in the radial direction while guiding light in the axial direction, a property that has been exploited to build NW-based antennas, lasers, and light-emitting diodes (LEDs). An example of a multicolor NW-based LED is shown in **Figure 3(a)** [11]. In the field of energy conversion, we mention that the typically low thermal

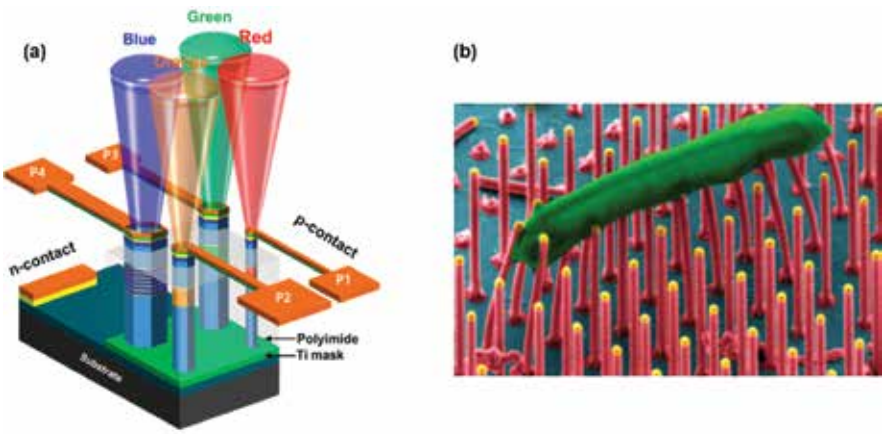

Figure 3. Two very recent examples of the technological power of NWs. (a) Schematic of monolithically integrated multicolor single InGaN/GaN dot-in-nanowire LED pixels on a single chip. Light emission wavelength is tuned across the visible spectrum by varying the nanowire diameter. Reproduced with permission from [11]. Copyright 2016, American Chemical Society. (b) SEM image showing the deformation of an array of InP NWs in direct contact with the body of a phytopathogen Xylella fastidiosa cell (colorized in green). The ordered NW array allows to evaluate single cell adhesion forces and to explore their dependence on organochemical surface compositions. Reproduced with permission from Ref. [14]. © 2016, American Chemical Society.

http://dx.doi.org/10.5772/65113

conductivity of NWs makes them ideal building blocks of thermoelectric devices able to convert wasted heat into electricity [12], while the high surface-to-volume ratio of NWs ensures great light absorption capability, which is currently exploited in the fabrication of high-efficiency solar cells [13]. Finally, interfacing NWs with living cells for delivering drugs or doing sensing activity is a very fascinating field. As an example, in **Figure 3(b)** we show an array of NWs acting as force sensors for bacterial cell adhesion [14].

After this brief overview on the NW world, including growth processes and technological applications, we will describe the properties of NWs that can be addressed by Raman spectroscopy. Indeed, a deep understanding of the NW properties is the starting point to design powerful devices as well as to perform important fundamental physics studies.

2. Experimental setup for Raman spectroscopy in nanowires

Whenever an electromagnetic radiation heats a sample, the light interacts with the sample. It may be reflected, absorbed or scattered. Raman spectroscopy relies on inelastic scattering of the radiation by the sample. It is a versatile and nondestructive technique based on the interaction between the radiation and the vibrational and/or rotational motions of the ions and it provides information such as crystal symmetry, composition, strain, lattice dynamics, and electronic band structure. In a Raman experiment, a monochromatic light is usually sent on the sample and the scattered light is collected and analyzed. When the frequency of the scattered radiation is analyzed, there will be not only the incident radiation wavelength (elastic or Rayleigh scattering component) but also radiation scattered at frequencies lower (Stokes) or higher (anti-Stokes) than the elastic one (inelastic scattering or Raman components). The intensity of the elastic component is much higher than the inelastic ones, thus special tricks are used to detect the weak Raman signal. Furthermore, the Stokes peak has intensity higher than the anti-Stokes peak, and their intensities depend on the temperature. The inelastic peaks appear at frequencies that differ from the incident one by a quantity called Raman shift, independent of the excitation frequency. The Raman shift is the most significant information in a Raman experiment.

In a typical Raman setup, the excitation energy is provided by a monochromatic laser source emitting in the visible range (488, 514, and 633 nm are the most common wavelengths). The laser light is filtered by a laser band pass filter and its polarization is cleaned from possible depolarized contributions with the use of a polarizer. Then, the beam is guided toward the sample with a set of mirrors and a polarization preserving beam splitter (typically 50:50). If nanostructures are investigated, like in our case, the laser light is focused via a microscope objective. A good objective has a high numerical aperture ($\sim$0.9 for 100× magnification), which results in a diffraction-limited laser spot able to provide submicrometric resolution. The nanostructure is positioned on an x–y piezoelectric stage, in such a way that its surface can be automatically scanned with high precision. The scattered Raman signal is collected by the same objective in the so-called backscattering geometry and focused to the entrance slit of a spectrometer equipped with diffraction gratings (typically with 1800 lines/mm). The signal is

dispersed in the spectrometer and then sent to a Si multichannel charge coupled device (CCD) detector. When standard, namely single stage spectrometers are used, a notch filter before the spectrometer is necessary to reject the intense elastic component, and only Raman shift larger than ~50 cm^{-1} can be detected. The best spectrometers existing for Raman spectroscopy are triple-stage spectrometers, where no notch is required, because the first two gratings are used for the rejection of the elastic contribution and of the stray light (in the so-called "subtractive mode"), while the third grating disperses the radiation components and determines the resolution. To provide an idea, a 1800 lines/mm grating mounted on a spectrometer with 0.5 m focal length gives a resolution of ~0.7 cm^{-1}. After the measurements, an accurate frequency calibration of the Raman spectra is usually performed exploiting the well-known energies of the emission lines of a neon lamp.

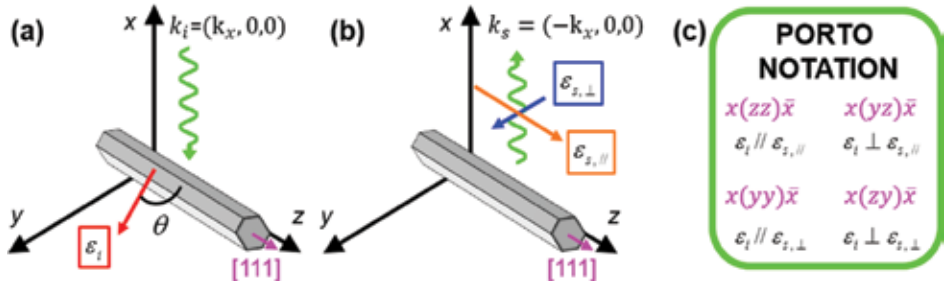

Figure 4. Sketch of a typical backscattering geometry used in polarization-resolved Raman experiments on a single ZB nanowire whose growth axis is in the crystallographic direction [111], aligned with the *z*-axis of the reference system. (a) The incident light wavevector k_i is parallel to the *x*-axis and its polarization vector ε_i varies, forming an angle θ with *z*. (b) The scattered light wavevector k_s is along -*x* and the components of its polarization vector ε_s either parallel or perpendicular to *z* are selected. (c) Four common scattering configurations are indicated in the Porto notation: $k_i(\varepsilon_i, \varepsilon_s)k_s$.

In **Figure 4**, a typical geometry for performing polarization-resolved Raman measurements on a single NW is sketched. Let us consider a NW with zinc blende (ZB) phase, grown along the [111] direction and having a hexagonal cross section, with facets of the {110} family. After transferring the wire on a substrate, the flat facet of the family {110} is perpendicular to the incident light wavevector (k_i) and the NW long symmetry axis is aligned with the *z*-axis of our reference system, as schematized in (a). In the used backscattering geometry, k_i is parallel to the *x*-axis and the scattered light wavevector (k_s) is opposite to it, see panel (b). As a consequence, all light polarization vectors lie in the *yz* plane. During the measurements, the polarization of the excitation (ε_i) is rotated by an angle θ with respect to the nanowire growth axis. The scattered radiation is analyzed by selecting the component of the polarization either parallel to the NW growth direction ($\varepsilon_{s,//}$) or perpendicular to it ($\varepsilon_{s,\perp}$). In the following, we will indicate the scattering configuration in the so-called Porto notation, $k_i(\varepsilon_i,\varepsilon_s)k_s$, where the outer terms, from left to right, refer to the directions of exciting and scattered light, respectively, and the inner bracket refers to the excitation and detection polarizations. Some examples of the most common scattering configurations as indicated in Porto notation are given in panel (c).

http://dx.doi.org/10.5772/65113

From the experimental point of view, ε_i of the incoming light is rotated by an angle θ with respect to the z-axis by using a lambda half plate whose fast axis forms an angle $\theta/2$ with the z-axis, while a polarizer before the spectrometer is used to select the scattered radiation with components of the polarization either parallel or perpendicular to the z-axis. Since the efficiency of a spectrometer depends on the polarization of the entering light, a lambda half plate at the entrance of the spectrometer is used to flip the polarization of the light into the most efficient direction.

By measuring the dependence of the scattered intensity on the incident and scattered polarization directions one can deduce the symmetry of the Raman tensors, thus the symmetry of the corresponding phonon, based on the comparison with the theoretical calculation of the intensity of the Raman signal for that specific experimental geometry. The intensity of the scattered light I_s into a solid angle dΩ is given by [15],

$$\mathrm{I_s} = \mathrm{I_i} \cdot \mathrm{k} \cdot |\varepsilon_i \cdot R \cdot \varepsilon_s|^2 \, \mathrm{d}\Omega \tag{1}$$

with I_i the irradiance of the radiation incident on the sample, $k = 2\pi a^2 \omega_s$ (a = 1/137 and ω_s frequency of the scattered light), and R the Raman scattering tensor, which is defined as $R = \left(\frac{\mathrm{d}\alpha}{\mathrm{d}Q_0}\right) \cdot Q\left(\omega_q\right)$, where α is the crystal polarizability, and Q the vector displacement of an atom induced by a phonon. It is usually convenient to transform the Raman tensors in a basis made by the three main crystallographic axes of the sample and to express the polarization vectors in that basis. From Eq. (1) one can calculate the selection rules for all modes in specific scattering geometries.

Once the basic principles of Raman spectroscopy in NWs and measurement setup have been summarized, the most significant results of Raman spectroscopy applied to NWs can be described.

3. Size effects in the Raman spectra of semiconductor nanowires

In a 3D-crystal with N atoms per primitive unit cell, the phonon dispersion (namely, the relation between the frequency and the wavevector of lattice vibrations) is composed of 3N branches (three of them are acoustic and the remaining 3N−3 are optical). Along high-symmetry directions the phonons are classified as transverse or longitudinal according to whether their displacements are perpendicular or parallel to the direction of the phonon wavevector q, respectively. Due to momentum and energy conservation rules, only the optical lattice modes at $q = 0$ (Γ point) can be studied by one-phonon spectroscopic techniques (infrared spectroscopy for odd parity modes and Raman scattering for both odd and even parity modes). In III–V ZB crystals and group IV crystals with the diamond structure, such as Si and Ge, there are six-phonon branches (because there are two atoms per primitive unit cell): two transverse and one longitudinal acoustical modes (TA and LA, respectively) and two transverse and one longitu-

dinal optical modes (TO and LO, respectively). The TO and LO near Γ are degenerate only in group IV crystals since the two atoms in the unit cell are identical.

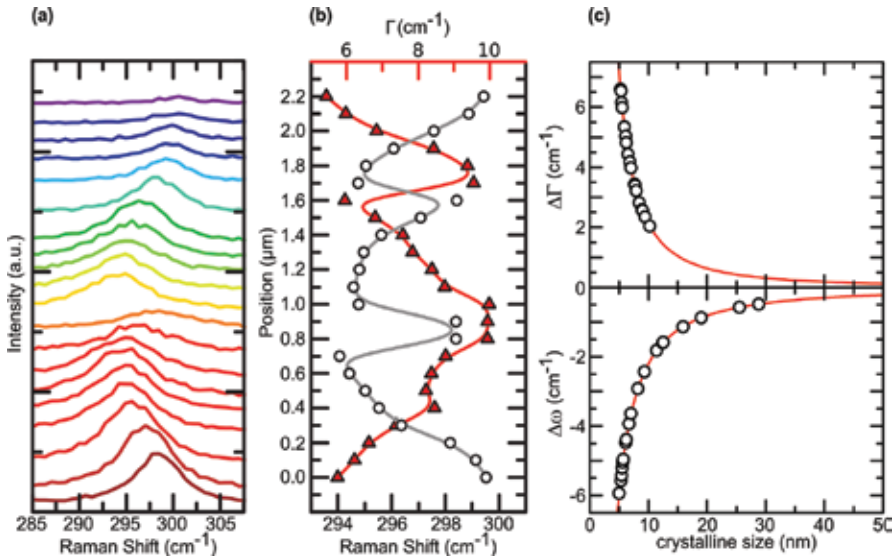

Figure 5. (a) Raman spectra recorded every 100 nm along a Ge NW with diameter of 86 nm. (b) Peak position (open circles, bottom scale) and FWHM Γ (full triangles, top scale) of the degenerate TO/LO modes as a function of the position. Solid lines are guides to the eyes. (c) Bottom: energy shift $\Delta\omega$ from the crystalline Ge Raman peak position (298 cm^{-1}). Top: broadening $\Delta\Gamma$ with respect to the natural FWHM of the crystalline Ge Raman peak (3.4 cm^{-1}). Open circles are the experimental values; solid lines come from the theoretical model.

In nanostructured materials it is usually observed that the energy of TO and LO modes is very similar to the bulk case. Differences may arise due to phonon confinement effects when scaling down the size of the crystal. Indeed, whenever the sizes of the "phonon wave packet" are comparable to the crystal size, an uncertainty in wavevector is introduced, which results in a contribution to the Raman peak at frequencies different from that at the Γ point. In other words, there is a relaxation of the $q = 0$ momentum conservation rule. As a consequence, the Raman line shifts (in a direction depending on the phonon dispersion) and broadens. **Figure 5(a)** shows Raman spectra taken along a single Ge nanowire consisting of a crystalline Ge core, whose diameter is inhomogeneous along the NW length, surrounded by an amorphous Ge layer [16]. The main band, attributed to the degenerate TO/LO phonons of the core, display variations in intensity and energy along the NW axis. Panel (b) shows the peak energy (open circles) and the full width at half maximum (FWHM) Γ (full triangles) of the phonon band as a function of the position (with steps of 100 nm). Since the downshift is mostly accompanied by a broadening, these effects point to phonon confinement in the core. By using a proper model and taking the experimental lattice constant of Ge NWs from the literature, an estimate of the size of the nanocrystal is determined by our experimental downshift ($\Delta\omega$) and broadening ($\Delta\Gamma$) of the TO/LO band, as displayed in panel (c). The observed $\Delta\omega$ correspond to a crystal size between 5 and 30 nm, in excellent agreement with the TEM analysis [16], while the

http://dx.doi.org/10.5772/65113

broadening gives values between 5 and 10 nm. We believe that the broadening data are less reliable because the inhomogeneity of the core in diameter (definitely probed by a ~1 μm laser spot) creates an additional broadening of the phonon band, resulting in crystal sizes smaller than the real ones.

In the context of size effects in NWs, in addition to phonon confinement also the high surface-to-volume ratio of NWs plays a role and creates differences with the bulk. As a matter of fact, the surfaces represent a new physical boundary. The crystal symmetry might be affected by the existence of the edges, which lead to a rearrangement of the lattice and can activate silent modes. Also, specific modes associated to the surface, such as surface optical (SO) modes or breathing modes, may appear [17]. The SO phonons are created at the interface between different materials with different dielectric constants and propagate along the interface. They are activated by a breaking of the translational symmetry of the surface potential, likely due to diameter variations along the NW length. Finally, since the surface atoms are "less bound" than the internal atoms, they "experience" a different local field. The propagation of optical phonons, where the oscillating dipoles, created by the out of phase oscillation of ions and cations, interact via a dipole-dipole interaction, is most affected by this.

Besides the appearance of the SO modes, the peculiar cylindrical shape with nanoscale dimensions of the NWs gives rise to the so-called dielectric mismatch effect, as will be discussed in the following. A representative example of the difference between NWs and the bulk is presented in **Figure 6** for zinc blende GaAs [18, 19]. In panel (a) we show a Raman spectrum of a ZB NW grown along the [111] direction (blue) and a spectrum of a (111)-oriented GaAs wafer (black) tilted by 90°. The spectra were, therefore, collected in the same scattering geometry, namely, $x(zz)\bar{x}$. The spectra are composed of a unique phonon mode, the E_1(TO), at ~267 cm^{-1}, as expected, based on the experimental geometry and the Raman tensors for ZB. The FWHM of this mode in the NW spectrum is ~2 cm^{-1} larger than in the bulk, which indicates a good crystal quality of the NW, the broadening being likely due to the presence of some twins in the crystal structure. Panel (b) displays the azimuthal dependence of parallel (full circles) and perpendicular (open squares) components of the scattered light of this mode for the bulk (left) and the NW (right). The measurements are performed as described in **Figure 4(a)** and **(b)**. In the bulk, the maximum intensity is found almost at the angles ($\theta \sim -20°$ for the parallel component and $\theta \sim 70°$ for the perpendicular) resulting from calculations based on Eq. (1). A same result is found in the NW for the parallel component. Instead, the perpendicular component is much less intense than in the bulk and it has no clear angular dependence. This difference points to a modification of the selection rules when passing from the bulk to the NW. This change can be attributed to the one-dimensional geometry of the NW. Indeed, in cylindrical-like crystals whose dielectric constant is larger than the one of the surrounding air, light absorption/emission is suppressed for light polarization perpendicular to the long symmetry axis because of image forces arising at the interface between the cylinder and its surroundings [20]. In NWs, this effect was observed also in photoluminescence measurements and it is strongly dependent on light wavelength and NW diameter. It exists in all NWs and in wurtzite NWs it has to be carefully taken into account when dealing with electronic

selection rules [21]. In Raman spectroscopy, because of this effect the phonon modes are more efficiently excited for parallel polarization, as we observe.

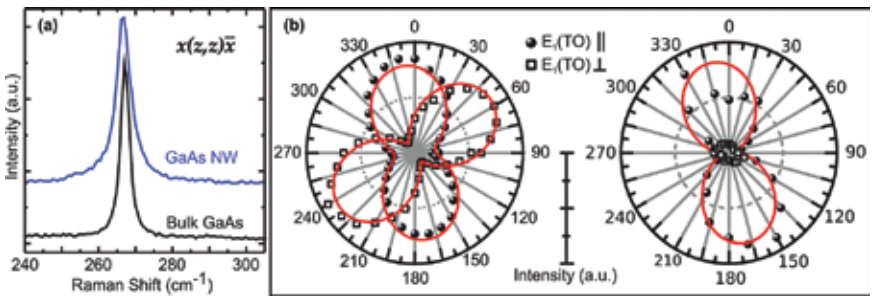

Figure 6. (a) Raman spectra of a NW grown along the [111] direction (blue) and of a (111)-oriented GaAs wafer (black) recorded in the same scattering geometry, $x(zz)\bar{x}$. (b) Azimuthal dependence of the TO mode of the bulk GaAs (left) and of the NW (right). Full circles and open squares represent the components of the Raman signal along the *z*- and *y*-axes, respectively. Solid lines are squared sine fits to the data.

4. Assessment of the crystal phase of nanowires

The crystallization of NWs in a crystalline phase that is not stable in the bulk form is one of the consequences related to the large surface-to-volume ratio of NWs, since the "unusual" crystal structure formation is favored for certain ranges of the relevant interface energies. For instance, non-nitrides III–V materials (such as GaAs, InAs, InP, etc.) that are notoriously stable in the cubic ZB phase in the bulk form can crystallize in the hexagonal wurtzite (WZ) phase when grown in the NW form under suitable VLS conditions. The occurrence of WZ in the lattice of these NWs is one of the most surprising findings in NWs and it provided the unprecedented opportunity to investigate this poorly known crystal phase. Many studies indicate that the WZ phase is favored in NWs featuring a high surface-to-volume ratio, such as in small diameters NWs [22], but an exhaustive picture of the reasons why WZ is formed in NWs is still lacking in the literature. It is worth stressing that the electronic and optical properties of the NWs strongly depend on their crystal phase [23] and thus engineering the crystal phase switching leads to the realization of heterostructures with additional degrees of freedom enabling novel optoelectronic devices [24, 25].

The differences between ZB and WZ properties are given by their different crystal structures. The ZB crystal is formed by two interpenetrating face-centered-cubic Bravais lattices (each of a different atomic species), whereas WZ is constructed from two interpenetrating hexagonal-close-packed lattices. The differences between ZB and WZ crystals are best understood by observing their structures in the [111] direction (that is the [0001] direction in WZ, usually known as the *c*-axis), along which both crystals look like stacked hexagonal layers, as shown in **Figure 7(a)** for a generic III–V crystal. Clearly, WZ and ZB are made by identical atoms within each layer, but these layers are alternated according to a different stacking sequence: ABABAB

http://dx.doi.org/10.5772/65113

in WZ and ABCABC in ZB. The length of the unit cell of the WZ phase along the [0001] direction is double of the cell of the ZB phase in the [111] direction [26]. Due to these crystallographic similarities, the principal features of the WZ electronic and phononic band structure can be understood starting from the ZB band structure and applying folding arguments. We will discuss in detail the phonon band structure, as it can be probed mainly by the Raman spectroscopy.

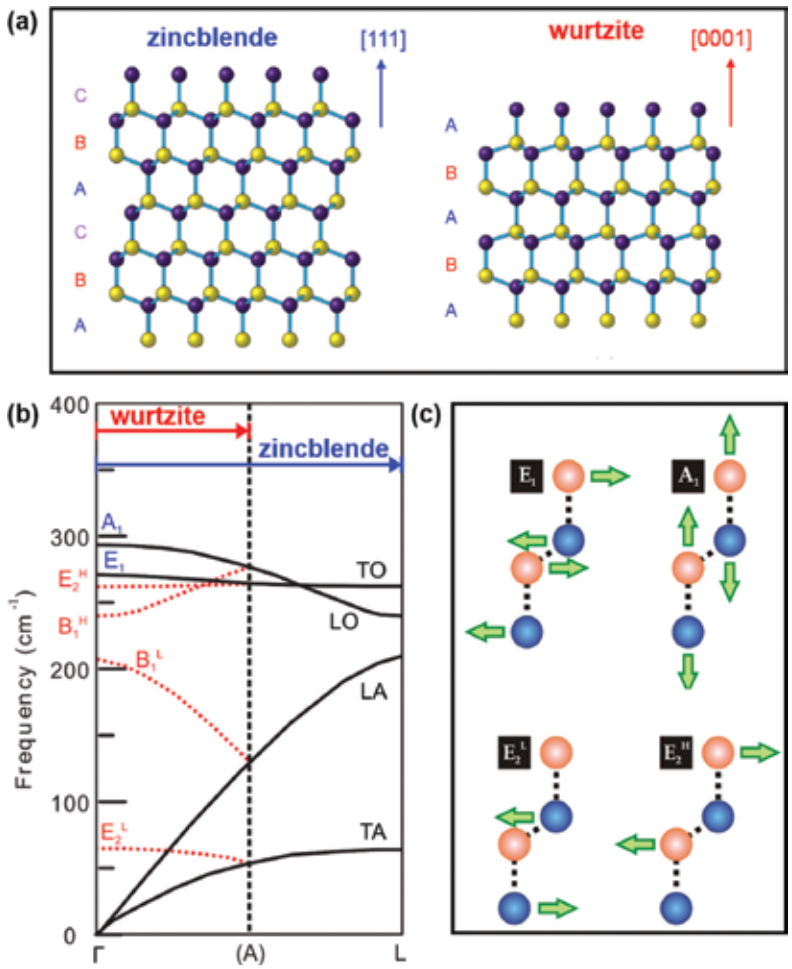

Figure 7. (a) Schematic drawing of the atomic arrangement in zinc blende (left) and wurtzite (right) structures of a III–V semiconductor. Each letter represents a bilayer. (b) Phonon dispersion of a typical III–V semiconductor (GaAs). The phonon branches of the ZB structure (solid lines) are folded to give rise to the phonon branches of the WZ structure (dashed lines). (c) Atomic displacements corresponding to the Raman active optical phonon modes in the WZ structure.

Figure 7(b) shows how the phonon dispersion of a III–V WZ crystal can be obtained by folding the one of the ZB structure along the [111] direction, namely from the Γ to the L point. We can

consider only this high symmetry direction because we will deal with one-phonon Raman scattering, which probes only phonons close to the Γ point. As discussed in the previous section for ZB GaAs crystals, there are six-phonon branches: 2TA, 1LA, 2TO, and 1LO. We stress that the dispersion curves of the TA modes are relatively flat near the zone edge and their energies are much lower than the LA phonon energy due to the covalent nature of bonds in these crystals. The LO phonon has higher energy than the TO phonons near Γ due to the ionic character of the bonds and the macroscopic electric field connected with the long wavelength LO phonon, at variance with group IV crystals where they are degenerate because no extra charge is carried by the two identical atoms in the unit cell.

In WZ, four new modes appear at the Γ point of the Brillouin zone. The folded modes are indicated with red dashed lines. Group theory predicts eight-phonon normal modes at the Γ point: $2A_1 + 2E_1 + 2B_1 + 2E_2$. Considering our scattering geometry described in **Figure 4** and the crystallographic axes of a typical WZ NW grown along the [0001] direction, only the A_1(LO), E_1(TO), E_2^H, and E_2^L modes can be experimentally observed. The atomic displacements associated to these modes are sketched in panel (c). The notation E_1 and A_1 denote modes vibrating perpendicular and along the growth axis, respectively. Since A_1 and E_1 modes are also found in ZB, the appearance of E_2^H and E_2^L modes in the Raman spectrum of III–V NW is the unambiguous signature of a WZ phase.

Polarization-resolved Raman measurements provide a reliable way to address the crystal phase of a given NW. To obtain such information it is necessary to calculate the selection rules for the modes specific to that crystal phase by using Eq. (1) and compare them with the experimental results. The Raman tensors of all existing crystal structures can be found in [27]. As summarized in table I in [19], in WZ III–V NWs grown along the [0001] direction (parallel to the *z*-axis in **Figure 4**) in backscattering configuration the A_1(TO) is expected to be observed only in the $x(yy)\bar{x}$ and $x(zz)\bar{x}$ configurations, the E_2^H and E_2^L only in $x(yy)\bar{x}$, and E_1 (TO) in $x(zy)\bar{x}$. Experimentally, the selection rules can be probed by measuring the dependence of the scattered intensity on the incident and scattered polarizations as done in **Figure 6**. **Figure 8** shows how this was made in GaAs NWs [19]. In panel (a) the Raman spectra obtained under the four main polarization configurations on the same pure-phase ZB NW of **Figure 6** are displayed. Only the A_1/E_1(TO) mode is visible and its intensity is maximum in the $x(zz)\bar{x}$ configuration, as clear also in the right panel of **Figure 6 (b)**. The reason for the sizable decrease in its intensity whenever the incident or scattered light are polarized perpendicular to the NW is the dielectric constant mismatch that we discussed in Section 3. In panel (b) of **Figure 8** we show the same measurement taken on a region of pure WZ phase in a mixed WZ/ZB NW. The E_2^L is not observed due to its very low energy, the A_1(TO) and E_1 (TO) are almost degenerate in GaAs and appear at ~266 cm^{-1}. In $x(zy)\bar{x}$ the A_1/E_1 peak should be mainly E_1 and in $x(yy)\bar{x}$ and $x(zz)\bar{x}$ mainly A_1. The shoulder at ~290 cm^{-1} can be ascribed to the theoretically forbidden A_1(LO), here most probably activated by the tilted facets of the hexagonal cross-section of the NW that are not perpendicular to k_i. Most importantly, we observe the E_2^H mode at ~256 cm^{-1}, with the highest intensity in the $x(yy)\bar{x}$ configuration, as distinctive of the WZ phase. Its full azimuthal dependence in (c) for detected polarizations parallel (full circles) and perpendicular (open squares) to the NW axis nicely confirms this attribution: the maximum intensity

http://dx.doi.org/10.5772/65113

of both detected polarizations is found when the polarization of incident light is perpendicular to the NW axis, though for the parallel detected polarization the dependence is less clear due to the low intensity.

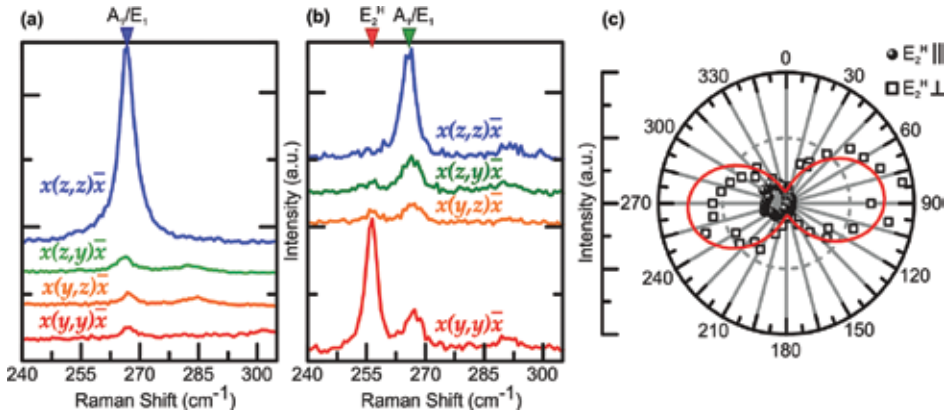

Figure 8. (a) Raman spectra of the ZB GaAs NW collected under the four main polarization configurations. The full azimuthal dependence is in the right panel of **Figure 6(b)**. (b) Same as (a) for a GaAs NW with WZ structure. (c) Azimuthal dependence of the parallel (full circles) and perpendicular (open squares) components of the E_2^H Raman mode with respect to NW growth axis. The solid red line is a squared sine fit to the data.

5. Assessment of the chemical composition and strain field in nanowires

In order to demonstrate the power of Raman spectroscopy to probe the chemical composition of NWs, it is worth focusing on alloyed NWs, while to investigate the strain state heterostructured NWs (e.g., core-shell NWs) are ideal. Here, we focus on core-shell $In_xGa_{1-x}As$/GaAs NWs as they fulfill both requirements. These NWs are called nanoneedles (NNs) because they are highly tapered. They feature a highly pure WZ phase [28].

The chemical composition x of the $In_xGa_{1-x}As$ core can be determined by Raman spectroscopy as displayed in **Figure 9**. Raman spectra of NNs with different indium composition capped with 30 nm of GaAs are shown in panel (a). Samples are labeled with the nominal In content and spectra were taken in the $x(yy)\bar{x}$ configuration. In agreement with the observations in **Figure 8(b)** for WZ GaAs, in $x(yy)\bar{x}$ both A_1 (TO) and E_2^H modes are observed (the E_2^H peak here is more intense than the A_1), while in the $x(zz)\bar{x}$ geometry (not shown here) only the A_1 (TO) is observed. The shoulder at about 235 cm^{-1} can be attributed either to a WZ InAs-like TO mode or to an interface mode. The Raman shift of all modes as determined by Lorentzian fits to the data (see for example the green solid lines in (a)) is reported in (c) as full squares (for data taken in $x(yy)\bar{x}$) and open circles (for $x(zz)\bar{x}$ data) as a function of the nominal In content. Solid lines represent the theoretical estimates of the GaAs-like and InAs-like modes energies obtained for ZB $In_xGa_{1-x}As$. No theoretical estimate is available for WZ $In_xGa_{1-x}As$, and so the energy of E_2^H, present in WZ only, has no theoretical comparison. The effective indium

compositions as extracted by the comparison between experiment and calculation for the GaAs-like TO modes are x = (0.22–0.24) for the sample with nominal x = 0.20, x = (0.17–0.22) for nominal x = 0.16, and x = (0.12–0.15) for nominal x = 0.12 [28].

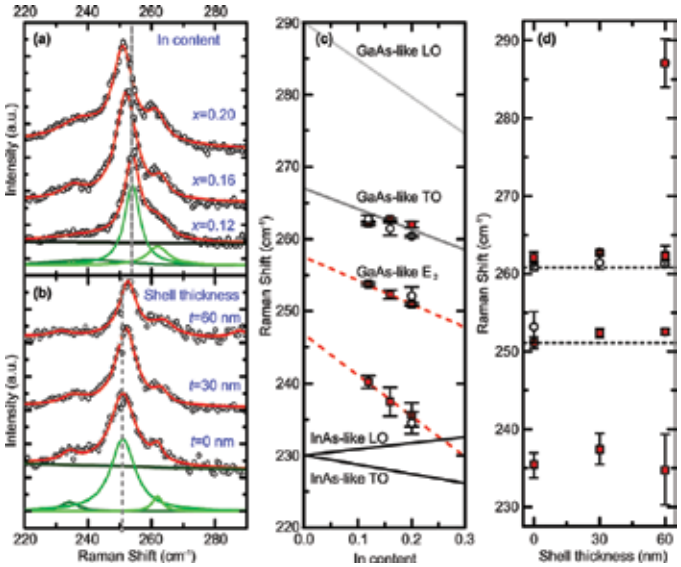

Figure 9. (a) Raman spectra (open circles) of $In_xGa_{1-x}As$ nanoneedles (with the indicated nominal In content, x) capped with 30 nm of GaAs. Spectra were taken in the $x(yy)\bar{x}$ scattering geometry and were normalized to the GaAs-like E_2^H phonon peak, whose energy is indicated by a dashed line in the spectra of the x = 0.12 sample. Red solid lines are Lorentzian fits to the data. The single contributions to a Lorentzian fit are represented by green solid lines in the x = 0.12 sample as an example. (b) Same as (a) for samples with the indicated GaAs shell thickness t and fixed In content (x = 0.16). The energy of the GaAs-like E_2^H phonon is indicated by a dashed line in the spectrum of the sample without shell. (c) Frequency of various optical phonons as a function of indium composition. Symbols represent experimental data points taken under the $x(zz)\bar{x}$ (open circles) and $x(yy)\bar{x}$ (full squares) scattering configurations. Solid lines indicate theoretical estimations for ZB $In_xGa_{1-x}As$ and dashed lines are linear fits to the data for the GaAs-like and InAs-like E_2^H modes. (d) Energy of phonon modes for an $In_xGa_{1-x}As$ NN with x = 0.16 a function of shell thickness. Symbols represent experimental data points taken under the $x(zz)\bar{x}$ (full squares) and $x(yy)\bar{x}$ (open circles) scattering configurations. Dashed lines indicate the energy of the GaAs-like A_1/E_1 (TO) and E_2^H modes for $In_xGa_{1-x}As$ without shell. Reproduced with permission from Ref. [28]. © 2014, American Chemical Society.

In these NNs, the possible presence of strain was also probed by Raman spectroscopy. In **Figure 9(b)**, we display spectra recorded in $x(yy)\bar{x}$ configuration from NNs with different GaAs shell thickness t and same indium composition (nominal x = 0.16). The peaks' attribution is the same as in panel (a). Here, the GaAs LO phonon mode is also observed, but only in the sample with the thickest shell. Its energy (~287 cm^{-1}) is downshifted by ~2 cm^{-1} with respect to the bulk, which could be due to tensile strain in the shell. The Raman shift of all modes as determined by Lorentzian fits to the spectra (the green solid lines in panel (b) are an example) are reported in panel (d) as full squares for $x(yy)\bar{x}$ data and open circles for $x(zz)\bar{x}$ data as a function of the nominal shell thickness. We do not observe any clear and consistent energy variation of the phonon modes with increasing shell thickness, neither an increase in their

http://dx.doi.org/10.5772/65113

FWHM, which allow us to exclude the presence of strain in the core. Possible compositional or shell thickness variations along the NN length can be also excluded, because Raman measurements performed on different points of a same NN do not display significant changes [28].

In this section, it is also worth mentioning that Raman spectroscopy in semiconductor NWs may be used to monitor the incorporation of dopants. At variance with electrical measurements, Raman measurements are not affected by spurious effects coming from the fabrication of contacts. Information on the type and concentration of dopants can be obtained by measuring, respectively, the energy and the intensity of the local vibrational modes associated with the impurities. As an example, we mention Reference [29], where *p*-type GaAs NWs were grown with different silicon doping concentrations and, depending on the growth conditions, the Si_{As} local mode (indicative of Si incorporation into As lattice) and the mode due to the formation of neutral Si_{As}-Si_{As} pairs were observed with different relative weights.

6. Resonant Raman scattering in nanowires

In this section, we highlight the power of Resonant Raman scattering (RRS) to investigate the electronic band structure and the electron-phonon interaction in semiconductor NWs. This investigation is possible because the scattering cross section contains the electron-radiation and the electron-phonon interaction Hamiltonians, as well as electronic states for electron-hole pair. In standard conditions, it is very difficult to have access to this information, due to summation over all the intermediate states, but if resonant conditions are achieved, the excitation energy matches electronic interband transitions and the electronic-related terms in the scattering cross section are sizably enhanced. Resonant conditions between excitation energy and electronic states may be reached by varying either the energy of the excitation (using a tunable laser) or the energy of the electronic states (for instance by applying an external pressure at fixed excitation energy). Indeed, the energy gap of semiconductors typically increases with pressure, thus if the pressure dependence of the energy gap is known, pressure-dependent RRS measurements give information on the electronic band structure of the material. We will discuss both methods focusing on InAs NWs with WZ phase [30], because in III–V NWs with WZ phase the electronic band structure is poorly known and RRS has proved to be a necessary tool to shine light on this highly debated topic [31].

Figure 10(a) shows some spectra collected from a single WZ InAs NW with growth axis aligned with *z*, as sketched in **Figure 4**, under two scattering configurations, $x(zz)\bar{x}$ (solid line) and $x(yy)\bar{x}$ (dashed line). Five different excitation energies comprised between 1.91 and 2.71 eV were used. All spectra exhibit an asymmetric peak at about 216 cm^{-1}, in the region of the TO mode, and an LO mode at ~238 cm^{-1}, more intense for higher excitation energies. The TO peak is asymmetric because it results from the convolution of two peaks: the A_1/E_1 (TO) mode at ~218 cm^{-1}, dominant in the $x(zz)\bar{x}$ configuration (where it is mainly A_1), and the E_2^H mode at ~214 cm^{-1}, dominant for $x(yy)\bar{x}$. This is in agreement with the results shown in **Figure 8(b)** for WZ GaAs. In the following we will refer to the convoluted A_1/E_1 and E_2^H modes simply as

TO. The measured Raman scattering cross sections (carefully normalized for the spectral response of the setup) of the TO (black squares) and LO (red circles) modes for the configuration $x(zz)\bar{x}$ (open symbols) and $x(yy)\bar{x}$ (filled symbols) are shown in panel (b). The intensity of the TO in $x(zz)\bar{x}$ configuration, that is mainly the A_1 (TO), and of the LO in both configurations, increases with energy in a monotonic way, while the intensity of the TO in $x(yy)\bar{x}$ configuration (where it is mainly given by the E_2^H mode), displays a resonance in the 2.41–2.60 eV energy region, which can be correlated with the WZ band structure since the E_2^H mode is peculiar to WZ phase. Actually, two separate resonances appear, but the number of experimental points is too limited to point out the exact energy at which the maxima occur.

These RRS data can be interpreted at the light of the following considerations. The three lowest energy electronic interband transitions in III–V WZ materials, labeled as A, B, and C, involve

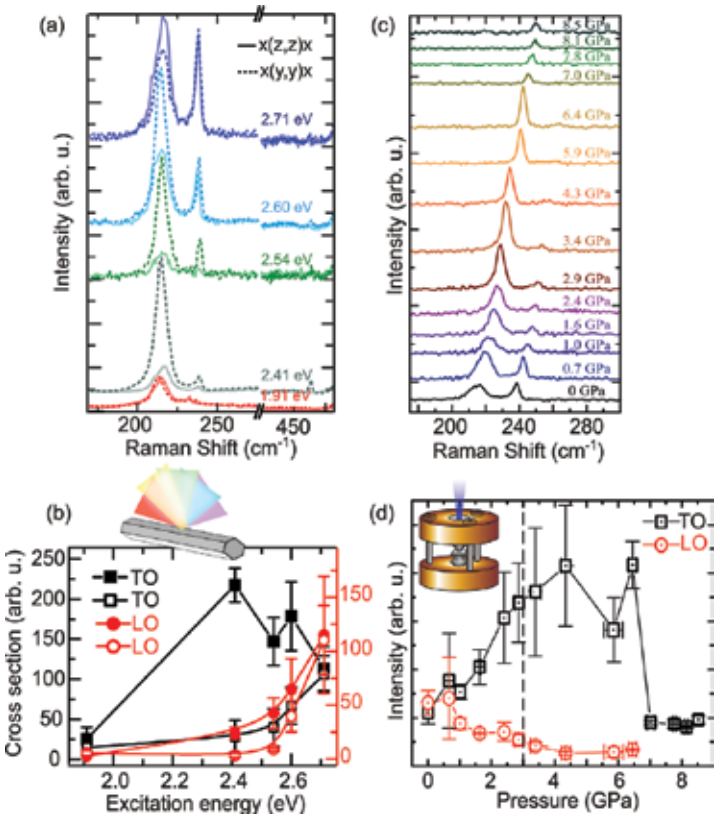

Figure 10. Resonant Raman experiments on WZ InAs NWs. (a) Spectra collected on a single NW with five different excitation energies in the $x(zz)\bar{x}$ (solid line) and $x(yy)\bar{x}$ (dashed line) configurations. (b) Raman scattering cross section of the TO as defined in the text (black squares and left scale) and LO (red circles and right scale) modes for the configuration $x(zz)\bar{x}$ (open symbols) and $x(yy)\bar{x}$ (filled symbols). The error bars come from the average of the Raman scattering cross sections of NWs with four different diameters. Solid lines are guides to the eyes. Reproduced with permission from [30]. Copyright 2013, American Chemical Society. (c) Spectra of a NW bundle for different applied pressures from 0 to 8.5 GPa. Excitation energy is fixed at 2.71 eV. (d) Average on the peaks intensities over two different bundles. The pressure at which the resonance is expected to occur in bulk InAs (based on the known pressure dependence of the E_1 band gap for this excitation energy) is indicated by a dashed line. The solid lines are a guide to the eyes.

http://dx.doi.org/10.5772/65113

the bottommost conduction band minimum, having a Γ_7^C symmetry, and the three valence band maxima, with Γ_9^V, $\Gamma_{7,+}^V$, and $\Gamma_{7,-}^V$ symmetries (in order of increasing hole energy). Due to the anisotropy of the hexagonal crystal lattice, there are special selection rules for these transitions: A is allowed only for light polarized perpendicular to the NW growth (like in $x(yy)\bar{x}$ and $x(yz,zy)\bar{x}$ configuration), B and C are allowed for both perpendicular and parallel polarized light (like in $x(yy)\bar{x}$, $x(yz,zy)\bar{x}$, and $x(zz)\bar{x}$ configurations). If we consider now the coupling of electronic states with the different phonon mode symmetries, the E_2^H mode, allowed in $x(yy)\bar{x}$, couples with the A transition, while the A_1 mode, in $x(zz)\bar{x}$, couples with B and C, and E_1, in $x(zy)\bar{x}$, couples with A, B, and C [30]. According to theoretical calculations on WZ InAs, the E_1 gap at A point involving the first valence band (the one with Γ_9^V symmetry at Γ) has an energy of ~2.4 eV, the E_1(A) gap involving $\Gamma_{7,+}^V$ band has an energy slightly higher than 2.6 eV, and the E_1(A) gap involving $\Gamma_{7,-}^V$ band has a much higher energy. Therefore, the resonance of the TO in $x(yy)\bar{x}$ (mainly E_2^H) at about 2.4 eV can be explained by the coupling between E_2^H and the E_1(A) gap involving the first valence band. We stress that the 2.4 eV value of the E_1(A) gap is reduced with respect to the ZB InAs E_1 gap, in agreement with band structure calculations. The increased intensity with no resonance of the TO in $x(zz)\bar{x}$ (mainly A_1) in the investigated energy region suggests that the resonance could be shifted to energies higher than 2.71 eV, which can be due to the sum of the contributions from the second and the third valence bands.

Let us now discuss high-pressure Raman measurements on the same NWs [30, 32]. Measurements were performed by exciting bundles of NWs with 2.71 eV. Hydrostatic pressure was applied by using a screw clamped opposing-plate diamond Anvil cell (DAC, as the one sketched in **Figure 10(d)**). The NWs were loaded together with a ruby microsphere in a sample chamber located in the center of a stainless steel gasket. A methanol-ethanol mixture (4:1) was used as pressure transmitting medium, and the ruby microsphere was used for determining the pressure through the ruby-fluorescence technique [33]. Raman spectra were collected in backscattering geometry without filtering light polarization, since it is not conserved through the diamond and anyhow the orientation of NWs in the bundle is unknown. Raman spectra collected from an InAs bundle are shown in **Figure 10(c)** for increasing applied pressure up to 8.5 GPa. At ambient pressure (0 GPa), the Raman spectrum is similar to the spectra in panel (a): the broad peak at ~216 $cm^{-1}$is due to convolution of the A_1/E_1 (TO) mode and the E_2^H TO mode (we continue to label the peak as TO), and the peak at ~238 cm^{-1} is due to LO mode. We notice that the frequency of the TO and LO increases with pressure, the FWHM of the TO decreases with pressure, the intensity of the LO peak decreases after 3 GPa and vanishes for pressures higher than 6.4 GPa, and the intensity of the TO increases (with a first maximum around 4 GPa and a second one around 6.5 GPa) and then decreases drastically without vanishing. The absolute intensities of the TO and LO modes (after averaging between two different bundles) are plotted in panel (d) as a function of the applied pressure. Red circles refer to LO, black squares to TO. In bulk ZB InAs, the pressure at which the resonance is expected to occur (based on the known pressure dependence of the E_1 band gap for 2.71 eV

excitation energy) is ~3 GPa, as indicated by a dashed line in panel (d). Here, the intensity increase for the TO mode is observed at a pressure slightly higher than 3 GPa due to a value of the E_1-gap slightly lower than the 2.71 eV. This finding confirms the results obtained by the energy-dependent Raman study. Indeed, assuming for the E_1 WZ band gap the same pressure dependence of the E_1 ZB gap and an energy gap at ambient pressure of 2.4 eV as the one determined from data in **Figure 10(b)**, the resonance is expected at about 4.2 GPa, in good agreement with the measurements. Moreover, the continuous decrease in intensity of the LO mode with pressure agrees with what expected from a gap which is already bigger than 2.71 eV at ambient pressure: with increasing pressure, and consequently increasing the relevant energy gap, the LO mode is going far and far from resonance conditions, leading to a continuously decreased intensity. This confirms its coupling with the gaps from the second and third valence bands at the A point. The disappearance of the LO mode at 6.4 GPa could be related to the structural phase transition that occurs in the ZB material, associated with the metallization of the system. We point out that the spectrum could be fully recovered after depressurizing the DAC, indicating a reversible structural transition.

We have shown that the present method, based on the combination of two RRS techniques, has proved to be a novel and powerful experimental tool for band structure investigation of nanoscale semiconductors.

In conclusion, we have provided valuable examples, mostly based on our experimental results, of how powerful is Raman spectroscopy in investigating all the most important aspects of the lattice dynamics of semiconductor nanowires.

Acknowledgements

The authors acknowledge S. Yazji and G. Abstreiter of Walter Shottky Institute of the Technische Universität München, A. Fontcuberta i Morral of the École Polytechnique Fédérale de Lausanne, and P. Postorino of Sapienza University of Rome for their precious contribution to data acquisition and interpretation. We acknowledge financial support from the Swiss National Science Foundation research grant (Project Grant No. 200021_165784).

Author details

Marta De Luca and Ilaria Zardo*

*Address all correspondence to: ilaria.zardo@unibas.ch

Department of Physics, University of Basel, Basel, Switzerland

References

[1] Yazawa M, Koguchi M, and Hiruma K. Heteroepitaxial ultrafine wire-like growth of InAs on GaAs substrates. Applied Physics Letters. 1991;58:1080.

[2] Hayden O, Agarwal R, and Lu W. Semiconductor nanowire devices. Nanotoday. 2008;3:12.

[3] Plissard S R, Slapak D R, Verheijen M A, Hocevar M, Immink G W G, van W I, Nadj-Perge S, Frolov S M, Kouwenhoven L P, and Bakkers E P A M. From InSb nanowires to nanocubes: Looking for the sweet spot. Nano Letters. 2012;12(4):1794–1798.

[4] De Luca M. Optical Studies in Semiconductor Nanowires. 1st ed. Roma: Sapienza Università Editrice; 2015. 248 p.

[5] Subramaniam M R, Devanathan S, and Kumaresan D. Synthesis of micrometer-sized hierarchical rutile TiO_2 flowers and their application in dye sensitized solar cells. RSC Advances. 2014;4:36791.

[6] Wagner R S and Ellis W C. Vapor-liquid-solid mechanism of single crystal growth. Applied Physics Letters. 1964;4:89.

[7] Dasgupta N P, Sun J, Liu C, Brittman S, Andrews S C, Lim J, Gao H, Yan R, and Yang P. 25th anniversary article: Semiconductor nanowires–synthesis, characterization, and applications. Advanced Materials. 2014;26:2137–2184.

[8] Dey A W, Svensson J, Borg B M, Ek M, and Wernersson L-E. Single InAs/GaSb nanowire low-power CMOS inverter. Nano Letters. 2012;12:5593.

[9] Rossi N, Braakman F R, Cadeddu D, Vasyukov D, Tütüncüoglu G, Fontcuberta i Morral A, Poggio M. Vectorial scanning force microscopy using a nanowire sensor. Nature Nanotechnology (in press). DOI: 10.1038/NNANO.2016.189.

[10] Weisse J M, Lee C H, Kim D R, and Zheng X. Fabrication of flexible and vertical silicon nanowire electronics. Nano Letters. 2012;12:3339.

[11] Ra Y-H, Wang R, Woo S Y, Djavid M, Sadaf S M, Lee J, Botton G A, and Mi Z. Full-color single nanowire pixels for projection displays. Nano Letters. 2016;16:4608.

[12] Yazji S, Swinkels M Y, De L M, Hoffmann E A, Ercolani D, Roddaro S, Abstreiter G, Sorba L, Bakkers E P A M, and Zardo I. Assessing the thermoelectric properties of single InSb nanowires: The role of thermal contact resistance. Semiconductor Science and Technology. 2016;31:064001.

[13] Krogstrup P, Jørgensen H I, Heiss M, Demichel O, Holm J V, Aagesen M, Nygard J, and Fontcuberta i Morral A. Single-nanowire solar cells beyond the Shockley–Queisser limit. Nature Photonics. 2013;7:306.

[14] Sahoo P K, Janissen R, Monteiro M P, Cavalli A, Murillo D M, Merfa M V, Cesar C L, Carvalho H F, de Souza A A, Bakkers E P A M, and Cotta M A. Nanowire arrays as cell

force sensors to investigate adhesin-enhanced holdfast of single cell bacteria and biofilm stability. Nano Letters. 2016;16:4656–4664. DOI: 10.1021/acs.nanolett.6b01998

[15] Turrel G and Corset J, editors. Raman Microscopy Developments and Applications. 1st ed. Malta: Academic Press; 1996. 463 p.

[16] Xiang Y, Zardo I, Cao L Y, Garma T, Heiss M, Morante J R, Arbiol J, Brongersma M, and Fontcuberta i Morral A. Spatially resolved Raman spectroscopy on indium-catalyzed core-shell germanium nanowires: Size effects. Nanotechnology. 2010;21:105703.

[17] Spirkoska D, Abstreiter G, and Fontcuberta i Morral A. Size and environment dependence of surface phonon modes of gallium arsenide nanowires as measured by Raman spectroscopy. Nanotechnology. 2008;19:435704.

[18] Zardo I, Abstreiter G, and Fontcuberta i Morral A. Raman spectroscopy on semiconductor nanowires. In: Paola Prete, editor. Nanowires. InTech; 2010. DOI: 10.5772/39514. Available from http://www.intechopen.com/books/nanowires/raman-spectroscopy-on-semiconductor-nanowires

[19] Zardo I, Conesa-Boj S, Peiro F, Morante J R, Arbiol J, Uccelli E, Abstreiter G, and Fontcuberta i Morral A. Raman spectroscopy of wurtzite and zinc-blende GaAs nanowires: Polarization dependence, selection rules, and strain effects. Physical Review B. 2009;80:245324.

[20] Ruda H E and Shik A. Polarization-sensitive optical phenomena in semiconducting and metallic nanowires. Physical Review B. 2005;72:115308.

[21] De Luca M, Zilli A, Fonseka H A, Mokkapati S, Miriametro A, Tan H H, Smith L M, Jagadish C, Capizzi M, and Polimeni A. Polarized light absorption in wurtzite InP nanowire ensembles. Nano Letters. 2015;15:998–1005.

[22] Glas F, Harmand J-C, and Patriarche G. Why does wurtzite form in nanowires of III-V zinc blende semiconductors? Physical Review Letters. 2007;99:146101.

[23] Caroff P, Bolinsson J, and Johansson J. Crystal phases in III–V nanowires: From random toward engineered Polytypism. IEEE Journal of Selected Topics. Quantum Electronics. 2011;17:829.

[24] Akopian N, Patriarche G, Liu L, Harmand J-C, and Zwiller V. Crystal phase quantum dots. Nano Letters. 2010;10(4):1198–1201.

[25] Assali S, Gagliano L, Oliveira D S, Verheijen M A, Plissard S R, Feiner L F, and Bakkers E P A M. Exploring crystal phase switching in GaP nanowires. Nano Letters. 2015;15:8062.

[26] Murayama M and Nakayama T. Chemical trend of band offsets at wurtzite/zinc-blende heterocrystalline semiconductor interfaces. Physical Review B. 1994;49:4710.

[27] Loudon R. The Raman effect in crystals. Advanced Physics. 1964;13:423–482.

[28] Wang X, Zardo I, Spirkoska D, Yazji S, Ng K W, Ko W, Chang-Hasnain C, Finley J, and Abstreiter G. Valence band splitting in wurtzite InGaAs nanoneedles studied by photoluminescence excitation spectroscopy. ACS Nano. 2014;8:11440.

[29] Ketterer B, Mikheev E, Uccelli E, and Fontcuberta i Morral A. Compensation mechanism in silicon-doped gallium arsenide nanowires. Applied Physics Letters. 2010;97:223103.

[30] Zardo I, Yazji S, Hörmann N, Hertenberger S, Funk S, Mangialardo S, Koblmüller G, Postorino P, and Abstreiter G. E1(A) Electronic band gap in wurtzite InAs nanowires studied by resonant Raman scattering. Nano Letters. 2013;13:3011.

[31] KettererB, Heiss M, Uccelli E, Arbiol J, and Fontcuberta i Morral A. Untangling the electronic band structure of wurtzite GaAs nanowires by resonant Raman spectroscopy. ACS Nano. 2011;5:7585.

[32] Yazji S, Zardo I, Hertenberger S, Morkötter S, Koblmüller G, Abstreiter G, and Postorino P. Pressure dependence of Raman spectrum in InAs nanowires. Journal of Physics: Condensed Matter. 2014;26:235301.

[33] Mao H K, Xu J, and Bell P M. Calibration of the ruby pressure gauge to 800 kbar under quasi-hydrostatic condition. Journal of Geophysical Research. 1986;91:4673–4676.

Chapter 5

Raman Study of the Crystalline-to-Amorphous State in Alpha-Decay–Damaged Materials

Ming Zhang

Additional information is available at the end of the chapter

http://dx.doi.org/10.5772/65910

Abstract

The stabilization and immobilization of high-level radioactive wastes in solid forms have become one of the most pressing industrial problems. Different crystalline mineral phases have been proposed as actinide-bearing crystalline hosts for waste materials. Self-radiation damage from alpha-decay of the incorporated actinides (such as U, Th) and other rare earth elements can lead to metamict state (amorphous state) and can affect the durability and long-term performance of these actinide-bearing phases. To investigate the impact of radiation on the nuclear waste forms and to obtain a better comprehension of the damage process and amorphization mechanism are important. The issues of interactions between high-energy particles and solids and radiation-induced structural modifications in crystalline-to-amorphous state are, in fact, an important and active area of fundamental researches. To study metamict state and metamictization is also important for geochemistry as the U-Pb isotope system is commonly used for age dating. Although radiation effect and naturally occurring radiation damage (the process is known as metamictization) have been the subject for many research investigations, there remain important and fundamental issues which need to be understood, for example, the structural changes at the atomic level caused by metamictization, the crystal structure of radiation-induced amorphous phases, solubility and diffusion of radioactive elements in damaged host phases, the effect of pressure and temperature on metamictization process and interaction of water and fluids with nuclear waste forms. Raman spectroscopy is found to be a very powerful tool for study and analysis of the damage effect and metamictization. This chapter describes and reviews recent Raman applications in zircon and titanite, which are proposed for nuclear waste forms. These applications are focused on radiation effect and structural damage process caused by alpha-decay process as well as recrystallization due to thermal annealing.

Keywords: Raman spectroscopy, radiation damage, metamictization, actinide, zircon, titanite

1. Introduction

Today, there are over 430 commercial nuclear power reactors in 31 countries which provide over 10% of the world electricity [1]. As a result, huge amounts of highly radioactive nuclear wastes are produced each year. One of the critical issues in nuclear energy industry is the safe disposal of nuclear wastes, especially high-level nuclear wastes (HLNW). The below are some minerals and synthetic materials proposed or developed as actinide-bearing crystalline hosts for waste materials [2–4]: zircon ($ZrSiO_4$), titanite ($CaTiSiO_5$), baddeleyite $(Zr,Hf,\ldots)O_2$, hafnon ($HfSiO_4$), perovskite $[(Ca,Gd,\ldots)(Al,Fe,Ti,\ldots)O_3]$, zirconolite [$CaZrTi_2O_7$ and $CaZrSi_2O_7$], apatite $[Ca_{10}(PO_4)_6(OH,F,Cl,B)_2]$, pyrochlore [$CaZrGd_2Ti_2O_7$, $Gd_2Zr_2O_7$, and $La_2Zr_2O_7$-$Nd_2Zr_2O_7$], monazite $[(La,Ce,\ldots)PO_4]$, and garnet $[(Ca,Fe,Gd,\ldots)_3(Al,Fe,Si,\ldots)_5O_{12}]$. Among them, zircon is one of the most studied and modeled minerals. Currently, pyrochlore has attracted attention because of its radiation damage resistance.

Self-radiation from alpha-decay of the incorporated actinides can lead to lattice damage resulting in structural change and transformation from crystalline state to an amorphous or aperiodic state, that is, metamict state (the process is known as metamictization) [5–7].

The effects of radiation damage on the structure of metamict minerals can be seen as systematic changes of its physical properties [8]: an increase in cell parameters and broadening of X-ray diffraction patterns [9–12]; a decrease in Raman and infrared intensities and dramatic band broadening [13, 14]; decreases in refractive index and birefringence [9, 15]; absorption of hydrous species [16–19]; an increase in fracture toughness [20]; a decrease in density [9, 10]; a variation of TEM diffraction patterns [10, 21, 22]; an increase of leach rate [23]; changes in bulk modulus and hardness [24]; a change of ^{29}Si NMR features [11, 25]; changes of diffuse X-ray scattering from single crystals [6]; occurrences of Huang type diffuse X-ray diffraction [26]; a change in EXAFS [27]; a variation of Mössbauer spectra [11, 28]; and a variation of positron annihilation lifetime [29]. Therefore, the durability and performance of these actinide-bearing phases can be altered by self-radiation damage from alpha-decay of the incorporated actinides. To gain better comprehension of the effect of radiation on crystal structure at the atomic level, the related damage process and damage mechanism are issues of critical importance.

Vibrational spectroscopy (Raman and infrared (IR) spectroscopy) is a very powerful tool in the analysis and study of structural variations related to medium- and short-range order [30]. Early analysis of alpha-decay damaged materials by Raman spectroscopy can be traced back to about two decades ago [31, 32]. The main advantages of vibrational spectroscopy (Raman and infrared spectroscopy) [30] are their fast response time (which can be in the range of ~10^{-12} s), short correlation length scale (which is in the order of a few unit cells), and good sensitivity to hydrous and hydroxyl species (e.g., H_2O and OH). In contrast to diffraction methods which are generally sensitive to periodicity of lattices and the crystallinity of a specimen, vibrational spectroscopy is mainly associated with the strength and length of interatomic bonds, as well as the atomic masses of the sample. Therefore, vibrational spectroscopy can give valuable information on phonon energy, bulk structure, chemical composition, and surface for not only crystalline materials, but also disordered phases. The method has, in fact, been widely applied in studying disordered and amorphous materials such as glasses.

http://dx.doi.org/10.5772/65910

This chapter illustrates recent applications of Raman spectroscopy in the study of radiation-damaged or metamict zircon and titanite. Being different from simple identification of damaged phases with Raman techniques, the investigations are focused on important issues such as: What happens at the atomic level during radiation damage and recrystallization? What are the possible structural modifications during metamictization? And whether decomposition into oxides is the final result of radiation damage. The experimental results provide a better understanding of the mechanism of radiation damage and the recrystallization processes.

2. Effects of alpha-decay radiation on Raman spectra of zircon and titanite

Zircon ($ZrSiO_4$) is a common accessory mineral in igneous rocks, in metamorphic rocks, and as detrital grains in sedimentary rocks. The work [33] has showed that zircon crystallizes to a tetragonal structure with space group D_{4h}^{19} or $I4_1/amd$ (with $Z = 4$), containing a chain of alternating, edge-sharing SiO_4 tetrahedra and ZrO_8 triangular dodecahedra extending parallel to the *c*-axis. Actinides such as U, Th and Pu can substitute Zr and locate in the Zr site. Because of their uranium and thorium content, some zircons undergo metamictization. Group theory predicts twelve Raman-active normal modes in zircon at $k = 0$: $2A_{1g} + 4B_{1g} + B_{2g} + 5E_g$ [34]. These Raman modes can be simply classified as internal modes and external modes. There are five ($2B_{1g} + 3E_g$) external modes and seven ($2A_{1g} + 2B_{1g} + B_{2g} + 2E_g$) internal modes. For Raman measurements of natural samples which are damaged by radiation of incorporated actinides, it is a good practice to use laser excitation with different wavelengths to ensure that spectral features recorded are due to phonon modes rather than features due to luminescence and impurities-related color centers (e.g., the work [8] used 514, 488, 457 and 632 nm lasers in its Raman measurement). Nine of the twelve predicted Raman modes can be seen in the most crystalline natural zircon (**Figure 1**). They are internal modes: 1008 cm^{-1} (B_{1g}, ν_3 stretching of SiO_4), 975 cm^{-1} (A_{1g}, ν_1 stretching), 439 cm^{-1} (A_{1g}, ν_2 bending), and 269 cm^{-1} (B_{2g}, ν_2 bending) and external modes: 393, 355, 225, 214 and 202 cm^{-1}. The other predicted Raman bands appear too weak to be observed in a common experimental arrangement.

The effect of alpha-decay radiation damage on the structure of zircon is evidenced by a decrease in band frequencies, a line broadening of Raman modes and a decrease in Raman intensity (**Figure 1**). Well-crystallized zircon samples have sharp and well-resolved Raman modes. With increasing alpha-decay radiation dose (the radiation dose of natural minerals is mainly related to sample's rock age and concentration of U and Th, and it can be calculated [9, 10]), the stretching modes of SiO_4 tetrahedra near 975 and 1008 cm^{-1} become weaker and broader, while the lower frequency modes become gradually weaker and could hardly be analyzed for high-dose cases. The broad Raman feature concurring near 950 cm^{-1} (the insert part in **Figure 1**) indicates the formation of amorphous phases in high-dose samples. The behavior of the band also suggests that SiO_4 tetrahedra remain in highly damaged zircon samples. As the 950 cm^{-1} feature is significantly away from the intense bands near 1008 cm^{-1} in terms of wavenumber, its appearance implies a new linkage of SiO_4 tetrahedra.

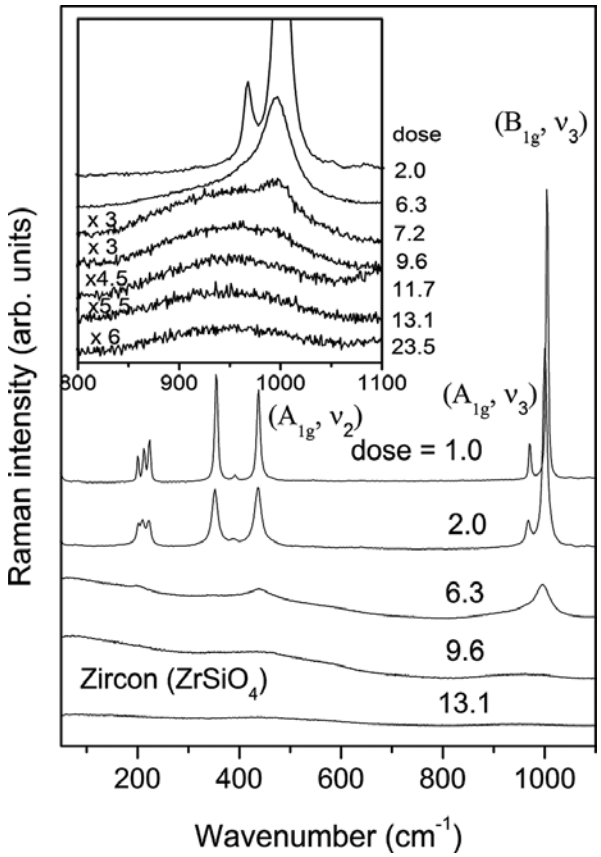

Figure 1. Micro-Raman spectra (with 488 nm excitation) of metamict zircon between 50 and 1100 cm^{-1} (Ref. [8], modified). The dosage is in the units of 10^{18} alpha-events g^{-1}.

The dose dependence of the frequency and full width at half maximum of the 1008 cm^{-1} stretching band of SiO_4 are shown in **Figure 2**. The data indicate that the Si-O bond strength exhibits a weakness, while the specific volume of the crystal increases, although radiation damage does not destroy SiO_4 and short-range ordering associated with the tetrahedral framework remains. The observation suggests that the increase in bond distances is probably depolarized by a rotation of the SiO_4 tetrahedra within the zircon structure. The data clearly show that the unit cell swelling in damaged zircon is associated with the SiO_4 tetrahedra which formed new linkage and play an important role in the zircon structure rather than isolated molecular complexes.

Raman band widths [full width at half maximum (FWHM)] and frequencies (especially those of the ν_3 band of SiO_4 near 1008 cm^{-1}) in zircon have been used for investigating the relationship between U-Pb isotopic discordance and metamictization [35–37]. More work is desirable to gain a better understanding of the behavior of this band during radiation damage and recrystallization, and the potential influence of chemical impurities on the band.

http://dx.doi.org/10.5772/65910

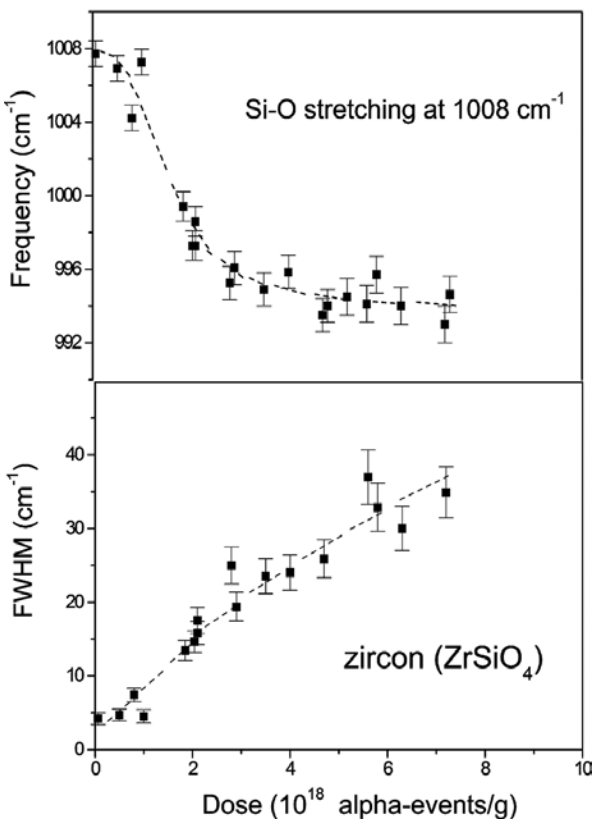

Figure 2. Phonon frequency and full width at half maximum (FWHM) of the ν_3 stretching band (B_{1g}) of SiO_4 in radiation-damaged zircon as a function of radiation dose (Ref. [8], modified). The lines are visual guides.

Another good example of Raman study of alpha-decay radiation damage is the application in metamict titanite. Titanite is a calcium titanium nesosilicate mineral, $CaTiSiO_5$. Taylor and Brown [38] synthesized pure titanite, and their X-ray data show that it is monoclinic (space group $P2_1/a$, $Z = 4$) with unit-cell parameters $a = 7.057$, $b = 8.707$, $c = 6.555$ Å, $\beta = 113.81°$. The crystal structure of $P2_1/a$ titanite phase contains chains of corner-sharing TiO_6 octahedra parallel along [1 0 0], which are cross-linked by edge-sharing CaO_7-polyhedra extending parallel to [1 0 1]. On heating, the $P2_1/a$ phase undergoes a phase transition to an $A2/a$ phase near 500 K [38]. The two phases have different optical active representations. For the $P2_1/a$ phase $\Gamma_{optic} = 24A_g + 24B_g + 23A_u + 22B_u$ (A_g and B_g are Raman-active, and A_u and B_u IR-active), whereas for the $A2/a$ phase $\Gamma_{optic} = 9A_g + 12B_g + 11A_u + 13B_u$ [39]. Therefore, the $P2_1/a$ phase is expected to have 48 Raman-active modes, whereas the $A2/a$ phase contains 21 Raman modes. Although pure synthetic titanite is in $P2_1/a$ symmetry, some well-crystalline natural titanite samples were surprisingly reported to be in the $A2/a$ structure [11]. This significant difference

in the total number of the Raman modes for the $P2_1/a$ and $A2/a$ phases is important and helpful for identifying the presence of the two phases [40].

Natural titanite occurs in igneous and metamorphic rock and incorporates a variety of impurity ions such as U, Th and other rare earth elements (REE). The structure of natural titanite is often metamict, as a result of self-radiation damage associated with the alpha-decay of the incorporated REEs. Raman spectra of crystalline or undamaged natural titanite (**Figure 3**) show spectral features similar to those of synthetic pure $P2_1/a$ titanite as reported previously [39]. The Raman work [41] suggested that anisotropy is preserved upon metamictization and that the structural state of highly metamict titanite should not be considered as quasi-amorphous. It was reported that the local structure of the amorphized regions contains a high degree of short-range order [42]. The effect of alpha-decay radiation on Raman spectrum of titanite is characterized by a dramatic decrease in intensity and line broadening (**Figure 3**).

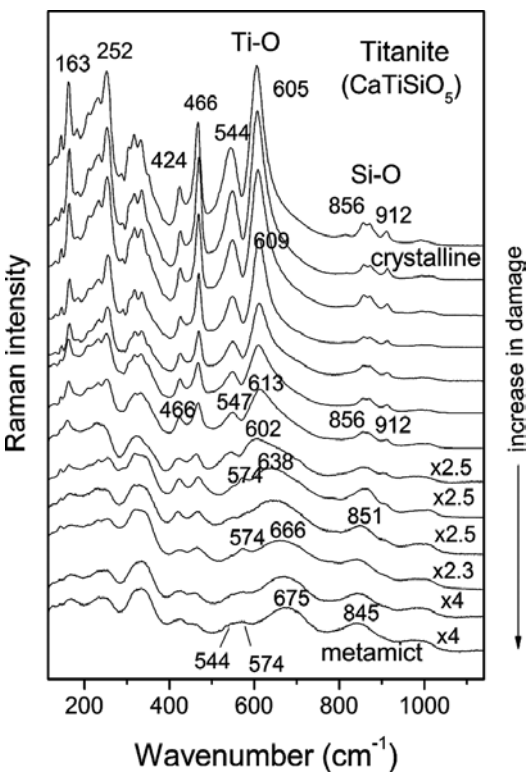

Figure 3. Raman spectra of fine powders of titanites ($CaTiSiO_5$) with different degrees of radiation damage (Ref. [40], modified). The top spectra are from well-crystallized samples, which show that the space group is the $P2_1/a$ symmetry [40]. Metamictization causes a loss of spectral details and a line broadening in the spectra of titanites. The Ti-O stretching band near 605 cm^{-1} shifts to a higher frequency, while a extra band near 574 cm^{-1} (which is due to the $A2/a$ phase) appears in partially damage samples. A relatively intense band is recorded near 675 cm^{-1} with a FWHM of about 80 cm^{-1} in heavily damaged titanite (in the bottom of the plot). The large FWFM indicates that this feature is related to radiation-induced disordered or amorphous phase. Crystalline titanites have the bands near 858 and 912 cm^{-1}, which are due to stretching vibrations of SiO_4 tetrahedra. These bands shift to lower frequencies in intermediately damaged samples and appear as a broad feature near 845 cm^{-1} in heavily damage samples (bottom).

http://dx.doi.org/10.5772/65910

The intense Ti-O band near 605 cm^{-1} shows the largest intensity decrease, indicating radiation effect on the TiO_6 octahedra. This change is consistent with the behavior of the infrared-active Ti-O stretching mode near 670 cm^{-1}, which is mostly affected by radiation damage and shifts to 710 cm^{-1} in heavily damaged titanite [43]. A Raman work on metamict titanite [44] proposed that radiation-induced periodic faults in the crystalline matrix of metamict titanite are related to the disturbance of SiO_4-TiO_6-SiO_4-TiO_6 rings comprising TiO_6 octahedra from different chains, whereas the radiation-induced amorphization is associated with the partial change of Ti coordination from octahedral to pyramidal and/or tetrahedral, which in turn violates the Ti-O-Ti intrachain linkages. In addition to these changes, radiation damage in titanite leads to the appearance of extra Raman signals (e.g., 574 cm^{-1}) in intermediately damaged samples (**Figure 3**). This behavior is not seen in metamict zircon. These additional phonon modes in these partially metamict titanite samples are, in fact, characteristic Raman bands of the *A*2/*a* phase [40]. The results indicate that as a result of the radiation, the $P2_1/a$ titanite first transforms to the *A*2/*a* structure, and then, with further radiation, the *A*2/*a* phase becomes an amorphous phase. Beirau et al. [45] reported in situ high-temperature Raman data of radiation-damaged titanite, and they found a structural anomaly near 500 K in partially metamict titanite, which was attributed to the $P2_1/a$-*A*2/*a* transition. These above findings explained why some of natural crystalline titanites were found to appear the *A*2/*a* structure [11], rather than the $P2_1/a$ phase. This could be due to the fact that natural titanite crystals commonly experienced radiation damage, which resulted in an alteration of the $P2_1/a$ crystal structure [40].

3. Issue of possible decomposition in radiation-damaged zircon

In the study of radiation effect and metamict state, what happens at the atomic level is an unclear and important question. Researchers have focused on issues such as possible changes in the coordination number of Zr [27], radiation-induced disordering rather than amorphization [31], damage-related distorted and disoriented isolated silica tetrahedra [16], the fraction of amorphized phase [14, 46], as well as whether metamictization leads to phase separation or damaged minerals decompose into their oxides, and what is the structural state of the decomposed phases [47, 48]. This issue of radiation-induced decomposition was, in fact, debated over decades [30]. Based on infrared data on metamict zircon, a two-stage damage process was proposed [49]. It was suggested that the first stage produces, throughout the lattice, highly stressed and expanded zircon with distorted SiO_4 tetrahedra, while the second stage was suggested to result in the decomposition of $ZrSiO_4$ to ZrO_2 and SiO_2, probably together with some aperiodic $ZrSiO_4$ [49]. However, the decomposition of damaged zircon was often reported in zircon samples only annealed experimentally at high temperatures, in which the decomposition commonly leads to different polymorphs of ZrO_2 and glassy silica. Monoclinic ZrO_2 was found in heavily damaged samples heated to 1373 K [50]. In a high-temperature study, Vance and Anderson [15] observed cubic and tetragonal ZrO_2 at 1073 and 1373 K, respectively. It was reported that highly metamict zircon contained randomly orientated ZrO_2 when annealed at 1173 K, and further annealing at 1523 K resulted in monoclinic ZrO_2, as well as a silica glass phase [51]. Ellsworth et al. [52] suggested that decomposition of metamict zircon into ZrO_2 and glassy SiO_2 could be one possible path for recrystallization. In contrast,

a high-temperature neutron work by [53] suggested that zircon decomposes into crystalline β-cristobalite (rather than silica glass) and tetragonal ZrO_2. An X-ray powder diffraction study at high temperatures reported the appearance of pseudo-cubic ZrO_2 [54]. Meldrum et al. [55] observed a decomposition of zircon into tetragonal ZrO_2 when irradiating zircon with heavy ions at around 950 K. As discussed by different works [56, 57], some of these previous works based on X-ray diffraction measurements might have experienced difficulties in the determination of cubic and tetragonal ZrO_2.

Vibrational (Raman and infrared) spectroscopy is a good analytical tool for resolving these problems related to decomposition of $ZrSiO_4$ into ZrO_2 and SiO_2, as pointed out by Ref. [30], because Raman and infrared spectra of zirconia (ZrO_2) have been well studied previously and also because vibrational spectroscopy has short length scales. ZrO_2 has three common polymorphs at different temperatures. The room-temperature phase is monoclinic, while the tetragonal and cubic phases occur at high temperatures [58]. The theoretical calculations [59, 60] have given the optical phonon modes (for zero wave vector) for each polymorph of zirconia ZrO_2. The monoclinic ZrO_2 has space group $C_{2h}^5/P2_1/c$ and $Z = 4$, and it has eighteen Raman modes and fifteen infrared modes [$9A_g(R) + 9B_g(R) + 8A_u$ (IR) + $7B_u(IR)$] (R indicating Raman-active and IR indicating infrared-active). In tetragonal ZrO_2 (with space group $D_{4h}^{15}/P4_2/nmc$ and $Z = 2$), the phase has six Raman modes and three infrared modes [$A_{1g}(R) + 2B_{1g}(R) + 3E_g(R) + A_{2u}(IR) + 2E_u(IR)$]. For cubic ZrO_2 (with space group $O_h^5/Fm3m$ and $Z = 1$), its vibrational spectra have only one Raman and one infrared modes [$F_{2g}(R) + F_{1u}(IR)$].

The data in **Figure 1** indicate that it is apparent that there is a lack of signals of ZrO_2 in highly damaged zircons. This shows that ZrO_2 and SiO_2 are not the final products of metamictization in zircon. Results from infrared spectroscopy of radiation-damaged zircon [14, 47] also support this observation. As mentioned early, although decomposed zircons were commonly reported in lab-treated samples, tetragonal ZrO_2 was recorded in only one natural sample [8], with an unknown thermal history, among a large number of natural zircon samples with different degrees of damage analyzed in Refs. [14, 47, 48]. In order to explore and examine high-temperature behavior of damaged zircon and the possible causes for decomposition in zircon, systematic works were carried out by different groups [47, 36, 61, 62]. These works show that thermal annealing of heavily damaged zircon at high-temperature experiments may lead to the decomposition of metamict zircon into tetragonal ZrO_2 and glassy SiO_2 at 1200 K, and upon further heating tetragonal ZrO_2 transforms to monoclinic ZrO_2 near 1400 K. Undamaged and weakly damaged zircons are less likely to show decomposition during high-temperature annealing. It was reported that the decomposition-induced silica tended to evaporate on further heating [61, 63]. As naturally damaged samples might experience high-temperature processes, some reported decomposed metamict zircon could be due to natural thermal annealing prior to experiments. In contrast to high-temperature annealing, the presence of ZrO_2 in some natural zircons might be due to the reaction of fluids with metamict zircons, because radiation damage may alternate the chemical stability of zircon. The observation of ZrO_2 in dissolution experiments was reported in highly damaged zircon samples [64]. Raman data of hydrothermally leached metamict zircon [65] showed the formation of

http://dx.doi.org/10.5772/65910

monoclinic ZrO_2. In general, the decomposition of zircon into ZrO_2 and SiO_2 is related to radiation-damaged zircons. Their crystal lattice is heavily damaged and has more defects. As a result, the durability of these heavily damaged samples is expected to be affected, and they are vulnerable to the impact of external physical and chemical conditions (e.g., water, solutions, high temperature, and even high pressure).

Raman data of metamict titanite (**Figure 3**) also show there is a lack of formation of oxides in highly damaged samples [40]. The findings are supported by X-ray measurements and TEM [11] and infrared data [43]. The observation further shows that phase decomposition into oxides is not the final state of alpha-decay damage in these materials, and the materials are safe to be used as nuclear waste forms. It has been found that decomposition of radiation-damaged zircon is commonly related to high-temperature heating (see a below section).

4. Metamict state *versus* glass state of $CaTiSiO_5$ and $ZrSiO_4$

One of the interesting issues related to radiation damage and metamictization is the similarities or differences between the amorphous phases produced by alpha-decay radiation damage and those produced through thermally quenched glass melts. Previous studies [47] have led to unanswered questions and concerns: for example, What is the relationship between the structural characteristics of disordered materials and the type of irradiation or physical process used to produce them?

As a type of disordered or amorphous materials, metamict minerals were commonly considered as "glass-like" materials in early studies on naturally occurring radiation effect and metamictization, and the metamict state was referred as a glassy state, which is somehow similar to that obtained by rapid quenching of high-temperature melts [30]. With experimental data gathering, evidences have emerged that indicate their important differences between the aperiodic states. The dispersion depends on the physical processes, which produce the amorphous states. Vibrational spectroscopy (Raman and infrared) is very useful to study this issue because of its sensitivity to local structures.

Raman data of metamict titanite ($CaTiSiO_5$) and its glass analogue (with the same chemical compositions) produced by quenching melts show that the two types of materials have different vibrational features (especially in the Ti-O and Si-O stretching regions) (**Figure 4**) [40], although they both are almost amorphous in terms of electron microscopy and X-ray diffraction analysis. The $CaTiSiO_5$ glasses produced from melts show a Si-O stretching band near 827 cm^{-1}, while metamict titanite has a relatively weak band in a higher wavenumber, 844 cm^{-1}. What is more, the quenched melts of $CaTiSiO_5$ have a relatively strong band peaked near 709 cm^{-1}, but this feature is almost absent in metamict titanite. The Raman observations are supported by the results for the same samples analyzed by infrared reflection and absorption spectroscopy [43]. These results suggest structural differences associated with Ti-O and Si-O bonds in the glasses and metamict phases. Interestingly, the glassy and metamict titanites also exhibit some similarities in a couple of band positions in the far infrared region (below 450 cm^{-1}). For example, they both have bands around 170, 330 and 430 cm^{-1}.

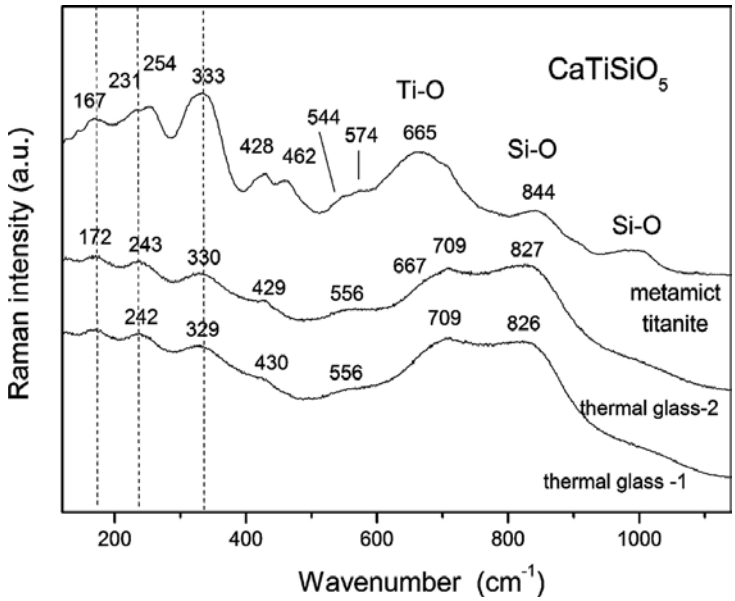

Figure 4. $CaTiSiO_5$ glasses produced by quenching titanite melts (thermal glass-1 and thermal glass-2 are prepared by quenching $CaTiSiO_5$ melts) show overall spectra patterns different from those of metamict titanite, especially in the region of 600 and 1100 cm^{-1} [Ref, [40], modified). This indicates the spectral dispersion related to Si-O and Ti-O vibrations in the two types of disordered materials. However, the two materials exhibit some local maximums with similar or close peak positions (indicated by dash lines) in the far infrared region (100 and 500 cm^{-1}).

Zircon has a high melting temperature (above 2700–2800 K), and crystalline ZrO_2 and a liquid of SiO_2 may coexist for a composition of $ZrSiO_4$ at a temperature region of ~1960 K and ~2670 K [66]. It is difficult to quench zircon melts without decomposition into ZrO_2 and SiO_2; however, glass-like zircon ($ZrSiO_4$) has been recorded with Raman spectroscopy in laser-treated zircon in a study with laser melting, near the boundaries between the unmolten and molten regions (where a relatively large temperature gradient could exist) [67]. The large temperature gradient is expected to increase the quench rate and facilitate a "freeze" of the local configuration of the $ZrSiO_4$ melts before the decomposition takes place. These experimental results indicate that the metamict state is different from the glassy state obtained by quenching melts. Apparently, the processes and structural states associated with metamictization and irradiation amorphization are more complex than those in common thermal glasses. The formation of the metamict state involves not only amorphization, but also defect accumulation caused by alpha-particle damage and further radiation or irradiation may lead to damage as well as recrystallization.

So far, although the issue remains under debates, there have been substantial evidences indicating characteristic discrepancies between two types of amorphous states (metamict and glass states) [68], for example: (i) the two types of materials commonly have spectral and structural discrepancies [40, 43, 69, 70]; (ii) high-energy heavy ion irradiation may lead to significant modifications in local structures of glasses [71–74]; (iii) upon heating, radiation-damaged minerals tend to recrystallize epitaxially and recover to their original

http://dx.doi.org/10.5772/65910

cryptographic orientations [48, 51, 75], while during high-temperature treatments, glasses commonly undergo a glass transition; and (iv) for common glasses, their glass transition temperatures are roughly defined, while various responses at different temperatures are seen in metamict minerals. For example, radiation-induced defects in metamict zircon may be annealed or healed at temperatures as low as 600 K accompanied by changes in the oxidation state of U ions; partial decomposition of $ZrSiO_4$ into SiO_2 and SiO_2 in heavily damaged zircon may take place at 1050 K; diffusion and conversions of hydrogen-related species together with dehydroxylation may occur between 1200 and 1600 K (e.g., [16, 18, 52, 76, 77], see for the transition point [6]).

5. Effect of thermal annealing on metamict zircon and titanite

Thermal annealing of metamict minerals at high temperatures is commonly used in studies of radiation-damaged minerals [30]. Its aims are to restore the original crystal structure for the purpose of studying recrystallization temperature, activation energy, types of radiation-induced local defects and phase identification, and to obtain a good comprehension of the recrystallization process and mechanism. Extensive studies were carried out to investigate changes at the atomic level in metamict materials during high-temperature annealing [10, 15, 36, 40, 44, 47, 48, 50, 52, 54, 55, 65, 75, 78–81]. However, controversies remain regarding the recrystallization path and activation energy.

Thermal annealing results in recrystallization of metamict zircon (**Figure 5**). The effect of annealing temperature on the structural recovery of damaged zircon can be clearly seen in the frequency and FWHM of the ν_3 Si-O stretching (B_{1g}) as a function of temperature (**Figure 6**). With increasing annealing temperature, the frequency of this mode shows, systematically, a large increase in the region between 800 and 1050 K and a weaker increase with temperature above 1050 K. This is due to the healing of the defective lattice and the recrystallization of remaining crystalline domains. Highly damaged zircon tends to decompose into tetragonal ZrO_2 and SiO_2 near 1100 K, and the transformation of tetragonal ZrO_2 into monoclinic ZrO_2 is reported at higher temperatures [47]. The findings may explain the cause of some previously reported ZrO_2 and SiO_2 in natural zircon, which likely experienced natural heating processes.

Spectroscopic data [47, 48, 61] revealed different recrystallization processes between partially and heavily damaged zircons, that is, the recrystallization process depends on the cumulative radiation dose (**Figure 5**, **6a** and **6b**). Being similar to metamict zircon [47], the thermal response of the damaged titanite ($CaTiSiO_5$) is affected by their initial degrees of damage, that is, at the same treatment conditions, weakly or partially damaged samples are more likely to recover to crystalline titanite as compared with highly metamict samples [40]. Intermediately and heavily damaged titanite samples show a recovery of Ti-O and Si-O bands after annealing at 1300–1400 K, and these recovered crystals are consistent with the $P2_1/a$ symmetry, although in terms of band widths, they are far from a fully recovering [40]. Similar results were reported by the work of another group [44] who thermally treated a metamict titanite sample, which has an accumulated radiation dose of 1.2×10^{18} alpha-event/g by multistep annealing up to 1173 K, and found it was insufficient to recover the crystalline structure of the studied sample.

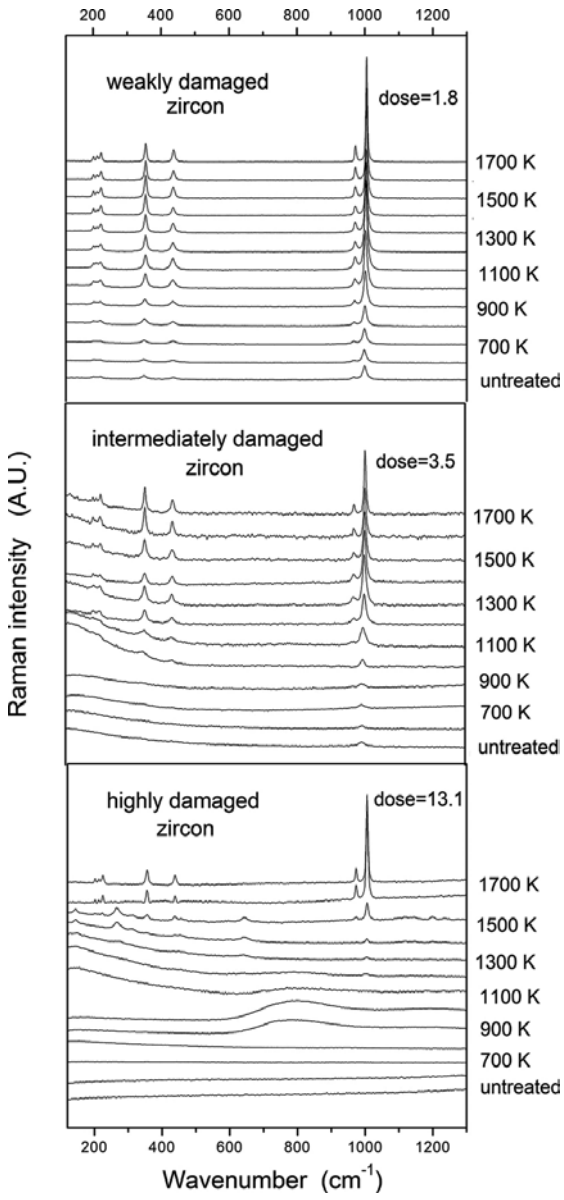

Figure 5. Raman spectra recorded from weakly metamict (dose = 1.8×10^{18} alpha-events g^{-1}), intermediately metamict (dose = 3.5) and highly metamict zircon (dose = 13.1) thermally treated in N_2 up to 1700 K and then punched (Ref. [47], modified).

The failure of a full recovery from the damage in thermally treated metamict titanite is also revealed by infrared spectroscopy [43]; however, the physics behind this remain unclear.

The thermally induced structural recovery and recrystallization of metamict zircon and titanite is also characterized a recovery of the anisotropy of the sample, which is restored

http://dx.doi.org/10.5772/65910

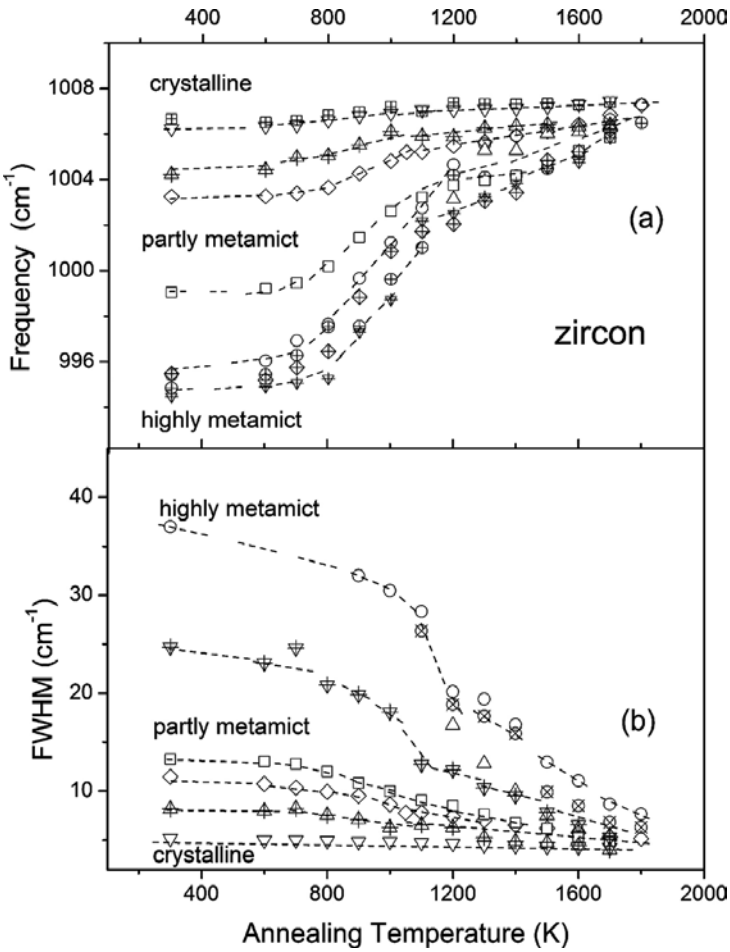

Figure 6. Phonon frequency and FWHM of the Raman ν_3 Si-O stretching (B_{1g}) in zircon ($ZrSiO_4$) with different degrees of damage as a function of annealing temperature (Ref. [47], modified with unpublished data).

during annealing, as evidenced by the recovery of orientational dependence of IR (as well as Raman) spectra along with the original crystallographic orientations as shown in **Figure 7**, which indicates an epitaxial recrystallization. This behavior indicates that in highly metamict zircon and titanite, crystalline nanodomains with original crystallographic orientations might still exist.

In conclusion, Raman spectroscopy, as shown above, is a very powerful tool for study of radiation damage in actinide-bearing phases and for estimation of their long-term durability of their physical properties and chemical stability. This type of Raman applications can provide a better understanding of the mechanism of radiation damage and thermal recrystallization processes. It has a wide usage in condensed mater physics, material science, nuclear material sciences, mineralogist, and geochemistry. It has also been used analysis other radiation-damaged minerals, such as fergusonite [82, 83], actinide-bearing monazite [32], titanoaeschynite (Nd) and

nioboaeschynite (Ce) [84], uranyl titanate mineral davidite-(La) [85], aeschynite-(Y) and polycrase-(Y) [86], and steenstrupine [87], and pyrochlore (Zietlow et al., personal communication).

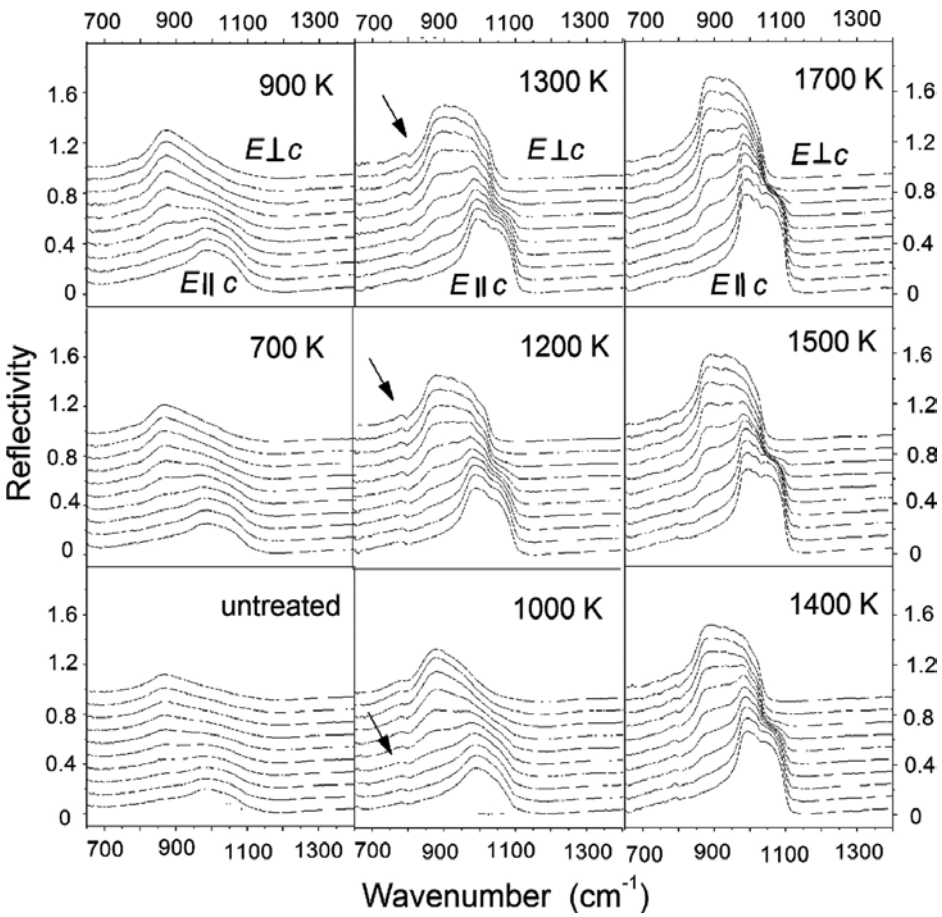

Figure 7. Orientational dependence of polarized infrared spectra of radiation-damaged zircon crystal (dose = 3.8×10^{18} alpha-events g^{-1}) annealed between 292 and 1700 K (Ref. [48], modified). The interval of the angle between the c-axis and the incident radiation E is 10°. The arrows indicate the appearance of an extra signal near 790 cm^{-1}, suggesting a possible intermediate phase. Thermal annealing results in a recovery of the anisotropy of the damage zircon crystal to its original crystallographic orientations.

Author details

Ming Zhang

Address all correspondence to: Ming_zhang@caep.cn

Institute of Materials, China Academy of Engineering Physics, Sichuan, China

References

[1] Ewing RC. Long-term storage of spent nuclear fuel. Nat. Mater. 2015;**14**:252–257.

[2] Ewing RC, Lutze W, Weber WJ. Zircon: a host-phase for the disposal of weapons plutonium. J. Mater. Res. 1995;**10**:243–246.

[3] Weber WJ, Ewing RC, Catlow CRA, de la Rubia TD, Hobbs LW, Kinoshita C, et al. Radiation effects in crystalline ceramics for the immobilization of high-level nuclear waste and plutonium. J. Mater. Res. 1998;**13**:1434–1484. doi:10.1557/JMR.1998.0205

[4] Ewing RC. The design and evaluation of nuclear-waste forms: clues from mineralogy. Can. Mineral. 2001;**39**:697–715. doi:10.2113/gscanmin.39.3.697

[5] Ewing RC. The metamict state: 1993—the centennial. Nucl. Instrum. Methods Phys. Res. Sect. B: Beam Interact. Mater. Atoms 1994;**B91**:22–29. doi:10.1016/0168-583X(94)96186-7

[6] Salje EKH, Chrosch J, Ewing RC. Is "metamictization" of zircon a phase transition? Am. Miner. 1999;**84**:1107–1116.

[7] Ewing RC, Meldrum A, Wang LM, Weber WJ, Corrales LR. Radiation effects in zircon. In Reviews in Mineralogy and Geochemistry, Vol 53, Edited by John Hanchar and Paul Hoskin; published by Mineralogical Society of America and Geochemical Society; 2003. p.387-425.

[8] Zhang M, Salje EKH, Farnan I, Graem-Barber A, Danial P, Ewing RC, Clark AM, Leroux H. Metamictization of zircon: Raman spectroscopic study. J. Phys. Condens. Matter. 2000;**12**:1915. doi:10.1088/0953-8984/12/8/333

[9] Holland HD, Gottfried D. The effect of nuclear radiation on the structure of zircon. Acta Crystallogr. 1955;**8**:291–300. doi:10.1107/S0365110X55000947

[10] Murakami T, Chakoumakos BC, Ewing RC, Lumpkin GR, Weber WJ. Alpha-decay event damage in zircon. Am. Miner. 1991;**76**:1510–1532.

[11] Hawthorne FC, Groat LA, Raudsepp M, Ball NA, Kimata M, Spike FD, Gaba R, Halden NM, Lumpkin GR, Ewing RC, Greegor RB, Lytle FW, Ercit TS, Rossman GR, Wicks FJ, Ramik RA, Sherriff BL, Fleet ME, Mccammon C. Alpha-decay damage in titanite. Am. Miner. 1991;**76**:370–396.

[12] Weber WJ. Alpha-decay-induced amorphization in complex silicate structures. J. Am. Ceram. Soc. 1993;**76**:1729–1738. doi:10.1111/j.1151-2916.1993.tb06641.x

[13] Nasdala L, Zhang M, Kempe U, Panczer G, Gaft M, Andrut M, Plötze M. Spectroscopic methods applied to zircon. Rev. Mineral. Geochem. 2003;**53**:427–467. doi:10.2113/0530427

[14] Zhang M, Salje EKH. Infrared spectroscopic analysis of zircon: radiation damage and the metamict state. J. Phys. Condens. Matter. 2001;**13**:3057–3071. doi:10.1088/0953-8984/13/13/317

[15] Vance ER, Anderson BW. Study of metamict ceylon zircons. Mineral. Mag. 1972;**38**:605–613. doi:10.1180/minmag.1972.038.297.09

[16] Woodhead JA, Rossman GR, Thomas AP. Hydrous species in zircon. Am. Miner. 1991;**76**:1533–1546.

[17] Zhang M, Groat LA, Salje EKH, Beran A. Hydrous species in crystalline and metamict titanites. Am. Miner. 2001;**86**:904–909.

[18] Zhang M, Salje EKH, Ewing RC. OH species, U ions, and CO/CO_2 in thermally annealed metamict zircon ($ZrSiO_4$). Am. Miner. 2010;**95**:1717–1724. doi:10.2138/am.2010.3567

[19] Salje EKH, Zhang M. Hydrous species in ceramics for the encapsulation of nuclear waste: OH in zircon. J. Phys. Condens. Matter. 2006;**18**:L277–L282. doi:10.1088/0953-8984/18/22/L01

[20] Chakoumakos BC, Murakami T, Lumpkin GR, Ewing RC. Alpha-decay-induced fracturing in zircon: the transition from the crystalline to the metamict state. Science (cover). 1987;**236**:1556–1559. doi:10.1126/science.236.4808.1556

[21] Yada K, Tanji T, Sunagawa I. Radiation-induced lattice-defects in natural zircon (zrsio4) observed at atomic resolution. Phys. Chem. Miner. 1987;**14**:197–204.

[22] Wang LM. Application of advanced electron microscopy techniques to the studies of radiation effects in ceramic materials. Nucl. Instrum. Methods Phys. Res. 1998;**B14**1:312–325.

[23] Ewing RC, Haaker RF, Lutze W. Leachability of zircon as a function of alpha dose. In Scientific Basis for Radioactive Waste Management V. Edited by Werner Lutze; Elsevier, Amsterdam, 1982: p. 389–397.

[24] Chakoumakos BC, Oliver WC, Lumpkin GR, Ewing RC. Hardness and elastic-modulus of zircon as a function of heavy-particle irradiation dose. I. *In situ* alpha-decay event damage. Radiat. Eff. Defects Solids. 1991;**118**:393–403. doi:10.1080/10420159108220764

[25] Farnan I. Si-29 NMR characterization of the crystalline-amorphous transition in $ZrSiO_4$. Phase Transitions. 1999;**69**:47–60.

[26] Ríos S, Salje EKH. Diffuse X-ray scattering from weakly metamict zircon. J. Phys. Condens. Matter. 1999;**11**:8947–8956.

[27] Farges F, Calas G. Structural-analysis of radiation-damage in zircon and thorite: an X-ray absorption spectroscopic study. Am. Miner. 1991;**76**:1–2.

[28] Salje EKH, Safarik DJ, Taylor RD, Pasternak MP, Modic KA, Groat LA, Lshley JC. Determination of iron sites and the amount of amorphization in radiation-damaged titanite ($CaSiTiO_5$). J. Phys. Condens. Matter. 2011;**23**:105402. doi:10.1088/0953-8984/23/10/105402

[29] Roberts J, Gaugliardo P, Farnan I, Zhang M, Vance ER, Davis J, et al. Positron annihilation lifetime study of radiation-damaged natural zircons. J. Nucl. Mater. 2016;**471**:44–50. doi:10.1016/j.jnucmat. 2015. 12.008

[30] Zhang M, Salje EKH. Spectroscopic characterization of metamictization and recrystallization in zircon and titanite. Phase Transit. 2003;**76**:117–136. doi:10.1080/0141159031000076093

[31] Nasdala L, Irmer G, Wolf D. The degree of metamictization in zircon: a Raman spectroscopic study. Eur. J. Mineral. 1995;**7**:471–478.

[32] Podor R. Raman spectra of the actinide-bearing monazites. Eur. J. Mineral. 1995;**7**:1353–1360.

[33] Hazen RM, Finger LW. Crystal-structure and compressibility of zircon at high-pressure. Am. Miner. 1979;**64**:196–201.

[34] Dawson P, Hargreave MM, Wilkinson GF. Vibrational spectrum of zircon ($ZrSiO_4$). J. Phys. C Solid State. 1971;**4**:240–256. doi:10.1088/0022-3719/4/2/014

[35] Nasdala L, Pidgeon RT, Wolf D, Irmer G. Metamictization and U-Pb isotopic discordance in single zircons: a combined Raman microprobe and SHRIMP ion probe study. Mineral. Petrol. 1998;**62**:1–27. doi:10.1007/BF01173760

[36] Geisler T, Pidgeon RT, van Bronswijk W, Pleysier R. Kinetics of thermal recovery and recrystallization of partially metamict zircon: a Raman spectroscopic study. Eur. J. Mineral. 2001;**13**:1163–1176. doi:10.1127/0935-1221/2001/0013-1163

[37] Xu XS, Zhang M, Zhu KY, Chen XM, He ZY. Reverse age zonation of zircon formed by metamictisation and hydrothermal fluid leaching. Lithos. 2011;**150**:256–267. doi:10.1016/j.lithos.2011.12.014

[38] Taylor M, Brown GE. High-temperature structural study of the $P2_1$-$A2/a$ phase-transition in synthetic titanite, $CaTiSiO_5$. Am. Miner. 1976;**61**:435–447.

[39] Salje EKH, Schmidt C, Bismayer U. Structural phase transition in titanite, $CaTiSiO_5$: a Raman spectroscopic study. Phys. Chem. Miner. 1993;**19**:502–506.

[40] Zhang M, Salje EKH, Redfern SAT, Bismayer U, Groat LA. Intermediate structures in radiation damaged titanite ($CaTiSiO_5$): a Raman spectroscopic study. J. Phys. Condens. Matter. 2013;**25**:115402. doi:10.1088/0953-8984/25/11/115402

[41] Beirau T, Bismayer U, Mihailova B, Paulmann C, Groat L. Structural phenomena of metamict titanite: a synchrotron, X-ray diffraction and vibrational spectroscopic study. Phase Transit. 2010;**83**:694–702. doi:10.1080/01411594.2010.502875

[42] Salje EKH, Taylor DR, Safarik DJ, Lashley JC, Groat LA, Bismayer U, James ER, Friedman R. Evidence for direct impact damage in metamict titanite $CaTiSiO_5$. J. Phys. Condens. Matter. 2011;**24**:052202. doi:10.1088/0953-8984/24/5/052202

[43] Zhang M, Salje EKH, Bismayer U, Groat L, Malcherek T. Metamictization and recrystallization of titanite: an infrared spectroscopic study. Am. Miner. 2002;**87**:882–890.

[44] Beirau T, Mihailova B, Matveeva G, Kolb U, Malcherek T, Groat LA, Bismayer U. Structural anisotropy and annealing-induced nanoscale atomic rearrangements in metamict titanite. Am. Miner. 2012;**97**:1354–1365. doi:10.2138/am.2012.4024

[45] Beirau T, Mihailova B, Malcherek T, Paulmann C, Groat LA, Bismayer U. Temperature-induced P21/c to c2/c phase transition in partially amorphous (metamict) titanite revealed by Raman spectroscopy. Can. Mineral. 2014;**52**:91–100. doi:10.3749/canmin.52.1.91

[46] Ríos S, Salje EKH, Zhang M, Ewing RC. Amorphization in natural zircon: evidence for direct impact damage. J. Phys. Condens. Matter. 2000;**12**:2401–2412.

[47] Zhang M, Salje EKH, Capitani GC, Leroux H, Clark AM, Schlüter J, Ewing RC. Annealing of alpha-decay damage in zircon: a Raman spectroscopic study. J. Phys. Condens. Matter. 2000;**12**:3131. doi:10.1088/0953-8984/12/13/321

[48] Zhang M, Salje EKH, Ewing RC, Farnan I, Ríos S, Schlüter J, Leggo P. Alpha-decay damage and recrystallization in zircon: evidence for an intermediate state from infrared spectroscopy. J. Phys. Condens. Matter. 2000;**12**:5189. doi:10.1088/0953-8984/12/24/310

[49] Wasilewski PJ, Senftle FE, Vaz JE, Thorpe AN, Alexander CC. A study of the natural a-recoil damage in zircon by infrared spectra. Radiat. Eff. 1973;**17**:191–199.

[50] Farges F. The structure of metamict zircon: a temperature-dependent EXAFS study. Phys. Chem. Miner. 1994;**20**:504–514.

[51] McLaren AC, Fitz JD, Williams IS, McLaren AC, Fitz JD, Williams IS. The microstructure of zircon and its influence on the age determination from Pb/U isotopic ratios measured by ion microprobe. Geochim. Cosmochim. Acta. 1994;**58**:993–1005.

[52] Ellsworth S, Navrotsky A, Ewing RC. Energetics of radiation-damage in natural zircon ($ZrSiO_4$). Phys. Chem. Miner. 1994;**21**:140–149. doi:10.1007/BF00203144

[53] Mursic Z, Vogt T, Frey F. High-temperature neutron powder diffraction study of $ZrSiO_4$ up to 1900 K. Acta Crystallogr. 1992;**B48**:584–590.

[54] Colombo M, Chrosch J. Annealing of natural metamict zircons: II high degree of radiation damage. Radiat. Phys. Chem. 1998;**53**:563–566. doi:10.1016/S0969-806X(98)00194-7

[55] Meldrum A, Zinkle SJ, Boatner LA, Ewing RC. A transient liquid-like phase in the displacement cascades of zircon, hafnon and thorite. Nature. 1998;**395**:56–58. doi:10.1038/25698

[56] Wittels MC, Steigler JO, Sherrill FA. Reactor sciences and technology. J. Nucl. Energy Parts A/B. 1962;**16**:237.

[57] Benyagoub A, Levesque F, Coureur F, Giber-Mougel C, Dufour C, Paumier E. Evidence of a phase transition induced in zirconia by high energy heavy ions. Appl. Phys. Lett. 2000;**77**:3197. doi:10.1063/1.1326483

[58] Smith DK, Newkirk HK. Crystal structure of baddeleyite (monoclinic ZrO_2) and its relation to polymorphism of ZrO_2. Acta Crystallogr. 1965;**18**:983–991. doi:10.1107/S0365110X65002402

[59] Keramidas VG, White WB. Raman-scattering study of crystallization and phase-transformations of ZrO_2. J. Am. Ceram. Soc. 1974;**57**:22–24.

[60] Anastassakis E, Papanicolaou B, Asher IM. Lattice-dynamics and light-scattering in hafnia and zirconia. J. Phys. Chem. Solids. 1975;**36**:667–676. doi:10.1016/0022-3697(75)90085-2

[61] Pavlik RS, Holland HJ, Payzant EA. Thermal decomposition of zircon refractories. J. Am. Ceram. Soc. 2001;**84**:2930–2936.

[62] Váciz T, Nasdala L, Wirth R, Mehofer M, Libowitzky E, Häger T. On the breakdown of zircon upon "dry" thermal annealing. Mineral. Petrol. 2009;**97**:129–138. doi:10.1007/s00710-009-0087-9

[63] Wang AH, Wang WY, Xie CS, Song WL, Zeng DW. CO_2 laser-induced structure changes on a zircon refractory. Appl. Surf. Sci. 2004;**227**:104–113. doi:10.1016/j.apsusc.2003.11.049

[64] Tole MP. The kinetics of dissolution of zircon ($ZrSiO_4$). Geochim. Cosmochim. Acta. 1985;**49**:453–458.

[65] Geisler T, Zhang M, Salje EKH. Recrystallization of almost fully amorphous zircon under hydrothermal conditions: an infrared spectroscopic study. J. Nucl. Mater. 2003;**320**:280–291. doi:10.1016/S0022-3115(03)00187-9

[66] Butterman WC, Foster WR. Zircon stability and ZrO_2-S10$_2$ Phase Diagram. Am. Miner. 1967;**52**:880–885.

[67] Zhang M, Salje EKH, Wang AH, Li XJ, Xie CS, Redfern SAT, Li RX. Vibrational spectroscopy of fast-quenched $ZrSiO_4$ melts produced by laser treatments: local structures and decomposed phases. J. Phys. Condens. Matter. 2005;**17**:6363–6376. doi:10.1088/0953-8984/17/41/007

[68] Zhang M, Ewing RC, Boatner LA, Salje EKH, Weber WJ, Daniel P, Zhang Y, Farnan I. Pb^+ irradiation of synthetic zircon ($ZrSiO_4$): infrared spectroscopic investigation—reply. Am. Mineral. 2009;**94**:856–858.

[69] Sales BC, Ramey JO, Boatner LA, McCallum JC. Structural inequivalence of the ion-damage-produced amorphous state and the glass state in lead pyrophosphate. Phys. Rev. Lett. 1989;**62**:1138–1141. doi:10.1103/PhysRevLett.62.1138

[70] Zhang M, Boatner L, Salje EKH, Ewing RC, Daniel P, Weber WJ, Zhang Y, Farnan I. Micro-Raman and micro-infrared spectroscopic studies of Pb- and Au-irradiated $ZrSiO_4$: optical properties, structural damage, and amorphization. Phys. Rev. B. 2008;**77**:144110. doi:10.1103/PhysRevB.77.144110

[71] Magruder RH, Morgan SH, Weeks RA, Zuhr RA. Effects of ion implantation on intermediate range order: IR spectra of silica. J. Non-Cryst. Solids. 1990;**120**:241–249.

[72] Magruder RH, Henderson DO, Morgan SH, Zuhr RA. Optical-spectra of pb implanted fused-silica. J. Non-Cryst. Solids. 1993;**152**:258–266. doi:10.1016/0022-3093(93)90259-Z

[73] Arnold GW, Brow RK, Myers DR. Characterization of the near-surface region of glass implanted with light elements. J. Non-Cryst. Solids. 1990;**120**:234–240.

[74] Arnold GW. Ion-implantation effects in glasses. Radiat. Eff. Defects Solids. 1998;**65**:17–30. doi:10.1080/00337578208216813

[75] Capitani GC, Leroux H, Doukhan JC, Ríos S, Zhang M, Salje EKH. A TEM investigation of natural metamict zircons: structure and recovery of amorphous domains. Phys. Chem. Miner. 2000;**27**:545–556. doi:10.1007/s002690000100

[76] Vance ER. Alpha-recoil damage in zircon. Radiat. Eff. 1975;**24**:1–6. doi:10.1080/00337577508239470

[77] Zhang M, Salje EKH, Ewing RC. Oxidation state of uranium in metamict and annealed zircon: near infrared spectroscopic quantitative analysis. J. Phys. Condens. Matter. 2003;**15**:3445–3470

[78] Weber WJ. Self-radiation damage and recovery in pu-doped zircon. Radiat. Eff. Defects Solids. 1991;**115**:341–349. doi:10.1080/10420159108220580

[79] Lumpkin GR, Foltyn EM, Ewing RC. Thermalrecrystallization of alpha-recoil damaged minerals of thepyrochlore structure type. J. Nucl. Mater. 1986;**139**:113. doi:10.1016/0022-3115(86)90029-2

[80] Chrosch J, Colombo M, Malcherek T, Salje EK, Groat LA, Bismayer U. Thermal annealing of radiation damaged titanite. Am. Miner. 1998;**83**:1083–1091.

[81] Nasdala L, Beran A, Libowitzky E, Wolf D. The incorporation of hydroxyl groups and molecular water in natural zircon ($ZrSiO_4$). Am. J. Sci. 2001;**301**:831–857. doi:10.2475/ajs.301.10.831

[82] Tomašić N, Gajović A, Bermanec V, Su DS, Rajić Linarić M, Ntaflos T, Schlögl R. Recrystallization mechanisms of fergusonite from metamict mineral precursors. Phys. Chem. Miner. 2006;**33**:145–159. doi:10.1007/s00269-006-0061-6

[83] Ruschel K, Nasdala L, Rhede D, Wirth R, Lengauer CL, Libowitzky E. Chemical alteration patterns in metamict fergusonite. Eur. J. Mineral. 2010;**22**:425–433. doi:10.1127/0935-1221/2010/0022-2031

[84] Xue LH, Gong W. A study on Raman and photoluminescence spectra of the aeschynite group minerals. J. Non-Cryst. Solids. 2000;**20**:827–829.

[85] Frost RL, Reddya BJ. The effect of metamictization on the Raman spectroscopy of the uranyl titanate mineral davidite (La,Ce)(Y,U,Fe^{2+})(Ti,Fe^{3+})(20)(O,OH)(38). Radiat. Eff. Defects Solids. 2011;**166**:131–136. doi:10.1080/10420150.2010.516394

[86] Tomašić N, Gajović A, Bermanec V, Rajić M. Recrystallization of metamict Nb-Ta-Ti-REE complex oxides: a coupled X-ray-diffraction and Raman spectroscopy study of aeschynite-(Y) and polycrase-(Y). Can. Mineral. 2004;**42**:1847–1857. doi:10.2113/gscanmin.42.6.1847

[87] Kusz J, Malczewski D, Zubko M, Häger T,Hofmeister T.High temperature study of metamict steenstrupine. Solid State Phenomena, 2010, 163:253-255

Chapter 6

Raman Spectroscopy for Monitoring Strain on Graphene and Oxidation Corrosion on Nuclear Claddings

Hongyi Mi, Zhenqiang Ma and James P. Blanchard

Additional information is available at the end of the chapter

http://dx.doi.org/10.5772/65111

Abstract

Raman scattering can explore a material's structure, composition, and condition. In this chapter, we demonstrate the application of Raman scattering to monitor the change in the physical properties and chemical composition of materials. We provide two examples: (1) the Raman peak profile and shift reveal the strain in graphene induced by nanostructure and (2) the appearance and intensity of the Raman peaks indicate the oxidation corrosion on Zircaloy nuclear fuel cladding. The Raman spectroscopy is capable of providing evident and precise signals for the monitoring tasks. Through this research, we propose Raman spectroscopy to be a sensitive, accurate, and nondestructive tool for monitoring material conditions.

Keywords: Raman scattering, phonon vibration, monitoring, mechanical strain, oxidation corrosion, graphene, zirconium alloy nuclear claddings, raman peak intensity, raman shift

1. Introduction

Raman scattering technology is able to reveal phonon/lattice vibrational mechanisms inside materials [1, 2]. By combining this technique with different optical systems, it is feasible for Raman spectroscopy to characterize the physical and chemical changes of materials, including crystal structure deformation and crystal component change [3, 4]. Attributed to its high sensitivity and noncontact detection, the sensing and monitoring applications of the Raman scattering technique for different materials have attracted great interest in both science and engineering fields.

Graphene is a two-dimensional (2D) material consisting of a flat monolayer or several layers of carbon atoms arranged in a honeycomb lattice structure [5, 6]. Because of its special Dirac cone structure which satisfies a linear dispersion relation, graphene has excellent electrical properties, and the charge carriers of graphene can transport as massless Dirac fermions with a mobility up to ~200,000 $cm^2 V^{-1} s^{-1}$ [7–10]. Combined with good mechanical strength [11], outstanding thermal conductivity [12], and excellent optical transparency [13], graphene consequently acts as an attractive candidate for future electronics and photonics applications [14–16]. Previous studies have found that the electrical and thermal characteristics of graphene including electrical resistivity [17], carrier mobility [18], band gap [19], and thermal conductivity [20] are sensitive to mechanical deformation as it alters the structure of the graphene band by confining or collimating the electrons and phonon vibration [19–23]. Therefore, the ability to engineer strain and monitor the mechanical strain condition on graphene is critical in order to fully utilize the electrical properties of graphene.

Through investigating phonon vibrations, Raman spectroscopy has been proven as an important, nondestructive tool to discover the properties of graphene [24, 25]. The mechanical strain can effectively change crystal phonon vibration based on the anharmonicity of the interatomic potentials of the atoms. In other words, the impact of strain on phonon vibration of graphene can be correlated with a change in the Raman characteristic peaks. Several studies using Raman spectroscopy to characterize the phonon vibration of graphene have been carried out with different strains induced by engineering methods [23, 26–29]. The strain on graphene can be clearly reflected in the shift of Raman characteristic peak shifts, and the shift rate is found proportional to the Grüneisen parameter [27, 28].

The management of spent nuclear fuel and other high-level nuclear wastes has drawn great attention from many fields [30]. The growth of an oxide corrosion layer on the cladding, such as zirconium alloy (Zircaloy), is a threat to the nuclear fuel cask storage system, where it may take years for the cladding to cool down due to the slow dissipation of the decay heat [31]. This oxidation process and its product oxide layer are detrimental to the Zircaloy cladding and may play a role in low-temperature creep and delayed hydride cracking [32].

Monitoring of nuclear fuel cladding in dry cask storage can assist with assurance of the integrity of the fuel within the storage canister and is a necessary path to estimate the health of the cladding. Several studies have been performed to understand the oxidation process of Zircaloy [33–36]. More importantly, many detection methods of oxide corrosion have been developed, including environmental monitoring [37], ultrasonic [38], ion beam radiation [39, 40], and optical spectrum methods [41–43]. Compared to other methods, the use of optical spectrum for observation and detection of the oxidation promises to be more flexible, economical, effective, and practical.

As one advanced optical method, Raman scattering technology has been employed to study the properties of zirconium oxide [44–47]. Based on the lattice mechanism, the Raman spectra can be used to identify zirconium oxide from other oxide materials [48] and provide detail of the formation of a textured oxide layer on the Zircaloy cladding [49]. The phonon vibration status of the crystal structure/phase of zirconium oxide (amorphous, tetragonal, and monoclinic polymorphs) can be finely revealed by the Raman characteristic peaks. These previous

http://dx.doi.org/10.5772/65111

studies have resulted in the foundation for further Raman scattering investigation on Zr-4 cladding health conditions and characteristics.

In this chapter, we demonstrated the employment of the Raman scattering technology to monitor the mechanical property changes of graphene and chemical corrosion in zirconium alloy nuclear fuel claddings. The positions, intensities, and profiles of the Raman characteristic peaks precisely and directly probe the physical and chemical changes within these materials. Therefore, Raman spectroscopy is proven to be a nondestructive tool for monitoring material conditions with high sensitivity and high resolution.

2. Raman scattering monitoring of mechanical strain on graphene

To date, several approaches to creating strain in graphene have been proposed [23, 24, 26, 28]. Although the graphene deformation methods are different, the Raman spectroscopy is always accepted as the most powerful and efficient tool to reveal the strain condition on graphene. In this section, we employ Raman scattering technology to observe biaxial strain on monolayer graphene. The strain was induced by deformation from a substrate with an array of SiO_2 nanopillars. The nanopillars (1 cm^2 in area, 80 nm in height, and 40 nm in pitch) were fabricated by employing a self-assembled block copolymer through simple dry etching and deposition processes. The graphene sheet was subsequently transferred to the array of SiO_2 nanopillars. The creation of biaxial tensile strain in graphene was validated based on high-resolution micro-Raman spectroscopy, and the strain values were quantitatively calculated through the Grüneisen parameter. Atomic force microscopy (AFM) and accompanying finite element simulations were employed to confirm the accuracy and reliability of the Raman spectroscopy monitoring results.

Figure 1 shows the schematic process to fabricate SiO_2 nanopillars patterned by self-assembled block copolymer. The fabrication began with forming periodic nanopatterns on 300 nm, thermally grown SiO_2/Si substrate by using a self-assembled block copolymer as a pattern template [50, 51]. A block copolymer layer, poly(styrene-*block*-methyl methacrylate) (PS-b-PMMA), on top of a ~5 nm neutral PS brush layer was used to define periodic nanopatterns (**Figure 1(a)–(c)**). The PMMA cylinders were selectively removed by exposure to UV irradiation and rinsing with acetic acid (CH_3COOH) to form the cylinder-shaped nanopattern template layer. The brush layer in the patterned cylinders was removed by O_2 plasma to allow the following evaporated material to deposit directly to the substrate in the next step. **Figure 2(a)** shows the block copolymer nanotemplate with a pitch (center-to-center distance between cylinders) size ~40 nm. A layer of 15 nm thick chromium (Cr) was deposited by e-beam evaporation and lifted off (**Figure 1(e)–(f)**). The array of Cr nanodots was uniformly created over the entire surface of SiO_2/Si substrate (**Figure 2(b)**). Then, the underlying SiO_2 layer was etched by Cr nanodots as a mask in the inductively coupled plasma (ICP) and the reactive ion etching (RIE) combination system. Finally, an array of SiO_2 nanopillars (80 nm in height and 40 nm in pitch) was formed on Si substrate after removing the Cr nanodots, as shown in **Figure 2(c)**.

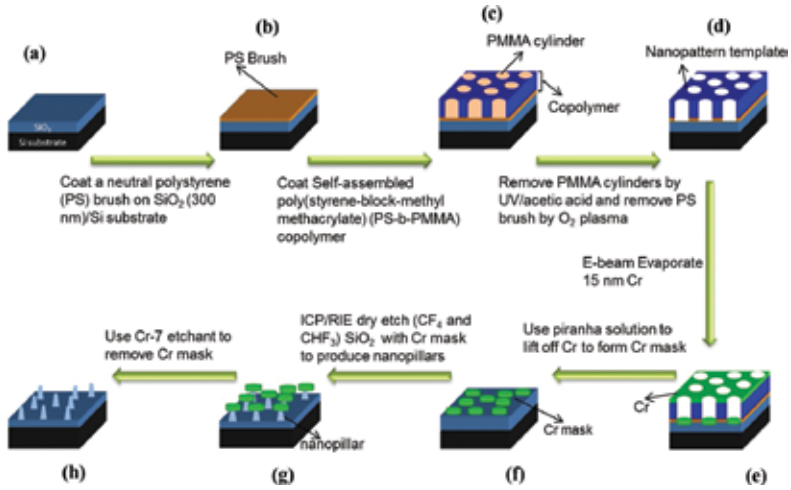

Figure 1. SiO_2 nanopillar fabrication process with assistant of self-assembled block copolymer. (a) original SiO_2/Si substrate, (b) PS coated on substrate, (c) self-assembled block copolymer coated on PS layer, (d)nanotemplate formed on substrate, (e) Cr evaporated on sample, (f) Cr nanodot on substrate after lift-off, (g) SiO_2 nanopillar formed after etching with Cr nanodot mask, and (h) clean SiO_2 nanopillar substrate after removing Cr nanodots.

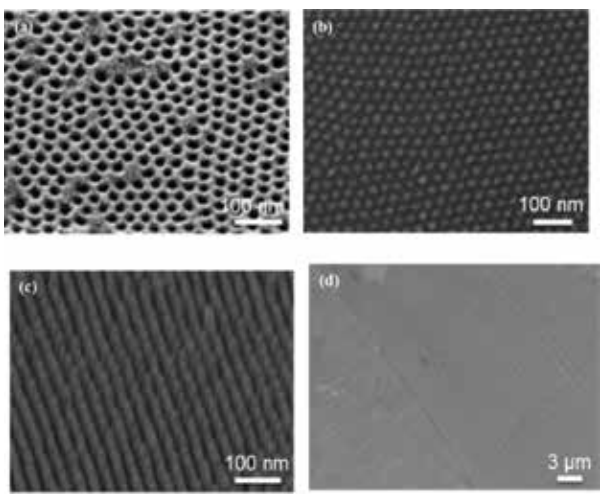

Figure 2. (a) Self-assembled block copolymer nanotemplate on SiO_2/Si substrate, (b) Cr nanodots after lift-off on SiO_2/Si substrate, (c) obtained SiO_2 nanopillars on SiO_2/Si substrate, and (d) CVD grown monolayer graphene on Cu foil substrate. From Ref. [52].

The monolayer graphene that was transferred onto the array of SiO_2 nanopillars was grown on a 25 μm thick 1″ × 1″ copper (Cu) foil by a chemical vapor deposition (CVD) [53, 54]. **Figure 2(d)** shows the SEM image of the grown monolayer graphene on Cu foil. A layer release-transfer method was employed to transfer the monolayer graphene film onto the pre-prepared SiO_2 nanopillar substrate as shown in **Figure 3**.

http://dx.doi.org/10.5772/65111

Firstly, in order to form a 150 nm thick PMMA supporting layer, the graphene layer on the back side of Cu foil was removed by oxygen plasma, followed by spin-coating PMMA on the top side of the graphene sample and baked at 130°C for 3 min (**Figure 3(a)–(c)**). Secondly, the PMMA-coated sample was dipped into 0.25 mol of Fe_3Cl etchant for 4 h to remove the Cu foil completely, and then the left PMMA/graphene membrane was floated on the solution surface (**Figure 3(d)–(e)**). After cleaning the sample in DI water, the floating PMMA/graphene membrane was scooped on the SiO_2 nanopillar substrate, and the PMMA layer was removed by acetone to only leave the graphene film on a SiO_2 nanopillar substrate (**Figure 3(f)–(h)**). The graphene/SiO_2 nanopillar substrate was dried on a hot plate at 105 °C for 1 min to evaporate solvent and water from the sample. With the help of water capillary action and van der Waals forces, the graphene film can be driven to follow the substrate profile. Namely, when the graphene/PMMA film was transferred to the SiO_2 nanopillar substrate, a 150 nm thick PMMA layer made it remain flat on the SiO_2 nanopillars. However, the graphene layer started to sag as the PMMA layer was removed and the capillary action of the water and the van der Waals forces between the graphene layer and the nanopillars helped the graphene layer depress and follow the profile of nanopillars. The schematic illumination for this process is shown in **Figure 4(a)**. During the SiO_2 nanopillar fabrication process, we intentionally left several unpatterned regions on the substrate to attach the graphene film tightly without strain after the transfer, which also can be used as unstrained reference regions in the following Raman spectroscopy study. **Figure 4(b)** is the 45°-angled SEM image showing that the deformed graphene film was supported by numerous and periodic SiO_2 nanopillars.

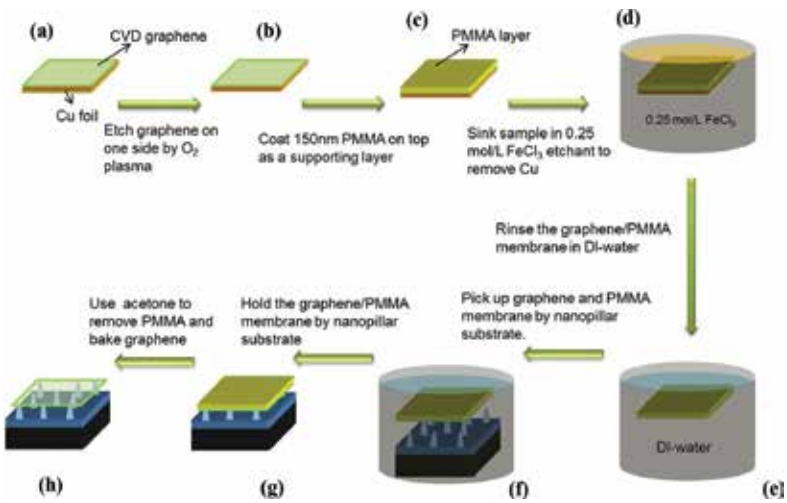

Figure 3. Transfer process of CVD graphene to prepared SiO_2 nanopillar substrate. (a) Graphene grown on Cu foil, (b) sample with back side graphene removed, (c)PMMA coated on graphen, (d) sample sunk in $FeCl_3$ solution to remove Cu, (e) PMMA/graphene layer in DI water for clean, (f) PMMA/graphene layer picked up by prepared SiO_2 nanopiller substrate, (g)Flat PMMA/graphene on top of SiO_2 nanopiller substrate, and (h) deformed graphene on SiO_2 nanopiller after removing PMMA.

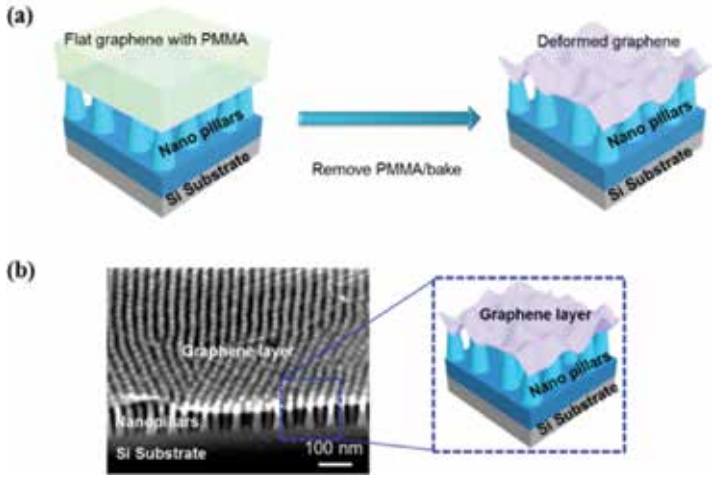

Figure 4. (a) Schematic illumination of graphene deformation process and (b) deformed graphene sheet standing on top of SiO_2 nanopillars.

A Horiba micro-Raman spectrometer (resolution of 0.045 cm^{-1}) with a 50× objective lens (a spot size of about 1 μm) and 18.5 mW of He-Ne (633 nm) was used to investigate the strain on the transferred monolayer graphene. The graphene on both flat regions and the SiO_2 nanopillars was examined at several different positions. From the Raman spectra as shown in **Figure 5(a)** and **(b)**, the intensity of the 2D band is about two times of that of the G band, which is corresponding to monolayer graphene Raman spectra [25, 54]. The graphene on the flat regions (no nanopillars) of the substrate without clear deformation was used as reference to study the strain on graphene. It is clear that there are substantial differences in the Raman spectrum G and 2D bands between the graphene on SiO_2 nanopillars and on the flat region. In **Figure 5(a)** and **(b)**, compared to the flat graphene, there are downshifts in the G band (average shift, 7.8 cm^{-1}) and 2D band (average shift, 16.3 cm^{-1}) of graphene on nanopillars in the peak positions. The downshift of the G band and the 2D band is attributed to the local strain on graphene induced by SiO_2 nanopillars.

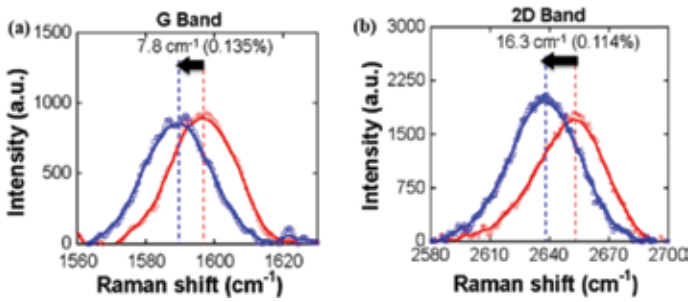

Figure 5. Raman spectra of the (a) G peak downshift and (b) 2D peak downshift taken on the flat surface (red) and on the nanopillars (blue). From Ref. [52].

http://dx.doi.org/10.5772/65111

In the Raman spectra of graphene, the G band is related to the doubly degenerated E_{2g} at the center of the Brillouin zone, while the 2D band is related to the momentum conservation of the scattering of two phonons with opposite waver vectors [26, 27]. The mechanical strain can influence the phonon variation in the crystal [3, 55]. The center-zone phonon vibration change due to the strain is shown in the G band shift, and the change in the double-resonance condition due to the strain, which affects the actual corresponding phonon, can be reflected by the 2D band in the Raman spectrum measurements. The local biaxial tensile strain induced by SiO_2 nanopillar can explain the downshift happening to G and 2D bands.

The Raman shifts were qualitatively studied to discover the biaxial strain through the Grüneisen parameter, which describes the vibrational effect on the crystal lattice property, by the following equation [24, 27, 55]:

$$\gamma = -\frac{1}{\omega_0}\frac{\delta\omega}{\delta\varepsilon_h} \tag{1}$$

where ω_0 is the Raman band frequency without strain, $\delta\omega$ is the Raman band shift, γ is the Grüneisen parameter for the corresponding band, and ε_h is the hydrostatic strain on the graphene film. For biaxial strain, ε_h can be expressed as $\varepsilon_h = \varepsilon_t + \varepsilon_l$ and $\varepsilon_t = \varepsilon_l$, in which ε_t and ε_l are the transversal and longitudinal components of the strain. From Eq. (1), based on previously reported Grüneisen parameters and the downshift characteristic bands collected from the test positions, the biaxial tensile strain $\varepsilon_l = \varepsilon_t$ can be calculated to have an average value of 0.135 % from the G band and 0.117 % from the 2D band.

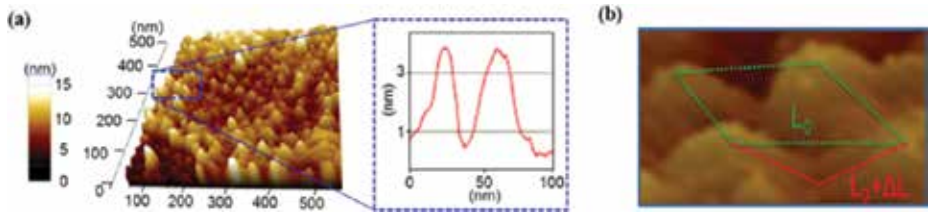

Figure 6. (a) Morphology of the transferred graphene film on the SiO_2 nanopillar substrate measured by AFM and (b) deformed graphene on four adjacent nanopillars (unit area). From Ref. [52].

In order to confirm the Raman spectroscopy defection results, the wavy morphology of the transferred graphene film on the SiO_2 nanopillars substrate was carefully measured by the noncontact-mode atomic force microscopy (AFM) over a 500 nm× 500 nm area as shown in **Figure 6**. It was clearly observed that the surface morphology of the transferred graphene film followed the SiO_2 nanopillar profile. The inserted 2D graphene surface profile in **Figure 6(a)** was taken from two adjacent SiO_2 nanopillars, which indicates how much the graphene layer was deformed. The peak-to-valley distances are found to have a range of about 0.5–5 nm. A subtle difference in the arrangement of the nanopillars and graphene sag condition creates a different degree of deformation on the graphene film. As described in the previous section,

just after transfer, the graphene/PMMA film was kept flat, and the length of the graphene between two pillars was L, while once the PMMA was removed, the graphene began to sag to follow the nanopillar profile, and the length of graphene between two pillars was changed to L + ΔL (**Figure 6(b)**). Then, the mechanical strain on graphene can be calculated by the following equation: strain = ΔL/L [24]. Based on the AFM-measured morphology of the graphene on the nanopillars, the local strain in the graphene can be extracted in the range from about 0.04 to 0.9 % with an average value about 0.17 % measured in a 1 μm^2 area.

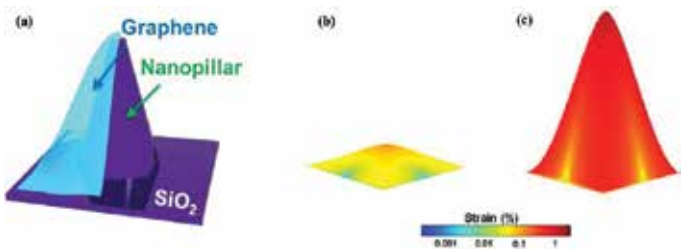

Figure 7. (a) A schematic illustration of strained graphene on top of a nanopillar. Simulated biaxial tensile strain on transferred graphene transferred by COMSOL Multiphysics; (b) with 0.5 nm; and (c) with 5 nm deformation toward. From Ref. [52].

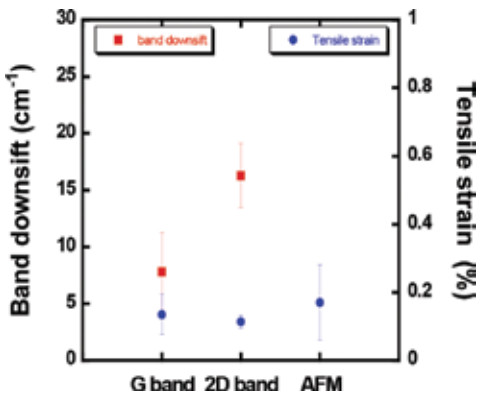

Figure 8. Comparison of the strain extracted from AFM and calculated from Raman band shift.

Furthermore, a strain distribution on graphene based on the deformation values we measured from the AFM was simulated by COMSOL Multiphysics. As shown in **Figure 7(a)**, we used the actual dimensions, structure, and material parameters in the simulation model. For graphene, we used Young's modulus of 1 TPa [11] and Poisson's ratio of 0.3 [56]. We took the two extreme cases, the largest and the smallest deformations which were the 0.5 and 5 nm of the peak-to-valley distances. For the smallest graphene deformation, the maximum strain in the graphene near the top part of the nanopillar is about 0.3 %, and most of the region shows an average strain of about 0.07 % as shown in **Figure 7(b)**. On the other hand, for the largest graphene deformation, the minimum strain in the graphene near the top part of the nanopillar

http://dx.doi.org/10.5772/65111

is as high as 3.5 %, and most of the region shows the average strain about 0.8 % as shown in **Figure 7(c)**. The simulated results confirm the analysis from the AFM measurement.

The Raman shift and strain conditions collected from Raman and AFM are shown in **Figure 8**. This biaxial strain value obtained from Raman spectroscopy detection matched to that obtained from accurate AFM measurement. This result demonstrates the accuracy and effectiveness for the Raman scattering technology to monitor the strain on graphene, even if the strain is induced by subtle nanostructures.

3. Raman scattering monitoring oxidation corrosion of nuclear fuel claddings

Acquiring and understanding the health condition of nuclear fuel cladding are vital for nuclear energy long-term fuel storage systems. In this section, we present the use of Raman scattering technology to monitor oxidation corrosion on nuclear fuel cladding. Systematic Raman scans were performed to study the relationship between typical Raman spectra and various oxidation corrosion layer thicknesses. The thicknesses of the oxide layers were confirmed by cross-sectional scanning electron microscopy (SEM) examination. The results reveal that each oxide layer thickness can be directly related to the Raman scattering characteristic peaks and have proven that Raman scattering technology is an accurate, nondestructive, and sensitive method to monitor the oxidation corrosion of zirconium-based cladding.

The tested Zr-4 cladding samples were cut by saw from 1 mm thick Zr-4 cladding into 1 cm × 1 cm specimens. The Zr-4 samples were ground and polished to remove the native surface oxide layer and provide a smooth sample surface. The morphology of the oxide may be affected by the cold-worked nature of the polished surface. The samples were loaded in a quartz tube with a 5 cm diameter and were oxidized in a Thermo Scientific F79335-70 furnace chamber at 500 °C in flowing air. Samples were oxidized for 5, 10, 20, 50, and 100 h, respectively, to achieve different corrosion layer thicknesses. These oxidation times were chosen such that the thickness of the oxide layer can be clearly distinguished. After oxidation, the polished side of each oxidized sample was ready for f Raman scattering investigation.

The Raman scattering spectra of the oxidized samples were measured with a Thermal Scientific DXR micro-Raman spectrometer. The excitation laser source is a DXR 532 nm green laser, and the output power was 10 mW. The spectra were acquired by a 50 μm aperture. The objective of the microscope was chosen as 10×, providing a laser beam spot size diameter of 2.1 μm. Raman spectra were collected from the entire 2.1 μm diameter spot. The scans implemented a 900 lines/mm grating to obtain full-range spectra and find the interested spectrum range. For each sample, systematic scans for several spots randomly selected at different regions on the sample were carried out. Then, the representative spectra which appeared most frequently were chosen for further analysis.

From the full-range scanned Raman spectra of bare Zr-4 as well as samples oxidized for 5, 10, 20, 50, and 100 h, the characteristic Raman scattering peaks appear between wave number of 160 and 800 cm^{-1}. **Figure 9** shows the selected representative Raman spectra in this wave

number range. A baseline has been subtracted from each spectrum, which allowed all the spectra to be put at the same level to permit selection of the best peaks for measuring the oxide layer thickness. As the Raman spectra reveal, the characteristic Raman scattering peaks become more obvious as the sample's oxidation time increases. In the spectrum from the non-oxidized sample, there is only one peak around 480 cm^{-1} with a very weak intensity. The spectrum from the 5 h sample exhibits the 480 cm^{-1} peak, which is similar to the bare sample. Meanwhile, two weak peaks around 180 and 630 cm^{-1} appear with a broad peak width. In the spectrum from the 10 h sample, the peaks at 180, 480, and 630 cm^{-1} become stronger and wider. In addition, two peaks at 340 and 380 cm^{-1} appear. The spectrum from the 20 h sample is similar to that of the 10 h sample, but the intensity of each peak increases slightly. The peaks at 180 and 630 cm^{-1} begin to split into two sub-peaks at 175 and 187 cm^{-1} and 613 and 638 cm^{-1}, respectively. In the spectrum from the 50 h sample, all these peaks still exist at the same positions but with much stronger intensities. New peaks at 220, 540, and 580 cm^{-1} also appear within this spectrum. The spectrum from the 100 h sample contains all the peaks in the 50 h sample's spectrum, but each of them displays an increase in intensity. Furthermore, there are two new peaks at 280 and 300 cm^{-1} with weak intensities.

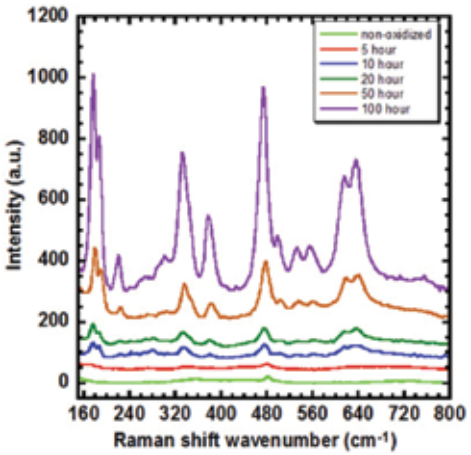

Figure 9. The selected representative Raman spectra of the non-oxidized, 5, 10, 20, 50, and 100 h oxidized Zr-4 cladding samples. As the oxidation time increases, there are 12 characteristic peaks appearing in the spectra. From Ref. [58].

As the oxidation time increases, a thicker oxide layer is grown on top of Zr-4, and in turn, the Raman spectrum of this sample can show stronger Raman scattering signals. Comparing all of these Raman spectra in detail, some characteristic peaks are helpful in identifying bare and oxidized samples. As discussed previously, there are 12 characteristic peaks appearing or enhanced in the spectra of the tested samples. In the spectra of the bare and 5 h samples, the differences are only observed for peaks at 180 and 630 cm^{-1}, which do not exist in the bare sample spectrum. These two peaks exist in all the spectra of the oxidized samples (from 5 to 100 h), and their intensities increase consistently as the oxidation time increases, although there is splitting happening in these two peaks for samples exposed for longer times. These split

http://dx.doi.org/10.5772/65111

peaks at 175, 187, 613, and 638 cm^{-1} correspond to the existence of the zirconium oxide tetragonal and monoclinic polymorphs in the oxide layer [44, 57]. When an oxide layer grows thicker, there will be more zirconium oxide in these polymorphs. Oxide layers grown in environments other than air will likely have a different morphology than those studied here. Future work is necessary to establish whether the approach used successfully in this study will apply to oxides grown under other conditions.

After the Raman spectrum measurement, the oxidized Zr-4 samples were prepared with phenolic mount for cross section measurement by SEM in order to examine the Raman results. Because of the different properties of phenolic, zirconium oxide, and Zr-4, these three materials can be easily distinguished by the white-black contrast. Zirconium oxide is a high dielectric constant material, so compared with Zr-4, the zirconium oxide layer has a darker gray color in SEM images, and the boundary between the oxide layer and the Zr-4 was obvious. Following this procedure, the zirconium oxide layer thickness can be measured accurately at different positions of cross section.

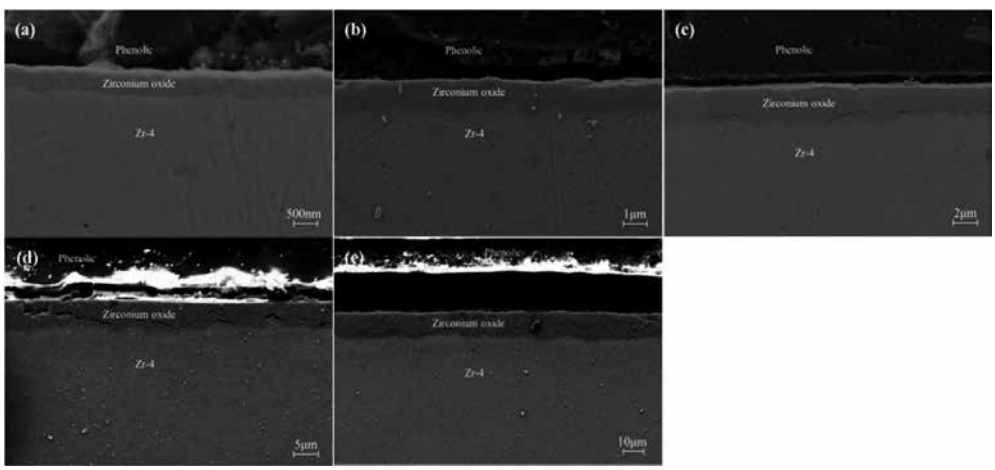

Figure 10. The cross-sectional SEM images of Zircaloy-4 samples oxidized at 500 °C in ambient air for (a) 5, (b) 10, (c) 20, (d) 50, and (e) 100 h. From Ref. [58].

The cross-sectional SEM images of the samples are shown in **Figure 10(a)–(e)**. The SEM images were taken in more than 20 different regions over the whole cross section of each sample, so they can be representative of the sample oxide layer thickness. The statistical average thickness and standard deviation of the top oxide layer are shown in **Figure 11**. The thickness of the oxide layer increases roughly linearly with oxidation time. For the 5 h sample, there is a very thin uniform oxide layer on the Zr-4. As the thickness increases, the top oxide layer becomes nonuniform, and the interface between zirconium oxide and Zr-4 becomes rougher. The average thickness of the oxide layer for the 5 h sample is about 0.55 μm with a deviation of about 0.066 μm. But for the 100 h sample, the average thickness of the oxide layer is about 10.13 μm with a deviation of about 3.08 μm. This suggests that during oxidation, the growth rate of the oxide layer varies across the sample, and the oxide layer will have an uneven profile.

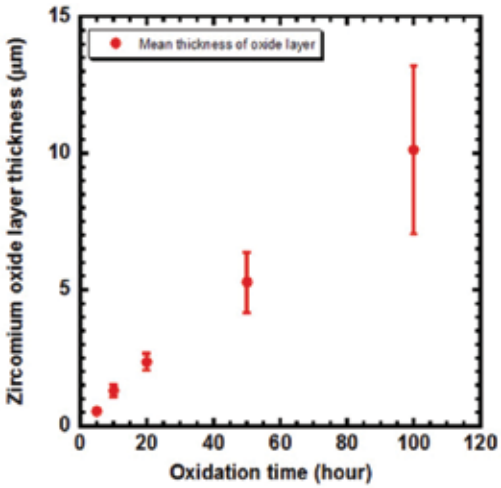

Figure 11. The calculated statistical average thickness and deviation of all oxidized samples as a function of oxidation time. From Ref. [58].

In order to analyze these two peaks quantitatively, the Gaussian-Lorentzian mode deconvolutions were carried out on two characteristic peaks around 180 and 630 cm^{-1}, which are candidate signals for detecting the Zr-4 cladding oxide layer thickness. **Figure 12** shows the deconvolution processes of these two characteristic peaks from the selected representative spectra of the 10 and 100 h samples. After deconvolution, the two sub-peaks can be replaced by individual peaks at the 175 and 187 cm^{-1} and 613 and 638 cm^{-1} positions, respectively. The intensities of these four peaks from the representative Raman spectra of all oxidized samples are shown in **Figure 12** as a function of the average thickness of the oxide layer. The intensities of these four deconvoluted peaks increase consistently as the oxide layer becomes thicker. For the 10 h sample with average oxide layer thickness of 1.30 μm, the intensities of the deconvoluted peaks are 44.1, 26.6, 21.3, and 39.5. For the 100 h sample with average oxide layer thickness of 10.13 μm, the intensities have increased greatly to 645.5, 405.5, 264.9, and 356.5.

The difference in intensities of the peaks at 175, 187, 613, and 638 cm^{-1} is able to identify each sample with the corresponding oxide layer thickness with high resolution as shown in **Figure 13**. Taking the peak at 175 cm^{-1} as an example, the peak intensity increases from 0 for a bare sample to 3.5, 44.1, 63.2, 186.6, and 645.5 for 0.55, 1.30, 2.36, 5.27, and 10.13 μm oxide layer thicknesses. Because there is no peak at these positions for the bare sample, it is easy to distinguish it from the oxidized samples, even for the 5 h sample with a 0.55 μm thick oxide layer. Among the oxidized samples, the average thickness difference between 5 and 10 h samples is only about 0.75 μm, but the signal intensity of the 10 h sample is almost 10 times higher than that of the 5 h sample. Another three peaks show similar trends. This result reflects that during the oxidation process at 500 °C, as oxidation time increases, the components of the tetragonal and monoclinic polymorph zirconium oxide become more, and consequently, they show much stronger characteristic peaks in the Raman spectra [44].

http://dx.doi.org/10.5772/65111

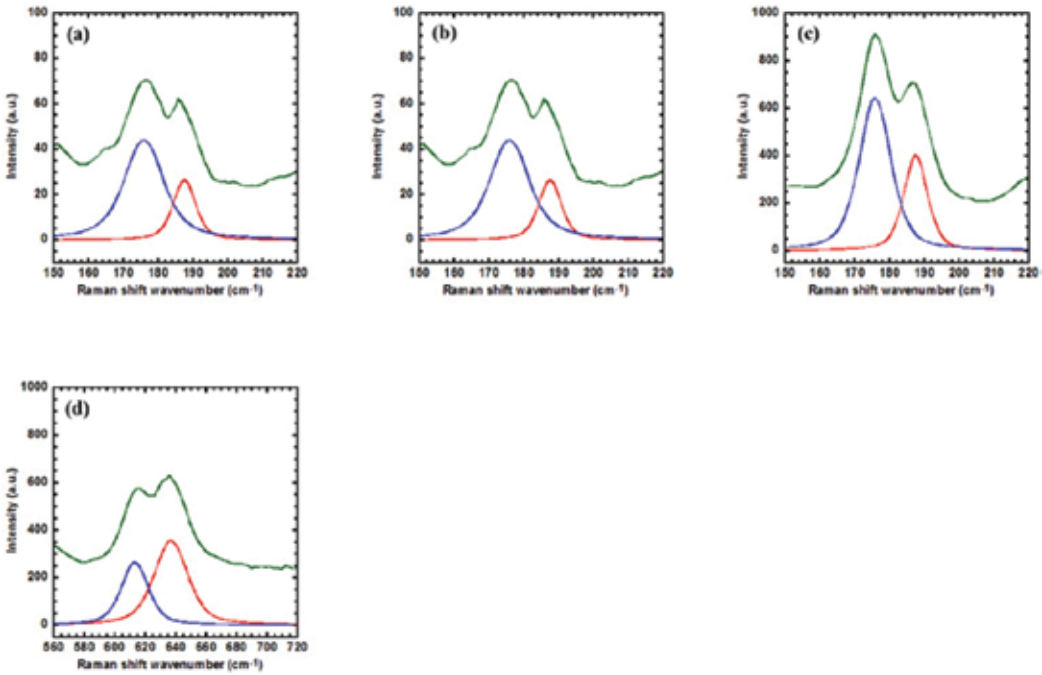

Figure 12. The Gaussian-Lorentzian deconvolution processes of characteristic peaks around 180 and 630 cm^{-1} from the selected representative Raman spectra of the 10 (a) (b) and 100 h (c) (d) oxidized samples. From Ref. [58].

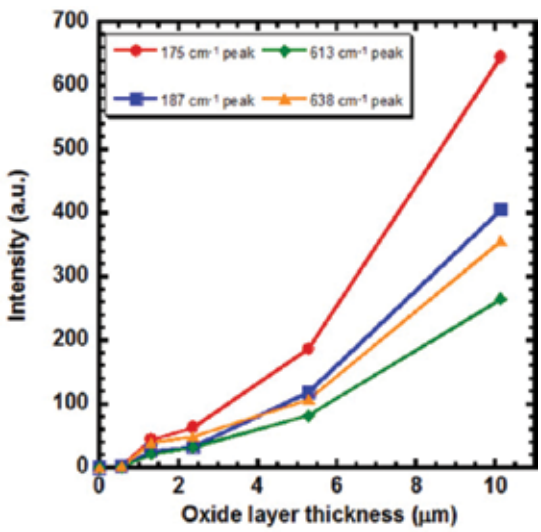

Figure 13. The intensities of the deconvoluted peaks at 175, 187, 613, and 638 cm^{-1} as a function of the average thickness of the oxide layer. From Ref. [58].

Figure 14 shows the maximum intensity deviation percentages of each characteristic peak from different test positions for all oxidized samples as a function of the average thickness of the oxide layer. It is observed that the maximum intensity deviations for these characteristic peaks are in the range from about 5 % to a little lower than 25 %. This intensity variation comes from the difference in the thickness of the oxide layer. This result means that the uneven condition of the oxide layer thickness for the sample can be roughly reflected in intensity variation of the characteristic peaks. After analysis of these characteristic peaks, they can be confidently considered as sufficient scattering signals to detect the oxide layer thickness on Zr-4 cladding and further employed to finish the task of converting the oxide layer thickness to detectable optical signals.

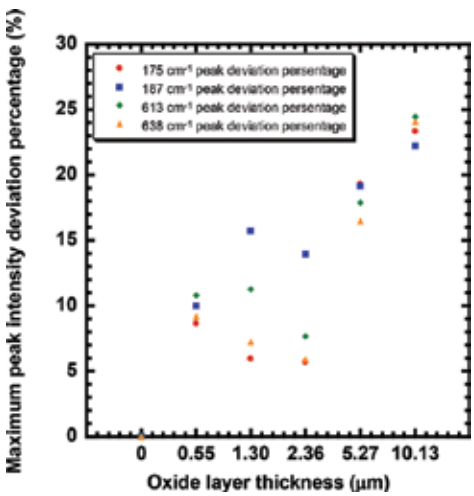

Figure 14. The maximum intensity deviation percentages of the characteristic peaks (deconvoluted) as a function of the average thickness of the oxide layer. From Ref. [58].

4. Conclusion

Raman spectroscopy has been demonstrated to successfully probe the tensile biaxial strain in monolayer graphene on the surface of SiO_2 nanopillars patterned by a self-assembled block copolymer. The characteristic Raman peaks of the G band and 2D band shifted due to the strain, and the Raman shifts accurately expressed the strain value distributed on graphene. The surface profile of the transferred graphene film on SiO_2 nanopillars was carefully investigated by AFM, and the biaxial tensile strain generated in the graphene was extracted from the physical deformation. Then, finite element simulations were used to validate the measurements. Both the AFM experimental investigation and FEM theory modeling matched the strain results achieved from Raman spectroscopy study and proved the capability of Raman scattering to monitor the subtle mechanical property change of graphene.

http://dx.doi.org/10.5772/65111

Raman scattering technology was studied to monitor spent fuel cladding oxidation. The air-oxidized Zr-4 cladding samples were systematically investigated by Raman spectroscopy. Straightforward Raman spectrum analysis reveals that there are characteristic peaks able to identify the bare and oxidized cladding samples and samples with different oxide layer thicknesses. SEM scans were carried out to visually examine oxide layer thicknesses on cladding. The comparison results confirmed this Raman scattering detection method displays high resolution in the determination of the oxidation corrosion degrees.

In summary, Raman scattering technology was proposed to monitor mechanical property of novel 2D carbon material and oxidation film thicknesses on nuclear fuel cladding Zircaloy. The positions and intensities of the characteristic peaks of the materials under test accurately and reliably revealed the changes in physical and chemical properties. The work reported in this chapter on observing materials with Raman spectroscopy extends the application of Raman scattering technology in monitoring new nanomaterial status and the health of nuclear storage systems in the research and engineering development.

Author details

Hongyi Mi[1], Zhenqiang Ma[1*] and James P. Blanchard[2]

*Address all correspondence to: mazq@engr.wisc.edu

1 Department of Electrical and Computer Engineering, University of Wisconsin-Madison, Madison-Wisconsin, United States of America

2 Department of Engineering Physics, University of Wisconsin-Madison, Madison-Wisconsin, United States of America

References

[1] W. H. Weber and R. Merlin, *Raman Scattering in Materials Science*. Springer-Verlag, Berlin Heidelberg, Germany 2000.

[2] S.-L. Zhang, *Raman Spectroscopy and its Application in Nanostructures*. John Wiley & Sons, Chichester, United Kingdom, 2012.

[3] A. Jorio, M. S. Dresselhaus, R. Saito, and G. Dresselhaus, *Raman Spectroscopy in Graphene Related Systems*. WILEY-VCH Verlag GmbH & Co. KGaA, Weinheim, Germany,2011.

[4] I. R. Lewis and H. Edwards, *Handbook of Raman Spectroscopy: From the Research Laboratory to the Process Line*. Marcel Dekker, Inc., New York, NY, United States of America, 2001.

[5] K. S. Novoselov, A. K. Geim, S. V. Morozov, D. Jiang, Y. Zhang, S. V. Dubonos, I. V. Grigorieva, and A. A. Firsov, "Electric field effect in atomically thin carbon films," *Science*, vol. 306, no. 5696, pp. 666–669, Oct. 2004.

[6] A. K. Geim and K. S. Novoselov, "The rise of graphene," *Nat. Mater.*, vol. 6, no. 3, pp. 183–191, Mar. 2007.

[7] K. S. Novoselov, A. K. Geim, S. V. Morozov, D. Jiang, M. I. Katsnelson, I. V. Grigorieva, S. V. Dubonos, and A. A. Firsov, "Two-dimensional gas of massless Dirac fermions in graphene," *Nature*, vol. 438, no. 7065, pp. 197–200, Nov. 2005.

[8] Y. Zhang, Y.-W. Tan, H. L. Stormer, and P. Kim, "Experimental observation of the quantum Hall effect and Berry's phase in graphene," *Nature*, vol. 438, no. 7065, pp. 201–204, Nov. 2005.

[9] K. I. Bolotin, K. J. Sikes, Z. Jiang, M. Klima, G. Fudenberg, J. Hone, P. Kim, and H. L. Stormer, "Ultrahigh electron mobility in suspended graphene," *Solid State Commun.*, vol. 146, no. 9–10, pp. 351–355, Jun. 2008.

[10] X. Du, I. Skachko, A. Barker, and E. Y. Andrei, "Approaching ballistic transport in suspended graphene," *Nat. Nanotechnol.*, vol. 3, no. 8, pp. 491–495, Aug. 2008.

[11] C. Lee, X. Wei, J. W. Kysar, and J. Hone, "Measurement of the elastic properties and intrinsic strength of monolayer graphene," *Science*, vol. 321, no. 5887, pp. 385–388, Jul. 2008.

[12] A. A. Balandin, S. Ghosh, W. Bao, I. Calizo, D. Teweldebrhan, F. Miao, and C. N. Lau, "Superior thermal conductivity of single-layer graphene," *Nano Lett.*, vol. 8, no. 3, pp. 902–907, Mar. 2008.

[13] R. R. Nair, P. Blake, A. N. Grigorenko, K. S. Novoselov, T. J. Booth, T. Stauber, N. M. R. Peres, and A. K. Geim, "Fine structure constant defines visual transparency of graphene," *Science*, vol. 320, no. 5881, pp. 1308–1308, Jun. 2008.

[14] Y.-M. Lin, C. Dimitrakopoulos, K. A. Jenkins, D. B. Farmer, H.-Y. Chiu, A. Grill, and P. Avouris, "100-GHz transistors from wafer-scale epitaxial graphene," *Science*, vol. 327, no. 5966, pp. 662–662, Feb. 2010.

[15] F. Bonaccorso, Z. Sun, T. Hasan, and A. C. Ferrari, "Graphene photonics and optoelectronics," *Nat. Photon.*, vol. 4, no. 9, pp. 611–622, Sep. 2010.

[16] F. Schwierz, "Graphene transistors," *Nat. Nanotechnol.*, vol. 5, no. 7, pp. 487–496, Jul. 2010.

[17] T. Sohier, M. Calandra, C.-H. Park, N. Bonini, N. Marzari, and F. Mauri, "Phonon-limited resistivity of graphene by first-principles calculations: electron-phonon interactions, strain-induced gauge field, and Boltzmann equation," *Phys. Rev. B*, vol. 90, no. 12, p. 125414, Sep. 2014.

http://dx.doi.org/10.5772/65111

[18] N. J. G. Couto, D. Costanzo, S. Engels, D.-K. Ki, K. Watanabe, T. Taniguchi, C. Stampfer, F. Guinea, and A. F. Morpurgo, "Random strain fluctuations as dominant disorder source for high-quality on-substrate graphene devices," *Phys. Rev. X*, vol. 4, no. 4, p. 041019, Oct. 2014.

[19] F. Guinea, M. I. Katsnelson, and A. K. Geim, "Energy gaps and a zero-field quantum Hall effect in graphene by strain engineering," *Nat. Phys.*, vol. 6, no. 1, pp. 30–33, Jan. 2010.

[20] N. Wei, L. Xu, H.-Q. Wang, and J.-C. Zheng, "Strain engineering of thermal conductivity in graphene sheets and nanoribbons: a demonstration of magic flexibility," *Nanotechnology*, vol. 22, no. 10, p. 105705, 2011.

[21] J. C. Meyer, A. K. Geim, M. I. Katsnelson, K. S. Novoselov, T. J. Booth, and S. Roth, "The structure of suspended graphene sheets," *Nature*, vol. 446, no. 7131, pp. 60–63, Mar. 2007.

[22] V. M. Pereira and A. H. Castro Neto, "Strain engineering of graphene's electronic structure," *Phys. Rev. Lett.*, vol. 103, no. 4, p. 046801, Jul. 2009.

[23] Z. H. Ni, T. Yu, Y. H. Lu, Y. Y. Wang, Y. P. Feng, and Z. X. Shen, "Uniaxial strain on graphene: Raman spectroscopy study and band-gap opening," *ACS Nano*, vol. 2, no. 11, pp. 2301–2305, Nov. 2008.

[24] C. Metzger, S. Rémi, M. Liu, S. V. Kusminskiy, A. H. Castro Neto, A. K. Swan, and B. B. Goldberg, "Biaxial strain in graphene adhered to shallow depressions," *Nano Lett.*, vol. 10, no. 1, pp. 6–10, Jan. 2010.

[25] A. C. Ferrari, J. C. Meyer, V. Scardaci, C. Casiraghi, M. Lazzeri, F. Mauri, S. Piscanec, D. Jiang, K. S. Novoselov, S. Roth, and A. K. Geim, "Raman spectrum of graphene and graphene layers," *Phys. Rev. Lett.*, vol. 97, no. 18, p. 187401, Oct. 2006.

[26] F. Ding, H. Ji, Y. Chen, A. Herklotz, K. Dörr, Y. Mei, A. Rastelli, and O. G. Schmidt, "Stretchable graphene: a close look at fundamental parameters through biaxial straining," *Nano Lett.*, vol. 10, no. 9, pp. 3453–3458, Sep. 2010.

[27] T. M. G. Mohiuddin, A. Lombardo, R. R. Nair, A. Bonetti, G. Savini, R. Jalil, N. Bonini, D. M. Basko, C. Galiotis, N. Marzari, K. S. Novoselov, A. K. Geim, and A. C. Ferrari, "Uniaxial strain in graphene by Raman spectroscopy: G peak splitting, Gr"uneisen parameters, and sample orientation," *Phys. Rev. B*, vol. 79, no. 20, p. 205433, May 2009.

[28] J. Zabel, R. R. Nair, A. Ott, T. Georgiou, A. K. Geim, K. S. Novoselov, and C. Casiraghi, "Raman spectroscopy of graphene and bilayer under biaxial strain: bubbles and balloons," *Nano Lett.*, vol. 12, no. 2, pp. 617–621, Feb. 2012.

[29] C. Metzger, S. Rémi, M. Liu, S. V. Kusminskiy, A. H. Castro Neto, A. K. Swan, and B. B. Goldberg, "Biaxial strain in graphene adhered to shallow depressions," *Nano Lett.*, vol. 10, no. 1, pp. 6–10, Jan. 2010.

[30] J. D. Werner, NRC: storage of spent nuclear fuel." *CRS. Rep. Congress*, May 2012.

[31] *Safety and Security of Commercial Spent Nuclear Fuel Storage: Public Report*. Washington, D.C.: National Academies Press, 2006.

[32] G. D. Moan and P. Rudling, *Zirconium in the Nuclear Industry: Thirteenth International Symposium*. ASTM International, West Conshohocken, PA, United States of America, 2002.

[33] D. G. Boase and T. T. Vandergraaf, "The Canadian spent fuel storage canister: some materials aspects," *Nucl. Technol.*, vol. 32, no. 1, pp. 60–71, Jan. 1977.

[34] J. S. Bryner, "The cyclic nature of corrosion of zircaloy-4 in 633 K water," *J. Nucl. Mater.*, vol. 82, no. 1, pp. 84–101, Jun. 1979.

[35] M. Suzuki and S. Kawasaki, "Oxidation of zircaloy cladding in air," *J. Nucl. Mater.*, vol. 140, no. 1, pp. 32–43, Aug. 1986.

[36] B. Cox, "Some thoughts on the mechanisms of in-reactor corrosion of zirconium alloys," *J. Nucl. Mater.*, vol. 336, no. 2–3, pp. 331–368, Feb. 2005.

[37] D. Shooter, "Chapter 3. Experimental methods for the study of heterogeneous reactions," in *Comprehensive Chemical Kinetics*, vol. 1, C. H. Bamford and C. F. H. Tipper, Ed. Elsevier, Amsterdam, the Netherlands, 1969, pp. 180–278.

[38] R. J. Grossman, "Continuous measurement of Zircaloy corrosion in air with an ultrasonic corrosion monitor," in *IEEE 1984 Ultrasonics Symposium*, 1984, pp. 860–865.

[39] I. S. Woolsey and J. R. Morris, "A study of Zircaloy-2 corrosion in high temperature water using ion beam methods," *Corrosion*, vol. 37, no. 10, pp. 575–585, Oct. 1981.

[40] K. Poulard, A. Chevarier, N. Moncoffre, P. Trocellier, and D. Crusset, "Study of zircaloy-4 fuel cladding corrosion using ion beams: application to long-term disposal of nuclear wastes," *Nucl. Instrum. Methods Phys. Res. Sect. B Beam Interact. Mater. At.*, vol. 181, no. 1–4, pp. 640–643, Jul. 2001.

[41] N. Ramasubramanian and V. C. Ling, "Fourier transform infrared reflection (FTIR) spectroscopy of corrosion films on irradiated zirconium alloys," *J. Nucl. Mater.*, vol. 175, no. 3, pp. 237–243, Dec. 1990.

[42] B. Cox and W. Yin-Mei, "Direct measurement of the thickness and optical properties of zirconia corrosion films," *J. Nucl. Mater.*, vol. 199, no. 3, pp. 258–271, Feb. 1993.

[43] I. Idarraga, M. Mermoux, C. Duriez, A. Crisci, and J. P. Mardon, "Raman investigation of pre- and post-breakaway oxide scales formed on Zircaloy-4 and M5® in air at high temperature," *J. Nucl. Mater.*, vol. 421, no. 1–3, pp. 160–171, Feb. 2012.

[44] V. G. Keramidas and W. B. White, "Raman scattering study of the crystallization and phase transformations of ZrO_2," *J. Am. Ceram. Soc.*, vol. 57, no. 1, pp. 22–24, Jan. 1974.

[45] R. Srinivasan, M. B. Harris, S. F. Simpson, R. J. De Angelis, and B. H. Davis, "Zirconium oxide crystal phase: the role of the pH and time to attain the final pH for precipitation of the hydrous oxide," *J. Mater. Res.*, vol. 3, no. 04, pp. 787–797, Aug. 1988.

[46] P. Barberis, T. Merle-Méjean, and P. Quintard, "On Raman spectroscopy of zirconium oxide films," *J. Nucl. Mater.*, vol. 246, no. 2, pp. 232–243, Aug. 1997.

[47] P. Barbéris, G. Corolleur-Thomas, R. Guinebretière, T. Merle-Mejean, A. Mirgorodsky, and P. Quintard, "Raman spectra of tetragonal zirconia: powder to zircaloy oxide frequency shift," *J. Nucl. Mater.*, vol. 288, no. 2–3, pp. 241–247, Feb. 2001.

[48] P. E. Quintard, P. Barbéris, A. P. Mirgorodsky, and T. Merle-Méjean, "Comparative lattice-dynamical study of the Raman spectra of monoclinic and tetragonal phases of zirconia and hafnia," *J. Am. Ceram. Soc.*, vol. 85, no. 7, pp. 1745–1749, Jul. 2002.

[49] J. S. Moya, M. Diaz, J. F. Bartolomé, E. Roman, J. L. Sacedon, and J. Izquierdo, "Zirconium oxide film formation on zircaloy by water corrosion," *Acta Mater.*, vol. 48, no. 18–19, pp. 4749–4754, Dec. 2000.

[50] R. Ruiz, H. Kang, F. A. Detcheverry, E. Dobisz, D. S. Kercher, T. R. Albrecht, J. J. de Pablo, and P. F. Nealey, "Density multiplication and improved lithography by directed block copolymer assembly," *Science*, vol. 321, no. 5891, pp. 936–939, Aug. 2008.

[51] A. J. Hong, C.-C. Liu, Y. Wang, J. Kim, F. Xiu, S. Ji, J. Zou, P. F. Nealey, and K. L. Wang, "Metal nanodot memory by self-assembled block copolymer lift-off," *Nano Lett.*, vol. 10, pp. 224–229, Jan. 2010.

[52] H. Mi, S. Mikael, C.-C. Liu, J.-H. Seo, G. Gui, A. L. Ma, P. F. Nealey, and Z. Ma, "Creating periodic local strain in monolayer graphene with nanopillars patterned by self-assembled block copolymer," *Appl. Phys. Lett.*, vol. 107, no. 14, p. 143107, Oct. 2015.

[53] X. Li, W. Cai, J. An, S. Kim, J. Nah, D. Yang, R. Piner, A. Velamakanni, I. Jung, E. Tutuc, S. K. Banerjee, L. Colombo, and R. S. Ruoff, "Large-area synthesis of high-quality and uniform graphene films on copper foils," *Science*, vol. 324, no. 5932, pp. 1312–1314, Jun. 2009.

[54] K. S. Kim, Y. Zhao, H. Jang, S. Y. Lee, J. M. Kim, K. S. Kim, J.-H. Ahn, P. Kim, J.-Y. Choi, and B. H. Hong, "Large-scale pattern growth of graphene films for stretchable transparent electrodes," *Nature*, vol. 457, no. 7230, pp. 706–710, Feb. 2009.

[55] G. Grimvall, *Thermophysical Properties of Materials*. Elsevier, Amsterdam, the Netherlands, 1999.

[56] E. Cadelano, P. L. Palla, S. Giordano, and L. Colombo, "Nonlinear elasticity of monolayer graphene," *Phys. Rev. Lett.*, vol. 102, no. 23, p. 235502, Jun. 2009.

[57] C. M. Phillippi and K. S. Mazdiyasni, "Infrared and Raman spectra of zirconia polymorphs," *J. Am. Ceram. Soc.*, vol. 54, no. 5, pp. 254–258, May 1971.

[58] H. Mi, S. Mikael, T. Allen, K. Sridharan, D. Butt, J. P. Blanchard, and Z. Ma, "Monitoring the oxidation of nuclear fuel cladding using Raman spectroscopy," *J. Nucl. Mater.*, vol. 445, no. 1–3, pp. 7–11, Feb. 2014.

Chapter 7

Boosting the Amount of Molecular Information Through Polarized Resolved Resonance Raman Scattering

Søren Hassing

Additional information is available at the end of the chapter

http://dx.doi.org/10.5772/65482

Abstract

Vibrational Raman spectroscopy, one of the experimental techniques available, is applied for characterization and analysis of molecular samples in different areas such as medical, food and environmental analysis. Application of the Raman technique is mostly similar to the application of infrared and near-infrared absorption spectroscopy, i.e. only the spectral distribution is analysed. The goal of the present chapter is to demonstrate that the amount of molecular information (also for solutions and powders) can be increased considerably by analysing also the polarization of the Raman and resonance Raman-scattered light. The goal is achieved through: (1) a discussion of the basic properties of Raman scattering with special focus on polarization and polarization dispersion. The discussion includes the rotational invariants of Raman tensors, the non-commuting generator approach to molecular symmetry as a tool for construction of state and Raman tensors for single molecules and dimers and higher aggregates and thereby predict the polarization; (2) a discussion of two illustrative case studies: Case study 1: Aggregation of haemoglobin in red blood cells (RBC); and Case study 2: *In vitro* polarization resolved RRS study of dye-sensitized solar cells.

Keywords: polarization, state tensor, Raman tensor, aggregation, non-commuting generators

1. Introduction

Raman spectroscopy is a fast, non-destructive and molecule-specific technique, which requires no or very little sample preparation. Raman spectroscopy is therefore attractive as an experimental technique for on-site investigations of molecular samples of very different

nature. A vibrational Raman spectrum contains the unique and highly resolved vibrational signature of the molecule and it is obtained by illuminating the sample with polarized laser light with wavenumbers in either the near-infrared (NIR), visible or ultraviolet (UV) regions and monitoring the backscattered light as a function of wavenumber. The main challenge of Raman spectroscopy has always been the low Raman cross-section, where typically 10^8 laser photons only generate a single Raman photon. The result is that the intensity in Raman spectra is generally low. Another challenge particular in Raman investigations of biomolecules is that the excitation of the Raman process is followed by a simultaneous excitation of fluorescence. Since the fluorescence cross-section is generally several orders of magnitude higher than the Raman cross-section, the Raman signal may be partly or completely hidden behind the fluorescence background.

However, because of the technical improvements in Raman instrumentation, the problems originating from the low Raman cross-section have largely been overcome so that the potential of Raman scattering can be utilized, and even though fluorescence may still be a problem in some cases and requires advanced signal processing, vibrational Raman spectroscopy is now applied as a standard technique in many areas such as medical, food and environmental analysis.

In most practical applications, only the positions and intensities of the Raman bands are analysed, i.e. the Raman technique is applied similarly to infrared (IR) and NIR spectroscopy. Although the polarization properties of Raman scattering have been known since the early days of Raman theory, see e.g. [1], and although Raman dispersion spectroscopy (including polarization) introduced by Mortensen [2] has been applied for many years to explore conformational perturbations in metallo-porphyrins and various proteins, see [3–7] and references therein, the advantage of applying polarization resolved Raman scattering is not yet common knowledge among the increasing group of practically working scientists and laboratory technicians representing very different areas, who apply vibrational Raman spectroscopy as one out of a large number of experimental techniques available for the characterization of molecular samples. Besides, polarization analysis of vibrational Raman data is not a standard option in most commercial Raman instruments.

A unique property of the Raman process is that the polarization of the scattered light is generally different from the polarization of the incident laser light. This holds for molecular solids, i.e. oriented molecules and (perhaps more surprisingly) also for powders and solutions, where the molecules are randomly oriented. In vibrational Raman scattering, the polarization change is found to be specific for each vibrational Raman mode and for excitations near an UV/Visible absorption in the molecule, i.e. in resonance or near-resonance Raman scattering, the change depends in general on the wavenumber difference between the excitation and the absorption as well as on the molecular configuration in the electronically excited state.

The goal of this chapter is to demonstrate why, how and when the application of polarized resolved Raman spectroscopy may increase the outcome of a Raman experiment. This goal is achieved through a discussion of the basic properties of Raman scattering with special focus on the polarization followed by a discussion of two illustrative case studies: Case study 1:

http://dx.doi.org/10.5772/65482

Aggregation of haemoglobin in red blood cells (RBC); Case study 2: *In vitro* polarization resolved RRS study of dye-sensitized solar cells (DSC).

2. A glimpse of Raman theory

A unified treatment of Raman theory can be found in Ref. [8] together with a long list of references to the Raman literature. The symmetry aspects of the polarization properties have been discussed by Mortensen and Hassing [9], while the vibronic aspects have been discussed by Siebrand and Zgierski [10] and we refer to these references for details.

Raman scattering is a two-photon process in which a primary photon with wavenumber $\tilde{\nu}_p$ and polarization vector $\boldsymbol{u}_p$ is absorbed and coherently replaced by a scattered photon with wavenumber $\tilde{\nu}_s$ and polarization vector $\boldsymbol{u}_s$. In a quantum mechanical description of the process in which the interaction between the molecule and radiation is used as perturbation, the Raman process is of second-order, which has the consequence that the Raman-scattered intensity into the solid angle $d\Omega(I_{\text{Raman}})$ becomes proportional to the absolute square of the scattering (Raman) tensor $|\boldsymbol{\alpha}^{a\to b}|^2$ which is a tensor of Rank 2. The basic scattering equations are collected in Eq. (1), while the expression for the components of the Raman tensor $\boldsymbol{\alpha}_{\varrho\sigma}^{a\to b}$ is given in Eq. (2).

$$I_{\text{Raman}} = \left(\frac{d\sigma}{d\Omega}\right) I_{\text{laser}}\, d\Omega \text{ and } \left(\frac{d\sigma}{d\Omega}\right) = 4\pi\, \boldsymbol{\alpha}_{\text{fsc}}^2\ \tilde{\nu}_s^4 \left| \sum_{\rho,\sigma} u_{s\rho}\, \boldsymbol{\alpha}_{\varrho\sigma}^{a\to b}\, u_{p\sigma} \right|^2 \tag{1}$$

where $\left(\frac{d\sigma}{d\Omega}\right)$ is the differential Raman cross-section and α_{fsc} is the fine structure constant. I_{laser} is the intensity of a collimated laser beam:

$$\boldsymbol{\alpha}_{\varrho\sigma}^{a\to b} = \sum_r \frac{\langle \boldsymbol{b}|\rho|r\rangle\langle r|\sigma|\boldsymbol{a}\rangle}{\tilde{\nu}_{pa} - \tilde{\nu}_p - i\,\gamma_r} + \frac{\langle \boldsymbol{b}|\sigma|r\rangle\ \langle r|\rho|\boldsymbol{a}\rangle}{\tilde{\nu}_{rb} + \tilde{\nu}_p + i\,\gamma_r} \tag{2}$$

where *a*, *b* and *r* stands for the initial, final and intermediate states of the process. $\tilde{\nu}_{r\boldsymbol{a}}$ is the energy difference between state $|r\rangle$ and $|\boldsymbol{a}\rangle$ The summation runs over all the (exact) eigenstates of the molecule and γ_r is the damping of the state $|r\rangle$ responsible for its exponential decay. ρ and ρ and σ are a shorthand notation for the Cartesian components of the electronic position vector $\sum_i r_i = \frac{\hat{\mu}}{e}$, where $\hat{\mu}$ and e are the electric dipole operator of the electrons and the electron charge, respectively, and the summation runs over all electrons in the molecule. ρ and σ refer either to the space-fixed coordinates *X*, *Y*,*Z* or to the molecule-fixed coordinates *x*, *y*, *z*. In non-resonance Raman scattering (RS), where the excitation wavenumber is chosen in a region, where the molecule does not absorb light, i.e. $\tilde{\nu}_b < \tilde{\nu}_p \ll \tilde{\nu}_{ra}$ for any state $|r\rangle$, the expression for $\boldsymbol{\alpha}_{\varrho\sigma}^{a\to b}$ becomes virtually independent of intermediate states and the polarizability theory first developed by Placzek applies [1]. See also the book by Long [11]. In the case of excitation close to an absorption energy, i.e. $\tilde{\nu}_p \sim \tilde{\nu}_{ra}$ for some intermediate states, the contribution from these states dominates and the Raman signal will be enhanced. The process is termed resonance Raman scattering (RRS). The enhancement, which may be a factor of 10^6, depends on the wavenumber difference between the resonating states $|r\rangle$ and the wavenumber of the laser $\tilde{\nu}_p$ as well as on the magnitude of the damping constants γ_r.

In polarization resolved Raman scattering two quantities are measured, the parallel and perpendicular components of the total scattering cross-section,

$$\left(\frac{d\sigma}{d\Omega}\right)_{\parallel} = 4\pi\, \boldsymbol{\alpha}_{\text{fsc}}^2\ \ \widetilde{\nu}_s^4\ \left|\alpha_{ZZ}^{a\to b}\right|^2 \tag{3}$$

$$\left(\frac{d\sigma}{d\Omega}\right)_{\perp} = 4\pi\, \boldsymbol{\alpha}_{\text{fsc}}^2\ \ \widetilde{\nu}_s^4\ \left|\boldsymbol{\alpha}_{YZ}^{a\to b}\right|^2 \tag{4}$$

$$DPR = \frac{\left(\frac{d\sigma}{d\Omega}\right)_{\perp}}{\left(\frac{d\sigma}{d\Omega}\right)_{\parallel}} = \frac{\left|\boldsymbol{\alpha}_{YZ}^{a\to b}\right|^2}{\left|\boldsymbol{\alpha}_{ZZ}^{a\to b}\right|^2} \tag{5}$$

where it is assumed that an oriented molecule is placed in the centre of a space-fixed coordinate system and that the Raman scattering is observed in the backscattering geometry. Besides the incoming light is taken to propagate along the *X*-axis and linearly polarized in the *Z*-direction. The parallel polarized scattered light is then also polarized in the *Z*-direction, while the perpendicular polarized scattered light is polarized in the *Y*-direction. The polarization is described by the depolarization ratio (DPR) defined in Eq. (5). The DPR is seen to be an absolute quantity.

For ensembles of randomly oriented molecules, i.e. powders and solutions, the parallel and perpendicular scattering cross-sections in Eqs. (3) and (4) must be averaged with respect to molecular orientation. The spatial average of the scattering components $\langle \left|\boldsymbol{\alpha}_{ZZ}^{a\to b}\right|^2 \rangle$ and $\langle \left|\boldsymbol{\alpha}_{YZ}^{a\to b}\right|^2 \rangle$ have been evaluated by Mortensen and Hassing by applying angular momentum theory [9]. The result is that $\langle \left|\boldsymbol{\alpha}_{ZZ}^{a\to b}\right|^2 \rangle$ and $\langle \left|\boldsymbol{\alpha}_{YZ}^{a\to b}\right|^2 \rangle$ are expressed in terms of the three rotational invariants of the Raman tensor Σ^0, Σ^1 and Σ^2, which contain combinations of the absolute squares of the tensor components. Σ^0 is the absolute square of the trace of Raman tensor and Σ^2 contains symmetric combinations of the off-diagonal tensor components and diagonal components and is termed the symmetric anisotropy. Σ^1 only contains anti-symmetric combinations of the tensor components, i.e. $\left|\boldsymbol{\alpha}_{\rho\sigma}^{a\to b} - \boldsymbol{\alpha}_{\sigma\rho}^{a\to b}\right|^2$. The complete relations between the invariants and the Raman tensor components are given in Ref. [9].

For randomly oriented systems Eqs. (3)–(5) must be then replaced by,

$$\left(\frac{d\sigma}{d\Omega}\right)_{\parallel} = 4\pi\, \boldsymbol{\alpha}_{\text{fsc}}^2\ \ \widetilde{\nu}_s^4\, \frac{1}{15}(5\,\Sigma^0 + 2\,\Sigma^2) \tag{6}$$

$$\left(\frac{d\sigma}{d\Omega}\right)_{\perp} = 4\pi\, \boldsymbol{\alpha}_{\text{fsc}}^2\ \ \widetilde{\nu}_s^4\, \frac{1}{15}\left(\frac{3}{2}\,\Sigma^2 + \frac{5}{2}\,\Sigma^1\right) \tag{7}$$

$$DPR = \frac{\left(\frac{d\sigma}{d\Omega}\right)_{\perp}}{\left(\frac{d\sigma}{d\Omega}\right)_{\parallel}} = \frac{3\,\Sigma^2 + 5\,\Sigma^1}{10\,\Sigma^0 + 4\,\Sigma^2} \tag{8}$$

First, it is noted that in RRS all three tensor invariants may be different from zero, while in RS the Raman tensor is found to be symmetric so that the scattering is determined by only Σ^0 and Σ^2, which has the consequence is that the DPR is limited to: $0 \le DPR \le \frac{3}{4}$. However, in RRS the DPR may take any number. But more important: the DPR may depend on the laser wavenumber, i.e. exhibit polarization dispersion.

We now see why polarized measurements performed on powders and solutions may provide extra information in Raman spectroscopy, while this is not the case in IR and NIR absorption.

http://dx.doi.org/10.5772/65482

Raman scattering includes in general three independent observables Σ^0, Σ^1 and Σ^2 while IR and NIR absorption only includes one observable, namely the spatially average of the electric dipole transition moment vector, i.e. its length. Polarized measurements in IR and NIR absorption may of course give additional information when the molecules can be spatially oriented.

2.1. State tensors and Raman tensors

In the discussion of the polarization properties of RRS, it is convenient to define for the state $|r\rangle$ the state tensor $\left[S_{\varrho\sigma}^{|r\rangle}\right]_{a\to b} = \langle b|\varrho|r\rangle\langle r|\sigma|a\rangle$. The Raman tensor for the Raman transition $|a\rangle \to |b\rangle$ is then given as a sum of state tensors, where each state tensor is weighted by the complex energy factor $\left(\tilde{\nu}_{ra} - \tilde{\nu}_p - i\gamma_r\right)^{-1}$. In the general case where the molecule has no symmetry all components of the state tensors $\left[S_{\varrho\sigma}^{|r\rangle}\right]_{a\to b}$ may be different, besides the state tensors $\left[S_{\varrho\sigma}^{|r\rangle}\right]_{a\to b}$ and $\left[S_{\varrho\sigma}^{|r\rangle}\right]_{a\to b}$ associated with different states $|r\rangle$ and $|s\rangle$ are also different in general. When the molecules have a certain amount of symmetry some of the components $\left[S_{\varrho\sigma}^{|r\rangle}\right]_{a\to b}$ vanish and some of the non-vanishing components become numerically related. However, the symmetry relations between the state tensor components $\left[S_{\varrho\sigma}^{|r\rangle}\right]_{a\to b}$ and $\left[S_{\varrho\sigma}^{|r\rangle}\right]_{a\to b}$ may still be different, depending on the symmetry relation between the states $|r\rangle$ and $|s\rangle$. The result is that a particular tensor component $\alpha_{\varrho\sigma}^{a\to b}$ of the Raman tensor $\alpha^{a\to b}$ will have contributions from selected states $|r\rangle$, while other components $\alpha_{\varrho'\sigma'}^{a\to b}$ will have contributions from other states $|s\rangle$. The important point is that the distribution of the state tensor components that contribute to a given Raman tensor $\alpha^{a\to b}$ will manifest itself in the measured DPR values. Thus, under-resonance or near-resonance excitations the value of the DPR may or may not depend on the excitation wavenumber (polarization dispersion). As already mentioned polarization dispersion has been applied in numerous resonance Raman studies of the structure and bio-functionality of proteins containing metallo-porphyrins [7, 12]. The ideal symmetry of the porphyrin (e.g. the haem group) is D_{4h}, but the real symmetry becomes lower when distortions are induced on the Tetra-pyrrole ring by its surroundings. Depending on the symmetry of the distortion the coupling between the doubly degenerate *B*- and *Q*-states of the chromophore induces changes in the state and Raman tensors, which give rise to a characteristic polarization dispersion of each Raman mode. Since the DPR is very sensitive to even small perturbations of the molecule, detailed information about intra-molecular interactions can be obtained as shown in the papers mentioned above. The challenge in performing Raman dispersion studies is that one has to monitor two Raman cross-sections, $\left(\frac{d\sigma}{d\Omega}\right)_{\parallel}$ and $\left(\frac{d\sigma}{d\Omega}\right)_{\perp}$ as a function of excitation wavenumber, which requires special laser sources and/or several lasers. The experiments may be rather time consuming as such, in particular when the fluorescence background changes with the excitation wavenumber. Besides, one has to keep track on the absolute intensity variations by the application of internal standards.

In non-resonance, vibrational Raman scattering the different contributions to the Raman tensor are 'washed out' and the Raman tensor becomes symmetric and as well known, the DPR values become either $DPR_{\text{asym}} = \frac{3}{4}$ for a-symmetric modes or $0 \le DPR_{\text{sym}} < \frac{3}{4}$ for totally symmetric modes.

For molecules with a well-defined nuclear configuration, the molecular symmetry can be discussed in terms of point-groups. As shown by Mortensen and Hassing [9], the general form of

the state tensors, determined by symmetry, can be evaluated by applying the method of non-commuting generators instead of conventional group representation theory [13]. The state tensors for almost all point groups have been derived in [9] and they have later been reproduced in [8]. Below it is demonstrated how this method can be extended to derive also the state tensors for aggregated molecules. Although the dimer is used as an illustrative example the method can easily be generalized to larger aggregates.

Finally, most treatments of vibrational Raman scattering are formulated within the adiabatic Born-Oppenheimer (ABO) approximation and we shall also do so here, since this will be sufficient for the discussion of the polarization. In any case, the results can be generalized to go beyond the ABO approximation by the application of perturbation theory. However, all results based on symmetry will be exact. Since we are mainly interested in larger molecules, i.e. solutions and powders, the rotational motion need not be explicitly considered. All states in the state and Raman tensors are therefore given as products of an electronic state and a vibrational sub-state, i.e. $|r\rangle = |e\rangle|v_1, v_2, v_3, \ldots\rangle$, where in the harmonic approximation the vibrational sub-states are also factorized.

2.2. State and Raman tensors for aggregated molecules

The non-commuting generator approach to molecular symmetry discussed by Mortensen in [13] is illustrated in **Figure 1**, using the point group D_4 as an example. The group is characterized by two generators $\widehat{C}_4$ and $\widehat{C}_{2y}$ and a commutation relation between the generators. The character table, used in group representation theory (shown to the right), is replaced by an eigenvalue table containing the eigenvalues of the generators (region I). Region II gives the eigenvalues under $\widehat{C}_{2y}$, but since this operator does not always commute with $\widehat{C}_4$ the transformation matrix showing how the two basis states $|E_x\rangle$ and $|E_y\rangle$ transform into each other is given instead. Notice that this is the particular information missing in group representation theory since only the characters (i.e. the traces) of the transformation matrices representing the symmetry operators are determined. It follows from **Figure 1** that the trace for both generators for the degenerate *E*-representation is equal to zero in accordance with the value in the character table.

The main task of symmetry is to calculate matrix elements or rather to point out the particular matrix elements that must vanish because of symmetry. The calculation of matrix elements and derivation of symmetry relations between matrix elements, using the non-commuting generator approach, is summarized in **Figure 2**.

In **Figure 2**, the possibility (I) is applied to derive spectroscopic selection rules, while possibility (II) is the one that can be applied to find numerical relations between matrix elements and to derive the general form of the state tensors and the Raman tensors for single molecules. The numerical relations between matrix elements are found by combining (I) and (II) and applying the Wigner Eckart theorem, see Ref. [13].

The state tensors obtained for a molecule with D_{4h} -symmetry, is given in the upper part of **Figure 4** for the Raman modes b_{1g}, b_{2g} and a_{2g} as examples. This applies to the haem, when assuming its ideal symmetry to be D_{4h}. The symmetry of the Raman mode is given in front of each tensor, while the symmetry inside the tensors is the symmetry of the electronic state, i.e. $|E_{Qx}\rangle$ or $|E_{Qy}\rangle$ responsible for that particular tensor component. The state tensors associated

http://dx.doi.org/10.5772/65482

A review of the non-commuting generator approach to molecular symmetry

The principles of the method in brief:

- Generators of the group and commutation relations
- Eigenvalue tables versus character tables, e.g. D_4.

Eigenvalue table

		$\lambda(\hat{C}_4)$	$\lambda(\hat{C}_{2y})$
I	A_1	1	1
	A_2	1	-1
	B_1	-1	1
	B_2	-1	-1
II	E_x E_y	$\begin{pmatrix} 0 & -1 \\ 1 & 0 \end{pmatrix}$	-1 1

Real basis

Character table

D_4	E	$2C_4$	C_2	$2C_2'$	$2C_2''$
A_1	1	1	1	1	1
A_2	1	1	1	-1	-1
B_1	1	-1	1	1	-1
B_2	1	-1	1	-1	1
E	2	0	-2	0	0

Generators in D_4: $\hat{R} = \hat{C}_4, \hat{C}_{2y}$

Commutation relation: $\hat{C}_{2y}\hat{C}_4 = \hat{C}_4^{-1}\hat{C}_{2y}$

Eigenvalues: $\lambda(\hat{R}) = e^{i\frac{2\pi}{n}k}$, k = 0, 1, 2, … n-1, (n = group order)

UNIVERSITY OF SOUTHERN DENMARK.DK

Figure 1. Eigenvalue table and character table for point group D_4. Group generators and their commutation relation are given.

Calculation of matrix elements by application of the non-commuting generator approach

Basic selection rule: $\hat{R}\langle b|\hat{O}|a\rangle = \langle b|\hat{O}|a\rangle$ (1)

for $\hat{R}$ equal to each group generator.

Possibility (I):

When the operator $\hat{O}$ and the states ⟨b| and |a⟩ **all** have eigenvalues under $\hat{R}$, application of (1) gives: $\lambda_b(\hat{R}) = \lambda_{\hat{O}}(\hat{R}) \cdot \lambda_a(\hat{R})$ (2)

Possibility (II):

When instead $\hat{O}$, ⟨b| and |a⟩ transform into other operators/states, then application of (1) gives rise to numerical relations between matrix elements.

These relations can be extracted from the eigenvalue tables.

Thus, the non-commuting generator approach may give additional information compared to conventional representation theory.

UNIVERSITY OF SOUTHERN DENMARK.DK

Figure 2. Calculation of symmetry based relations between matrix elements through the application of non-commuting generator approach [13].

with the vibrational sub-states are found by taking the direct product of the symmetry of the electronic state and the symmetry of the Raman mode. Having calculated the distribution of state tensors the Raman tensors and the invariants can be calculated and finally the DPR is calculated from Eq. (8). The DPR values are listed behind the state tensors. Notice that due the high symmetry no polarization dispersion occurs.

When the configuration of the haem is perturbed so that the symmetry becomes lower than D_{4h} the energy of $|E_{Qx}\rangle, |E_{Qy}\rangle$ and of the next excited states $|E_{Bx}\rangle, |E_{By}\rangle$ (Soret absorption band) split up due to coupling induced by the perturbations. As shown by Siebrand and Zgierski [10] and Schweitzer Stenner et al. [14] this will give rise to a mixing of the Raman tensors for different modes and result in characteristic polarization dispersion curves for most Raman modes, from which detailed information about the symmetry lowering perturbations can be extracted. We shall not consider these cases further, but refer to the papers just mentioned. Instead we consider the construction of state and Raman tensors for molecular aggregates using the non-commuting generator approach. The molecular dimer of two coupled haem-groups is chosen as an illustrative case. For simplicity only the excitonic coupling between the $|E_{Qx}\rangle, |E_{Qy}\rangle$-states is considered.

The construction of the state tensors for the molecular dimer by the application of the non-commuting generator approach consists of three steps, which are summarized in **Figure 3**.

In step 1, the coupling matrix describing the electronic coupling between the *Q*-states of the monomers is defined. Considering, e.g. a H-type dimer the elements in the coupling matrix are $h_{xx} = h_{yy} \equiv h_e$ and $h_{xy} = h_{yx} \equiv h'_e$.

In step 2, the eigenstates and eigenvalues are determined by diagonalisation of the coupling matrix. Finally, in step 3 the state tensors of the dimer in the basis of the monomers are evaluated by inserting the eigenstates and the components of the dipole moment operator of the dimer and applying the symmetry relations between the tensor elements of the monomers.

The state tensors obtained for the H-type dimer for the Raman modes b_{1g}, b_{2g} and b_{1g}, b_{2g} and a_{2g} is shown **Figure 4(b)**. From the state tensor patterns the Raman tensors can then be evaluated by adopting the Franck-Condon principle for the symmetric modes and the general vibronic relation $S_{\varrho\sigma}^{|e,0\rangle} = S_{\sigma\varrho}^{|e,1\rangle}$ for the asymmetric modes.

The following should be noticed from **Figure 4**: (1) only 2 of the 4 basis states termed $|R_1\rangle$ and $|R_2\rangle$ contribute to the scattering. (2) The state tensors contain 4 elements instead of 2 as for the monomers. (3) The numerical relations between these tensor elements depend on the symmetry of the Raman mode. (4) The energy factors depends linearly on the coupling parameters h_e and h_e and h'_e. Because of the changed state tensor pattern of the dimer as compared to the monomers, changes are introduced in the Raman tensors with the consequence that the DPR now exhibit polarization dispersion. A similar calculation can be made for J-type dimer as well. The simulated polarization dispersion curves of H-type and J-type

dimers of molecules with D_{4h} symmetry shown in **Figure 5(b)** demonstrate that it is possible to determine the kind of dimerization by polarized resolved RRS.

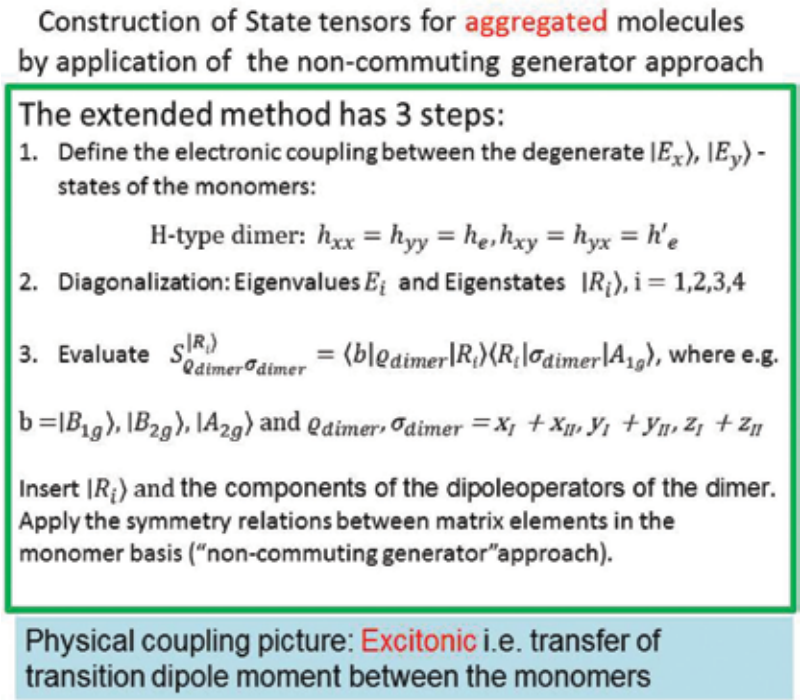

Figure 3. Construction of state tensors for excitonic coupled molecules illustrated by an H-type dimer.

In Ref. [15], a discussion based on a physical and vibronic model of polarization dispersion in H-type and J-type dimers is presented and it is concluded that polarization resolved RRS (i.e. DPR) appears to be a powerful tool for determining the geometries and coupling strengths for molecular dimers and larger aggregates.

2.2.1. Case study 1: aggregation of haemoglobin in red blood cells

Aggregation of biomolecules plays an important role in various biophysical processes, e.g. oxygen uptake, processes involving drug uptake by human cells [16, 17]. In nature many of these important biophysical processes are dependent upon various minor changes of the molecular configurations as well as on various aggregation processes of the biomolecules involved. As already mentioned an important class of biomolecules is the metallo-porphyrins, where extensive systematic studies applying polarized Raman dispersion spectroscopy and including vibronic theory as well as experiments, have been performed [4, 6, 7, 12, 14, 18–22].

Theoretical quantum computations, e.g. density functional theory (DFT), and normal coordinate structural decomposition (NSD) have also been applied [23–26]. The oxidation state of haemoglobin in a single red blood cell (RBC) has been studied *in vivo* applying RRS with different excitation wavelengths by Wood and McNaughton [27], while Ramser et al. have demonstrated that single RBC's can be studied by trapping the cell with optical tweezers [28].

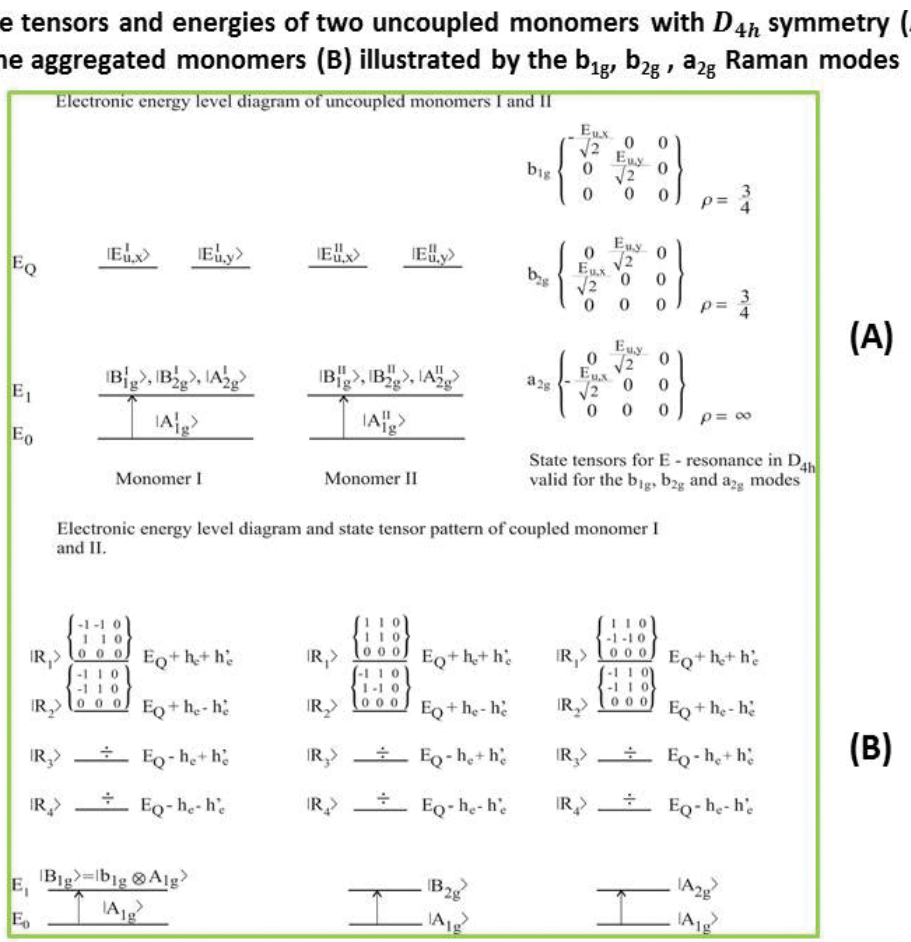

Figure 4. Energy level scheme and state tensors for uncoupled monomers and for the H-type dimer. Monomers: the symmetry written in the tensor means that the number in that position is due to a state with that symmetry, while the signs show the quantitative relation between the tensor elements. Dimer: The numerical relations between the tensor elements are indicated with ±1. The Wigner-Eckart theorem has been applied.

In the following the aggregation of haemoglobin molecules in living RBC's of human blood is discussed. First, the polarized resolved Raman study on spatially oriented RBCs performed by Wood et al. in Ref. [29] is discussed. The coordinates, which constitutes the laboratory frame, are designated ⊥ and ∥ and for the molecular frame these are designated *X*, *Y*, *Z*. The erythrocytes were affixed in a horizontal and vertical direction relative to a petri dish surface. In the horizontal situation the Petri dish surface is parallel to the ⊥, ∥ –plane, while in the vertical situation it is perpendicular to this plane. The polarization of the laser is directed

http://dx.doi.org/10.5772/65482

along ∥-axis and is, besides, identical in the two situations. Subsequently 30 Raman spectra were measured in each situation, where in each case both the parallel and perpendicular polarization of the scattering were measured. The polarized Raman experiment may now be described by the following equations,

$$\left(\frac{d\sigma}{d\Omega}\right)_{\parallel}^{(1)} = 4\pi\,\alpha_{fsc}^2\;\;\tilde{\nu}_s^4\left|\alpha_{ZZ}^{RBC}\right|^2\;;\;\left(\frac{d\sigma}{d\Omega}\right)_{\perp}^{(1)} = 4\pi\,\alpha_{fsc}^2\;\;\tilde{\nu}_s^4\left|\alpha_{XZ}^{RBC}\right|^2 \tag{9}$$

$$DP\,R_1^{RBC} = \frac{\left|\alpha_{XZ}^{RBC}\right|^2}{\left|\alpha_{ZZ}^{RBC}\right|^2} \tag{10}$$

$$\left(\frac{d\sigma}{d\Omega}\right)_{\parallel}^{(2)} = 4\pi\,\alpha_{fsc}^2\;\;\tilde{\nu}_s^4\left|\alpha_{ZZ}^{RBC}\right|^2\;;\;\left(\frac{d\sigma}{d\Omega}\right)_{\perp}^{(2)} = 4\pi\,\alpha_{fsc}^2\;\;\tilde{\nu}_s^4\left|\alpha_{YZ}^{RBC}\right|^2 \tag{11}$$

$$DP\,R_2^{RBC} = \frac{\left|\alpha_{YZ}^{RBC}\right|^2}{\left|\alpha_{ZZ}^{RBC}\right|^2} \tag{12}$$

The philosophy behind the polarized Raman experiments performed with the spatially oriented RBC's in [29] is that if no aggregation between the haemoglobin molecules takes place inside the RBCs, then $DP\,R_1^{RBC} \approx DP\,R_2^{RBC}$, whereas if an aggregation takes place $DP\,R_1^{RBC} \neq DP\,R_2^{RBC}$. The parallel polarized spectra of the horizontally and the vertically oriented RBCs were compared by applying a principal component analysis (PCA) to the data. The same analysis was performed for the perpendicular polarized spectra. Since the PCA performed on both sets of data containing the polarization parameter showed significantly different results, it was concluded that a distinct ordering of the haemoglobin took place in the erythrocytes.

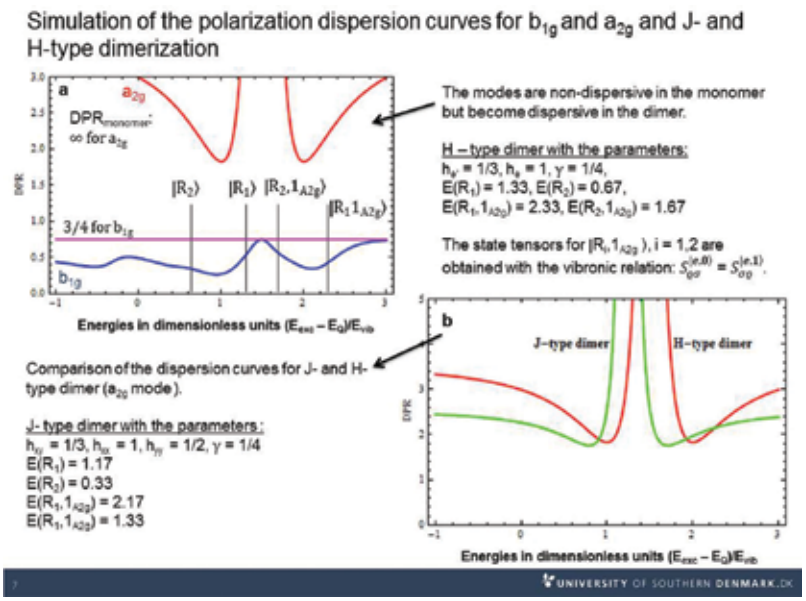

Figure 5. Simulated polarization dispersion curves for dimers. (a) Illustrates that non-dispersive modes become dispersive due to aggregation. (b) Demonstrates that it is possible to distinguish between J-type and H-type dimerization by polarization resolved RRS.

It is important, when studying the properties of biomolecules and biophysical processes, to mimic the natural surrounding conditions. When for example carrying out Raman studies of the aggregation process of haemoglobin in RBCs, this means that it is preferable to perform the polarization resolved measurements directly on a solution of the RBCs and thereby avoiding the consequences of a molecular fixation used by Ramser et al. [28] and by Wood et al. [29]. The basis for such an investigation is the results expressed in Eqs. (6)–(8). In our measurements the procedure was as follows: First, the polarized resolved RRS spectra were measured on a sample containing a number of randomly oriented erythrocytes (i.e. a dilute solution where no aggregation between the RBCs occurs). Secondly, the polarized resolved RRS spectra were measured of a reference sample containing a number of randomly oriented haemoglobin molecules (i.e. a dilute solution where no aggregation occurs). After inspection of the visible absorption spectra of selected haem-proteins, measured in [30], the excitation was chosen as 532 nm, which corresponds to resonance with the vibronic part of the *Q*-band. The DPR values obtained from the most intense Raman modes in the two cases were then compared. As opposed to the experiments with the oriented/fixed RBCs in [29] our results shown in **Figure 6**, demonstrate that the application of PCA is unnecessary when proving the aggregation of haemoglobin, since the changes in the DPR of most Raman active modes are large. In particular, the DPR of the inversely polarized a_{2g} modes exhibits large changes.

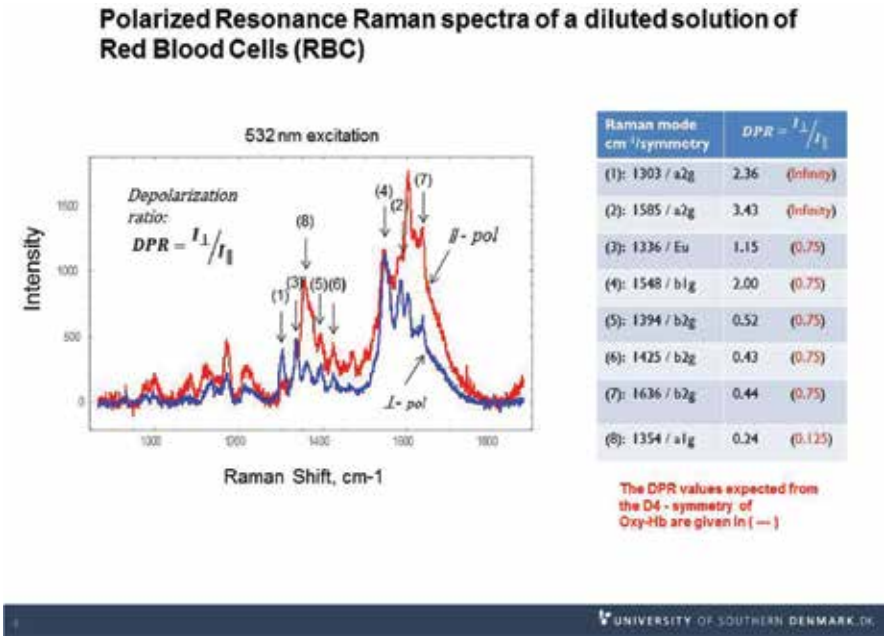

Figure 6. Left: polarized resolved, fluorescence corrected RRS spectra of a diluted solution of RBCs. Right: DPR values obtained for most intense modes.

http://dx.doi.org/10.5772/65482

Figure 7 illustrates a comparison of the experimental results in **Figure 6** with simulations of the polarization dispersion curves based on the molecular H-type dimer model shown in **Figure 4**. The particular shape of the dispersion curves clearly illustrate that they depend strongly on the nature of the Raman modes. It should be noticed the simulations are based on only one adjustable parameter. The remaining parameters are estimated from Raman and other experiments.

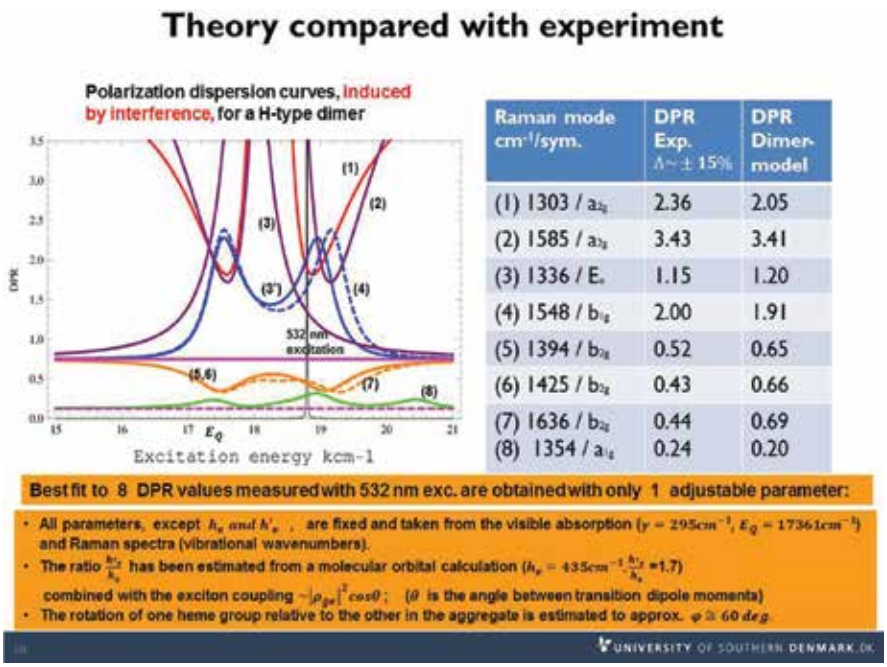

Figure 7. Theoretical interpretation of the experimental results in **Figure 6** based on a H-type dimer model.

2.2.1.1. Conclusion of case study 1

The polarized resolved RRS study of the RBC demonstrates that aggregation between the haem-protein molecules inside the RBCs can be studied *in vivo*, which, e.g. opens for the possibility of monitoring the effects of drugs added to the blood. It should be noticed that the method applies to aggregation of symmetric molecules in general.

2.2.2. Case study 2: in vitro, polarization resolved RRS study of dye-sensitized solar cells (DSC)

The basis for the polarization resolved RRS study of aggregation illustrated in Case study 1 is the observation that the DPR is very sensitive to changes in the structure of the state tensors, i.e. the number of components and the numerical relations between these. As demonstrated these changes were induced by the excitonic coupling (i.e. weak coupling) between the isolated molecules.

In the present case study, it is demonstrated that it is possible to discriminate between very similar molecules (i.e. molecules where the unpolarized Raman spectra are almost identical) by utilizing a combination of the polarization dispersion of Raman modes with a small spectral change in the visible absorption spectra. The dye-sensitized solar cells (DSC) is an illustrative example, but the method has general applicability. The idea is quite simple; the resonance condition for a given molecule depends on the wavenumber difference between the electronic absorption and the laser. Due to the spectral shift in the absorption the dispersion curve for a dispersive Raman mode will be displaced so that the excitation will 'hit' a different point on the dispersion curve. The shift in the DPR value measured at the wavenumber of the laser will depend on the nature of the dispersion (see, e.g. **Figure 5(a)** or **7**), the magnitude of spectral shift in the absorption and of the wavenumber of the laser chosen for the excitation.

When the molecules have low or no symmetry most Raman modes will in general be dispersive. When the molecular symmetry is higher the numerical relations between some of tensor elements will limit the number of dispersive modes, like in the haem-protein case, where the ideal symmetry of the chromophore (haem) is D_{4h}. However, as already emphasized the real symmetry for most proteins is lowered due to perturbations of the haem-group, with the result that several modes exhibit dispersion. Thus in reality, dispersive Raman modes are quite common.

As said, the DSCs will be considered as an example. The discussion is based on the studies performed by Hassing et al. in [31, 32], in which the stability of the Ruthenium-based dye (N719) and the properties of dye-sensitized solar cells (DSC) based on N719 was studied by polarization resolved RRS. Reference to these papers is made for details and for references to the special literature on DSCs.

The working efficiency of a DSC depends on essentially of two parameters: The long-term stability of the dye itself and on the microscopic structure of the dye-semiconductor interface (N719-TiO_2). Raman spectroscopy is an attractive technique for on-site investigations of DSCs, since no sample preparations are required, the measurements can be performed through the cover glass of the DSC and Raman spectra have in general a high molecular specificity. The chemical structure of N719 and of its main degradation product N719-TBP is shown in **Figure 1** in [32]. In the investigations of the dye stability one must be able to discriminate between these molecules. The unpolarized RRS spectra measured on solutions of N719 and N719-TBP [31] show that the spectra are nearly identical with respect to the main spectroscopic features, which might lead to the conclusion that N719 has not degraded. The unpolarized RRS spectra obtained from DSC samples fabricated with a different relative amount of N719 and N719-TBP gives the same result for the prominent and well-defined spectral features. Although certain spectral changes are found these are small and only related to the Raman bands with very low intensity [33]. Another issue in the RRS investigation of the performance of the DSC is to estimate the relative amount of N719 molecules adsorbed to the surface of the TiO_2 semiconductor and as compared to those which are desorbed, see [34]. The measured unpolarized RRS spectra originate from a mixture of adsorbed and desorbed N719 molecules. These spectra cannot be discriminated since both the spectra of the adsorbed and desorbed molecules are approximately equally resonance enhanced (see **Figure 8**) and besides similar. The same situation holds for the N719-TBP molecules.

http://dx.doi.org/10.5772/65482

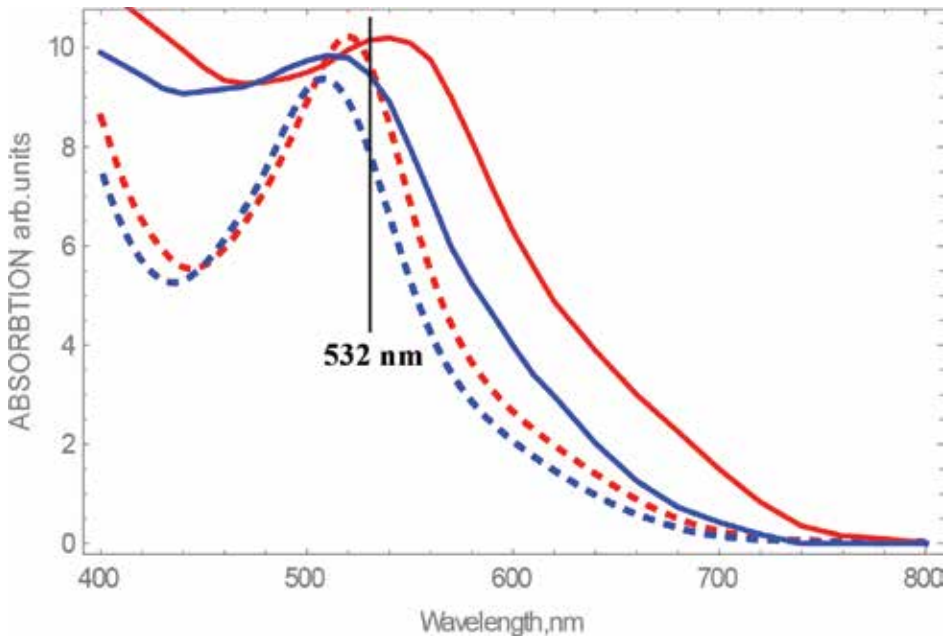

Figure 8. Visible absorption spectra of $DSC_{100/0}$ (solid red), $DSC_{0/100}$ (solid blue), N719 in methanol (dashed red) and N719-TBP in methanol (dashed blue). Laser wavelength for RRS is 532 nm. The spectral shifts between the spectra are in the region 13–30 nm.

Figure 8 shows the visible absorption spectra of DSC samples with 100% N719 ($DSC_{100/0}$), 100% N719-TBP ($DSC_{0/100}$) and solutions of N719 and N719-TBP.

The DPR values obtained from the polarization resolved and fluorescence subtracted RRS spectra for the solutions of N719 and N719-TBP in methanol and for the DSC-samples $DSC_{100/0}$ and $DSC_{0/100}$ have been collected in **Figure 9** for comparison.

It follows from **Figure 9** that although the positions of the Raman bands are almost the same for the four molecules considered (the shifts in band positions lie between 0 and 2 cm^{-1}) most of the DPR values will change when comparing either the values for the solutions of N719 and N719-TBP or the values for the DSC-samples $DSC_{100/0}$ and $DSC_{0/100}$. The observed shifts in the DPR values originate from the combined effect of the spectral shift in the electronic absorption spectra (e.g. ~13mm for the solutions) and the fact that the modes are dispersive. Since the observed changes in most DPR values are significant and also related to the most intense Raman bands, the polarized resolved RRS has a larger potential for monitoring the stability than the unpolarized RRS, where the conclusions have to rely on small spectral changes in bands with low signal-to-noise (S/N) ratio.

However, the most striking result reflected in **Figure 9** is the large change in the DPR values observed between adsorbed and non-adsorbed N719 molecules and/or between adsorbed and non-adsorbed N719-TBP molecules.

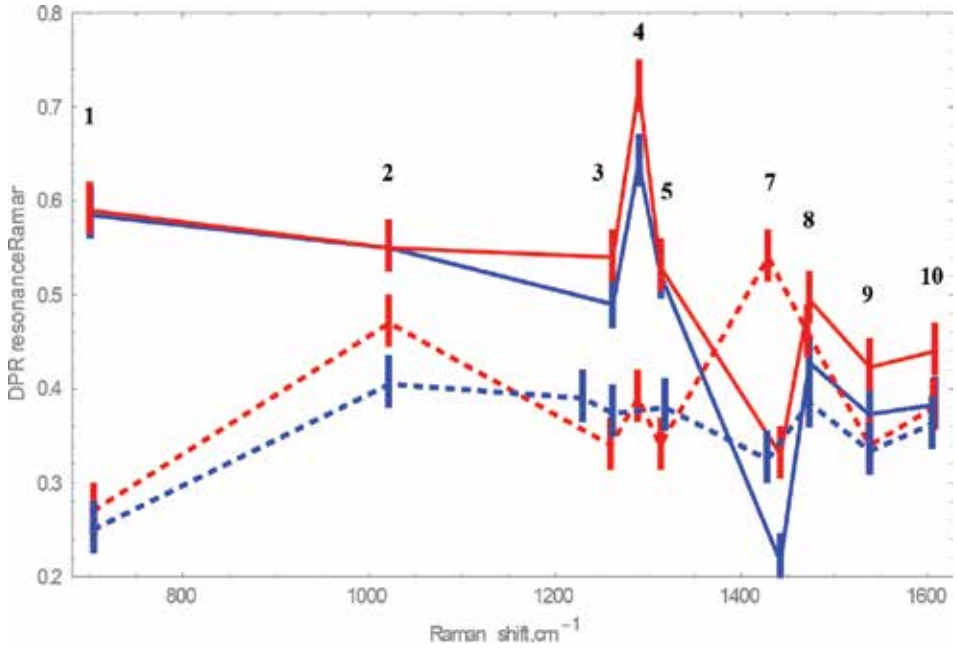

Figure 9. DPR values and estimated uncertainty ±0.025 for the DSC samples: $DSC_{100,0}$ (solid, red) and $DSC_{0,100}$ (solid, blue), for the solutions of N719 (dashed, red) and N719-TBP (dashed, blue) for the most prominent Raman bands 1–10, see Ref. [32] for details.

The explaination for this is probably that while the non-adsorbed molecules are randomly oriented, the molecules adsorbed to the TiO_2 surface are partially oriented. Thus, the scattering conditions for the Raman processes in the two situations are very different. From the theoretical section it follows that the polarized Raman signals (and the DPR) obtained from an oriented molecule are determined by the absolute square of those components of the Raman tensor that are selected by the molecular orientation in the coordinate system defined by the laser polarization and the polarization analyzers. For randomly oriented molecules the polarized Raman signals (and the DPR) are determined by the rotational invariants of the Raman tensor. The change in the DPR values between the adsorbed and non-adsorbed molecules that reflects both the molecular orientation and the wavenumber of the absorption spectra are changed. The large average increase of the DPR values, observed e.g. for the $DSC_{100/0}$ relative to the N719 in solution, is probably due to the partial orientation exhibited by the N719 molecules, when they are adsorbed to the TiO_2. The similarity between the DPR-graphs for the DSCs and the solutions shows that these variations are essentially due to the shifts in the absorption spectra combined with the dispersive property of the individual Raman modes. Finally, since we observe very small wavenumber shifts (0–2 cm^{-1}) in the Raman spectra for the resonance-enhanced Raman modes the nature of these modes must be similar for adsorbed and non-adsorbed molecules.

The average orientation of the adsorbed molecules depends on the physical details of the adsorption process and on the spatial structure of the TiO_2 substrate. Since for oriented molecules the DPR is determined essentially by the ratio between the absolute square of those components of the Raman tensor, which are selected by the molecular orientation, it seems

http://dx.doi.org/10.5772/65482

that more information about the adsorption process can be extracted from an extended analysis, involving the design of polarization resolved RRS experiments with this in mind.

3. Concluding remarks and challenges

As shown, the reliability as well as the kind and amount of molecular information can be improved by extending a Raman analysis to include polarization resolved experiments. For example in the studies of DSCs in [33] the spectral distribution of the strongest Raman bands in fresh and aged DSCs was found to be practically identical, while significant changes of the DPR ratios were observed in [32]. Thus, the conclusions about dye stability become more reliable, when the polarization is measured. Furthermore, the possibility for studying the adsorption-desorption at the Dye-TiO_2 interface seems promising. The polarized RBC study demonstrated that aggregation between the haem molecules inside the RBCs can be studied *in vivo*, which, e.g. opens for the possibility of monitoring the effects of drugs added to the blood. Recently, Jernshøj et al. applied a combination of dynamic light-scattering and polarization resolved RRS to study, among other things, the aggregation versus pH of Arenicola Marina extracellular haemoglobin (a giant molecule with mass ~**3.6 10^6 Da** and 144 oxygen binding sites) [30]. This study demonstrates the high applicability of polarized resolved RRS with respect to extracting rather detailed information about molecular systems involving very large molecules.

Finally, three challenges that one has to face when applying polarization resolved RRS should be mentioned:

(1) *Simultaneous measurements of perpendicular and parallel polarized RRS components are mandatory*.

(2) *The determination of the depolarization ratios is sensitive to fluorescence background subtraction*.

(3) *Deconvolution of 'crowded' Raman spectra is not trivial*.

Since CCD-cameras are applied in Raman microscopes, it is in fact possible through a modification of the collection optics to monitor the parallel and perpendicular polarized spectra simultaneously. This has three important implications: the accuracy of the measured DPR is improved, since modifications of the sample induced by the laser appear in both signals, the S/N ratio can be increased through averaging a large amount of spectra and most importantly it open for performing polarized resolved Raman imaging.

Author details

Søren Hassing

Address all correspondence to: sh@kbm.sdu.dk

Institute of Chemical Engineering, Biotechnology and Environmental Technology, University of Southern Denmark, Odense M, Denmark

References

[1] Placzek G; in Handbuch der Radiologie, Ed.: Marx E, Leipzig, 1934, 2, 209–374, Akademische Verlagsgesellschaft.

[2] Sonnich Mortensen O; Raman Dispersion Spectroscopy (RADIS). J.Raman Spectrosc., 1981, 11, 329–333.

[3] Hedegaard M; Hassing S; Application of Raman dispersion spectroscopy in 3-way multivariate data analysis. J.Raman spectrosc. 2008, 39(4), 478–489.

[4] Lemke C; Dreybrodt W; Shelnutt J; Quirke J M E.; Schweitzer-Stenner R; Polarized Raman Dispersion Spectroscopy probes planar and non-planar distortions ofNi(II)-porphyrins with different peripheral substituents. J. Raman Spectrosc., 1998, 29, 945–953.

[5] Nagar S; Schweitzer-Stenner R; Dreybrodt W; Mayer A; Determination of the Raman Tensor of the Haem Group in Myoglobin by Resonance Raman Scattering in Solution and Single Crystals. Biophys Struct Mech, 1984, 10, 257–273.

[6] Bobinger U; Schweitzer-Stenner R; Dreybrodt W; Highly resolved depolarization dispersion and excitation profiles of Raman fundamentals of protoporphyrin IX in a cytochrome c matrix. J.Raman Spectrosc.1989, 20, 191–202

[7] Schweitzer-Stenner R; Wedekind D; Dreybrodt W; Detection of heme perturbations caused by the quaternary R->T transition in oxyhemoglobin trout IV by resonance Raman scattering. Biophys. J. 1989,55, 703–712.

[8] Long D A; The Raman Effect; John Wiley & Sons, Chichester (UK), 2002.

[9] Mortensen O S; Hassing S; Polarization and Interference Phenomena in resonance Raman scattering; In: Clarke R J H, Hester R E , editors. Advances in Infrared and Raman Spectroscopy, Vol. 6, Chapter 1, Wiley, New York (US) , 1980.

[10] Siebrand W; Zgierski M Z; In: Lim C; editor, Excited States Vol. 4, 1–134, Academic Press. Inc. New York, 1979.

[11] Long D A; Raman Spectroscopy, McGraw Hill, London UK, 1977

[12] Schweitzer-Stenner R; Polarized Resonance Raman Dispersion Spectroscopy on Metalporphyrins. J. Porphyr. Phthal. 5, 198–224, 2001.

[13] Sonnich Mortensen O; In: Structure and Bonding 69, 1–38; Springer-Verlag, 1987.

[14] Schweitzer-Stenner R; Bosenbeck M; Dreybrodt W; Raman dispersion spectroscopy probes heme distortions in deoxy-Hb trout IV involved in its T-state Bohr-effect. Biophysical Journal, 1993, 64, 1194–1209.

[15] Kelley A M; A multimode vibronic treatment of absorption, resonance Raman, and hyper-Rayleigh scattering of excitonically coupled molecular dimers. J. Chem Phys, 2003, 119(6), 3320–3331.

[16] Wood B R; McNaughton D; Resonance Raman spectroscopy in malaria research. Expert Rev. Proteomics, 2006, 3(5), 525–544.

[17] Frosch T; Koncarevic S; Becker K; Popp J; Morphology-sensitive Raman modes of the malaria pigment hemozoin. Analyst, 2009, 134,1126–1132.

[18] Shelnutt J A; Cheung L D; Chang R C C; Yu N; Felton, L H; Resonance Raman spectra of metalloporphyrins. Effects of Jahn-Teller instability and nuclear distortion on excitation profiles of Stokes fundamentals. J. Chem. Phys., 1977, 66, 3387–3398.

[19] Shelnutt J A; O'Shea D C; Resonance Raman spectra of copper tetraphenylporphyrin: Effects of strong vibronic coupling on excitation profiles and the absorption spectrum. J. Chem. Phys., 1978, 69, 5361–5374.

[20] Zgierski M Z; Pawlikowski M; Chemical Physics 1982, 65, 335–367.

[21] Schweitzer-Stenner R; Revisited Depolarization Ratio Dispersion of Raman Fundamentals from Heme c in Ferrocytochrome c Confirms That Asymmetric Perturbations Affect the Electronic and Vibrational Structure of the Chromophore's Macrocycle. J. Phys. Chem., 1994, 98, 9374–9379.

[22] Huang G; Szigeti K; Fidy J; Schweitzer-Stenner R; Structural Disorder of Native Horseradish Peroxidase C probed by Resonance Raman and Low Temperature Optical Absorption spectroscopy. J.Phys.Chem. B, 2003, 107,2822–2830.

[23] Jentzen M; Ma J; Shelnutt J A; Conservation of the Conformation of the Porphyrin Macrocycle in Hemoproteins Biophysical Journal, 1998, 74,753–763.

[24] Haddad R E; Gazeau S; P´ecaut J; Marchon J; Medforth C J; Craig J; Shelnutt J A. Origin of the Red Shifts in the Optical Absorption Bands of Nonplanar Tetraalkylporphyrins. J. Am. Chem. Soc., 2003, 125, 1253–1268.

[25] Xu L; Li Z; Tan W; He T; Liu F; Chen D; Density functional theory studies on the Raman and IR spectra of *meso*-tetraphenylporphyrin diacid. Spectrochimica Acta Part A, 2005, 62, 850–862.

[26] Ma Y P; He S G; Ding X L; Wang Z C; Xue W; Shi Q; Theoretical study of intermolecular interactions in meso-tetraphenylporphyrin diacid dimer (H4TPPCl2)2 . Physical Chemistry Chemical Physics, 2009, 11, 2543–2552

[27] Wood B R; McNaughton D; Raman excitation wavelength investigation of single red blood cells in vivo. J. Raman Spectrosc., 2002, 33, 517–523.

[28] Ramser K; Logg K; Goksör M; Enger J; Käll M; Hanstorp D; Resonance Raman spectroscopy of optically trapped functional erythrocytes. Journal of Biomedical Optics, 2004, 9(3), 593–600.

[29] Wood B R; Hammer L; McNaughton D; Resonance Raman spectroscopy provides evidence of heme ordering within the functional erythrocyte. Vibrational Spectroscopy, 2005, 38, 71–78.

[30] Jernshøj K D; Hassing S; Olsen L F; A combination of dynamic light scattering and polarized resonance Raman scattering applied in the study of Arenicola Marina extracellular hemoglobin. J Chem Phys, 2013, 139 (6), 065104–1–10.

[31] Hassing S; Jernshøj K D; Nguyen P T; Lund T; J. Investigation of the Stability of the Ruthenium-Based Dye (N719) Utililizing the Polarization Properties of Dispersive Raman Modes and/or of the Fluorescent Emission. J. Physical Chemistry C, 2013, 117, 23500–23506.

[32] Hassing S; Jernshøj K D; Nguyen P T; Lund T; In Vitro Polarized Resonance Raman Study of N719 and N719-TBP in Dye Sensitized Solar Cells. J. Technology Innovations in Renewable Energy, 2016, 5, 21–32.

[33] Likodimos V; Stergiopoulos T; Falaras P; Hariksun R; Desilvestro J; Tulloch, G; Prolonged Light and Thermal Stress Effects on Industrial Dye-Sensitized Solar Cells: A Micro-Raman Investigation on the Long-Term Stability of Aged Cells. J. Phys. Chem. C 2009; 113, 9412–9422.

[34] Perez Leon C; Kador L; Peng B; Thelakkat M; Characterization of the Adsorption of Ru-bpy Dyes on Mesoporous TiO2 Films with UV-Vis, Raman and FTIR Spectroscopy. J. Chem. Phys. B, 2006, 110 (17), 8723–8730.

Chapter 8

Petrographical and Mineralogical Applications of Raman Mapping

Frédéric Foucher, Guillaume Guimbretière,
Nicolas Bost and Frances Westall

Additional information is available at the end of the chapter

http://dx.doi.org/10.5772/65112

Abstract

Raman spectroscopy has undergone rapid development over the last few decades. The ability to acquire a spectrum in only a few tens of milliseconds allows use of Raman mapping as a routine technique. However, with respect to classical single spectrum measurement, this technique is not still as widely used as it could be, in particular for mineralogy and petrography. Here, we explain the advantages of Raman mapping for obtaining additional information compared to single spot analyses. The principle and the limits of the technique are first explained in 2D and 3D. Data processing techniques are then described using different types of rocks and minerals to demonstrate the utility of Raman mapping for obtaining information about the general composition, identification of small phases, as well as for distinguishing minerals that are spectrally very close. More "exotic" uses of the collected signal are also described. Finally, a gallery of images from representative samples is used to illustrate the discussion.

Keywords: Raman mapping, petrography, mineralogy

1. Introduction

The Raman effect was described for the first time by Chandrasekhara Venkata Rāman in 1928. Raman spectroscopy is a very powerful technique allowing study of atomic bonds and identification of crystalline structures. Contrary to energy dispersive X-ray spectroscopy (EDX) or the electron microprobe, for example, Raman does not give the elemental composition of the sample but can identify organic molecules and mineralogical phases. No sample preparation is required, and the analysis can be made on the sample surface or below the surface, depending

on sample transparency. For technical reasons, the technique began to be widely used only at the beginning of the 1980s with the generalisation of lasers. At the end of the 1990s, Raman spectroscopy underwent a second phase of development with the introduction of Charge Couple Device (CCD) technology, which has widely improved the sensitivity of spectrometers. These technical revolutions allow acquisition of a Raman spectrum in only few milliseconds. This strong decrease in the acquisition time permitted development of new applications, in particular Raman mapping. This technique consists of scanning the sample with the laser while acquiring spectra so that spatial distribution can be added to structural information.

Here, we present the principle of the technique and the basis of the associated data processing followed by an overview of the information that can be extracted from Raman mapping to improve mineralogical and petrological analyses. In particular, we discuss how it can be used to study the general composition of rocks, to detect and identify small phases, or to differentiate minerals whose spectra are very close. More exotic uses of the collected signal are also presented, e.g., detection of particular phases using luminescence. Finally, we illustrate the discussion using a number of different types of rocks and minerals.

2. Principle and instrumentation

2.1. Raman spectroscopy

The Raman effect is due to inelastic interaction between photons and atomic bonds. In this process, the scattered photons lose or gain energy with respect to the incident photons by vibrating or stabilising the atomic bonds of the sample. This effect leads to a shift in energy called the Stokes shift if the photons lose energy and the Anti-Stokes shift if the photons gain energy. At room conditions, the Stokes part of the Raman signal is generally stronger and is, therefore, generally used in Raman analysis. Due to the quantification of the energy and to the activated vibrational modes, photons are only scattered for particular energies and thus for particular wavelengths. Therefore, Raman scattering of a monochromatic light by molecular entities or an ordered solid will give spectra consisting of sharp spectral lines. Most systems today use a CCD camera interfaced with the spectrometer. The collected signal is then represented in a graph showing the number of photons versus wavenumber, i.e., the shift in cm^{-1} with respect to the incident beam, the laser wavelength corresponding then to 0 cm^{-1}. The spectral resolution is limited by the CCD camera resolution and by the grating used to diffract the light. It also depends on the laser wavelength. Since the Raman effect is sensitive to atomic bonds, a Raman spectrum is associated with only one compound and its intensity is proportional to its concentration. Polymorphic minerals (similar compositions but different crystalline structures) will thus have different spectra. For example, anatase, rutile and brookite have different Raman spectra despite their similar composition (TiO_2). It is important to note that different parameters may influence the Raman signal, such as instrumental setup, structural defects, traces elements, internal stresses or temperature [1–3] (**Figure 1**). Although these parameters may sometimes complicate interpretation, some of them can also be used to measure particular properties, for example, the shift related to internal stresses [4].

http://dx.doi.org/10.5772/65112

Finally, the Raman effect is relatively complex to model, and the identification of a compound is generally made by comparison with reference spectra found in the literature or in databases. More information about the Raman effect can be found in this book or others [5–7].

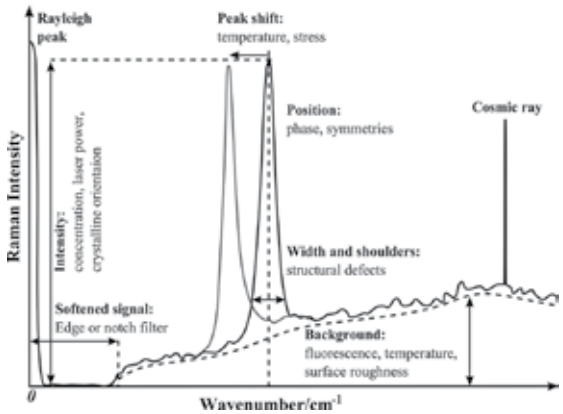

Figure 1. Origins of the parameters and modifications of the Raman spectrum [1].

2.2. Instrumentation

Raman mapping consists of scanning a sample with the laser beam while acquiring spectra. For the study example, we present here, a WITec Alpha500 RA Raman spectrometer was used. Other systems from Renishaw, Horiba Jobin Yvon, Thermo Fisher or Bruker, for example, may use slightly different methods for mapping, but the general principle of scanning remains the same. The general discussion of this chapter can thus be applied to any other system.

This study was made using a CW green Nd:YAG frequency doubled laser with a wavelength of λ = 532 nm. The laser beam is focused on the sample using optical microscope objectives and optical observations of the analysed area are made with a camera. The spectral resolution of the spectrometer is of 1 and 3 cm^{-1} using 1800 and 600 g/mm gratings, respectively. Surface scanning is made by moving the sample below the objective along successive lines using motorised and/or piezoelectric scan tables. The instrument used is equipped with two positioning systems: (1) a small-scale system working with piezoelectric ceramics that can analyse an area of 200 × 200 μm in the horizontal plan and 20 μm in the vertical direction and (2) a large-scale motorised system that can move the sample over a distance of 15 × 10 cm horizontally and 2 cm vertically.

Raman mapping systems are generally confocal, i.e. only the signal coming from the near object focal plane is redirected to the spectrometer. This is done by placing a pin hole in the image focal plane of the microscope. The volume used for the analysis is then reduced and the in-plane resolution is slightly increased, depending on the size of the pin hole, the objective and the laser wavelength. The main interest of the confocality is to permit 3D imaging using a stacking process by acquiring Raman maps at different depths. It is important to note that the

depth of analysis depends on the refractive index of the material; there is a difference between the apparent depth, corresponding to the distance with respect to the sample surface, and the true depth of analysis (**Figure 2**).

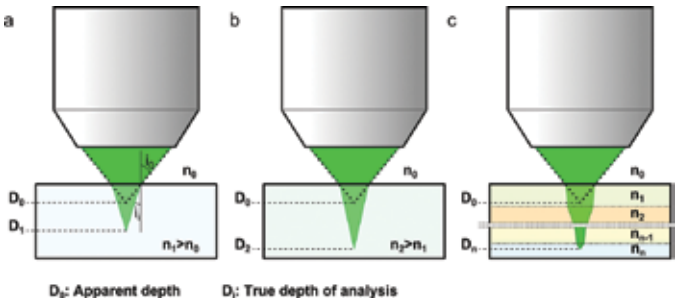

Figure 2. Apparent depth D_0 versus true depth D_i of analysis in optical microscopy when analysing (a) a material with a refractive index equal to n_1, (b) a material with a refractive index equal to n_2 with $n_2 > n_1$ and (c) when analysing across n different materials of refractive index n_i and thickness e_i.

The ratio between the true depth D_i and the apparent depth D_0 is given by the following equation:

$$\frac{D_i}{D_0} = \frac{\tan i_0}{\tan i_1} \tag{1}$$

where i_0 and i_1 are the maximal angle with respect to the optical axis in the observation medium (e.g. air, water or oil) and in the analysed material, respectively (see **Figure 2a**). The famous Snell-Descartes law and the definition of the numerical aperture NA give:

$$NA = n_0.\sin i_0 = n_i.\sin i_i \tag{2}$$

where n_0 and n_i are the refractive index of the observation medium and of the analysed material, respectively. Using Eq. (2), and noting that:

$$\tan\left(\arcsin x\right) = \frac{x}{\sqrt{1-x^2}} \tag{3}$$

Eq. (1) finally writes:

$$\frac{D_i}{D_0} = \sqrt{\frac{n_i^2 - NA^2}{n_0^2 - NA^2}} \tag{4}$$

http://dx.doi.org/10.5772/65112

This ratio is thus all the more important when the difference in refractive index is high (see **Figure 2b**). For example, when analysing quartz (n_{qz} = 1.55) in air (n_{air} = 1) with an objective having a numerical aperture of NA = 0.9, the true depth of analysis is ~2.9 times deeper than the apparent depth corresponding to the mechanical vertical displacement.

In the case where several phases are crossed by the laser (see **Figure 2c**), Eq. (4) can be generalised into:

$$\frac{D_n}{D_0} = \sum_{i=1}^{n} e_i \sqrt{\frac{n_i^2 - NA^2}{n_0^2 - NA^2}} \tag{5}$$

where e_i is the thickness of the phase i. For 2D maps, the depth of the measurement and the volume analysed are thus different for each phase, and for 3D Raman maps, the volume and the depth of the different phases are associated with different scales in the raw data.

2.3. Raman mapping

As explained above, Raman mapping consists of scanning the sample with the laser beam while acquiring spectra. The scanned area is then divided into a pixel-assigned array of spectral elements, sometimes called "spexels" [8], as shown in **Figure 3a**.

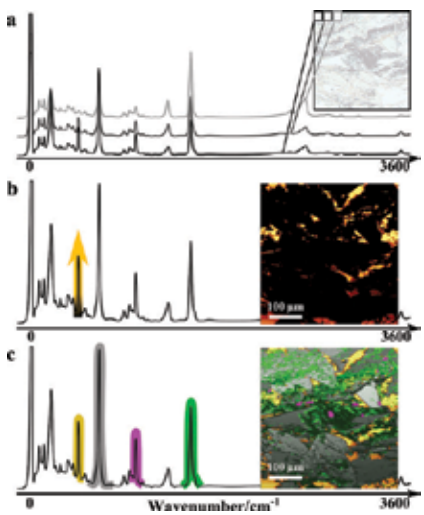

Figure 3. (a) Principles of Raman mapping illustrated using a polished thin section of a metachert from the 3.8 billion years old Isua Greenstone belt, Greenland. The scanned area of the sample is divided into small squares, or spexels, each associated with a Raman spectrum. (b) Raman map of the concentration of quartz in the sample, as identified by the intensity of the main peak at 465 cm^{-1}. (c) Raman map of the composition of the sample obtained by attributing a colour to the main spectral peak of each mineral (yellow for quartz, grey for cumingtonite, pink for apatite and green for graphite). Scan size: 500 × 500 μm^2.

Historically, the first Raman maps were constructed manually by making a map point by point. The sample was then not scanned continuously but was immobile beneath the laser beam during the acquisition of each spectrum (**Figure 4**). These first maps were interesting for the study of homogeneity in materials, but, because of the limited number of spectra associated with this time-consuming method, imaging was not very efficient. With the recent development in fine positioning systems and synchronisation between the positioning system and the CCD detector, automated scanning is now available. This automation allows high resolution mapping point by point as well as by continuous scanning.

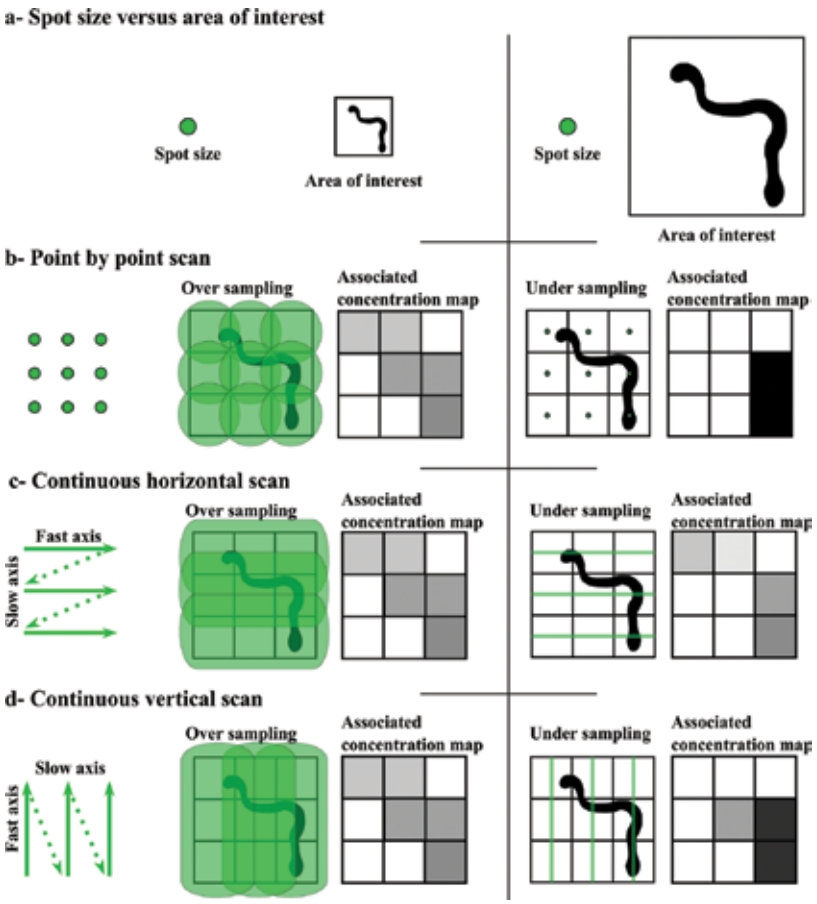

Figure 4. Principle of Raman mapping. (a) Laser spot size versus area of interest and different ways of scanning, (b) point by point, (c) continuously and horizontally and (d) continuously and vertically. The spectrum associated to each pixel corresponds to the average spectrum of the different associated phases. The concentration map is thus darker where the vermicular structure is analysed. If the spot size is larger than the pixel size (left row), there is oversampling, and the associated maps are the same whatever the method used. However, if the laser spot size is small in comparison with the pixel size (right row), there is undersampling and the associated maps depend on the type of the scan.

In all scanning methods of imaging (e.g. Raman mapping as well as atomic force microscopy, scanning electron microscopy, etc.), the lines are accumulated one by one and the spatial

http://dx.doi.org/10.5772/65112

resolution is fixed by the ratio of the width and height of the scanned area over the number of lines and rows, respectively. Then, for a square scan, the time needed to go down a row is very long compared to the time needed to go along a line (for a horizontal scan). The axis parallel to the lines is thus called the fast axis, and the axis perpendicular to the lines is called the slow axis (see **Figure 4**). This notion must be kept in mind while scanning a small area where thermal or mechanical drift may induce deformation in the images (shearing) and/or a loss of focus with the time. During Raman mapping, the spectra are generally accumulated continuously during the scan. The spectrum associated with each point corresponds thus to the average spectrum acquired over a line whose length is fixed by the spatial resolution but whose thickness is equal to the laser spot size. If the spot size is higher than the resolution, the associated map is then under-sampled since not all the area are scanned; a scan obtained over the same area rotated by 90° would give a different result (**Figure 4**). To avoid this effect, the chosen resolution must be at least equal to the spot size. On the other hand, the Rayleigh criterion implies that the resolution cannot be physically higher than half of the spot size as given by the Airy disk equation:

$$S = 1.22\frac{\lambda}{NA} \tag{6}$$

where λ is the laser wavelength, S is the laser spot diameter, and NA is the numerical aperture of the objective. Using a green laser (λ = 532 nm) and the 100× objective (with a numerical aperture of 0.9), the spot size is thus $S \sim 720$ nm in diameter and the maximal physical resolution is thus ~360 nm/pixel. Using a confocal system, this resolution can be slightly decreased by ~10% [6]. However, even if using a higher resolution does not give more information, over-sampling could provide a better contrast.

In conclusion, continuous scanning is generally the best choice for imaging due to its rapidity, but point-by-point mapping may be useful when the sample contains fluorescent phases that may drown out the Raman signal of the other phases in the average spectra acquired with the continuous scan method.

3. Data processing

We have chosen a number of different rocks and minerals to illustrate methods of data processing for improving image quality and for obtaining specific information. Measurements were made mainly on polished thin sections as well as on polished rock surfaces.

3.1. Classical maps

Raman scans are mostly used to map the composition of a sample over a particular area. The interest of mapping with respect to single spectrum analysis is that it is possible to observe the association and spatial distribution of different phases (see **Figure 5**). These kinds of images

are obtained by selecting a peak in the spectrum of each phase and by plotting its intensity in order to obtain an image of its concentration (**Figures 3b** and **5b**), or by associating a colour to a given peak in order to obtain an image in which each phase is represented by a colour (**Figures 3c** and **5d**). However, the quality of the images can be improved by more complex data processing. The use of the peak area instead of the peak intensity leads to slightly better contrast, in particular if the peak is wide (**Figure 5c**). A second step involves extracting the spectrum of each phase and using a correlation process with the global data set to dissociate phases when there is partial overlap of their peaks (**Figure 5d–f**). Calculations can be applied to the data set, such as derivatives to eliminate the background or to use the square or the cube of the data set to increase the signal/nose ratio. Finally, more advanced tools can be used, such as principal component analysis, to improve the detection of different phases [9].

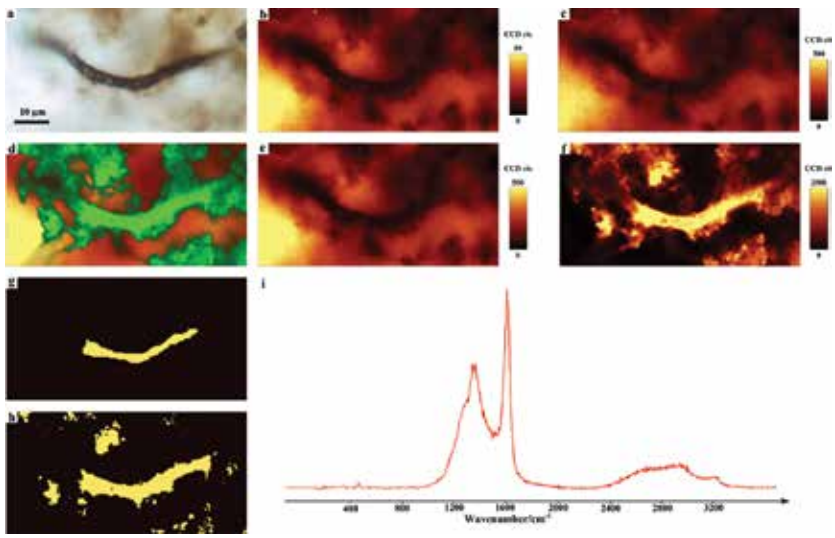

Figure 5. Raman mapping of silicified microorganisms from the Gunflint formation and average spectrum of carbonaceous matter. (a) Optical microscopy image in transmitted light. Associated Raman images of quartz obtained (b) using the intensity of the main peak of quartz at 465 cm^{-1} and (c) the area of the same peak. (d) Raman compositional map with quartz in orange and carbonaceous matter in green corresponding to the superimposition of the Raman images obtained using the full spectrum correlation of (e) quartz and (f) carbonaceous matter. Boolean masks (0 in black and 1 in yellow) can be obtained by directly drawing on the image (g) or by using a mathematical threshold filter (h) in order to obtain a high signal/noise ratio average spectrum of the fossilised filament (i).

Mapping also permits by obtaining high quality spectra of a phase. Indeed, it is possible to create a mask (i.e. Boolean image) by directly drawing on an image (**Figure 5g**) or by using thresholds (**Figure 5f**) to select the areas of interest, to multiply it to the data set in order to select only the associated spectra, and finally to average these spectra to obtain the corresponding average spectrum (**Figure 5i**). Different masks can be applied to the same data set. For example, it is possible to use a mask corresponding to the area where the signal of the phase is the highest and a second one corresponding to the areas where the background level is the lowest. The average spectrum thus obtained can be more representative than that

http://dx.doi.org/10.5772/65112

obtained in only one point. Of course, the map can also be used to locate the area where the signal is highest before acquiring a single spot spectrum.

3.2. Detection and identification of small phases

Although the spatial resolution of Raman spectroscopy is the same as that of optical microscopy, each pixel of an image is not just a colour but corresponds to a spectrum. Raman spectroscopy may thus permit identification of very small grains that are difficult to identify using classical optical microscopy (e.g. the pyrite grain shown by the black arrow in **Figure 6c** or the grain of SiC in **Figure 9d**). A mineral phase may also be invisible in optical microscopy, and Raman mapping is then the only way to detect it, as shown in **Figure 6**. Finally, at larger scales, mapping can be a good means to localise phases present in minor or trace amounts in a sample.

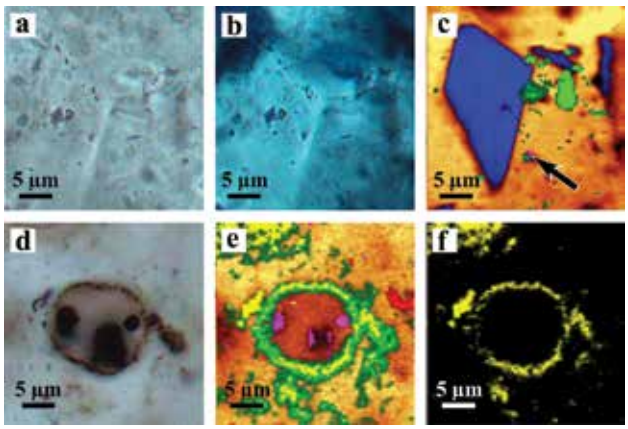

Figure 6. Optical and associated Raman maps of (a–c) a polished thin section of a hydrothermal vein from the quarry of Neuvial, Mazerier, Allier, France and (d–f) a thin section of the ~800 My-old Draken Formation, Svalbard (see [10] for more information). The Raman map (c) shows the presence of carbonaceous matter (green), orthoclase (blue) and a pyrite grain (pink and black arrow) in the quartz matrix (orange). The carbonaceous matter and the pyrite grain were invisible in the optical microscopy image (a), and the orthoclase was too small to be identified by polarised optical microscopy (b). The optical image (d) shows a fossil planktonic microorganism. The presence of opal (in yellow) and anatase (in red) is highlighted in the composition (e) and opal (f) Raman maps, whereas they are invisible in optical microscopy. The quartz matrix is in orange in (e). Image size 30 × 30 µm².

3.3. Identification of spectrally close phases

Not only is the spatial resolution better than mapping but also the spectral resolution. Indeed, due to the high number of spectra accumulated for each image, very small spectral changes can be statistically detected. **Figure 7** shows the position of the centre of mass of the main peak of a quartz spectrum during analysis of crushed samples of various grain sizes (see Ref. [1] for more information). Although the resolution of the Raman spectrometer is ~1 cm^{-1}, the image highlights peak shifts lower than 0.5 cm^{-1}. Such small variations would not be identifiable using single spectrum analysis, while they are statistically obvious in this image.

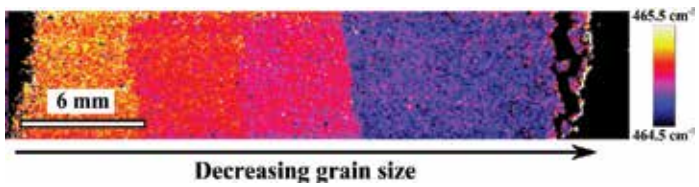

Figure 7. Raman analysis of quartz powders of four different grain sizes (decreasing grain size from left to right) showing the shift of the main peak at ~465 cm^{-1} towards the lower values with the decreasing grain size (see Ref. [1] for more information).

A similar approach can be helpful for mineralogy because it is often difficult to distinguish minerals having relatively similar Raman spectra, for example, carbonates [11]. However, by using peak position and the full width of the peaks at half maximum (FWHM) or the background level, it is possible to distinguish and identify different phases in the images. **Figure 8** shows different Raman images obtained from the same data set of carbonate deposits in a vesicle in basalt from Svalbard (see Refs. [12] and [13] for more information). The different carbonate phases can be distinguished because of the variation in the ratio Mg/Ca during deposition, resulting in phases ranging from dolomite to magnesite.

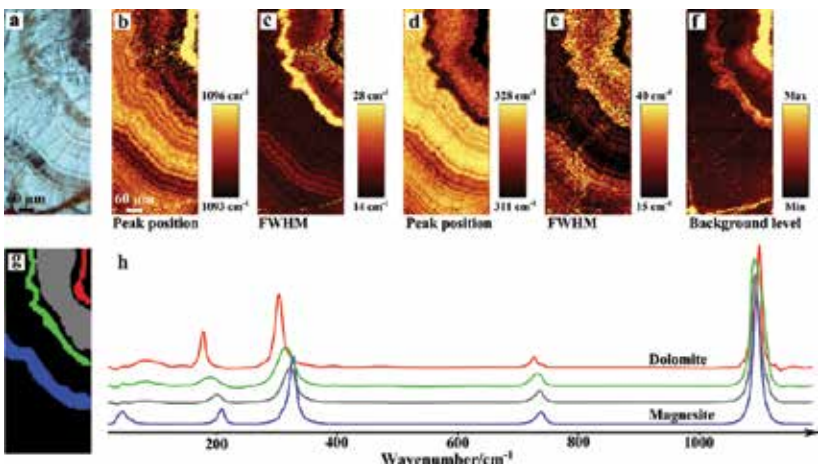

Figure 8. (a) Optical image and Raman maps of (b) the position, (c) the FWHM of the main peak position around 1000 cm^{-1}, (d) and (e) of the second carbonate peak around 320 cm^{-1} and (f) the background level illustrating different phases in carbonate deposited in a vesicle formed in basalt from Svalbard (see Ref. [13] for more information). The corresponding areas can be selected (g) in order to obtain the associated average spectra (h).

3.4. Exotic uses

As noted above, the collected signal depends on different parameters that can be used to make images. More complex maps can thus be obtained by applying different calculations to the images; for instance, the ratio of peak intensity can distinguish changes in crystal orientation, as shown in **Figure 9**. The image of background intensity is also a particularly interesting

http://dx.doi.org/10.5772/65112

example. We have seen above that it can be used to make masks, but it can also be used to show variations in composition or to distinguish relatively similar phases (**Figure 8**). The Raman signal can also be modified by defects in the sample, such as cracks or fluid inclusions, as shown in **Figure 9**. Finally, the signal is also associated with fluorescence and could thus give some information about the trace element composition of a mineral.

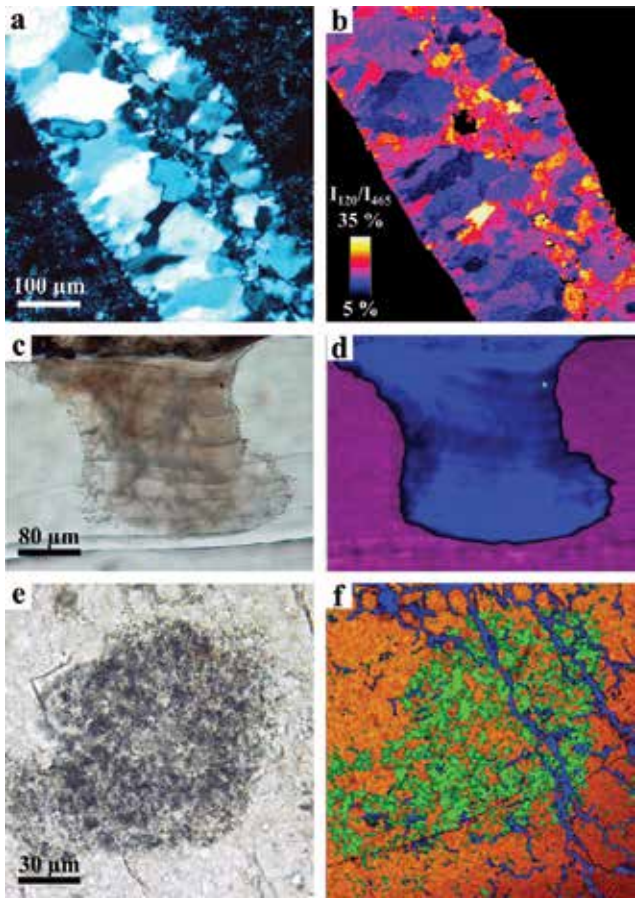

Figure 9. (a) Optical image in polarised/analysed transmitted light microscopy and (b) associated compositional Raman map of a polished thin section of hydrothermal quartz vein (Barberton, South Africa). The image of the intensity ratio of the peak located at 465 cm^{-1} over the peak located at 120 cm^{-1} permits highlighting differences in crystalline orientation. (c) Optical image and (d) associated compositional Raman map of a polished thin section of a pearl showing aragonite in purple and vaterite in dark blue. The background intensity image is used to show the vaterite (see Ref. [14] for more information). A small grain of SiC, coming from the polishing process, is also detected (in light blue in d). (e) Optical image and (f) associated compositional Raman map of a chert sample having undergone atmospheric entry (analogue meteorite, see Ref. [15] for more information). The quartz is in orange and the carbonaceous matter in green. The background intensity is displayed in dark blue and highlights cracks in the sample due to stresses related to atmospheric entry.

To conclude, various processing methods applied to Raman mapping data set can highlight particular properties of the mineral phases in a scanned sample. Further examples of such

processing include making several scans of the same area using different environmental parameters (different laser wavelengths, external stress, temperature, etc.).

3.5. Statistical treatment

In all the above maps, the increase in information due to the statistics of a great number of spectra is implemented visually by plotting the appropriate classic spectral parameters. When the components of the sample are unknown, the reference spectra are not available, and the spectral sources are not well identified from spectrum to spectrum, or to extract very fine spectral modification of a single compound, mathematical treatment based on the statistical structure of the hyperspectral data can be implemented. Nowadays, numerous mathematical treatments exist and are tested by spectroscopists in various kinds of applications [9, 16, 17]. As an illustration, **Figure 10** shows the principal component analysis extraction of spectral sources of interest in the Raman mapping of a uranium dioxide ceramic and the corresponding

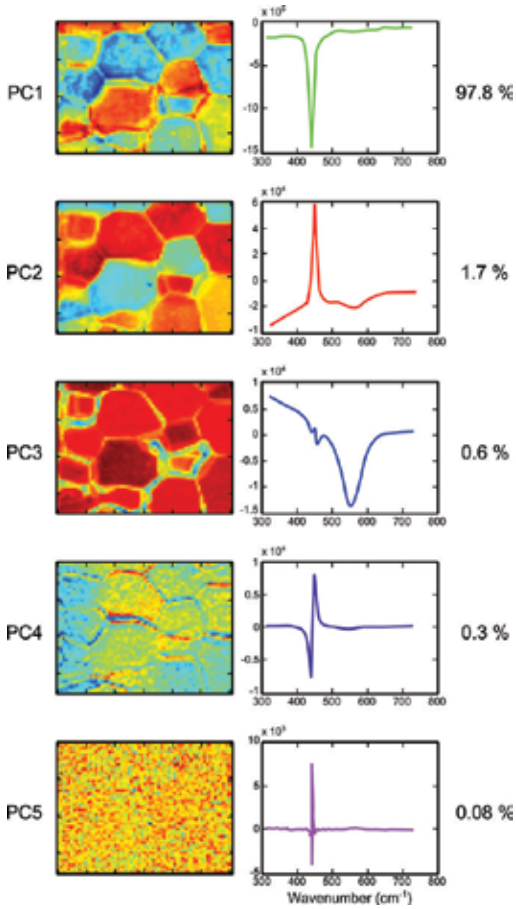

Figure 10. Principal component analysis of a Raman mapping of a uranium dioxide ceramic. At right, the spectral sources with their percentages and at left, the corresponding maps [9].

http://dx.doi.org/10.5772/65112

map [9]. The percentages to the right are the percentage of data variance coming from the corresponding spectral source. The maps show that only the first four sources have any significance, the fifth being only noise. Analysis of the information given by the spectral sources is complex. An initial analysis demonstrates the fact that different types of maps highlight either the grains or the grain borders in the ceramic (see Ref. [9] for more details).

4. Gallery

Figure 11 shows various examples of Raman maps made on polished thin sections of various rocks. As described below, the mineralogical determination and the interpretation of minerals in their context are greatly facilitated by Raman mapping.

4.1. Sedimentary samples

The sample in **Figure 11a** is a sandstone with an oxide matrix coming from the Hettangien formation (203.6–199.6 My), Chéniers France (see Ref. [18] for more information). This formation was occasionally exploited for iron and manganese since the Iron Age and also contains barite mineralisation. The grains consist of quartz and plagioclase (**Figure 11a1**). The different phases of iron oxide crystallisation in the holes of the rock, where hematite is altered to goethite, are highlighted by Raman mapping (**Figure 11a2**). These minerals are difficult to distinguish in transmitted light by optical microscopy. A small grain of barite is also visible in the Raman map.

4.2. Magmatic sample

Magmatic rocks are in most cases relatively easy to study using optical microscopy (the crystals are large and euhedral). However, Raman mapping can reveal small variations in mineralogical phases or crystal orientation. **Figure 11b1** shows an optical view of a granite from Autun, Saône-et-Loire, France (see Ref. [19] for more information). This rock is composed of large grains of quartz and labradorite associated with biotite, phlogopite, plagioclase and accessory minerals (titanite, apatite, rutile and brookite; **Figure 11b2**).

4.3. Volcanic samples

The sample shown in **Figure 11c** is a basalt from El Teide volcano, Tenerife, Spain. Basaltic rocks containing glass and microlitic crystals tend to be rather opaque in thin section, and identification of the individual minerals using optical microscopy is difficult, as shown in **Figure 11c1**. On the other hand, Raman mapping reveals easily all the microlitic paragenesis (labradorite, augite, analcime, apatite, anatase and hematite; **Figure 11c2**). Analcime occurs in vesicles and is a secondary mineral in this basalt. **Figure 11c3** shows the crystalline orientation of the plagioclases phases with polysynthetic twinning obtained from the intensity ratio of the spectral peaks at 195 and 514 cm^{-1}. With this type of sample, a statistic treatment of the image could provide information on the orientation of the minerals and, consequently, lava flow direction.

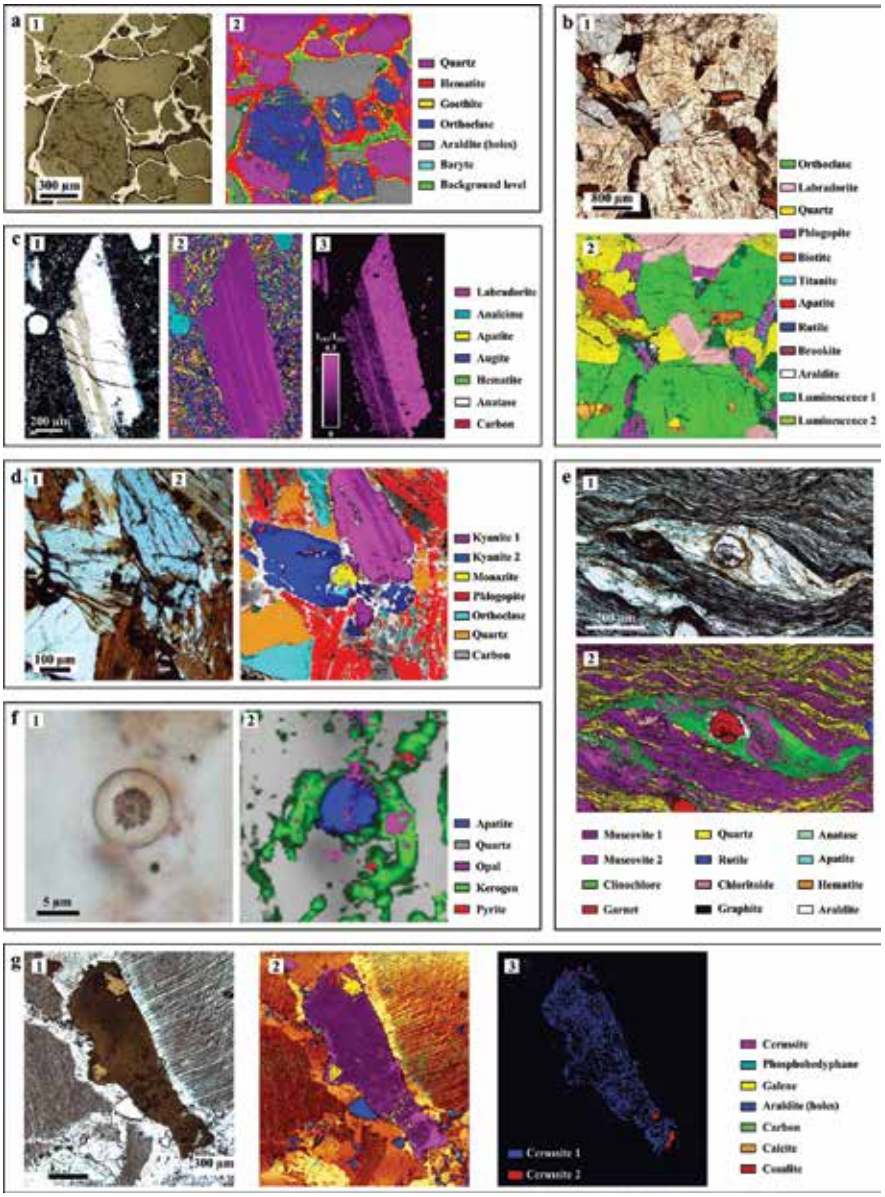

Figure 11. Image gallery made on polished thin sections of different samples. (a) Sandstone from the Chéniers mine, Sacierges-Saint-Martin, Indre, France, (a1) optical view in reflected light, (a2) Raman map. (b) Granite from Autun, Saône-et-Loire, France (b1) optical view of the rock, (b2) Raman map. (c) Basalt from El Teide volcano, Tenerife, Spain (c1) optical view in transmitted light, (c2) Raman map and (c3) detail of the orientation in a plagioclase crystal obtained from the intensity ratio of the spectral peaks at 195 and 514 cm^{-1}. (d) Garnet-kyanite granulite xenoliths in gneiss from La ferme des Saugères, Allier, France (d1) optical view in transmitted light, (d2) Raman map. (e) Highly deformed micaschist from the Sierra Alhamilla, Alméria, Spain (e1) optical view of a pressure shadow around a garnet in transmitted light, (e2) Raman map. (f) Microfossil from the Draken formation, Svalbard (f1) optical view in transmitted light, (f2) Raman map. (g) "Calamine" (Zn ore rocks) sample from BeniTajite mine, Haut Atlas, Morocco (g1) optical view, (g2) Raman map and (g3) detail of two generations of cerussite.

http://dx.doi.org/10.5772/65112

4.4. Metamorphic samples

Metamorphic rocks are characterised by very different mineral paragenesis, which can be difficult to identify in optical microscopy but easily resolvable using Raman mapping.

The sample in **Figure 11d** is a garnet-kyanite granulite from the gneissic upper unit (USG), La Ferme des Saugères in the Sioule metamorphic series, Allier, France (see Refs. [20] and [21] for more information). This rock is composed of quartz and granoblastic orthoclase that are readily visible in the Raman map (**Figure 11d2** A particularity of this sample is that it presents a retromorphosed facies associated with the destabilisation of the garnet and kyanite to phlogopite. Identification of the Al_2SiO_5 polymorphs (andalousite, sillimanite and kyanite) by optical microscopy is difficult but not with Raman mapping. The information thus obtained could be helpful for establishing the conditions of formation of the rock (e.g. in a P-T-t diagram). **Figure 11d2** is a Raman map based on peak parameters that have been modified by changes in the crystal orientation of kyanite. Note that carbon is present because the sample was coated for analysis by scanning electron microscopy and electron microprobe.

The second metamorphic sample is a highly deformed micaschist from the Sierra Alhamilla, Alméria, Spain (see Ref. [22] for more information). **Figure 11e1** is an optical micrograph demonstrating the high degree of deformation of the rock, making identification of the individual phases difficult. Raman mapping, on the other hand, reveals that the rock contains chloritoïde relics as well as various accessory minerals such as rutile, anatase, apatite, graphite and hematite in a small alteration vein. A pressure shadow filled by clinochlore and a new generation of muscovite can be observed. With its ability to distinguish structural changes in individual minerals, Raman mapping also highlights the direction of deformation, as indicated by the quartz and muscovite crystals (**Figure 11e2**).

4.5. Application for micropaleontology

Figure 11f is a dolomitised conglomerate from the Draken Formation (−800 to −700 My), Svarlbard. This conglomerate includes cherty lenses rich in microbial mat/planktonic microfossil assemblages (**Figure 11f1**) [23]. Two colourless phases that are not distinguishable in optical microscopy are revealed by Raman mapping to be opal and hydroxyapatite (**Figure 11f2**) (see Ref. [10] for more information). Some small spots of pyrite are also observed.

4.6. Application for metallogeny

Mineral identification in metallogeny is very important for understanding the mineralisation process. **Figure 11g1** shows calamine deposit from the BeniTajite mine, Haut Atlas, Morocco, developed in a karstic area (see Ref. [24] for more information). The Raman map in **Figure 11g2, 3** shows the presence of cerussite formed by the alteration of galena. The cerussite has a botryoidal banded texture and forms a crust shielding the galena from oxidation. Some cerussite recrystallised during evolution of the karst, resulting in two generations of the mineral, each characterised by very specific textures that are invisible to optical or electronic microscopy but are readily visible in Raman mapping. Other minerals, such as calcite, cosalite

(a Pb-Bi-sulphur) and phosophohedyphane (a Pb-phosphate), can also be identified by Raman mapping.

5. Conclusion

Raman mapping is a powerful technique for mineralogy and petrography. The small spatial resolution of the laser beam allows detection and identification of very small mineral phases that are impossible to identify by optical microscopy. The spectral resolution is also considerably improved by the rapid acquisition of several thousands of spectra. Finally, various data processing methods can be used to characterise particular structural or compositional properties of individual crystalline phases, thus vastly improving analytical possibilities. In the near future, mapping is likely to become the standard procedure for Raman analysis.

Acknowledgements

We acknowledge Olga A. Maslova for the mapping and analysis of UO2 ceramics. R. Augier, F. Choulet, D. DoCouto and F. Rull for the samples from Sierra Alhamilla, Morocco and Autun, la Sioule and Tenerife, respectively. We also acknowledge P. Bost for his help in sampling at Chéniers.

Author details

Frédéric Foucher[1*], Guillaume Guimbretière[2], Nicolas Bost[2] and Frances Westall[1]

*Address all correspondence to: frederic.foucher@cnrs-orleans.fr

1 CNRS, Centre de Biophysique Moléculaire, France

2 CNRS, Conditions Extrêmes: Matériaux, Hautes Températures et Irradiation, France

References

[1] Foucher F, Lopez-Reyes G, Bost N, Rull Pérez F, Russmann P, Westall F. Effect of grain size distribution on Raman analyses and the consequences for in situ planetary missions. Journal of Raman Spectroscopy. 2013;44:916–925.

[2] Guimbretière G, Desgranges L, Canizares A, Carlot G, Caraballo R, Jegou C, Duval F, Raimboux N, Ammar M-R, Simon P. Determination of in depth damaged profile by

http://dx.doi.org/10.5772/65112

micro-Raman line mapping in a pre-cut irradiated UO2. Applied Physics Letters. 2012;100:251914.

[3] Guimbretière G, Canizarès A, Raimboux N, Joseph J, Desgardin P, Desgranges L, Jegou C, Simon P. High temperature Raman study of UO2: A possible tool for in situ estimation of irradiation-induced heating. Journal of Raman Spectroscopy. 2015;46:418–420.

[4] Gries T, Vandenbulcke L, Simon P, Canizares A. Anisotropic biaxial stresses in diamond films by polarized Raman spectroscopy of cubic polycrystals. Journal of Applied Physics. 2008;104:023524.

[5] Poilblanc R, Crasnier F. Spectroscopies infrarouge et Raman. In: Bornarel J, editor. Collection Grenoble Sciences, Les Ulis, France: Grenoble, EDP Sciences; 2006. 674 p.

[6] Dieing T, Hollricher O, Toporski J, editors. Confocal Raman Microscopy. Springer Series in Optical Sciences, 156th ed. Berlin, Germany: Springer; 2010. 289 p.

[7] Dubessy J, Caumon M-C, Rull Pérez F, editors. Raman Spectroscopy Applied to Earth Sciences and Cultural Heritage. EMU Notes in Mineralogy, 12th ed. Twickenham, United Kingdom: The Mineralogical Society of Great Britain and Ireland; 2012. 504 p.

[8] Schopf JW, Kudryavtsev AB, Agresti DG, Czaja AD, Wdowiak TJ. Raman imagery: A new approach to assess the geochemical maturity and biogenecity of permineralized precambrian fossils. Astrobiology. 2005;5(3):333–371.

[9] Maslova OA. Caractérisation de matériaux heterogenes par spectroscopie Raman [thesis]. University of Orléans, France; 2014.

[10] Foucher F, Westall F. Raman imaging of metastable opal in carbonaceous microfossils of the 700–800 Ma old Draken formation. Astrobiology. 2013;13(1):57–67.

[11] Rividi N, van Zuilen M, Philippot P, Ménez B, Godard G, Poidatz E. Calibration of carbonate composition using micro-Raman analysis: Application to planetary surface exploration. Astrobiology. 2010;10(3):293–309.

[12] Treiman AH, Amundsen HEF, Blake DF, Bunch T. Hydrothermal origin for carbonate globules in Martina meteorite ALH84001: Terrestrial analogue from Spitsbergen (Norway). Earth and Planetary Science Letters. 2002;204:323–332.

[13] Bost N, Westall F, Ramboz C, Foucher F, Pullan D, Meunier A, Petit S, Fleischer I, Klingelhöfer G, Vago J. Missions to Mars: Characterisation of Mars analogue rocks for the International Space Analogue Rockstore (ISAR). Planetary and Space Science. 2013;82–83:113–127.

[14] Bourrat X, Foucher F, Guegan R, Feng Q, Stemfle P, Chateigner D, Westall F. AFM-Raman coupling to study mesocrystal polymorpism in nacre. In: GeoRaman Xth. France: Nancy; 2012. p. 27.

[15] Foucher F, Westall F, Brandstätter F, Demets R, Parnell J, Cockell CS, Edwards HGM, Bény J-M, Brack A. Testing the survival of microfossils in artificial martian sedimentary

meteorites during entry into Earth's atmosphere: The STONE 6 experiment. Icarus. 2010;207:616–630.

[16] Vajna B, Patyi G, Nagy Z, Bodis A, Farkas A, Marosi G. Comparison of chemometric methods in the analysis of pharmaceuticals with hyperspectral Raman imaging. Journal of Raman Spectroscopy. 2011;42:1977–1986.

[17] Gendrin C, Roggo Y, Collet C. Pharmaceutical applications of vibrational chemical imaging and chemometrics: A review. Journal of Pharmaceutical and Biomedical Analysis. 2008;48:533–553.

[18] Vincienne H. Rapport géologique sur le gisement de fer du bassin de Chaillac (Indre). Chambre de commerce et d'industrie de l'Indre, France 1948; p. 26.

[19] Choulet F, Faure M, Fabbri O, Monié P. Relationships between magmatism and extension along the Autun-La Serre fault system in the Variscan Belt of the eastern French Massif Central. International Journal of Earth Science (GeolRundsch). 2012;101:393–413.

[20] Ravier J, Chenevoy M. Présence de formations granulitiques jalonnant un linéament crustal dans la série cristallophylienne de la Sioule (Massif Central Français). Compte Rendu de l'Académie des Sciences de Paris. 1979;288(II):1703–1706.

[21] DoCouto D. Signification géologique des datations chimiques sur monazite. Application à la série polymétamorphique de la Sioule (Nord du Massif Central) [Master 2 thesis]. Université d'Orléans, France ; 2009.

[22] Augier R, Agard P, Monié P, Jolivet L, Robin C, Booth-Rea G. Exhumation, doming and slab retreat in the Betic Cordillera (SE Spain): In situ 40Ar/39Ar ages and P–T–d–t paths for the Nevado-Filabride complex. Journal of Metamorphic Geology. 2005;23:357–381.

[23] Knoll AH, Fairchild IJ, Swett K. Calcified microbes in Neoproterozoic carbonates: Implications for our understanding of the Proterozoic/Cambrian transition. Palaios. 1993;8(6):512–525.

[24] Charles N, Barbanson L, Sizaret S, Ennaciri A, Branquet Y, Badra L, Chen Y, El Hassani L, Guillou-Frottier L. Les gisements à ZN non-sulfurés du Haut-Atlas marocain. Ressources minérales: la vision du mineur. In: Ecole thématique CNRS/INSU/MINES. Paris: Tech; 2012.

Chapter 9

Stimulated Raman Scattering for All Optical Switches

Ariel Flores-Rosas, Evgeny A. Kuzin,
Orlando Díaz-Hernández,
Gerardo J. Escalera-Santos, Roberto Arceo-Reyes,
Baldemar Ibarra-Escamilla and Víctor I. Ruiz-Pérez

Additional information is available at the end of the chapter

http://dx.doi.org/10.5772/66320

Abstract

We theoretically and experimentally investigate an all optical switch based on stimulated Raman scattering in optical fibers. The experimental setup consists of a Raman circuit of two stages connected in series through a bandpass filter. In the first stage, we have a saturated amplifier, in this stage the pump pulses are saturated when pump and signal are launched to the input or the pump pulses remain without saturation when pump only is launched at the input. The second stage works as the Raman amplifier; for this stage amplification is directly dependent on the pump power entering from the first stage. For the case when pump pulse only is launched at the input pass to the second stage without saturation and amplifies the signal entering in the second stage, very intense signal pulses appear at the output of this stage. For the case when both pump and signal pulses are launched to the input, the pump pulse is saturated in the first stage and the filter rejected the amplified signal, so that only low power pump enters the second stage and consequently no signal pulses appear at the output. We show that the contrast can be improved when using fibers with normal and anomalous dispersion connected in series in the first stage. The best contrast (the ratio of energies) obtained was 15 dB at 6 W pump peak power.

Keywords: fiber optics, fiber nonlinearities, optical signal processing, stimulated Raman scattering, optical switch

1. Introduction

All-optical signal processing can be applied in the fields of optical communication and computation for its high speed. As a fundamental and key part for all-optical signal processing,

whose operation relies on nonlinear optical phenomena, has raised great interests in recent years as an alternative to electronic switching in optical communication systems [1, 2]. These devices have a strong potential and can be very useful for a number of applications in diverse areas such as ultrahigh-speed optical telecommunications, wavelength conversion, pulse regeneration, optical monitoring, optical computing, etc. Nonlinear effects will be particularly important in the next generation of optical networks, which will rely on all-optical functions for higher speed and greater capacity. Many principles and devices have been reported; of them a great part is performed by devices based on the Kerr effect in optical fibers, such as the nonlinear optical loop mirror (NOLM) first proposed by Doran and Wood [3], devices based on cross-phase modulation (XPM) proposed by Mamyshev and four-wave mixing (FWM) proposed by Caramella and Stefano [4, 5], logic gates [6], and wavelength conversion [7]. First reports were followed by numerous investigations proving high performance of all-fiber devices. The NOLM was investigated for soliton switch [8], wavelength demultiplexing [9], mode locking [10], etc. Some interferometric devices such as NOLM present an oscillating power transfer function but the ideal characteristic is the step-like function. The power transfer function of the FWM-based devices approaches the step-like function; nevertheless, for an only stage scheme, a flat response is obtained only at spaces, whereas at marks an oscillating dependence was measured [11]. A flat response was shown in double stage scheme at both spaces and marks [12].

Recently, there has been a lot of interest in stimulated Raman scattering (SRS) and is considered one of the most important nonlinear effects in optical fibers. SRS is one of the oldest and most well-studied optical phenomena and can anticipate great advantages for optical signal processing circuits because of high amplification of the signal and naturally existing possibility for wavelength conversion. In spite of that, SRS has just obtained some attention in the context of Raman amplifiers and only a few works were published on the use of SRS for designing optical signal processing circuits and optical switches. Furthermore, SRS can be hoped to present many advantages due to high amplification of the signal and intrinsical compatibility with communications systems using Raman amplification of signals [13]. The strong dependence of the Raman amplification on pump power that was considered for wavelength conversion with high extinction ratio of the output signal and can be base for the design of Raman circuits [14]. In this work, the output signal pulses at Stokes wavelength are generated as result of the Raman amplification caused by input signal used as the pump. Because of the strong dependence of Raman amplification on pump power, the extinction ratio of the output signal can be much higher than that of the input signal. The exploitation of pump saturation in presence of the signal was shown in [15]. In this work, the pulses at Stokes wavelength are used as input signal, and the pump pulses are considered as an output signal. In the absence of the Stokes pulse (spaces), the pump pulse travel in the fiber without saturation and has high power at the fiber output (marks), whereas in presence of the Stokes signal (marks) the pump pulse is depleted and has a low power at the fiber output (spaces). Disadvantage of this approach is the low extinction ration of the output signal. The most interesting work was suggested by Belotiskii [16] where authors used a two-stage setup. In this work, we consider experimentally, the Raman circuit using the approach suggested in [16] and show that it allows the step-like power transfer function with high differential gain and low input signals.

http://dx.doi.org/10.5772/66320

2. Theoretical analysis

In this section, we present simple numerical calculations to show the basic principles and potential of the approach [17]. **Figure 1** presents the diagram of the Raman circuit, it consists of two stages. In stage 1, the pump pulses are saturated if the signal is at "ON" or passes through stage 1 without saturation if the signal is at "OFF," this means that stage 1 woks as saturated amplifier. The amplification in stage 2 depends on the pump power entering from stage 1; that is, stage 2 works as Raman amplifier. When the pump pulse enters stage 2 without saturation as a result of that the input signal is at "OFF," then this will result in the generation of the high output pulses at the Stokes wavelength, this mean that the output signal is at "ON." For the opposite case when the input signal is at "ON," then the pump pulse is depleted in stage 1, the input signal is at "ONs" and therefore the output signal is at "OFF," so in this way the Raman circuit works as an inverter. For this operation of the Raman circuit one should take into account the following considerations: (a) the pump power has to be high enough to provide strong amplification of the signal and (b) at the same time the pump power has to be lower than the SRS threshold at which strong Stokes pulses and pump depletion appears as a result of the amplification of the initial spontaneous Stokes waves. The wavelength of the continuous wave (CW) seeding laser wave defines the wavelength of the output signal. The walk-off effect between pump and Stokes pulses is inevitable because of the big difference between pump and signal wavelengths. To avoid the degradation of the operation of the Raman circuit because of walk-off effect we propose to use the dispersion management using the special fibers, which they are formed by connecting the fibers in which the signal travels faster than pump with the fibers in which the signal travels slower than pump. We must consider that if we use the fibers with anomalous, the modulation instability (MI) effect can be expected, which will complicate circuit operation drastically.

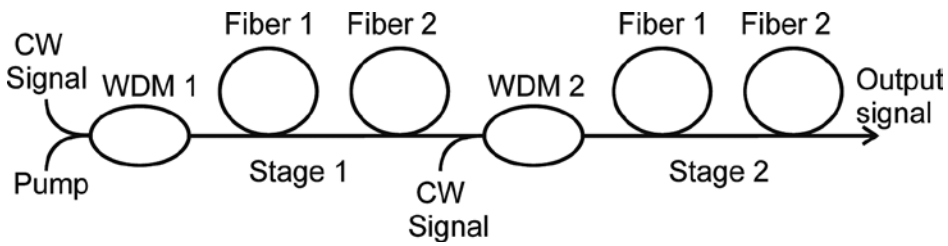

Figure 1. Setup of Raman circuit.

Because of its speed and good results split-step Fourier method (SSFM) is the most commonly used method for numerical analysis of the nonlinear equation of Schrödinger (NLSE), which uses the algorithm's finite Fourier transforms. We use this method to evaluate the operation of the Raman circuit based on the coupled equations for pump A_{P}, and Stokes A_{S}, pulses:

$$\frac{\partial A_S(t)}{\partial z} + \left(\frac{1}{V_P} - \frac{1}{V_S}\right)\frac{\partial A_S(t)}{\partial t} + i\frac{\beta_2}{2}\frac{\partial^2 A_S(T,z)}{\partial t^2} = \frac{g}{2}A_S(t)\left|A_P(t)\right|^2 \quad (1)$$

$$\frac{\partial A_p(t)}{\partial z} + i\frac{\beta_2}{2}\frac{\partial^2 A_p(T,z)}{\partial t^2} = -\frac{g}{2}A_p(t)\left|A_p(t)\right|^2 \quad (2)$$

where β_2 is the group velocity dispersion (GVD) parameter considered equal for pump and Stokes wavelengths; g is the Raman gain coefficient equal to 10^{-13} m/W for silica glass at 1550 nm wavelength; V_P and V_S are the group velocity of pump and Stokes pulses, respectively. Here we do not consider the effects connected to the Kerr effect and widening of the pulses due to GVD that is possible if the fiber length is less than the scattering length. The parameters of the fibers used in calculations correspond to the fibers used in experiments. Fiber 1, Corning SMF-LS dispersion shifted fiber with normal dispersion; Fiber 2, SMF-28 fiber with anomalous dispersion; and Fiber 3, OFS True Wave fiber with anomalous dispersion. **Figure 2** shows examples of the pump pulses at the output of Fiber 1 (**Figure 2a**) and at the output of Fiber 2 (**Figure 2b**). Input pulse is shown by the solid line and the output by dashed line.

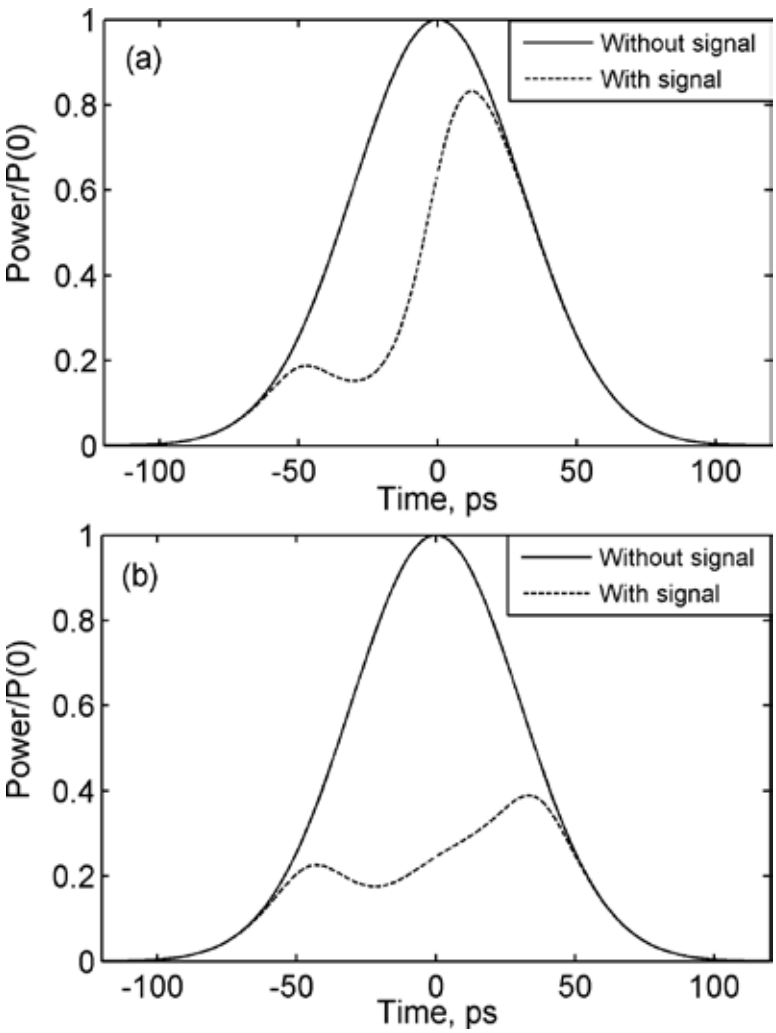

Figure 2. Input (solid line) and output (dashed line) waveforms of the pump at the end of (a) fiber 1 and (b) fiber 2.

http://dx.doi.org/10.5772/66320

The parameters used for calculations were as follow: Fiber 1 SMF-LS with 100 m length, Fiber 2 SMF-28 with 25 m length. The pump pulse presents the Gaussian shape of 100 ps and 25 W of power. The input Stokes pulse has a super Gaussian shape with 300 ps and a peak power of 1 mW and effective area of fibers of 50 μm^2. Fiber 1 has normal dispersion, so Stokes pulse has high speed and the first half of pulse manifests stronger depletion than the second half of pulse. Depletion can be made large when normal dispersion fiber is spliced with a fiber with anomalous dispersion, see **Figure 2(b)**, this happens because in fiber with normal dispersion the signal travels faster than the pump and the fibers with anomalous dispersion the signal travels slower than the pump, therefore pumping depletion becomes stronger in this case [18].

To calculate the depletion of the pump pulse we use as a ratio between the pulse energies at the output and the input. **Figure 3** shows the dependencies of the depletion of the pump on the input Stokes signal peak power. In the figure, the solid line represents the depletion when only the SMF-LS fiber is considered; the fiber length is equals to 100 m (pump power is equals to 30 W). For the dashed line we have 100 m of SMF-LS fiber added with 40 m of SMF-28 fiber (pump power equals to 24 W to have the same total Raman amplification as it was in the first case). Finally, we show the depletion for dotted line and for this case we used 100 m of fiber 1 with low GVD so that walk-off length is much longer than the length of the fiber (pump power was 30 W). It can be seen that the best results obtained are for the fiber with low dispersion; however, in practice it is not easy to fulfill the condition that the walk-off length is larger than the length of the fiber, a special case is when we have low potencies and for this case are required large fiber lengths. However, a simple dispersion management technique using fibers with normal and anomalous dispersion may provide switching with a contrast (the ratio between the energies of the signals at the second stage output) of about 20 dB at input power less than 10^{-3} of pump power [17].

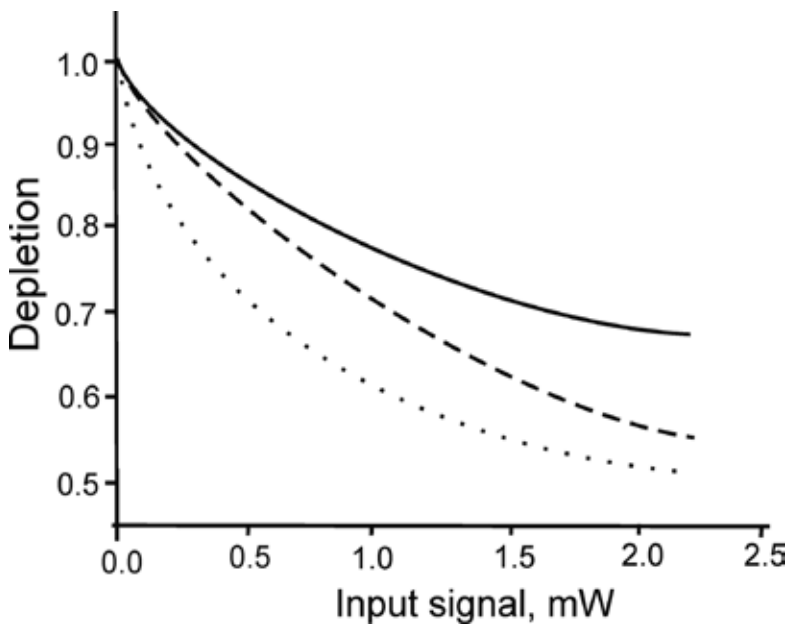

Figure 3. Depletion of the pump at first stage. Solid line is for fiber 1, dashed line is for fiber 1 + fiber 2, and dotted line is for fiber 1 with low dispersion.

We calculate the energy of Stokes pulse of the input in the output circuit depending on the power input Stokes in the first state. The calculations were made with SSFM with $g = 0.6\times10^{-13}$ m/W corresponding to the maximum Raman gain for the pump wavelength 1550 nm, the pulse duration pump of input is 100 ps with a power of 15 W, and the effective area of the fibers is 50 μm^2. Three types of fibers with different GVD were used: fiber 1 D = −6 ps/(nm-km); fiber 2 D = 20 ps/(nm-km); fiber 3 D = −0.01 ps/(nm-km). Fiber 1 corresponds to dispersion shifted fiber, fiber 2 is the SMF-28 fiber, and fiber 3 corresponds to the fiber without walk-off between pulses pump and Stokes. **Figure 4** shows the results for three different configurations of stage 1. Stage 1 is only of fiber 1 with 295 m of length (solid line). Stage 1 is comprised of three fibers connected in series: 150 m of fiber 1, 45 m of fiber 2, and 100 m of fiber 3 (dashed line). Stage 1 is also comprised of 295 m of fiber 3 (the dotted line). For the three cases 350 m of fiber 3 was used for stage 2. The best result is provided by the fiber with low dispersion.

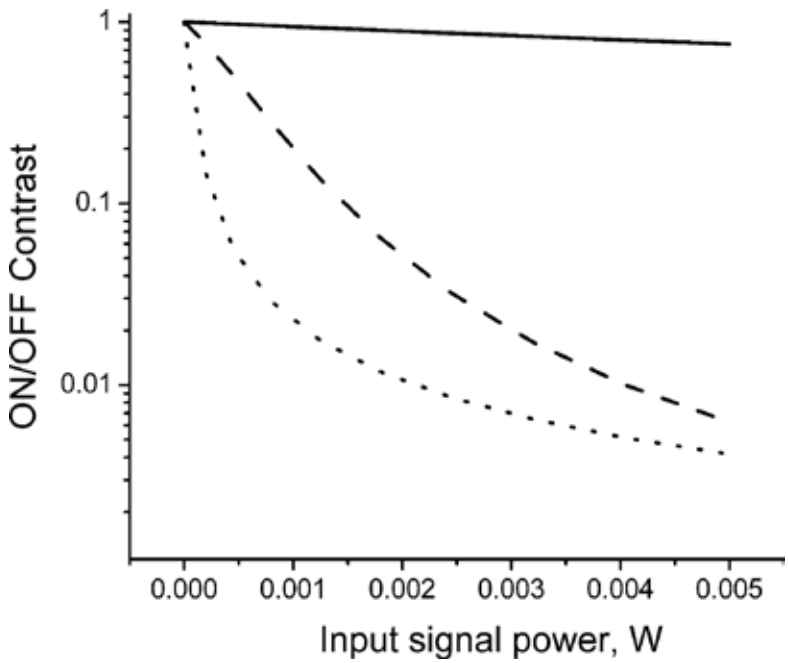

Figure 4. Energy of Stokes pulses at the output of the circuit.

The characteristics of a circuit of two stages depend on the attenuation between them, and two circuits connected in series provide the step-like dependence. The dependence of two circuits for the case when stage 1 is comprised of only fiber 3 and stage 2 is comprised of fiber 3 is shown in **Figure 5(a)**. The dependence for the case when stage 1 is comprised of three fibers connected in series, fiber 1, fiber 2, and fiber 3, and for stage 2 that is comprised of fiber 3 is shown in **Figure 5(b)**. As mentioned earlier, the dependence of two circuits depends on the attenuation between them, and for **Figure 5(a)** and **(b)** the attenuation is different and shows the dependence of the circuits connected in series.

http://dx.doi.org/10.5772/66320

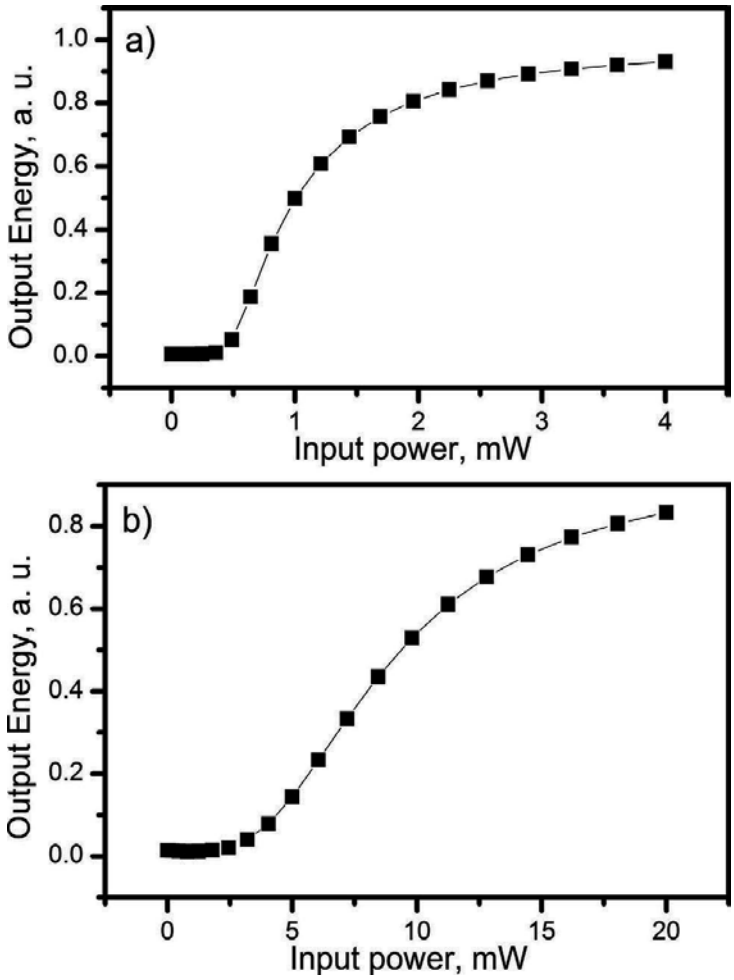

Figure 5. Dependencies of the output Stokes energy on the input power for two circuits connected in series: (a) attenuation is 10 times and (b) attenuation is 3 times.

A strong dependence of the output signal energy on the input signal power allows for improved signal-to-noise ratio of the signal. To show it, we put Gaussian noise to input Stokes. The Gaussian noise added to input Stokes is shown in **Figure 6a)** and the result of the input Stokes with Gaussian noise is shown in **Figure 6(b)**. We can consider two possibilities: one possibility, when input signal is "OFF," Gaussian noise is launched for fiber 1, and two possibility when input signal is "ON," Stokes more Gaussian noise is launched for fiber 1. We applied random noise and the results are show in **Figure 7** for 10 Stokes pulses when input signal is "ON" and "OFF." The parameters of the setup used for calculations were as follows: 100 m of fiber 1, 40 m of fiber 2, and 300 m of fiber 3, input pump power of 24 W, and the power of the input signal of 1 mW. As we can see, the output Stokes pulses are well distinguished [18].

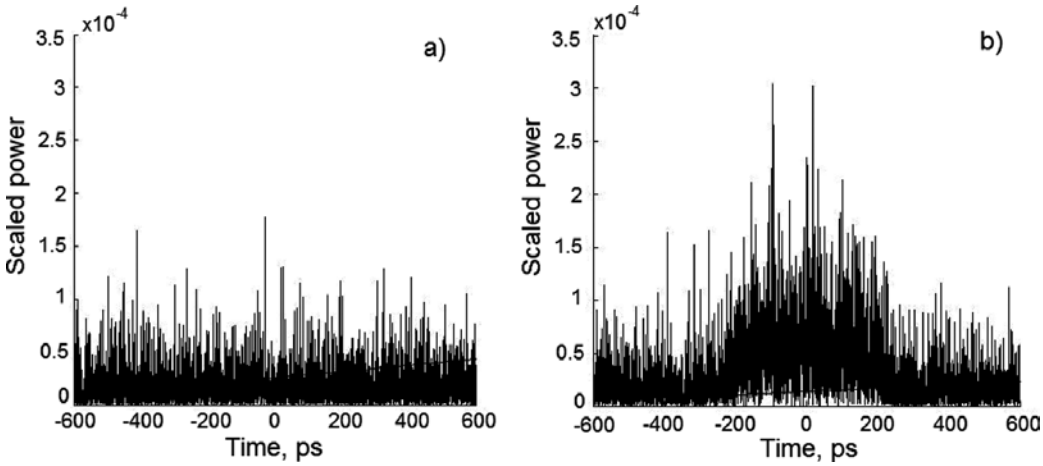

Figure 6. The input signal "off" (a) and the input signal "on" (b) in the presence of random noise.

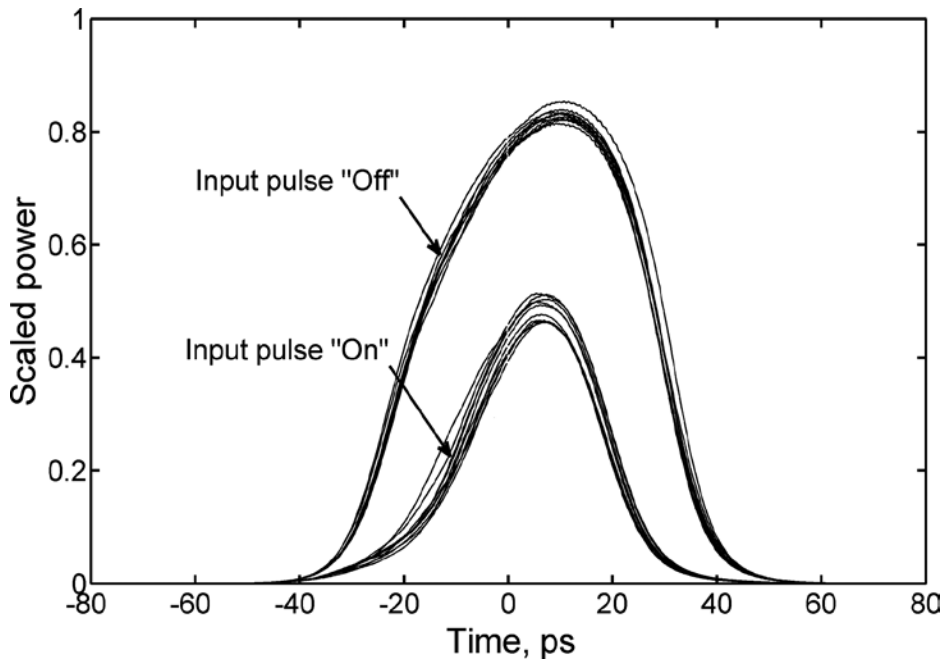

Figure 7. Output Stokes pulses for input pulses "ON" and "OFF."

From the above results, we can say that the setup of Raman circuit allows effective optical switching, logic operation, and noise reduction with signal of low power of the pump power. As we show above, to improve the operation of the Raman circuit we proposed the connection in series of fibers with normal and anomalous dispersion. We must consider that the power required for strong Raman amplification is lower than that required for the effects of MI and

http://dx.doi.org/10.5772/66320

pulse breakup in fibers with anomalous GVD [19]. The pulse breakup will affect the depletion of the pump pulse and amplification of the Stokes pulses. There are few works that are related to this problem, especially related to supercontinuum generation and Raman amplification [20].

3. Experimental results

Figure 8 shows the experimental setup, the setup used as a source of pump pulse is a diode laser with λ = 1528 nm. This diode laser is directly modulated by the pulse generator to generate pulses with duration of 2 ns. The pulses from the diode laser are amplified by an Erbium Doped Fiber Amplifier (EDFA) for power of several tens of Watts [21]. The pump pulses are introduced to the Coupler 1 (85/15), whose 85% port is spliced with the first stage comprising Fiber 1 + Fiber 2. In Fiber 1 we used the Corning SMF-28 fiber with anomalous GVD equal to 20 ps/nm-km, in the Fiber 2 we used the Corning SMF-LS dispersion shifted fiber with GVD equal to −6 ps/nm-km (normal dispersion at pump wavelength). The CW radiation with wavelength equal to 1620 nm is also introduced using the coupler 3 for two stages, the signal power introduced into Fiber 1 was 0.5 mW. The polarization controller inserted after the EDFA allows adjusting the polarization of the pump to provide maximum Raman amplification in the fibers because Raman amplification depends on polarization states of the pump and Stokes [22, 23]. The SRS in the first stage causes the signal amplification of 1620 nm and depletion pump pulse. In the experiment, two filters were used to reject the 1620 nm radiation at the end of the first stage. The Fabry-Perot (FP) filter and a broadband filter were used. For the launch the 1528 nm pump pulses and 1620 nm CW signal to the second stage of the experimental setup was used, Coupler 2 (90/10). The signal power of 1620 nm launched into fiber 3 was of 0.5 mW. We used 4.5 km of OFS True Wave (RS) fiber as fiber 3. With this configuration, we can measure simultaneously the pump pulse at the input of the first stage (pump monitoring, output 1), the pump output of the first stage (output 3), and pulses Stokes at the output of the second stage (output 2). We use the laser at this wavelength because it was what was available, but as the displacement of the wavelength between the signal and pumping must be very close to the maximum gain Raman (about 110 nm for the band of 1550 nm), thought we could use other lasers of around 1550 nm and can get a good operation of the device.

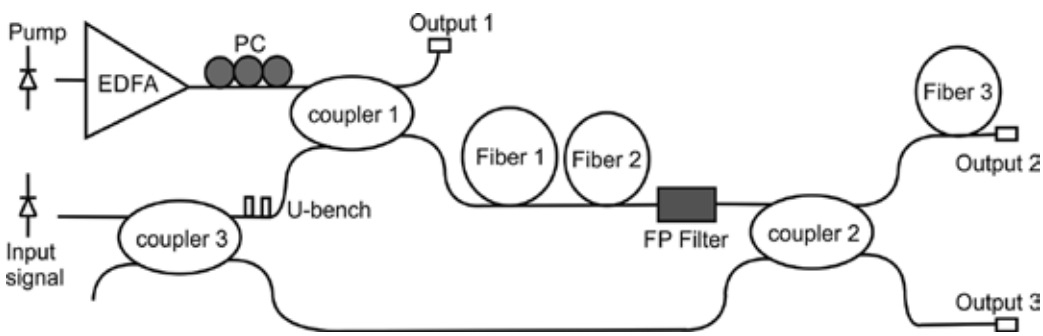

Figure 8. Experimental setup of Raman circuit.

To measure the Raman gains were launched to test fibers 0.5 mW of power with CW diode at 1620 nm. Stokes signal at output 3 of **Figure 8** was measured with a monochromator. The fiber used was SMF-28 with 100, 200, 300, 600, and 4500 m of length. The polarization of the pump was adjusted with the PC for maximum Raman amplification. The dependencies of powers Stokes with pump powers fit well with an exponential dependence, which corresponds to the Raman amplification given by exp (gP_bL/A_{eff}), where g is the coefficient of Raman amplification, P_b is the pumping power, A_{eff} is the effective area of the fiber core, and L is fiber length. In the results are also shown the critical power for breaking pulses. From these results we can say that the breaking of the pulse always starts with lower power compared to the Raman effect threshold. This can affect the efficiency of the switch since the breakup of the pulse starts before Raman amplification reaches significant values. The Raman gain average experimental value = 0.72 W^{-1}/km and the theoretical value for linearly polarized pump and Stokes = 0.72 W^{-1}/km (see **Figure 9**). Theoretical calculations agree well with the experiment.

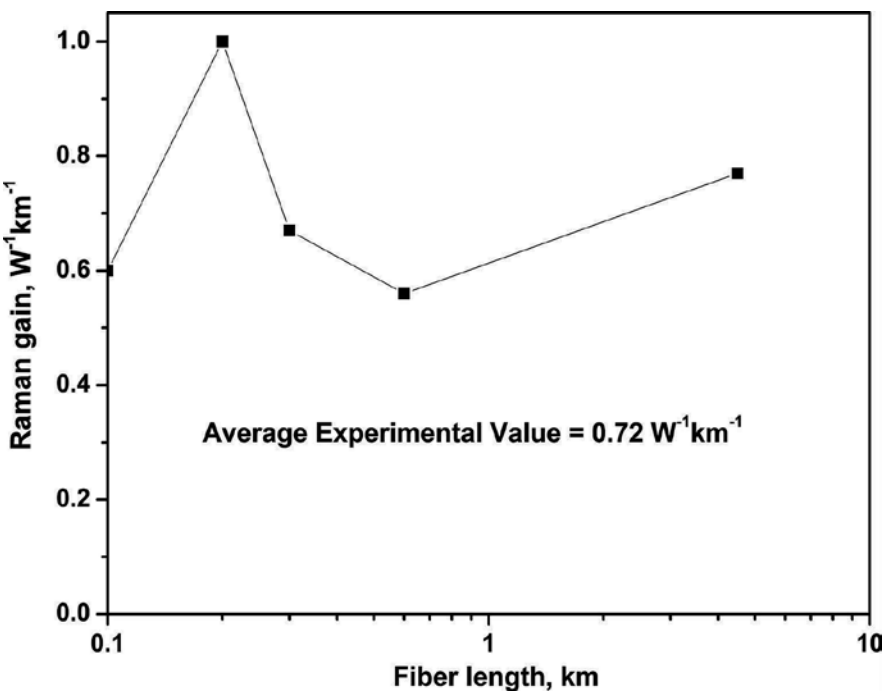

Figure 9. Raman gain.

The experimental setup is shown in **Figure 8**. We used the composed fiber, which consists of different spans of fiber 1 and fiber 2 for the investigated pump saturation in the first stage. **Figure 10** presents the results of waveforms of pump pulses at the output of the filter for different pump powers when only fiber 1 was used in the first stage. In the experiment, we used different span of fiber SMF-28. **Figure 10(a)** was obtained with a fiber length of 300 m and the inset is for the fiber with a length of 600 m. Strong depletion of the pump pulse was observed for the 300 m y 600 m of fiber even if the 1620 nm radiation was not applied. In this case, the effect of

http://dx.doi.org/10.5772/66320

the 1620 nm radiation on the pulse depletion was not detected. The maximum power at the FP filter output was measured to be equal to 7 W for 300 m y 3 w for 600 m. The pump depletion is caused by the pulse breakup process followed by the soliton self-frequency shift that results in broadening of the spectrum and the decrease of the power at the output of the FP filter.

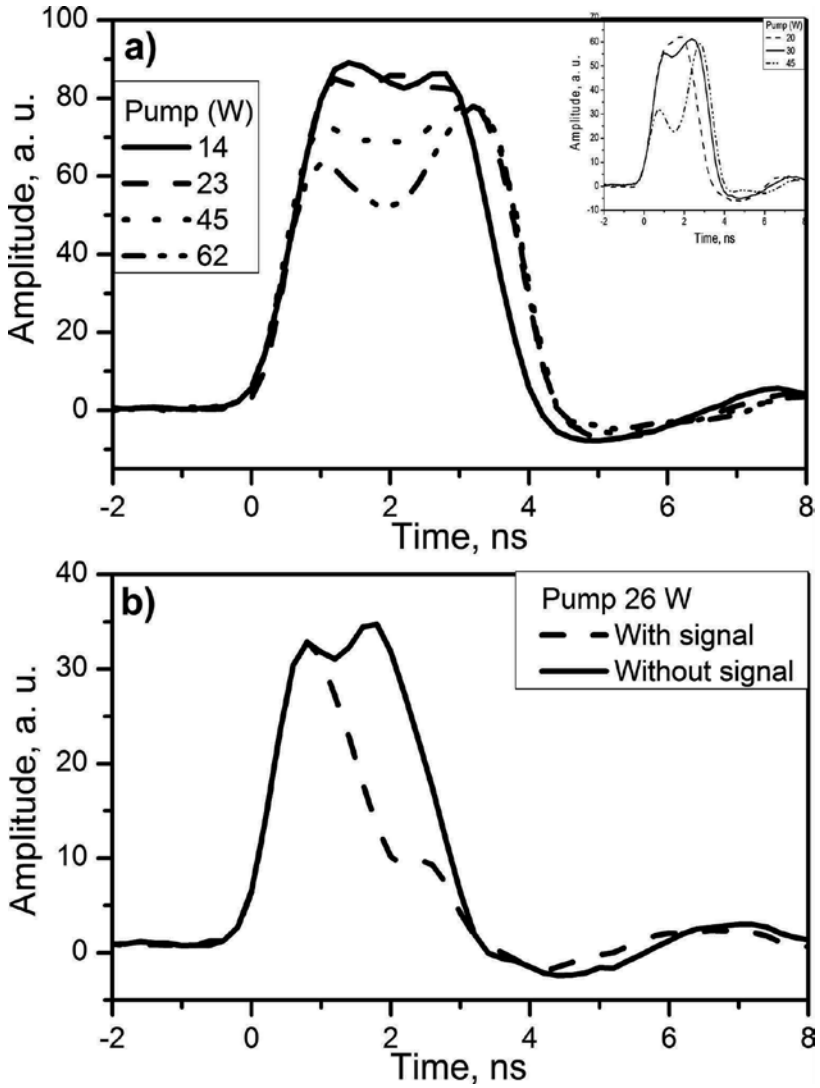

Figure 10. Pump pulses at the output of the FP filter when the SMF-28 fiber was used as the Fiber 1; (a) fiber length is equal to 300 m and the inset 600 m; (b) fiber length is equal to 1 km.

According to previous results, it can be concluded that for fiber lengths long critical power required for breaking pulses decays slower compared to the power required for Raman amplification. Therefore we assume that the effect of input radiation 1620 nm may be larger for larger fiber lengths. The pump saturation for 1 km of fiber SMF-28 is shown in **Figure 10(b)**,

the dashed line shows the pulse when radiation 1620 nm is off, and the solid line shows when we have 0.5 mW of 1620 nm radiation. The delay between pump pulses of 1528 nm and Stokes pulse 1620 nm for SMF-28 fiber is 2 ns for 1 km fiber, for this reason only the second half of the pulse is reduced. Depletion of the pump pulse when there was no input signal revealed that an effect of breaking pulse appears. The pump power for **Figure 10(b)** is 26 W.

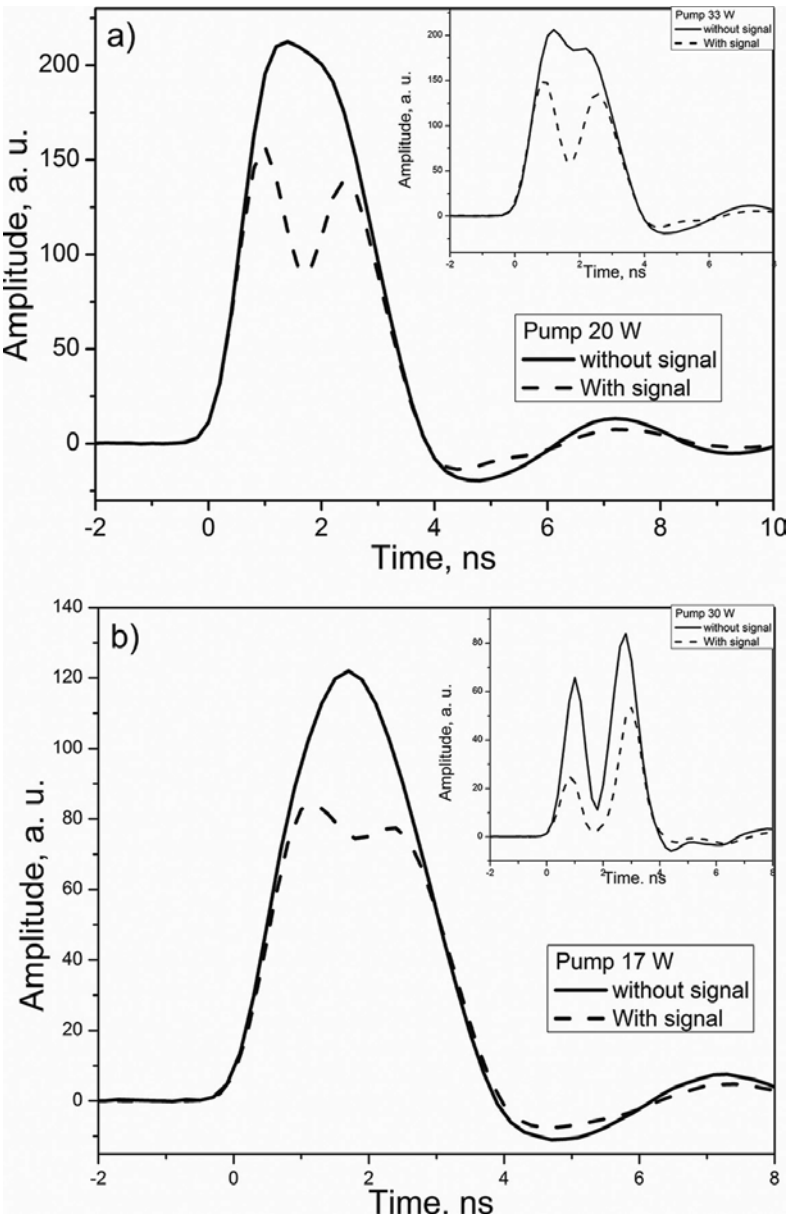

Figure 11. (a) Saturation of the pump by the input signal with 350 m of SMF-LS fiber for 20 W and the inset for 33 W pump power and (b) for 550 m SMF-Ls for 17 W and the inset for 30 W pump power.

http://dx.doi.org/10.5772/66320

Also tested in the experiment is the SMF-LS fiber, this fiber has normal dispersion for a wavelength of 1528 nm and so the effect of MI and breaking pulses are suppressed. The fiber shows conventional saturation of the pump and corroborates well with the simulations based on Eq. (1). **Figure 11** presents the results for a fiber of 350 and 550 m of length. **Figure 11(a)** shows pump power equal to 20 W and the inset of 33 W for 350 m of SMF-LS; **Figure 11(b)** shows pump power equal to 17 W and the inset of 30 W for 550 m of SMF-LS. Without input signal (solid line), no change in the waveform of the pump pulse is observed for **Figure 11(a)** and **(b)**. However, at 0.5 mW strong depletion of signal input power (dashed line) can be seen in **Figure 11(a)** and **(b)**. At 33 W for 350 m of SMF-LS and 30 W for 550 m of SMF-LS pumps power the depletion (solid line) is observed even without input signal, see insets of **Figure 11**.

We use a special fiber, consisting of a span of SMF-LS fiber spliced with another span of SMF-28 fiber, which was also tested in the experiment. Several tests were done and found that if the span of the fiber SMF-28 was respectively shorter than approximately 300 m, the effect of this span of fiber in low powers was negligible and depletion of the pump was determined by the fiber SMF-LS. For the case when we used 600 m of SMF-28 fiber spliced with 550 m fiber SMF-LS the effect of SMF-28 fiber was significant (with pump powers of 18 and 23 W). From these results, we can conclude that the effect of saturation of the pump by input signal was observed if the length of SMF-LS fiber is at least two times longer than the length of the SMF-28 fiber. For this case, the power required for MI effect is higher than that required for effective pump depletion. **Figure 12** presents an example of the output pump pulses for the first stage and the composed fiber consisted of a 550 m span of SMF-LS spliced with 300 m span of SMF-28, with pump power of 17 W and the inset for 20 W [17].

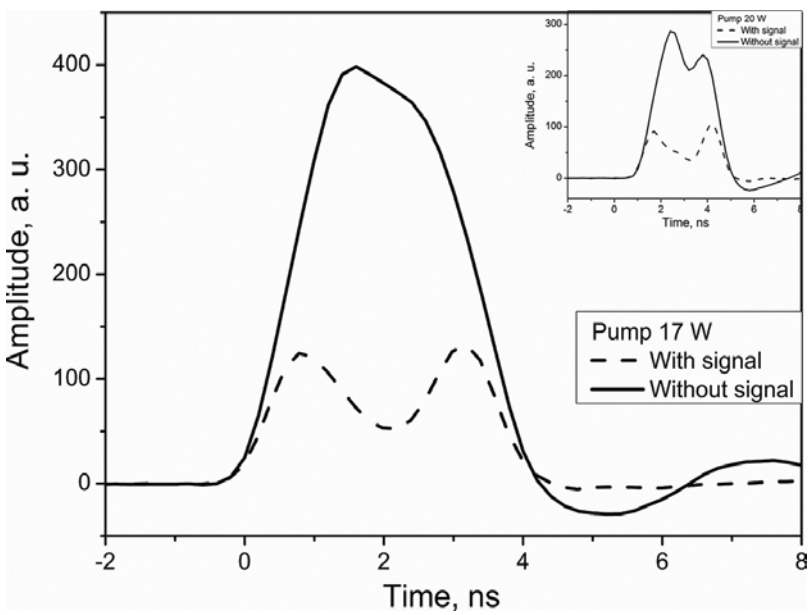

Figure 12. Saturation of the pump by the input signal if the first stage comprises a 550 m SMF-LS fiber connected to a 300 m SMF-28; pump power is 17 W and the inset for 20 W.

We can say that using the broadband filter obtain a considerable improvement in pump saturation, and with this result, we obtain a considerable improvement to the efficiency of the switch. The saturation measured for the composed fibers, which consists of a span of SMF-28 fiber spliced with another span of SMF-LS fiber, is shown in **Figure 13** and it presents the results of saturation for these fibers. **Figure 13(a)** presents results for 350 m SMF-LS fiber spliced with 300 m SMF-28 fiber, and **Figure 13(b)** presents results for 350 m SMF-LS fiber spliced with 600 m SMF-28 fiber. These graphs were obtained when using the broadband filter and spectral filter. We can see that when connecting the SMF-LS fiber, SMF-28 fiber can increase the saturation of the pump.

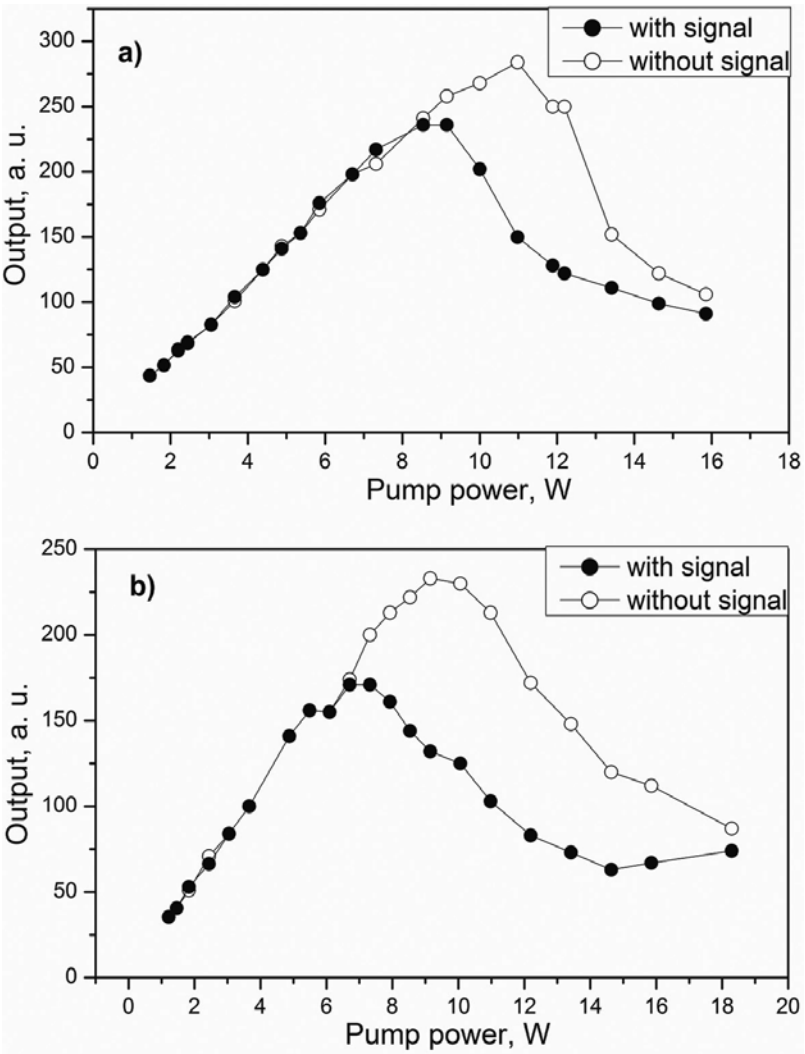

Figure 13. Saturation of peak power pump for variety of pump powers for two configurations: (a) 350 m SMF-LS fiber + 350 m SMF-28 fiber and (b) 350 m SMF-LS + 600 m SMF-28.

http://dx.doi.org/10.5772/66320

If the pump depletion in the first state of the SMF-28 fiber is determined by the MI, the depletion has to be dependent on the bandwidth of the filter inserted between the first and second stage. To show this, we use a broadband filter which is made with a spam of SMF-28 fiber. The difference between losses is sufficient to measure the depletion of pump of the broadband filter. **Figure 14** shows the results of the depletion measured with the broadband filter and the inset shows the results of the depletion measured with Fabry-Perot filter. We can see from the figure that with the narrow band filter pump depletion occurs in low power pump (about 5 W) and for the case with the broadband filter pump depletion occurs in about 30 W of pump power. We can conclude that the problem connected with the MI could be overcome using wideband filter between the first and the second stage. We can consider, for example, a filter based on a liquid filled photonic crystal fiber filter [24].

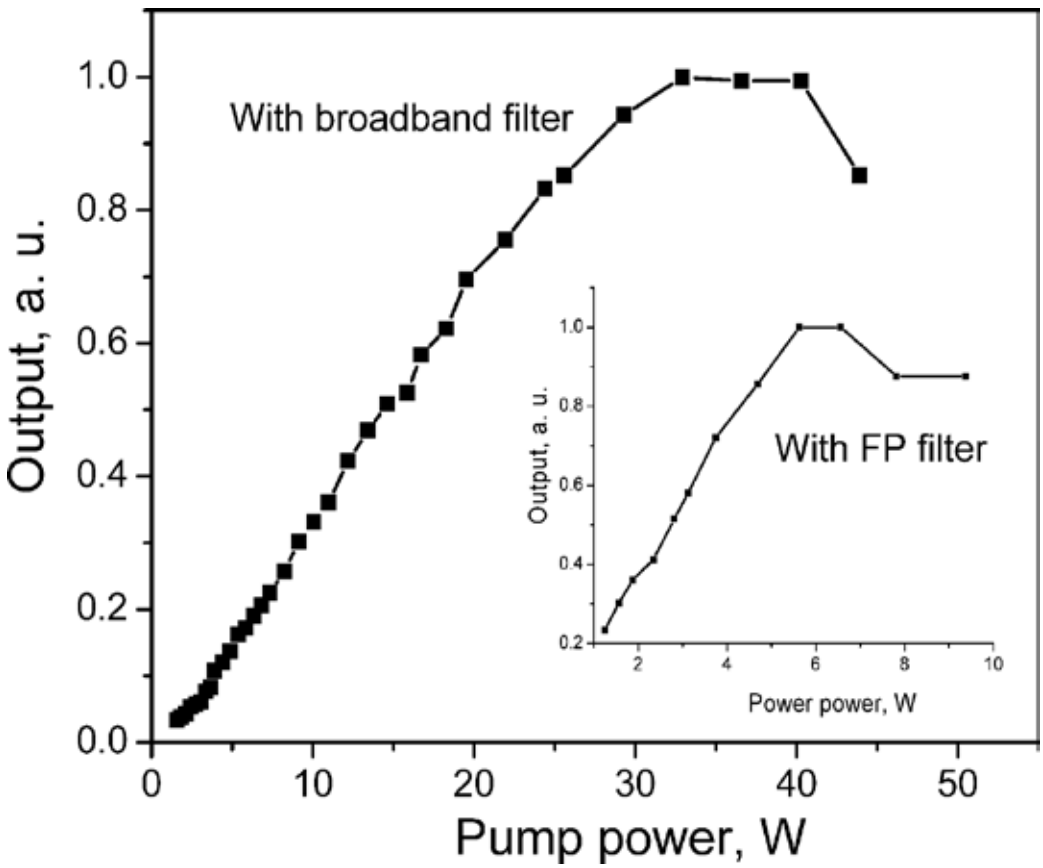

Figure 14. Saturation of pump measured with broadband and narrowband filter.

We investigate the experimental setup of the Raman circuit composed of two stages. In stage 1, we used different combinations of the SMF-LS fiber and SMF-28 fiber, and for stage 2, we used OFS True Wave (RS) fiber with 4.5 km of length. The results show the waveforms of the signal

pulses at the output 2 of the experimental setup. We used for stage 1: SMF-LS with different length; the composed fibers, which consists of a span of SMF-LS fiber spliced with another span of SMF-28 fiber. The results of **Figure 15(a)** were obtained with 350 m of SMF-LS as the first stage at 37 W pump power and the inset is for 550 m of SMF-LS at 23 W; the results of **Figure 15(b)** were obtained with 550 m of SMF-LS spliced with 600 m of SMF-28 used as the first stage at 18 W pump power. The inset of **Figure 15(b)** show magnifications of the output signal when input signal is applied.

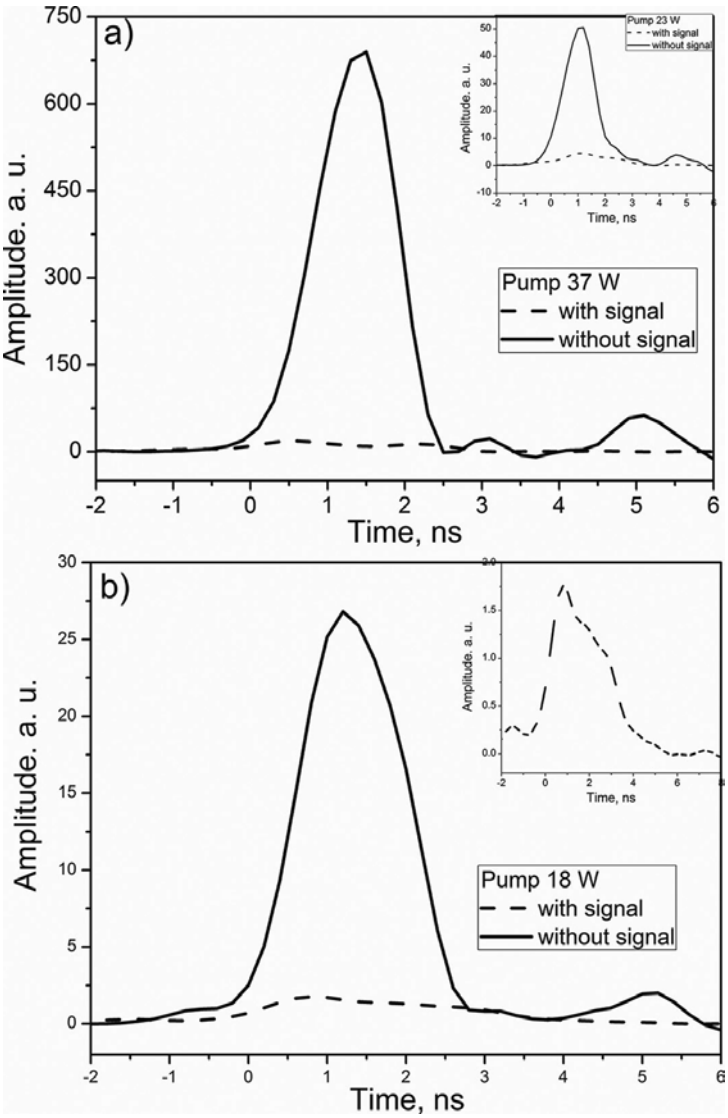

Figure 15. The waveforms of the output signal at 1620 nm at the output 2 of the experimental setup; dashed line with input signal (OFF), solid line without input signal (ON). The first stage consists of the 350 m of the SMF-LS fiber and the inset for 550 m of SMF-LS fiber (a); the first stage consists or of the 350 m SMF-LS connected to the 600 m SMF-28 the inset show the magnification of the when input signal is applied (b).

http://dx.doi.org/10.5772/66320

Finally, we measured the ratio of output energy without input signal ("OFF") and with input signal ("ON") for different pump powers. **Figure 16** shows the dependencies of the contrast on the pump power. The dependencies are shown for the first stage consisting of the 350 m SMF-LS fiber, **Figure 16(a)**, and for the first stage consisting of the 350-m SMF-LS and the 600 m SMF-28 fiber, **Figure 16(b)**. We can see that the best results from our configuration are for 350 m from the SMF-LS fiber in the first stage. For this configuration, the contrast OFF/ON came up to 27. With 500 m of SMF-LS in the first stage maximum contrast was equal to 7 and for configuration of 600 m of SMF-28 m spliced with 500 m of SMF-LS increase the contrast to 13.

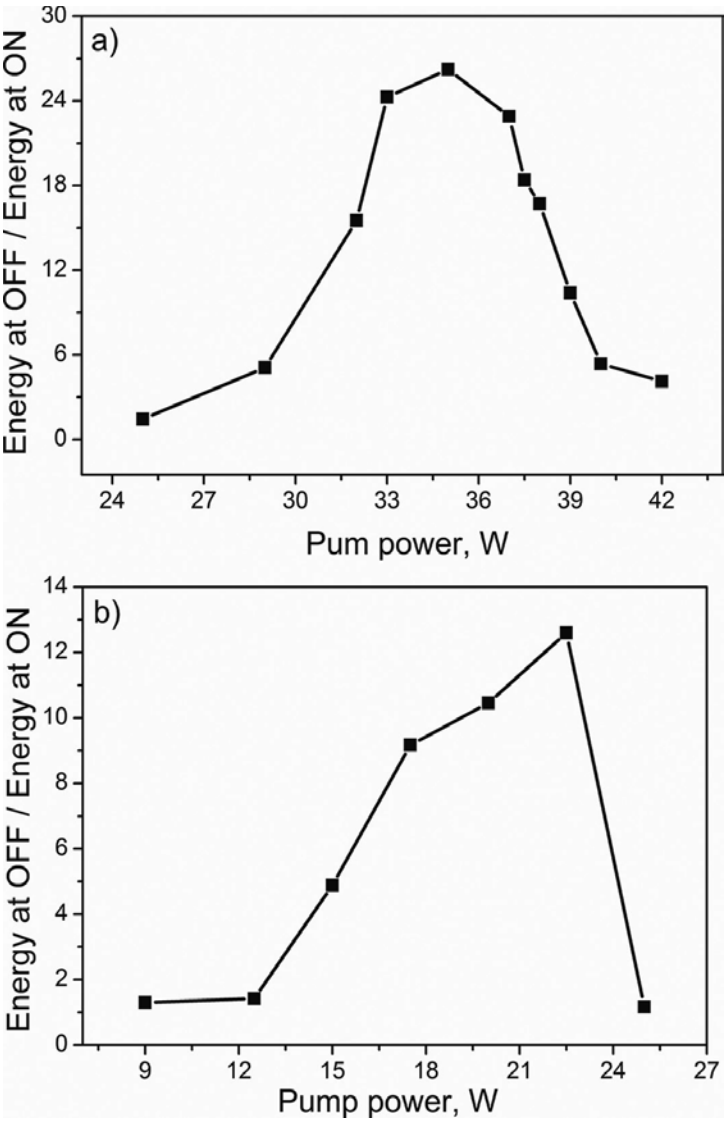

Figure 16. Energy of Stokes pulses, (a) for 350 m SMF-LS in the first stage; (b) for 550 m SMF-LS + 600 m SMF-28 in the first stage.

4. Conclusions

We investigate experimentally and theoretically an all-optical switch based on the SRS and demonstrate its viability. The use of SRS to design an all-optical switch circuit makes it possible to use very low powers of signal to control respectively strong pulses. The best contrast (the ratio of signal energy at the output when the input signal is ON/OFF) was 15 dB in pump peak power of 6 W and input signal only of 0.5 mW. Since there is a big difference between the wavelengths of pumping and signal, the walk-off between pump and Stokes is inevitable. We investigate the possibility to avoid degradation of circuit operation by the walk-off effect connecting fibers with normal and anomalous dispersion. We found that fibers with anomalous GVD effect of the MI and the breaking pulse appear lower than those required for a strong Raman amplification powers. We propose to use the spectral filter large bandwidth between states of Raman circuit for reducing problems of breaking pulses. We have built a simple configuration of the device with efficient switching and low power pump. Therefore, the experimental setup is compact and can be carried to another laboratory, and results are repeatable, i.e., the measurements are not dependent on environmental parameters.

Acknowledgements

The authors thank the Mexican Council for Science and Technology (CONACyT) for providing financial support for the realization of this project and the Proyecto PROMEP (Profocie) DSA/103.5/15/7129.

Author details

Ariel Flores-Rosas[1]*, Evgeny A. Kuzin[2], Orlando Díaz-Hernández[1], Gerardo J. Escalera-Santos[1], Roberto Arceo-Reyes[1], Baldemar Ibarra-Escamilla[2] and Víctor I. Ruiz-Pérez[3]

*Address all correspondence to: ariel.flores@unach.mx

1 Facultad de Ciencias en Física y Matemáticas, Universidad Autónoma de Chiapas, Tuxtla Gutiérrez, Chiapas, México

2 Departamento de Óptica, Instituto Nacional de Astrofísica, Óptica y Electrónica (INAOE), Puebla, México

3 Instituto Tecnológico de Culiacán, Culiacán, Sinaloa, México

References

[1] N. Nishizawa and Y. Ukai. Ultrafast all optical switching using pulse trapping in birefringent fibers. Optics Express. 2005;**13**(20):8128–8135. DOI: 10.1364/OPEX.13.008128

[2] M. Bajcsy, S. Hofferberth, V. Balic, T. Peyronel, M. Hafezi, A.S. Zibrov, V. Vuletic, and M.D. Lukin. Efficient all-optical switching using slow light within a hollow fiber. Physical Review Letters. 2009;**102**(20):203902. DOI: http://dx.doi.org/10.1103/PhysRevLett.102.203902

[3] N. J. Doran and David Wood. Nonlinear-optical loop mirror. Optics Letters. 1988;**13**(1):56–58. DOI: 10.1364/OL.13.000056

[4] B.E. Olsson and D.J. Blumenthal. All-optical demultiplexing using fiber cross-phase modulation (XPM) and optical filtering. IEEE Photonics Technology Letters. 2001;**13**(8):875–877. DOI: 10.1109/68.935833

[5] E. Ciaramella and T. Stefano. All-optical signal reshaping via four-wave mixing in optical fibers. IEEE Photonics Technology Letters. 2000;**12**(7):849–851. DOI: 10.1109/68.853523

[6] T. Fujisawa and M. Koshiba. All-optical logic gates based on nonlinear slot-waveguide couplers. Journal of the Optical Society of America B. 2006;**23**(4):684–691. DOI: 10.1364/JOSAB.23.000684

[7] R. Dekker, A. Driessen, T. Wahlbrink, C. Moormann, J. Niehusmann, and M. Först. Ultrafast Kerr-induced all-optical wavelength conversion in silicon waveguides using 1.55 μm femtosecond pulses. Optics Express. 2006;**14**(18):8336–8346. DOI: 10.1364/OE.14.008336

[8] M.N. Islam, C.E. Soccolich, and D.A.B. Miller. Low-energy ultrafast fiber soliton logic gates. Optics Letters. 1990;**15**(16):909–911. DOI: 10.1364/OL.15.000909

[9] A.I. Siahlo, L.K. Oxenløwe, K.S. Berg, A.T. Clausen, P.A. Andersen, C. Peucheret, A. Tersigni, P. Jeppesen, K.P. Hansen, and J.R. Folkenberg. A high-speed demultiplexer based on a nonlinear. IEEE Photonics Technology Letters. 2003;**15**(8):1147–1149. DOI: http://orbit.dtu.dk/fedora/objects/orbit:18529/datastreams/file_4226957/content.

[10] B. Ibarra-Escamilla, E.A. Kuzin, D.E. Gomez-Garcia, F. Gutierrez-Zainos, S. Mendoza-Vasquez, and J.W. Haus. A mode-locked fibre laser using a Sagnac interferometer and nonlinear polarization rotation. Journal of Optics A: Pure and Applied Optics. 2003;**5**(5):S225. DOI: http://dx.doi.org/10.1088/1464-4258/5/5/370

[11] E. Ciaramella, F. Curti, and S. Trillo. All-optical signal reshaping by means of four-wave mixing in optical fibers. IEEE Photonics Technology Letters. 2001;**13**(2):142–144. DOI: 10.1109/68.910515

[12] S. Yamashita and S. Mazumder. Optical 2R regeneration using cascaded fiber four-wave mixing with suppressed spectral spread. IEEE Photonics Technology Letters. 2006;**18**(9):1064–1066. DOI: 10.1109/LPT.2006.873475

[13] C. Headley and G. P. Agrawal. Raman Amplification in Fiber Optical Communication. 1st ed. San Diego, CA, USA: Elsevier Academic Press; 2005. 152 p. DOI: 012044506-9

[14] A. Uchida, M. Takeoka, T. Nakata, and F. Kannari. Wide-range all-optical wavelength conversion using dual-wavelength-pumped fiber Raman converter. Journal of Lightwave Technology. 1998;**16**(1):92–99. DOI: 10.1109/50.654989

[15] F. Ahmed and N. Kishi. All-fiber wavelength conversion of ultra-fast signal with enhanced extinction ratio using stimulated Raman scattering. Optical Review. 2003;**10**(1):43–46. DOI: 10.1007/s10043-003-0043-6

[16] V.I. Belotitskii, E.A. Kuzin, M.P. Petrov, and V.V. Spirin. Demonstration of over 100 million round trips in recirculating fibre loop with all-optical regeneration. Electronics Letters. 1993;**29**(1):49–50. DOI: 0013-5194

[17] A. Flores-Rosas, E.A. Kuzin, O. Pottiez, B. Ibarra-Escamilla, and M. Duran-Sánchez. Optical switch based on stimulated Raman scattering. Optical Engineering. 2011;**50**(7):071101-7. DOI: 10.1117/1.3558851

[18] A. Flores-Rosas, E.A. Kuzin, B. Ibarra-Escamilla, O. Pottiez, and M. Duran-Sánchez. The on-off contrast in an all optical switch based on stimulated Raman scattering in optical fibers. In: Benjamin J. Eggleton; Alexander L. Gaeta; Neil G. R. Broderick, editors. Nonlinear Optics and Applications IV; June 04, 2010; Brussels, Belgium. Bellingham, USA: Spie Digital Library; 2010. p. 7728. DOI: 10.1117/12.854737

[19] G. P Agrawal. Nonlinear Fiber Optics. 1st ed. San Diego, CA, USA: Academic Press; 2001. 442 p. DOI: 012045144-1

[20] A. E. El-Taher, J. D. Ania-Castañon, V. Karalekas, and P. Harper. High efficiency supercontinuum generation using ultra-long Raman fiber cavities. Optics Express. 2009;**17**(20):17909–17915. DOI: 10.1364/OE.17.017909

[21] M. Bello-Jimenez, E. A. Kuzin, B. Ibarra-Escamilla, and A. Flores-Rosas. Optimization of the two-stage single-pump erbium-doped fiber amplifier with high amplification for low frequency nanoscale pulses. Optical Engineering. 2007;**46**(12):125007. DOI: 10.1117/1.2823495

[22] Q. Lin and G.P. Agrawal. Vector theory of stimulated Raman scattering and its application to fiber-based Raman amplifiers. Journal of the Optical Society of America B. 2003;**20**(8):1616–1631. DOI: 10.1364/JOSAB.20.001616

[23] S. Sergeyev, S. Popov, and A.T. Friberg. Modeling polarization-dependent gain in fiber Raman amplifiers with randomly varying birefringence. Optics Communications. 2006;**262**(1):114–119. DOI: 10.1016/j.optcom.2005.12.045

[24] S. Torres-Peiró, A. Díez, J.L. Cruz, and M.V. Andrés. Fundamental-mode cutoff in liquid-filled Y-shaped microstructured fibers with Ge-doped core. Optics Letters. 2008;**33**(22):2578–2580. DOI: 10.1364/OL.33.002578

Chapter 10

Raman Spectroscopy of Amino Acid Crystals

Paulo T.C. Freire, Felipe M. Barboza, José A. Lima Jr.,
Francisco E.A. Melo and Josué Mendes Filho

Additional information is available at the end of the chapter

http://dx.doi.org/10.5772/65480

Abstract

In this chapter, we investigate the Raman spectra of proteinogenic amino acid crystals. Amino acids are fundamental organic molecules that compose polypeptides (a linear chain of amino acids) and proteins (folded polypeptides with specific functions) found in all living beings. Surprisingly, the number of these basic molecules is not more than 22 (20 of them commonly known as the standard amino acids, plus pyrrolysine and selenocysteine). They are defined as a molecule formed by an NH_2 group, a COOH group, a lateral chain (the R group), and a hydrogen atom, all of them connected to a single carbon, the α-carbon. Interestingly, α-amino acids show chirality, i.e., they present different distributions of group of atoms around the α-carbon, being defined as L- and D-form. For amino acids and proteins found in the living beings, the L-form is the dominant form, although some exceptions have been discovered in the last decades. In this chapter, we present the Raman spectra of all standard amino acids and discuss the different kinds of vibrations found, comparing them. As complementary part of the work, we present results on vibrational properties of some amino acids using Raman spectroscopy when subjected to specific conditions, with variation in temperature or pressure. Finally, we present some perspectives as the investigation of purines, a group of molecules associated with the DNA molecule.

Keywords: amino acid, raman spectroscopy, vibrational property

1. Introduction

Amino acids constitute an impressive and mysterious class of organic molecules, impressive because they form all proteins of living beings and mysterious because of their simplicity. In fact, amino acids — in their α form and in the *zwitterion* charge distribution conformation —are

constituted by one carbon, one NH_3^+ group, one CO_2^- group, and a group denominated as radical. The radical (*R*) characterizes the different types of amino acids; for example, *R* = H for glycine, *R* = CH_3 for alanine, *R* = CH_2-OH for serine, etc.

As it is well established, every cell of the living being on the Earth uses a set of 20 amino acids to produce all kinds of proteins [1, 2]. The 20 standard amino acids can be classified as (i) unpolar (alanine, valine, leucine, isoleucine, methionine, proline, phenylalanine, and tryptophan) and (ii) polar (glycine, arginine, asparagine, cysteine, glutamine, lysine, aspartic acid, glutamic acid, serine, threonine, tyrosine, and histidine). Additionally, some compendia include selenocysteine and pyrrolysine as belonging to the group of proteinogenic amino acids, but this is not unanimity yet. In the last years, a series of studies have investigated the vibrational and structural properties of amino acid crystals [3–42].

One of the main techniques to investigate vibrational properties of materials, whatever it is, is Raman spectroscopy. The technique consists in the interaction of light from a laser source with the material and further scattering of the light. The scattered light carries information about the rotational, vibrational, and, eventually, electronic states of the material. Concerning the Raman scattering effect, a pivotal concept is the scattering cross-section, σ, which represents a likelihood of a scattering event to occur [43]. It is defined as the rate at which energy is removed from the incident photon by the scattering substance, divided by the rate at which energy in the incident photon crosses a unit area perpendicular to its direction of propagation [43], expressed as in Eq. (1):

$$\sigma = h\omega_I / (2\pi\tau I_I) \tag{1}$$

In this equation, *h* represents the Planck constant, ω_I represents the angular frequency of the incident light, $1/\tau$ is the transition rate of the scattering process, and I_I is the surface power density, given in units of energy/[time × area]. $1/\tau$ is calculated through time-dependent perturbation theory from quantum mechanics. Obviously, if we are using quantum theory we need to define a Hamiltonian representing the system, as well as the states of the system. It is possible to define a Hamiltonian composed of two parts: (i) one unperturbed (H_0), represented by the contribution of the scattering medium and by the radiation field and (ii) one perturbed (H_p), with contributions from the electron-radiation interaction and electron-phonon interaction. An eigenstate of H_0 is ψ_i that encompasses information about incident and scattered photons, phonons, and about the electrons. The process involves the excitation of the medium due to the incident photon, leading the system to an intermediate state, creating an electron-hole pair. Such pair is scattered in a different intermediate state; finally, the electron-hole pair recombines, occurring the emission of a photon. This scattered phonon will have the information about the system. Using time-dependent perturbation theory we can show that

$$1/\tau = \quad d/dt \sum |\Psi_f{}^* \exp[-i\,(H_0 + H_p)\,(2\pi/h)]\,\Psi_i|^2 \tag{2}$$

http://dx.doi.org/10.5772/65480

with the sum performed over all possible eigenstates Ψ_f. After a crusty work using third-order perturbation theory, we can present the cross-section for the so-called one-phonon Stokes process in a relation such as:

$$\sigma = h\omega_I/(2\pi I_0) \sum (8\pi/h^2) \left| \{[\langle f| H_{er} |b\rangle \langle b| H_{ep} |a\rangle \langle a| H_{er} |i\rangle] / (E_I - E_{eh} + i\xi_1)(E_I - (E_q + E_{eh}) + i\xi_2)\}\right|^2 \delta(E_I - (Es + E_q)) \quad (3)$$

In this expression, the kets $|a\rangle$ and $|b\rangle$ represent intermediate states with small lifetime — called virtual states — H_{er} represents the electron-radiation interaction, H_{ep} represents the electron-phonon interaction, E_I represents the energy of the incident phonon, E_s represents the energy of the scattered photon, E_q represents the phonon energy, and ξ_1 and ξ_2 are small parameters. Other processes are also possible such as those involving two phonons that require the use of perturbation theory in order higher than third. However, in the present text, the results are related to one-phonon processes and, consequently, at first, all quantitative analysis can be achieved with the use of Eq. (3).

In this chapter, we summarize the main studies on Raman spectroscopy applied to proteinogenic amino acid molecules and crystals and point new perspectives on the subject.

2. Experimental details

In the present work, we have used two experimental set-ups: an instrument using Fourier transform mechanism and a dispersive (conventional) spectrometer. On the one hand, FT-Raman spectra were recorded using a Bruker RFS100/S FTR system and a D418-T detector, with the sample excited by means of the 1064 nm line of a Nd:YAG laser. In these cases, the spectral resolution was 4 cm^{-1}. On the other hand, the conventional Raman spectra were excited with the 514.5 nm line of argon ion lasers and the scattered light was analyzed in a Jobin-Yvon T64000 spectrometer equipped with the nitrogen cooled CCD system. Typically, the spectral resolution in the conventional Raman experiments was 2 cm^{-1}. Theoretically, the bands appearing in the Raman spectrum are independent of the excitation energy of the laser, although the intensity of the scattered light is proportional to λ^{-4} (λ is the wavelength of the laser) and, consequently, long-wavenumber excitation will produce a weaker Raman spectrum. However, in some cases, the exciting photons—mainly in the visible—are sufficient to excite the system into the lowest energy electronic states, and further relaxation to the ground state will appear as a broadband fluorescence in the Raman spectrum. Regarding the samples of amino acids, we have utilized two kinds: those used to obtain FT-Raman spectra were commercial reagents, while those where polarized Raman spectra are shown, were crystals obtained through aqueous solutions at several temperatures.

3. Nonpolar amino acids

In the discussion, we will separate the discussion according to the polarity of the lateral groups of the amino acids. We begin with the apolar amino acids. This group is composed of the following amino acids: glycine, alanine, valine, leucine, isoleucine, phenylalanine, methionine, tryptophan, and proline.

Glycine is the simplest amino acid, having as the radical a hydrogen atom. Although the molecular simplicity, glycine can crystallize in three different forms at atmospheric pressure and room temperature. The α-form shows a $P2_1/n$ monoclinic structure where hydrogen bonds appear in double antiparallel layers; the β-form shows a $P2_1$ monoclinic structure and individual parallel layers are linked by hydrogen bonds in a three-dimensional network; the γ-form shows a $P3_1$ trigonal structure with zwitterions forming helixes linked in a three-dimensional network [6]. The problem is that the three forms of glycine generally crystallize simultaneously from the same solution. In order to obtain crystals of the γ-form, it is necessary to prepare aqueous solution containing small seeds of the γ-glycine; the metastable β-form can be obtained by a mixture of water and acetic acid having the β-glycine as a seed, among other possibilities [6]. The three forms were studied under high pressure or under temperature variation. From these studies different results were obtained. The α-glycine under pressure is stable up to 23 GPa [7]. The β polymorphic form of glycine

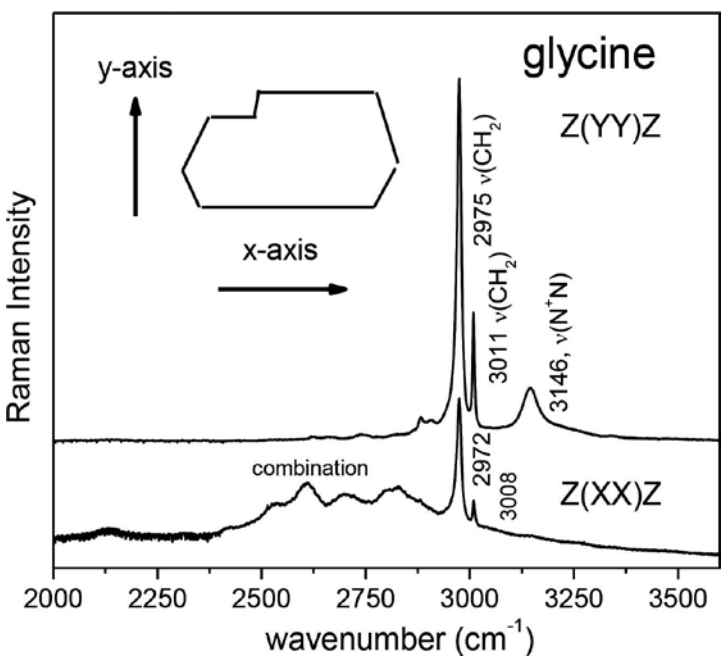

Figure 1. Polarized Raman spectra of glycine (α-form) for two scattering geometries in the high wavenumber region of the spectrum.

http://dx.doi.org/10.5772/65480

presents a phase transition at 0.76 GPa [8]; the new phase, β' is noted by the jumps and kinks at the curve of wavenumber vs. pressure as observed in experiment of Raman spectroscopy. Although the γ-form is the most stable among the three atmospheric pressure possibilities, it is possible to observe at ~ 440 K the $\gamma \rightarrow \alpha$ phase transition [9]. Also, under pressure, a phase transition from the γ-form to a new δ-form is verified, starting at ~ 2.7 GPa [10]. Additionally, when the δ-form is decompressed, between 0.95 and 0.2 GPa, a new polymorph is obtained, the ζ-glycine [11]. In relation to the Raman spectroscopy, as it is expected, each of the different polymorphs exhibits different spectrum. To give an example, **Figure 1** shows the Raman spectra of the (predominantly) α-form of glycine in the high wavenumber region for two scattering geometries, Z(YY)Z and Z(XX)Z. In this figure, it is possible to observe bands associated with symmetric stretching of CH_2, $\nu_S(CH_2)$, at 2971 cm $^{-1}$; antisymmetric stretching of CH_2, $\nu_A(CH_2)$, at 3006 cm^{-1}, and stretching of NH, ν(NH), at 3145 cm^{-1}. Depending on the kind of polymorph, the stretching of NH, in particular, is observed at different wavenumbers and with different intensities.

Although the chirality itself is a theme of great relevance, in the present chapter we discuss only the properties of the L-chiral sister of amino acid crystals (those present in the proteins) and do not furnish further information about the phenomenon. The simplest chiral amino acid is ***alanine***. It crystallizes in an orthorhombic $P2_12_12_1$ space group with four molecules per unit cell. The Raman spectrum of L-alanine was studied in a series of papers throughout the years [12–14]. Two studies have furnished the assignment of the normal modes through the analysis of deuterated analogs [13, 14]. Under temperature variation, L-alanine seems to be stable in the interval of 20–300 K, as indicated by several studies, including both infrared spectroscopy [15] and Raman scattering [16] studies. **Figure 2** shows the Raman spectrum of L-alanine recorded at room temperature in the interval of 300–700 cm^{-1}. This spectral range presents two important vibrations, e.g., the torsion of NH_3^+, $\tau(NH_3)$, and the rocking of CO_2^- unit, $r(CO_2)$. The study of the $\tau(NH_3)$ mode as a function of pressure showed that its wavenumber presents $dw/dP < 0$, in contrast with other amino acid crystals, such as L-threonine and taurine. Such fact was interpreted as a consequence of the behavior of hydrogen bonds that due to the short dimension should move away the N, H, and O atoms (that participate of a specific hydrogen bond) from a straight line, instead of to approximate the N and O atoms [17]. The discussion about the effect of pressure on L-alanine crystal is also of relevance. A first work indicated that L-alanine crystal undergoes a phase transition at ~ 2.2 GPa [18]. Additionally, the same work showed that the bands appearing at 42 and 48 cm^{-1} change intensity above the pressure where the supposed phase transition occurs [18] and the variation of intensity of the two bands was also noted by Tumanov et al. [19]. However, two studies point that instead of a phase transition, in fact, at 2.2 GPa, only the inversion of the **a** and **c** crystallographic axes occurs [19, 20]. Because at ~2.2 GPa, the two crystallographic axes had the same dimensions, technically, at this specific pressure, the structure should be tetragonal, but above the critical pressure value, the structure continues with its original orthorhombic structure. Therefore, L-alanine is an interesting example where the union of both Raman spectroscopy and X-ray diffraction furnished a wide picture about the behavior of the system.

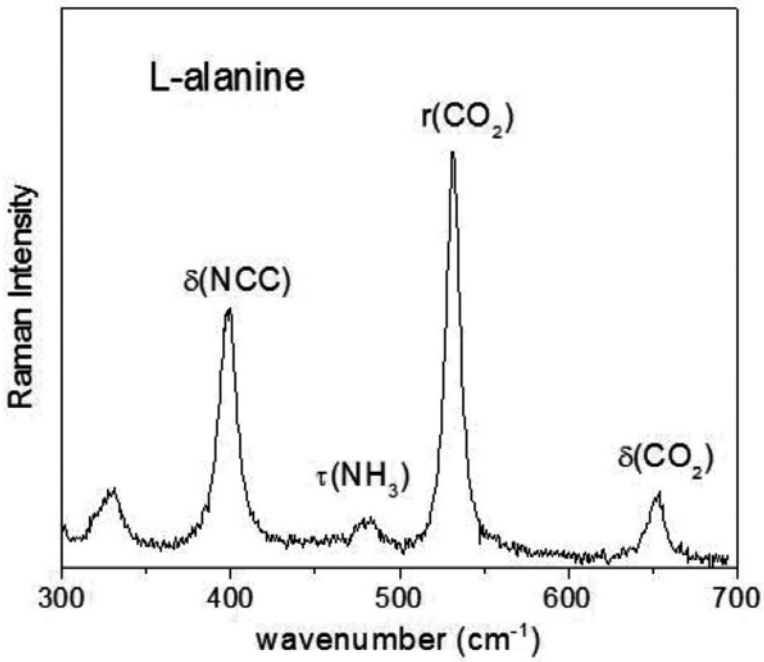

Figure 2. Raman spectrum of L-alanine in the spectral range from 300 to 700 cm^{-1}. Some important modes related to hydrogen bonds are shown, as rocking of CO_2^-, $r(CO_2^-)$, and torsion of NH_3^+, $\tau(NH_3^+)$.

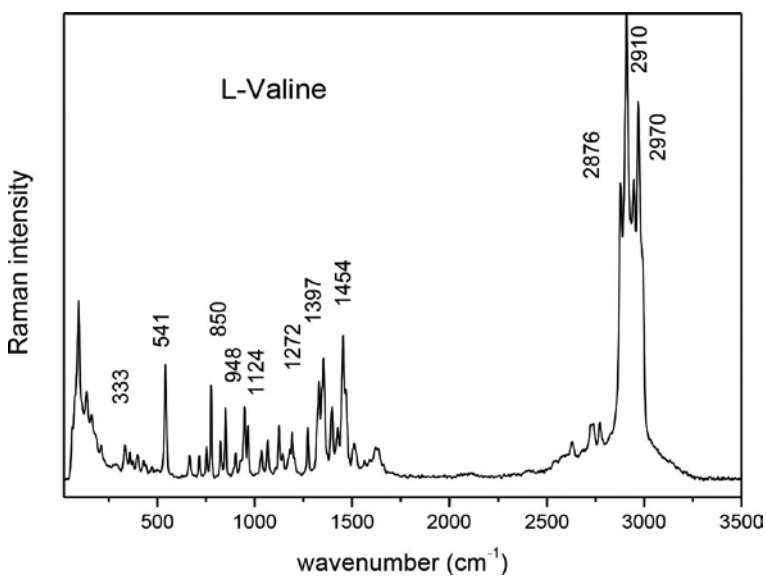

Figure 3. FT-Raman spectra of L-valine in the spectral range from 20 to 3500 cm^{-1}. The most intense peaks appear in the high wavenumber region of the spectrum.

http://dx.doi.org/10.5772/65480

Figure 3 shows the FT-Raman spectrum of ***L-valine*** in the range of 20–3500 cm^{-1}. This aliphatic amino acid crystallizes in a monoclinic structure with a $P2_1$ space group. L-valine is characterized by the $(CH_3)_2$-(CH) groups as radicals [L-leucine and L-isoleucine, which are discussed below, are characterized by $(CH_3)_2$-CH_2-CH_2]. There are four molecules per unit cell of L-valine, two of them in the *trans* conformation and two of them in the *gauche I* conformation. As usual, the modes in the high wavenumber region are associated with the stretching of CH and CH_3; modes related to the bending of CH_3, $\delta(CH_3)$, were assigned for the bands between 1400 and 1460 cm^{-1}; modes assigned as rocking of CH_3, $r(CH_3)$, were observed between 1125 and 1200 cm^{-1}; bands identified as the stretching of CC, ν(CC), were observed between 900 and 970 cm^{-1} [21]. The lattice modes were assigned as bands with wavenumber lower than 177 cm^{-1} and the torsion of CO_2, $\tau(CO_2)$, was identified with a band at 185 cm^{-1}. A Raman spectroscopic study showed that the L-valine crystal seems to undergo a phase transition at ~100 K, as indicated by changes in the lattice mode region of the spectrum [21]. In fact, unless the crystal is ferroelastic and presents domains, modification in the lattice mode spectral region means change in the symmetry of the unit cell. This behavior differs from the behavior of the L-alanine crystal, for example, that is stable under cryogenic conditions.

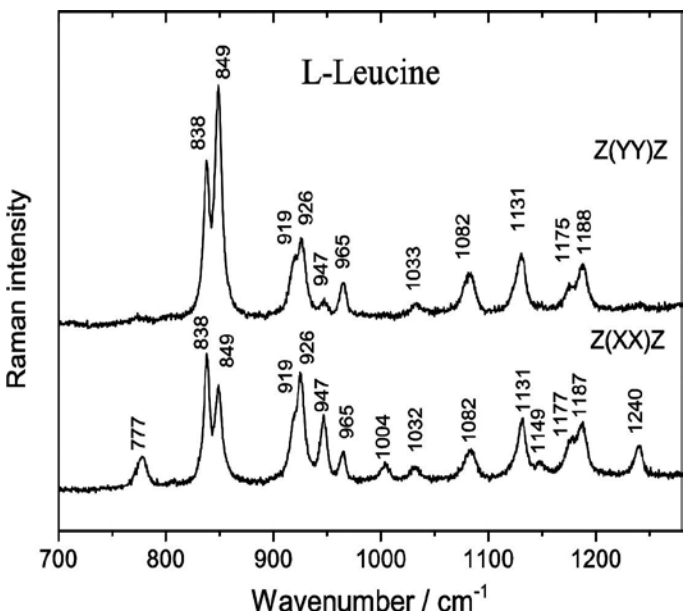

Figure 4. Raman spectra of L-leucine in the spectral range from 700 to 1280 cm^{-1} for two scattering geometries.

Another amino acid with nonpolar characteristics is ***L-leucine***. This amino acid crystallizes in a monoclinic structure, space group $P2_1$, and $Z = 2$. The carboxyl and the amino groups are hydrogen bonded in a double layer, in a similar fashion to L-valine and L-isoleucine [22]. **Figure 4** presents the Raman spectra of L-leucine for two scattering geometries in the spectral range from 700 to 1280 cm^{-1}. The band observed at 777 cm^{-1} is assigned as bending of CO_2^-, $\delta(CO_2^-)$;

at 838 cm^{-1} as out-of-plane vibration of CO_2, $\gamma(CO_2)$; 849 cm^{-1} as rocking of CH_2, $r(CH_2)$. The bands between 919 and 1004 cm^{-1} are assigned as stretching vibration of CC, ν(CC), and the bands at 1032 and 1083 cm^{-1} are assigned as stretching of CN, ν(CN), while the band at 1131 cm^{-1} is assigned as rocking of NH_3^+, $r(NH_3^+)$ unit [22]. The Raman spectroscopic study showed a series of modifications at about 353 K in both the internal and lattice modes of L-leucine, indicating a possible modification of the structure. This was interpreted as a phase transition from a C_2 to a C_S structure, even with the appearance of a TO mode at high temperature. L-leucine was also investigated under high pressure with the scrutiny of Raman spectroscopy [23]. Anomalous behavior was observed in two ranges, from 0 to 0.46 GPa and from 0.8 to 1.46 GPa. The first anomaly was realized through the observation of the disappearance of a band in the CH and CH_3 stretching region of the spectrum. The second anomaly is verified through the disappearance of lattice modes and splitting of modes in the high wavenumber region. Obviously, some of the modifications must involve molecular rearrangements due to changes of hydrogen bonds. Again, Raman spectroscopy appears as a powerful tool in order to study the phase transitions.

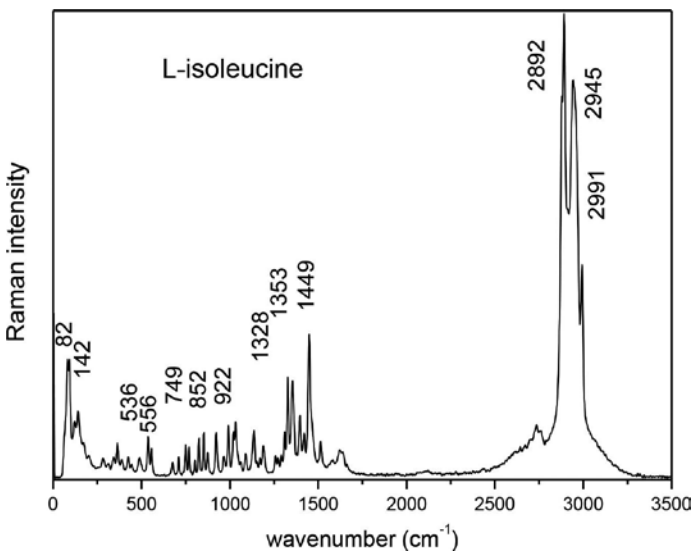

Figure 5. FT-Raman spectra of L-isoleucine in the spectral range from 20 to 3500 cm^{-1}. The most intense peaks appear in the high wavenumber region of the spectrum.

Figure 5 presents the FT-Raman spectrum of ***L-isoleucine*** in the spectral range from 20 to 3500 cm^{-1}. We observe that the most intense bands is located in the high wavenumber region of the spectrum, corresponding to bands associated with stretching of CH, CH_2, and CH_3; in fact, the spectral range of 2700–3200 cm^{-1} presents a very complex profile, with at least seven different bands [24]. On the other hand, the region between about 1700 and 2700 cm^{-1} does not present bands, as occurs with most proteinogenic amino acids (exception to cysteine that presents bands associated with SH stretching vibration at about 2500 cm^{-1}). A series of bands is observed between 500 and 1650 cm^{-1}, including vibrations associated with stretching of CC, ν(CC), from

http://dx.doi.org/10.5772/65480

872 to 1018 cm^{-1}, stretching CN, ν(CN), at 1033 and 1091 cm^{-1}, rocking of CH_3, rocking of CO_2^-, at 536 cm^{-1} etc. Several modes associated with bending vibrations are observed in the 300–500 cm^{-1} spectral range. The vibration associated with torsion of CO_2^-, $\tau(CO_2^-)$, is observed at ~ 177 cm^{-1}; such vibration is common to most amino acid crystals. Finally, below 170 cm^{-1} bands are observed that are generically associated with the lattice modes of the crystal. In relation to the behavior of the crystal under low temperature conditions, Raman spectroscopy showed that the L-isoleucine crystal does not present any evidence of phase transition, similarly to L-alanine and L-leucine, but differently from L-valine, which presents a modification at about 100 K. Such fact is very curious and future investigations are demanded in order to shed light in this problem.

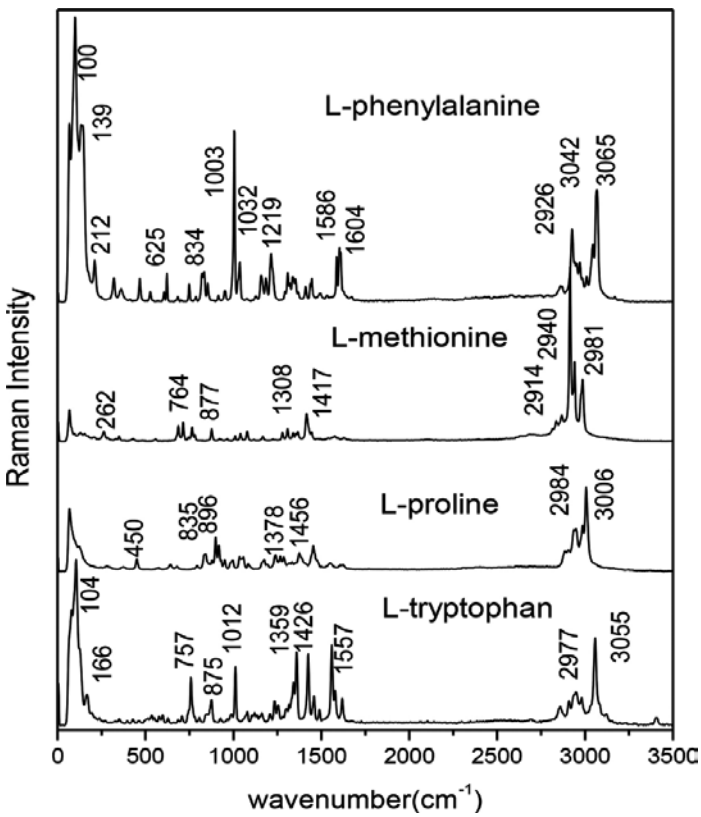

Figure 6. FT-Raman spectra of L-phenylalanine, L-methionine, L-proline and L-tryptophan in the spectral range from 20 to 3500 cm^{-1}.

The Raman spectra of ***L-phenylalanine***, ***L-methionine***, ***L-proline***, and ***L-tryptophan*** are shown in **Figure 6**. It is very difficult to grow crystals of L-phenylalanine and L-tryptophan in their pure forms. L-proline grows mainly in a hydrated form, while it is relatively easy to grow L-methionine. As a consequence there are few studies reporting vibrational properties of L-phenylalanine [25] and L-tryptophan [26], as well L-proline [5], and a little more on

L-methionine [27]. In relation to the previous amino acid presented in this chapter, phenylalanine and tryptophan show an additional benzene ring. As a consequence, this unit presents vibrations associated with it: stretching of CH at 2979, 3030, and 3057 cm^{-1}; rocking at ~1260 cm^{-1}; deformation at about 704 cm^{-1}; ring breathing at ~ 1010 cm^{-1} and wagging at ~ 744 cm^{-1}, for L-tryptophan [25]. The L-phenylalanine shows that vibrations related to the benzene ring are observed at 848, 912, and 949 cm^{-1} (out-of-plane bending); 1001 cm^{-1} (breathing of the ring); 1025 and 1076 cm^{-1} (in-plane bending); 1600 cm^{-1} (stretching of CC in the ring). Some results on L-proline monohydrated were presented in reference [5], where a high pressure investigation is furnished; the work shows evidence of two phase transitions, between 0.0 and 1.1 GPa and another between 6.5 and 7.8 GPa. In relation to L-methionine, a detailed study of the Raman spectra of the crystal under high pressure was revealed in reference [27]. Although the methionine molecule presents a sulfur atom, differently from the cysteine, in the methionine there is a connection linking two carbon atoms, C–S–C; as a consequence, the very intense band observed at ~ 2500 cm^{-1} appearing in the Raman spectrum of cysteine due to the S-H stretching is not observed in the Raman spectrum of methionine. However, a very characteristic band associated with the C-S stretching vibration is observed at 659 cm^{-1} in the spectrum of L-methionine. Following this band, when the L-methionine crystal was subjected to high pressure into a diamond anvil cell, it was observed an impressive modification that was associated with a phase transition undergone by the crystal at about 2.2 GPa [27]. Also interesting is the fact that the phase transition occurs with a hysteresis of ~ 0.8 GPa, suggesting the transition can be classified as a first-order one.

4. Neutral, polar amino acids

Among the polar amino acids, serine, cysteine, asparagine, glutamine, threonine, and tyrosine are neutral. **Figure 7** shows the Raman spectra of L-cysteine.HCl, L-serine, L-glutamine, and L-asparagine.H_2O as obtained through a Fourier-transform Raman spectrometer in the spectral range from 50 to 3500 cm^{-1}. From 1800 to 2800 cm^{-1} no mode is observed, except in the spectrum of L-cysteine.HCl, where a stretching vibration of SH appears at ~ 2550 cm^{-1}. In fact, as mentioned in the previous paragraph, cysteine is the only proteinogenic amino acid that presents an S-H bond and, as a consequence, is the only amino acid to present a peak in this region.

It is important to remember that ***L-cysteine*** can be found without HCl ions in the unit cell. L-cysteine can be obtained under ambient conditions in two different crystalline polymorphs, orthorhombic, and monoclinic. The orthorhombic structure of L-cysteine crystallizes with $Z = 4$ and space group $P2_12_12_1$. One of the important characteristics among the amino acid crystals is the fact that L-cysteine presents the S-H…S hydrogen bond, extending along the **b** crystallographic direction. As a consequence, L-cysteine constitutes a model to understand the important sulfur hydrogen bonds involved in some proteins of the human being. In a polarized Raman spectroscopic study, it was observed that at low temperatures, the S-H…S hydrogen bonds contribute to form an ordered crystal structure, but upon heating, the thiol-groups appear slightly disordered [28]. As pointed out in this reference, some of the S-H…S

http://dx.doi.org/10.5772/65480

hydrogen bonds are substituted by S-H…O bonds in such a way that at room temperature the number of the two species of hydrogen bonds is approximately the same. Interestingly enough is the fact that the change of hydrogen bonds with the substitution of sulfur by oxygen is not sharp, but occurs through a series of intermediate states [28]. We remember that L-alanine, when submitted to low temperature conditions, also presents a pathological behavior, i.e., the **c** crystallographic parameter decreases in a succession of steps and plateaus. The jumps on the **c** parameter were interpreted for L-alanine as attempts to relax some frustration [29]. Returning to the L-cysteine case, the modification in the thiol group is related to different orientations of the cysteine zwitterion, which are tuned by the strong N-H…O hydrogen bonds. Additionally, it was observed that different groups (NH_3, SH, CH, and CH_2) are activated in different temperature ranges, similarly with was observed for the NH_3 and CH_3 groups of L-alanine [30]. Under high pressure, the Raman spectrum of orthorhombic L-cysteine presents noticeable modifications that can be summarized as follows [31]. Above 0.1 GPa redistribution of intensities of the components of the bands associated with stretching of SH, ν(SH), suggests a continuous decrease in the number of sulfhydryl groups participating of S-H…S hydrogen bonds. This tendency remains until the pressure arrive to 1.6–1.9 GPa, when is observed an impressive change in the Raman spectrum, associated with a phase transition. One of these changes is the downshift of the wavenumber of ν(SH) by ~ 40 cm^{-1}, as well as the splitting of this band; such facts suggest both (i) the S-H…S hydrogen bond

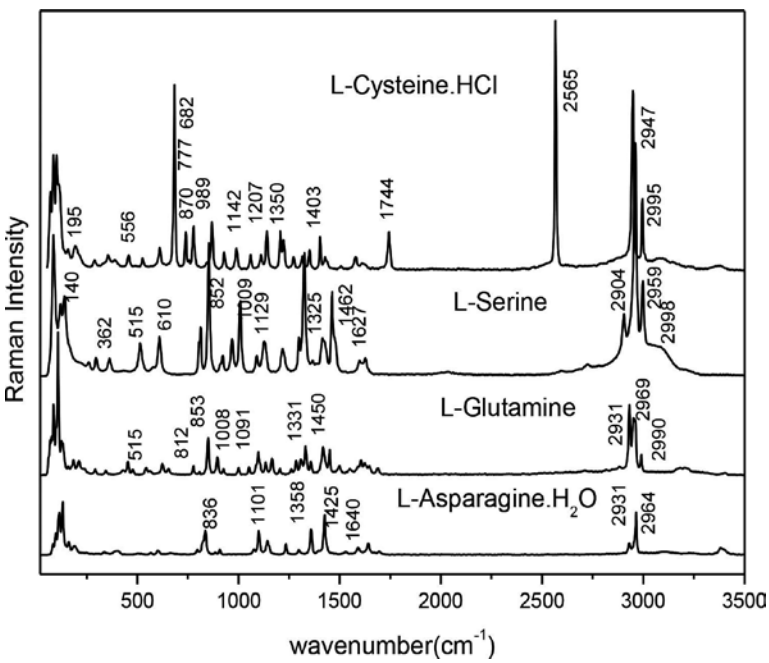

Figure 7. FT-Raman spectra of polar (neutral) amino acids L-serine, L-glutamine and compounds L-cysteine.HCl and L-asparagine.H_2O. In the spectrum of L-cysteine.HCl stands out an intense band associated with the S-H stretching, ν(SH), similar to the monoclinic phase of L-cysteine, but different from the orthorhombic phase, where broad split bands are observed (see text).

strengthen and (ii) increasing of disorder of SH group. Above 2.3 GPa, the wavenumber of ν(SH) presents a upshift of 30 cm^{-1}, indicating the weakening of hydrogen bonds related to S-H groups. However, the modes are split above this pressure, and we can consider that the sulfhydryl groups are still disordered.

Obviously, if you change the sulfur atom by an oxygen atom, the hydrogen bonds involving SH groups cease to exist. As a molecule, ***serine*** is a copy of cysteine but with oxygen replacing the sulfur atom. L-serine crystallizes in an orthorhombic structure with space group $P2_12_12_1$, the same of one of the polymorphs of L-cysteine. A Raman spectroscopic study showed that L-serine presents changes at ~ 140 K. the changes were interpreted as reorientation of the side chain CH_2OH with respect to the C-C bonds of the skeleton of the molecule [32]. As a consequence, a positional disorder of the O-H...O intermolecular hydrogen bond is verified. Such a fact was realized through the analysis of the behavior of stretching of OH, ν(OH), allowing to separate the temperature evolution of O-H...O hydrogen bond among the other formed by serine molecules in the crystal structure: N-H...O in the head-to-tail chains, N-H...O between antiparallel chains and N-H...O between **ab** layers [32]. This constitutes a very beautiful example of the power of Raman spectroscopy to play light in a so complicated theme as is hydrogen bond.

Glutamine is the more abundant proteinogenic amino acid in the human blood, occupying a pivotal position in the nitrogen metabolism. The radical of the amino acid is characterized by the groups NH_2-(C=O)-CH_2-CH_2. As a consequence, the high spectral region of the Raman spectrum of L-glutamine presents a rich profile. In the FT-Raman spectrum a very strong band observed at 2933 cm^{-1} is associated with the symmetric stretching of CH_2, $\nu_S(CH_2)$; a doublet at 2952 and 2962 cm^{-1} is associated, respectively, with the stretching CH, ν(CH), and the symmetric stretching of CH_2, $\nu_S(CH_2)$; a peak observed at 2991 cm^{-1} is assigned as antisymmetric stretching of CH_2, $\nu_A(CH_2)$. Above 3100 cm^{-1} it is possible to observe bands with low intensity associated with NH_2 and NH_3^+ groups: at 3176 cm^{-1}, assigned as symmetric stretching of NH_2; at 3210 cm^{-1}, assigned as symmetric stretching of NH_3^+ and at 3403 cm^{-1}, assigned as antisymmetric stretching of NH_2. Such assignment, performed on reference [33] with the use of deuterated L-glutamine samples will be fundamental to understand the behavior of the crystal submitted to extreme conditions e.g., high pressure and low temperatures.

The radical NH_2-(C=O)-CH_2 characterizes the amino acid L-***asparagine***. Although is possible to grow small crystals of the pure form, most of the studies on vibrational spectroscopy deals with the hydrate form, monohydrated L-asparagine (MLA). This crystal was studied in a series of papers [34, 35]. A Raman spectroscopic study revealed that under low temperature MLA undergoes a phase transition between 140 and 150 K. The modification is clearly realized through the observation of splitting of a band assigned as lattice modes, at ~ 130 cm^{-1} [34]. Under high temperature, MLA also presents a phase transition, as it was shown by Raman scattering measurements [35]. At about 363 K, the orthorhombic $P2_12_12_1$ structure of MLA change drastically, as it is possible to infer from the impressive modifications of the Raman spectra above this temperature. Interesting enough, while in the low temperature phase transition the modifications are observed mainly in the low wavenumber region of the Raman spectrum, in the high temperature phase transition modifications occur in all spectral range.

http://dx.doi.org/10.5772/65480

Something that also deserves attention is the behavior of MLA under high pressure. In a recent work [36] authors have investigated the material up to 30 GPa. This is the highest pressure value utilized in experiments on the vibrational properties of amino acid crystals up to now (we remember that L-alanine presents a crystal-amorphous phase transition at 15 GPa, half of the pressure value reached in the experiment with MLA). In this work, analyzing most of the Raman bands in the spectral range 30–3600 cm^{-1}, it was possible to note modifications that were correlated with phase transition undergone by MLA, as well as, with conformational changes of the molecules in the unit cell of the crystal. The changes observed at approximately 10 GPa were associated with a phase transition and other modifications between 2.1 and 3.1 GPa and between 15.0 and 17.0 GPa were associated with conformational changes. In particular, the most impressive modifications occur in the high wavenumber region of the spectrum. Very suggestive is the fact that the wavenumbers of the antisymmetric stretching of NH_2, $\nu_A(NH_2)$ and symmetric stretching of H_2O, $\nu_S(H_2O)$ decrease in the interval at 1 atm and 8.5 GPa, indicating that hydrogen bonds are strengthened in this pressure interval. The explanation for the anomalous behavior is because N-H…O hydrogen bond interaction is stiffened due the approximation of molecules under compression, weakening the covalent N-H interaction and, consequently, shifting the wavenumber of the two modes to lower values. During the transition at 10 GPa, the bands associated with stretching of water molecule show a positive jump, indicating a new environment for the molecules. However, between 10.6 and 15 GPa and above 17.9 GPa the symmetric stretching of water goes, respectively, to higher and to lower wavenumbers, signaling different behavior of the hydrogen bonds. As a résumé for the data on MLA, we can affirm that Raman spectroscopy furnished a precise picture about the hydrogen bonds allocated in the unit cell of the crystal.

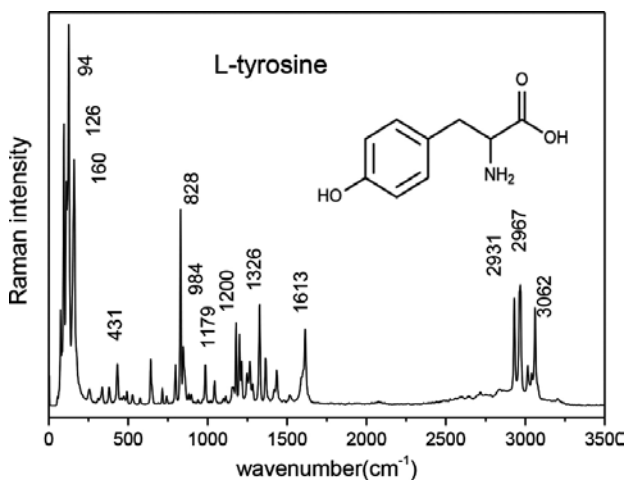

Figure 8. FT-Raman spectrum of L-tyrosine. It is interesting to observe the intense peaks characterizing the low wavenumber of the spectrum. The inset presents a representation of the molecule.

The FT-Raman spectrum of ***L-tyrosine*** is shown in **Figure 8** (the inset shows a representation of the molecular formula). As occurs with L-phenylalanine and L-tryptophan, L-tyrosine

presents a benzene ring in its radical. Consequently, it is expected that vibrations associated with breathing of the benzene ring and CC stretching related to the atoms of the ring appear in the Raman spectrum of L-tyrosine with frequencies similar to those of L-phenylalanine and L-tryptophan. It is also interesting to observe that the low wavenumber bands are the most intense bands appearing in the Raman spectrum. Because these bands are assigned mainly as lattice modes, it will be of interest in future studies where one should search for eventual phase transitions. In the high wavenumber region of the Raman spectrum, it is possible to observe distinctly five different bands that are associated with the stretching vibrations of CH and CH_2, ν(CH) and ν(CH_2), respectively. Up to now, there is no work published in the literature discussing the vibrational behavior of L-tyrosine subjected to neither low temperature nor high pressure conditions, among other extreme conditions.

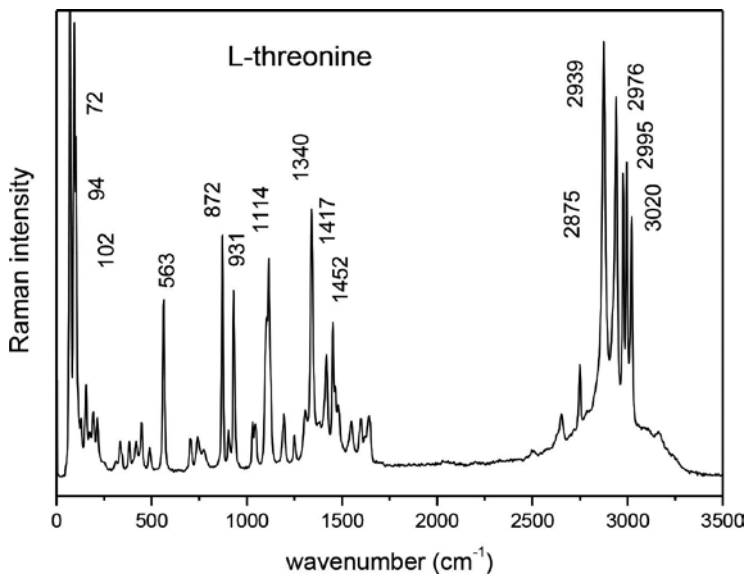

Figure 9. FT-Raman spectrum of L-threonine in the spectral range 20–3500 cm^{-1} recorded at room temperature. It is interesting the observation of a very complex profile in the high wavenumber region of the spectrum although threonine is a relatively simple molecule.

Figure 9 shows the FT-Raman spectrum of ***L-threonine*** in the spectral range from 20 to 3500 cm^{-1}. Most of the bands appearing in the low wavenumber region are associated with lattice modes and, as a consequence, their behavior can furnish information about the stability of the unit cell [37]. L-threonine crystallizes in an orthorhombic structure with space group $P2_12_12_1$. Vibrations associated with CC stretching are observed as bands in the spectral range 907–940 cm^{-1}. Rocking of CO_2^-, r(CO_2^-) is observed at ~ 568 cm^{-1}. It is interesting in this point remember that r(CO_2^-) vibration is observed at 515 cm^{-1} in L-serine, 530 cm^{-1} in L-histidine hydrochloride monohydrated, 553 cm^{-1} in L-asparagine monohydrated and in L-cysteine, 545 cm^{-1} in L-methionine and 541 cm^{-1} in L-valine. So, this kind of vibration that appears in the Raman spectrum as a band of relatively high intensity presents a well-specific range where

it is observed. It is also relevant to point out that the torsion of NH_3^+, $\tau(NH_3^+)$, is observed in L-threonine at 497 cm^{-1}. A recent Raman scattering study—where a sample of L-threonine was put into a diamond anvil cell set up—showed an impressive phase transition close to 2 GPa, another between 8.2 and 9.2 GPa, and a third between 14 and 15.5 GPa. The principal indication for the occurrence of these pressure-induced phase transitions is the modification in the bands associated with external modes. Additional changes observed in bands related to CO_2, NH_3, and CH_3 units of the threonine molecule also corroborate the occurrence of the three-phase transition [38]. However, although the maximum pressure reached in the experiment was 27 GPa, no evidence of amorphization was observed. This point is being analyzed because, on the contrary, L-alanine undergoes a crystal — amorphous phase transition for pressure of only 15 GPa. Additionally, a comparative study looking for a correlation between the behavior of NH_3 torsional modes of L-alanine, L-threonine, and taurine with the hydrogen bond dimensions was given in reference [17]. A possible connection between the hydrogen bond dimensions and the amorphous state of the amino acid crystal can give interesting insights about the phenomenon.

5. Acidic, polar amino acids

Figure 10 shows the FT-Raman spectra of ***L-aspartic acid*** and ***L-glutamic acid*** in the spectral range from 20 to 3500 cm^{-1}. In some aspects, the two spectra are similar, e.g., the lattice modes appear as very intense bands in the low wavenumber region of the spectrum and the profiles of the Raman spectra in the high wavenumber region are very similar for the two crystals. L-glutamic acid crystallizes in two possible polymorphs, called α (like prisms) and β (as platelets). Both polymorphs crystallize in an orthorhombic structure in a $P2_12_12_1$ space group. In **Figure 10**, the main contribution for the FT-Raman spectrum of L-glutamic acid is from the β-form. For this polymorph, there is no intramolecular hydrogen bond, but a strong hydrogen bond between two carboxylic groups in neighboring molecules is observed; such a bond form links along the ***b***-direction. In the L-glutamic acid, the symmetric stretching of NH_3^+ appears— as occurs with most of the amino acid crystals—as a weak band, observed at 3073 cm^{-1}. A very strong band associated with the stretching of CH_2 is observed at 2974 and 2938 cm^{-1}. Vibrations associated with rocking of NH_3^+ are observed at 1128 and 1149 cm^{-1} and the stretching of CC is observed at 970 and 1062 cm^{-1}. At 804 and 866 cm^{-1} (the last one as a very strong band) bands are associated with rocking of CH_2. Vibrations associated with the skeleton of the L-glutamic acid are observed in the spectral range of 240–398 cm^{-1}. Finally, the torsion of CO_2^- unit is observed at 199 cm^{-1} and bands with wavenumber lower than this value are associated with the lattice vibrations of the crystal. Raman spectroscopy was used to investigate the vibrational properties of a crystal of L-glutamic acid in its β–form. From this study, authors have observed modifications that can be considered as evidence that the crystal undergoes some phase transitions. One modification in the Raman spectrum was observed between 0.5 and 1.3 GPa. The second modification was noted between 2.6 and 3.1 GPa; the third modification was observed for pressures between 5.4 and 6.4 GPa and the fourth change in the Raman spectra was observed for pressures between 13.9 and 15.9. Again,

it is important to inform that at these pressures there is no evidence of amorphization for the crystal of L-glutamic acid; in fact, even at the highest pressure reached in the experiments (21.5 GPa), the crystal shows all bands, given no evidence of an amorphous phase [39].

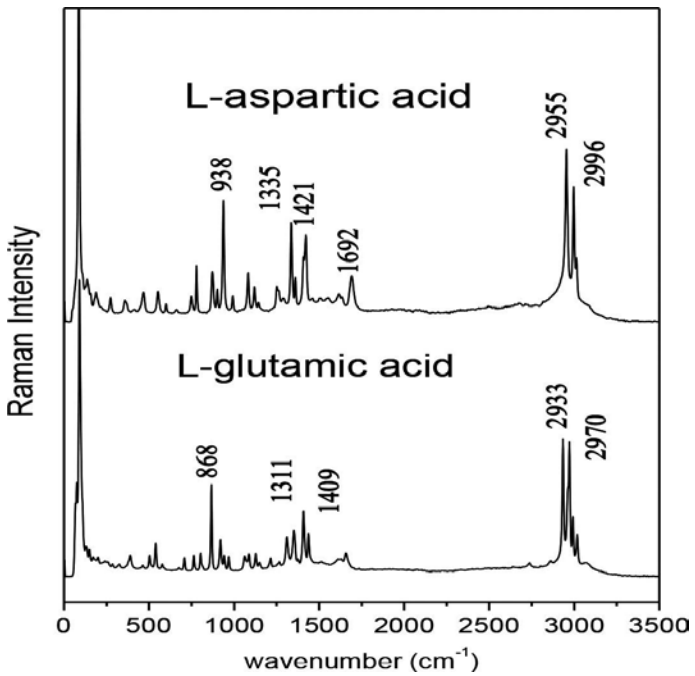

Figure 10. FT-Raman spectra of L-aspartic acid and L-glutamic acid in the spectral range 20–3500 cm^{-1} recorded at room temperature.

6. Basic, polar amino acids

L-Lysine, ***L-arginine*** and ***L-histidine*** are the basic, polar amino acids. Lysine has as characteristic a radical composed of the following group of atoms CH_2–CH_2–CH_2–CH_2–NH_2. Almost no work on Raman spectroscopy of L-lysine was published. However, Hernández et al. [40] showed the assignment of the main modes of the Raman spectrum of L-lysine. For example, the stretching of CC is observed at 1012, 1033, 1063, and 1076 cm^{-1}; the antisymmetric rocking of NH_3^+ is observed at 1143 and 1183 cm^{-1}; the antisymmetric bending of NH_3^+ appears as bands at 1615 and 1650 cm^{-1}; the symmetric stretching of CO_2^- at 1415 cm^{-1} and the antisymmetric stretching of CO_2^- at 1598 cm^{-1}. Hernández et al. [40] also presented a tentative assignment of most bands appearing in the Raman spectrum of L-arginine. The radical characterizing L-arginine is CH_2–CH_2–CH_2–NH–C–NH–NH_2. The Raman spectrum of L-arginine shows bands at 1011 and 1035 cm^{-1} which are associated with CC stretching, while a band at 970 cm^{-1} is associated with CN stretching. Rocking of NH_3^+ is observed at 1164 cm

$^{-1}$ and antisymmetric bending of CNH_2 is observed at 1176 cm^{-1}. The symmetric stretching of CO_2^- is observed at 1581 cm^{-1} and the antisymmetric stretching of CO_2^- appears at 1581 cm^{-1} [40].

L-histidine was investigated through Raman spectroscopy in a recent paper that explored the vibrational behavior of the crystal under cryogenic conditions [41]. L-histidine can crystallize in two different polymorphs with monoclinic or orthorhombic symmetry. The work of reference [41] has investigated the orthorhombic form of the crystal that presents a $P2_12_12_1$ space group with four molecules per unit cell. It is interesting to note that many of the amino acids crystallize in a $P2_12_12_1$ space group with orthorhombic structure or in a $P2_1$ space group with monoclinic structure; this possibly is related to the packing of molecules in the unit cell, but this point will not be explored in the present text. Returning to the case of L-histidine, the Raman scattering study in reference [41] showed a series of discontinuity in the wavenumber of bands at about 165 K. This was interpreted as consequence of a conformational phase transition through involving both CO_2^- and NH_3^+ groups. It is interesting to add the information that L-arginine and L-histidine can also easily grow as hydrated and as chloride hydrated crystals. In **Figure 11**, the Raman spectra of L-histidine hydrochloride monohydrated crystal are shown for three different scattering geometries in order to illustrate a case of an amino acid crystallizing with water and HCl units.

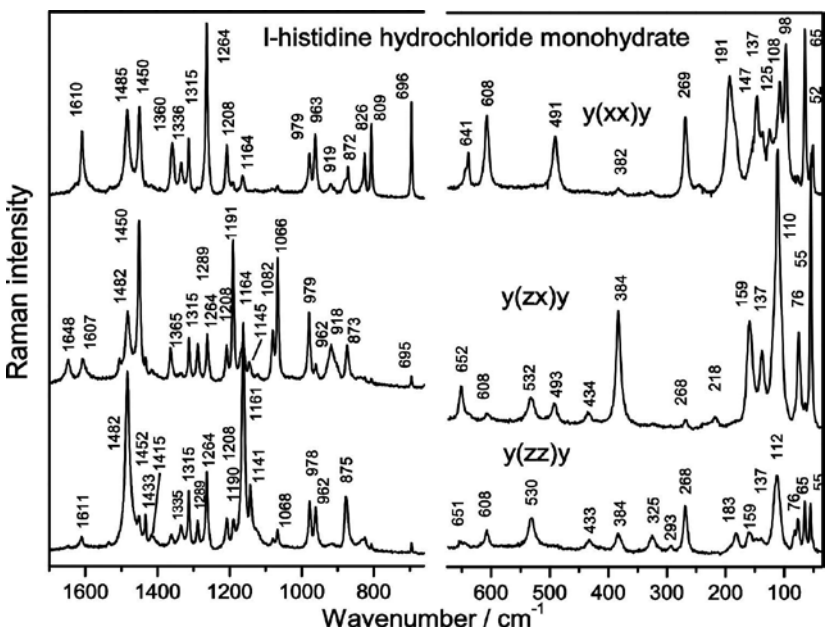

Figure 11. Raman spectra of L-histidine hydrochloride monohydrate in three scattering geometries (adapted from reference [43]).

Up to now, the Raman scattering investigations have furnished an interesting picture about the vibrational aspects of diverse amino acids. Some studies have even studied the behavior

of the crystals under extreme conditions, low temperature or high pressure. However, a complete understanding involving connections, for example, between the hydrogen bonds and the physical properties of the crystal is still lacking. Obviously, some preliminary attempts are already known, such as a possible connection between the dimensions of hydrogen bonds and the behavior of torsional vibration of NH_3^+ under high pressure (for L-alanine, L-threonine, and taurine [17]). A fundamental question in biochemistry is to realize why the proteins of all living beings are formed by the L-form of amino acids (the D-form is found only isolated in the plasma of certain cells). Some glimpses were given by Abdus Salam who speculates the occurrence of a phase transition explained through BCS theory, gauge field theory, and Higgs mechanism [44]. There is also suggestion that ultraviolet radiation should be able to select one of the chiral forms of the amino acid, but, in fact, all these suggestions are suppositions waiting for confirmation. This problem deserves future investigations. But, is the behavior of D-amino acid crystals the same of L-amino acids under extreme conditions? At first, the answer to this question should be positive because both L- and D-forms of the amino acids are equivalent from an energetic point of view. However, some preliminary results point to different behavior for the two forms in some special cases, but we do not have space to discuss such intriguing point in this chapter. Maybe, surprising information is waiting for us in the coming years.

7. Beyond amino acids

The success obtained by the investigation of amino acids has incentivized the study of other simple organic molecules of living beings. After furnishing a more or less closed picture about amino acids, the next natural step is the study of peptides, but we will not discuss them in this chapter. We prefer to analyze another natural choose, molecules involved in the DNA structure. One example we will explore in this chapter is thymidine, a nucleoside constituted of a deoxyribose and the pyrimidine base thymine. It is found in the DNA of all living organisms. The Raman spectrum presents a very intense set of bands in the low wavenumber region that are associated with the lattice modes (**Figure 12**). This is very interesting because in future analysis of the crystal under extreme conditions, the behavior of the lattice modes should be a pivotal point in order to understand eventual structural modification. A strong band observed at 1665 cm^{-1} is assigned as in-plane vibration involving C = O and C = C and a band at 1690 cm^{-1} is assigned as stretching C = O, ν(C=O). Bending of CH_3, δ(CH_3), is identified as the band at 1438, 1457, and 1480 cm^{-1}. The band observed at 1031 cm^{-1} is associated with bending of CNH, δ(CNH), and the band at 1000 cm^{-1} is associated with bending OCH, δ(OCH). An out-of-plane vibration involving CH is observed at 972 cm^{-1} and a pyrimidine ring breathing is observed at 773 cm^{-1}. Additionally, out-of-plane vibration involving CCH_3 group is observed at 396 and 378 cm^{-1} and in plane vibration involving the same group is observed at 276 and 306 cm^{-1}. In the high wavenumber region of the Raman spectrum is possible to observe a series of bands, among them one observed at 3298 cm^{-1} that was assigned as stretching of OH, ν(OH). A series of bands is observed at 2952, 2965, 2973, and 2991 cm^{-1} and they are classified as stretching of CH, CH_2, and CH_3 units. Finally, let us single out an important point related to the study of thymidine, its behavior as a function of temperature.

In order to make the presentation of this section more complete, we have performed study of thymidine crystal under low temperature. Analysis of the Raman spectra of thymidine showed that the wavenumber of several bands presents jumps at about 160 K, suggesting the occurrence of a conformational modification due change of hydrogen bonds. A comparison with the behavior of amino acid crystals will be welcome, and we hope that in a few time we will have an overview of the subject.

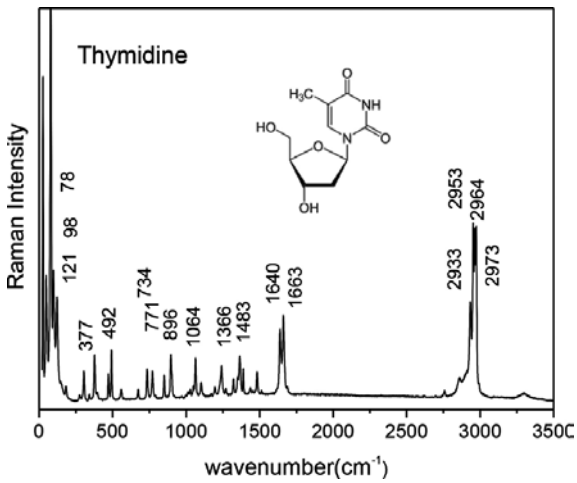

Figure 12. Raman spectrum of thymidine; in the inset a representation of the molecule.

In résumé, in this chapter, a complete picture about the Raman spectra of the 20 proteinogenic amino acid crystals was furnished and some aspects related to the modification of these spectra under extreme conditions were also discussed. As additional information we discussed the Raman spectrum of thymidine, an organic molecule involved in the formation of DNA.

Acknowledgements

The authors acknowledge financial support from CNPq and FUNCAP through PRONEX program.

Author details

Paulo T.C. Freire*, Felipe M. Barboza, José A. Lima Jr., Francisco E.A. Melo and Josué Mendes Filho

*Address all correspondence to: tarso@fisica.ufc.br

Department of Physics, Federal University of Ceará, Fortaleza, Ceará, Brazil

References

[1] Fleck M, Petrosyan AM, Salts of Amino Acids: Crystallization, Structure and Properties. Heidelberg: Springer; 2011. 574 p. DOI: 10.1007/978-3-319-06299-0_1.

[2] Boldyreva E, Crystalline Amino Acids: A Link between Chemistry, Materials Science and Biology, In: Boyens JCA, Ogilvie JF, editors. Models, Mysteries, and Magic of Molecules. Netherlands: Springer; 2007. pp. 167–192. DOI: 10.1007/978-1-4020-5941-4.

[3] Freire PTC, Pressure-Induced Phase Transitions in Crystalline Amino Acids, In: Boldyreva E, Dera P, editors, High Pressure Crystallography – From Fundamental Phenomena to Technological Applications. New York: Springer; 2010. pp. 559–572. DOI: 10.1007/978-90-481-9258-8.

[4] Görbitz CH, Crystal structures of amino acids: from bond lengths in glycine to metal complexes and high-pressure polymorphs, Crystallography Reviews 2015; 21: 160–212, DOI: 10.1080/0889311X.2014.964229.

[5] Freire PTC, Lima Jr JA, Abagaro BTO, Pinheiro GS, Silva JAF, Filho JM, Melo FEA, High Pressure Raman Spectra of Amino Acid Crystals. In: Dominique de Caro, editor. Vibrational Spectroscopy. Rijeka: InTech; 2012. pp. 37–58. DOI: 10.5772/1345. ch2

[6] Boldyreva EV, Drebushchak VA, Drebushchak TN, Paukov IE, Kovalevskaya YA, Shutova ES, Polymorphism of glycine. Thermodynamic aspects. Part I: Relative stability of the polymorphs, Journal of Thermal Analysis and Calorimetry. 2003; 73: 409–418. DOI: 10.1023/A:1025405508035.

[7] Murli C, Sharma SM, Karmakar S, Sikka SK, α-glycine under high pressures: a Raman study, Physica B 2003; 339: 23–30. DOI: 10.1016/S0921-4526(03)00446-0.

[8] Goryainov SV, Kolesnik EN, Boldyreva EV, A reversible pressure-induced phase transition in β-glycine at 0.76 GPa, Physica B 2005; 357: 340–357. DOI: 10.1016/j.physb.2004.11.089.

[9] Boldyreva EV, Drebushchak VA, Drebushchak TN, Paukov IE, Kovalevskaya YA, Shutova ES, Polymorphism of glycine, Part II, Journal of Thermal Analysis and Calorimetry 2003; 73: 419–428. DOI: 10.1023/A:1025457524874.

[10] Boldyreva EV, Ivashevskaya SN, Sowa H, Ahsbahs H, Weber H-P, Effect of hydrostatic pressure on the γ-polymorph of glycine 1. A polymorphic transition into a new δ-form, Zeitschrift für Kristallographie 2005; 220: 50–57. DOI: 10.1524/zkri.220.1.50.58886.

[11] Goryainov SV, Boldyreva EV, Kolesnik EM, Raman observation of a new (ζ) polymorph of glycine? Chemical Physics Letters 2006; 419: 406–500. DOI: 10.1016/j.cplett.2005.11.123.

[12] Wang CH, Storms RD, Raman study of hydrogen bonding and long-wavelength lattice modes in an L-alanine single crystal, Journal of Chemical Physics 1971; 55: 5110–5119. DOI: 10.1063/1.1675629.

[13] Susi H, Byler DM, Vibrational analysis of L-alanine and deuterated analogs, Journal of Molecular Structure 1980; 63: 1–11. DOI: 10.1016/0022-2860(80)85305-1.

[14] Diem M, Polavarapu PL, Oboodi M, Nafie LA, Vibrational circular dichroism in amino acids and peptides. 4. Vibrational analysis, assignments, and solution-phase Raman spectra of deuterated isotopomers of alanine, Journal of American Chemistry Society 1982; 104: 3329–3336. DOI: 10.1021/ja00376a014.

[15] Rozenberg M, Shoham G, Reva I, Fausto R, Low-temperature Fourier transform infrared spectra and hydrogen bonding in polycrystalline L-alanine, Spectrochimica Acta A 2003; 59: 3253–3266. DOI: 10.1016/S1386-1425(03)00159-8.

[16] Vik AF, Yuzyuk YI, Barthes M, Sauvajol J-L, Low-wavenumber dynamics of L-alanine, Journal of Raman Spectroscopy 2005; 36: 749–754. DOI: 10.1002/jrs.1328.

[17] Freire PTC, Melo FEA, Mendes Filho J, Lima RJC, Teixeira AMR, The behavior of NH_3 torsional vibration of L-alanine, L-threonine and taurine crystals under high pressure: a Raman spectroscopic stugy, Vibrational Spectroscopy 2007; 45: 99–102. DOI: 10.1016/j.vibspec.2007.05.003.

[18] Teixeira AMR, Freire PTC, Moreno AJD, Sasaki JM, Ayala AP, Mendes Filho J, Melo FEA, High-pressure Raman study of L-alanine crystal, Solid State Communications 2000; 116: 405–409. DOI: 10.1016/S0038-1098(00)00342-2.

[19] Tumanov NA, Boldyreva EV, Kolesov BA, Kurnosov AV, Cabrera RQ, Pressure-induced phase transitions in L-alanine, revisited, Acta Crystallographica 2010; B 66: 458–471. DOI: 10.1107/5010876811001983X.

[20] Funnell NP, Dawson A, Francis D, Lennie AR, Marshall WG, Moggach AS, Warren JE, Parsons S, The effect of pressure on the crystal structure of L-alanine, CrysEngComm 2010; 12: 2573–2583. DOI: 10.1039/c001296c.

[21] Lima Jr. JA, Freire PTC, Lima RJC, Moreno AJD, Mendes Filho J, Melo FEA, Raman scattering of L-valine crystals, Journal of Raman Spectroscopy 2005; 36: 1076–1081. DOI: 10.1002/jrs.1410.

[22] Façanha Filho PF, Freire PTC, Lima KVC, Mendes Filho J, Melo FEA, Pizani PS, High temperature Raman spectra of L-leucine crystals, Brazilian Journal of Physics 2008; 38: 131–137. DOI: 10.1590/S0103-97332008000100024.

[23] Façanha Filho PF, Freire PTC, Melo FEA, Lemos V, Mendes Filho J, Pizani PS, Rossatto DZ, Pressure-induced phase transitions in L-leucine crystals, Journal of Raman Spectroscopy 2009; 40: 46–51. DOI: 10.1002/jrs.2071.

[24] Almeida FM, Freire PTC, Lima RJC, Remédios CMR, Mendes Filho J, Melo FEA, Raman spectra of L-isoleucine crystals, Journal of Raman Spectroscopy 2006; 37: 1296–1301. DOI: 10.1002/jrs.1553.

[25] Olsztynska S, Komorowska M, Vrielynck L, Dupuy N, Vibrational spectroscopic study of L-phenylalanine: effect of pH, Applied Spectroscopy 2001; 55: 901–907. DOI: 0003-7028/01/5507-0901.

[26] Chuang C-H, Chen Y-T, Raman scattering of L-tryptophan enhanced by surface Plasmon of silver nanoparticles: vibrational assignment and structural determination, Journal of Raman Spectroscopy 2009; 40: 150–156. DOI:10.1002/jrs.2097

[27] Lima JA, Freire PTC, Melho FEA, Lemos V, Mendes Filho J, Pizani PS, High pressure Raman spectra of L-methionine crystal, Journal of Raman Spectroscopy 2008; 39: 1356–1363. DOI: 10.1002/jrs.2005

[28] Kolesov BA, Minkov VS, Boldyreva EV, Drebushchak TN. Phase transitions in the crystals of L- and DL-cysteine on cooling: intermolecular hydrogen bonds distortions and the side-chain motions of thiol-groups. 1. L-cysteine, Journal of Physical Chemistry B 2008; 112: 12827–12839. DOI: 10.1021/jp804142c.

[29] Barthes M, Bordallo HN, Dénoyer F, Lorenzo J-E, Zaccaro J, Robert A, Zontone F. Micro-transitions or breathers in L-alanine? The European Physical Journal B 2004; 37: 375–382. DOI: 10.1140/epjb/e2004-00069-1.

[30] Souza JM, Freire PTC, Bordallo HN, Argyriou DN. Structural isotopic effects in the smallest chiral amino acid: observation of a structural phase transition in fully deuterated alanine. Journal of Physical Chemistry B 2007; 111: 5034–5039. DOI: 10.1021/jp070366z.

[31] Minkov VS, Krylov AS, Boldyreva EV, Goryainov SV, Bizyaev SN Vtyurin AN, Pressure-induced phase transitions in crystalline L- and DL-cysteine, Journal of Physical Chemistry B 2008; 112: 8851–8854. DOI: 13.1021/jp8020276.

[32] Kolesov BA, Boldyreva EV, Difference in the dynamic properties of chiral and racemic crystals of serine studied by Raman spectroscopy at 3–295 K, Journal of Physical Chemistry B 2007; 111: 14387–14397. DOI: 10.1021/jp076083o.

[33] Dhamelincourt P, Famirez FJ, Polarized micro-Raman and FT-IR spectra of L-glutamine, Applied Spectroscopy 1993; 47: 446–451. DOI: 10.1366/0003702934335083.

[34] Moreno AJD, Freire PTC, Melo FEA, Mendes Filho J, Nogueira MAM, Almeida MA, Miranda MAR, Remédios CMR, Sasaki JM, Low-temperature Raman spectra of monohydrated L-asparagine crystals, Journal of Raman Spectroscopy 2004; 35: 236–241. DOI: 10.1002/jrs.1141.

[35] Bento ICV, Freire PTC, Melo FEA, Mendes Filho J, Moreno AJC, Joya MR, Pizani PS, High temperature phase transition in monohydrated L-asparagine crystal, Solid State Communications 2007; 141: 29–32. DOI: 10.1016/j.ssc.2006.09.041.

[36] Silva JAF, Freire PTC, Lima JA, Mendes Filho J, Melo FEA, Moreno AJD, Polian A, Raman spectroscopy of monohydrated L-asparagine up to 30 GPa, Vibrational Spectroscopy 2015; 77: 35–39. DOI: 10.1016/j.vibspec.2015.02.006.

[37] Silva BL, Freire PTC, Guedes I, Araújo-Silva MA, Mendes Filho J, Moreno AJD, Polarized Raman spectra and infrared analysis of vibrational modes in L-threonine crystals, Brazilian Journal of Physics 1998; 28: 19–24. DOI: 10.1590/S0103-97331998000100003.

[38] Holanda RO, Lima JA, Freire PTC, Melo FEA, Mendes Filho J, Polian A, New pressure-induced phase transitions of L-threonine crystal: a Raman spectroscopic study, Journal of Molecular Structure 2015; 1092: 160–165. DOI: 10.1016/j.molstruc.2015.03.024.

[39] Luz-Lima C, Sousa GP, Lima Jr. JA, Melo FEA, Mendes Filho J, Polian A, Freire PTC, High pressure Raman spectra of β form of L-glutamic acid, Vibrational Spectroscopy 2012; 48: 181–187. DOI: 10.1016/j.vibspec.2011.12.005.

[40] Hernández B, Pflüger F, Derbel N, De Coninck J, Ghomi M, Vibrational analysis of amino acids and short peptides in hydrated media. VI. Amino acids with positively charged side chains: L-Lysine and L-Arginine, Journal of Physical Chemistry B 2010; 114: 1077–1088. DOI: 10.1021/jp909517r.

[41] De Sousa GP, Freire PTC, Mendes Filho J, Melo FEA, Lima CL, Low-temperature Raman spectra of L-histidine crystals, Brazilian Journal of Physics 2013; 43: 137–144. DOI: 10.1007/s13538-013-0132-3.

[42] Faria JLB, Almeida FM, Pilla O, Rossi F, Sasaki JM, Melo FEA, Mendes Filho J, Freire PTC, Raman spectra of L-histidine hydrochloride monohydrate crystal, Journal of Raman Spectroscopy 2004; 35: 242–248. DOI: 10.1002/jrs.1142.

[43] Long DA, The Raman Effect, John Wiley & Sons, Chichester 2002. DOI: 10.1002/0470845767.

[44] Salam A, Chirality, phase transitions and their induction in amino acids, Physics Letters B 1992; 288: 153–160. DOI: 10.1016/0370-2693(92)91970-K.

Chapter 11

Raman Spectroscopy with X-Rays

Piter Sybren Miedema

Additional information is available at the end of the chapter

http://dx.doi.org/10.5772/65427

Abstract

The Raman effect in the X-ray wavelength regime as applied to spectroscopy is described in this chapter: The concepts of these X-ray Raman spectroscopies, (nonresonant) X-ray Raman spectroscopy, and resonant X-ray Raman spectroscopy, better known under the name resonant inelastic X-ray scattering, have been shortly described, and this chapter further focuses on (why) using these spectroscopic methods by showing some current applications of these techniques. As well, some possible future applications are mentioned.

Keywords: X-ray Raman spectroscopy, resonant inelastic X-ray scattering (RIXS), synchrotrons, X-ray free-electron lasers, X-ray absorption spectroscopy, X-ray emission spectroscopy

1. Introduction

Raman spectroscopy studies are commonly employed in the UV and visible light (UV-VIS) regime, making use of an easily available monochromatic UV-VIS (laser) incoming beam and measuring energy losses (or energy gains) related to vibrational and rotational states of the system of interest. As such, Raman spectroscopy is used in chemistry to provide fingerprints by which molecules can be identified. The principle of Raman spectroscopy is the Raman effect of a photon upon interaction with matter: when a photon is scattered from an atom or molecule (or crystal), a small fraction of the scattered photons are scattered by an excitation, with the scattered photons having an energy different from that of the incident photons. In most cases, the scattered energy is lower, which is called Stokes Raman scattering, and in the less common case, when the scattered energy is increased, it is called anti-Stokes Raman scattering. Thus, Raman relies on inelastic scattering (Raman scattering) of monochromatic light, usually from a laser in the visible, near-infrared, or ultraviolet range.

However, based on the basics of the Raman effect mentioned above, there is no reason why the Raman effect should not be present in other wavelength regimes, and this chapter deals with the Raman analogues in the X-ray regime: X-ray Raman spectroscopy (XRS) and resonant X-ray Raman spectroscopy or the more commonly used term resonant inelastic X-ray scattering (RIXS). This chapter provides details concerning this X-ray regime Raman spectroscopy being not only a fingerprint for molecules but even an element-dependent electronic structure fingerprint. In general, X-ray spectroscopies may supply electronic structure information on element-specific oxidation and spin states.

As well as for the UV-VIS regime, XRS and RIXS can deal with vibrational or phonon energy losses and/or gains, which will only be shortly discussed in Section 3. Besides, since X-ray photons have much higher energy than UV-VIS photons, one may observe much bigger energy losses, which will be explained in detail in Section 3. Some applications of XRS will be covered in Section 4. In Section 5, RIXS will be explained and Section 6 shows some applications of RIXS spectroscopy. But at first we take a step back in Section 2, where some basics on X-ray spectroscopies in general are covered.

2. Some basics about X-ray spectroscopies – absorption spectroscopy

While moving in the wavelength regime from UV-VIS to X-rays, one must realize that X-ray photons have substantially more energy than UV-VIS photons. Whereas UV-VIS photons above certain energy can excite valence electrons into the conduction band, the energy of X-ray photons can be applied to excite core electrons into the conduction band. In general, the unit electronvolt (eV) is used in X-ray spectroscopies, which corresponds to 1 eV = 1.60210 × 10^{-19} J = 8065.73 cm^{-1}. As for other absorption spectroscopies, X-ray absorption spectroscopy (XAS) is a matter of measuring the difference between the intensity of the incoming beam and transmitted beam following the Lambert–Beer's law:

$$I_t = I_0 e^{-\mu t} \tag{1}$$

where t is the sample thickness and μ is the absorption coefficient. I_t is the transmitted intensity and I_0 is the incoming intensity. For XAS, the absorption coefficient μ gives the probability that X-rays will be absorbed. At most X-ray energies, the absorption coefficient is a smooth function of energy, with a value that depends on the sample density ϱ, the atomic number Z, atomic mass A, and the X-ray energy E roughly as:

$$\approx \frac{\rho Z^4}{AE^3} \tag{2}$$

The strong dependence of μ on both atomic number Z and energy E is a fundamental property of X-rays. With X-ray spectroscopies, one can gain information about selected elements by

choosing the right X-ray energy range; due to the high energy of X-ray photons, these photons may lead to the excitation of core electrons to unoccupied levels. The energy of these core electron levels is determined by the type of element. That is, in a nutshell why X-ray absorption-related spectroscopies are element-specific. As an example the X-ray transmission of cobalt and iron is shown in **Figure 1** for sample thicknesses of 0.2 μ. The energy level of the iron 1s core level is at about 7112 eV (black dotted line in **Figure 1**), and the energy level of the next neighbor in the periodic table cobalt 1s lies at about 7709 eV (red solid line in **Figure 1**) as can be seen from the decrease in the transmission of X-rays around this energy. A difference of 600 eV is substantial keeping in mind that 1 eV corresponds to 8065.73 cm^{-1}.

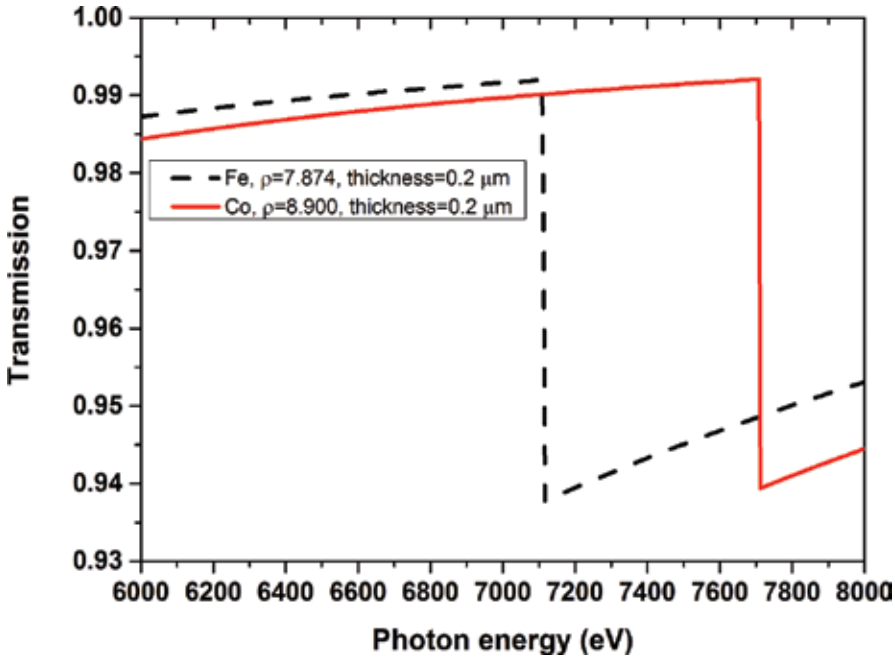

Figure 1. X-ray transmission for iron and cobalt with thicknesses of 0.2 μm as available from CXRO (henke.lbl.gov/optical_constants/filter2.html).

One prerequisite for XAS (and as well for many other X-ray spectroscopies) is a widely energy-tunable X-ray source, and in general, synchrotron radiation is required. Table-top tunable X-ray sources are coming up as well, but the required brilliance for photon-in photon-out spectroscopies such as XRS and RIXS is only available at synchrotrons and X-ray free-electron lasers (X-ray FELs). For an overview of available synchrotrons and FELs, see www.lightsources.org.

Because the core-level energies are so different for different types of atoms, it means that the absorption of an X-ray photon is element-specific. In addition, many X-ray spectroscopies are as well able to identify relative oxidation states (see for example Refs. [1, 2]) and spin states (see for example Refs. [1, 3, 4]). For the heavier elements, there will be more than one core

level. For example, for the previously mentioned iron, there is the 1s core level (K-edge), and 2s (L_1-edge), and 2p levels ($L_{2,3}$-edge), and the 3s (M_1-edge) and 3p levels ($M_{2,3}$-edge) may also be considered as core levels. The word "edge" comes historically from the fact that at certain X-ray energies, there is a steep change in absorption: these sharp rises in X-ray absorption (or deep decreases in X-ray transmission as seen in **Figure 1**) are due to reaching the binding energy of a certain core level. The edges are named after the excited core-level electron as indicated in between brackets above (K-edge, L-edge, etc.).

From the chemistry perspective, one would like to use the X-ray edge, which is sharpest with the best energy resolution or in other words with the best chemical resolution. These "best chemical resolution edges" appear for all elements between 40 and 1000 eV [5], in the so-called (VUV to) soft X-ray regime.

In general, X-ray energies above 2000 eV are considered to be part of the hard X-ray regime. The energy region between 1000 and 2000 eV is some intermediate tender X-ray regime, which is sometimes considered to be a separate part and sometimes part of either the soft X-ray regime or the hard X-ray regime. The terms hard X-ray and soft X-ray refer to their penetration depth in air. Soft X-ray photons below 1000 eV do not penetrate far through air (due to absorption by CO_2, O_2, and N_2), and that is why in the soft X-ray regime, measurements are normally performed under vacuum. Hard X-rays do penetrate through air, and in this regime, Röntgen originally discovered X-ray radiation. As hard X-rays do penetrate through air, experiments with hard X-rays normally are performed with safety lead shields around the experiment in order to absorb the hard X-rays and protect the surrounding, for example, the spectroscopists/scientists from exposure to X-rays.

Note that in hospitals, they actually make use of the penetration depth of hard X-rays for X-ray CT scans: since bones absorb stronger than other parts of the human body, but still a substantial part of the incident X-ray beam is completely transmitted through the body, this CT scan tells you something about bone breaking.

As mentioned previously, the best chemical resolution edges are in the soft X-ray regime and this X-ray regime has limits on the measurement conditions: in general high vacuum operation conditions (below 10^{-7} mbar), although there are developments into operation under milder vacuum conditions, for example, soft X-ray emission on liquids in the 10^{-3} mbar regime [6] and X-ray photoelectron and electron yield X-ray absorption spectroscopy on solids in the 1 mbar [7–9] to 1 bar regime [10].

In the next section, it will become clear how X-ray Raman spectroscopy circumvents the constraints of the soft X-ray regime, while still leading to spectra that resemble the soft X-ray edge with the best chemical resolution.

3. X-ray Raman spectroscopy

X-ray Raman Spectroscopy (XRS) or nonresonant inelastic X-ray scattering (NIXS) is a spectroscopy that makes use of the Raman concept as sketched in **Figure 2**; there is a mono-

chromatic incoming X-ray beam with energy E_0, and the scattered X-rays are measured as function of the emitted energy E_f. The incoming and scattered X-rays do not have to directly correspond to an X-ray edge; however, the Raman energy loss ΔE due to a scattering event may be related to some core-level excitation (or to phonon excitation like in typical Raman spectroscopies).

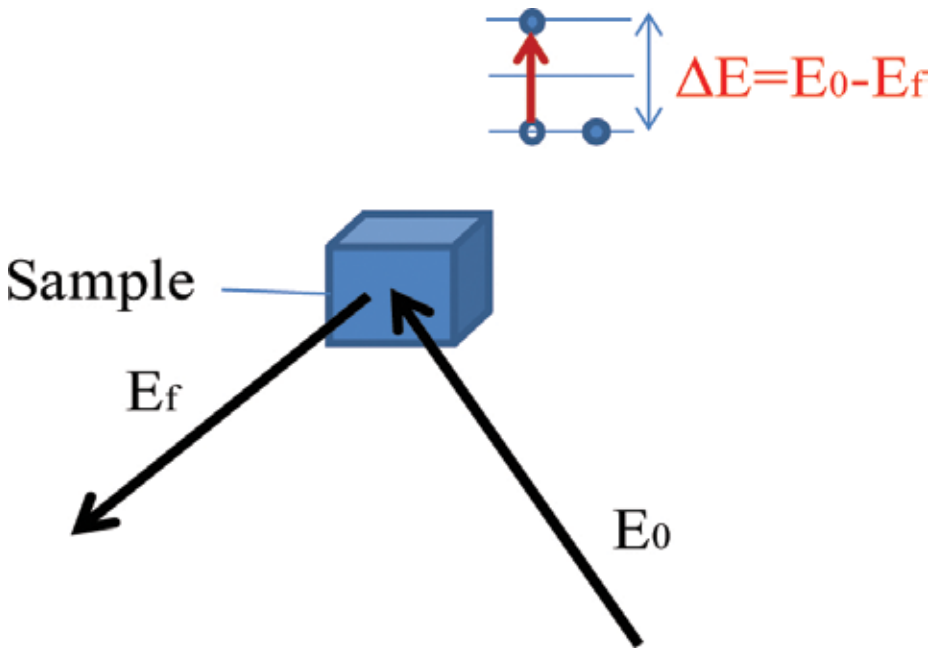

Figure 2. Schematic representation of the X-ray Raman process.

Note that in this scattering process, there are other events which are much more likely, elastic (Rayleigh) scattering and Compton scattering (see for example the relative intensities in **Figure 1** of Ref. [11]). Initially, the low cross section of XRS made this technique impractical, but intense new X-ray facilities, third-generation synchrotrons and X-ray free-electron lasers (FELs), and improvements in X-ray optics helped XRS to become an interesting spectroscopic tool.

XRS is a technique that retains the experimental advantages of hard X-ray measurements, for example, deeper probing depth implying more realistic samples, less beam damage due to lower scattering cross section, experiments in a gas or liquid environment or under higher pressures, while revealing the information equivalent to the soft X-ray XAS. In particular, for K-edges of the light-weight elements, which have really low VUV to soft X-ray energies as their edge, leading to a substantial low penetration depth, XRS can circumvent the problems related to soft X-rays. The difference between XRS and XAS is the transition operator. In XAS, the electronic transition can be approximated as a dipole transition, while for XRS also higher-order transitions (quadrupole) are allowed, depending on the q-vector, related to the angle

between incident and scattered X-rays. At low values for q, only dipole transitions are allowed, so far low-q XRS compares well with XAS. For high-q, higher-order transitions are present in XRS, which will be shortly discussed in the next section.

XRS, RIXS, and nonresonant X-ray emission spectroscopy (XES), where RIXS and XES will be discussed in more detail later on, are second-order optical processes where the excitation and de-excitation processes are coherently correlated by the Kramers-Heisenberg formula depicted here:

$$F(\Omega,\omega) = \sum_j \left| \sum_i \frac{\langle j|T_2|i\rangle\langle i|T_1|g\rangle}{E_g+\hbar\Omega-E_i+i\Gamma_i} \right|^2 \delta(E_g + \hbar\Omega - \mathrm{E}_j - \hbar\omega) \quad (3)$$

Where $\hbar\omega$ and $\hbar\Omega$ are the energies of the incident X-ray and emitted/scattered X-ray energy, respectively. j, i, and g present the final, intermediate, and ground states, respectively. T_1 and T_2 represent the radiative transitions by incident and emitted photons, and Γ_i represents the spectral broadening due to the core-hole lifetime in the intermediate state. δ is the energy conservation of the process with difference in the ground state energy plus the X-ray emitted energy with the final state energy plus the incident X-ray energy. As this formula shows there is a dependence on the core-hole lifetime, which can be made use of to study core-hole state dynamics in RIXS spectroscopy (discussed later in Section 6).

In electron spectroscopies, a spectroscopy equivalent to XRS exists, which is called electron energy-loss spectroscopy (EELS). Both XRS and EELS give information similar to XAS, but because the transitions in XRS and EELS occur in a different way, the transition operator is different. However, at low momentum transfer (low q-vector), the transition operator in EELS and XRS can be approximated as a dipole operator, and in that case, the spectral shape agrees with XAS.

XRS can be measured in two modes: (A) the direct analogue of common Raman spectroscopy: a monochromatic X-ray beam is used and the emitted X-ray beam is measured as function of energy loss (or emission energy). (B) The emitted X-ray energy is fixed and the incoming X-ray beam is varied, the so-called inverse energy scan technique. Currently, mode B is applied more often since it is easier to change the incoming monochromatic energy than the settings of the emission spectrometer for different emission energies; however, with dispersive X-ray emission spectrometers [12], mode A may become the standard mode, which would be beneficial for (femtosecond) time-resolved studies with X-ray FELs.

Besides the use of XRS as some correspondence spectroscopy to XAS, one can also measure low-loss features such as phonons (vibrations for molecules) and plasmons as with traditional Raman spectroscopy. In this meV energy-loss scale, the technique is actually often called as NIXS or IXS. The advantage of NIXS compared to traditional (UV-VIS regime) Raman spectroscopy is that the X-rays penetrate deeper in materials than UV-VIS photons, so the energy loss obtained related to phonons and plasmons with NIXS might give a more bulk-like picture of the phonon and plasmon behavior of the system of interest. As well a wider energy

http://dx.doi.org/10.5772/65427

and momentum space can be probed with synchrotron radiation. This NIXS will not be discussed further, one is referred to Refs. [13–16].

4. Some applications of X-ray Raman spectroscopy

4.1. *In situ* X-ray spectra of light elements

XAS of light elements, such as lithium (Li), boron (B) and carbon (C), occurs in the soft X-ray energy range at about 60, 180, and 280 eV, respectively. In general, XAS can be measured in transmission, electron, or ion yield or fluorescence yield mode. Due to the path lengths of soft X-rays, transmission X-ray absorption measurements in this soft X-ray energy range of 50–300 eV are very difficult. The electron yield mode of XAS is an alternative surface-sensitive measure for the standard transmission XAS mode. Concerning *in situ* XAS studies, it can as yet only be performed at the mbar to bar pressure range, for example, as shown in Refs. [7, 9]. Fluorescence yield XAS probes deeper into the sample, but this probe has very low yield for soft X-ray energies and may suffer from saturation effects in concentrated systems. At the same time, the incoming X-ray probe of 60–280 eV does not penetrate deep enough and still mostly surface is probed with fluorescence yield XAS. With XRS, one is able to measure more bulk-like properties of light elements [11]. There are a few dedicated XRS setups in the world, where I would like to mention a setup at the European Synchrotron Radiation Facility (ESRF) [17, 18] and another setup at the Stanford Synchrotron Radiation Lightsource (SSRL) [19, 20].

As an example, we discuss XRS measurements performed on (nanosized) $LiBH_4$ hydrogen storage materials [21, 22] at the setup of SSRL [19]. For those experiments, the XRS scans were performed using the inverse energy scan technique with a fixed analyzer energy of 6462.20 eV (mode B mentioned in Section 3). The XRS spectra of this example were measured using 25 detector crystals with an average q-vector of 1.3 atomic units, implying essentially pure dipole transitions, while this dedicated XRS setup had many more detector crystals (at that time 40) which may allow as well higher-order transitions [19], see next sections, but for these studies the other detector crystals were covered. The main additional reason besides the issues mentioned at the beginning of this subchapter for performing XRS experiments on these hydrogen storage materials was that the samples need to be under humid-free environment, and with hydrogen release as well as the pressure is rising, measurements with soft X-rays would be difficult. This example showed that it is possible to study the electronic properties of Li, B, and C of bulk and $LiBH_4$-carbon nanocomposites ($LiBH_4$-C) during de-hydrogenation and the first step of re-hydrogenation.

In particular, for nanocomposites, this is important since there are no many techniques, like XRD used on the bulk samples, able to grasp the electronic structure information on such small and often amorphous materials. In addition, XRS was used to study the decomposition of $NaBH_4$–C nanocomposites (shown in the ESI,† Section S10 of Ref [22]). Note that XRS studies on the lithium edge have as well become relevant for other lithium systems [23] and battery applications, *in situ* de- and re-charging [20]. On the other hand, there are other borohydrides

where the B K-edge XRS (and in addition the Mg L-edge XRS) has recently been measured for another possible hydrogen storage material, $Mg(BH_4)_2$ [24].

4.2. Materials under pressure and in the liquid phase

Although the previously mentioned hydrogen storage materials were only under 1 bar of nitrogen/hydrogen, XRS is also applied in studies with even higher pressures to study the effect of it on materials [25], for example, on iron to gain information on the behavior of it in the inner core of earth [26]. In these higher-pressure studies, phonon scattering is often studied with XRS [27, 28] (NIXS or IXS mentioned in the previous section) to study pressure-induced phase transitions and how the phonon spectrum changes. Since XRS is applied in the hard X-ray regime, it is also easier to get electronic structure measures, similar to direct XAS, on liquid phase systems [29, 30].

4.3. Higher-order electronic transitions

In Section 3, it was mentioned that XRS and XAS may give similar results, but with XRS one is as well able to obtain higher-order transitions above the dipole transition. It has been shown in Ref [31] that octupole transitions can be observed in XRS on rare earth phosphates $RePO_4$ with Re = La, Ce, Pr, and Nd. In this respect, XRS might potentially be used in measuring otherwise spectroscopically unavailable excited states or "optically dark states."

4.4. Summary

In summary, XRS has been mostly used for (*in situ*) electronic structure studies on light elements as the alternative to XAS, and there is a strong focus on materials under high-pressure conditions. In general, XRS studies may become important as well for studies on (heterogenous) catalysts under (close to) industrial operation conditions, because of the advantage of the edge with best chemical resolution without the constraints of the soft X-ray regime (vacuum). As well, XRS is used to gain understanding of the momentum space of phonons of materials of interest (which was not covered in this section).

5. RIXS

Resonant X-ray Raman spectroscopy is now more commonly known as RIXS, but other terms such as resonant X-ray fluorescence spectroscopy (RXFS) and resonant X-ray emission spectroscopy (RXES) have also been used in the past. With RIXS, the incoming X-ray photon energy corresponds (or is close) to an X-ray edge in contrast to XRS. The RIXS process is schematically shown with an one-electron scheme in **Figure 3** next to schematically shown XAS and XES process. The first step of the RIXS process is the same as the XAS process. The second transition is emission from some state, and here it is shown as emission from an occupied state. The XES process is similar to that second step. The processes of RIXS are here only shortly described. For more details on (theory of) RIXS one is referred to Refs. [1, 32–35].

However, for RIXS, the excited electron can relax back into the core hole (elastic emission) and in parallel create an additional excitation from the occupied valence into the unoccupied valence with some energy loss related to this valence excitation as opposed to XES: following the X-ray excitation, subsequent X-ray emission may take place (side-note: Auger decay is stronger than emission decay in the soft X-ray regime). There are a few possibilities that the excited electron decays itself (participator decay channel), which may lead to elastic X-ray scattering, but the excited electron could also have traveled over some excited potential energy surface during the core-hole lifetime which may lead to emission to a vibrationally excited state. Another option for the participator channel is that the excited electron decays itself and transfers energy to an electron in the valence band which gets excited into some unoccupied state (e.g., a so-called charge transfer state or a valence-valence excitation). Also an electron from the valence band (spectator decay channel) may decay instead of the excited electron (participator channel). This may lead effectively to the same final situation from this one-electron picture of **Figure 3**.

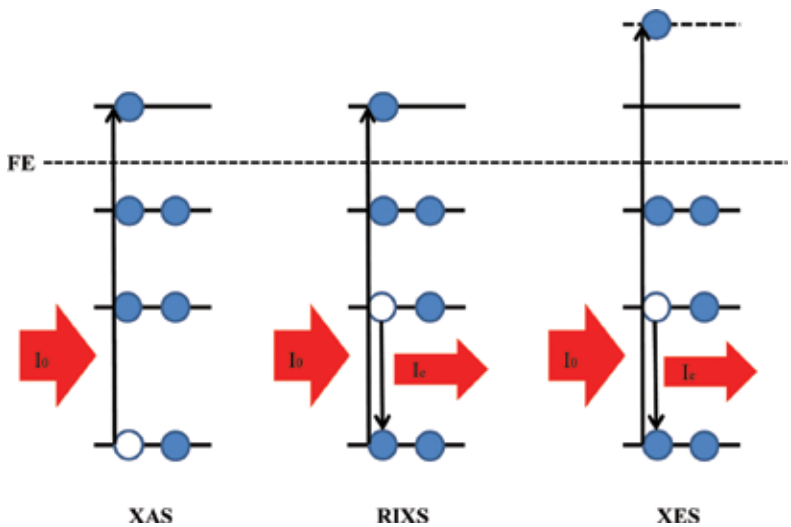

Figure 3. Schematic representation of the different core spectroscopies: X-ray absorption spectroscopy (XAS), resonant inelastic X-ray scattering (RIXS), and (nonresonant) X-ray emission spectroscopy (XES). FE indicated the Fermi level. Solid horizontal lines indicate unoccupied states within the system, while the dotted line indicates a virtual state for electrons ("free electrons"). Red lines indicate incident and emitted radiation.

So, **Figure 3** showed the XAS, XES, and RIXS processes by single-electron movements. However, one should think about these processes in total energy terms. The case for the combination of XAS, RIXS, and XES is shown in **Figure 4**.

As simplified above, RIXS is a combination of XAS (the absorption of the photon) and XES (the emission of a photon), and **Figure 4** shows that with RIXS it is then possible to reach excited states of the material. Here it is not stressed what kind of excited states these are, since this can be any type of excited state. That means that with RIXS (and sufficient resolution in the emission spectrometer) one can obtain information on electronic excited states (e.g., dd

excitations in 3d-materials) but as well on vibrationally and magnetically excited states [36]. The figure does not show energy gains (anti-Stokes Raman), but in principle this is possible if the system before the X-ray excitation is already in an excited state.

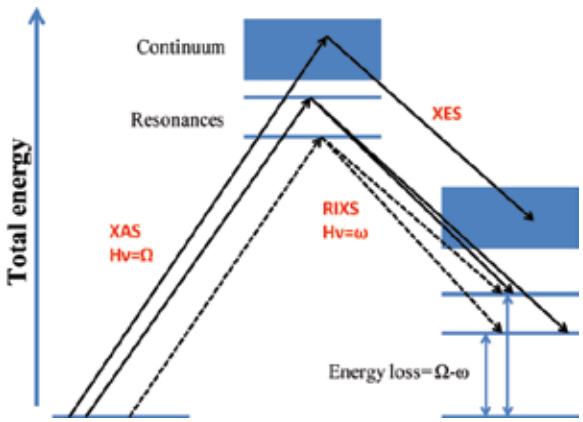

Figure 4. Total energy scheme of the processes of X-ray absorption (XAS), X-ray emission (XES) and resonant inelastic X-ray scattering (RIXS) with X-ray absorption resonances and the continuum as possible excitation channels (intermediate state for RIXS/XES) and final states for RIXS at different energy (energy loss) than the original ground state.

In the earlier days of RIXS, Butorin showed advantages of the RIXS technique, such as clear band showing allowed dd excitations compared to EELS and UV-VIS absorption spectra where dd transitions often appear as weak structures [37]. RIXS spectroscopy gained increased interest with the advances on the brilliance of synchrotrons and X-ray free-electron lasers as well as advances in more efficient detectors. More information on RIXS and its capabilities can be found in Refs. [5, 38, 39].

6. Some applications of RIXS

6.1. Soft X-ray RIXS on cuprates

In the early days, soft X-ray RIXS with moderate resolution was performed a lot on standard compounds such as manganese oxide (MnO) [37, 40], cobalt oxide (CoO) [40], and nickel oxide (NiO) [40–43]. Interestingly, in the soft X-ray regime when the SAXES spectrometer [44] became available with a much better energy resolution, and the general improved resolution was established on MnO [45], CoO [46], and NiO [47], high-energy resolution RIXS was focused mostly on the Cu L-edge of high-temperature superconductors (HT-SC) and representative HT-SC model compounds and as well with some measurements at the oxygen K-edge to gain understanding of superconducting properties related to phonon, magnon, and electronic structure, for example, Refs [48–52] for Cu L-edge and Refs. [53, 54] for the oxygen K-edge RIXS of HT-SC (model) compounds.

Nowadays, with more high-resolution RIXS spectrometers becoming available with even advanced features [55], high-resolution soft X-ray RIXS studies toward other 3d- (e.g., iron selenides, manganites, nickelates, or cobalt), 4d-, and 5d-metal (e.g., iridium) materials and to 4f-materials are expected for investigations into solid-state applications like superconductivity (FeSe-related), multiferroics, topological insulators, etc.

6.2. RIXS on metal organics – hard X-ray RIXS: 1s2p and 1s3p RIXS

In general, organic materials suffer from the X-ray probe, for example, the X-rays create beam damage. Hard X-rays have a lower cross section with metallic components in metal organics, such as proteins and homogeneous metal-containing catalysts than soft X-rays. In order to decrease the chances of beam damage, hard X-ray RIXS is often applied on these biologically/homogeneous catalysis relevant materials, especially focusing on properties concerning the active metal center of these systems.

In line with XRS, hard X-ray RIXS can also be used to study the edges with best chemical resolution indirectly [56, 57]. For example, for iron one can excite the (pre-)K-edge (1s core hole with excitation into the 3d-shell-related states) and probe the Ka (2p emission) or Kb (3p) emission. In these cases, the final state of the RIXS process is similar to the normal 2p XAS or 3p XAS (a hole in the 2p/3p and an additional electron in 3d). The emission resembles then the normal 2p (3p) XAS measured in the soft X-ray regime, but the spectrum measured via 1s2p (1s3p) RIXS may have additional features [58] due to quadrupole and monopole contributions, since with RIXS as a two-photon process the dipole selection rule has to be twice taken into account.

6.3. RIXS on simple semiconductors: electron-phonon coupling, band gap properties

In the hard X-ray regime, RIXS has been applied as well to study electron-phonon interactions of cuprates by focusing on the phonon progression [59], and in essence, the same technique can be performed in soft X-ray RIXS with high-energy resolution as long as there are not too many different phonon modes interfering. In the soft X-ray regime, electron-phonon scattering properties have been analyzed by measuring both RIXS and X-ray emission spectroscopy (XES) with a relatively low-energy resolution RIXS spectrometer [60] compared to the current standard as function of temperature for silicon and silicon carbide.

Resonant inelastic X-ray scattering and X-ray emission are very often applied in a similar fashion. Above certain energies, for example, well above the X-ray resonances, in the ionization regime, when one observes emitted X-ray photons, one speaks simply of *normal* XES.

By applying the combination of RIXS and XES, one could get (relative) measures on the angular and crystal momentum transfer due to electron-phonon scattering. This gives you an average electron-phonon scattering picture, so it is perfectly fine if there are many phonon modes. Comparing the different results on these compounds, a form of silicon carbide (6H-SiC) showed a much stronger electron-phonon scattering effect than pure silicon for both crystal momentum transfer and angular momentum transfer [61, 62]. In **Figure 5**, comparison of calculated silicon partial density of states (DOS) of 6H-SiC with the difference in XES as

function of temperature with reference to room temperature is given. One sees that as function of temperature, the XES difference shows a decrease related to s-DOS and an increase related to p-DOS, while the core hole is of 2p character. In general, s-(and d-)DOS is expected in the XES with a Si 2p core hole and the increase in p-DOS with temperature is therefore a measure for the amount of angular momentum transfer events in the core-hole lifetime.

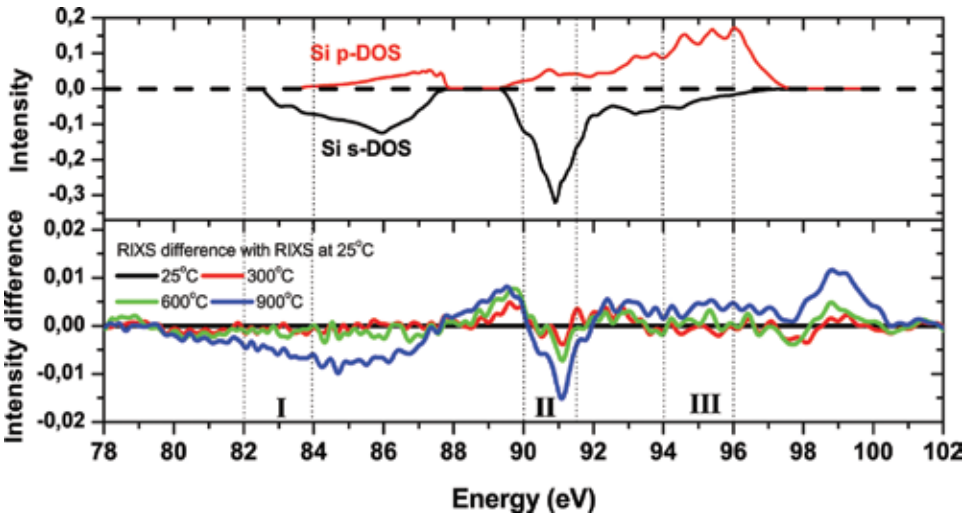

Figure 5. Top: calculated Si s-DOS and p-DOS for silicon carbide (6H-SiC). Bottom: difference in the XES with the XES at room temperature for 6H-SiC. This figure was adapted from Ref. [62] and is taken with permission.

For insulators and semiconductors, the first electronic energy loss observed in RIXS is directly related to the (element-specific) band gap, and by combining the information of RIXS with XAS and XES, one is able to identify the valence and conduction band behavior as a function of temperature [63, 64], which is important to know for semiconductor applications under extreme temperature conditions.

6.4. RIXS on liquids and on ions and organic molecules solved in liquid

In general, liquids at synchrotrons are measured by flow cells or liquid jets. For hard X-ray RIXS measurements, there are in principal no side conditions, but for soft X-ray RIXS measurements, you need to stay below a certain pressure in order to still be able to get X-rays on the liquid and to measure the emitted X-rays. There are a few setups in the world that can perform these measurements routinely, for example, the setups explained in Refs. [6, 65]. For liquids, the soft X-ray regime of RIXS [66, 67] is more important because often you want to study resonantly the oxygen K-edge and nitrogen K-edges which are at about 500 and 400 eV in the soft X-ray regime, respectively. Liquid jet RIXS with relatively low-energy resolution (~500 meV) has now, for example, been successfully employed on liquid and gas phase water [68, 69], methanol and other alcohols [70], 3d-metal ions solved in water, for example, Mn^{2+} (and Mn^{2+} organic complexes) [71] and Ni^{2+} in water [72], $Fe(CO)_5$ solved in ethanol [73, 74],

$Fe(CN)_6$ solved in water [74–76], 2-mercaptopyridine solved in water [77] and (models for) biologically relevant proteins in solution [71, 78–80].

As an example of RIXS on liquids, **Figure 6** shows the oxygen K-edge RIXS on resonance and far above the resonance (nonresonant X-ray emission) for methanol, ethanol, propanol, butanol, pentanol, and hexanol. It shows the main double-peak structure for all these alcohols, where the interpretation of this double-peak structure has been under debate for oxygen K-edge of water. As explained by Schreck et al., the relative ratio of this main double-peak structure corresponds to the amount of hydrogen bonds (expected from simulations) [70].

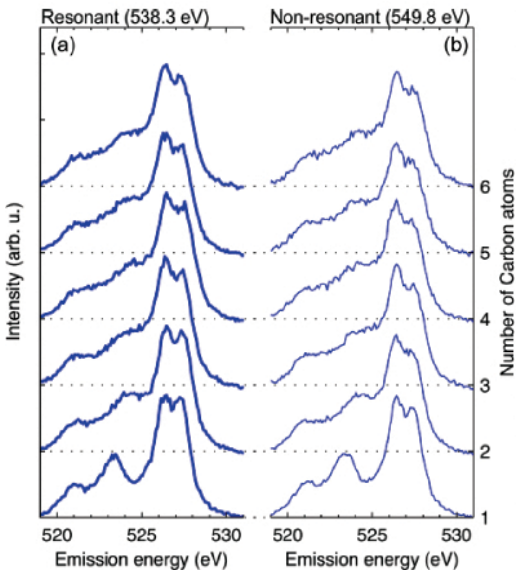

Figure 6. From top to bottom: oxygen K-edge on resonance (a) and oxygen K-edge nonresonant X-ray emission (b) of liquid hexanol, pentanol, butanol, propanol, ethanol and methanol. Figure taken from Ref. [70].

For the more sophisticated RIXS spectrometers with high resolution (~50 meV), flow cells are preferred in order to keep good vacuum conditions in the overall vacuum chamber and in the spectrometer. With the first high-resolution RIXS spectrometer available at the Swiss Light Source [44, 81], RIXS with vibrational-resolved resolution was acquired and analyzed for water [68] and acetone and the acetone-chloroform complex [82], and for the latter, two systems ground state potential energy surfaces could be reconstructed from the vibrational progression observed with vibrationally resolved RIXS.

By combining pump-laser probe-X-ray photons, one can get time-resolved information on materials. In this case, it is possible that the pump-laser excites the material to some excited state and the probe X-ray followed by X-ray scattering may lead to anti-stokes RIXS features (that is features observed at X-ray emission energies higher than the probe X-ray excitation energy). The first indications have been shown in X-ray free-electron laser experiments on $Fe(CO)_5$ solved in ethanol [74].

7. Summary

A short overview of X-ray Raman spectroscopy and resonant X-ray Raman spectroscopy (RIXS) has been given with special attention to what these element-specific spectroscopies can contribute to a better understanding of materials, or in other words how chemistry might benefit from Raman spectroscopy studies in the X-ray regime. Here it was shown that XRS and RIXS can supply information on (local, occupied, and unoccupied valence) electronic structure relevant to chemical activity, as well as supplying data to coupling of electronic structure with vibrational (electron-phonon interaction) and spin structure (electron-magnon interaction). In addition, with X-ray FELs, XRS and RIXS can be applied to (optically) excited states, and in particular the shift of these spectroscopies from synchrotrons to X-ray free-electron lasers [83] may become an important transition for time-dependent electronic and phononic structure studies. As well, (future) diffraction-limited storage rings will enhance the energy resolution for XRS and RIXS [84].

Author details

Piter Sybren Miedema

Address all correspondence to: p.s.miedema@gmail.com

Institute of Methods and Instrumentation for Synchrotron Radiation Research (FG-ISRR), Helmholtz-Zentrum Berlin, Germany

References

[1] F. de Groot and A. Kotani, Core Level Spectroscopy of Solids. CRC Press, Boca Raton, Florida, 2008

[2] L. A. Grunes, "Study of the K edges of 3d transition metals in pure and oxide form by X-ray absorption spectroscopy," *Phys. Rev. B*, vol. 27, no. 4, pp. 2111–2131, 1983.

[3] P.S. Miedema, "X-ray Spectroscopy of Inorganic Materials," PhD thesis, Utrecht University, Utrecht, The Netherlands, 2012.

[4] G. van der Laan and A. I. Figueroa, "X-ray magnetic circular dichroism—A versatile tool to study magnetism," *Coord. Chem. Rev.*, vol. 277–278, pp. 95–129, Mar. 2014.

[5] F. J. Himpsel, "Photon-in photon-out soft X-ray spectroscopy for materials science," *Phys. Stat. Sol.*, vol. 248, no. 2, pp. 292–298, Feb. 2011.

[6] K. Kunnus, I. Rajkovic, S. Schreck, W. Quevedo, S. Eckert, M. Beye, E. Suljoti, C. Weniger, C. Kalus, S. Grübel, M. Scholz, D. Nordlund, W. Zhang, R. W. Hartsock, K. J.

Gaffney, W. F. Schlotter, J. J. Turner, B. Kennedy, F. Hennies, S. Techert, P. Wernet, A. Föhlisch, "A setup for resonant inelastic soft X-ray scattering on liquids at free electron laser light sources.," *Rev. Sci. Instrum.*, vol. 83, no. 12, p. 123109, Dec. 2012.

[7] P. S. Miedema, M. M. van Schooneveld, R. Bogerd, T. C. R. Rocha, M. Hävecker, A. Knop-Gericke, F. M. F. de Groot, "Oxygen binding to cobalt and iron phthalocyanines as determined from in situ x-ray absorption spectroscopy," *J. Phys. Chem. C*, vol. 115, no. 51, pp. 25422–25428, Dec. 2011.

[8] H. Bluhm, "Photoelectron spectroscopy of surfaces under humid conditions," *J. Electron Spectrosc. Relat. Phenom.*, vol. 177, no. 2–3, pp. 71–84, 2010.

[9] M. Hävecker, T. Schedel-niedrig, R. Schlögl, I. Chemistry, F. Mpg, "High-pressure low-energy XAS: a new tool for probing reacting surfaces of heterogeneous catalysts," *Top. Catal.*, vol. 10, pp. 187–198, 2000.

[10] J. J. Velasco-Vélez, V. Pfeifer, M. Hävecker, R. Wang, A. Centeno, A. Zurutuza, G. Algara-Siller, E. Stotz, K. Skorupska, D. Teschner, P. Kube, P. Braeuninger-Weimer, S. Hofmann, R. Schlögl, A. Knop-Gericke, "Atmospheric pressure X-ray photoelectron spectroscopy apparatus: bridging the pressure gap," *Rev. Sci. Instrum.*, vol. 87, p. 053121, 2016.

[11] U. Bergmann, P. Glatzel, S. P. Cramer, "Bulk-sensitive XAS characterization of light elements: from X-ray Raman scattering to X-ray Raman spectroscopy," *Microchem. J.*, vol. 71, no. 2–3, pp. 221–230, Apr. 2002.

[12] R. Alonso-Mori, J. Kern, D. Sokaras, T. C. Weng, D. Nordlund, R. Tran, P. Montanez, J. Delor, V. K. Yachandra, J. Yano, U. Bergmann, "A multi-crystal wavelength dispersive X-ray spectrometer," *Rev. Sci. Instrum.*, vol. 83, p. 073114, 2012.

[13] E. Burkel, "Phonon spectroscopy by inelastic X-ray scattering," *Rep. Prog. Phys.*, vol. 63, no. 2, pp. 171–232, Feb. 2000.

[14] F. Sette, M. H. Krisch, C. Masciovecchio, G. Ruocco, G. Monaco, "Dynamics of glasses and glass-forming liquids studied by inelastic X-ray scattering," *Science (80-.).*, vol. 280, no. 5369, pp. 1550–1555, 1998.

[15] O. Chubar, G. Geloni, V. Kocharyan, A. Madsen, E. Saldin, S. Serkez, Y. Shvyd'ko, J. Sutter, "Ultra-high-resolution inelastic X-ray scattering at high-repetition-rate self-seeded X-ray free-electron lasers," *J. Synchrotron Radiat.*, vol. 23, no. 2, pp. 410–424, 2016.

[16] A. Q. R. Baron, Y. Tanaka, D. Miwa, D. Ishikawa, T. Mochizuki, K. Takeshita, S. Goto, T. Matsushita, H. Kimura, F. Yamamoto, T. Ishikawa, "Early commissioning of the SPring-8 beamline for high resolution inelastic X-ray scattering," *Nucl. Instrum. Methods Phys. Res. A Accel. Spectrom., Detect. Assoc. Equip.*, vol. 467–468, pp. 627–630, 2001.

[17] S. Huotari, G. Vankó, F. Albergamo, C. Ponchut, H. Graafsma, C. Henriquet, R. Verbeni, G. Monaco, "Improving the performance of high-resolution X-ray spectrometers with position-sensitive pixel detectors," *J. Synchrotron Radiat.*, vol. 12, pp. 467–472, 2005.

[18] S. Huotari, F. Albergamo, G. Vankó, R. Verbeni, G. Monaco, "Resonant inelastic hard X-ray scattering with diced analyzer crystals and position-sensitive detectors," *Rev. Sci. Instrum*., vol. 77, p. 053102, 2006.

[19] D. Sokaras, D. Nordlund, T. C. Weng, R. A. Mori, P. Velikov, D. Wenger, A. Garachtchenko, M. George, V. Borzenets, B. Johnson, Q. Qian, T. Rabedeau, U. Bergmann, "A high resolution and large solid angle X-ray Raman spectroscopy end-station at the Stanford Synchrotron Radiation Lightsource," *Rev. Sci. Instrum*., vol. 83, p. 043112, 2012.

[20] A. Braun, D. Nordlund, S. W. Song, T. W. Huang, D. Sokaras, X. Liu, W. Yang, T. C. Weng, Z. Liu, "Hard X-rays in-soft X-rays out: an operando piggyback view deep into a charging lithium ion battery with X-ray Raman spectroscopy," *J. Electron Spectrosc. Relat. Phenom*., vol. 200, pp. 257–263, 2015.

[21] P. S. Miedema, P. Ngene, A. M. J. van der Eerden, T.-C. Weng, D. Nordlund, D. Sokaras, R. Alonso-Mori, A. Juhin, P. E. de Jongh, F. M. F. de Groot, "In situ X-ray Raman spectroscopy of $LiBH_4$," *Phys. Chem. Chem. Phys*., vol. 14, no. 16, pp. 5581–7, Apr. 2012.

[22] P. S. Miedema, P. Ngene, A. M. J. van der Eerden, D. Sokaras, T.-C. Weng, D. Nordlund, Y. S. Au, F. M. F. de Groot, "In situ X-ray Raman spectroscopy study of the hydrogen sorption properties of lithium borohydride nanocomposites.," *Phys. Chem. Chem. Phys*., vol. 16, no. 41, pp. 22651–22658, Oct. 2014.

[23] T. A. Pascal, U. Boesenberg, R. Kostecki, T. J. Richardson, T. C. Weng, D. Sokaras, D. Nordlund, E. McDermott, A. Moewes, J. Cabana, D. Prendergast, "Finite temperature effects on the X-ray absorption spectra of lithium compounds: first-principles interpretation of X-ray Raman measurements," *J. Chem. Phys*., vol. 140, p. 034107, 2014.

[24] C. J. Sahle, S. Kujawski, A. Remhof, Y. Yan, N. Stadie, A. Al-Zein, M. Tolan, S. Huotari, M. Krisch, C. Sternemann, "*In-situ* characterization of the decomposition behavior of $Mg(BH_4)_2$ by X-ray Raman scattering spectroscopy," *Phys. Chem. Chem. Phys*., vol. 18, pp. 5397–5403, 2016.

[25] J. P. Rueff, A. Shukla, "Inelastic X-ray scattering by electronic excitations under high pressure," *Rev. Mod. Phys*., vol. 82, pp. 847–896, 2010.

[26] A. Nyrow, J. S. Tse, N. Hiraoka, S. Desgreniers, T. Büning, K. Mende, M. Tolan, M. Wilke, C. Sternemann, "Pressure induced spin transition revealed by iron M2,3-edge spectroscopy," *Appl. Phys. Lett*., vol. 104, no. 26, p. 262408, Jun. 2014.

[27] V. M. Giordano, M. Krisch, G. Monaco, "Phonon spectroscopy at high pressure by inelastic X-ray scattering," *J. Synchrotron Radiat*., vol. 16, pp. 707–713, 2009.

[28] M. Krisch, "Status of phonon studies at high pressure by inelastic X-ray scattering," *J. Raman Spectrosc*., vol. 34, no. 7–8, pp. 628–632, 2003.

[29] J. Niskanen, C. J. Sahle, I. Juurinen, J. Koskelo, S. Lehtola, R. Verbeni, H. Müller, M. Hakala, S. Huotari, "Protonation dynamics and hydrogen bonding in aqueous sulfuric acid," J. Phys. Chem. B, vol. 119. pp. 11732–11739, 2015.

[30] C. J. Sahle, M. a Schroer, I. Juurinen, J. Niskanen, "Influence of TMAO and urea on the structure of water studied by inelastic X-ray scattering.," *Phys. Chem. Chem. Phys.*, vol. 18, pp. 16518–16526, 2016.

[31] S. Huotari, E. Suljoti, C. J. Sahle, S. Rädel, G. Monaco, F. M. F. De Groot, "High-resolution nonresonant X-ray Raman scattering study on rare earth phosphate nanoparticles," *New J. Phys.*, vol. 17, p. 043041, 2015.

[32] A. Kotani and S. Shin, "Resonant inelastic X-ray scattering spectra for electrons in solids," *Rev. Mod. Phys.*, vol. 73, no. January, pp. 203–246, 2001.

[33] L. J. P. Ament, M. van Veenendaal, T. P. Devereaux, J. P. Hill, J. van den Brink, "Resonant inelastic X-ray scattering studies of elementary excitations," *Rev. Mod. Phys.*, vol. 83, no. 2, pp. 705–767, Jun. 2011.

[34] P. Glatzel, M. Sikora, G. Smolentsev, M. Fernández-García, "Hard X-ray photon-in photon-out spectroscopy," *Catal. Today*, vol. 145, pp. 294–299, 2009.

[35] F. Gel'mukhanov, H. Agren, "Resonant X-ray Raman scattering," *Phys. Rep.*, vol. 312, pp. 87–330, 1999.

[36] S. Fatale, S. Moser, M. Grioni, "Magnetic excitations in soft X-ray RIXS: recent developments," *J. Electron Spectrosc. Relat. Phenom.*, vol. 200, pp. 274–281, 2015.

[37] S. Butorin, J.-H. Guo, M. Magnuson, P. Kuiper, J. Nordgren, "Low-energy d-d excitations in MnO studied by resonant X-ray fluorescence spectroscopy," *Phys. Rev. B*, vol. 54, no. 7, pp. 4405–4408, 1996.

[38] A. Kotani, "Resonant inelastic X-ray scattering in d and f electron systems," *Eur. Phys. J. B*, vol. 47, no. 1, pp. 3–27, Sep. 2005.

[39] P. Glatzel, T.-C. Weng, K. Kvashnina, J. Swarbrick, M. Sikora, E. Gallo, N. Smolentsev, R. A. Mori, "Reflections on hard X-ray photon-in/photon-out spectroscopy for electronic structure studies," *J. Electron Spectrosc. Relat. Phenom.*, vol. 188, pp. 17–25, Jun. 2013.

[40] S. M. Butorin, "Resonant inelastic X-ray scattering as a probe of optical scale excitations in strongly electron-correlated systems: quasi-localized view," *J. Electron Spectrosc. Relat. Phenom.*, vol. 110–111, pp. 213–233, Oct. 2000.

[41] M. Magnuson, S. M. Butorin, A. Agui, J. Nordgren, "Resonant soft X-ray Raman scattering of NiO," *J. Phys. Condens. Matter*, vol. 14, pp. 3669–3676, 2002.

[42] L. Braicovich, C. Dallera, G. Ghiringhelli, N. B. Brookes, J. B. Goedkoop, M. A. Van Veenendaal, "X-ray L2,3 resonant Raman scattering from NiO: spin flip and intermediate-state relaxation," *Phys. Rev. B*, vol. 55, no. 24, pp. 989–992, 1997.

[43] H. Ishii, Y. Ishiwata, R. Eguchi, Y. Harada, M. Watanabe, A. Chainani, S. Shin, "Resonant soft X-ray emission spectroscopy of NiO across the Ni L2,3 thresholds," *J. Phys. Soc. Jpn.*, vol. 70, no. 6, pp. 1813–1816, 2001.

[44] G. Ghiringhelli, A. Piazzalunga, C. Dallera, G. Trezzi, L. Braicovich, T. Schmitt, V. N. Strocov, R. Betemps, L. Patthey, X. Wang, M. Grioni, "SAXES, a high resolution spectrometer for resonant X-ray emission in the 400-1600 eV energy range," *Rev. Sci. Instrum.*, vol. 77, p. 113108, 2006.

[45] G. Ghiringhelli, M. Matsubara, C. Dallera, F. Fracassi, A. Tagliaferri, N. B. Brookes, A. Kotani, L. Braicovich, "Resonant inelastic X-ray scattering of MnO◎: L 2, 3 edge measurements and assessment of their interpretation," *Phys. Rev. B*, vol. 73, pp. 8–11, 2006.

[46] S. Chiuzbăian, T. Schmitt, M. Matsubara, A. Kotani, G. Ghiringhelli, C. Dallera, A. Tagliaferri, L. Braicovich, V. Scagnoli, N. Brookes, U. Staub, L. Patthey, "Combining M- and L-edge resonant inelastic X-ray scattering for studies of 3d transition metal compounds," *Phys. Rev. B*, vol. 78, no. 24, p. 245102, Dec. 2008.

[47] G. Ghiringhelli, M. Matsubara, C. Dallera, F. Fracassi, R. Gusmeroli, A. Piazzalunga, A. Tagliaferri, N. B. Brookes, A. Kotani, L. Braicovich, "NiO as a test case for high resolution resonant inelastic soft X-ray scattering," *J. Phys. Condens. Matter*, vol. 17, no. 35, pp. 5397–5412, Sep. 2005.

[48] L. Braicovich, M. Moretti Sala, L. J. P. Ament, V. Bisogni, M. Minola, G. Balestrino, D. Di Castro, G. M. De Luca, M. Salluzzo, G. Ghiringhelli, J. Van Den Brink, "Momentum and polarization dependence of single-magnon spectral weight for Cu L3-edge resonant inelastic X-ray scattering from layered cuprates," *Phys. Rev. B*, vol. 81, p. 174533, 2010.

[49] L. Braicovich, J. van den Brink, V. Bisogni, M. M. Sala, L. J. P. Ament, N. B. Brookes, G. M. De Luca, M. Salluzzo, T. Schmitt, V. N. Strocov, G. Ghiringhelli, "Magnetic excitations and phase separation in the underdoped La_{2-x}Sr_{x}CuO_{4} superconductor measured by resonant inelastic X-ray scattering," *Phys. Rev. Lett.*, vol. 104, no. 7, p. 077002, Feb. 2010.

[50] L. Braicovich, L. J. P. Ament, V. Bisogni, F. Forte, C. Aruta, G. Balestrino, N. B. Brookes, G. M. De Luca, P. G. Medaglia, F. M. Granozio, M. Radovic, M. Salluzzo, J. Van Den Brink, G. Ghiringhelli, "Dispersion of magnetic excitations in the cuprate La_2CuO_4 and $CaCuO_2$ compounds measured using resonant X-ray scattering," *Phys. Rev. Lett.*, vol. 102, no. 16, pp. 22–25, 2009.

[51] C. Monney, V. Bisogni, K.-J. Zhou, R. Kraus, V. N. Strocov, G. Behr, J. Málek, R. Kuzian, S.-L. Drechsler, S. Johnston, A. Revcolevschi, B. Büchner, H. M. Rønnow, J. van den Brink, J. Geck, T. Schmitt, "Determining the short-range spin correlations in the spin-chain Li_2CuO_2 and $CuGeO_3$ compounds using resonant inelastic X-ray scattering," *Phys. Rev. Lett.*, vol. 110, no. 8, p. 087403, 2013.

[52] C. Monney, T. Schmitt, C. E. Matt, J. Mesot, V. N. Strocov, O. J. Lipscombe, S. M. Hayden, J. Chang, "Resonant inelastic X-ray scattering study of the spin and charge excitations in the overdoped superconductor $La_{1.77}Sr_{0.23}CuO_4$," *Phys. Rev. B*, vol. 93, no. 7, p. 075103, 2016.

[53] B. Freelon, A. Augustsson, J. H. Guo, P. G. Medaglia, A. Tebano, G. Balestrino, C. L. Dong, C. L. Chang, P. a. Glans, T. Learmonth, K. E. Smith, J. Nordgren, Z. Hussain, "Low energy electronic spectroscopy of an infinite-layer cuprate: a resonant inelastic X-ray scattering study of $CaCuO_2$," *Phys. C*, vol. 470, no. 3, pp. 187–192, 2010.

[54] C. C. Chen, M. Sentef, Y. F. Kung, C. J. Jia, R. Thomale, B. Moritz, a. P. Kampf, T. P. Devereaux, "Doping evolution of the oxygen K-edge X-ray absorption spectra of cuprate superconductors using a three-orbital Hubbard model," *Phys. Rev. B*, vol. 87, p. 165144, 2013.

[55] L. Braicovich, M. Minola, G. Dellea, M. Le Tacon, M. Moretti Sala, C. Morawe, J. C. Peffen, R. Supruangnet, F. Yakhou, G. Ghiringhelli, N. B. Brookes, "The simultaneous measurement of energy and linear polarization of the scattered radiation in resonant inelastic soft X-ray scattering, " *Rev. Sci. Instrum*., vol. 85, no. 11, pp. 115104, 2014.

[56] F. M. F. de Groot, P. Glatzel, U. Bergmann, P. a van Aken, R. a Barrea, S. Klemme, M. Hävecker, A. Knop-Gericke, W. M. Heijboer, B. M. Weckhuysen, "1s2p resonant inelastic X-ray scattering of iron oxides.," *J. Phys. Chem. B*, vol. 109, no. 44, pp. 20751–20762, Nov. 2005.

[57] M. Lundberg, T. Kroll, S. DeBeer, U. Bergmann, S. A Wilson, P. Glatzel, D. Nordlund, B. Hedman, K. O. Hodgson, E. I. Solomon, "Metal-ligand covalency of iron complexes from high-resolution resonant inelastic X-ray scattering.," *J. Am. Chem. Soc*., vol. 135, no. 45, pp. 17121–17134, Nov. 2013.

[58] T. Kroll, R. G. Hadt, S. A. Wilson, M. Lundberg, J. J. Yan, T. C. Weng, D. Sokaras, R. Alonso-Mori, D. Casa, M. H. Upton, B. Hedman, K. O. Hodgson, E. I. Solomon, "Resonant inelastic X-ray scattering on ferrous and ferric bis-imidazole porphyrin and cytochrome c: nature and role of the axial methionine-fe bond," *J. Am. Chem. Soc*., vol. 136, no. 52, pp. 18087–18099, 2014.

[59] H. Yavaş, M. van Veenendaal, J. van den Brink, L. J. P. Ament, A. Alatas, B. M. Leu, M.-O. Apostu, N. Wizent, G. Behr, W. Sturhahn, H. Sinn, E. E. Alp, "Observation of phonons with resonant inelastic X-ray scattering.," *J. Phys. Condens. Matter*, vol. 22, p. 485601, 2010.

[60] J. Nordgren, G. Bray, S. Cramm, R. Nyholm, J.-E. Rubensson, N. Wassdahl, "Soft X-ray emission spectroscopy using monochromatized synchrotron radiation (invited)," *Rev. Sci. Instrum*., vol. 60, no. 7, p. 1690, 1989.

[61] M. Beye, F. Hennies, M. Deppe, E. Suljoti, M. Nagasono, W. Wurth, A. Föhlisch, "Dynamics of electron-phonon scattering: crystal- and angular-momentum transfer probed by resonant inelastic X-ray scattering," *Phys. Rev. Lett*., vol. 103, no. 23, p. 237401, Dec. 2009.

[62] P. S. Miedema, M. Beye, R. Könnecke, G. Schiwietz, A. Föhlisch, "The angular- and crystal-momentum transfer through electron–phonon coupling in silicon and silicon-carbide: similarities and differences," *New J. Phys*., vol. 16, no. 9, p. 093056, Sep. 2014.

[63] M. Beye, F. Hennies, M. Deppe, E. Suljoti, M. Nagasono, W. Wurth, A. Föhlisch, "Measurement of the predicted asymmetric closing behaviour of the band gap of silicon using X-ray absorption and emission spectroscopy," *New J. Phys*., vol. 12, no. 4, p. 043011, Apr. 2010.

[64] P. S. Miedema, M. Beye, R. Könnecke, G. Schiwietz, A. Föhlisch, "Thermal evolution of the band edges of 6H-SiC: X-ray methods compared to the optical band gap," *J. Electron Spectrosc. Relat. Phenom*., vol. 197, pp. 37–42, Dec. 2014.

[65] L. Weinhardt, M. Blum, O. Fuchs, A. Benkert, F. Meyer, M. Bär, J. D. Denlinger, W. Yang, F. Reinert, C. Heske, "RIXS investigations of liquids, solutions, and liquid/solid interfaces," *J. Electron Spectrosc. Relat. Phenom*., vol. 188, pp. 111–120, Jun. 2013.

[66] J. E. Rubensson, F. Hennies, A. Pietzsch, "High-resolution resonant inelastic soft X-ray scattering applied to liquids," *J. Electron Spectrosc. Relat. Phenom*., vol. 188, pp. 79–83, 2013.

[67] J.-E. Rubensson, "Resonant inelastic soft X-ray scattering applied to molecular materials," *J. Electron Spectrosc. Relat. Phenom*., vol. 200, pp. 239–246, 2015.

[68] A. Pietzsch, F. Hennies, P. S. Miedema, B. Kennedy, J. Schlappa, T. Schmitt, V. N. Strocov, A. Föhlisch, "Snapshots of the fluctuating hydrogen bond network in liquid water on the sub-femtosecond timescale with vibrational resonant inelastic X-ray scattering," *Phys. Rev. Lett*., vol. 114, p. 088302, 2015.

[69] L. Weinhardt, A. Benkert, F. Meyer, M. Blum, R. G. Wilks, W. Yang, M. Bär, F. Reinert, C. Heske, "Nuclear dynamics and spectator effects in resonant inelastic soft X-ray scattering of gas-phase water molecules," *J. Chem. Phys*., vol. 136, no. 14, 2012.

[70] S. Schreck, A. Pietzsch, K. Kunnus, B. Kennedy, W. Quevedo, P. S. Miedema, P. Wernet, A. Föhlisch, "Dynamics of the OH group and the electronic structure of liquid alcohols," *Struct. Dyn*., vol. 1, no. 5, p. 054901, Sep. 2014.

[71] S. I. Bokarev, M. Khan, M. K. Abdel-Latif, J. Xiao, R. Hilal, S. G. Aziz, E. F. Aziz, O. Kühn, "Unraveling the electronic structure of photocatalytic manganese complexes by L-Edge X-ray spectroscopy," *J. Phys. Chem. C*, vol. 119, no. 33, pp. 19192–19200, 2015.

[72] K. Kunnus, I. Josefsson, S. Schreck, W. Quevedo, P. S. Miedema, S. Techert, F. M. F. de Groot, M. Odelius, P. Wernet, A. Föhlisch, "From ligand fields to molecular orbitals: probing the local valence electronic structure of Ni(2+) in aqueous solution with resonant inelastic X-ray scattering.," *J. Phys. Chem. B*, vol. 117, no. 51, pp. 16512–16521, Dec. 2013.

[73] P. Wernet, K. Kunnus, I. Josefsson, I. Rajkovic, W. Quevedo, M. Beye, S. Schreck, S. Grübel, M. Scholz, D. Nordlund, W. Zhang, R. W. Hartsock, W. F. Schlotter, J. J. Turner, B. Kennedy, F. Hennies, F. M. F. de Groot, K. J. Gaffney, S. Techert, M. Odelius, A. Föhlisch, "Orbital-specific mapping of the ligand exchange dynamics of Fe(CO)5 in solution," *Nature*, vol. 520, pp. 78–81, 2015.

[74] K. Kunnus, "Probing dynamic pathways and electronic structure of coordination complexes with soft X-ray spectroscopy," Universität Potsdam, 2014.

[75] N. Engel, S. I. Bokarev, E. Suljoti, R. Garcia-Diez, K. M. Lange, K. Atak, R. Golnak, A. Kothe, M. Dantz, O. Kühn, E. F. Aziz, "Chemical bonding in aqueous ferrocyanide: experimental and theoretical X-ray spectroscopic study," *J. Phys. Chem. B*, vol. 118, no. 6, pp. 1555–1563, 2014.

[76] K. Kunnus, W. Zhang, M. G. Delcey, R. V Pinjari, P. S. Miedema, S. Schreck, W. Quevedo, H. Schroeder, A. Föhlisch, K. J. Gaffney, M. Lundberg, M. Odelius, P. Wernet, "Viewing the valence electronic structure of ferric and ferrous hexacyanide in solution from the Fe and cyanide perspectives," *J. Phys. Chem. B*, vol. 120, pp. 7182–7194, 2016.

[77] S. Eckert, P. S. Miedema, W. Quevedo, B. O'Cinneide, M. Fondell, M. Beye, A. Pietzsch, M. Ross, M. Khalil, A. Föhlisch, "Molecular structures and protonation state of 2-Mercaptopyridine in aqueous solution," *Chem. Phys. Lett*., vol. 647, pp. 103–106, 2016.

[78] N. Bergmann, S. Bonhommeau, K. M. Lange, S. M. Greil, S. Eisebitt, F. de Groot, M. Chergui, E. F. Aziz, "On the enzymatic activity of catalase: an iron L-edge X-ray absorption study of the active centre.," *Phys. Chem. Chem. Phys*., vol. 12, no. 18, pp. 4827–4832, 2010.

[79] R. Golnak, J. Xiao, M. Pohl, C. Schwanke, A. Neubauer, K. M. Lange, K. Atak, E. F. Aziz, "Influence of the outer ligands on metal-to-ligand charge transfer in solvated manganese porphyrins," *Inorg. Chem*., vol. 55, no. 1, pp. 22–28, 2016.

[80] K. Atak, R. Golnak, J. Xiao, E. Suljoti, M. Pflüger, T. Brandenburg, B. Winter, E. F. Aziz, "Electronic structure of hemin in solution studied by resonant X-ray emission spectroscopy and electronic structure calculations.," *J. Phys. Chem. B*, vol. 118, no. 33, pp. 9938–9943, 2014.

[81] V. N. Strocov, T. Schmitt, U. Flechsig, T. Schmidt, A. Imhof, Q. Chen, J. Raabe, R. Betemps, D. Zimoch, J. Krempasky, X. Wang, M. Grioni, A. Piazzalunga, L. Patthey, "High-resolution soft X-ray beamline ADRESS at the Swiss Light Source for resonant inelastic X-ray scattering and angle-resolved photoelectron spectroscopies," *J. Synchrotron Radiat*., vol. 17, no. 5, pp. 631–643, 2010.

[82] S. Schreck, A. Pietzsch, B. Kennedy, W. Quevedo, P. S. Miedema, C. Såthe, S. Techert, J. A. Terschlüsen, V. N. Strocov, T. Schmitt, F. Hennies, J.-E. Rubensson, P. Wernet, A. Föhlisch, "Ground state potential energy surfaces around selected atoms from resonant inelastic X-ray scattering.," *Sci. Rep*., vol. 6, p. 20054, 2016.

[83] R. Alonso-Mori, D. Sokaras, D. Zhu, T. Kroll, M. Chollet, Y. Feng, J. M. Glownia, J. Kern, H. T. Lemke, D. Nordlund, A. Robert, M. Sikorski, S. Song, T. C. Weng, U. Bergmann, "Photon-in photon-out hard X-ray spectroscopy at the Linac Coherent Light Source," *J. Synchrotron Radiat*., vol. 22, pp. 612–620, 2015.

[84] T. Schmitt, F. M. F. de Groot, J. E. Rubensson, "Prospects of high-resolution resonant X-ray inelastic scattering studies on solid materials, liquids and gases at diffraction-limited storage rings.," *J. Synchrotron Radiat*., vol. 21, no. Pt 5, pp. 1065–1076, Sep. 2014.

Chapter 12

Using Raman Spectroscopy to Improve Hyperpolarized Noble Gas Production for Clinical Lung Imaging Techniques

Jonathan Birchall, Nicholas Whiting, Jason Skinner,

Michael J. Barlow and Boyd M. Goodson

Additional information is available at the end of the chapter

http://dx.doi.org/10.5772/65114

Abstract

Spin-exchange optical pumping (SEOP) can be used to "hyperpolarize" ^{129}Xe for human lung MRI. SEOP involves transfer of angular momentum from light to an alkali metal (Rb) vapor, and then onto ^{129}Xe nuclear spins during collisions; collisions between excited Rb and N_2 ensure that incident optical energy is nonradiatively converted into heat. However, because variables that govern SEOP are temperature-dependent, the excess heat can complicate efforts to maximize spin polarization—particularly at high laser fluxes and xenon densities. Ultra-low frequency Raman spectroscopy may be used to perform *in situ* gas temperature measurements to investigate the interplay of energy thermalization and SEOP dynamics. Experimental configurations include an "orthogonal" pump-and-probe design and a newer "inline" design (with source and detector on the same axis) that has provided a >20-fold improvement in SNR. The relationship between ^{129}Xe polarization and the spatiotemporal distribution of N_2 rotational temperatures has been investigated as a function of incident laser flux, exterior cell temperature, and gas composition. Significantly elevated gas temperatures have been observed —hundreds of degrees hotter than exterior cell surfaces—and variances with position and time can indicate underlying energy transport, convection, and Rb mass-transport processes that, if not controlled, can negatively impact ^{129}Xe hyperpolarization.

Keywords: low-frequency Raman, hyperpolarization, spin-exchange optical pumping, xenon NMR/MRI, low-field NMR, remote temperature measurement

1. Introduction

Magnetic resonance imaging (MRI) is a powerful tool for diagnostic imaging of soft tissue, combining superior contrast, dynamic capability, and no risk of damage caused by ionizing radiation compared to computerized tomography (CT) [1]. Most MRI techniques conveniently detect the nuclear spin of protons in water, which makes up a significant portion of the human body. This detection modality poses a problem within the lungs, however, as the low proton density translates to greatly reduced signal-to-noise ratios for conventional MRI techniques. Even at high magnetic field strengths, the equilibrium nuclear spin polarization is very low (~10^{-4} to 10^{-6}). To facilitate MRI inside the lungs, far greater signal-to-noise ratios are needed, requiring nuclear spin polarizations to be increased far above equilibrium levels—a process known as hyperpolarization. Indeed, inhalation of hyperpolarized gases provides greatly improved sensitivity and bright images, outweighing the low spin densities of the gas phase. Gas hyperpolarization can now be readily achieved using established techniques; however in these approaches, maximizing the available spin polarization is hampered by complex system dynamics and codependence of many variables that are heavily temperature-dependent.

In most studies relevant to lung imaging, this hyperpolarized state is achieved by utilizing circularly polarized photons to shift particles with a nonzero magnetic moment between discrete spin states. During gas-phase collisions, spin angular momentum is transferred from alkali metal electrons to noble gas nuclei, a technique known as spin-exchange optical pumping (SEOP) [2]. Noble gases are used in SEOP because of their lack of reactivity with alkali metal vapors and their ultra-long hyperpolarization lifetimes. Nitrogen is present as a buffer gas to prevent radiation trapping, helping to maximize the alkali metal electron spin polarization—and hence, the noble gas nuclear spin polarization. Thus, inhalation of a hyperpolarized noble gas sample such as ^{129}Xe while inside the MRI scanner enables both structural and functional high-resolution imaging of the lungs in real time. Despite significant advances in polarizer technology in recent years, many underlying aspects of the SEOP process, such as energy- and mass transport mechanisms within the OP cell and the temperature dependences of many parameters, remain poorly understood. Ironically, the desire to maximize the available nuclear spin magnetization leads to a demand for higher pump laser powers and richer noble gas mixtures, which only serve to compound this issue.

In an attempt to overcome these challenges, Raman spectroscopy may be used to complement more commonly used techniques such as optical absorption spectroscopy and low-field NMR in order to optimize the multidimensional SEOP parameter space, thereby improving the ^{129}Xe hyperpolarization process for MR applications. Conventional temperature measurement (e.g., using a thermocouple) would be challenging to implement, given that the SEOP process takes place inside a sealed vessel, within a magnetic field, and under constant uniform illumination by high-power laser light; moreover, temperature measurement of the exterior cell walls may often provide only a poor reflection of the true gas behavior within the cell. However, if optical access is available, Raman spectroscopy can be used to acquire *in situ* rotational and vibrational temperature measurements of the nitrogen buffer gas—and hence, an accurate picture of the true gas temperature at a given location within the cell. This capability should provide a more complete

http://dx.doi.org/10.5772/65114

insight into the energy deposition, transport, and dissipation processes that occur during the SEOP process, which in turn may further enable optimization of the efficiency of noble gas hyperpolarization—thereby improving the diagnostic capability of HP noble gases in clinical settings.

2. Theory

2.1. Spin-exchange optical pumping

The SEOP process consists of two major steps. Firstly, circularly polarized photons (necessary to satisfy the selection rules for optical absorption) are used to transfer angular momentum to a gaseous target with nonzero spin, such as spin-½ electrons. A vaporized alkali metal such as rubidium is typically used, since its single outer shell electron is easier to manipulate and existing laser technology at the required transition wavelengths is well developed. The net polarization, P, of the alkali metal can then be given by [3]

$$P = S_z \frac{R}{\Gamma_{SD} + R} \tag{1}$$

where S_z is the photon spin of the circularly polarized laser light, R is the optical pumping rate, and Γ_{SD} is the rate of spin destruction or spin relaxation due to collisions with the walls of the system or other gas-phase species (particularly xenon atoms). Assuming the optical pumping rate exceeds the rate of relaxation, a large population excess will accumulate in one of the two electronic spin states, leading to the alkali metal as a whole becoming highly polarized. The particular favored state depends on the directional helicity of the light.

The second stage in the SEOP process is that of spin-exchange. Bringing an unpolarized gaseous system into contact with the polarized alkali metal vapor results in spin-coupling via a hyperfine interaction. Gas phase collisions then lead to transfer of polarization from alkali metal electrons to noble gas nuclei on short timescales. The net spin polarization of the noble gas during the spin-exchange process is calculated using [3]

$$P_G = P_A \frac{\Gamma_{SE}}{\Gamma_{SE} + \Gamma_{SD}} \left[1 - e^{-t(\Gamma_{SE} + \Gamma_{SD})}\right] \tag{2}$$

where P_G and P_A represent the net spin polarizations of the gas and alkali metal, respectively, Γ_{SE} is the rate of spin exchange between alkali metal electrons and gas nuclei, Γ_{SD} is the rate of alkali metal electron spin destruction, and t is the time elapsed after the commencement of laser polarization in seconds. The SEOP process requires temperatures on the order of 100°C to ensure sufficient alkali metal vapor density. Buffer gases such as nitrogen is commonly used to quench radiation trapping and slow the rate of electron spin relaxation to help maintain high net spin polarizations by preventing unwanted fluorescence and reabsorption of unpolarized light [4] by alkali metal electrons. An overview of the SEOP process is illustrated in **Figure 1**.

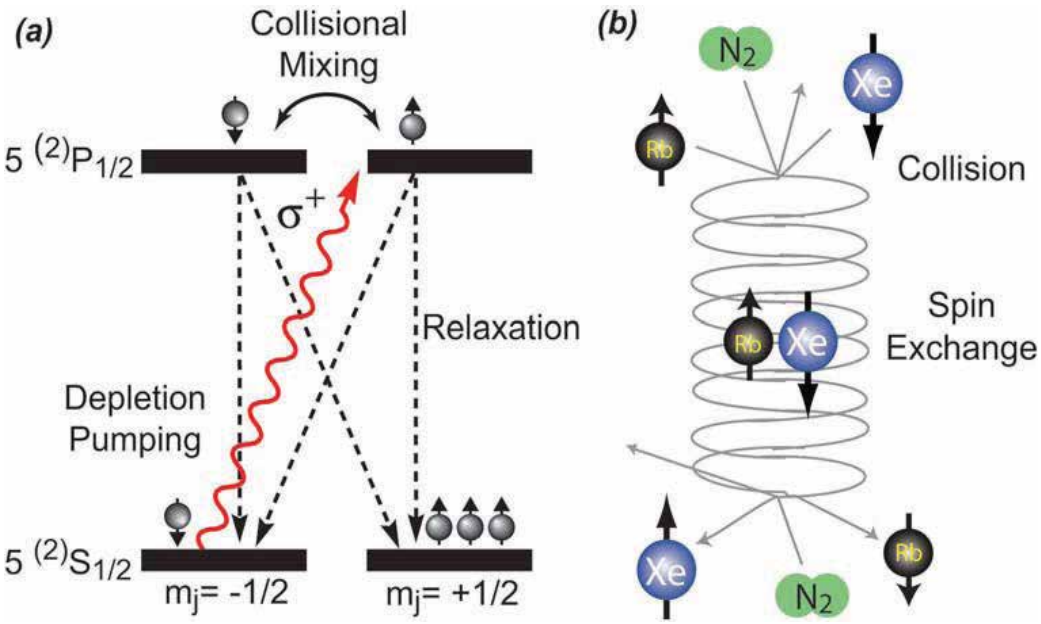

Figure 1. The spin-exchange optical pumping (SEOP) process. (a) Optical pumping and collisional mixing of the alkali metal electron spin states using circularly polarized light. (b) Polarization of noble gas nuclei via collision and spin-exchange process in the formation and breakup of an alkali-metal/noble-gas van der Waals molecule. Figures adapted from [7].

As previously mentioned, temperature is one of the most important variables governing the SEOP process. Elevated temperatures raise the alkali metal vapor density within the cell, increasing the probability of collisions between pump laser photons and alkali metal electrons and more importantly resulting in increased spin-exchange rates. As evidenced by Eq. (2), the latter effect should lead to a greater net spin polarization of the noble gas, provided there is sufficient pump light intensity to maintain good illumination of the optical cell (and hence, good alkali metal polarization). This prediction holds to a certain extent—as temperature continues to rise however, the alkali metal number density can increase rapidly in a self-propagating fashion; the alkali metal vapor absorbs more light, whose energy is rapidly converted to heat, which can in turn lead to even more alkali metal vaporization. This results in the form of optical opacity, whereby pump laser light is unable to penetrate the length of the optical cell. This actually reduces the efficiency of optical pumping in the areas of the cell furthest from the pump laser, because although the spin-exchange rate may be quite high, the alkali metal polarization in much of the cell is low, greatly reducing noble gas polarization. This is known as a "runaway" process [5, 6], and is clearly detrimental to a stable, efficient SEOP process. In the interest of obtaining the highest possible NMR signal, it is desirable to conduct experiments at an optimal temperature where net spin polarization and build-up rates are maximized, while avoiding the unstable runaway regime.

2.2. Temperature measurement using Raman spectroscopy

As mentioned above, the presence of nitrogen gas inside the optical cell is primarily meant to quench the rate of radiative spin-destruction, achieved by collisions with electronically excited

http://dx.doi.org/10.5772/65114

alkali metal atoms. The energy transferred as a result of these collisions is pooled in the rotational and vibrational modes of the N_2 molecules; these modes quickly relax to the translational degrees of freedom, thereby increasing the local gas temperature inside of the cell. Since SEOP must take place inside a closed system due to the high reactivity of alkali metals in air, physical insertion of a thermocouple is impractical for the reasons listed above, and merely measuring the cell surface temperature does not provide a true account of the internal temperature, nor the corresponding energy transport processes occurring within the cell. Additionally, progressively stronger light sources have been utilized for SEOP over the years, and lasers emitting tens or hundreds of watts of energy are now standard [6]. Virtually all of the laser energy absorbed by Rb is transferred to the rotational and vibrational degrees of freedom in the N_2 buffer gas, which then rapidly equilibrates with the translational temperature (corresponding to the local temperature of the gas mixture). These changes in temperature are capable of significantly affecting SEOP (hence, xenon polarization) through changes to the alkali metal density and absorption profile [8], degradation of organic coatings on the OP cell surface [9], and convective gas transport that may bring xenon in closer proximity to paramagnetic relaxation centers in the cell wall surface [4, 10, 11]; changes to temperature-dependent cross-sections that govern polarization and depolarization rates in SEOP may also occur. Remote sensing of the N_2 rotational (and vibrational) temperatures inside the pump cell during SEOP can be achieved using *in situ* Raman spectroscopy.

Hickman et al. [12] demonstrated that the intensity of each peak, numbered J, in the N_2 Raman spectrum follows the relation

$$I(J) \propto \nu^4 g(J)(2J+1) P_{J \to J'} e^{-\frac{BJ(J+1)}{k_B T}} \tag{3}$$

where ν is the frequency of the rotational line in Hertz, $g(J)$ is the ground state degeneracy due to the nuclear spin, B is the rotational constant for nitrogen (taken to be ~2), k_B is Boltzmann's constant, J is the peak number, and

$$P_{J \to J'} = \frac{3(J+1)(J+2)}{2(2J-1)(2J+1)} \tag{4}$$

Combining Eqns. (3) and (4) produces the relation

$$-BJ(J+1)\frac{hc}{k_B T} = ln\frac{S(J)}{g(J)f(J)} + 4ln\frac{1}{\nu} \tag{5}$$

where $S(J)$ is the measured intensity of the Raman peak, h is the Planck constant, c is the speed of light in m s^{-1}, and

$$f(J) = \frac{3(J+1)(J+2)}{2(2J+3)} \tag{6}$$

A plot of $F(J) = ln\left[\frac{S(J)}{g(J)f(J)}\right]$ against $J(J+1)$ then yields a straight line with gradient $m = \frac{Bhc}{k_B T}$. Rearranging this equation for T thus allows calculation of the rotational temperature of N_2.

2.3. Hyperpolarized lung imaging

Any noble gas isotope with nonzero spin can theoretically be used as a hyperpolarized contrast agent with a view for clinical lung MRI. Traditionally, helium-3 was most commonly used due to its high gyromagnetic ratio—resulting in stronger MRI signals. However, due to its insolubility in blood and water, perfusion across the alveolar wall cannot occur, primarily limiting the use of ^{3}He to gas-phase ventilation and diffusion imaging. The difficulty in wide-spread clinical ^{3}He adoption is further compounded by the difficulty and expense of acquisition, since ^{3}He is a nonrenewable by-product of tritium decay in nuclear reactors. As such, most current clinical studies on hyperpolarized noble gases use ^{129}Xe for its solubility in tissue and blood, significant chemical shift range, low cost of acquisition, and high natural abundance.

As discussed previously, higher net spin polarizations directly result in stronger MR signal generation and hence, improved image contrast between areas of interest and background noise. Recent hyperpolarization methods can create near-unity net spin polarizations [13], resulting in spectroscopic signals four to five orders of magnitude greater than nonhyperpolarized samples. Such improvements in image quality facilitate the use of HP noble gas MRI within the lungs as a diagnostic imaging tool for characterizing lung structure and function [14], and consequently may potentially enable earlier and more reliable diagnosis of various respiratory disorders, such as idiopathic pulmonary fibrosis (IPF) and chronic obstructive pulmonary disease (COPD) 7]. An example of a HP ^{129}Xe lung ventilation image can be seen in **Figure 2**.

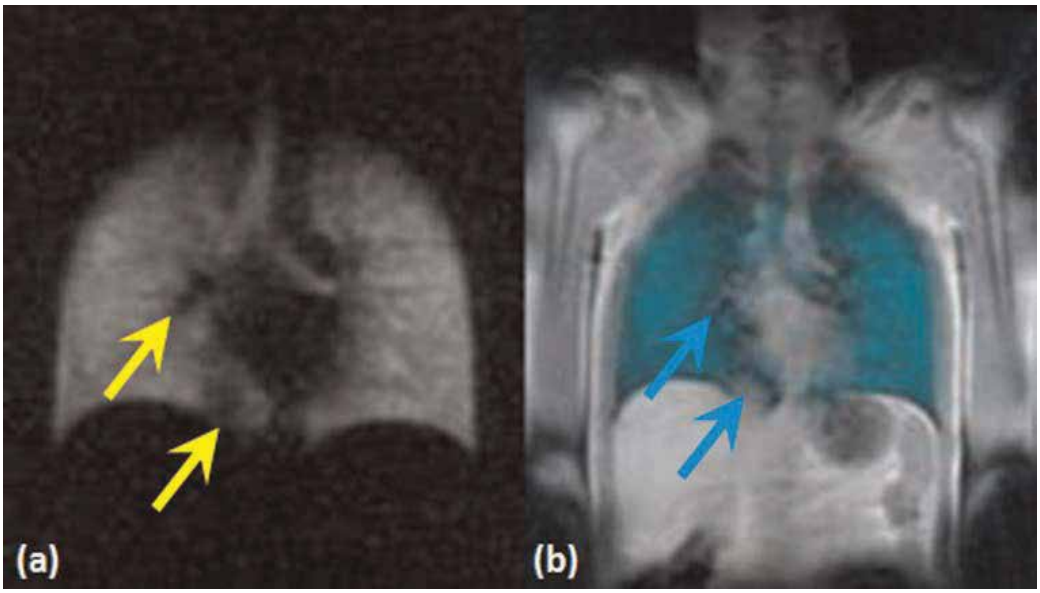

Figure 2. (a) Coronal plane 25 mm slice ^{129}Xe-MR ventilation image of a healthy adult male, with ^{129}Xe appearing bright, upper airways are clearly delineated. (b) Second coronal plane 25 mm slice fused ^{129}Xe-MR ventilation and proton coregistration image, with ^{129}Xe appearing green blue-green. On the fused image, it can be seen that ventilation defects on the ventilation image (yellow arrows) correspond to a diaphragmatic eventration and pulmonary vasculature on the fused image (blue arrows) [15].

http://dx.doi.org/10.5772/65114

3. Methodology

Early studies carried out by Happer and coworkers [4] used the N_2 rotational temperature to monitor energy transport during optical pumping. These experiments primarily used pump cells loaded with helium and nitrogen gases, and operated under the same experimental conditions as SEOP (without the NMR-active noble gas) using a broadband (2 nm linewidth) 795 nm Rb D_1 pump laser. The Raman setup shown in **Figure 3(a)** consisted of a 514.5 nm probe beam from an argon-ion laser (6 W) that could be focused to a 1 mm waist anywhere within the pump cell; the scattered light was collected using a planoconvex lens and directed into a Spex 1404 double Raman spectrometer (0.85 m focal length) and the photons were counted using a bi-alkali photomultiplier tube (PMT) with computer readout. The results of this work include the observation of convective heat transfer during optical pumping, as the N_2 rotational temperature deviated from a linear relationship with absorbed pump laser power, shown in **Figure 3(b)**. This convective heat transfer was further studied by measuring the N_2 temperature at differing spatial locations throughout the pump cell as a function of pump laser absorption. For low values of laser absorption (2.9 W), the calculated Rayleigh number (which provides a measure of convective vs. conductive transfer by comparing buoyant and viscous forces) indicates conductive heat transfer to the pump cell walls. As the absorption of the pump laser is increased to 15 W, the Rayleigh number indicates convective heat transfer; this is important in SEOP, as convection can affect the residing time of polarized ^{129}Xe nuclei near the pump cell walls and lead to depolarization. Switching between a cell loading of predominantly helium gas with some nitrogen (1.0 and 0.33 amagat) to a cell with only high density nitrogen (3.2 amagat) increased the Rayleigh number by a factor of 70; simply changing the pump cell volume and geometry further increased the Rayleigh number by an additional factor of 29. This demonstrates how gas composition, density, and pump cell geometry can affect energy transport during SEOP.

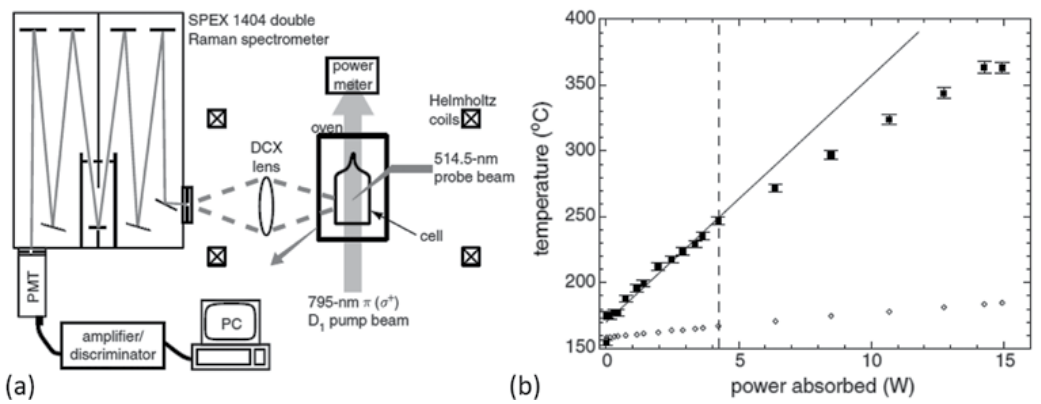

Figure 3. (a) Schematic representation of Happer's experimental setup showing SEOP pump cell, 795 nm Rb excitation source, and orthogonal Raman probe/detect configuration. 514.5 nm Raman probe beam furnished by a 15 W water cooled argon-ion laser, with resulting Raman scattering imaged directly into spectrometer. (b) N_2 rotational temperature (solid squares) as a function of absorbed laser power for a cell loading of 2 amg He and 0.33 amg N_2 in a 40 cm^3 OP cell, with an external cell surface temperature of 170°C (open diamonds). Solid line fits to data points up to 4.3 W of absorbed energy, after which the experimental data deviate significantly from a purely conductive energy dissipation model [2].

Happer et al. also noticed that the N_2 rotational temperature was elevated compared to the surface temperature of the glass walls of the pump cell (measured via thermocouple). The extent of the temperature elevation changed with absorbed pump laser power and gas loading (density/composition), and often varied from 100 to 200°C above the cell wall temperature. Because of the slower vibrational-to-rotational cross-relaxation, N_2 vibrational temperatures were found to be significantly elevated in pump cells containing only nitrogen (T_{vib} ~ 900°C). Upon the addition of helium gas, N_2 vibration temperatures were only elevated ~120°C above the cell surface temperature, due to the significantly faster relaxation time with the helium translational temperature. These studies, which were the first to use Raman spectroscopy to remotely monitor gas temperatures during SEOP, utilized relatively low resonant laser powers and predominantly helium-rich gas loadings—both of which lessen the degree to which energy accumulates in the N_2 rotational-vibrational manifold. The authors noted that additional studies would be warranted under conditions of high resonant laser power and the absence of helium buffer gas.

3.1. Orthogonal configuration

Recent advances in laser diode array (LDA) technology have resulted in not only an increase in overall laser power (hundreds of watts), but also a narrowing of the spectral output from several nanometers to a few tenths of a nanometer. This increase in resonant flux leads to more efficient absorption by the relatively narrow alkali metal D_1 absorption line (c.a. ~0.1 nm), with the consequence of additional thermal management concerns [6]. Furthermore, recent advances in using high xenon partial pressures (p_{Xe}) in SEOP in the absence of helium to attain high xenon nuclear spin polarization values (p_{Xe}) [16], and its further application in clinical-scale xenon hyperpolarizers used for pulmonary imaging [6], have furthered the interest in binary Xe/N_2 gas mixtures for SEOP. The absence of helium, with its favorable thermal conductivity, is expected to further exacerbate thermal management concerns. Because of these demands of high resonant laser flux and gas density/composition, additional studies of energy transport under these conditions is warranted.

Further work from Whiting et al. [17] conducted remote temperature sensing using Raman scattering to observe energy thermalization during $Rb/^{129}Xe$ SEOP under conditions of high xenon partial pressures and resonant laser powers. These studies used a laser diode array (~70 W) that was frequency-narrowed (~0.25 nm linewidth) using an internal volume holographic grating; this SEOP pump laser was spectrally tunable independent of output power to allow comparative studies at different excitation frequencies. The cylindrical optical pumping cell (2.5 cm inner diameter; 15.5 cm length) was surrounded by an outer glass cylinder that served as a forced-air oven and allowed 360° optical access [18]. Miniature NMR coils were placed directly under the OP cell to allow correlative low-field NMR studies of HP ^{129}Xe gas along with Raman scattering measurements of nitrogen buffer gas. The Raman apparatus shown in **Figure 4**(**a**, **c**) consisted of a Verdi V5 532 nm excitation laser (5 W) that was fiber-coupled to a modular lens assembly box to focus the light into the OP cell. Scattered light was collected by a similar lens box (positioned orthogonal to the probe laser) that was fiber-coupled to a Horiba Jobin-Yvon U1000 double 1-m Raman spectrometer with 2400 l/mm grating and CCD receiver. Spatial filtering of the laser and Rayleigh scatter was achieved through

http://dx.doi.org/10.5772/65114

adjustment of the internal baffles of the spectrometer; this provided spectra that displayed Stokes and anti-Stokes rotational Raman lines within 6 cm^{-1} of the laser line without the use of notch or edge filters—see **Figure 4(b)**. The N_2 rotational temperature was calculated using the methods explained in Section 2.2, and calibration studies showed a good correlation with different N_2 gas temperatures in the absence of optical pumping as shown in **Figure 4(d)**.

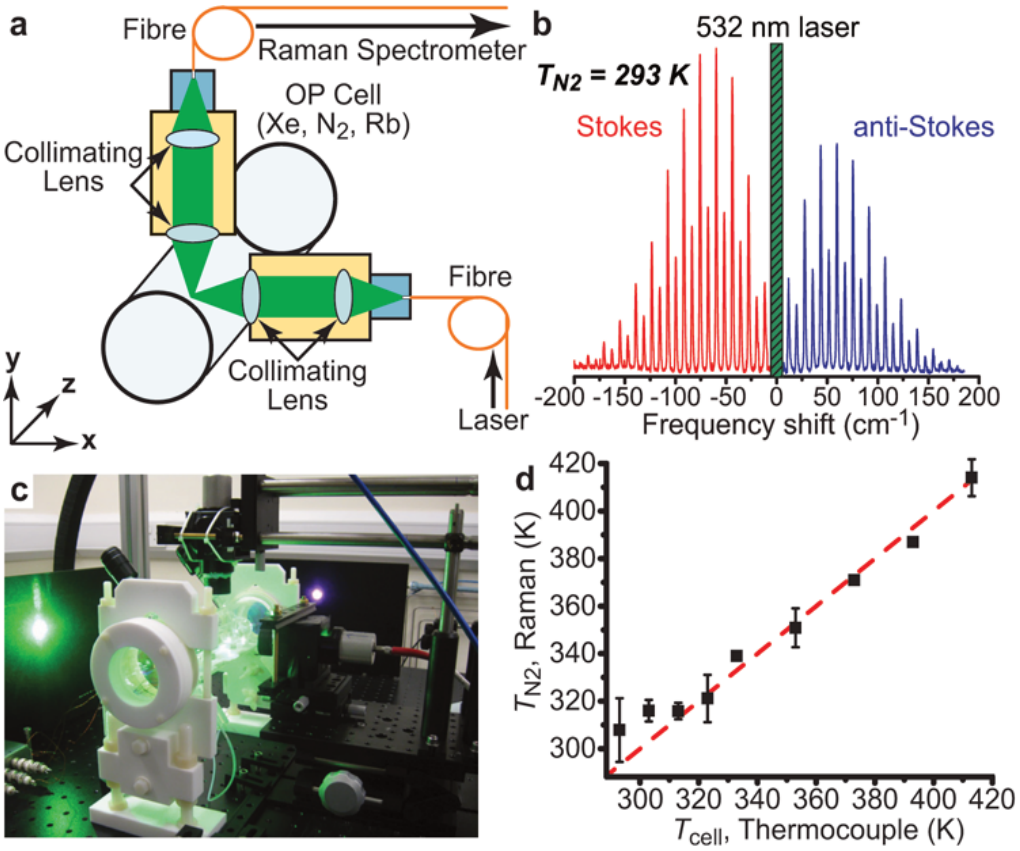

Figure 4. (a) Schematic representation of orthogonal Raman apparatus. (b) Example N_2 rotational Raman spectrum (baseline-corrected) at room temperature, without SEOP (3 atm N_2). (c) Photograph of orthogonal Raman apparatus. (d) Plot of oven temperature (T_{cell}) measured via thermocouple (located in the oven inlet airstream) versus T_{N2} measured via Raman spectroscopy without SEOP; experimental data (squares) are shown in comparison with simulation assuming 1:1 correlation (dotted line); error bars are least-squares fit errors of *Bhc*/*kT* plots [19].

In this work, different xenon partial pressures were studied to determine the effects from increasing incident laser power on both ^{129}Xe hyperpolarization level and N_2 rotational temperature—see **Figure 5(a, b)**. Both HP ^{129}Xe signal and N_2 rotational temperatures increased with laser power for the different gas loadings (100/1900, 500/1500, and 1500/500 Torr Xe/N_2), with the highest ^{129}Xe signal and N_2 temperature observed at the highest xenon partial pressure. This increased temperature at high xenon partial pressure was not primarily attributed to increased laser absorption, but rather to the combination of the lower concentration of nitrogen (increasing the energy absorption per N_2) and low thermal conductivity of xenon

(which was the significant fraction of total gas volume). Gas loadings with the lowest xenon partial pressure exhibited a relatively weak dependence of N_2 rotational temperature on incident laser light. Despite the high nitrogen temperatures, the high xenon density loading provided the highest overall ^{129}Xe NMR signal—typically the overall figure of merit for applications of hyperpolarized contrast agents.

Additional studies examined the effects of heating as a function of longitudinal position within the cylindrical pump cell. Because the external heat source was provided in the rear of the cell, and the forced air oven was poorly insulated, there was a significant temperature gradient (~30–40°C surface temperature) along the length of the cell. Both the ^{129}Xe NMR signal and the N_2 rotational temperature reflected the presence of this gradient and showed the maximal values were at the rear of the cell (close to the heating source). This type of back-to-front temperature gradient has both benefits and detriments. One benefit is that the total cell illumination may improve, as the optical density of absorbers gradually increases with penetration depth (unlike other OP systems, which may have conditions where all the laser light is absorbed in the front portion of the cell—leaving the rear of the cell optically opaque); this improved illumination should increase global HP ^{129}Xe signal. On the other hand, an unfavorable result of temperature gradients is longitudinal convective heat transport, which potentially brings the polarized gas in close contact with paramagnetic relaxation centers in the cell wall surface for longer periods of time. These studies were carried out at different illumination wavelengths to examine how changes to the Rb D1 lineshape [6] (through altering the gas density and composition) affect the N_2 rotational temperature. The highest HP ^{129}Xe NMR signals and N_2 rotational temperatures were found nearest to the Rb D_1 line, and elevated values were observed at red-shifted excitation wavelengths (as expected, given the effects of different gas loadings on the Rb absorption lineshape [6]).

The effects of slight changes in temperature of the forced air oven on both HP ^{129}Xe NMR signal and N_2 rotational temperature over the course of an SEOP experiment were also monitored—see **Figure 5(c, d)**. Increasing the external cell temperature from ~110°C to ~140°C resulted in significant changes to these parameters. At the lower cell temperature, the N_2 rotational temperature reached steady state (~190°C) quickly and held the value throughout the course of the experiment (40 min); correspondingly, other conditions within the OP cell remained stable (e.g., laser absorption, Rb density, P_{Xe} value, etc.). By raising the external cell temperature a mere ~30°C, the N_2 rotational temperature climbed to ~730°C in less than 15 minutes of OP; a steep rise in HP ^{129}Xe signal was also observed in the initial portion of the SEOP experiment. However, once the N_2 rotational temperature peaks, both it and the P_{Xe} values begin to drop significantly. The N_2 rotational temperature remains quite high (~530°C), but fluctuates greatly over the remainder of the experiment; the amount of absorbed laser light continues to increase for the remainder of the experiment. These occurrences likely indicate both Rb runaway as well as increased turbulence inside the OP cell. These results, showing the effects of slight external cell surface temperature changes on the SEOP efficiency, indicate that (under some experimental regimes) overall cell illumination can be more critical than the Rb/^{129}Xe spin-exchange rate (which is often viewed as the most important parameter of SEOP).

In summary, this work expanded on the previous studies of Happer et al. [4] by examining a regime of high resonant laser power and xenon-dominant binary gas mixtures in the absence of

http://dx.doi.org/10.5772/65114

helium. It also used *in situ* low-field ^{129}Xe NMR in addition to the N_2 rotational temperatures observed using Raman spectroscopy. These relatively extreme conditions showed that elevated N_2 rotational temperatures correlated with ^{129}Xe hyperpolarization across a range of experimental conditions and that internal gas temperatures of ~730°C could be observed within 15 minutes of SEOP. While the results of these experiments effectively displayed the interdependence of laser power, cell temperature, gas density/composition, and laser centroid offset during SEOP, the experimental Raman setup could be significantly improved. Although the internal baffles of the Raman spectrometer were used for spectral/spatial filtering (in the absence of notch or edge filters), detection sensitivity was an issue, as were significant problems with the baseline. Furthermore, the orthogonal excitation/detection setup was difficult to precisely focus (with an associated hysteresis). Both the probe beam and Raman scattering collection optics needed to be focused to the same point within ~1 mm spatial resolution in three dimensions using only manual translational stages. An improved design, in which the excitation and collection optics were colinear, would simplify the setup and overcome many of these shortfalls.

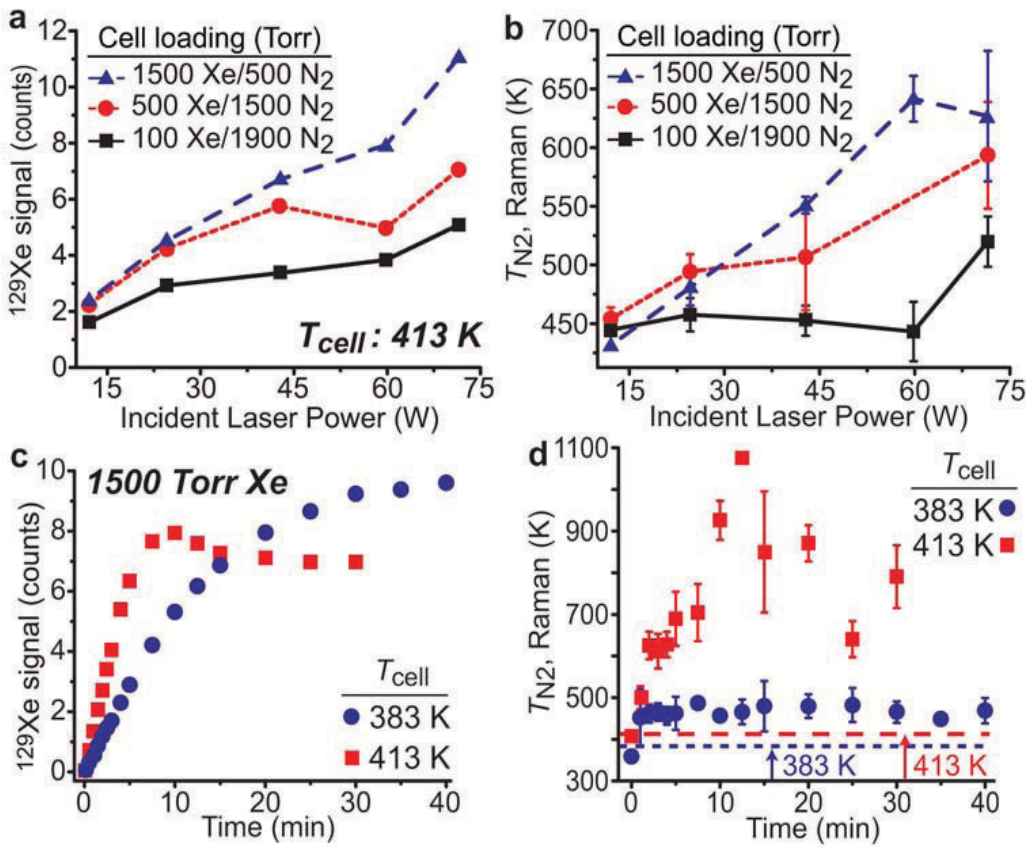

Figure 5. (a) Plot of ^{129}Xe NMR signal versus incident laser power for three Xe/N_2 gas mixtures (values in Torr): 100/1900 (solid); 500/1500 (dotted); and 1500/500 (dashed). (b) Concurrent N_2 rotational temperatures for the experiment in (a) (*y*-axis baseline set to T_{cell}). (c) Time course of ^{129}Xe NMR signal recorded during SEOP performed at two different oven surface temperatures: 383 K (squares) and 413 K (circles) for a cell loading of 1500/500 Torr Xe/N_2. (d) Concurrent N_2 rotational temperatures for the experiment in (c). Upper limits of T_{cell} are shown as dotted (383 K) and dashed (413 K) lines [17].

3.2. In-line superhead

In an attempt to overcome the limitations of the orthogonal Raman probe arrangement, a confocal approach was taken whereby scattered photons were detected in the same plane as probe laser photon emission. To realize this, the same 532 nm probe laser and Horiba Jobin-Yvon U1000 double 1-m Raman spectrometer (from Section 3.1) were fiber-coupled instead to an on-axis optical module. This design greatly improved the sensitivity and reliability of the measurements due to the significantly reduced chance of misalignment relative to the orthogonal arrangement. Two ultra-narrow-band VHG notch filters were used to discard the vast majority of dominant Rayleigh scattered light, allowing resolution of both Stokes and anti-Stokes ultra-low frequency Raman lines as close as 10 cm^{-1} to the probe laser wavelength. Rayleigh scattered light was further reduced by an order of magnitude through the inclusion of an ultra-narrow-band beamsplitter filter, which also facilitated the minimization of spontaneous laser diode emissions and fluorescence, thus greatly improving the spectra of the incoming probe photons [19]. Additionally, the entire configuration is mounted on a translational x-axis stage, allowing different positions within the optical cell to be probed independently. Schematics of the inline configuration are shown in **Figure 6**, along with a typical Raman spectrum and temperature calibration plot to illustrate the improvements in sensitivity.

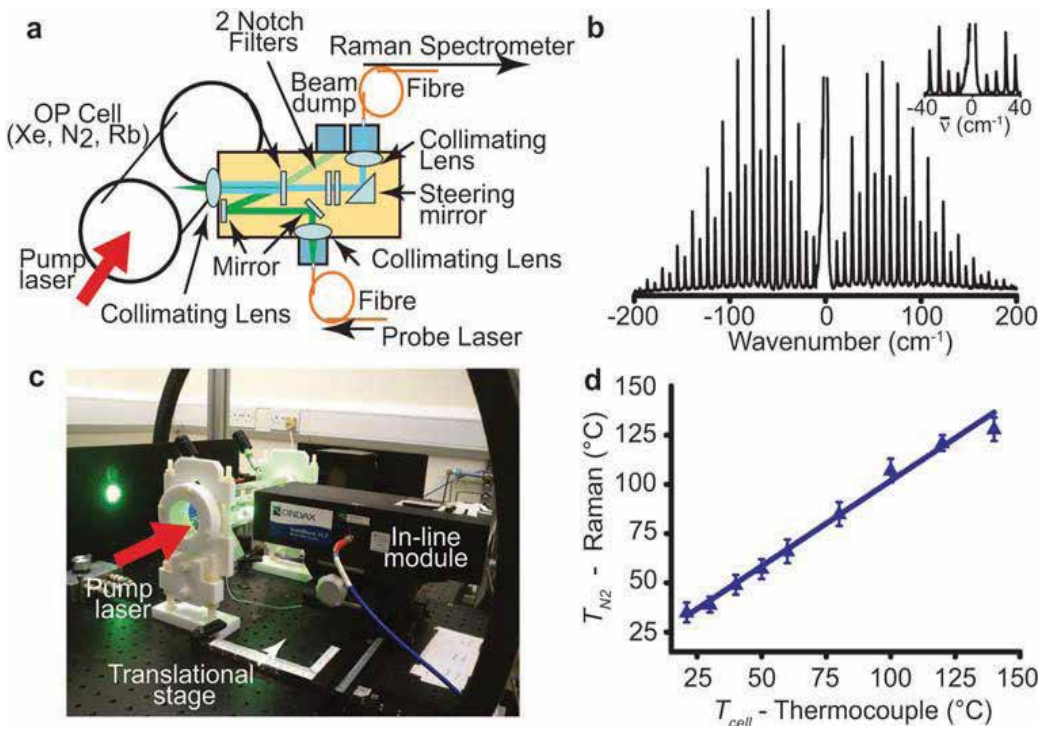

Figure 6. (a) Schematic representation of in-line Raman module. (b) Example N_2 rotational Raman spectrum (baseline-corrected) at room temperature, without SEOP (3 atm N_2). The inset shows a close-up of the ultra-low frequency region that is spectrally resolvable using the in-line apparatus. (c) Photograph of in-line Raman module. The inline module is mounted onto a translational stage to allow three-dimensional mapping of T_{N2} within the cell. (d) Plot of oven temperature (T_{cell}) measured via thermocouple (located in the oven inlet airstream) versus T_{N2} measured via Raman spectroscopy; experimental data (triangles) are shown in comparison with simulation assuming 1:1 correlation (line); error bars are least-squares fit errors of *Bhc*/*kT* plots [19].

http://dx.doi.org/10.5772/65114

A comparison of Raman spectra acquired using the orthogonal and in-line methods was made under identical conditions at room temperature, with no pump laser illumination and over a 15 s integration time in an optical cell containing 100/1900 Torr Xe/N_2. The results of this experiment are shown in **Figure 7**, indicating a ~23-fold improvement in SNR [19], facilitating much more accurate determination of temperature. It can be seen from the spectra that additional Raman signals arise from atmospheric N_2 and O_2 along the optical path of the probe laser external to the optical cell. In later studies, these contributions to the Raman spectrum were mitigated by collection of spectra from an evacuated optical cell, which were subsequently subtracted from the data to remove "background" signals. Care must be taken during this correction process, however, as spectral drift can result in unrealistic difference spectra and less precise temperature measurements.

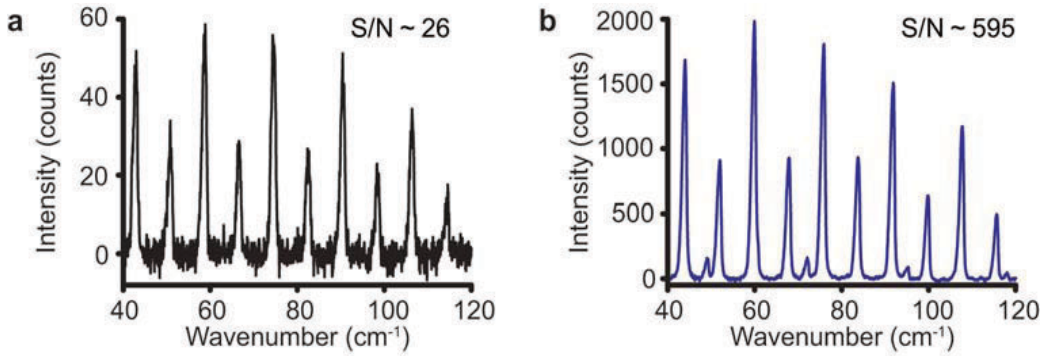

Figure 7. Comparison of typical rotational Raman spectra from N_2 gas at 24°C using the 'orthogonal' detection system (a) or the 'inline' module (b). Spectra were obtained under identical conditions (OP cell containing 100/1900 Torr Xe/N_2, 15 s acquisition time, no pump laser illumination), and indicate a SNR improvement of ~23-fold when using the in-line apparatus [19].

As an initial demonstration of temperature determination *in situ* during SEOP, the effects of cell heating due to the pump laser were investigated by comparing the T_{N2} spatial profile along the *z*-axis after 5 min of pump laser illumination at 60 W, for both a frequency-narrowed and broadband laser diode array. The gas mixture was an identical 100/1900 Torr Xe/N_2 mixture, while the temperature at the inlet to the external forced air oven was 150°C. Measurements were taken across the optical cell at intervals of 1 mm transverse to the pump laser beam, at an *x*-position 21 mm behind the front window. The resulting Raman spectra were analyzed to calculate T_{N2} across the width of the cell. It was observed that for both pump laser sources, temperatures were elevated relative to thermocouple readings in the external forced air oven; by roughly 40°C in the case of broadband pump laser illumination, but by as much as 200°C when using the frequency-narrowed pump laser. This can be explained by a greater proportion of photons from the frequency-narrowed pump laser possessing the energy required to induce an energy level transition within the alkali metal electrons. The higher number of polarized electrons directly leads to an increase in the amount of energy imparted to the rovibrational states of N_2 as a result of quenching collisions. The results of this experiment are shown in **Figure 8** along with spectral profiles of the two different lasers used.

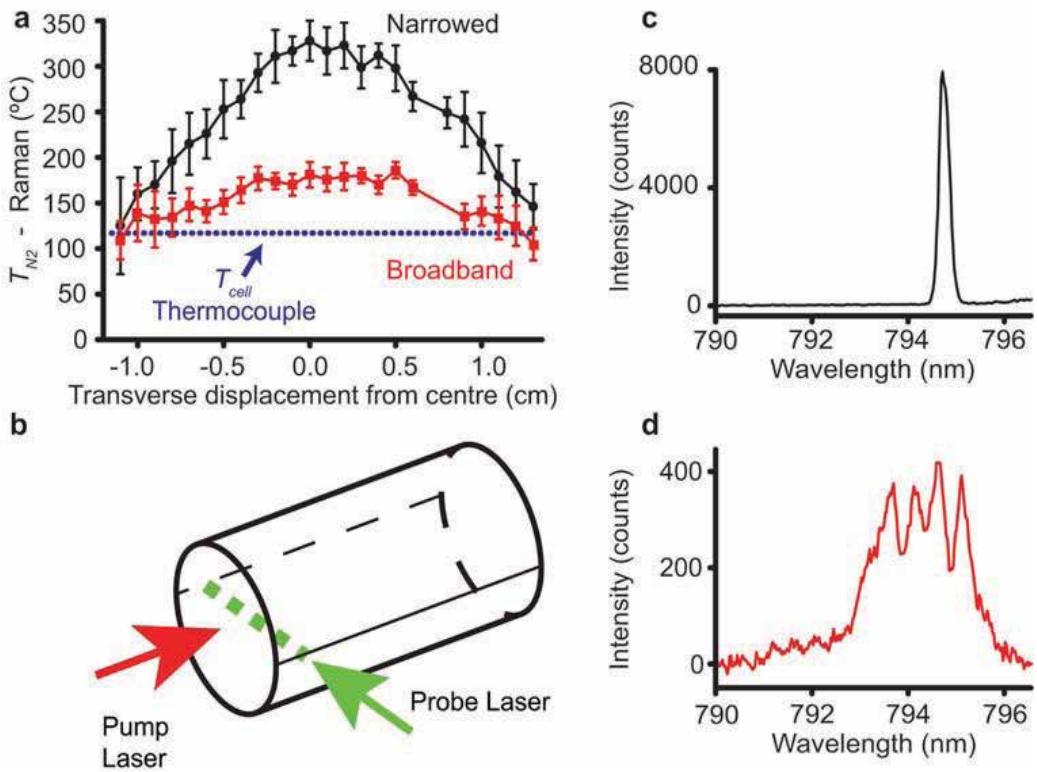

Figure 8. (a) Plots showing the spatial variation of the steady-state values of T_{N2} during SEOP, as induced by the 'pump' LDAs [acquired after 5 min of illumination by either a 60 W broadband (red squares) or 60 W VHG-narrowed LDA (black circles)]. Plots are compared to the temperature of the external glass wall near the front of the cell, as measured with a thermocouple (dotted line). (b) Schematic representation detailing the collection of T_{N2} data; values for T_{N2} were measured in 1-mm increments by translating the focused spot horizontally across the cross-section of the cell, transverse to the pump beam. (c, d) Spectral profiles of the VHG-narrowed and broadband LDAs, respectively; FWHM = 0.26 and 2.13 nm [19].

4. Current work and future directions

Since demonstrating its utility and improved performance, the in-line Raman module has become central to our current work: a series of experiments that provide greater insight into xenon-rich stopped-flow SEOP. So far, these experiments have examined SEOP as a function of (1) buffer gas, in which the ratio of N_2 to He was varied; (2) position within the optical cell, in which the portable nature of the in-line Raman module was harnessed to probe in-cell temperatures at multiple points along the length of the optical cell; and (3) alkali metal ratio (the so-called hybrid SEOP), in which pure Rb SEOP was compared to SEOP with Cs also present in the optical cell in varying amounts. The rationale, results, and implications of these experiments are described in the following sections.

4.1. Function of buffer gas/mixture composition

There are two primary buffer gases that are typically utilized in SEOP experiments—N_2 and He. N_2 is used to perform radiation trapping, quenching the emission of resonant unpolarized photons by excited alkali metal atoms that would otherwise depolarize other Rb atoms. He meanwhile was originally added in high fractions to collisionally broaden the absorption line of the alkali metal to more optimally couple the incident laser line [20], a job to which it was well suited due to its low Rb spin-destruction rate—see **Table 1**. N_2 also provides pressure-broadening effects, albeit at the cost of increased spin-destruction. This practice was necessary because the pump laser linewidths were initially at least an order of magnitude wider than the Rb D_1 transition line, resulting in inefficient optical pumping. Although the role of He for pressure-broadening has become increasingly redundant as pump laser linewidths narrow to approach the Rb linewidth, its high thermal conductivity relative to N_2 and Xe is important to note. In the emerging regime of ^{129}Xe-rich stopped-flow SEOP, where both the poor thermal conductivity of the Xe and longer gas residence time in the cell compound thermal runaway issues, He may be uniquely situated to facilitate the dissipation of thermal energy from the optical cell, ultimately improving yields of polarized ^{129}Xe.

Gas	Thermal conductivity (10^{-2} W m^{-1} K^{-1})	Spin destruction rate (cm^3 s^{-1})
Xenon	0.70	6.02×10^{-15} (T/298 K)
Nitrogen	3.09	3.44×10^{-18} (T/298 K)
Helium	17.77	3.45×10^{-19} (T/298 K)

Table 1. Thermal conductivities and spin destruction rates for Xe and N_2/He buffer gases used in the SEOP hyperpolarization process [21].

The impact of He on the thermal behavior within the optical cell can be seen in **Figure 9**. Here, three SEOP experiments are compared in which the partial pressure of Xe and the total cell pressure were held constant at 100 Torr and 2000 Torr, respectively, but increasing amounts of He gas were substituted in place of N_2. As the fraction of He within the cell was increased it can be seen that T_{N2} is reduced from roughly 200°C with no He present, to 100°C with 1400 Torr He included in the mixture. The onset of Rb runaway is evident from the sharp spike in ^{129}Xe polarization in the first mix, where the polarization initially climbs sharply, peaking abruptly at ~6 min before dropping. At this point the high Rb vapor density creates optical opacity that limits the polarization process. It can be seen that this effect is suppressed as more He is added to the mixture at little cost to the ultimate ^{129}Xe polarization. Given that existing ^{129}Xe-rich stopped-flow polarizers operate with substantially higher powered lasers, which only further exacerbate these thermal management issues, it may be that He becomes a valuable tool for optimization.

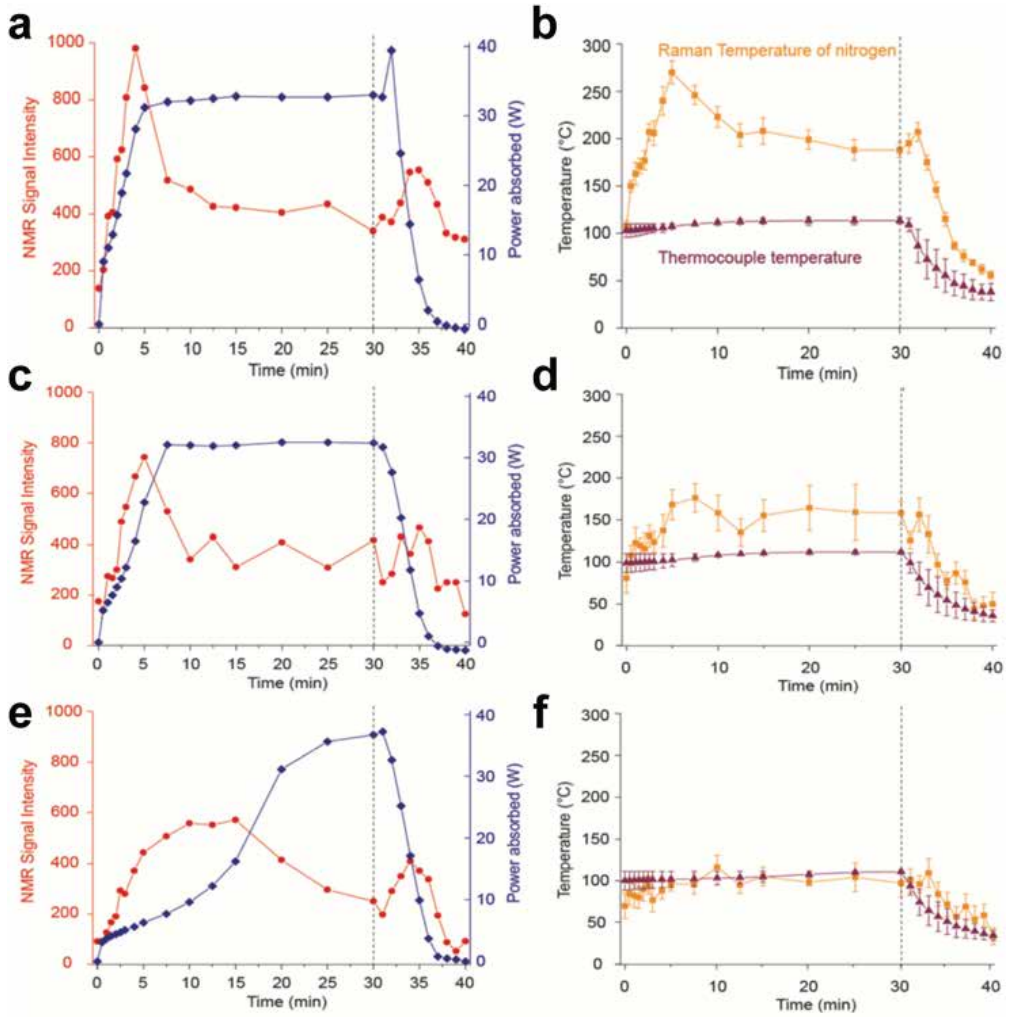

Figure 9. Comparison of SEOP as a function of buffer gas composition—(a), (c), and (e) show Xe polarization (red) and power absorbed (blue). (b), (d), and (f) show N_2 Raman temperature (orange) and oven thermocouple temperature (green). Gas compositions were 100/1900 Torr Xe/N_2 with no He (a, b), 100/1700 Torr Xe/N_2 and 200 Torr He (c, d), and 100/500 Torr Xe/N_2 and 1400 Torr He (e, f) [22].

4.2. Position-dependent temperature mapping

The experiments that vary buffer gas density/composition indicate that polarization and temperature are likely to vary along the length of the cell, particularly under conditions of Rb runaway. **Figure 10** illustrates how Raman measurements were taken at coincident locations to NMR measurements at the front, middle, and back of the optical cell (a) using the translational stage (b). **Figure 11** shows the results of two experiments where this configuration was used. Both experiments were conducted on a gas mix of 1000/1000 Torr Xe/N_2 but at oven temperatures of 120 and 130°C, respectively. At 120°C, the temperature at the front, middle, and back correspond well to the xenon polarizations, which are both highest at the back for the cell.

http://dx.doi.org/10.5772/65114

However, it can be seen that a mere 10°C increase in oven temperature is enough to induce significant variation in T_{N2} along the length of the cell. Closer examination shows that after 4 min of pump laser illumination during SEOP, when the ^{129}Xe polarization prematurely spikes, a switch in the Raman temperatures occurs–indicative of a change in the thermal flow patterns within the cell. This effect is likely caused by Rb runaway, a conclusion corroborated by the elevated pump laser light absorption, which indicates a spike in absorbers.

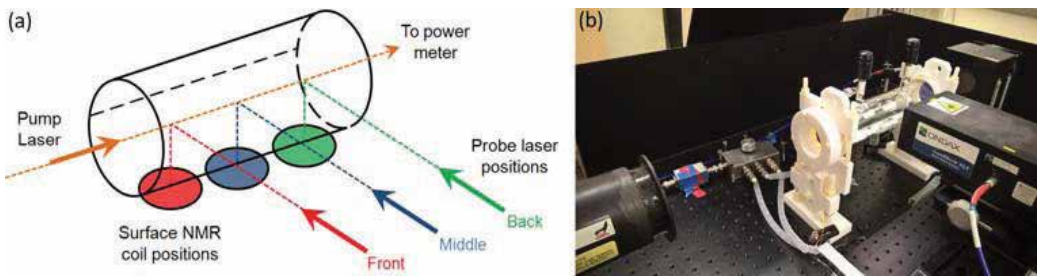

Figure 10. (a) Schematic representation showing in-line Raman module probe and NMR surface coil alignment at three positions within the optical pumping cell. (b) Photograph of in-line Raman module and NMR surface coils placed within the oven [23].

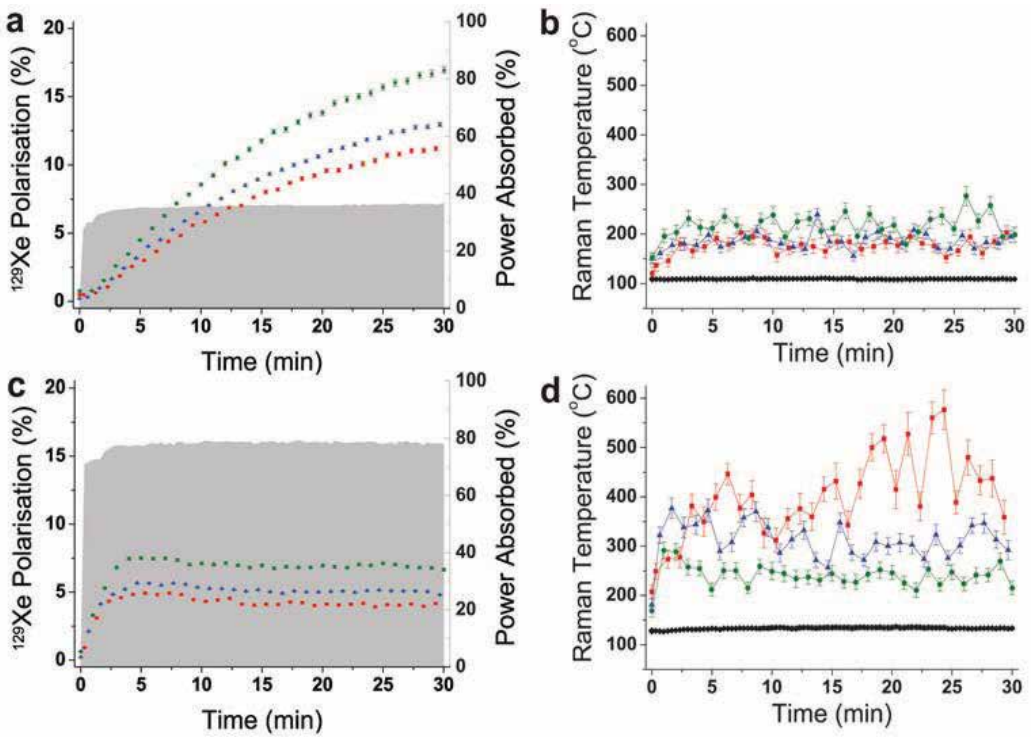

Figure 11. Comparison of Xe polarization build-up and T_{N2} Raman measurements during a 30-min SEOP experiment in an optical pumping cell containing 1000/1000 Torr Xe/N_2 at 120°C (a, b) and 130°C (c, d). Line color is indicative of cell position as outlined in **Figure 10(a)**. The shaded area in figures (a) and (c) represents the percentage of pump laser light absorbed [23].

These measurements as a function of position will be improved by introducing an automated translational stage that will permit more reliable positioning of the Raman probe relative to the cell with increased speed and precision. This will facilitate N_2 temperature maps in two dimensions—both along the width and the length of the optical cell.

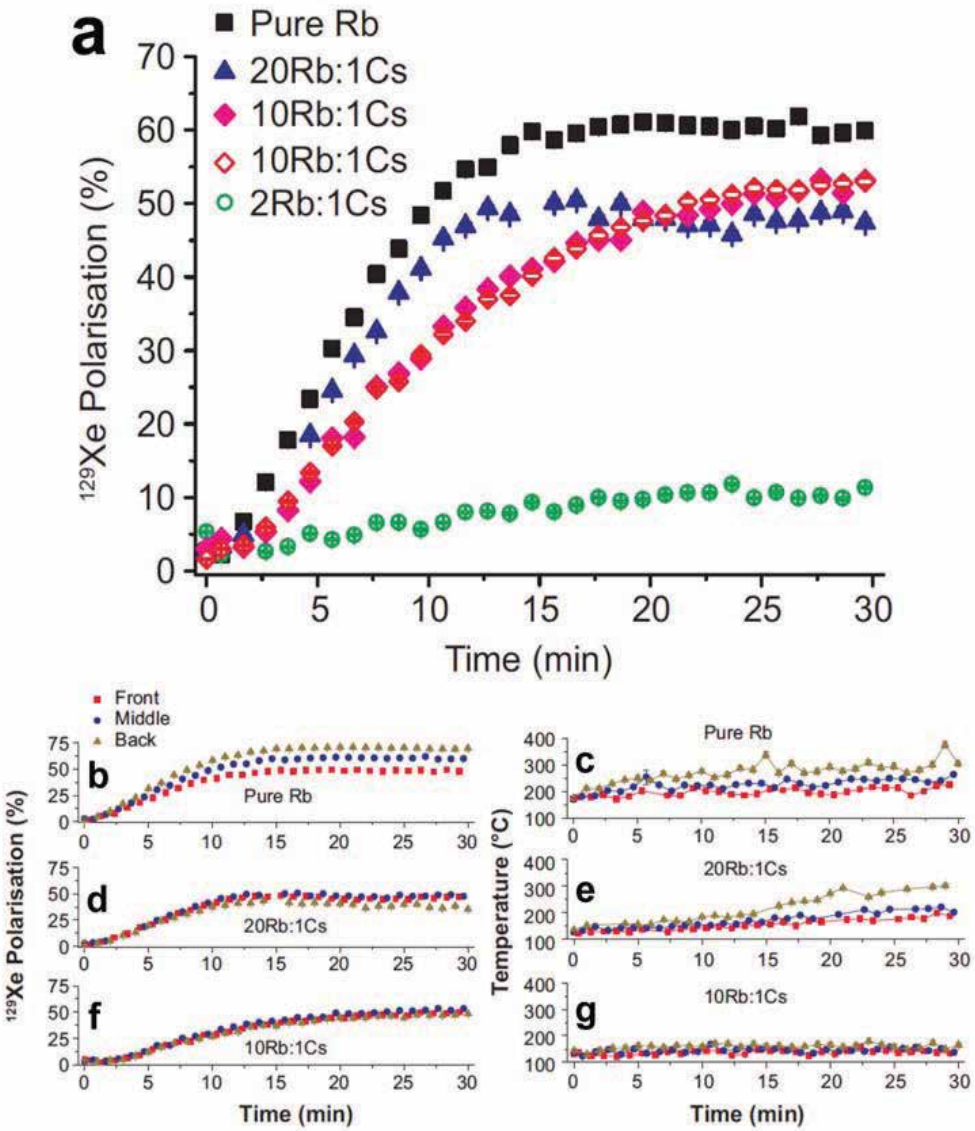

Figure 12. Rb-Cs hybrid SEOP. (a) ^{129}Xe polarization build-up curves using pure Rb, 20Rb:1Cs, 10Rb:1Cs, 2Rb:1Cs. Solid colored symbols denote a premixing of the AMs before loading; empty symbols denote separate loading. (b), (d), and (f) show xenon polarizations for the front middle and back positions within the cell for pure Rb, 20Rb:1Cs, 10Rb:1Cs and (c), (e), and (g) show the corresponding Raman temperatures. Cell oven temperature was set to 140°C and the gas mixture was 100/1900 Torr Xe/N_2 [24].

http://dx.doi.org/10.5772/65114

4.3. Function of alkali metal ratio (Rb-Cs hybrid SEOP)

Rubidium has long been the alkali metal of choice for SEOP, owing to its large absorption cross-section and the availability of affordable, high-powered lasers that are well matched to its D_1 transition line. Additionally, Rb is solid at room temperature, with a low melting point that facilitates easy storage and transfer into optical cells. However, it has been shown that cesium can produce greater polarization under similar experimental conditions [25], but comparably high-powered lasers at the Cs D_1 transition wavelength are not commonplace. Alternatively, for ^{3}He hyperpolarization by SEOP, it was shown that using two alkali metals simultaneously—rubidium and potassium—resulted in four times faster build-up of net spin polarization once the optimal ratio of the alkali metals had been achieved [26]. In this example it was Rb that underwent optical pumping, with angular momentum transferred to He by two distinct spin-exchange routes; one directly from Rb to He, and from Rb to He via K. The reason for the increase in speed is that the exchange cross sections for Rb-K and K-He are both larger than those for Rb-He alone. Inspired by these findings, we conducted analogous experiments in an Rb-Cs SEOP system to hyperpolarize ^{129}Xe. The SE cross-sections for Rb-Cs and Cs-Xe have been shown to be greater than for Rb-Xe in separate experiments [27, 28]. If successful, the performance of existing polarizers could be improved with the simple addition of Cs to the existing Rb within the optical cell. As with previous studies, a 60 W pump laser tuned to the Rb D_1 transition wavelength was used for polarization.

Figure 12(a) shows a summary of major hybrid results to date. From this figure it can be seen that, contrary to that suggested by the SE cross-sections, the resulting ^{129}Xe polarization in our initial efforts decreases as more Cs is added to the alkali metal hybrid mixture. The data in **Figure 12(b–g)** can be used to explain this observation, indicating that ^{129}Xe polarization and T_{N2} actually decrease with increasing Cs fraction. The latter is indicative of decreasing rates of optical pumping, likely caused by a suppression of the Rb vapor by a dominant Cs vapor. Indeed, the intrinsic vapor pressure of Cs is higher than that of rubidium due to its lower boiling point, a relation that is reversed in the analogous K-Rb system for ^{3}He hyperpolarization. Thus, our Rb-Cs hybrid experiments to date indicate that the addition of Cs to the standard Rb-^{129}Xe SEOP method serves only to suppress the ^{129}Xe polarization. However, considering only a small number of different Rb-Cs ratios and conditions have been investigated, future studies on leaner Cs mixtures, where the Rb vapor density is not suppressed to such an extent, may yet yield a more favorable outcome.

5. Conclusions

An overview of gas temperature measurement using Raman spectroscopy and its potential as a diagnostic tool for improving understanding of energy transport processes during spin-exchange optical pumping has been discussed. The main approaches taken to correlate low-field NMR with Raman spectroscopy, using both orthogonal and in-line detection methods, have been compared and contrasted to relevant historical studies as well as each other to provide insight on poorly understood thermal processes present during SEOP. Future research will aim to build upon the in-line configuration, where automation of the translational stage

could allow three-dimensional temperature mapping for improved characterization of these processes with greater resolution. Additionally, the demand for higher laser powers and richer Xe mixtures will likely result in thermal management becoming paramount, as the tightrope between maximizing polarization efficiency and avoiding the perilous "runaway" regime becomes narrower still.

This improved understanding of such thermal and energy transport processes should be directly translated to improving the next generation of clinical hyperpolarizers for use in producing HP noble gas for MRI studies in the lungs, which will hopefully facilitate safer, earlier, and more reliable diagnosis of a variety of serious and life-threatening diseases. Such advances will serve to streamline the diagnostic process, improving cost-effectiveness and reducing strain on medical services alongside the obvious benefit to those in society.

Author details

Jonathan Birchall[1]*, Nicholas Whiting[2], Jason Skinner[1], Michael J. Barlow[1] and Boyd M. Goodson[3]

*Address all correspondence to: msxjrb@nottingham.ac.uk

1 Sir Peter Mansfield Imaging Centre, University of Nottingham, Nottingham, UK

2 The University of Texas MD Anderson Cancer Center, Houston, TX, USA

3 Department of Chemistry and Biochemistry, Southern Illinois University, Carbondale, IL, USA

References

[1] Erkonen WE, Smith WL, editors. Radiology 101: The Basics and Fundamentals of Imaging. 3rd ed. Philadelphia: Lippincott, Williams and Wilkins; 2010. 8 p. DOI: http://dx.doi.org/10.1016/j.acra.2010.01.022.

[2] Walker TG, Happer W, Spin-exchange optical pumping of noble-gas nuclei. Reviews of Modern Physics. 1997;69:629. DOI: http://dx.doi.org/10.1103/RevModPhys.69.629.

[3] Appelt S, Ünlü T, Zilles K, Shah NJ. Experimental studies of rubidium absolute polarization at high temperatures. Applied Physics Letters. 1999;75:428. DOI: 10.1063/S0003-6951(99)03229-5.

[4] Walter DK, Griffith WM, Happer W. Energy transport in high-density spin-exchange optical pumping cells. Physical Review Letters. 2001;86:3264-3267. DOI: http://dx.doi.org/10.1103/PhysRevLett.86.3264.

[5] Zook AL, Adhyaru BB, Bowers CR. High capacity production of > 65% spin polarized xenon-129 for NMR spectroscopy and imaging. Journal of Magnetic Resonance. 2002;159:175-182. DOI: 10.1016/S1090-7807(02)00030-7.

[6] Whiting N, Nikolaou P, Eschmann NA, Goodson NM, Barlow MJ. Interdependence of in-cell xenon density and temperature during Rb/^{129}Xe spin-exchange optical pumping using VHG-narrowed laser diode arrays. Journal of Magnetic Resonance. 2011;208:298-304. DOI: 10.1016/j.jmr.2010.11.016.

[7] Goodson BM, Nuclear magnetic resonance of laser-polarized noble gases in molecules, materials, and organisms. Journal of Magnetic Resonance. 2002;155:157-216. DOI: 10.1006/jmre.2001.2341.

[8] Romalis MV, Miron E, Cates GD. Pressure broadening of Rb D_1 and D_2 lines by ^{3}He, ^{4}He, N_2, and Xe: Line cores and near wings. Physical Review A. 1997;56:4569-4578. DOI: http://dx.doi.org/10.1103/PhysRevA.56.4569

[9] Breeze SR, Lang S, Moudrakovski I, Ratcliffe CI, Ripmeester JA, Santyr G et al. Coatings for optical pumping cells and short-term storage of hyperpolarized xenon. Journal of Applied Physics. 2000;87:8013-8017. DOI: http://dx.doi.org/10.1063/1.373489.

[10] Fink A, Baumer D, Brunner E. Production of hyperpolarized xenon in a static pump cell: Numerical simulations and experiments. Physical Review A. 2005;72:053411. DOI: http://dx.doi.org/10.1103/PhysRevA.72.053411.

[11] Fink A, Brunner E. Optimization of continuous flow pump cells used for the production of hyperpolarized ^{129}Xe: A theoretical study. Applied Physics B. 2007;89:65-71. DOI: 10.1007/s00340-007-2754-z.

[12] Hickman RS, Liang LH. Rotational temperature measurement in nitrogen using Raman spectroscopy. Review of Scientific Instruments. 1972;43:796–799. DOI: http://dx.doi.org/10.1063/1.1685760.

[13] Nikolaou P, Coffey AM, Walkup LL, Gust BM, Whiting N, Newton H, et al. Near-unity nuclear polarization with an 'Open-Source' ^{129}Xe hyperpolarizer for NMR and MRI. Proceedings of the National Academy of Sciences 2013;110:14150–14155. DOI: www.pnas.org/cgi/doi/10.1073/pnas.1306586110.

[14] Dregely I, Mugler JP 3rd, Ruset IC, Altes TA, Mata JF, Miller GW, et al. Hyperpolarized xenon-129 gas-exchange imaging of lung microstructure: first case studies in subjects with obstructive lung disease. Journal of Magnetic Resonance Imaging 2011;33:1052–1062. DOI: http://dx.doi.org/10.1002%2Fjmri.22533.

[15] Safavi S, Barlow M, Hall I. Clinical ^{129}Xe aspects of translation of HP Xenon-129. Manuscript in preparation.

[16] Whiting N, Nikolaou P, Eschmann NA, Barlow MJ, Lammert R, Ungar J, et al. Using frequency-narrowed, tunable laser diode arrays with integrated volume holographic gratings for spin-exchange optical pumping at high resonant fluxes and xenon densities. Applied Physics B 2012;106:775–788. DOI: 10.1007/s00340-01204924-x.

[17] Whiting N. Manuscript in preparation.

[18] Rosen MS, Chupp TE, Coulter KP, Welsh RC. Polarized ^{129}Xe optical pumping/spin exchange and delivery system for magnetic resonance spectroscopy and imaging studies. Review of Scientific Instruments. 1999;70:1546-1552. DOI: 10.1063/1.1149622.

[19] Newton H, Walkup LL, Whiting N, West L, Carriere J, Havermeyer F, et al. Comparative study of in situ N2 rotational Raman spectroscopy methods for probing energy thermalisation processes during spin-exchange optical pumping. Applied Physics B 2014;115:167–172. DOI: 10.1007/s00340-013-5588-x.

[20] Driehuys B, Cates GD, Miron E, Sauer K, Walter DK, Happer W. High-volume production of laser-polarized ^{129}Xe. Applied Physics Letters. 1996;69:1668-1670. DOI: 10.1063/1.117022

[21] Tables of Physical & Chemical Constants (16th edition 1995). 2.3.7 Thermal conductivities [homepage on the Internet]. Kaye & Laby Online. [updated c2005; cited 2016 Sep 26]. Available from: http://www.kayelaby.npl.co.uk/general_physics/2_3/2_3_7.html

[22] Newton H, Smith J, Walkup L, Whiting N, Barlow M, Morris P et al. Effects of gas composition on optical pumping and energy transport for hyperpolarized 129Xe using in situ Raman spectroscopy and NMR. Poster session presented at: Exotica, 54th Experimental Nuclear Magnetic Resonance Conference; 2013 Apr 14-19; Pacific Grove, CA.

[23] Birchall J. Manuscript in preparation.

[24] Newton H, Skinner J, Birchall J, Whiting N, Gust BM, Ranta K et al. Can We Utilise Rb/Cs Hybrid optical pumping to hyperpolarise noble gases? Presentation given at: Sensitivity and Resolution: Pushing the Boundaries, 55th Experimental Nuclear Magnetic Resonance Conference; 2014 Mar 23-28; Boston, MA.

[25] Whiting N, Eschmann NA, Goodson BM. ^{129}Xe-Cs (D_1,D_2) versus ^{129}Xe-Rb (D_1) spin-exchange optical pumping at high xenon densities using high-power laser diode arrays. Physical Review A 2011;83:053428. DOI: http://dx.doi.org/10.1103/PhysRevA.83.053428.

[26] Babcock E, Nelson I, Kadlecek S, Driehuys B, Anderson LW, Hersman FW, et al. Hybrid spin-exchange optical pumping of ^{3}He. Physical Review Letters. 2003;91:123003. DOI: http://dx.doi.org/10.1103/PhysRevLett.91.123003.

[27] Gibbs H, Hull R. Spin-exchange cross sections for Rb^{87}-Rb^{87} and Rb^{87}-Cs^{133} collisions. Physical Review. 1967;153:132. DOI: http://dx.doi.org/10.1103/PhysRev.153.132.

[28] Jau Y-Y, Kuzma NN, Happer W. High-field measurement of the ^{129}Xe − Rb spin-exchange rate due to binary collisions. Physical Review A 2002;66:052710. DOI: http://dx.doi.org/10.1103/PhysRevA.66.052710.

Chapter 13

Inverse Raman Scattering in Femtosecond Broadband Transient Absorption Experiments

Antonio Aloi and Raffaele Tommasi

Additional information is available at the end of the chapter

http://dx.doi.org/10.5772/65479

Abstract

This chapter reports on one of the nonlinear spectral features, the inverse Raman scattering (IRS), observed upon the interaction of ultrafast-pulsed lasers in a Raman-active medium. Hereby, a comprehensive theoretical description of the IRS is exposed. Furthermore, the investigation carried out on synthetic eumelanin dispersions is addressed to show how the transient absorption measurements can be influenced by the IRS, if probing at energies close to Stokes and anti-Stokes vibrational modes of the medium. A thorough analysis demonstrates that the IRS affects the sign of dynamics but not relaxation times. A specific kind of spectroscopy based on the IRS effect (ultrafast Raman loss spectroscopy) is eventually illustrated as valuable tool to characterize the structure of molecules and to investigate their dynamics during chemical reactions, even occurring at ultrafast timescales.

Keywords: nonlinear Raman spectroscopy, stimulated Raman scattering, inverse Raman-scattering, femtosecond transient absorption spectroscopy, stimulated Raman gain spectroscopy (SRGS), ultrafast Raman loss spectroscopy (URLS)

1. Introduction

Nowadays, the possibility to investigate optical nonlinearities offers great insights on material properties and the interaction between light and matter. After the interaction with a strong optical field, the response of the material will be no longer linearly dependent on its strength, instead nonlinear effects start playing major roles. Due to crystal structures and symmetries of media, the third order is the nonlinearity of the lowest order that can be observed in all media [1], and thus has become a valuable tool to investigate structural and dynamic aspects

of matter. Among the third-order nonlinear effects (e.g., third-harmonic generation, optical Kerr effect), the four-wave mixing (FWM) is the mostly explored since it generalizes all the third-order nonlinearities. The FWM relies on the mixing of three input signals, which results in the generation of a fourth output field. When one of the input signals is resonant with the frequencies of the material, the FWM process can be enhanced and is called *stimulated Raman scattering* (SRS). Coupling this process with laser pulses delayed in time, namely using a pump-probe setup, it is possible to investigate the temporal behavior of the material and the evolution of its properties. Nonlinear Raman spectroscopy is an example of such combination between third-order nonlinear optical effect and pump-probe technique [2].

In this chapter, we discuss one of the FWM processes which contributes to the stimulated Raman scattering, called inverse Raman scattering (IRS). The theory behind the IRS effect will be explained, resorting to Feynman dual-time line (FDTL) diagrams [3], as well as its application as a spectroscopic tool. Furthermore, the connection held between the IRS and the femtosecond transient absorption (FTA) spectroscopy will be clarified, pointing out the important role the IRS effect plays on the temporal evolution of relaxation dynamics in FTA.

2. Inverse Raman scattering: theory

To describe the SRS and its origin, we begin by discussing the interaction of an optical field of frequency ω_L with a Raman-active medium, restricted to the scalar approximation. A vibrational mode in a Raman-active medium can be described as a simple harmonic oscillator with frequency ω_v. Due to vibrations, the optical polarizability of the molecules will change in time, depending on their reciprocal distance (internuclear separation). The periodic variation of the molecule polarizability will generate a modulation in the refractive index, which in turn will modify an incoming light beam of frequency ω_L. Specifically, the frequencies $\omega_L \pm \omega_v$ will be superimposed upon the transmitted light beam. The stimulated Raman scattering can be visually understood in terms of the interactions shown in **Figure 1**. **Figure 1a**

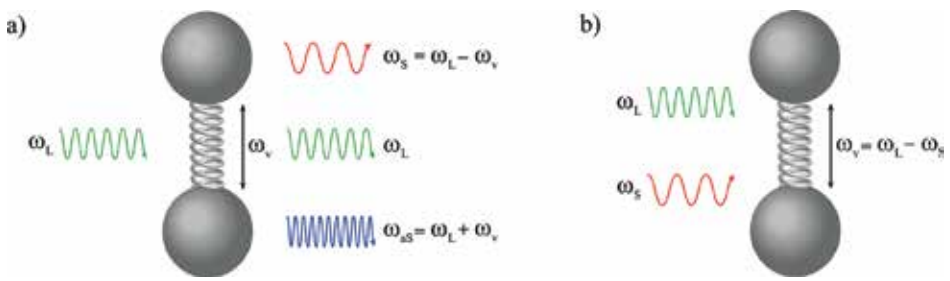

Figure 1. Schematic showing the stimulated Raman-scattering process. The molecules in the Raman-active medium are described by harmonic oscillators of frequency ω_v. The incoming laser beam has frequency ω_L. (a) Modulation of the refractive index and subsequent emission of Stokes and anti-Stokes radiation and (b) beating of the Stokes frequency with the laser field reinforcing the vibrational oscillation of the molecule.

http://dx.doi.org/10.5772/65479

shows the modulation of the refractive index due to the vibrational frequencies of the medium, thereby the transmitted light will carry the Stokes ($\omega_S = \omega_L - \omega_v$) and anti-Stokes ($\omega_{aS} = \omega_L + \omega_v$) frequencies besides the laser frequency ω_L. At the same time, one of the newly generated frequencies can beat with the incoming laser beam frequency, modulating the amplitude of the molecular vibrations (**Figure 1b**).

The two processes hereby depicted reinforce one another: the modulation of the vibrational frequencies interacts with the incoming laser beam frequency, leading to a Stokes field which increases the amplitude of the vibrational oscillation, and eventually strengthens the Stokes frequencies. This condition of amplification is called vibrational coherence, and it can be probed by a third laser beam, determining the stimulated Raman scattering [4]. The mathematical expressions of energy conservation and phase matching are given below:

$$\begin{aligned} \omega_{\mathrm{SRS}} &= \left(\omega_L - \omega_S\right) \pm \omega_L = \omega_v \pm \omega_L \\ \boldsymbol{k}_{\mathrm{SRS}} &= \left(\boldsymbol{k}_L - \boldsymbol{k}_S\right) \pm \boldsymbol{k}_L = \boldsymbol{k}_v \pm \boldsymbol{k}_L \end{aligned} \tag{1}$$

with ω_{SRS} and $\boldsymbol{k}_{\mathrm{SRS}}$ the frequency and the wave vector of the SRS signal, respectively. If the incoming optical field is a femtosecond pulse, and the probing beam is a broadband white-light continuum (WLC), then the process is called *femtosecond stimulated Raman scattering* (FSRS), and is one of the four-wave-mixing processes. Among all the possible interactions of the fields involved, these can be narrowed down to two main terms called stimulated Raman scattering, and inverse Raman scattering [2]. Hereby, we focus on the inverse Raman-scattering effect.

The probability of annihilation of a photon with frequency ω_L and the simultaneous creation of another photon with frequency $\omega_1 = \omega_L \pm \omega_{v'}$ according to the Kramers-Heisenberg dispersion formula, is given by [5]

$$P = \frac{16\pi^4}{h^4} \int |\mu|^2 \rho_0 \left(\rho_1 + \frac{8\pi h \omega_1^3}{c^3} \right) d\omega_0, \tag{2}$$

where μ is the probability of the two-photon process, $\rho_0 \rho_1$ is associated to the IRS process, while $\rho_0 8\pi h \omega_1^3$ takes into account the spontaneous Raman scattering. A generalization of Eq. (2) was proposed by Mukamel to describe the stimulated Raman-scattering signal as [6]

$$\begin{aligned}\tilde{S}_{SRS}\left(\omega_{pu},\omega_{pr}\right)=4\pi N\sum_{g,g',e,f}P(g)\left|\varepsilon_{pu}\right|^2\left|\varepsilon_{pr}\right|^2\left|T^{(2)}_{g'g}\left(\omega_{pu}\right)\right|^2\delta\left(\omega_{pu}-\omega_{pr}-\omega_{g'g}\right)\\ -P(g)\left|\varepsilon_{pu}\right|^2\left|\varepsilon_{pr}\right|^2\left|T^{(2)}_{g'g}\left(\omega_{pr}\right)\right|^2\delta\left(\omega_{pr}-\omega_{pu}-\omega_{g'g}\right)\\ +P(g)\left|\varepsilon_{pr}\right|^2\left|T^{(1)}_{eg}\right|^2\delta\left(\omega_{pr}-\omega_{eg}\right)\\ -P(g)\left|\varepsilon_{pr}T^{(1)}_{eg}+\left|\varepsilon_{pu}\right|^2\varepsilon_{pr}T^{(3)}_{eg}\left(\omega_{pr}-\omega_{pu},\omega_{pr}\right)\right|^2\\ +\left|\varepsilon_{pu}\right|^2\varepsilon_{pr}T^{(3)}_{eg}\left(\omega_{pr}-\omega_{pu},\omega_{pu}\right)\delta\left(\omega_{pr}-\omega_{eg}\right).\end{aligned} \tag{3}$$

Here, N is the number of molecules involved in the scattering process, $\varepsilon_{\mathrm{pu}}$ ($\varepsilon_{\mathrm{pr}}$) and ω_{pu} (ω_{pr}) are the amplitudes and frequencies, respectively, of the pump (probe) field. $P(g)$ indicates the ground-state population at equilibrium $|g\rangle$, while $T^{(1)}_{\mathrm{eg}}$ is a matrix defining the scattering process, showing the order of the transition (i = 2 two-photon process, i = 3 three-photon process, etc.), and the initial and final states involved. Eq. (3) can be explained as follows: the first term describes the loss of a photon with frequency ω_{pu}, and the emission of a photon (gain process) with frequency ω_{pr}. Conversely, the second term takes into account the emission of a pump-beam photon after the annihilation of a photon of the probe beam (loss process). Both third and fourth terms describe the perturbation in the probe-field absorption due to the coexistence of the pump field [7].

As stated in Eq. (3), the absorption of a photon with frequency ω_{pu}, or the emission at frequency ω_{1}, depends on the population of the states involved in the transition, and specifically on the ratio between the number of molecules in the excited vibrational state and the number of molecules in the ground state. At room temperature, the excited states are scarcely populated; hence, a radiation is most likely emitted at Stokes frequencies, while absorbed at anti-Stokes frequencies [8].

Even if there are other nonlinear processes involved, due to the intensity of the laser field typically used, the treatment of the SRS can be narrowed down to three relevant equations in the classical description, reporting on the laser excitation frequency ω_{pu}, and the Stokes and anti-Stokes frequencies ω_S, ω_{aS}:

$$\frac{dA_m\left(\omega_{pu}\right)}{dz}=\frac{2\pi i\omega_{pu}}{n_{pu}c}\chi_{mjkl}A_j\left(\omega_S\right)A_k\left(\omega_{aS}\right)A_l^*\left(\omega_{pu}\right)e^{-i\Delta kz}+\sum_{\mu=L,S,aS}\chi_{mjkl}A_j\left(\omega_{pu}\right)A_k\left(\omega_\mu\right)A_l^*\left(\omega_\mu\right), \tag{4}$$

$$\frac{dA_k\left(\omega_S\right)}{dz}=\frac{2\pi i\omega_S}{n_Sc}\chi_{kjml}A_j\left(\omega_{pu}\right)A_m^*\left(\omega_{aS}\right)A_l\left(\omega_{pu}\right)e^{i\Delta kz}+\sum_{\mu=L,aS,S}\chi_{klmn}A_l\left(\omega_S\right)A_m\left(\omega_\mu\right)A_n^*\left(\omega_\mu\right), \tag{5}$$

http://dx.doi.org/10.5772/65479

$$\frac{dA_j^*(\omega_{aS})}{dz} = -\frac{2\pi i\omega_{aS}}{n_{aS}c}\chi_{jklm}A_k^*(\omega_{pu})A_l(\omega_S)A_m^*(\omega_{pu})e^{-i\Delta kz} + \sum_{\mu=L,aS,S}\chi_{jklm}A_k^*(\omega_{aS})A_l(\omega_\mu)A_m^*(\omega_\mu). \quad (6)$$

Here, χ_{mjkl} are the nonlinear susceptibilities at the interacting frequencies, while n is the refractive index modulated by the fields at their specific frequency. The wave vectors are related to one another by the phase-matching condition $\Delta\boldsymbol{k} = 2\boldsymbol{k}_{\mathrm{pu}} - \boldsymbol{k}_S - \boldsymbol{k}_{aS} = 0$. On one hand, the real part of the susceptibility describes the refractive index modulation due to the incoming field, and thus expresses the phase modulation. The imaginary part, on the other hand, accounts for the nonlinear Raman scattering and the two-photon absorption. Resorting to Eqs. (4)–(6), it is possible to describe all the processes involved in the SRS effect. The equations needed to describe the IRS effect alone are fewer, though. To simplify the theoretical treatment, few assumptions can be done without loss of generality. In fact, it can be expected that the incoming light intensity is stronger than the scattered one, that is, $I_{\mathrm{pu}} \gg I_S,\quad I_{aS}$. Furthermore, the intensity of the IRS is stronger than the spontaneous Raman scattering if detected at the same frequency. Thus, in the scalar approximation for the susceptibility, Eqs. (4)–(6) can be rewritten as

$$\frac{dA_s}{dz} = \frac{2\pi i\omega_S}{n_S c}\left(\chi\left|A_{pu}\right|^2 A_S + \chi A_{pu}^* A_{aS}^* e^{i\Delta kz}\right), \quad (7)$$

$$\frac{dA_{as}}{dz} = -\frac{2\pi i\omega_{aS}}{n_{aS}c}\left(\chi A_{pu}^* A_S^* e^{-i\Delta kz} + \chi\left|A_{pu}\right|^2 A_{aS}^*\right), \quad (8)$$

assuming that the incoming field intensity is constant, that is, $dA_{\mathrm{pu}}/dz = 0$. It follows that the intensities of the Stokes and anti-Stokes fields are

$$I_S(z) = r_1^2\exp\left(2|g|I_{pu}z\right) + r_2^2\exp\left(-2|g|I_{pu}z\right) + 2r_1r_2\cos\left(\Delta kz + \delta\phi\right), \quad (9)$$

$$I_{aS}(z) = \alpha_1 r_1^2\exp\left(2|g|I_{pu}z\right) + \alpha_2 r_2^2\exp\left(-2|g|I_{pu}z\right) - 2r_1r_2\cos\left(\Delta kz + \delta\phi\right). \quad (10)$$

where $g = (2\pi\omega/nc)\Im\chi$. The terms r_i and α_i are defined by the initial conditions, and specifically $\alpha_1 \le 1,\quad \alpha_2 \ge 1$; $\delta\phi$ is the initial phase shift at the front of the sample. Depending on the ratio $gI_{\mathrm{pu}}/\Delta k$ and hence on the Stokes-anti-Stokes coupling, three different solutions to the system can be found [8]. Here, the solution for zero coupling ($gI_{\mathrm{pu}} < \Delta k$) will be presented, due to the noncollinear geometry of the pump-probe setup (for the other solutions, refer to

Weigmann's paper [8]). The condition hereby described predicts an enhancement of the IRS signal, with the intensities at the Stokes and anti-Stokes frequencies given by

$$I_S(z) \simeq r_1^2 \exp\left(2|g|I_{pu}z\right), \tag{11}$$

$$I_{aS}(z) \simeq \alpha_2 r_2^2 \exp\left(-2|g|I_{pu}z\right). \tag{12}$$

It follows that the intensities at the anti-Stokes frequencies are higher than the corresponding ones at the Stokes frequencies [7, 9, 10]. In the spontaneous Raman scattering, at room temperature the populations in the excited vibrational levels are negligible, as described by Boltzmann distribution, thus the anti-Stokes peaks are weak. However, in the stimulated process (such as IRS) the Boltzmann distribution does not describe anymore the energy levels population, and a strong anti-Stokes emission can be observed [11].

3. Inverse Raman scattering: spectroscopy

The IRS effect can be described by the Feynman dual-time line (FDTL) diagrams in the Liouville space with the ket and bra evolution (**Figure 2**) [12]. Using the FDTL diagrams and the related energy level diagrams, it is possible to illustrate the temporal evolution of the density matrix in the four-wave mixing process, which the IRS is based on. The temporal evolution goes from τ_3 to t when the third-order polarization induced in the medium is computed [3]. The arrows pointing into the time line represent the absorption from the ground state $\left|\Psi_{g0}\right\rangle$ to the excited state $\left|\Psi_{e}\right\rangle$ and the related wave vector is **+k** On the contrary, the arrows pointing far from the time line illustrate the stimulated emission from $\left|\Psi_{e}\right\rangle$ to $\left|\Psi_{g0}\right\rangle$ and their wave vector is **−k**.

In the energy diagrams, $\boldsymbol{E}_{\mathrm{pr}}$, $\boldsymbol{E}_{\mathrm{pu}}$, and $\boldsymbol{E}^{*}_{\mathrm{pu}}$ are the vectors of the fields involved in the interaction in the medium, having frequencies ω_{pr}, ω_{pu}, and ω_{pu} respectively. In both IRS (I) and IRS (II) processes, the wave vectors of the incoming pump fields, that is, $\boldsymbol{k}_{\mathrm{pu}}$ and $\boldsymbol{k}^{*}_{\mathrm{pu}}$, vanish, leading to a third-order polarization having the same direction of the incoming pump pulse [12]. The difference between the IRS (I) and IRS (II) lays in the sequence with which pump and probe pulses reach the sample. In the IRS (I) (**Figure 2a**), the excitation process is started by the probe pulse alone at frequencies higher than those of pump pulse, that is, in the anti-Stokes region. The vibrational coherence persists as long as the pump pulse overlaps with the probe pulse, then a photon with frequency ω_{pr} is annihilated due to the interaction between the two pulses, and a loss in intensity in the probe spectrum is observed at the specified anti-Stokes frequency [13]. In the IRS (II) (**Figure 2b**), the pump pulse is followed by the probe pulse, it induces the excitation in the sample and due to the interaction of the two fields, the vibrational coherence is achieved. A photon having frequency ω_{pr} and wave vector $\boldsymbol{k}_{\boldsymbol{S}}$ (i.e., same direction of the

http://dx.doi.org/10.5772/65479

Stokes radiation) is created, and it adds to the probe pulse, leading to an intensity gain in the probe spectrum at the specified frequency. According to the energy conservation, a loss in energy, equal to the gain obtained at the Stokes frequency, is observed in the pump pulse [4]. This is clearly shown in the bottom part of **Figure 2a** and **2b**, where the frequency of the outcoming beam is higher (lower) than the one of the pump fields for the anti-Stokes (Stokes) signal.

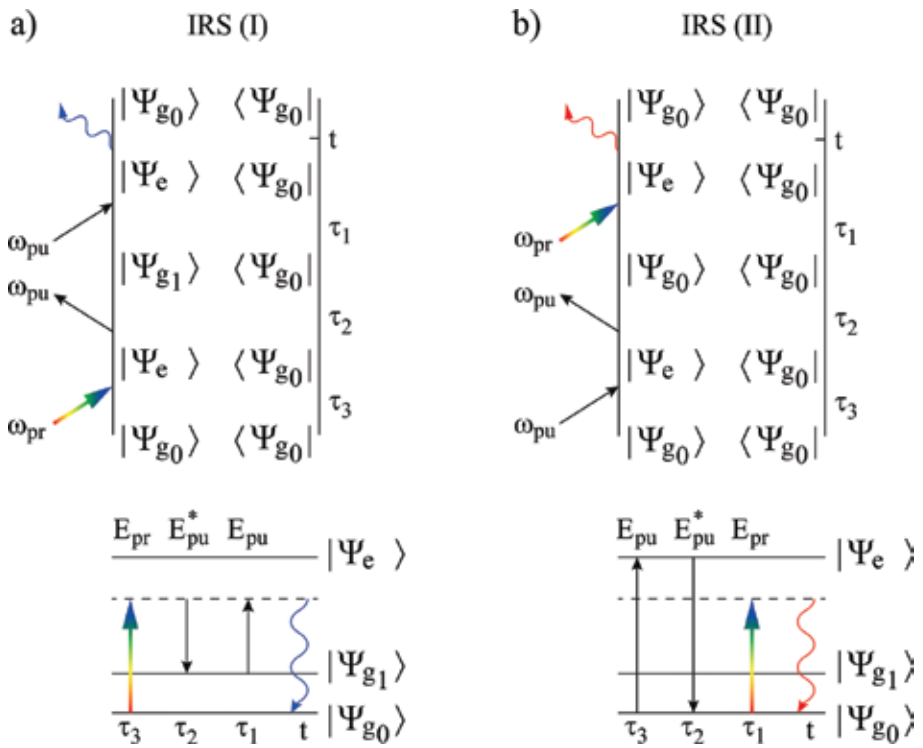

Figure 2. Feynman dual-time line (FDTL) diagrams (top) and energy-level diagrams (bottom) describing the IRS effect. The wavy line is the field coming out from the stimulated Raman-scattering process, and illustrates the third-order polarization of the involved energetic states. In the energy diagrams, the solid and the dashed lines represent the real and the virtual levels, respectively. (a) The pump pulse arrives after the probe pulse, and excites the sample. This originates the anti-Stokes line since the outcoming frequency is higher than the one of the incoming pump fields. This is called IRS (I) process and (b) the probe pulse follows temporally the pump pulse and the Stokes line is generated because the outcoming frequency is smaller than the incoming one. This is the IRS (II) process.

According to Lee's papers [3, 14], it is possible to extrapolate the mathematical expression of the third-order polarization from the FDTL diagrams. The time-dependent third-order polarization in the IRS effect in the probe direction (i.e., wave vector $\boldsymbol{k}_{pr}$, is given by the overlap of the wave packet on the ket side of the time line and a ground vibrational state on the bra side. It depends on the transition dipole moment μ_{ge} on the inhomogeneous broadening of the wave packet $G(t)$ and it is integrated over the time intervals $t, \tau_1, \tau_2,$ and τ_3 :

$$P^{(3)}_{IRS(I)}(t)=\left(\frac{i}{\hbar}\right)^3\int_0^t d\tau_1\int_0^{\tau_1}d\tau_2\int_0^{\tau_2}d\tau_3 \times exp\left[-\frac{\gamma_g t}{2\hbar}-\frac{\gamma_e(t-\tau_1)}{2\hbar}-\frac{\gamma_d(\tau_1-\tau_2)}{\hbar}-\frac{\gamma_g(\tau_1-\tau_2)}{2\hbar}-\frac{\gamma_e(\tau_2-\tau_3)}{2\hbar}-\frac{\gamma_g\tau_3}{2\hbar}\right] \times E_{pu}(\tau_1)E^*_{pu}(\tau_2)E_{pr}(\tau_3)G(t-\tau_1+\tau_2-\tau_3)I(t,\tau_1,\tau_2,\tau_3) \tag{13}$$

$$P^{(3)}_{IRS(II)}(t)=\left(\frac{i}{\hbar}\right)^3\int_0^t d\tau_1\int_0^{\tau_1}d\tau_2\int_0^{\tau_2}d\tau_3 \times exp\left[-\frac{\gamma_g t}{2\hbar}-\frac{\gamma_e(t-\tau_1)}{2\hbar}-\frac{\gamma_d(\tau_1-\tau_2)}{\hbar}-\frac{\gamma_g(\tau_1-\tau_2)}{2\hbar}-\frac{\gamma_e(\tau_2-\tau_3)}{2\hbar}-\frac{\gamma_g\tau_3}{2\hbar}\right] \times E_{pr}(\tau_1)E^*_{pu}(\tau_2)E_{pu}(\tau_3)G(t-\tau_1+\tau_2-\tau_3)I(t,\tau_1,\tau_2,\tau_3) \tag{14}$$

Here, the four-time correlation function $I(t,\tau_1,\tau_2,\tau_3)$ is defined as follows:

$$I(t,\tau_1,\tau_2,\tau_3) = \left\langle \Psi_{g0}(\boldsymbol{Q})|e^{i\boldsymbol{h}_g/\hbar}\mu_{ge}e^{i\boldsymbol{h}_e(t-\tau_1)/\hbar}\times\mu_{eg}e^{i\boldsymbol{h}_g(\tau_1-\tau_2)/\hbar}\mu_{ge}e^{i\boldsymbol{h}_e(\tau_2-\tau_3)/\hbar}\times\mu_{eg}e^{i\boldsymbol{h}_g\tau_3/\hbar}|\Psi_{g0}(\boldsymbol{Q})\right\rangle \tag{15}$$

where $\boldsymbol{Q}$ is the multidimensional vibrational coordinate, $|\Psi_{g0}(\boldsymbol{Q})\rangle$ the initial ground vibrational state of the electronic ground state $|g\rangle$, and $\boldsymbol{h}_g$ and $\boldsymbol{h}_e$ the vibrational multidimensional Hamiltonians associated to the energetic levels involved in the transition $|g\rangle$ and $|e\rangle$ The terms γ_g and γ_e in Eqs. (13) and (14) are the line bandwidths of the two energetic levels, while γ_d is the time interval between τ_2 and τ_1, during which the vibrational coherence is lost (Raman vibrational dephasing time) [3].

Once defined the third-order polarization for both effects IRS (I) and IRS (II), it is possible to show the variation in intensity of the stimulated Raman signal as function of the frequencies, to be given by

$$\Delta I_{IRS}(\omega)=-\frac{8\pi^2 lC}{3n}\omega\,\Im\left\{E^*_{pr}(\omega)P^{(3)}_{IRS}(\omega)\right\} \tag{16}$$

where l is the optical path length, C the number of molecules per unit volume, and n the refractive index of the Raman-active medium. $E^*_{\mathrm{pr}}(\omega)$ is the incoming probe field with frequency ω and $P^{(3)}_{\mathrm{IRS}}(\omega)$ is the Fourier transform of the third-order polarization calculated using Eqs. (13) and (14). The variation in intensity $\Delta I_{\mathrm{IRS}}(\omega)$ is directly depending on the imaginary

http://dx.doi.org/10.5772/65479

part of the third-order Raman polarization, and hence on the Raman susceptibility as already stated in the previous section [15]. $\Im\left\{\chi^{(3)}(\omega)\right\}$ is negative at the Stokes frequencies ($\omega_S = \omega_L - \omega_v$) and positive at anti-Stokes frequencies ($\omega_{aS} = \omega_L + \omega_v$), as depicted in **Figure 3**, where the relation between the Stokes and anti-Stokes susceptibilities is presented. It follows that the Raman spectrum will be positive at the Stokes frequencies, experiencing a gain in the probe-beam intensity for each frequency which fulfills $\omega_S = \omega_L - \omega_v$. On the contrary, $\Delta I_{\mathrm{IRS}}(\omega) < 0$ in the anti-Stokes region. Here, the probe-beam intensity will be decreased for all those frequencies which meet the condition $\omega_{aS} = \omega_L + \omega_v$.

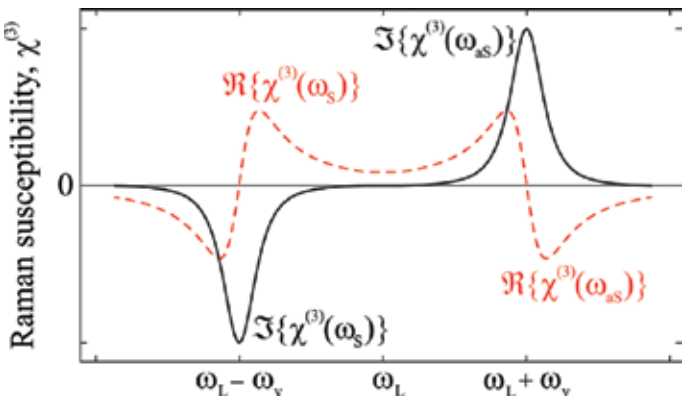

Figure 3. Relation between the Stokes and anti-Stokes susceptibilities. The solid black line is the imaginary part of the Raman susceptibility; the red dashed line is the real part of the Raman susceptibility.

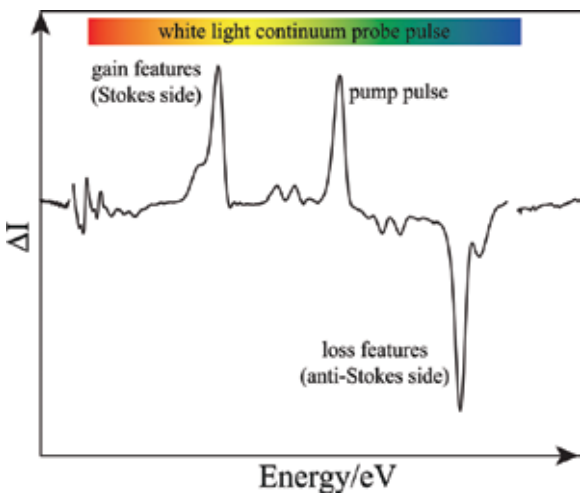

Figure 4. Extracted Raman spectrum of eumelanin dispersion in DMSO-methanol mixture.

The aforementioned variation in intensity $\Delta I_{\mathrm{IRS}}(\omega)$ will be analyzed for a case of study of a dispersion of eumelanin in dimethyl sulfoxide DMSO-methanol mixture (1:20 ratio) in the following. In **Figure 4**, the extracted Raman spectrum of the dispersion is depicted. On the red side of the white-light broadband spectrum (Stokes side), some frequencies resonate with the vibrational modes of the Raman-active medium. Hence, the signal appears as gain features in the probe pulse at those specific frequencies. At the same time, on the blue side (anti-Stokes side) a loss in the intensity is achieved at frequencies $\omega_{aS} = \omega_{pu} + \omega_{v}$.

4. Inverse Raman scattering: experiments

4.1. Experimental setup

To carry out FTA measurements, a noncollinear geometry in the pump-probe setup is used. A diode-pumped Ti:Sapphire femtosecond oscillator generates a ~100 fs pulse at a repetition rate of 78 MHz. The so-generated pulses are stretched and amplified by a regenerative Ti:Sapphire amplifier, pumped by a Q-switched Nd^{3+}:YLF laser at 1-KHz repetition rate, and eventually compressed, leading to 4 mJ, ~100 fs pulses at 798 nm. A beam splitter sends 90% of the outcoming pulse to an optical parametric amplifier to provide tunability over a broad spectral range (290–2600 nm). This tuneable laser pulse is sent through a depolarizer, an optical chopper, and finally focused on the sample in 1 mm spot, yielding an excitation density of 5×10^{14} photon $pulse^{-1}$ cm^{-2}. The remaining 10% of the radiation is delayed in time by an optical delay line and focused on a CaF_2 crystal to generate a white-light continuum radiation, spanning between 450 and 800 nm. The WLC radiation is used as probe beam spatially overlapped to the pump pulse on the sample. The light transmitted by the sample is coupled into an optical fiber and sent to a charge-coupled device (CCD) spectrometer. The temporal resolution (~200 fs) is determined by the cross-correlation between the width of pump and probe pulses overlapping on the sample. The chromatic aberrations are removed by chirp correction software.

4.2. The IRS related to FTA experiments

So far, the nature of the IRS has been described. In this section, the IRS will be treated in relation with femtosecond transient absorption (FTA) experiments. In an FTA experiment, the intensity transmitted by an unexcited medium is given by $I_{\mathrm{pr}}^{0}(\hbar\omega)$, when the medium is excited by a pump pulse, a difference in the probe intensity is detected, and can be described as

$$\Delta I_{FTA}(\hbar\omega,\tau) = I_{pr}^{0}(\hbar\omega) - I_{pr}^{pu}(\hbar\omega,\tau), \tag{17}$$

where $I_{\mathrm{pr}}^{\mathrm{pu}}(\hbar\omega,\tau)$ is the probe intensity transmitted by the sample in the presence of the pump, and τ is the time delay between pump and probe pulses. Conversely, the variation in intensity

http://dx.doi.org/10.5772/65479

measured at the Stokes and anti-Stokes frequencies in the broadband spectrum of the probe pulse will be measured as the difference between the signal with and without the pump pulse: $I_{\text{pump}-\text{on}} - I_{\text{pump}-\text{off}}$ [16]. It results that

$$\Delta I_{IRS}(\omega,\tau) \propto -\Delta I_{FTA}(\hbar\omega,\tau). \tag{18}$$

By expressing the transient absorption signal as function of the detected difference in intensity, Eq. (19) can be obtained

$$\Delta A(\hbar\omega,\tau) = -\log_{10}\left[1 - \frac{\Delta I_{FTA}(\hbar\omega,\tau)}{I^0_{pr}(\hbar\omega)}\right], \tag{19}$$

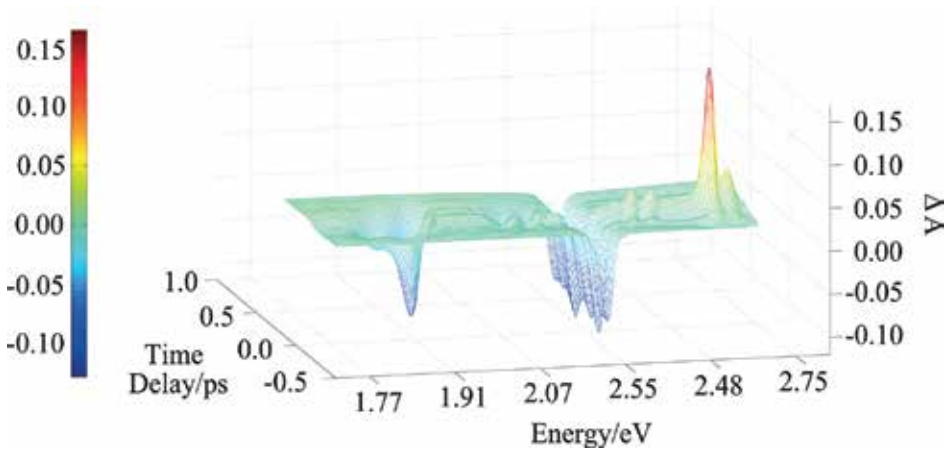

Figure 5. Three-dimensional plot of a femtosecond transient absorption experiment performed in eumelanin dispersed in a DMSO-methanol mixture. The sample was excited at 2.294 eV and probed over a range spanning from 1.548 to 2.753 eV. From left to right, the Stokes, laser pump, and anti-Stokes peaks can be identified. The $\Delta A(\hbar\omega,\tau)$ is shown in the first picosecond of time delay between the pump and probe pulses to clearly exhibit the Raman peaks.

and, thus, it is possible to directly relate the IRS effect to the FTA measurements. At Stokes frequencies, the probe-beam field experiences gain in intensity as already described above. Hence, the argument of the logarithm in Eq. (19) is larger than 1 and the transient absorption $\Delta A(\hbar\omega,\tau) < 0$. In fact, an increase in the photon flux is detected in the transmitted probe beam. Conversely, at anti-Stokes frequencies, a loss in intensity is experienced in the Raman-active medium, due to the annihilation of a photon of frequency ω_{aS}. Experimentally, the decrease in intensity in the transmitted probe beam can be treated as a real absorption by the sample, being $\Delta A(\hbar\omega,\tau) > 0$. This is precisely illustrated in **Figure 5**. In the middle, the scattered radiation from the incoming pump beam is evident. Symmetrically located with respect to the

pump laser, the upside-down peaks at low energies are the Stokes lines, while the intense peaks at high energies are the anti-Stokes lines.

Due to the different amount of photons detected in the femtosecond transient absorption experiments caused by the inverse Raman-scattering effect, it is crucial to recognize the presence of such coherent artifact to avoid misinterpretation in the analysis of the FTA spectra. Hereafter, the relaxation dynamics of a dispersion of eumelanin suspended in a DMSO-methanol mixture (1:20 ratio) is investigated by means of FTA. This sample was chosen to demonstrate the influence of the IRS, whose signal arises from the solvent used, in the temporal relaxation of the eumelanin pigments.

4.3. Decoupling IRS features from FTA dynamics

To investigate the influence of the IRS on the transient absorption dynamics, suitable probing energies have to be chosen accurately. To this end, the temporal evolutions of the Raman features have been analyzed. From **Figure 6**, it is clear that probing the sample dynamics at $\hbar\omega_{\mathrm{pr}}$ = 1.741 eV allows the investigation of a region free from IRS features (probe frequency lower than the Stokes peaks, $\hbar\omega_{\mathrm{pr}} < \hbar\omega_S$). Furthermore, this is the energy at which the pigment is showing its maximum absorption, as illustrated in the inset of **Figure 6**. The other two regions where it is worth to investigate the dynamics are $\hbar\omega_{\mathrm{pr}}$ = 1.823 and $\hbar\omega_{\mathrm{pr}}$ = 2.460 eV. These two probing energies allow to study regions near the IRS features at energies lower (between the Stokes and the pump frequencies, $\hbar\omega_S < \hbar\omega_{\mathrm{pr}} < \hbar\omega_{\mathrm{pu}}$) and higher (between the pump and the anti-Stokes frequencies, $\hbar\omega_{\mathrm{pu}} < \hbar\omega_{\mathrm{pr}} < \hbar\omega_{aS}$) than the incoming pump pulse, respectively.

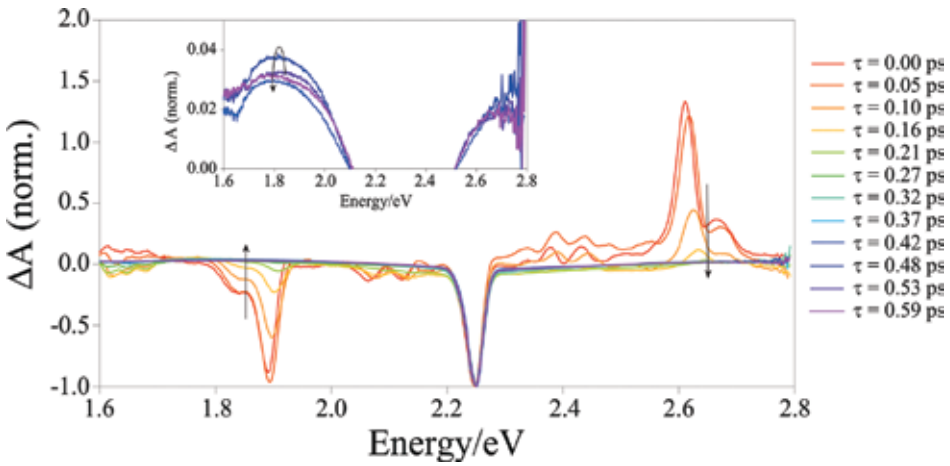

Figure 6. Temporal evolution of the synthetic eumelanin transient absorption spectra acquired in DMSO-methanol mixture after excitation at 2.254 eV. The spectra have been normalized to the pump-pulse intensity. The τ on the right illustrates the delay times between the pump and the probe pulses at which the spectra were acquired. The inset points out the rising of the eumelanin absorption signal, in an enlarged scale.

http://dx.doi.org/10.5772/65479

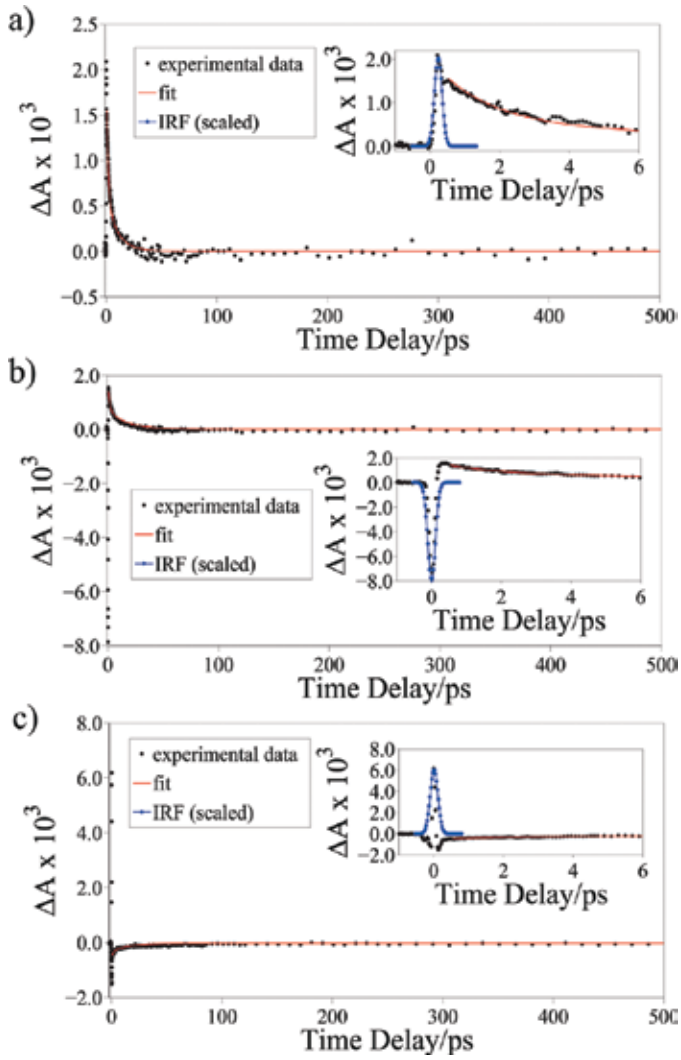

Figure 7. Transient absorption dynamics acquired in synthetic eumelanin dispersed in DMSO-methanol mixture. Dispersion has been excited at 2.254 eV and probed at energies $\hbar\omega_{\mathrm{pr}} < \hbar\omega_S$ (a), $\hbar\omega_S < \hbar\omega_{\mathrm{pr}} < \hbar\omega_{\mathrm{pu}}$ (b) and $\hbar\omega_{\mathrm{pu}} < \hbar\omega_{\mathrm{pr}} < \hbar\omega_{aS}$ (c), that is, 1.741, 1.823, and 2.460 eV, respectively. The experimental data (full circles) were fitted by a bi-exponential decay function (red solid line); the blue line shows the instrumental response function (IRF). Figure revised from [17].

The dynamics in the aforementioned regions is shown in **Figure 7** for the eumelanin suspension in DMSO-methanol mixture [17]. The temporal relaxation of these pigments is well reported [18], and is consistent with the data herein shown. At the same time, it is possible to appreciate a change in the sign of the differential absorption at very short time delays (first hundreds of femtoseconds) upon the probed energy, disclosing the influence of the IRS. When the probe-beam frequency is lower than the one at which the Stokes features appears, an IRS-free FTA

dynamics is observed. In fact, as presented in **Figure 7a** ($\hbar\omega_{pr}$ = 1.741 eV), the FTA dynamics shows a positive ΔA signal which decreases in time in a multi-exponential way. This signal is indicative of a photo-induced absorption, where the intensity of the transmitted probe beam in the presence of excitation by the pump pulse is lower than the one collected in the absence of the pump beam. In fact, upon excitation at $\hbar\omega_{pu}$ = 2.254 eV, an excited-state absorption (ESA) process, involving optically allowed transitions to higher-energy states, occurs in the eumelanin dispersion [19, 20]. When the response of the sample is probed at frequencies between the Stokes features and the incoming pump pulse, a profile like the one shown in **Figure 7b** is observed. Here, the dynamics is made out of a negative ΔA signal at ultrashort time delay followed by a sharp rise, ending by a bi-exponential decay. The observed signal is a convolution of two processes: the absorption of the pigments and the IRS effect arising from the solvent. As observed in the previous case, the eumelanin absorption leads to a positive ΔA signal at every time delay between pump and probe pulses.

The second contribution occurs only in the first hundreds of femtoseconds instead. This is due to the fact that the vibrational coherence needed to achieve the inverse Raman scattering persists as long as pump and probe pulses are temporally overlapped. Since the frequency of the probe pulse resonates with one of the Stokes features, a reinforcement of the vibrational modes of the solvent follows. Due to the resonance at the Stokes frequency, a gain in the intensity of the probe beam is achieved and the IRS appears as an emission of photons as described by the theoretical model presented by Rai et al. [4]. An increase in transmitted intensity is registered as a negative ΔA signal in an FTA experiment. Being a stimulated process, the IRS intensity overwhelms the absorption signal carried by the eumelanin pigments until the vibrational coherence lasts. When the delay between pump and probe pulses increases, the IRS artifact disappears, revealing the positive absorption of the eumelanin. Right after, the suspension relaxes back to the ground state following a bi-exponential decay.

In **Figure 7c**, the FTA dynamics of the eumelanin probed at frequencies between the incoming pump beam and the anti-Stokes features is presented. If $\hbar\omega_{pu} < \hbar\omega_{pr}$, a depletion of the ground state is achieved through the action of the pump pulse. This process is called ground-state bleaching and results in a negative ΔA signal, since the transmitted intensity of the probe beam is higher when the sample is excited. However, the ground-state bleaching cannot explain the presence of a sharp and intense positive peak in the first few hundreds of femtoseconds of the dynamics. Again, the IRS effect plays a major role at ultrashort delay times. In fact, the resonance between the incoming fields and the vibrational modes of the solvent occurring this time at the anti-Stokes frequencies leads to the stimulated Raman process. The loss in intensity experienced by the probe pulse can be accounted for as additional absorption, described by a positive ΔA signal. When the pump and probe pulse are no more overlapped in the sample, the phase-matching condition for the IRS is not satisfied, and the eumelanin dynamics is disclosed, recovering the signal in a bi-exponential fashion.

The decay time obtained from the fit of the eumelanin dynamics is reported in **Table 1** for the DMSO-methanol suspension. It is worth noting that regardless of the frequency of the probe pulse, the decay times of the samples are comparable. In fact, the IRS does not affect the

relaxation dynamics of the pigment. However, the IRS influences the sign and the amplitude of the FTA measurements.

Solvent	Probe energy (eV)	τ_1 (ps)	τ_2 (ps)
DMSO-methanol	1.741	1.5 ± 0.2	10.1 ± 0.9
	1.823	1.6 ± 0.3	16.9 ± 1.4
	2.460	1.5 ± 0.1	15.3 ± 1.2

Table 1. Fitting decay time values of eumelanin suspensions, carried out in DMSO-methanol mixture. The suspension was excited at 2.254 eV. Table adapted from [17].

4.4. Ultrafast Raman loss spectroscopy as diagnostic tool

The very need of high spatial and temporal resolution to investigate molecular reaction pathways has pushed toward the development of femtosecond stimulated Raman scattering. The aim is to be able to follow structural changes in molecules during a reaction occurring on short timescales, spanning from femtoseconds to picoseconds. The ability of femtosecond stimulated Raman spectroscopy lies in the high temporal resolution with which molecular vibrations can be collected, giving deep insights into reaction dynamics. Charge-transfer processes have been intensely investigated by FSRS; for example, long-debated studies on 4-(dimethylamino)benzonitrile, due to the discrepancy between the structural simplicity of this push-pull molecule and the complexity of the excited electronic levels, have been recently come to an end. In fact, the crucial role played by intramolecular and solvent reorganizations has been at the forefront of a systematic investigation, regarding three different dynamics on various timescales: the $\pi\pi^*$ relaxation, the internal conversion, and the vibrational relaxation [21, 22]. By investigating the excited-state proton transfer by FSRS, Fang et al. attributed to the skeletal motions the origin of the fluorescent form of a green fluorescent protein from *Aequorea victoria*, which is famous for its efficient bioluminescence [23]. Indeed, by looking separately at the low vibrational frequencies of specific modes, it was possible to identify an out-of-phase motion of the phenoxil ring in the chromophore, and thus to optimize the chemical structure of the chromophore for improving the excited-state proton transfer. Another important role in which FSRS is actively utilized is to help reveal the role that molecular symmetry plays in vibrational coherence activity in photosynthetic systems (as carotenoids) and in photochemistry. In particular, internal conversion processes and coupling between electronic states are ruled out [24, 25]. Finally, the vast majority of chemical reactions studied by FSRS concerns the isomerization, because of its key function in chromophores of high significance in biology. For example, Kuramochi et al. presented the first information pertaining to the vibrations in early instants of the photodynamics observed in the chromophore of the photoactive yellow protein. This study provided more insights on how to trigger the photoreceptive functions of the chromophore when embedded in the protein [26]. Kukura et al., instead, explored the spectral evolution of specific vibrational modes explaining how the activation of rhodopsin, a light

receptor, is driven by geometric changes in the retinal backbone [27]. These are just few of the large number of examples that can be recalled to demonstrate the power of FSRS to unravel reaction coordinates, chemical configurations, and nuclear dynamics.

One of the specific methods enrolled by the femtosecond-stimulated Raman spectroscopy relies on the IRS effect and is called femtosecond inverse Raman scattering (FIRS) [2], or ultrafast Raman loss spectroscopy (URLS) [4]. In URLS, the decrease in intensity of the probe beam, as described in Section 4.2, is completely described by the IRS effect and is used as fingerprint to follow in time the reaction pathways. Moreover, this spectroscopic tool shows some beneficial features missing in the general FSRS. The intensity of the Raman peaks at the anti-Stokes frequencies results higher than what is measured at the Stokes frequencies (Raman gain), leading to a better signal-to-noise ratio [7, 9, 10]. Second, looking at the blue side of the pump pulse to identify the spectral features of the sample helps to reject the fluorescence signal, which appears on the red side [2]. Finally, the detector dynamic range has higher efficiencies on the anti-Stokes than on the Stokes side, minimizing the noise levels and thus allowing for clearer imaging (FIRS microscopy) [28–32], for example, in tissues [33] and drug-delivery processes [34–36].

In the previous paragraph, it was shown that investigating the temporal evolution of the ΔA signal at specific probing energies can be used to determine the influence of the IRS coherent artifact on the dynamics of the eumelanin pigments. Focusing now on the IRS features, the dynamics of specific bonds, induced by photoexcitation processes, can be probed [37, 38].

First, it is of crucial importance to identify the spectral features encountered in the FTA measurements, and ascribe them to specific vibrational modes. To this end, the Raman spectrum of the solvent mixture (DMSO-methanol, 1:20 in ratio) was collected. As can be seen in **Figure 8a**, the Raman spectrum is dominated by three narrow peaks and a broad band. These features are recognized as follows: CO stretching and SO stretching in methanol and in DMSO, overlapping at 0.125 eV (peak I); CH_2 bending in methanol at 0.177 eV (peak II); CH stretching in methanol at 0.352 and 0.365 eV (symmetric and antisymmetric vibrational mode), and in DMSO at 0.361 eV (peak III); OH stretching in methanol at 0.414 eV (peak IV) [39–41]. A direct correspondence of the Raman peaks shown in **Figure 8a** is found in the FTA measurements depicted in **Figure 8b**. In fact, the spectral evolution at ultrashort time delays shows specifically the same Raman features occurring symmetrically to the pump pulse at Stokes and anti-Stokes frequencies.

Tuning the pump pulse to lower energies, the spectral features follow the energy shift, maintaining constant the energy difference between each of them and the pump pulse (spectra from red to blue in **Figure 8b**). Computing $\Delta E = \hbar\omega_{\mathrm{pu}} - \hbar\omega_{i'}$ that is, the difference in energy between the pump pulse and the spectral features, this equals the Raman shift values displayed on the x-axes for each Raman peak reported in **Figure 8a**. By this analysis, the authors proved that the observed coherent artifact in the FTA measurements at ultrashort time delay is a feature originating from the stimulated Raman-scattering process [17].

http://dx.doi.org/10.5772/65479

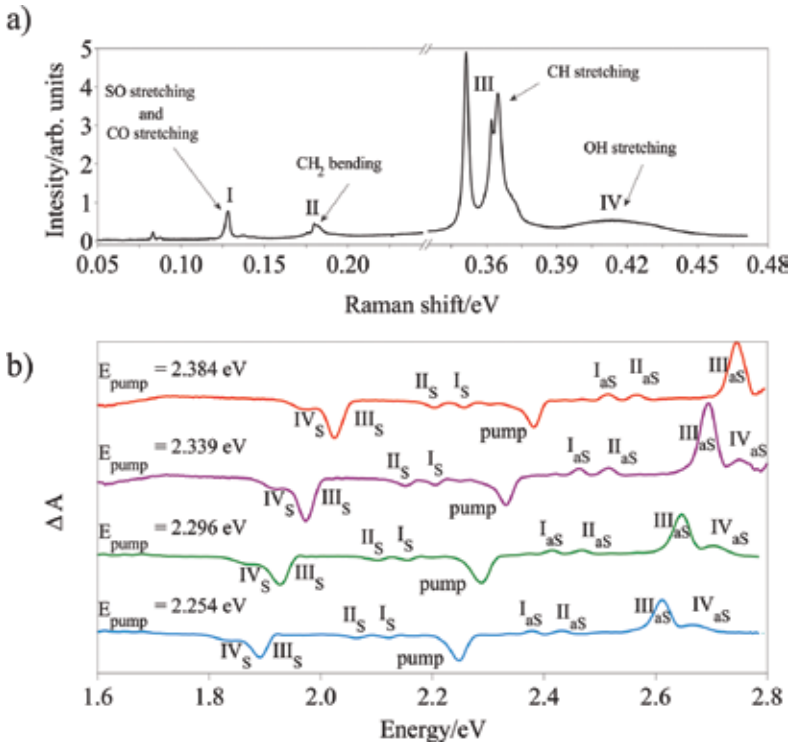

Figure 8. (a) Raman spectrum of DMSO-methanol mixture (λ_{ex} = 488 nm, $P_{incident}$ = 6 mW, acquisition time: 30 s) and (b) Spectral evolution of the transient absorption signal detected at $\tau \sim 0$ in the DMSO-methanol mixture for different pump-pulse energies. The curves are vertically shifted for clarity. Figure taken from [17].

Once identified the Raman vibrational modes, it is possible by URLS to investigate them specifically and, in particular, to address their spectral evolution in time. This can give insights on the transient structure of the molecules and on the dynamics of the specific vibrational modes. Here, we report on a very preliminary analysis ran in such direction on the aforementioned sample; in **Figure 9** the C—H Raman vibrational mode located at 2.641 eV, upon pumping the sample at $\hbar\omega_{pu}$ = 2.525 eV, is examined in terms of peak shift and intensity over time. The spectra shown in **Figure 9a** have been normalized to the intensity of the incoming pump pulse. The peak position experiences a shift toward the blue region of the spectrum as the temporal decoupling of pump and probe pulses occurs. This can be clearly seen in **Figure 9b** within the first picoseconds. At the same time, its intensity decreases at an exponential rate (**Figure 9c**).

This example should visually explain the potential and the strength of the URLS as spectroscopic tool. In fact, the results here collected, and the many more presented in literature [37, 38, 42], unambiguously demonstrate the ability of the technique to select specific bonds and study their dynamics upon photoexcitation, at ultrafast timescales. However, further investigations are required to relate the experimental observations to the ultimate structure of the solvent molecules.

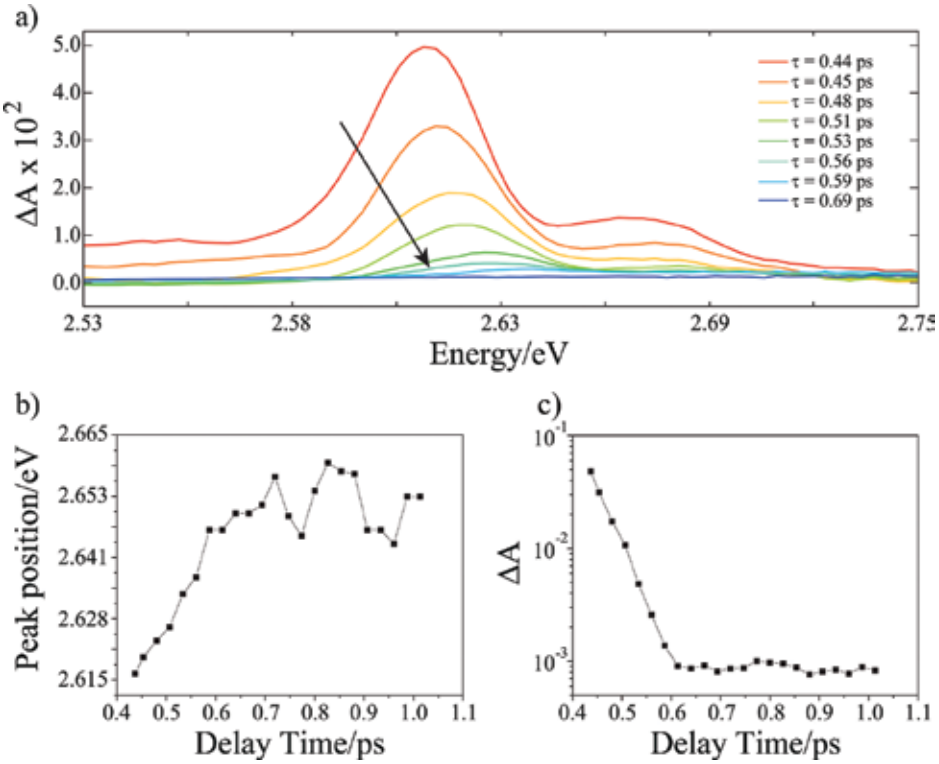

Figure 9. (a) ΔA signal in the blue region of the pump pulse. The peak taken into account is the anti-Stokes feature related to the stretching of the C—H bond in methanol and DMSO, (b) evolution of the Raman peak position as function of delay time between the pump and the probe pulses, and (c) temporal evolution of the intensity of the Raman peak.

5. Conclusions

In this chapter, the authors presented a complete description of the inverse Raman scattering effect, one of the four-wave mixing processes contributing to the stimulated Raman scattering process. Feynman dual-time line diagrams and energy level diagrams were used to explain the theory behind the IRS effect. Once addressed the nature of the IRS effect, its close relation with the transient absorption pump-probe experiment was described, as well as the influence on the temporal evolution of the sample dynamics. To this end, the dynamics of eumelanin dispersions carried out at different exciting energies were shown, pointing out the crucial role of the IRS in the relaxation dynamics of the sample. Finally, the implementation of the IRS effect as diagnostic tool in determining the structures and interactions among molecules was presented. In fact, the high resolution achieved in the time and spectral domains showed by ultrafast loss Raman spectroscopy enables to follow specifically the electronic structure of molecules while undergoing chemical reactions, even on ultrafast timescales.

http://dx.doi.org/10.5772/65479

Author details

Antonio Aloi[1,2] and Raffaele Tommasi[3,4*]

*Address all correspondence to: raffaele.tommasi@uniba.it

1 Institute for Complex Molecular Systems (ICMS), Eindhoven University of Technology, Eindhoven, Netherlands

2 Laboratory of Macromolecular and Organic Chemistry, Department of Chemical Engineering and Chemistry, Eindhoven University of Technology, Eindhoven, Netherlands

3 Department of Basic Medical Sciences, Neuroscience and Sense Organs, University of Bari Aldo Moro, Bari, Italy

4 CNR-IPCF Bari Divison, c/o Chemistry Department, Bari, Italy

References

[1] Wei, J. Nonlinear Super-Resolution Nano-Optics and Applications. 1st ed. Springer-Verlag Berlin Heidelberg; 2015. DOI: 10.1007/978-3-662-44488-7.

[2] Dietze, D.R.; Mathies, R.A. Femtosecond stimulated Raman spectroscopy. Chem. Phys. Chem. 2016; 17:1–29. DOI: 10.1002/cphc.201600331

[3] Qiu, X.; Li, X.; Niu, K.; Lee, S.Y. Inverse Raman bands in ultrafast Raman loss spectroscopy. J. Chem. Phys. 2011; 135:164502-1-8. DOI: 10.1063/1.3653940.

[4] Rai, N.K.; Lakshmanna, A.Y.; Namboodiri, V.V.; Umapathy, S. Basic principles of ultrafast Raman loss spectroscopy. J. Chem. Sci. 2012; 124:177–186. DOI: 10.1007/s12039-012-0214-8.

[5] Jones, W.J.; Sticheff, B.P. Inverse Raman spectra: induced absorption at optical frequencies. Phys. Rev. Lett. 1964; 13:657–660. DOI: 10.1103/PhysRevLett.13.657.

[6] Roslyak, O.; Marx, C.A.; Mukamel, S. Generalized Kramers-Heisenberg expressions for stimulated Raman scattering and two-photon absorption. Phys. Rev. A. 2009; 79:063927-1-12. DOI: 10.1103/PhysRevA.79.063827.

[7] Mallick, B.; Lakhsmanna, A.Y.; Umapathy, S. Ultrafast Raman loss spectroscopy (URLS): instrumentation and principles. J. Raman Spectrosc. 2011; 42:1883–1890. DOI: 10.1002/jrs.2996.

[8] Lau, A.; Werncke, W.; Pfeiffer, M.; Lenz, K.; Weigmann, H.J. Inverse Raman scattering. Sov. J. Quant. Electron. 1976; 6:402–409. DOI: 10.1070/QE1976v006n04ABEH011129/meta.

[9] Umapathy, S.; Lakhsmanna, A.Y.; Mallick, B. Ultrafast Raman spectroscopy. J. Raman Spectrosc. 2009; 40:235–237. DOI: 10.1002/jrs.2199.

[10] Lakhsmanna, A.Y.; Mallick, B.; Umapathy, S. Ultrafast Raman loss spectroscopy: a new approach to vibrational structure determination. Curr. Sci. 2009; 97:210–216.

[11] Abramczyk, H. Introduction to laser spectroscopy. 1st. ed. Elsevier; Radarweg 29, P.O. Box 211, 1000 AE Amsterdam, The Netherlands; 2005. DOI: 9780444516626.

[12] Niu, K.; Lee, S.Y. Analysis of time resolved femtosecond and femtosecond/picosecond coherent anti-Stokes Raman spectroscopy: Application to toluene and Rhodamine 6G. J. Chem. Phys. 2012; 136:064504-1-11. DOI: 10.1063/1.3682470.

[13] Frontiera, R.R.; Shim, S.; Mathies, R.A. Origin of negative and dispersive features in anti-Stokes and resonance femtosecond stimulated Raman spectroscopy. J. Chem. Phys. 2008; 129:064507-1-6. DOI: 10.1063/1.2966361.

[14] Niu, K.; Cong, S.; Lee, S.Y. Femtosecond stimulated Raman scattering for polyatomics with harmonic potentials: application to rhodamine 6G. J. Chem. Phys. 2009; 131:054311-1-14. DOI: 10.1063/1.3198473.

[15] Boyd, R. Nonlinear Optics. 3rd. ed. Academic Press; 30 Corporate Drive, Suite 400, Burlington, MA 01803, USA, 525 B Street, Suite 1900, San Diego, California 92101-4495, USA, 84 Theobald's Road, London WC1X 8RR, UK; 2008. DOI: 9780123694706.

[16] Sun, Z.; Lu, J.; Zhang, D.H.; Lee, S.Y. Quantum theory of (femtosecond) time-resolved stimulated Raman scattering. J. Chem. Phys. 2008; 128:144114-1-13. DOI: 10.1063/1.2888551.

[17] Aloi, A.; Brunetti, A.; Perna, G.; Lasalvia, M.; Capozzi, V.; Tommasi, R. Ultrafast transient absorption of eumelanin suspensions: the role of inverse Raman scattering. Biomed. Opt. Express. 2015; 6:4000–4013. DOI: 10.1364/BOE.6.004000.

[18] Matthews, T.E.; Wilson, J.W.; Degan, S.; Simpson, M.J.; Jin, J.Y.; Zhang, J.Y.; Warren, W.S. In vivo and ex vivo epi-mode pump-probe imaging of melanin and microvasculature. Biomed. Opt. Express. 2011; 2:1576–1583. DOI: 10.1364/BOE.2.001576.

[19] Berera, R.; van Grondelle, R.; Kennis, J.T.M. Ultrafast transient absorption spectroscopy: principles and application to photosynthetic systems. Photosynth. Res. 2009; 101:105–118. DOI: 10.1007/s11120-009-9454-y.

[20] Meredith, P.; Sarna, T. The physical and chemical properties of eumelanin. Pigment Cell Res. 2006; 19:572–594. DOI: 10.1111/j.1600-0749.2006.00345.x.

[21] Rhinehart, J.M.; Mehlenbacher, R.D.; McCamant, D.W. Probing the charge transfer reaction coordinate of 4-(Dimethylamino)benzonitrile with femtosecond stimulated Raman spectroscopy. J. Phys. Chem. B. 2010; 114:14646–14656. DOI: 10.1021/jp1023982.

[22] Rhinehart, J.M.; Challa, J.R.; McCamant, D.W. Multimode charge-transfer dynamics of 4-(Dimethylamino)benzonitrile probed with ultraviolet femtosecond stimulated Raman spectroscopy. J. Phys. Chem. B. 2012; 116:10522–10534. DOI: 10.1021/jp3020645.

[23] Fang, C.; Frontiera, R.R.; Tran, R.; Mathies, R.A. Mapping GFP structure evolution during proton transfer with femtosecond Raman spectroscopy. Nature. 2009; 462:200–205. DOI: 10.1038/nature08527.

[24] Hashimoto, H.; Sugisaki, M.; Yoshizawa, M. Ultrafast time-resolved vibrational spectroscopies of carotenoids in photosynthesis. Biochim. Biophys. Acta Bioenerg. 2015; 1847:69–78. DOI: 10.1016/j.bbabio.2014.09.001.

[25] Buckup, T.; Motzkus, M. Multidimensional time-resolved spectroscopy of vibrational coherence in biopolyenes. Annu. Rev. Phys. Chem. 2014; 65:39–57. DOI: 10.1146/annurev-physchem-040513-103619.

[26] Kuramochi, H.; Takeuchi, S.; Tahara, T. Ultrafast structural evolution of photoactive yellow protein chromophore revealed by ultraviolet resonance femtosecond stimulated Raman spectroscopy. J. Phys. Chem. Lett. 2012; 3:2025–2029. DOI: 10.1021/jz300542f.

[27] Kukura, P.; McCamant, D.W.; Yoon, S.; Wandschneider, D.B.; Mathies, R.A. Structural observation of the primary isomerization in vision with femtosecond-stimulated Raman. Science. 2005; 310:1006–1009. DOI: 10.1126/science.1118379.

[28] Robles, F.E.; Fischer, M.C.; Warren, W.S. Dispersion-based stimulated Raman scattering spectroscopy, holography, and optical coherence tomography. Opt. Express. 2016; 24:485–498. DOI: 10.1364/OE.24.000485.

[29] Puppels, G.J.; de Mul, F.F.; Otto, C.; Greve, J.; Robert-Nicoud, M.; Arndt-Jovin, D.J.; Jovin, T.M. Studying single living cells and chromosomes by confocal Raman microspectroscopy. Nature. 1990; 347:301–303. DOI: 10.1038/347301a0.

[30] Zumbusch, A.; Holtom, G.R.; Xie, X.S. Three-dimensional vibrational imaging by coherent anti-Stokes Raman scattering. Phys. Rev. Lett. 1999; 82:4142–4145. DOI: 10.1103/PhysRevLett.82.4142.

[31] Cui, M.; Bachler, B.R.; Ogilvie, J.P. Comparing coherent and spontaneous Raman scattering under biological imaging conditions. Opt. Lett. 2009; 34:773–775. DOI: 10.1364/OL.34.000773.

[32] Simpson, M.J.; Wilson, J.W.; Phipps, M.A.; Robles, F.E.; Selim, M.A.; Warren, W.S. Nonlinear microscopy of eumelanin and pheomelanin with subcellular resolution. J. Invest. Dermatol. 2013; 133:1822–1826. DOI: 10.1038/jid.2013.37.

[33] Ji, M.; Orringer, D.A.; Freudiger, C.W.; Ramkissoon, S.; Liu, X.; Lau, D.; Golby, A.J.; Norton, I.; Hayashi, M.; Agar, N.Y.R.; Young, G.S.; Spino, C.; Santagata, S.; Camelo-Piragua, S.; Ligon, K.L.; Sagher, O.; Xie, X.S. Rapid, label-free detection of brain tumors with stimulated Raman scattering microscopy. Sci. Transl. Med. 2013; 5:201ra119-1-10. DOI: 10.1126/scitranslmed.3005954.

[34] Fu, D.; Yu, Y.; Folick, A.; Currie, E.; Farese, R.V.Jr.; Tsai, T.-H.; Xie, X.S.; Wang, M.C. In vivo metabolic fingerprinting of neutral lipids with hyperspectral stimulated Raman scattering microscopy. J. Am. Chem. Soc. 2014; 136:8820–8828. DOI: 10.1021/ja504199s.

[35] Fu, D.; Zhou, J.; Zhu, W.S.; Manley, P.W.; Wang, Y.K.; Hood, T.; Wylie, A.; Xie, X.S. Imaging the intracellular distribution of tyrosine kinase inhibitors in living cells with quantitative hyperspectral stimulated Raman scattering. Nat. Chem. 2014; 6:614–622. DOI: 10.1038/nchem.1961.

[36] Tipping, W.J.; Lee, M.; Serrels, A.; Bruntonb, V.G.; Hulme, A.N. Stimulated Raman scattering microscopy: an emerging tool for drug discovery. Chem. Soc. Rev. 2016; 45:2075–2089. DOI: 10.1039/C5CS00693G.

[37] Umapathy, S.; Roy, K.; Kayal, S.; Rai, N.; Venkatraman, R.K. Structure and dynamics from time resolved absorption and Raman spectroscopy. Springer Netherlands; 2014. DOI: 10.1007/978-94-017-8550-1_3.

[38] Hoffman, D.P.; Mathies, R.A. Femtosecond stimulated Raman exposes the role of vibrational coherence in condensed-phase photoreactivity. Acc. Chem. Res. 2016; 49:616–625. DOI: 10.1021/acs.accounts.5b00508.

[39] Martens, W.N.; Frost, R.L.; Kristof, J.; Kloprogge, J.T. Raman spectroscopy of dimethyl sulphoxide and deuterated dimethyl sulphoxide at 298 and 77 K. J. Raman Spectrosc. 2002; 33:84–91. DOI: 10.1002/jrs.827.

[40] Cheng, J.X.; Xie, X.S. Coherent Raman scattering microscopy. CRC Press; Taylor & Francis Group, 6000 Broken Sound Parkway NW, Suite 300, Boca Raton, FL 33487-2742; 2012. DOI:9781439867655.

[41] Ellis, A.; Zehentbauer, F.M.; Kieferab, J. Probing the balance of attraction and repulsion in binary mixtures of dimethyl sulfoxide and n-alcohols. Phys. Chem. Chem. Phys. 2013; 15:1093–1096. DOI: 10.1039/C2CP42902K.

[42] Kukura, P.; McCamant, D.W.; Mathies, R.A. Femtosecond stimulated Raman spectroscopy. Annu. Rev. Phys. Chem. 2007; 58:461–488. DOI: 10.1146/annurev.physchem.58.032806.104456.

Section 2

Surface Enhanced Raman Spectroscopy

Chapter 14

Surface-Enhanced Raman Scattering

Ujjal Kumar Sur

Additional information is available at the end of the chapter

http://dx.doi.org/10.5772/66084

Abstract

The steady and fast development of surface and interfacial science have set up innovative openings for new diagnostic probes for analytical characterization of the adsorbates and determination of the microscopic structure of surfaces and interfaces. Regrettably Raman spectroscopy, being a weak scattering surface phenomenon, had seized no part in it, until the discovery and development of Surface Enhanced Raman Scattering (SERS) in the early 1970's that has opened up broad research fields both in the physics and chemistry of interfaces. The discovery of SERS by Fleischmann and coworkers in 1974 at the University of Southampton, United Kingdom is closely connected with the electrochemical systems. They reported an extraordinary million-fold enhancement of weak Raman signal from pyridine molecules adsorbed onto electrochemically roughened silver electrode compared to that from free molecules in liquid environment. In early 1976, Richard P. Van Duyne and David Jeanmaire at Northwestern University observed the effect and in early 1977, M. G. Albrecht and J. A. Creighton reported similar observation. This review article deals with the development of SERS research with special importance is given to the fabrication of various SERS-active substrates, mechanism of SERS effect and its various potential applications ranging from sensors to biomedical applications.

Keywords: Raman scattering, surface-enhanced Raman scattering, electromagnetic (EM) enhancement effect, hot spots, sensors, SERS active substrates

1. Introduction

Raman scattering arises as a result of interaction of electromagnetic radiation with matter resulting in the alteration of frequency or wavelength of the incident radiation. With the invention of strong, monochromatic, polarized and tunable lasers, the Raman spectroscopy has grown as a highly sensitive technique to probe structural details of a complex molecular structure. However, the applications of traditional or conventional Raman spectroscopy are restricted by the low scattering cross section involved with the Raman scattering process,

which are ~ 12–14 orders of magnitude lower than the fluorescence cross section for various biological and organic molecules, which are highly fluorescent in nature [1–7]. Therefore, the discovery of Fleischmann and coworkers from the University of Southamption, UK in 1974 [8], which demonstrated the unexpected high Raman signals obtained from pyridine molecules adsorbed on a rough silver electrode, has attracted considerable attention of researchers from various fields such as physics, chemistry, biology, mathematics, and engineering. In a published paper, Fleischmann et al. reported an extraordinary million-fold enhancement of Raman signal from pyridine molecules adsorbed onto electrochemically roughened silver electrode compared to that from free molecules in a liquid environment [8]. Surface-enhanced Raman scattering (SERS) effect deals with the gigantic amplification of the weak Raman scattering intensity by molecules in the presence of a nanostructured metallic surface [5–8]. The SERS enhancement factor can be defined as the ratio between the Raman signals obtained from a given number of molecules in the presence and in the absence of the metal nanostructure and this factor is dependent largely on the size and morphology of the nanostructures. In general, SERS enhancement value is around 10^6, but it may reach value as high as 10^{10} at definite highly effective subwavelength regions of the surface [5–8].

Since its discovery in the year 1974, surface-enhanced Raman scattering (SERS) has attracted significant interest of researchers [1–7]. The discovery of SERS has opened up a promising way to overcome the low-sensitivity problem associated with conventional Raman spectroscopy. Introduction of the SERS technique not only improves the overall surface sensitivity making Raman spectroscopy more applicable but also stimulates the study of the interfacial processes involving enhanced optical scattering from adsorbates on metal surfaces [9].

This review article covers the current development in SERS research along with brief discussion on the fabrication of various SERS active substrates, the various theoretical explanations of the mechanism of SERS effect and its various diverse applications in sensing, diagnostics, and catalysis. The article first deals with a short historical assessment of the SERS effect, followed by an overview on the preparation of various SERS active substrates. The article concludes with the citations of some recent applications of SERS from the literature. Due to insufficiency in space, a comprehensive review of all current work based on SERS is impossible. However, we have summarized a few representative examples including our own results to demonstrate the recent advancement in the SERS research.

2. Historical background and gradual development of SERS

Raman spectroscopy is a spectroscopic technique based on molecular vibration and is dependent on the inelastic scattering of monochromatic light, usually from a laser in the visible, near-infrared, or near-ultraviolet range of electromagnetic spectra. This effect was discovered by famous Indian physicist Professor C.V. Raman in 1928 [10].

Figure 1 shows the schematic diagram to explain the principle of Raman scattering. The weak Raman signal observed in conventional Raman spectroscopy can be explained by the low scat-

tering cross section (~10^{-30} molecule cm^{-2}). Therefore, Raman spectroscopy will provide low sensitivity in terms of signal and is the main reason for its inapplicability in practical fields for a long period [5–7]. For an extremely low scattering cross section in the range 10^{12}–10^{14} molecule cm^{-2}, usually present in a monolayer, it is very difficult to detect signal obtained from a Raman probe molecule even by the most effective modern and sophisticated Raman spectrometer. Raman spectroscopy is competent enough to obtain fingerprint information of species by detecting the vibrational bands. In Raman spectroscopy, the sample containing the Raman probe molecule is illuminated with a laser beam of appropriate wavelength. Wavelengths close to the laser line arises as a result the Rayleigh scattering is filtered out, while the rest of the unfiltered light is dispersed onto a detector. Spontaneous Raman scattering is very weak as compare to the Rayleigh scattering and identification and partition of these two signals are important to obtain a high quality Raman spectrum. Traditionally, holographic diffraction gratings are employed in Raman spectrometers to yield a high degree of laser rejection. On the other hand, modern instrumentation unanimously employs notch filters for laser rejection. Development of modern instrumentation along with the introduction of fast-Fourier transform (FFT)-based spectrometers, confocal microscopes, and charge coupled device (CCD) detectors has brought a new dimension in Raman instruments, providing very high sensitivity. **Figure 2** demonstrates the development of Raman instrumentation from the Raman spectrometer of C. V. Raman to the latest sophisticated Horiba-Jobin model of micro-Raman system.

However, the intensity of Raman signal obtained from most of the systems is very weak and is only about 10^{-10} times the intensity of the incident laser. Fleischmann and his group from the University of Southampton, UK, carried out Raman spectroscopic study with expected high intensity of signal by increasing the number of adsorbed molecules on a roughened metal electrode surface. In 1974, they reported very high quality Raman spectra of pyridine molecule (Raman probe molecule with high scattering cross section) adsorbed on electrochemically roughened Ag electrodes [8]. The authors attributed the enhancement in the Raman intensity to an increase in the surface area of the Ag electrode by the electrochemical

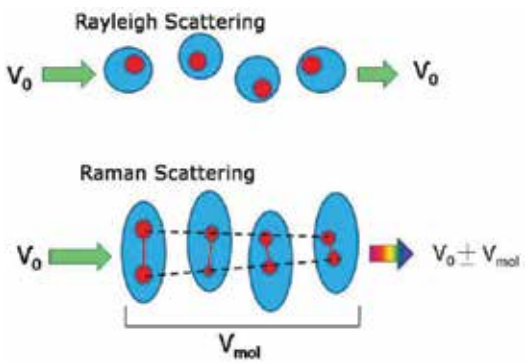

Figure 1. Schematic diagram to explain the principle of Raman scattering and Rayleigh scattering.

Figure 2. The development of Raman instrumentation from the Raman spectrometer of C. V. Raman to the latest sophisticated Horiba-Jobin model of the micro-Raman system.

roughening method. **Figure 3** illustrates the schematic diagram to explain the principle of SERS. The technique is so sensitive that even single molecule can be detected.

Figure 4 shows the photograph of Fleischmann, who invented SERS. Fleischmann, Hendra, and Mcquillan of University of Southampton, UK, discovered surface-enhanced Raman scattering (SERS) spectroscopy by chance when they tried to carry out Raman study with pyridine (Py) molecule having very high Raman cross section on the roughened silver (Ag) electrode [8]. The spectra were found to be dependent on the applied electrode potential.

http://dx.doi.org/10.5772/66084

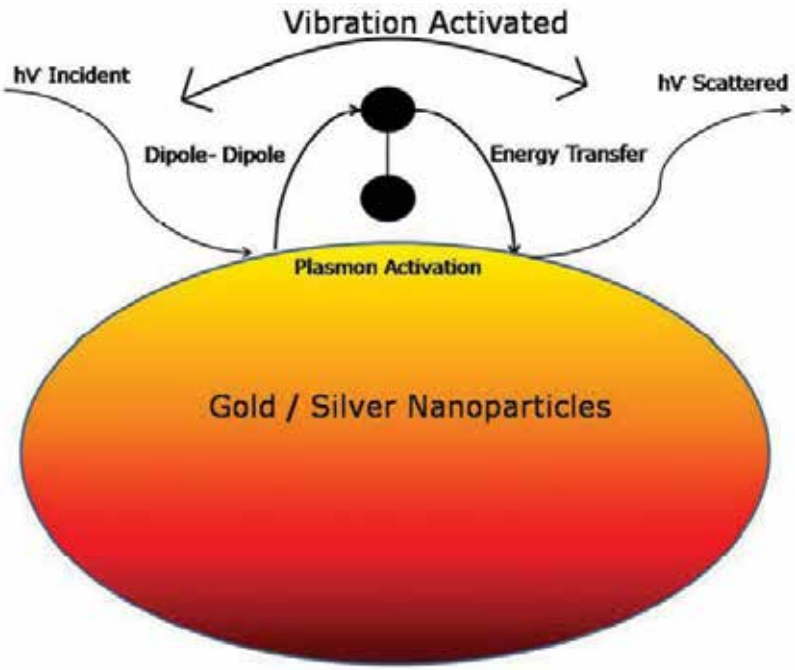

Figure 3. Schematic diagram to explain the principle of SERS.

Initially, it was thought that an increase of surface area to be responsible for the enhancement of Raman signal. Afterward, in 1977 Jeanmaire and Van Duyne [11], from Northwestern University, USA, first realized that the surface area is not the key point in the above phenomenon. Albrecht and Creighton [12] of University of Kent, UK, reported a similar result in the same year. Both the groups independently supported enough proofs to exhibit that the strong surface Raman signal must be created by an authentic augmentation of the Raman scattering efficiency (10^5 to 10^6 enhancement). Later, this effect was referred as surface-enhanced Raman scattering and now, it is a unanimously acknowledged surface analytical technique. In spite of the fact, the first SERS spectra were obtained employing an electrochemical system (Py + roughened Ag electrode), all significant reactions occurring on various surfaces like metal and semiconductors can be investigated by the SERS technique. The technique is so sensitive that even single molecule can be detected in addition to various electrochemical processes.

The precise mechanism responsible for the enhancement effect observed in SERS is still highly controversial as found from the literature. There are two major mechanisms that are responsible for the large enhancement of weak Raman signal obtained from pyridine molecules adsorbed on electrochemically roughened Ag surface. Jeanmaire and Van Duyne first proposed a theory based on the electromagnetic effect responsible for the enhancement of Raman signal [11]. This is known as the electromagnetic theory of SERS effect and is based on the excitation of localized surface plasmons (LSP). Albrecht and Creighton first proposed a theory

based on the charge transfer effect of the adsorbed molecule on the enhancement of Raman signal [12]. This is known as the chemical enhancement. This chemical enhancement theory depends on the charge transfer complex formation of the adsorbed molecule by absorption of photon of the suitable wavelength. Nevertheless, it is extremely complicated to separate these two effects experimentally and understand the overall mechanism of SERS.

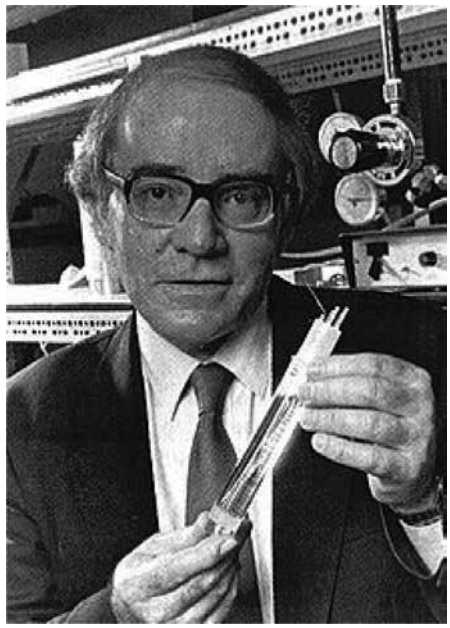

Figure 4. The photograph of Fleischmann, the inventor of SERS.

In the mid-1980s, the spotlight on SERS research diverted to the exploitation of SERS effect for new and novel analytical and biological applications from the basic understanding of the mechanism responsible for the SERS phenomenon. However, it was extremely difficult to record high-quality, highly reproducible and stable SERS spectra as demonstrated by some of the investigations carried out in the mid-1980s as well as the early 1990s. The SERS spectra obtained were highly irreproducible, which can be explained by the small variations in the fabrication of SERS substrates. This shortcoming has prevented the development of SERS as a quantitative tool for long period. For that reason, fabrication of an SERS active substrate is very important in SERS research so that highly uniform, stable, and highly reproducible SERS signals can be obtained.

In the mid-1990s, VIIIB transition metals were employed as SERS active substrates to carry out electrochemical surface-enhanced Raman spectroscopy (EC-SERS) and these SERS substrates were further utilized for electrochemistry and catalysis [13]. Professor Tian and his coworkers at the Xiamen University, China, first introduced quite a few surface roughening procedures and demonstrated that the SERS effect can be directly obtained from transition metals such

http://dx.doi.org/10.5772/66084

as pure Pt, Ru, Rh, Pd, Fe, Co, and Ni electrodes with a surface enhancement factor in the range between 1–3 orders of magnitude [14]. Since the early-2000s, the randomly roughened surfaces were replaced by the well-controlled nanostructures of both coinage (e.g., Au, Ag, and Cu) and transition metals due to the gradual and rapid development of nanoscience and nanotechnology. These nanostructures were considered as a very promising class of excellent SERS-active substrate. Up to now, molecular-level investigations by Raman spectroscopy on diverse adsorbates at various electrodes had been carried out.

The next major landmark in the field of SERS research was the observation of SERS spectra from single molecules (SM-SERS) by two independent research groups in the year 1997 [15, 16]. The detection of single molecules using the SERS technique and attainment of ultimate limit of detection in any analytical detection was possible by combining other techniques, for instance, fluorescence spectroscopy and scanning tunneling methods along with SERS technique.

Under suitable conditions, SERS enhancements in the order of 10^{14} can be obtained. It is important to mention here that special sites, sometimes referred to as "hot spots," are responsible for the observed enhancement in the SERS effect to a large extent. On the basis of these considerations, a great deal of the current research work in SERS is focused on the controlled and reproducible fabrication of metallic nanostructures which can create hot geometries like "hot spots" where the Raman probe molecules are correctly and inevitably located for gigantic Raman enhancement. This will provide new information in novel research areas like plasmonics.

3. SERS active substrates

The metals that are selected to be used as an SERS active substrate can be determined by the plasmon resonance frequency. Both, visible and near-infrared radiation (NIR) can generally be used for excitation of the Raman modes. Silver (Ag), gold (Au), and copper (Cu) are typically utilized for carrying out SERS experiments because their plasmon resonance frequencies are in the region of above-mentioned wavelength of electromagnetic spectrum, providing maximal enhancement for visible and NIR light [5–7]. Recently, transition metals such as platinum (Pt), ruthenium (Ru), palladium (Pd), iron (Fe), cobalt (Co), and nickel (Ni) have been utilized as SERS active substrates. These transition metals can display enhancements between 1–3 orders of magnitude and these enhancement factor values are very low compared to the enhancement factors obtained for metals such as Au and Ag. This can be explained by the fact that excitation of the surface plasmon resonances in the visible light region is extremely difficult. Nevertheless, large enhancement (~ 10^4) values can be obtained from the transition metals using excitation wavelength in the near ultra-violet (UV) region. The major features of the SERS technique are abridged briefly as follows:

- SERS is highly surface sensitive, nondestructive and *in-situ* vibrational spectroscopic analytical technique.

- SERS occurs as a result of bringing the Raman probe molecules closer within the few nanometers of the surface of SERS substrates of different morphologies.
- The SERS technique will exhibit exceptionally high spatial resolution, in which the enhancement range is several nanometers, effective for one or several molecular layers close to the SERS active substrate.
- SERS activity is strongly dependent on the type of metal and surface roughness of the SERS active substrate employed for the study.

Therefore, the fabrication of an SERS active substrate is a very important field from the point of view of SERS research. The two most commonly used SERS substrates are metallic colloids of Au, Ag, and Cu obtained from chemical reduction and the metal electrode surfaces roughened by one or more electrochemical oxidation-reduction cycles. Surface and substrate generality are the major limitations associated with the SERS effect and many research groups all over the world have tried to surmount these two major problems by obtaining SERS activity from other metallic surfaces other than Ag, Au, and Cu and from atomically flat (single crystal) surfaces rather than roughened surfaces. However, most of the metals used as SERS substrates will exhibit poor biological compatibility. For that reason, it is essential to provide new novel substrates for SERS study. For an ideal SERS substrate, the material should be economical, easily accessible, chemically inert, as well as biocompatible.

The SERS substrates can be approximately divided into three categories: (1) metal nanoparticles (MNPs) in suspension, (2) metal nanoparticles immobilized on solid substrates, and (3) metal nanostructures fabricated directly on solid substrates by nanolithography and template based synthesis [7, 17]. Although both nanoparticles and nanoparticle film electrodes can exhibit good surface uniformity, as a result difficulty in controlling the spacing of the nanoparticles will not be able to optimize the SERS activity. Only template-based fabrication methods can be employed to obtain highly ordered SERS substrates with controlled interparticle spacing. Amid different template-based methods, nanosphere lithography (NSL), and anodic aluminum oxide (AAO) films are most commonly employed to fabricate highly ordered SERS active substrates. The Langmuir-Blodgett technique can also be utilized to fabricate highly ordered SERS active substrates. **Figure 5** illustrates the different SERS active substrates used in recent years. As a result of fast advancement in nanoscience and nanotechnology, several methods are accessible now for the fabrication of various metallic nanostructures with different size, shape, which can be further utilized as SERS active substrates. This has facilitated in a significant enhancement in the citations of new SERS active substrates available in the literature in the last 5 years and we are expecting a further improvement in the upcoming years.

Metal nanoparticles in suspension are the simplest of all SERS active substrates used so far, where the SERS effect can be studied in the presence of definite concentration of analytes (Raman probe molecules). However, aggregation of metallic nanoparticles can prevent to obtain highly reproducible SERS spectra. Alternatively, aggregation is sometimes essential for obtaining high quality, highly reproducible SERS signal [15]. MNPs suspension must be mixed with the analyte solution for carrying out the SERS experiment, a sampling require-

http://dx.doi.org/10.5772/66084

ment that might be limiting for a few real-life applications, such as quantitative analysis of adsorbates on nonSERS active surfaces like semiconductors and fruits. In spite of the problems such as reproducibility in experimental results and potential sampling, MNPs suspensions are extensively employed as an SERS active substrate due to their high SERS-performance, good stability, and simplicity in production. Actually, this kind of substrate was employed in the early years for carrying out single molecule SERS experiments. The drawback of sampling has been recently overcome by Professor Tian and his research group at the Xiamen University, China [18]. They introduced a completely original shell-isolated MNPs as an SERS enhancing smart dust, which was successfully employed for probing hydrogen adsorbed on the single crystal Pt surface, and direct detection of pesticides residues in the form of contamination in citrus fruits such as oranges. This new borrowing SERS technique is referred by them as shell-isolated nanoparticle-enhanced Raman spectroscopy (SHINERS) [18].

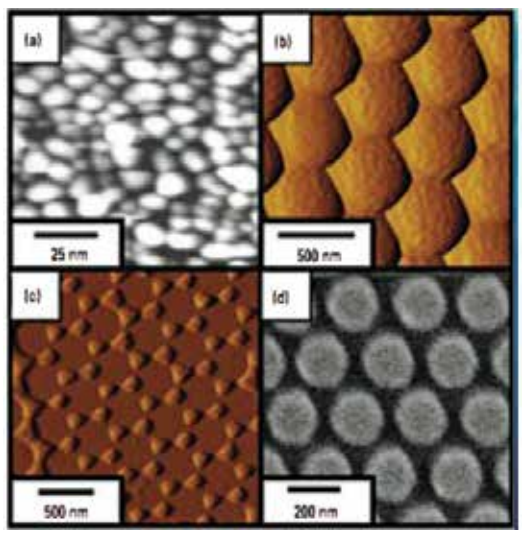

Figure 5. The different SERS active substrates fabricated by nanotechnology. Reproduced with permission from Haynes et al. [36]. Copyright @ American Chemical Society. (a) Rough silver film on glass; (b) Silver coating on top of PS beads; (c) Nanosphere lithography; (d) Silver column produced by e-beam lithography. after the word by nanotechnology

For crucial evaluation, the SERS substrates covered in this review article can be limited to only three general types of substrates, classified according to their fabrication technique: (1) MNPs immobilized in planar solid supports, (2) metallic nanostructures fabricated using nanolithographic methods, and (3) metallic nanostructures fabricated using template-based techniques.

The dispersed and aggregated MNPs cannot be used as a SERS active substrate in real analytical problems as a result of the poor reproducibility of SERS enhancement factor, which can be solved by immobilizing the MNPs on some kind of solid support. Since the first report of an SERS substrate consisting of MNPs synthesized by a wet chemical method and afterward immobilizing them onto a solid support [19], the process has become extremely popular and several papers have been published based on this process as found from the literature survey.

The top-down nanolithography and associated nanoimprint lithographic-based fabrication techniques were employed to fabricate highly ordered metallic nanostructures array. In this technique, a layer of polymeric photoresist (positive or negative) is cast on the solid substrates (such as Si, glass, or Au film). It was followed by direct patterning on the photoresist surface or indirect patterning with the assistance of a mold using ultraviolet (UV) light, an electron beam, or a focused ion beam. Afterward, the residual photoresist can be utilized as a mold, on which SERS-active metals are deposited by a physical vapor deposition technique under vacuum conditions. The mold was lifted off and a highly ordered nanostructured SERS-active substrate with a structure identical or complementary to that of the mold is formed. Highly ordered and uniform SERS active substrates with interparticle spacings below 10 nm can be produced by employing the nanolithographic method with a broad variety of shapes and geometries. However, nanolithographic techniques are still time-consuming and very expensive due to the use of high energy focused ion beam (FIB) or electron beam (EB) for the fabrication of the SERS substrate with a large area. Both, FIB and EB lithographic techniques can be employed to make molds for the nanoimprint lithography technique. In the nanoimprint lithographic technique, the desired nanopatterns are produced by direct writing on the Si or quartz slide by using an electron beam, which can be subsequently used as the mold. Next, the mold is aligned and pressed into the photoresist covering on the substrate and finally, the mold is lifted off after curing. Subsequently, the substrate is deposited with the desired metal to be used as an SERS active substrate. A highly ordered nanostructure with good SERS activity can be fabricated by completely removing the photoresist. Nanoimprint lithographic techniques are more efficient and inexpensive as compared to nanolithographic techniques.

Van Duyne and his group developed the nanosphere lithographic technique in 2001 [20, 21]. In this technique, highly ordered single or multi-layer colloidal crystal templates are produced from the self-assembly of monodispersed polystyrene or SiO_2 nanospheres of the desired diameter on clean conducting substrates such as indium tin oxide (ITO) or evaporated metal substrate over glass. Afterward, a metal layer is deposited by the physical vapor deposition or electrochemical deposition method on the substrate with a controlled thickness. Three types of structured SERS substrate can be produced by the nanosphere lithographic technique: (1) Ag metal "film over nanosphere" (FON) surfaces are formed due to physical vapor deposition on the nanosphere template; (2) surface confined nanoparticles with a triangular footprint are produced by the removal of nanospheres of the FON surfaces by sonication in a solvent; (3) thin nanostructured films containing regular hexagonal array of uniform segment sphere voids are formed by electrochemical deposition followed by removal of spheres. One can control the shape, size, and interparticle spacing of the fabricated nanostructures by tuning the size of the nanospheres and the thickness of the deposited metal with the ultimate objective that the localized surface plasmon resonance (LSPR) position can be adjusted to match the excitation wavelength with an optimized SERS enhancement.

Arrays of silver (Ag) nanoparticles with a precisely controlled gap up to 5 nm are electrochemically grown by Wang et al. [22] by utilizing the porous AAO film as a template material. This Ag/AAO system with tunable sub-10 nm interparticle gap can be further utilized as highly ordered, uniform SERS active substrate with high value of SERS enhancement factor (~10^8). It is extremely difficult to precisely control of interparticle gaps between nanostructures on an SERS-active substrate in the sub-10 nm regime as known from the

existing literature. Such studies are crucial for the fabrication of SERS active substrates with uniformly high enhancement factors, and for overall understanding of collective surface plasmons existing inside the gaps. The "hot junction" or "hot spot" located at the interparticle gap of these nanostructure-based SERS substrates can enhance the SERS activity, which is an important aspect for large electromagnetic field enhancement and excellent SERS sensitivity. Wang et al. experimentally demonstrated the first quantitative study of the collective SERS effect on a substrate with precisely controlled "hot junctions" in the sub-10 nm regime, and confirmed the theoretical prediction of interparticle-coupling-induced Raman enhancement. This Ag/AAO-based SERS substrates fabricated by Wang et al. [22] with highly uniform and reproducible SERS signals can be utilized as both a biosensor and a chemical sensor with extremely high sensitivity. Using these SERS substrates, concentration up to picomolar level has been detected. This excellent SERS substrate can be further exploited for single molecule SERS study increasing the overall detection limit and SERS sensitivity.

The Langmuir-Blodgett (LB) technique can be employed for the large-scale production of a fully defect-free SERS substrate over a large area of few hundred of cm^2. The LB method was initially employed to form a large-area surface film of amphiphilic molecules on solid substrates. In this procedure, the amphiphilic molecules such as stearic acid is dissolved in a volatile solvent like benzene or chloroform, which is completely immiscible with water, and soon after, the solution is dispersed on the surface of the water phase. As a result, a monomolecular film of the amphiphilic molecule will form at the air/water interface with complete evaporation of the volatile solvent. The film can be deposited on the substrate by the dipping and pulling method. Similarly, a nanoparticle film can be fabricated by the LB method. In this procedure, the surfaces of nanoparticles are modified with hydrophobic molecules and dispersed directly into a highly volatile solvent, which is immiscible with water. By dispersion of the solution into the water phase, a layer of randomly distributed nanoparticles will be left at the interface after complete evaporation of the volatile solvent. By compressing the layer through moving the barrier, one can control the density of the monolayer film. Subsequently, an ordered layer of nanoparticles will be formed on the surface. A systematic SERS study was carried out by Yang and his group using an SERS active substrate fabricated by the LB technique [23]. The LB technique was employed by them to successfully fabricate most uniform SERS substrates of films of nanorods, nanowires, and spherical, cubic, cuboctahedral and octahedral Ag nanoparticles [23].

4. Enhancement mechanism observed in the SERS effect

Even though, several theoretical and experimental research studies based on the SERS phenomena have been carried out and a great deal of research publications based on these works are well cited in the literature, the correct nature of the gigantic enhancement in Raman intensity found in the SERS effect is still controversial. However, it is generally accepted that two enhancement mechanisms, a long-range electromagnetic (EM) effect and a short-range chemical (CM) effect, are functioning simultaneously. The EM mechanism is based on the amplification of the electromagnetic field generated by coupling of the radiation field with the localized

surface plasmons (LSP) of the metal nanoparticles. The localized surface plasmon resonanace (LSPR) arises as a result of resonance condition between the incident wavelength of light and the electrons in the nanoparticles. This facilitates a combined oscillation of the conduction electrons and it will give rise to two main consequences. The first consequence is the absorption of the wavelengths of light selectively by nanoparticles, which is responsible for this collective oscillation. The second consequence is the enhancement of electromagnetic fields that extend from the nanoparticle surfaces. These fields are mainly responsible for the large enhancement observed in SERS. The enhancement is approximately proportional to $|E^4|$ and generally in the order of 10^8 or more, where E is the intensity of the electromagnetic field.

Localized surface plasmon resonance (LSPR), the lightning rod effect, and the image field effect, all these effects are responsible for the enhancement in SERS. Among them, LSPR contributes mainly to the electromagnetic field enhancement and SERS effect. Anisotropic metallic nanostructures have all of the characteristics of excellent SERS active substrates with good stability and high reproducibility. It has been demonstrated in the literature that anisotropic nanostructures such as nanorods, nanodisks, and nanoprisms will exhibit interesting size and shape-dependent properties. Anisotropic metal nanoparticles will exhibit "lightning-rod effect" [24], which is a new kind of field enhancement refers to enhanced charge density localization at a tip or vertex of a nanoparticle. The theory based on "lightning-rod effect" was developed by Liao and Wokaun in the year 1982. The excitation of the free electrons of a metallic tip by an electromagnetic field (laser light) will generate an extremely localized, sturdy electric field at these sharp tips or vertex with large curvatures leading to large field enhancement in those regions. This effect gives rise to high SERS activity of the anisotropic nanostructures. Anisotropic metallic nanostructures have been extensively utilized as an effective SERS active substrate with high SERS activity [25, 26] as found in the literature.

The chemical enhancement (CM) mechanism corresponds to the enhancement effect arises as a result of the chemical interaction between the adsorbates and the metal surface. The CM mechanism can also be referred as the charge transfer (CT) mechanism, involving the photo-induced transfer of an electron from the Fermi level of the metal to an unoccupied molecular orbital of the adsorbate (LUMO) or vice versa. The enhancement factor of CM is generally in the order of $10–10^2$. EM has a long-range effect, for which rough metallic surfaces can be used as an SERS active substrate, while CM has a short-range effect taking place on the molecular scale. The two mechanisms of EM and CM are not reciprocally restricted, but these two effects work simultaneously to generate the overall SERS effect. However, it is very hard to differentiate CM from the EM effect. Several research groups all over the world have tried to solve this problem, but the problem is unsolved so far.

5. Applications of SERS

SERS is highly sensitive analytical spectroscopic technique available among the modern scientific communities and can contribute both to surface science and nanoscience. It is also associated with a broad range of other surface sensitive techniques to study various fundamental

and applied research topics such as, corrosion, catalysis, advanced materials, diagnostics, biomedical applications, biological process, and sensing.

The SERS-active Ag/AAO nanostructured system as mentioned earlier in this chapter has been used by Liu et al. to investigate antibiotic-induced chemical changes in bacterial cell wall [27]. They recorded high quality, highly reproducible SERS spectra, which are also sensitive and stable. The "chemical features" observed from the SERS spectra of bacterial cell wall facilitates fast identification of drug-resistant bacteria within an hour both qualitatively and quantitatively. Furthermore, the characteristic changes in the SERS spectra were clearly observed in the drug-sensitive bacteria at the near the beginning (i.e., 1 hour) of antibiotic exposure, which could be utilized to differentiate them from the drug-resistant ones. The rapid detection of pathogens such as bacteria and viruses using the SERS technique provides a novel approach for microbial diagnostics. The SERS-based novel technique was applied to a single bacterium. This rapid SERS detection of pathogens makes possible direct analysis of clinical specimen as an alternative to a pure culture specimen. Traditional diagnostic protocols for diagnosing bacterial infections are based on the isolation of pure culture of the bacterium, which is followed by the resolving of the nature of the isolate and an extensive assessment of the isolates responses to several antibiotics proliferation or viability. For such biological assays, an incubation period varying from days to weeks or even months is essential for the growth of bacteria with such a density that can be handled by the available diagnostic tools. Different PCR-based protocols have been inducted for the quantitative identification of bacteria. Mass spectrometry can also be alternatively utilized for culture-free bacterial diagnostics. Nevertheless, just like the PCR-based method, mass spectrometry-based protocol is dependent on the existing previous information in the literature about the pathogens. Finally, neither of the PCR or mass spectrometry-based protocols can be applied to a live bacterial sample to observe their responses to antibiotics or to carry out different functional tests. On the other hand, SERS-based spectroscopic technique can resolve the limitation of PCR-based identification methods for pathogens. The SERS active substrates based on the Ag/AAO system can be utilized for the fine changes observed in the bacterial cell wall during different stages of bacterium's growth and also for the bacterium's response to antibiotic treatment during the early period of antibiotic exposure.

In a recent development, Ankamwar et al. [28] fabricated a highly stable and almost homogeneous SERS active substrate from silver nanoparticles synthesized from the leaf extract of *Neolamarckia cadamba* for the rapid detection of two strains of bacteria, Gram-positive (*Staphylococcus aureus*) and Gram-negative (*Escherichia coli*) bacteria. **Figure 6** demonstrates the TEM image of the as-synthesized silver nanoparticles along with their UV-visible spectrum, SAED pattern, and the resultant SERS spectra generated upon interaction with *S. aureus* and *E. coli*.

These silver nanoparticles upon interaction with bacteria can exhibit a large Raman enhancement factor ($(3 \pm 0.20) \times 10^7$ and $(5 \pm 0.40) \times 10^7$ for *S. aureus* and *E. coli* bacteria, respectively) with almost zero fluctuations. The SERS substrate developed by them is almost homogeneous with a relative standard deviation value of 6.32 calculated from 50 repeated measurements from various locations on the SERS substrate. In addition to this, the fabricated SERS substrates are extremely stable even after 3 months. Using this almost homogeneous, a stable SERS active substrate, Gram-positive bacteria can be differentiated from Gram-negative bacteria. The SERS

data presented in the above study is highly stable, uniform, and reproducible, which shows the versatility of the biosynthesized SERS active substrate. This SERS active substrate is capable of detecting extremely low concentrations (10^3 CFU ml^{-1}) of *E. coli* within a very short time of 1–5 s and also exhibits high sensitivity (see **Figure 7**). **Figure 7** demonstrates the SERS calibration curve obtained with SERS intensity of the peak at 1330 cm^{-1} (C–N stretching mode) as a function of concentration of bacteria *E. coli*. The 1330 cm^{-1} peak became detectable at 10^3 CFU/ml of *E. coli* concentration. The SERS intensity increases with the concentration of the bacterial solution, as it is exponentially correlated to the concentration of *E. coli* bacterial cells in the sample between 10^3 and 10^8 CFU/ml. Experiments were repeated five times with each bacterial concentration, and the standard errors of the mean for each concentration are also shown in **Figure 7**. The major intention of this SERS study using biosynthesized Ag nanoparticles was to develop a rapid fingerprinting method for the characterization of bacteria particularly *E. coli*, which is associated with urinary tract infection (UTI), a common disease among most people of all age groups in developed countries such as India and China.

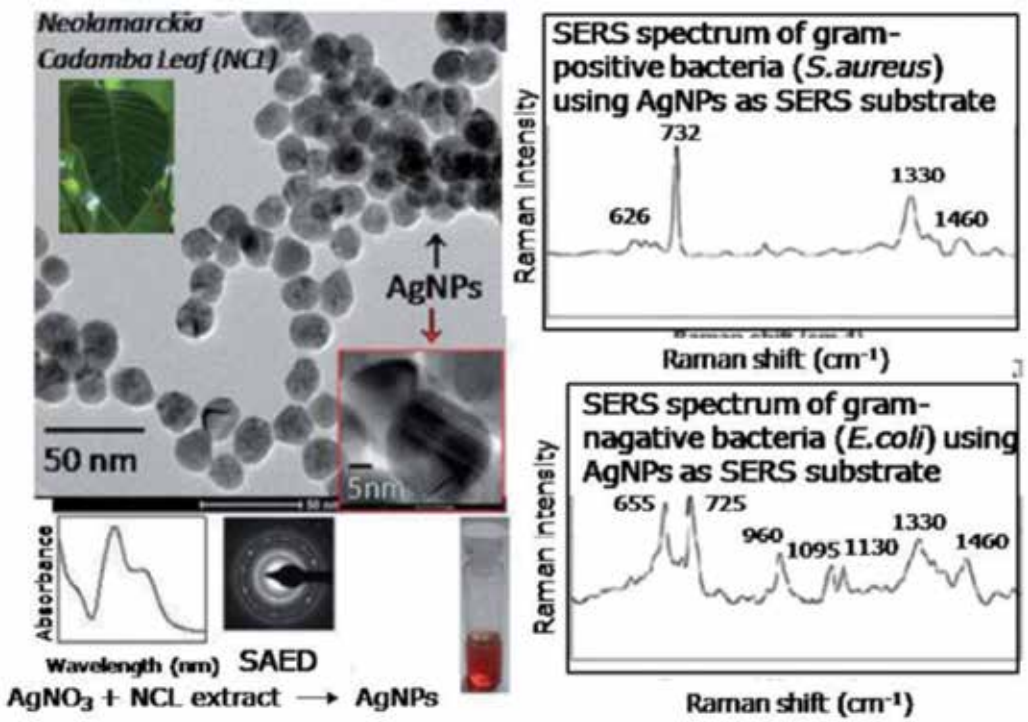

Figure 6. The TEM image of the as-synthesized silver nanoparticles along with their UV-visible spectrum, SAED pattern, and the resultant SERS spectra generated upon interaction with bacteria *S. aureus* and *E. coli*. Reproduced with permission from Ankamwar et al. [28]. Copyright @ Royal Society of Chemistry, Inc.

The SERS-based pathogen detection method is especially useful for the analysis of slow-growing bacteria, which typically may take few weeks during laboratory tests. The SERS spectra described above to detect and quantify bacteria lacks the molecular level specificity

compared to other commonly used techniques. The SERS-based technique demonstrates a novel approach for rapid microbial diagnostics, where SERS can be directly applied on the clinical sample rather than pure cultured bacteria.

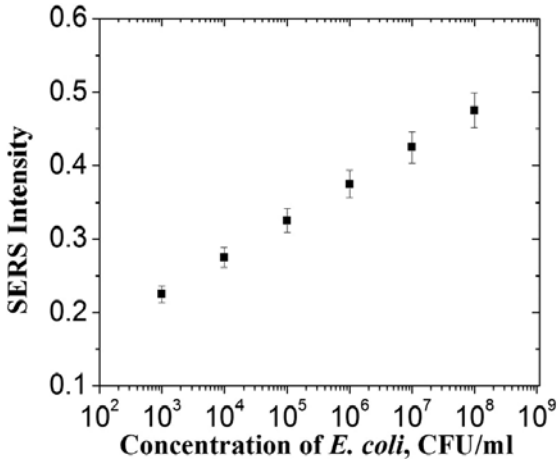

Figure 7. The SERS calibration curve obtained with SERS peak area or SERS intensity of the peak at 1330 cm^{-1} (C–N stretching mode) as a function of concentration of bacteria *E. coli*. Reproduced with permission from Ankamwar et al. [28]. Copyright @ Royal Society of Chemistry, Inc.

Nie and Emory [15] carried out a single-molecule SERS experiment by employing the SERS technique along with the transmission electron microscopy (TEM) and scanning tunneling microscopy (STM) techniques. They observed surface Raman enhancement in the order of 10^{14}–10^{15} for single rhodamine 6G (R6G) molecule adsorbed on selected Ag nanoparticles. For the single-molecule SERS study, a single event was observed rather than an ensemble averaged value usually attained for traditional SERS measurements. Advancement of the single molecule SERS technique has brought a new aspect in biomedical research, as it can act as a versatile probing tool to investigate various biological molecules such as virus, bacteria, and protein.

The limitation arises out of surface generality of the SERS effect has been resolved by the invention of tip-enhanced Raman spectroscopy (TERS) technique in 2004 [29], which is a modification of the conventional SERS technique. This new and novel technique is derived from the enhancement of the surface Raman scattering intensity (SERS signal) by merging Raman spectroscopy with a scanning probe microscopy technique such as atomic force microscopy (AFM) or scanning tunneling microscopy (STM). The experimental setup in the TERS technique consists of AFM or STM tip placed in a nearby surrounding area of an ultrasmooth substrate, generally single crystal metal surfaces and illuminated by an electromagnetic radiation of suitable wavelength. The contact or tunneling mode of AFM/STM can be used in the experimental setup of TERS. Irradiating with a laser beam of suitable wavelength, a localized surface plasmons are excited in the tip-substrate gap, generating a huge, local enhancement of electromagnetic field in comparison to the incident radiation. TERS was used to probe malachite green isothiocyanate, a dye molecule adsorbed on the Au(111) surface [29]. TERS

has been used to study surface reactions on single crystal and smooth surfaces, as surface roughness of the substrate does not play any role in this enhancement.

Surface-enhanced Raman scattering spectroscopy (SERS) can be used for the identification short-live reaction intermediates such as radical and radical ions on the electrode surface and elucidation of the reaction mechanism in general. Tian and his research group at Xiamen University, China, carried out the first *in situ* electrochemical SERS (EC-SERS) investigation on the electrochemical reduction of $PhCH_2Cl$ in acetonitrile (CH_3CN) on the Ag electrode [30]. The benzyl radical anion as a reaction intermediate and 3-phenylpropanenitrile as the major reaction product were detected from the SERS study for the above surface reaction. The complete reaction mechanism enlightening the adsorption process of $PhCH_2Cl$ on the Ag surface and all other possible interactions including the solvent molecule have been determined from the systematic SERS study. The SERS results were further validated by quantum mechanical density functional theory (DFT) calculations, which confirm the detection of the reaction intermediate and products.

It was established by Mulvihill et al. that LB assemblies made of various polyhedral Ag nanocrystals can be utilized as high quality SERS active substrates for the high-sensitivity detection of arsenate and arsenite ions in aqueous solutions with a detection limit of 1 ppb [31]. The detection limit resulted from the analysis carried out by the SERS-based technique is an order of magnitude lower than the existing yardstick set by the World Health Organization (WHO). The SERS substrate can be used as a chemical sensor, which is simultaneously highly reproducible and portable, and therefore, this could be easily executed in field detection. The SERS technique can be further employed in environmental analysis. Pesticides, herbicides, pharmaceutical chemicals in water, banned food dyes, aromatic chemicals in regular aqueous solutions and in sea water, chlorophenol derivatives and amino acids, chemical warfare species, explosives, and various organic pollutants [32, 33] can qualitatively and quantitatively analyzed by the SERS-based detection technique. The partition property of SERS substrates as well as surface chemistry facilitates the complete separation of pollutants and analysis of complex environmental samples in real environmental analysis and monitoring.

Immobilized metal nanoparticles in the form of SERS substrates can be used for biomedical diagnostics. For instance, the SERS substrate can be used as a glucose sensor to detect glucose in human blood. Although glucose is most commonly monitored by electrochemical-based sensors, a substitute protocol using SERS substrates fabricated by the NSL technique has been employed to detect glucose in blood [34]. In this new protocol, the SERS-based glucose sensor was developed by growing silver film over nanospheres (AgFON) surfaces prepared by the NSL technique. Nevertheless, glucose sensing on a bare AgFON surface was not successful and glucose was brought within the range of electromagnetic enhancement of the AgFON surface by formation of a self-assembled monolayer (SAM) on its surface to partition the analyte of interest, in a manner similar to the technique used to generate the stationary phase in high-performance liquid chromatography. Numerous SAMs were studied to partition glucose effectively to the AgFON surface and it was observed that both

straight-chain alkanethiols and ethyleneglycol-terminated alkanethiols partitioned glucose most effectively. The key for the detection of glucose by the SERS-based technique was the surface chemistry of alkanethiol molecule on the AgFON surface. The SERS substrate was modified with an alkanethiol partition layer to facilitate the glucose adsorption to the metal surface. Real-time sensing and quantitative detection of glucose in bovine plasma by SERS has been reported in the literature [35].

6. Summary

Even though, the appropriate theory and principles to elucidate the correct mechanism of the SERS phenomenon is yet to be developed, the 40 years of this versatile technique has reached a new height due to the increased efficiency of the modern Raman instrumentation and recent advancement in nanoscience and nanotechnology. Controlled and reproducible fabrication of SERS-active substrates [36] and understanding the in depth connection between the nanoparticle structure and SERS activity remains noteworthy challenges in this field of research. We believe that the fast and gradual development of nanoscience and nanotechnology will eventually allow an absolute understanding of the SERS effect and a broad range application of SERS in both analytical sciences and biomedical sciences.

Acknowledgements

UKS would like to acknowledge the Indian National Science Academy (INSA), New Delhi, India, for providing INSA Visiting Scientist Fellowship (SP/VF-9/2014-15/273/01 April, 2014) under the guidance of BA at Bio-inspired Materials Science Laboratory, Department of Chemistry, Savitribai Phule Pune University, Ganeshkind, Pune, India. UKS would like to acknowledge the financial support received from the projects funded by the UGC, New Delhi (grant no. PSW-045/13-14-ERO) and UGC-DAE CSR, Kolkata centre, Collaborative Research Schemes (UGC-DAE-CSR-KC/CRS/13/RC11/0984/0988). UKS would like to thank all the authors and publishers of various journals and books (Elsevier, RSC, ACS, Springer, Techno Press, Intech Inc, and Indian Academy of Sciences) from which various figures and text portions has been reproduced in this chapter. Finally, special acknowledgement should be given to Techno Press, the publisher of the journal *Advances in Nano research* [7] from which some portion of the text has been reproduced.

Author details

Ujjal Kumar Sur

Address all correspondence to: uksur99@yahoo.co.in

Department of Chemistry, Jadavpur University, Kolkata, India

References

[1] Van Duyne R P. In: Moore C B. editors. Chemical and Biological Applications of Lasers. New York: Academic, Press; 1979.

[2] Chang R K, Furtak T E. editors. Surface Enhanced Raman Scattering. New York: Plenum Press; 1982.

[3] Aroca R. Surface Enhanced Vibrational Spectroscopy. United Kingdom: John Wiley and Sons, Ltd; 2006.

[4] Tian Z Q, Ren B. In: Unwin P, Bard A J, Stratmann M. editors. Encyclopedia of Electrochemistry. Weinheim: Wiley-VCH; 2003. 572 p.

[5] Sur U K. Surface-enhanced Raman spectroscopy: recent advancement of Raman spectroscopy. Resonance. 2010; **15**: 154–164. DOI: 10.1007/s12045-010-0016-6

[6] Sur U K, Chowdhury J. Surface-enhanced Raman scattering: overview of a versatile technique used in electrochemistry and nanoscience. Curr Sci. 2013; **105**: 923–939.

[7] Sur U K. Surface-enhanced Raman scattering (SERS) spectroscopy: a versatile spectroscopic and analytical technique used in nanoscience and nanotechnology. Adv Nano Res. 2013; **1**: 111–124. DOI: http://dx.doi.org/10.12989/anr.2013.1.2.111

[8] Fleischmann M, Hendra P J, McQuillan A J. Raman spectra of pyridine adsorbed at a silver electrode. Chem Phys Lett. 1974, **26**; 163–166. DOI: 10.1016/0002614(74)85388-1

[9] Cooney R P, Mahoney M R, McQuillan A J. In: Clark R J H, Hester R E. editors. Advances of Infrared and Raman Spectroscopy. London: Heyden; 1982. 188 p.

[10] Raman C V, Krishnan K S. A new type of secondary radiation. Nature. 1928; **121**: 501–502.

[11] Jeanmaire D L, Van Duyne R P. Surface Raman electrochemistry. Part 1. Heterocyclic, aromatic and aliphatic amines adsorbed on the anodized silver electrode. J Electroanal Chem. 1977; **84**: 1–20. DOI: 10.1016/S0022-0728(77)80224-6

[12] Albrecht M G, Creighton J A. Anomalously intense Raman spectra of pyridine at a silver electrode. J Am Chem Soc. 1977; **99**: 5215–5217. DOI: 10.1021/ja00457a071

[13] Tian Z Q, Ren B. Adsorption and reaction at electrochemical interfaces as probed by surface-enhanced Raman spectroscopy. Annu Rev Phys Chem. 2004; **55**: 197–229. DOI: 10.1146/annurev.physchem.54.011002.103833

[14] Tian Z Q, Ren B, Wu D Y. Surface-enhanced Raman scattering: from noble to transition metals and from rough surfaces to ordered nanostructures. J Phys Chem B. 2002; **106**: 9463–9483. DOI: 10.1021/jp0257449

[15] Nie S, Emory S R. Probing single molecules and single nanoparticles by surface-enhanced Raman scattering. Science.1997; **275**: 1102–1106. DOI: 10.1126/science.275.5303.1102

[16] Kneipp K, Wang Y, Kneipp H, Perelman L T, Itzkan I, Dasari R R, Field M S. Single molecule detection using surface-enhanced Raman scattering (SERS). Phys Rev Lett. 1997; **78**: 1667–1670. DOI: http://dx.doi.org/10.1103/PhysRevLett.78.1667

[17] Lin X M, Cui Y, Xu Y H, Ren B, Tian Z Q. Surface-enhanced Raman spectroscopy: substrate-related issues. Anal Bioanal Chem. 2009; **394**: 1729–1745. DOI: 10.1007/s00216-009-2761-5

[18] Li J F, et al. Shell-isolated nanoparticle-enhanced Raman spectroscopy. Nature. 2010; **464**: 392–395. DOI: 10.1038/nature08907

[19] Freeman R G, Grabar K C, Allison K J, Bright R M, Davis J A, Guthrie A P, Hommer M B, Jackson M A, Smith P C, Walter D G, Natan M J. Self-assembled metal colloid monolayers: an approach to SERS substrates. Science. 1995; **267**: 1629–1632. DOI: 10.1126/science.267.5204.1629

[20] Willets K A, Van Duyne R P. Localized surface plasmon resonance spectroscopy and sensing. Annu Rev Phys Chem. 2007; **58**: 267–297. DOI: 10.1146/annurev.physchem.58.032806.104607

[21] Haynes C L, Van Duyne R P. Nanosphere lithography: a versatile nanofabrication tool for studies of size-dependent nanoparticle optics. J Phys Chem B. 2001; **105**: 5599–5611. DOI: 10.1021/jp010657m

[22] Wang H H, Liu C Y, Wu S B, Liu N W, Peng C Y, Chan T H, Hsu C F, Wang J K, Wang Y L. Highly Raman-enhancing substrates based on silver nanoparticle arrays with tunable sub-10 nm gaps. Adv Mater. 2006; **18**: 491–495. DOI: 10.1002/adma.200501875

[23] Tao A, Kim F, Hess C, Goldberger J, He R R, Sun Y G, Xia Y N, Yang P D. Langmuir-Blodgett silver nanowire monolayers for molecular sensing using surface-enhanced Raman spectroscopy. Nano Lett. 2003; **3**: 1229–1233. DOI: 10.1021/nl0344209

[24] Liao P F, Wokaun A. Lightning rod effect in surface enhanced Raman scattering. J Chem Phys. 1982; **76**: 751–752. DOI: http://dx.doi.org/10.1063/1.442690

[25] Orendorff C J, Gole A, Sau T K, Murphy C J. Surface enhanced Raman spectroscopy of self-assembled monolayers: sandwich architecture and nanoparticle shape dependence. Anal Chem. 2005; **77**: 3261–3266. DOI: 10.1021/ac048176x

[26] Hu J Q, Chen Q, Xie Z X, Han G B, Wang R H, Ren B. A simple and effective route for the synthesis of crystalline silver nanorods and nanowires. Adv Funct Mater. 2004; **14**: 183–189. DOI: 10.1002/adfm.200304421

[27] Liu T T, Lin Y H, Hung C S, Liu T J, Chen Y, Huang Y C, Tsai T H, Wang H H, Wang D W, Wang J K, Wang Y L, Lin C H. A high speed detection platform based on surface-enhanced Raman scattering for monitoring antibiotic-induced chemical changes in bacteria cell wall. PLoS One. 2009; **4**: 1–9.

[28] Ankamwar B, Sur U K, Das P. SERS study of bacteria using biosynthesized silver nanoparticles as SERS substrate. Anal Methods. 2016; **8**: 2335–2340. DOI: 10.1039/c5ay03014e

[29] Pettinger B, Ren B, Picardi G, Schuster R, Ertl G. Nanoscale probing of adsorbed species by tip-enhanced Raman spectroscopy. Phys Rev Lett. 2004; **92**: 096101–096104. DOI: 10.1103/PhysRevLett.92.096101

[30] Wang A, Huang Y F, Sur U K, Wu D Y, Ren B, Rondinini S, Amatore C, Tian Z Q. *In Situ* identification of intermediates of benzyl chloride reduction at a silver electrode by SERS coupled with DFT calculations. J Am Chem Soc. 2010; **13**: 9534–9536. DOI: 10.1021/ja1024639

[31] Mulvihill M, Tao A, Benjauthrit K, Arnold J, Yang, P. Surface-enhanced Raman spectroscopy for trace arsenic detection in contaminated water. Angew Chem Int Ed. 2008; **47**: 6456–6460. DOI: 10.1002/anie.200800776

[32] Liu S Q, Tang Z Y. Nanoparticle assemblies for biological and chemical sensing. J Mater Chem. 2010; **20**: 24–35. DOI: 10.1039/B911328M

[33] Fan M, Andrade G F S, Brolo A G. A review on the fabrication of substrates for surface enhanced Raman spectroscopy and their applications in analytical chemistry. Anal Chim Acta. 2011; **693**: 7–25. DOI: 10.1016/j.aca.2011.03.002

[34] Shafer-Peltier K E, Haynes C L, Glucksberg M R, Van Duyne R P. Toward a glucose biosensor based on surface-enhanced Raman scattering. J Am Chem Soc. 2003; **125**: 588–593. DOI: 10.1021/ja028255v

[35] Lyandres O, Shah N C, Yonzon C R, Walsh J T, Glucksberg M R, Van Duyne R P. Real-time glucose sensing by surface-enhanced Raman spectroscopy in bovine plasma facilitated by a mixed decanethiol/mercaptohexanol partition layer. Anal Chem. 2005; **77**: 6134–6139. DOI: 10.1021/ac051357u

[36] Haynes C L, McFarland A D, Van Duyne R P. Surface-enhanced Raman spectroscopy. Anal Chem. 2005; **77**: 338A–346A. DOI: 10.1021/ac053456d

Chapter 15

The Intricate Nature of SERS: Real-Life Applications and Challenges

Nicoleta Elena Dina and Alia Colniță

Additional information is available at the end of the chapter

http://dx.doi.org/10.5772/65478

Abstract

Testing for the presence of microorganisms in biological samples in order to diagnose infections is very common at all levels of health care. There is a growing need to ensure appropriate diagnosis by also minimizing the analysis time, both being very important concerns related to the risk of developing an antimicrobial resistance. Moreover, there are important medical and financial implications associated with infections. In this chapter, we will discuss the latest ultrasensitive and selective, but simple, rapid and inexpensive bacteria detection and identification methods by using receptor-free and innovative immobilization principles of the biomass. Raman spectroscopy, which combines the selectivity of the method with the sensitivity of the surface-enhanced Raman scattering (SERS) effect, is used in correlation with chemometric techniques in order to develop biosensors for pathogenic microorganisms.

Keywords: surface-enhanced Raman scattering (SERS), single-cell detection, label-free, principal component analysis (PCA), biosensors

1. Introduction

Lately, the pathogens can be individually identified by using surface-enhanced Raman scattering (SERS), without the need of labeling or specific receptor usage like antibodies, for instance. Colloidal metallic suspensions offer the advantage of ambient conditions, fast completion, and minimal number of reactants, being economical, and resulting in a ready-to-use product. However, despite the progress achieved, concerns and problems with the preparation of metal nanoparticles (NPs) remain, such as the byproducts from the reducing agent, the multiple steps

often required, and the high concentration of protective agents. Furthermore, it has been a major bottleneck to elucidate the key factors (other than surface roughness enhanced electromagnetic fields) that play important roles in the SERS process of adsorbed biomolecules. The understanding of the mechanisms involved in the interaction of biological systems with inorganic materials is of interest in both fundamental and applied disciplines. Herein, the decisive know-how in investigating biological samples by using several SERS-active platforms will be described.

1.1. SERS effect

Raman spectroscopy requires the illumination of a sample with monochromatic light. The inelastic scattering of a small fraction (approximately one in a million) of the incident photons toward lower (Stokes scattering) or higher frequencies (anti-Stokes scattering) than the incident light is known as Raman scattering. A typical Raman spectrum plots the intensity of the scattered light versus the number of probed molecules. There are several noteworthy advantages of this technique, such as speed, versatility, and the functionality under ambient conditions in nonspecific environments (by using portable, miniaturized spectrometers); the simplicity of sample preparation; the possibility of remote detection of Raman signals by using optical fiber probes; the chance to examine transparent samples; and the obliviousness to water, ubiquitous element for biological samples. Probably the biggest disadvantage lies in the extremely small cross section, typically (10^{-30}–10^{-25}) cm^2/molecule, which can be translated into long acquisition times and considerable high sample concentrations.

Raman spectra can be used for the identification and classification of microorganisms once a procedure with good reproducibility and reliability is established [1–4]. However, the spontaneous Raman effect is so weak that fluorescence, when it occurs, obscures the Raman spectrum. SERS represents the enhancement of Raman-active vibrations associated with the intimate contact (within few nanometers) to a surface covered with plasmonic NPs. Moreover, additional modes not found in the traditional Raman spectrum can be present in the SERS spectrum, while other modes can disappear.

The surface-selection rules that apply to infrared and Raman spectroscopies are extended for surface-enhanced vibrational spectroscopy (SEVS) by taking into account the local field and/or the roughness of the surface. SEVS spectra are the expression of the analyte-radiation interaction when the molecule is in the close proximity or adsorbed on the metallic nanostructure, which supports the surface plasmons [5]. So the presence of the plasmon resonance, for instance, will define the observed spectral intensities. When electromagnetic radiation with the same frequency is incident upon the nanostructure, the electric field of the radiation drives the conduction electrons into collective oscillation. Electromagnetic enhancement, the major contribution in the SERS effect, relies on the Raman-active molecules being confined within large electromagnetic fields (EFs), generated by the excitation of the local surface plasmon resonance (LSPR). So the extreme sensitivity of SERS to small increases in the local field is easily seen since it scales roughly as ω^4 (where ω = frequency). Therefore, the fall-off in intensity of high frequency vibrations is also explained; the driving field and scattered field cannot simultaneously excite the particle resonance if they are of very different frequencies. This explains also

http://dx.doi.org/10.5772/65478

the different excitation profiles for different bands; maxima for higher frequency vibrations occur at shorter wavelengths, as the scattered field is brought closer to resonance [6].

SERS represents a relatively inexpensive alternative, compared to the conventional detection methods that also meet the clinical tools' requirements: simplicity, reliability, uniformity (for testing various pathogens), and high specificity. It completely overcomes the shortcoming of Raman small cross sections. SERS is capable to characterize [7–10], identify [11, 12], and differentiate [13, 14] pathogenic microorganisms in synergy with chemometrics, based on the biochemical, chemical, and their structural properties.

Even though SERS is a highly specific and sensitive detection method, well suited for biological issues, SERS measurements still suffer from low reproducibility of spectra. Fluctuations of spectral characteristics are induced by variation between different colloid batches, colloid concentration dependence, and inconsistent enhancement even within one colloid batch mainly due to an inhomogeneous and a rather uncontrollable aggregation of NPs [15]. The main issues consist in the difficulty to generate uniform distributed EFs, large EFs occurring only at localized positions (hot-spots) and the polydispersity of colloidal clusters. As Nie and coworkers [16, 17] have already quite convincingly demonstrated, the enhancement factor depends on the wavelength of exciting radiation, or rather on the relation between the wavelength and the size of the Ag NPs.

Still, for real-world applications, reproducibility is considered in particular cases more important than enhancement factors. Background signal from the food and environmental matrices represents a real challenge. In addition, proper and simplified sample pretreatment is needed before conducting a SERS measurement. For instance, sample preparation for SERS detection of bacteria is quite inconsistent referring to colloids as SERS-active substrates. The NPs can be either coated on the outside of the bacterial cell wall or directed to the interior of the bacterial cells. Whereas the first preparation results in spectral information mainly derived from cell wall components, the second one contains additional cytoplasmic information [18, 19]. **Figure 1** shows the SERS signal acquisition process from a microbiologic sample, when the silver coverage of the bacteria (in blue) is successful.

Conclusively, the SERS effect depends on a wide range of parameters, such as the particular features of the laser excitation (wavelength, polarization, and angle of incidence), the experimental setup (scattering configuration), substrate-related parameters (geometry, adsorption, orientation with respect to the incident beam direction, and polarization), and is distance-dependent. However, readiness remains an important parameter in choosing the suitable, fast, and reliable tool for detection at trace level, for large-scale applications.

1.2. Gold or silver NPs in biomedical applications?

Gold NPs (Au NPs) are promising SERS candidates in biomedicine and have already been successfully tested for various biomedical applications. They are easy to prepare, significantly more stable than other metallic NPs (not easily oxidized), and are highly biocompatible. They can act as artificial antibodies due to their simple surface chemistry, precise binding affinity, and possibility of tuning by varying the density of ligands on their surfaces. Lately, a continuous effort was made to develop new low-cost and easier synthesis strategies for increasing

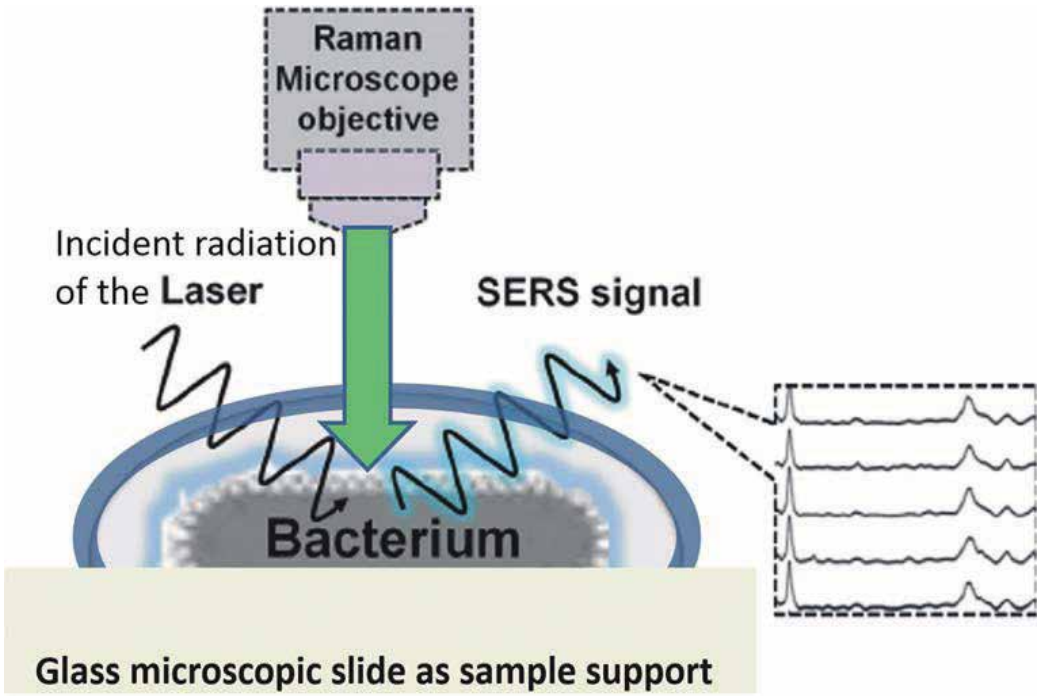

Figure 1. SERS signal acquisition from bacteria while irradiated with the laser light in backscattering configuration.

their cellular biocompatibility, by varying their geometries, their physical dimensions, and functionality. The mixing rate of the reactants could greatly influence the physical properties of the Au NPs, their stability over long periods of time, and their SERS sensitivity. It is reported that when the gold salt solution is rapidly added to the reaction mixture, preponderant spherical short- and long-chain polyethylene glycol (PEG) Au NPs with a mean diameter of 15 nm are obtained, whereas a drop-wise addition of the gold salt leads to a seeding effect and to Au NPs with a mean diameter of 60 nm [20]. The most common surface ligand used in biomedical applications is thiolated PEG (PEG-SH), which ensures the desired hydrophilicity and increased circulatory half-life *in vivo* systems [21]. Proteins, such as bovine serum albumin or collagen, can also serve as capping and stabilizing agents in the one-step synthesis of gold colloidal nanoassemblies and spherical Au NPs with tunable shape and size [22, 23]. Furthermore, the *in vitro* uptake and toxicity effect of Au NPs grown with a native collagen shell exhibit a lower toxic effect on cervical carcinoma and lung adenocarcinoma cells than synthetic polymer-coated Au NPs [24]. Additionally, due to their ability to efficiently convert light into heat, gold NPs can specifically allow thermal ablation of the targeted biological region and by absorbing high amounts of X-ray radiation become enhancers in cancer radiation therapy or computed tomography [21].

However, silver NPs (Ag NPs) show stronger plasmon fields than Au NPs due to the simple fact that their plasmon band does not overlap with the interband electronic transitions, as in the case of Au NPs [25]. **Figure 2** presents our recent results obtained by using different SERS-

http://dx.doi.org/10.5772/65478

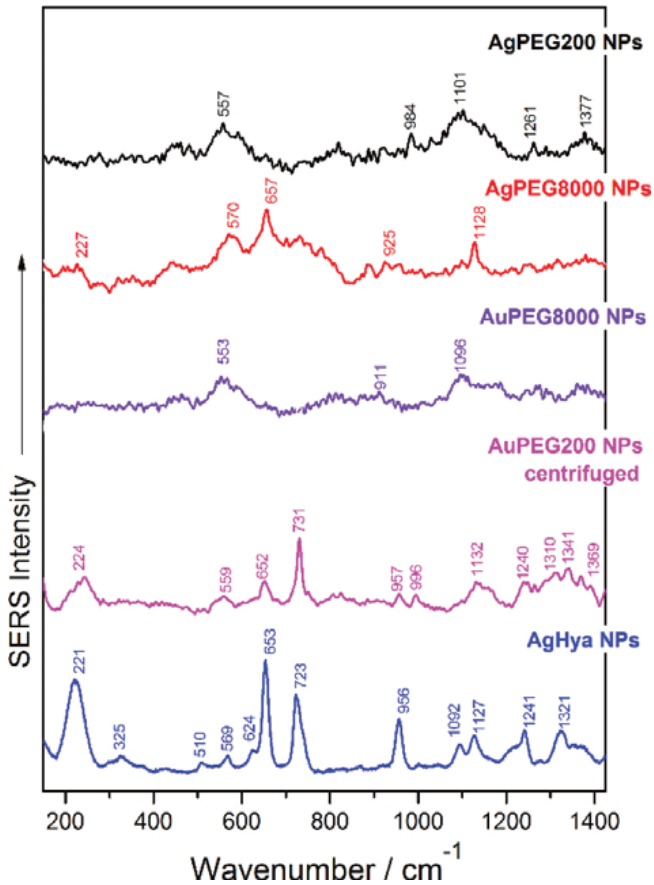

Figure 2. SERS spectra of *E. coli* by using five distinct platforms of detection: AgPEG200NPs/AgPEG8000NPs—silver NPs with PEG200/PEG8000 layer, AuPEG200NPs/AuPEG8000NPs—gold NPs with PEG200/PEG8000 layer, and Ag Hya NPs–*in situ* silver synthesized NPs by reduction with hydroxylamine hydrochloride.

active substrates for the detection of *E. coli*. We synthesized several types of Ag and Au sols by using PEG with two chain lengths as reducing agent [20] and compared the obtained SERS signals with the *in situ* synthesized Ag NPs SERS signal of bacteria. The SERS spectra were recorded using a Raman microscope (Lab RAM HR, HORIBA Jobin Yvon, Japan). The 633-nm line of a HeNe laser was used as the excitation source. The excitation wavelength dependency of the SERS enhancement can be explained by the optical absorption of the silver colloidal suspensions. We already characterized the herein used NPs in our previous work; the Ag Hya NPs particles feature a plasmon resonance band of around 402 nm. Hence, excitation with the 532 nm laser line is favorable as compared to longer wavelengths (633 nm), being closer to the plasmonic band. However, in the case of the Au PEG NPs the plasmon resonance band is specific to gold and was determined around 540–560 nm, depending on the particles' diameter. Generally, we waited 30 min as incubation time in order to obtain the higher and more stable SERS signal from the irradiated sample. As an effect of incubation time we observed an increasing agglomeration of the SERS-active colloids, leading to a coupling of the plasmon

resonances, which again leads to a red-shift of the main absorption. In consequence, we achieved in these earlier works the best SERS performance with the 633 nm excitation wavelength. As an indicator we selected the intensity of the marker band found at 732 cm^{-1} which was about fivefold higher for the *in situ* approach. Even when we preconcentrated the Au PEG NPs by centrifugation (38× more concentrated Au colloidal suspension), the enhancement factor was not comparable with the one obtained for the hydroxylamine reduced *in situ* Ag colloid [12]. Moreover, the single-cell detection of bacteria was successfully obtained by using the *in situ* method, while the other tested colloids enabled us to detect bacteria only in rather high concentrations (>10^3 CFU/ml). For single-cell detection assays, this aspect could make a difference in selecting the SERS detection platform.

2. Label-free SERS-based assays

The impact on the public health demands sensitive analytical tools for detecting pathogens. Rapid, culture-free, ultrasensitive pathogens' detection and identification are of paramount importance, since there are infections caused by a single microorganism (mycobacteria) and some pathogens need 20 days to proceed through one division cycle (while some *E. coli* strains take only 20 min), making laboratory culture a slow process.

Conventional methods currently used for microorganisms' identification are nucleic acid-based polymerase chain reaction (PCR, qPCR, and real-time PCR), on-chip nucleic acid amplification [26], enzyme-linked immunosorbent assay (ELISA) [27], chemiluminescence-based microarrays [28, 29], and matrix-assisted laser desorption/ionization (MALDI, MALDI-TOF) [30, 31]. Major drawbacks of these culture-based detection techniques are the time required, the high costs, the need of prelabeling, and/or use of antibodies or DNA sequencing, and also the concerning increased rate of false negatives and false positives. In addition, biosensors for bacteria detection still rely on the specific capture of the targeted pathogen by using antibodies [9, 11, 32], aptamers [33], and substrates that contain metallic nanosculptured thin films [34], or other different complex surface morphologies fabricated by using photolithography combined with deposition techniques [35]. This approach leads to costly microarrays, which can only be handled by trained personnel, in laboratory conditions. However, before any of these whole-organism fingerprint techniques can be used to analyze the samples, the microorganisms must be cultured in order to isolate the microorganism of interest from other sample constituents and/or produce sufficient biomass for analysis.

Recently, spectroscopic techniques look more and more promising with the development of low-cost, label-free, and ultrasensitive detection protocols enabling for the first time to be fast, specific, and sensitive enough in vital issues as healthcare. Particularly, Raman spectroscopy is a nonintrusive *in situ* analysis method, requiring small efforts for sample preparation and can be easily used outdoors with portable, miniaturized, and even handheld Raman spectrometers. Moreover, when using SERS, the spectral fingerprint reflects the physiological state of a bacterial cell, e.g., when pathogenic bacteria were cultured under conditions known to affect virulence, their SERS fingerprints changed significantly. It is also known that bacteria respond to environmental triggers, such as temperature, pH, and nutrient concentrations, by switching

http://dx.doi.org/10.5772/65478

to different physiological changes in their biochemical profile, including the number and composition of outer membrane proteins, lipopolysaccharides (LPS), and cellular fatty acids [36].

For SERS detection of bacteria, several innovative approaches are reported. Sengupta and coworkers [37–39] reported straightforward analysis of a colloidal-bacterial mixture in an optical glass cuvette. The preferred excitation laser line is 514.5 nm in their study of the pH influence and the time-dependent behavior of colloidal-bacterial suspensions, even if this wavelength is too long to resonate with excitations of the aromatic ring breathing mode.

By using the same excitation wavelength, Kahraman et al. [40] developed a uniform bacterial sample preparation method based on the convective assembly. Aggregation and clustering was frequently applied for obtaining higher SERS signal from "hot-spots" [41]. Knauer and others [9, 11, 42] optimized the microarray detection of single-bacterium by using different Ag sols and aggregation with sodium chloride or sodium azide in low concentrations. However, in these studies, the 633 nm laser line was selected for SERS-based detection on the antibody-activated microarray and the substrate used for enhancement was an Ag colloid produced by using a modified Leopold and Lendl method [43].

Efrima and Zeiri also proposed a novel approach, to use colloid produced in the presence of the biomass [18, 19]. The authors used the 633 nm laser line as an excitation wavelength, therefore they were able to report the ring breathing mode band observed at 1004 cm^{-1} and assigned to the phenylalanine residue [10]. Excepting Knauer's group work [9, 11, 42] and recent studies reported by Zhou et al. [12–14, 44], when applying the *in situ* approach, the Leopold and Lendl SERS active substrate was not so exploited in the bacteria detection, as the usage of the 633 nm laser line is mere. The hydroxylamine-reduced silver colloid was shown as ideal for obtaining SERS structural information on biological molecules contained in the bacterial cell wall, since it provides a high enhancement factor and shows almost no anomalies in the spectral band position upon aggregation [45] in comparison to the citrate-reduced Ag sols.

Another bacteria detection assay reported used crystal violet (CV) as Gram stain [46]: the procedure involved staining bacterial samples with CV which binds to the peptidoglycan layer of the Gram-positive and Gram-negative bacteria. Despite the simple and robust methodology of staining, the detection relies on optical microscopy, which is often susceptible to user-dependent sampling error. Therefore, by developing magneto-fluorescent NPs, the detection was improved and was successfully tested for both Gram-positive and Gram-negative bacteria (*E. coli* and *S. aureus*).

Label-free SERS-based detection is a very promising alternative for rapid monitoring real samples, offering single-cell sensitivity [1, 47], providing spectra with no contribution from the aqueous environment (prominent in the biological samples), and a high precision classification of bacteria, at strain level [1–3]. Recently, innovative approaches for the rapid SERS label-free detection of bacteria were developed:

(i). Simple, receptor-free immobilization of bacteria on the glass surface [14]. Mircescu et al., based on molecular-specific SERS spectra of uropathogens at single-cell level, discriminated

between rough and smooth strains of *E. coli* and *P. mirabilis*. The innovative and effective principle of bacteria immobilization through electrostatic forces, by inducing a positive charge on the silanized microarray surface was demonstrated for Gram-negative bacteria. In addition, the monitoring of single-cell SERS spectra of bacteria in different growth phases was assessed. (ii). *In situ* silver NPs preparation in the presence of bacteria (Bacteria@ Ag NPs) [12]. Zhou et al. developed the *in situ* Ag colloid synthesis in two steps, resulting in coating the bacterial cell wall with a silver SERS-active layer. The assay requires about 10 min and only one sample droplet of 3 μl. By using this novel strategy, SERS detection (about 30-fold higher enhanced SERS signal) and hierarchy cluster analysis (HCA) discrimination of three strains of *E. coli* and one strain of *S. epidermidis* was reported.

2.1. *In situ* Ag NPs synthesis: extended approach

Currently and also in the future, biosensors with integrated nanotechnology promise to address the analytical needs in practical pathogen diagnosis. Recently, comprehensive reviews concerning the bacteria detection by using Raman and SERS spectroscopies were reported [15, 48, 49]. The increased sensitivity and high information content of SERS is acknowledged, mostly when this powerful tool is used in conjunction with advanced analysis and classification techniques. The key advantages that SERS-based biosensors include are the easy-to-use detection platforms and reduced testing time resulting in immediate diagnostic (within 5–15 min) [50, 51], superior sensitivity and multiplex capability [52], reduced sample volume, and high sensitivity and specificity. Thus, a great deal of research has been invested into the development of SERS-based biosensors for pathogenic microorganisms.

For instance, SERS mapping by using Ag dendrites [53] as SERS active substrate, both for Gram-negative and Gram-positive bacteria was reported. Not so promising results were obtained in case of the Gram-positive bacteria, probably due to their different membrane structure, containing less outside proteins. Usually, the marker bands used for detection of the pathogens are either the 1332 cm^{-1} band assigned to the CH deformations in proteins [53], either the 730 cm^{-1} band assigned to adenine [14, 54].

In this section we will mainly focus on the latest studies involving *in situ* Ag NPs synthesis approach for SERS detection in biomedical applications. In a more recent study, Zhou et al. [13] applied the Bacteria@ Ag NPs approach for live and dead bacteria counting/discrimination.

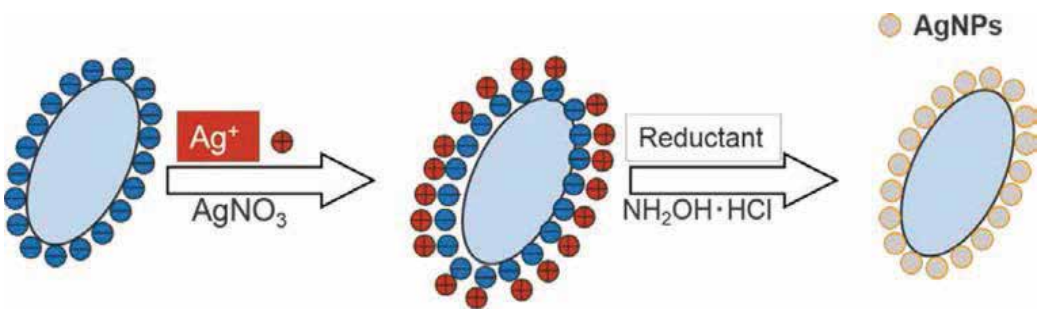

Figure 3. Scheme describing the *in situ* AgNPs synthesis on the bacterial cell wall.

http://dx.doi.org/10.5772/65478

Moreover, by using antibiotics (ampicillin, polymyxin B, and chloramphenicol) with different action mechanisms on bacteria and by monitoring the SERS signal decay in time, they were able to determine which microorganism is or not developing a drug resistance in less than 4 h. Lately, the same group [44] completed the previous work by applying the Bacteria@ Ag NPs approach on a microarray (containing antibodies). **Figure 3** exhibits the schematic protocol of generating the Bacteria@ Ag NPs for SERS detection of microorganisms at single-cell level.

Since Efrima's group reported on producing *in situ* NPs through external (bacterial cell-wall) or internal (interior components mode) synthesis on bacteria [18], the use of *in situ* synthesized Ag colloids for bacteria detection was demonstrated in several assays only by Haisch's group [12–14, 44, 54].

Recently, a label-free NIR-SERS detection and discrimination of bacteria after pretreatment of bacterial cell membrane with disrupting agents was presented, featuring a sensitivity down to 10^3 CFU/ml and a measuring time of less than 5 min [55]. Latest studies underline the applicability of the *in situ* synthesized Ag colloids also in environmental research, for instance, for the detection of bacteria in plant roots [56] and for pesticide monitoring in spinach leaves [57]. These results demonstrate the applicability of SERS-based noninvasive detection approaches for identification and characterization of pathogens and their secreted metabolites. The *in situ* synthesis of Ag colloid ensures the structural integrity of the coated bacterial cells and thus helps to rapidly generate spectral bacterial signatures with high sensitivity and specificity. **Figure 4** contains a collection of microscopic images illustrating the reproducible coverage of *E. coli* cells with a silver layer by using the *in situ* synthesis approach.

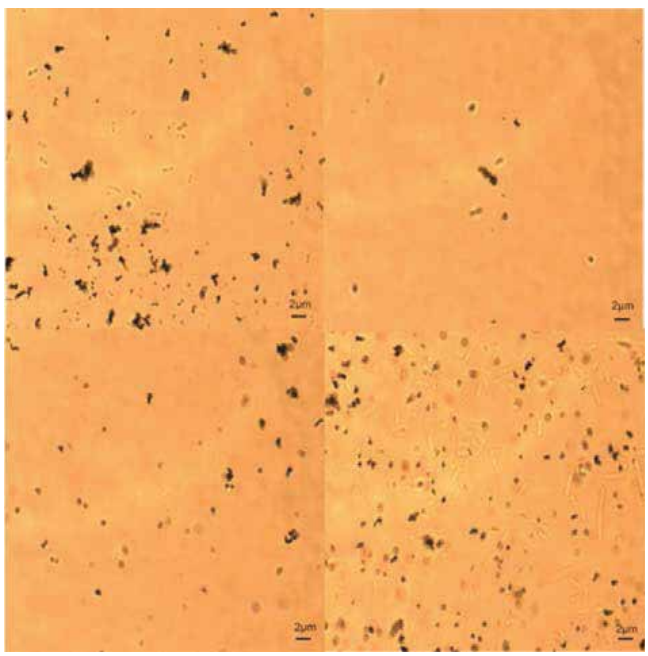

Figure 4. Microscopic 100× images showing the Ag NPs coverage of bacteria (*E. coli*) when using the *in situ* synthesis approach (Bacteria@ Ag NPs).

The influence at strain level of the O-antigen presence was already demonstrated by using unspecific surface chemistry as means of bacteria adsorption and the *in situ* synthesis approach [14]. O-antigen is the terminal structural part of the Gram-negative bacterial outer membrane that contains the significant variation between virulent strains and lab-designed strains. The differences in the composition of the monosaccharide units and sugar linkages translate into strain discrimination, by using molecular serotyping tests and chemometric analysis. Considering all this, O-antigen is the most variable cell constituent and of great importance when dealing with bacteria identification at strain level.

Raw SERS spectra collected from single cells of four different strains of *E. coli* are shown in **Figure 5.** For the accurate detection and discrimination between these strains, one has to make sure that all experimental conditions are standardized for each measurement. In this context, we established a constant timeline in the preparation steps of the samples and we used constant experimental parameters in acquiring the SERS spectra. The used *E. coli* strains are rough (K12)–MG1655, TOP 10 (**Figure 5A** and **C**) and smooth strains (B2)-536, UTI89 (**Figure 5B** and **D**).

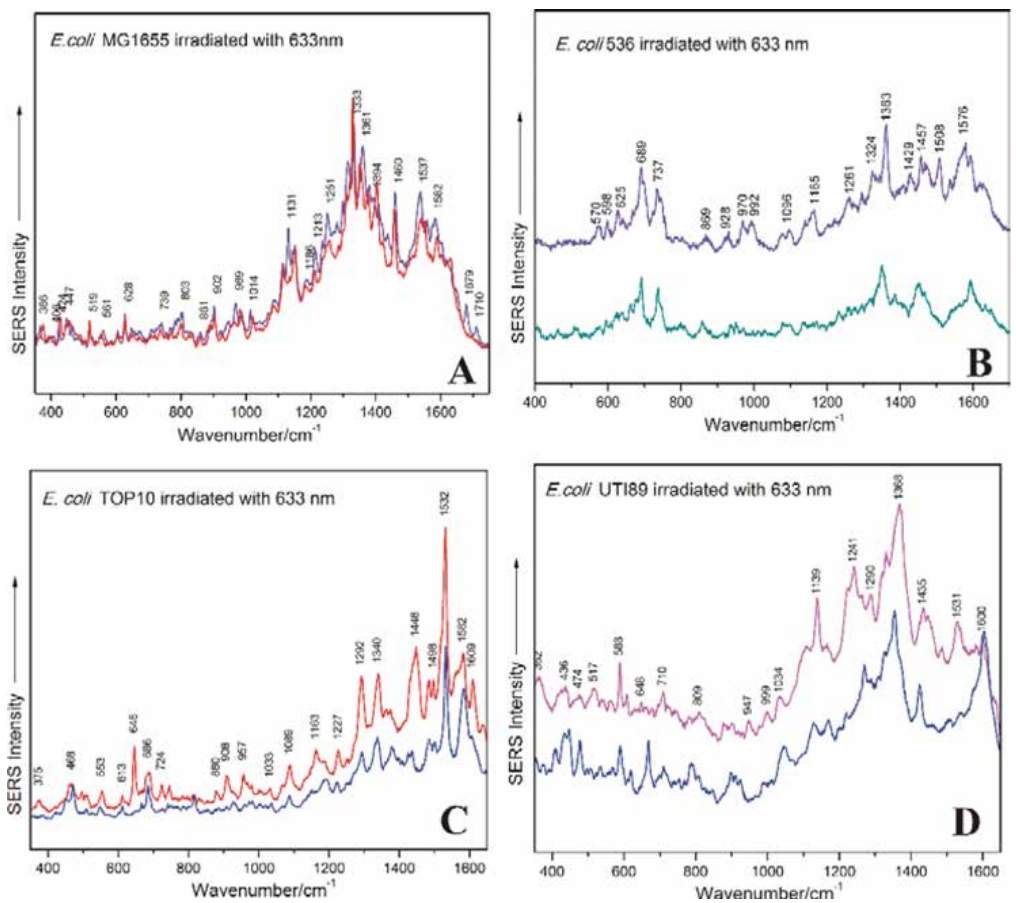

Figure 5. Raw SERS spectra of rough (A and C) and smooth (B and D) *E. coli* strains collected by using the *in situ* synthesis approach (Bacteria@ Ag NPs).

http://dx.doi.org/10.5772/65478

Specific SERS bands in each case (with or without the O-antigen) are discussed in our previous study [14], where a clear discrimination between K12 and B2 strains is demonstrated by using chemometrics (principal component analysis, PCA).

In the last decades, SERS was used to identify: DNA bases [58], a wide range of explosives and trace materials [59], food additives [60], therapeutic agents [61], different species of pathogenic and nonpathogenic bacteria [62–64], protozoa [65], fungi [66, 67], and their spores [68], respectively. Furthermore, as previously described, vibrational spectroscopy can be used to study the uniqueness of microorganisms. Consequently, we envision that the *in situ* synthesis approach could be used to some extent in other microorganisms' detection as well, not only bacteria.

Particularly, Raman and SERS spectroscopies were already applied in the detection, characterization, and monitoring of growth cycle for fungi. For example, various pathogens such as *Candida albicans, C. glabrata,* and *C. tropicalis* isolated from blood cultures have been rapidly identified [66]. Rapid diagnosis of infections caused by fungi from *Candida* genus is extremely important, since intra-abdominal infections caused by these fungi lead to high mortality rates [67]. Yang and Irudayaraj [69] were able to easily identify *A. niger* and *F. verticillioides* pathogenic fungi from apple surface, using FT-Raman spectroscopy. Szeghalmi and coworkers [70] studied the growth of *A. nidulans* strain A28 hyphae over the Au-coated Klarite SERS substrate, and they detected a strong signal in the close proximity of the hyphal cell wall because of the excretion of some extracellular components during growth.

Another field of interest in fungi studies using Raman spectroscopy and SERS is the characterization of various bioactive compounds extracted from different fungi. De Oliveira and coworkers [71] successfully identified the chemical composition of the extracts obtained from *P. sanguineus* fungus. The major bioactive components of *P. sanguineus* extracts are *ergosterol* and *cinnabarin*, the last one being responsible for the antibiotic activity of the extract [72].

Zinc oxide nanoparticles (ZnO NPs) were tested for their antifungal activity against *B. cinerea* and *P. expansum* fungi. He and coworkers [73] used traditional microbiological plating, along with SEM and Raman spectroscopy and showed that a concentration higher than 3 mmol/l of ZnO NPs can significantly inhibit the growth of *B. cinerea* and *P. expansum*. The last one is more sensitive to the action of ZnO NPs because these inhibit the development of conidiophores and conidia, resulting in the death of fungal hyphae. The detection of fungal infection in mice lungs with *P. brasiliensis* and follow-up treatment with magnetic NPs functionalized with amphotericin B can be achieved using SERS analysis [74].

SERS imaging and analysis have been effectively used for the characterization of *in vitro* biosynthesis of NPs by different species of fungi. In this regard, Mukherjee and coworkers [75] established a controlled biosynthetic route to obtain the nanocrystalline Ag particles using *T. asperellum*. Using TEM and XRD, the obtained Ag NPs were found to be in a range of 13–18 nm. *C. cladosporioides* was also reported to be able of Ag NPs extracellular biosynthesis [76]. In fact, fungi are not only able to biosynthesize Ag NPs, but also Au NPs. Extract from the filamentous fungi *A. nidulans* was used in the formation of Au NPs within and adjacent to hyphae. Also, the *Neurospora crassa* extract was tested by Quester and his coworkers [77] for the formation of Au NPs under different experimental conditions. The authors were able to

synthesize Au NPs with different shapes and sizes ranging from 3 to 200 nm by using methylene blue as target molecule.

Concluding this chapter, it is a challenge to entrench how to use most effectively the SERS effect in our favor. The simple reasoning is that SERS is still a not fully understood phenomenon. However, the ongoing studies in the biomedical area show the huge potential of this ultrasensitive technique to actually improve our life quality and the diagnosis procedures of infections and to significantly prevail essential real-life issues. Apart from infections diagnostics, cancer treatment or imaging, drug delivery, and personalized medicine or other health care branches can greatly benefit from Raman/SERS detection and mapping in synergy with functionalized NPs and high-performance support vector machines.

Acknowledgements

This chapter could not be written to its fullest without Dr. Nicolae Leopold, Prof. Dr. Vasile Chis (Biomolecular Physics Department, Babes-Bolyai University, Cluj-Napoca, Romania), and Dr. Christoph Haisch (Analytical Chemistry Chair, Technische Universität München, Germany) who served as my supervisors, as well as partners who challenged and encouraged me throughout my time spent as a PhD student. They would have never accepted anything less than my best efforts, and for that, I sincerely thank them. This work was supported by a grant of the Romanian National Authority for Scientific Research and Innovation, CNCS – UEFISCDI, project number PN-II-RU TE-2014-4-0862.

Author details

Nicoleta Elena Dina* and Alia Colniță

*Address all correspondence to: nicoleta.dina@itim-cj.ro

National Institute of R & D of Isotopic and Molecular Technologies, Donat, Cluj-Napoca, Romania

References

[1] Harz M, Rösch P, Popp J. Vibrational spectroscopy—a powerful tool for the rapid identification of microbial cells at the single-cell level. Cytom. Part A. 2009;**75A**(2):104–113. DOI: 10.1002/cyto.a.20682

[2] Kemmler M, Rodner E, Rösch P, Popp J, Denzler J. Automatic identification of novel bacteria using Raman spectroscopy and Gaussian processes. Anal. Chim. Acta. 2013;**794**:29–37. DOI: 10.1016/j.aca.2013.07.051

[3] Kloß S, Kampe B, Sachse S, Rösch P, Straube E, Pfister W, Kiehntopf M, Popp J. Culture independent Raman spectroscopic identification of urinary tract infection pathogens: A proof of principle study. Anal. Chem. 2013;**85**(20):9610–9616. DOI: 10.1021/ac401806f

[4] Meisel S, Stöckel S, Elschner M, Melzer F, Rösch P, Popp J. Raman spectroscopy as a potential tool for detection of Brucella spp. in milk. Appl. Environ. Microbiol. 2012;**78**(16):5575–5583. DOI: 10.1128/aem.00637-12

[5] Aroca R. Surface-enhanced vibrational spectroscopy. John Wiley & Sons Ltd: Atrium, England, 2006. DOI: 10.1002/9780470035641

[6] Campion A. Raman spectroscopy of molecules adsorbed on solid surfaces. Annu. Rev. Phys. Chem. 1985;**36**:549–572. DOI: 10.1146/annurev.pc.36.100185.003001

[7] Schuster KC, Reese I, Urlaub E, Gapes JR, Lendl B. Multidimensional information on the chemical composition of single bacterial cells by confocal Raman microspectroscopy. Anal. Chem. 2000;**72**(22):5529–5534. DOI: 10.1021/ac000718x

[8] Schuster KC, Urlaub E, Gapes JR. Single-cell analysis of bacteria by Raman microscopy: Spectral information on the chemical composition of cells and on the heterogeneity in a culture. J. Microbiol. Methods. 2000;**42**(1):29–38. DOI: 10.1016/S0167-7012(00)00169-X

[9] Knauer M, Ivleva NP, Niessner R, Haisch C. Optimized surface-enhanced Raman scattering (SERS) colloids for the characterization of microorganisms. Anal. Sci. 2010;**26**(7):761–766. DOI: 10.2116/analsci.26.761

[10] Zeiri L, Bronk BV, Shabtai Y, Eichler J, Efrima S. Surface-enhanced Raman spectroscopy as a tool for probing specific biochemical components in bacteria. Appl. Spectrosc. 2004;**58**(1):33–40. DOI: 10.1366/000370204322729441

[11] Knauer M, Ivleva NP, Liu X, Niessner R, Haisch C. Surface-enhanced Raman scattering-based label-free microarray readout for the detection of microorganisms. Anal. Chem. 2010;**82**(7):2766–2772. DOI: 10.1021/ac902696y

[12] Zhou H, Yang D, Ivleva NP, Mircescu NE, Niessner R, Haisch C. SERS detection of bacteria in water by *in situ* coating with Ag nanoparticles. Anal. Chem. 2014;**86**(3):1525–1533. DOI: 10.1021/ac402935p

[13] Zhou H, Yang D, Ivleva NP, Mircescu NE, Schubert S, Niessner R, Wieser A, Haisch C. Label-free *in situ* discrimination of live and dead bacteria by surface-enhanced Raman scattering. Anal. Chem. 2015;**87**(13):6553–6561. DOI: 10.1021/acs.analchem.5b01271

[14] Mircescu NE, Zhou H, Leopold N, Chis V, Ivleva NP, Niessner R, Wieser A, Haisch C. Towards a receptor-free immobilization and SERS detection of urinary tract infections causative pathogens. Anal. Bioanal. Chem. 2014;**406**(13):3051–3058. DOI: 10.1007/s00216-014-7761-4

[15] Cialla D, März A, Böhme R, Theil F, Weber K, Schmitt M, Popp J. Surface-enhanced raman spectroscopy (SERS): Progress and trends. Anal. Bioanal. Chem. 2012;**403**(1):27–54. DOI: 10.1007/s00216-011-5631-x

[16] Emory SR, Haskins WE, Nie SM. Direct observation of size-dependent optical enhancement in single metal nanoparticles. J. Am. Chem. Soc. 1998;**120**(31):8009–8010. DOI: 10.1021/ja9815677

[17] Nie SM, Emory SR. Probing single molecules and single nanoparticles by surface-enhanced Raman scattering. Science. 1997;**275**:1102–1106. DOI: 10.1126/science.275.5303.1102

[18] Efrima S, Bronk BV. Silver colloids impregnating or coating bacteria. J. Phys. Chem. B. 1998;**102**(31):5947–5950. DOI: 10.1021/jp9813903

[19] Efrima S, Zeiri L. Understanding SERS of bacteria. J. Raman Spectrosc. 2009;**40**(3):277–288. DOI: 10.1002/jrs.2121

[20] Leopold N, Chis V, Mircescu NE, Marisca OT, Buja OM, Leopold LF, Socaciu C, Braicu C, Irimie A, Berindan-Neagoe I. One step synthesis of SERS active colloidal gold nanoparticles by reduction with polyethylene glycol. Colloids Surf., A. 2013;**436**:133–138. DOI: 10.1016/j.colsurfa.2013.05.075

[21] Dreaden EC, Alkilany AM, Huang XH, Murphy CJ, El-Sayed MA. The golden age: Gold nanoparticles for biomedicine. Chem. Soc. Rev. 2012;**41**(7):2740–2779. DOI: 10.1039/c1cs15237h

[22] Tódor IS, Szabó L, Marisca OT, Chis V, Leopold N. Gold nanoparticle assemblies of controllable size obtained by hydroxylamine reduction at room temperature. J. Nanopart. Res. 2014;**16**(12):1–8. DOI: 10.1007/s11051-014-2740-4

[23] Vlad IE, Marișca OT, Vulpoi A, Șimon S, Leopold N, Anghel SD. Simple approach for gold nanoparticle synthesis using an Ar-bubbled plasma setup. J. Nanopart. Res. 2014;**16**(10):1–11. DOI: 10.1007/s11051-014-2633-6

[24] Marișca O, Kantner K, Pfeiffer C, Zhang Q, Pelaz B, Leopold N, Parak W, Rejman J. Comparison of the *in vitro* uptake and toxicity of collagen- and synthetic polymer-coated gold nanoparticles. Nanomaterials. 2015;**5**(3):1418. DOI: 10.3390/nano5031418

[25] Pinchuk A, Plessen Gv, Kreibig U. Influence of interband electronic transitions on the optical absorption in metallic nanoparticles. J. Phys. D Appl. Phys. 2004;**37**(22):3133. DOI: 10.1088/0022-3727/37/22/012

[26] Kunze A, Dilcher M, Abd El Wahed A, Hufert F, Niessner R, Seidel M. On-chip isothermal nucleic acid amplification on flow-based chemiluminescence microarray analysis platform for the detection of viruses and bacteria. Anal. Chem. 2016;**88**(1):898–905. DOI: 10.1021/acs.analchem.5b03540

[27] Guven B, Basaran-Akgul N, Temur E, Tamer U, Boyac IH. SERS-based sandwich immunoassay using antibody coated magnetic nanoparticles for *Escherichia coli* enumeration. Analyst. 2011;**136**(4):740–748. DOI: 10.1039/c0an00473a

[28] Szkola A, Linares EM, Worbs S, Dorner BG, Dietrich R, Martlbauer E, Niessner R, Seidel M. Rapid and simultaneous detection of ricin, Staphylococcal enterotoxin B and saxitoxin by chemiluminescence-based microarray immunoassay. Analyst. 2014;**139**(22):5885–5892. DOI: 10.1039/C4AN00345D

[29] Seidel M, Niessner R. Chemiluminescence microarrays in analytical chemistry: A critical review. Anal. Bioanal. Chem. 2014;**406**(23):5589–5612. DOI: 10.1007/s00216-014-7968-4

[30] Wieser A, Schneider L, Jung JT, Schubert S. MALDI-TOF MS in microbiological diagnostics-identification of microorganisms and beyond (mini review). Appl. Microbiol. Biotechnol. 2012;**93**(3):965–974. DOI: 0.1007/s00253-011-3783-4

[31] Sören SS, Kirsten KW, Chris CW, Beatrix BG, Andreas AW, Thomas TM, Markus MK. Novel, improved sample preparation for rapid, direct identification from positive blood cultures using matrix-assisted laser desorption/ionization time-of-flight (MALDI-TOF) Mass Spectrometry. J. Mol. Diagn. 2011;**13**(6):701–706. DOI: 10.1016/j.jmoldx.2011.07.004

[32] Xiao N, Wang C, Yu C. A self-referencing detection of microorganisms using surface enhanced Raman scattering nanoprobes in a test-in-a-tube platform. Biosensors. 2013;**3** (3):312–326. DOI: 10.3390/bios3030312

[33] Ravindranath SP, Wang Y, Irudayaraj J. SERS driven cross-platform based multiplex pathogen detection. Sensor. Actuat. B Chem. 2011;**152**(2):183–190. DOI: 10.1016/j.snb.2010.12.005

[34] Srivastava SK, Hamo HB, Kushmaro A, Marks RS, Gruner C, Rauschenbach B, Abdulhalim I. Highly sensitive and specific detection of *E. coli* by a SERS nanobiosensor chip utilizing metallic nanosculptured thin films. Analyst. 2015;**140**(9):3201–3209. DOI: 10.1039/C5AN00209E

[35] Shamsi MH, Choi K, Ng AHC, Wheeler AR. A digital microfluidic electrochemical immunoassay. Lab. Chip. 2014;**14**(3):547–554. DOI: 10.1039/c3lc51063h

[36] Grow AE, Wood LL, Claycomb JL, Thompson PA. New biochip technology for label-free detection of pathogens and their toxins. J. Microbiol. Methods. 2003;**53**(2):221–233. DOI: 10.1016/S0167-7012(03)00026-5

[37] Sengupta A, Mujacic M, Davis EJ. Detection of bacteria by surface-enhanced Raman spectroscopy. Anal. Bioanal. Chem. 2006;**386**(5):1379–1386. DOI: 10.1007/s00216-006-0711-z

[38] Sengupta A, Laucks ML, Dildine N, Drapala E, Davis EJ. Bioaerosol characterization by surface-enhanced Raman spectroscopy (SERS). J. Aerosol Sci. 2005;**36**(5–6):651–664. DOI: 10.1016/j.jaerosci.2004.11.001

[39] Sengupta A, Laucks ML, Davis EJ. Surface-enhanced Raman spectroscopy of bacteria and pollen. Appl. Spectrosc. 2005;**59**:1016–1023. DOI: 10.1366/0003702054615124

[40] Kahraman M, Yazıcı MM, Sahin F, Culha M. Convective assembly of bacteria for surface-enhanced Raman scattering. Langmuir. 2008;**24**(3):894–901. DOI: 10.1021/la702240q

[41] Kahraman M, Yazici MM, Sahin F, Bayrak ÖF, Çulha M. Reproducible surface-enhanced Raman scattering spectra of bacteria on aggregated silver nanoparticles. Appl. Spectrosc. 2007;**61**(5):479–485. DOI: 10.1366/000370207780807731

[42] Knauer M, Ivleva N, Niessner R, Haisch C. A flow-through microarray cell for the online SERS detection of antibody-captured *E. coli* bacteria. Anal. Bioanal. Chem. 2012;**402**(8):2663–2667. DOI: 10.1007/s00216-011-5398-0

[43] Leopold N, Lendl B. A new method for fast preparation of highly surface-enhanced Raman scattering (SERS) active silver colloids at room temperature by reduction of silver nitrate with hydroxylamine hydrochloride. J. Phys. Chem. B. 2003;**107**(24):5723–5727. DOI: 10.1021/jp027460u

[44] Zhou H, Yang D, Mircescu N, Ivleva N, Schwarzmeier K, Wieser A, Schubert S, Niessner R, Haisch C. Surface-enhanced Raman scattering detection of bacteria on microarrays at single cell levels using silver nanoparticles. Microchim. Acta. 2015;**182**(13–14):2259–2266. DOI: 10.1007/s00604-015-1570-0

[45] Yaffe NR, Blanch EW. Effects and anomalies that can occur in SERS spectra of biological molecules when using a wide range of aggregating agents for hydroxylamine-reduced and citrate-reduced silver colloids. Vib. Spectrosc. 2008;**48**(2):196–201. DOI: 10.1016/j.vibspec.2007.12.002

[46] Budin G, Chung HJ, Lee H, Weissleder R. A magnetic Gram stain for bacterial detection. Angew. Chem. Int. Ed. 2012;**51**(31):7752–7755. DOI: 10.1002/anie.201202982

[47] Kneipp J, Kneipp H, Kneipp K. SERS-a single-molecule and nanoscale tool for bioanalytics. Chem. Soc. Rev. 2008;**37**(5):1052–1060. DOI: 10.1039/b708459p

[48] Kastanos EK, Kyriakides A, Hadjigeorgiou K, Pitris C. A novel method for urinary tract infection diagnosis and antibiogram using Raman spectroscopy. J. Raman Spectrosc. 2010;**41**(9):958–963. DOI: 10.1002/jrs.2540

[49] Haisch C. Raman-based microarray readout: A review. Anal. Bioanal. Chem. 2016;**408**(17):4535–4545. DOI: 10.1007/s00216-016-9444-9

[50] Cheng I-F, Chang H-C, Chen T-Y, Hu C, Yang F-L. Rapid (<5 min) identification of pathogen in human blood by electrokinetic concentration and surface-enhanced Raman spectroscopy. Sci. Rep. 2013;**3**(2365):1–8. DOI: 10.1038/srep02365

[51] Zhang JY, Do J, Premasiri WR, Ziegler LD, Klapperich CM. Rapid point-of-care concentration of bacteria in a disposable microfluidic device using meniscus dragging effect. Lab on a Chip. 2010;**10**(23):3265–3270. DOI: 10.1039/c0lc00051e

[52] Yoo SM, Lee SY. Optical biosensors for the detection of pathogenic microorganisms. Trends Biotechnol. 2016;**34**(1):7–25. DOI: 10.1016/j.tibtech.2015.09.012

[53] Wang P, Pang S, Chen J, McLandsborough L, Nugen SR, Fan M, He L. Label-free mapping of single bacterial cells using surface-enhanced Raman spectroscopy. Analyst. 2016;**141**(4):1356–1362. DOI: 10.1039/C5AN02175H

[54] Kubryk P, Niessner R, Ivleva NP. The origin of the band at around 730 cm^{-1} in the SERS spectra of bacteria: A stable isotope approach. Analyst. 2016;**141**(10):2874–2878. DOI: 10.1039/C6AN00306K

[55] Chen L, Mungroo N, Daikuara L, Neethirajan S. Label-free NIR-SERS discrimination and detection of foodborne bacteria by *in situ* synthesis of Ag colloids. J. Nanobiotechnol. 2015;**13**(1):1–9. DOI: 10.1186/s12951-015-0106-4

[56] Polisetti S, Bible AN, Morrell-Falvey JL, Bohn PW. Raman chemical imaging of the rhizosphere bacterium P*antoea sp.* Yr343 and its co-culture with *Arabidopsis thaliana*. Analyst. 2016;**141**(7):2175–2182. DOI: 10.1039/C6AN00080K

[57] Yang T, Zhang Z, Zhao B, Hou R, Kinchla A, Clark JM, He L. Real-time and *in situ* monitoring of pesticide penetration in edible leaves by surface-enhanced Raman scattering mapping. Anal. Chem. 2016;**88**(10):5243–5250. DOI: 10.1021/acs.analchem.6b00320

[58] Kneipp K, Kneipp H, Manoharan R, Itzkan I, Dasari RR, Feld MS. Surface-enhanced Raman scattering (SERS)—a new tool for single molecule detection and identification. Bioimaging. 1998;**6**(2):104–110. DOI: 10.1002/1361-6374(199806)6:2<104::aid-bio6>3.0.co;2-t

[59] Bertone JF, Spencer KM, Sylvia JM. Fingerprinting CBRNE materials using surface-enhanced Raman scattering. Proc. SPIE. Chemical, biological, radiological, nuclear, and explosives (CBRNE) sensing IX, Bellingham, Wash.: Society of Photo-optical Instrumentation Engineers 2008;69540J-1–69540J-7, ISSN: 0277786X, ISBN: 9780819471451 [0819471453].

[60] Lin M, He L, Awika J, Yang L, Ledoux DR, Li H, Mustapha A. Detection of melamine in gluten, chicken feed, and processed foods using surface-enhanced Raman spectroscopy and HPLC. J. Food Sci. 2008;**73**(8):T129–T134. DOI: 10.1111/j.1750-3841.2008.00901.x

[61] Stokes RJ, McBride E, Wilson CG, Girkin JM, Smith WE, Graham D. Surface-enhanced Raman scattering spectroscopy as a sensitive and selective technique for the detection of folic acid in water and human serum. Appl. Spectrosc. 2008;**62**(4):371–376. DOI: 10.1366/000370208784046812

[62] Golightly RS, Doering WE, Natan MJ. Surface-enhanced Raman spectroscopy and homeland security: A perfect match? ACS Nano. 2009;**3**(10):2859–2869. DOI: 10.1021/nn9013593

[63] Liu Y, Chao K, Nou X, Chen Y-R. Feasibility of colloidal silver SERS for rapid bacterial screening. Sens. Instrumen. Food Qual. 2009;**3**(2):100–107. DOI: 10.1007/s11694-008-9064-y

[64] Jarvis RM, Brooker A, Goodacre R. Surface-enhanced Raman scattering for the rapid discrimination of bacteria. Faraday Discuss. 2006;**132**:281–292. DOI: 10.1039/B506413A

[65] Rule KL, Vikesland PJ. Surface-enhanced resonance Raman spectroscopy for the rapid detection of C*ryptosporidium parvum* and *Giardia lamblia*. Environ. Sci. Technol. 2009;**43**(4):1147–1152. DOI: 10.1021/es801531t

[66] Maquelin K, Kirschner C, Choo-Smith LP, Ngo Thi NA, Van Vreeswijk T, Stammler M, Endtz HP, Bruining HA, Naumann D, Puppels GJ. Prospective study of the performance of vibrational spectroscopies for rapid identification of bacterial and fungal pathogens recovered from blood cultures. J. Clin. Microbiol. 2003;**41**:324–329. DOI: 10.1128/JCM.41.1.324-329.2003

[67] Hoerauf A, Hammer S, Muller-Myhsok B, Rupprecht H. Intra-abdominal *Candida* infection during acute necrotizing pancreatitis has a high prevalence and is associated with increased mortality. Crit. Care Med. 1998;**26**(12):2010–2015.

[68] De Gussem K, Vandenabeele P, Verbeken A, Moens L. Raman spectroscopic study of *Lactarius* spores (russulales, fungi). Spectrochim. Acta. A. 2005;**61**(13–14):2896–2908. DOI: 10.1016/j.saa.2004.10.038

[69] Yang H, Irudayaraj J. Rapid detection of foodborne microorganisms on food surface using Fourier transform Raman spectroscopy. J. Mol. Struct. 2003;**646**(1–3):35–43. DOI: 10.1016/S0022-2860(02)00575-6

[70] Szeghalmi A, Kaminskyj S, Rösch P, Popp J, Gough KM. Time fluctuations and imaging in the SERS spectra of fungal hypha grown on nanostructured substrates. J. Phys. Chem. B. 2007;**111**(44):12916–12924. DOI: 10.1021/jp075422a

[71] De Oliveira LFC, Le Hyaric M, Berg MM, De Almeida MV, Edwards HGM. Raman spectroscopic characterization of cinnabarin produced by the fungus *Pycnoporus sanguineus (fr.) murr.* J. Raman Spectrosc. 2007;**38**(12):1628–1632. DOI: 10.1002/jrs.1881

[72] Smânia A, Monache FD, Smânia EFA, Gil ML, Benchetrit LC, Cruz FS. Antibacterial activity of a substance produced by the fungus *Pycnoporus sanguineus (fr.) murr.* J. Ethnopharmacol. 1995;**45**(3):177–181. DOI: 10.1016/0378-8741(94)01212-I

[73] He L, Liu Y, Mustapha A, Lin M. Antifungal activity of zinc oxide nanoparticles against B*otrytis cinerea* and P*enicillium expansum*. Microbiol. Res. 2011;**166**(3):207–215. DOI: 10.1016/j.micres.2010.03.003

[74] Santos CMB, Da Silva SW, Saldanha CA, Santos MFMA, Garcia MP, Azevedo RB, Morais PC. SERS as a valuable tool for detection and treatment follow-up of fungal infection in mice lungs: Use of Amphotericin B and its nanoencapsulation onto magnetic nanoparticles. J. Raman Spectrosc. 2013;**44**(5):695–702. DOI: 10.1002/jrs.4259

[75] Mukherjee P, Roy M, Mandal BP, Dey GK, Mukherjee PK, Ghatak J, Tyagi AK, Kale SP. Green synthesis of highly stabilized nanocrystalline silver particles by a non-pathogenic and agriculturally important fungus *T. asperellum.* Nanotechnology. 2008;**19**(7):075103. DOI: 10.1088/0957-4484/19/7/075103

[76] Balaji DS, Basavaraja S, Deshpande R, Mahesh DB, Prabhakar BK, Venkataraman A. Extracellular biosynthesis of functionalized silver nanoparticles by strains of *Cladosporium cladosporioides* fungus. Colloids Surf. B. 2009;**68**(1):88–92. DOI: 10.1016/j.colsurfb.2008.09.022

[77] Quester K, Avalos-Borja M, Vilchis-Nestor AR, Camacho-López MA, Castro-Longoria E. SERS properties of different sized and shaped gold nanoparticles biosynthesized under different environmental conditions by *Neurospora crassa* extract. PLoS One. 2013;**8**(10): e77486. DOI: 10.1371/journal.pone.0077486

Chapter 16

Precision Target Guide Strategy for Applying SERS into Environmental Monitoring

Lei Ouyang, Dingyi Li, Lihua Zhu and Heqing Tang

Additional information is available at the end of the chapter

http://dx.doi.org/10.5772/64813

Abstract

Surface enhanced Raman spectroscopy (SERS) is a promising analytical technique that exhibits various applications in trace detection and identification. When it is applied into environmental monitoring, we should concern several key points to improve detection sensitivity and selectivity for the detection in complex matrix. In this tutorial review, we mainly focus on the strategies for improving the use of SERS into environmental application. The strategies are summarized for enhancing the ability of the substrate to selectively capture specific targets, and for achieving separation and concentration of the analytes from the matrix and the assembly structures for multiple phase detection. We have also introduced several newly developed detection systems using portable instruments and miniaturized devices that are more suitable for infield applications. In addition, we discuss the present challenges that hide it from wide real application and give the outlook for the future development in applying SERS in environmental monitoring.

Keywords: SERS, environmental monitoring, pollutant, target capture, concentration, separation, infield detection

1. Introduction

Tremendous achievements have been made in industrial, agricultural and medical fields in the last several decades, which also led much pressure on our living environment. The uncontrollable releasing of various toxic and potentially harmful chemicals and/or biological products into the environment results in serious damages to ourselves. The pollution in water, soil and air is becoming main threat to ecosystem and health, and the pollutants include inorganic gases, irons, pathogenic organisms and organic pollutants such as persistent organic pollutants (POPs),

antibiotics and pesticides [1, 2]. It is urgent to develop rapid and sensitive strategy to classify, quantify and assess them from the environment, which is the basic information to early warning for their threats and getting the precondition for solving these problems. Environmental monitoring requires the analysis of pollutants at (very) low concentrations since many of the pollutants have serious consequence at even extremely low levels. In addition, the methods to be used should also be simple and rapid for their operations in the real application.

Different techniques including chromatography, spectroscopy, mass-spectra methods are well established in environmental analysis [3–5], but most of these methods require sophisticated instruments and some of them are lack of sufficiently recognition capacity, which limit their wide applications for infield application. Recently, advanced nanomaterial-based methods have contributed a lot to this area, such as microfluidics, electrochemical sensor, surface plasmon resonance (SPR) method, single-molecule spectroscopy and hyperspectroscopy [6–8]. Among these methods, surface-enhanced Raman spectroscopy (SERS) is one of the most promising methods for environmental monitoring. As a molecular vibrational spectroscopy, SERS holds several outstanding advantages compared to the traditional techniques. Firstly, by making use of the SPR-induced strong electromagnetic field to enhance signals of the analytes, SERS has high sensitivity which enables detection at low concentrations, even as low as to single molecule level [9]. Secondly, the obtained Raman spectra contains abundant molecular information of the analytes, and the finger-print information is valuable for identification and classification [10]. Thirdly, the Raman character peaks have very narrow width, which enables multiple detection or complex identification. Unlike other vibrational spectroscopy such as infrared spectroscopy, SERS can be applied directly in solution since water has little background signal. SERS technique is also compatible with different sample conditions including aqueous, solidary and even gaseous state, and it needs less sample preparation and preoperation. This technique can get the character signal within seconds to minutes, which is suitable for rapid signal readout. SERS is also very convenient and cost-effective to be combined with miniaturized Raman spectrometers and offers good practical utility for real application, even for infield detection.

The above-mentioned remarkable advantages have led many significant achievements of SERS in the environmental detection [11]. Recently, several review articles have covered different considerations, such as facing various targets such as organics, [12] ions [13] or pathogens [14]. Considering the real condition when performing SERS in environmental application, we believe that special attention should be paid to the following aspect in order to fully realize the potential of SERS method. (1) SERS phenomenon only takes effect when the analyte is near the surface of the SERS substrate, which usually needs to be within several nanometers [15]. While for most of the environmental targets, their interaction with the bare substrate is not strong enough to get them close to the substrate; thus, it is important to shorten the distance between them. (2) The matrix of the environmental samples is complex, which will interrupt the effective interaction between the substrate and the analytes, and hence, the proposed method should have specific selectivity to the interested targets. (3) In many cases, the proposed method should have the ability to concentrate the target in order to meet the demands of sensitivity. (4) For most of infield detections, a strategy is required to be compatible

http://dx.doi.org/10.5772/64813

with portable instruments (or miniaturized devices). In this chapter, therefore, we mainly focus on the recent achievements with the goal of developing target-specific SERS-based methods for pollutant detection, the strategies for realizing selective target capture, concentration and separation. We also summarize detection systems that are compatible with specific complex matrix and newly proposed devices suitable for infield application. This review further covers the current challenge and future prospect for better application of SERS in environmental protection.

2. Strategies for selective target capture

The SERS effect is known to be a localized first-layer effect. The observed enhanced Raman signal comes from the analytes close to the metallic structures with a distance no longer than 5 nm, and the signal intensity exponentially decreases with increasing the distance [15]. The analytes may be divided into two groups. In the first group, the analytes have strong affinity to the bare surface of metallic structures due to their functional groups such as amino ($-NH_2$) and thiol (−SH) groups. These analytes are easily absorbed on the substrate, and their SERS responses are obtained directly if they are SERS active. As the second group of analytes, most of which are pollutants to be concerned, they have no strong affinity to the unmodified substrate, and hence, the distance between the analyte and the SERS substrate is too large to producing enough SERS-enhancing effect. Therefore, it is important to functionalize the surface of the substrate to capture such weakly affinitive targets. In addition, it should be noted that many SERS substrates are made with wet chemical synthesis methods. These wet chemically synthesized SERS substrates usually contain one or more surfactants and/or other organic species being used as the shape control reagents and/or reducing agents during the synthesis. The presence of these species may hinder the effective contact of analytes with the substrate surface, and hence, surface replacement of these capping species is needed to avoid the interference and further enhance the capture capacity of the substrate for the specific targets. Concerning targets with weak Raman response, surface functionalization can be used to increase the sensitivity by producing special interaction or generating specific complexes between analytes and modified molecules which could be used for the indirect detection [16, 17]. The detailed measures may aim at one or more of the following five types of interaction enhancement.

2.1. Electrostatic or hydrophobic interaction

Different function structures or molecules are used to enrich targets from the matrix, one of the functions is to modify the SERS substrate surface with improved electrostatic or hydrophobic interactions. For example, in most common colloidal systems (such as citrate reduced Ag or Au NPs), the substrate surface is negatively charged. To enhance the attractive interaction between the particle surface and the negatively charged target molecules, a substrate with controllable surface charge is favorable. By employing aliphatic amino acids as reductant and modifier, controllable surface charge range from −60 to +30 mV was obtained, which is favorable to smaller electrostatic repulsion and even attraction to increase analyte retention

[18]. Besides, the SERS substrate are often hydrophilic, but various toxic organic pollutants bearing aromatic structures are highly hydrophobic. Polycyclic aromatic hydrocarbons (PAHs) are a family of these pollutants, which consist of fused aromatic rings and contain no substituent that can absorb to the hydrophilic surface. The affinity between such hydrophobic analytes and the hydrophilic substrate may be enhanced by making use of the hydrophobic interaction. For example, Jing et al. reported thiol-functionalized magnetic nanoparticles (NPs) for the SERS detection of eight kinds of PAHs including benzene and naphthalene with limits of detection (LODs) down to 10^{-7} mol L^{-1} [19]. Similarly, alkyl dithiol was modified onto the metal particles to enhance the affinity of pesticides to the substrate, and this greatly promoted adsorption constant and led to the LOD down 10^{-8} mol L^{-1}, proving a solid basis for identification and quantitative analysis of organochlorine pesticides [20]. For the detection of aromatic organics, π-π stacking could also be used, where the modifying molecules could be aromatic molecules and also special materials like graphene or carbon nitride with absorption ability [21, 22]. The capture strategies by making use of electrostatic or hydrophobic interaction could effectively enhance the detection activity to targets, but the selectivity is still weak due to the low selectivity of these interactions.

2.2. Forming surface complex

Surface modification with molecules that can selectively bond to the target by forming a complex is an effective method to enable selective detection. For example, mercury ion (Hg(II)) is one of the most toxic pollutants with bioaccumulative activity. It holds weak SERS response and weak interaction to the common SERS substrate, and thus, it is difficult to be detected by SERS directly. By modifying the gold nanomaterials with tryptophan (a SERS-active molecule that can interact with Hg(II) to form a complex with a weak SERS response), an easy and highly selective method was proposed to recognize Hg(II) with the LOD down to 5 ppb level [23]. By making use of the specific interaction between Hg(II) and single-stranded DNA to convert into a hairpin structure through forming of thymine–Hg(II)–thymine complex, Hg(II) ions at concentrations as low as to 0.2 ppt (1p mol L^{-1}) were readily discriminated, being much lower than conventional analytical methods (usually nanomolar level) [24]. Due to the high binding specificity of DNAzyme to Pb^{2+} ions, a SERS DNAsyme biosensor was developed to detection of Pb^{2+}, such detection was further accomplished by SERS nanoprobe labeled with both DNA and Raman probe for signal amplification [25]. Another example of making use of the surface complex is the SERS detection of trinitrotoluene (TNT) with cysteine. Cysteine-modified gold nanoparticles (NPs) could selectively recognize of TNT molecules due to the formation of Meisenheimer complex, which underwent aggregation via electrostatic interaction to form hot spots and further enhanced the Raman signal of the complex by nine orders. High sensitivity (low to 2 pico molar level) and selectivity were observed for the detection of TNT without dye tagging [26]. Similarly, the surface-modified gold NPs with (aminomethyl)phosphoric acid were synthesized to selectively capture uranium(U) ions by making use of its phosphonic tails as terminal group. Without any pretreatment, the proposed method was performed directly for detection of uranium in contaminated water even under low pH and high salts conditions [27].

http://dx.doi.org/10.5772/64813

2.3. Host–guest interaction

The above-mentioned strategies for detection of targets by forming surface complex can greatly increase the sensitivity and selectivity, and the key point is to find a specific interaction between the analyte and the modifier; such analyte–receptor systems are not limited to the complex formation, but also many other interactions, such as host–guest interaction, molecular imprinting (MIP) recognition and antibody–antigen interaction. These interactions all have been successfully applied into promoting the selectivity of SERS-based method into specific target monitoring [28–31].

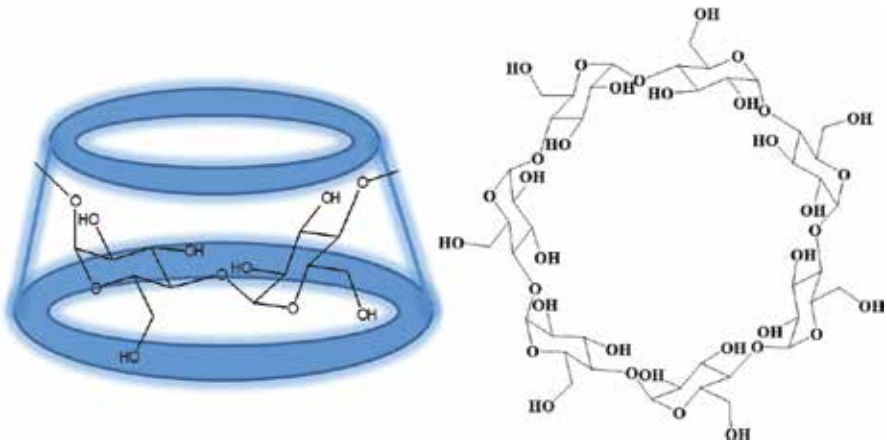

Figure 1. Molecular structure of β-CD.

Host–guest interaction is an important phenomenon in supramolecular chemistry, which describes the special interaction between the host molecules with unique structure and the guest smaller molecules or ions. It encompasses the idea of molecular recognition and interaction through noncovalent bonding (such as hydrogen bonds, ionic binds, van der Waals forces and hydrophobic interactions) [32]. It has been widely used in the drug delivery, the removal of hazardous materials from the environment and for sensing called indicator–spacer–receptor approach [33]. It also can be used for the SERS detection of the specific guest molecules by making use of the host structures as a modifier. Several typical host molecules have been applied as functional modifiers, such as viologen host lucigenin for the selective detection of PAHs or pesticides [34–36], dithiocarbamate calix [4] arene derivatives for the capture and detection of organic pollutants such as pyrene and PAHs [28, 37], and cucurbit[n]uril for the SERS monitoring of diaminostilbene [38]. Cyclodextrins (CDs) are another class of host molecules in supramolecular chemistry, and they have cyclic oligosaccharide structures with hydrophobic internal cavities which can selectively capture suitable nanosized guest molecules [39]. The most widely used cyclodextrin is β-cyclodextrin (β-CD) with seven glucose units, which is a natural product of specific bacteria. As shown in **Figure 1**, the cavity diameter is 6.4 À, which contributes to the interaction with guest molecules [39].

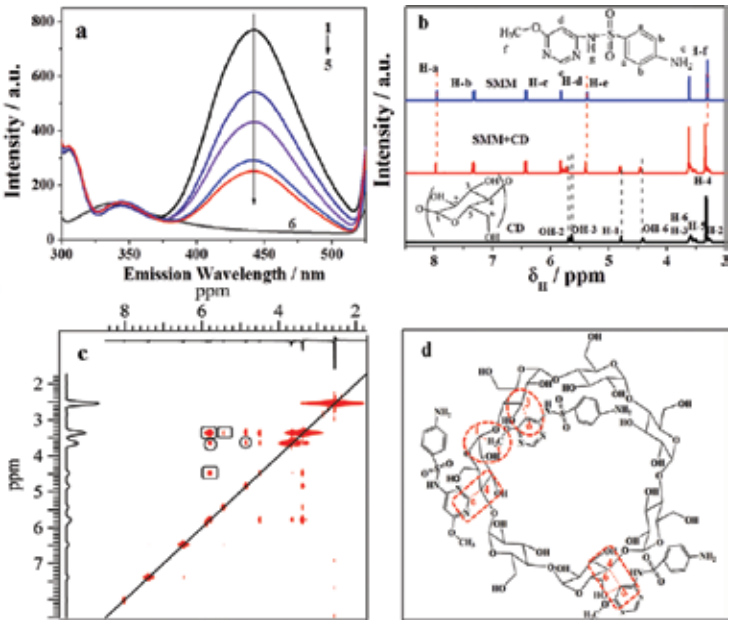

Figure 2. Molecular interaction between SMM and CD. Reproduced with permission from Ref. [45].

As a functional modifier, β-CD has been used for the SERS detection of both organic pollutants and inorganic ions, such as polychlorinated biphenyls (PCB-77, PCB-1) down to 3 μM, [40] methyl parathion at picomolar level, [41] PAHs (anthracene, pyrene or anthrecene) [39, 42] and micromolar Pb^{2+} ions [29]. In most of the reported works, thio-modified β-CD (such as per-6-deoxy-(6-thio)-β-CD) was used because of the weak modifying efficiency of natural β-CD onto the surface of the metal structure. In our earlier work, we proposed an in situ reduction strategy to synthesize β-CD modified Ag nanoparticles by making use of the reducing activity of the natural β-CD under heat and alkaline condition [43, 44]. The obtained substrate was successfully applied to detection of sulfonamide antibiotics with the LOD as low as 10 ng mL^{-1} [45]. Our results showed that by employing β-CD as both reductant and shape-controlling agent, the β-CD-modified Ag NPs could be easily obtained with controllable size and distribution, and much enhanced detection ability was observed with enhancement factor (EF factor) up to 1.97×10^6. The mechanism for the promoted recognition ability was further studied by fluorescence and ^{1}H NMR methods. As shown in **Figure 2a**, the character fluorescence emission at 445 nm of sulfamonomethoxine (SMM) solution was significantly decreased with the addition of β-CD, and such a quenching effect suggests a considerably strong interaction between SMM and β-CD. More detailed information for the interaction from the molecular level was obtained from NMR analysis. **Figure 2b** shows the ^{1}H NMR spectra of SMM, β-CD and SMM-β-CD complex. After assigning the character chemical shift to each proton, obvious shift of several protons was observed, such as H-a, H-e and H-f of SMM by 0.01–0.03 ppm, and H-1, H-4, OH-2, OH-3 and OH-6 protons by 0.01–0.10 ppm. In order to get insight into the exact interaction sites, we further performed the 2D NMR characterization which could not

only give the chemical shifts similar to ^{1}H NMR, but also reveals the correlation between the interacted protons. The obtained 2D NOESY NMR spectra of the SMM-β-CD complex are shown in **Figure 2c**. As indicated in the spectra, these cross-peaks indicate a close interaction of β-CD with SMM, since such cross-peaks could only be observed when the distance of relative molecules is shorter than 0.5 nm, such as H-3 with H-d, H-1 with H-f, these cross-peaks comes from the protons of SMM and interior cavity of β-CD, as marked by elliptic circles. Besides that, cross-peak from the SMM with the outside face of β-CD cavity was also obtained, as marked by rectangles in **Figure 2c**. These results provide us the interaction pattern of β-CD with SMM: It could not only set SMM into its cavity by host–guest interaction, but it also acts as a scaffold or a bridge to pull the SMM close to the out-surface of the cavity which yield greatly enhanced activity in SERS detection of SMM. The strategy of using native β-CD as scaffold for analytes with low affinity to the substrate shows wide application prospect in selectively capture and sense other concerning pollutants.

2.4. Antibody–antigen interaction

Antibody–antigen interaction is the most specific and useful recognition interaction that has been widely used in clinical diagnose. The highly specific binding is due to the specific chemical constitution of each antibody. The antigenic determinant or epitope is recognized by the paratope of antibody, situated at variable regions of polypeptide chain which also has unique hypervariable regions in each antibody [46]. The strategy of using antibody as modifier for selective SERS detection of antigens is commonly applied in the biological detection and imaging, and also for environmental monitoring, and it is widely used for the detection of pathogen organisms with both label and label-free methods [47, 48]. There are several reviews that summarized the achievement of such strategy in the pathogen detection [49–51]. Beside the common antibody modification, other interactions that base on immunological recognition has also been applied into the detection of specific pollutants recently. For example, aptamer is made of single-stranded DNA oligomer that can be selected against specific target (biological macromolecule or small organic molecule) come from systematic evolution of ligands by exponential enrichment (SELEX) [31]. On the basis of capture and enrichment by the PCB-77 specific aptamer, the improved detection of PCB77 was accomplished with a LOD down to 1×10^{-8} mol L^{-1} [52]. The aptamer-based strategy was used to detect bisphenol A, one of the most important endocrine disrupting chemicals, with a LOD as low as 3.9 pg/mL with excellent recovery for real sample detection [53]. Aptamer-based SERS sensor has also been developed for the selective detection of Hg^{2+} by employing the structure-switching aptamer in the presence of spermine [54]. These antibody, aptamer or other recognition structures such as phage that making use of the immunological reaction have the advantage of high selectivity, but also have some limitations that need further study, due to their low stability under harsh conditions.

2.5. Artificial antibody–antigen interaction (molecular imprinting effect)

Molecular imprinting (MIP) is a powerful technique to create specific recognition site in polymer by employing target molecules or molecules with similar structures as templates. The

recognition cavities after removing the templates provide the capability and functionality to selectively rebind specific targets without interference from other molecules. The surface MIP technique has been used for selective detection and removing of organic pollutants from the complex matrix [30, 55]. Such a strategy could be performed to functionalize the surface of the substrate to promote the recognition ability of the SERS method. Zhang et al. proposed a ligand replacement approach to rapid determination of penicilloic acid in the penicillin by using a molecularly imprinted monolayer as recognition surface, which efficiently excluded the interference of penicillin and provided a selective determination down to 0.1‰ (w/w) [56]. Similarly, thiol-terminated MIP microspheres which have been immobilized on a gold-coated substrate were used for the selective capture of nicotine, showing good capture efficiency and SERS response [57]. In considering of using MIPs techniques for selective SERS detection, two key points should be kept in mind. The first is that the imprinted layer should be thin thick because a thick layer will interfere the enhancement from the under layer metal structure. The second is that the polymer film should have clear background signal to prevent any interference to the detection of target molecules.

3. Strategies for target concentration and separation

In order to get satisfactory result, the strategy for target concentration and separation after selectively capture is also important. In various environmental cases, the concentrations of the interested targets are usually rather low and the matrix is complex. Therefore, preconcentrating the targets is required to increase the sensitivity. The combination of SERS-active structures with magnetic materials is an effective method to endow the substrate with facile recycle property, many different magnetic structures were applied into the SERS detection of pollutant, the improved ability of recycle and separation benefits a lot to the fast and convenient observation [17, 48, 58, 59]. In addition to the magnetic field-assisted separation strategy, some other techniques were also performed for effectively separating the substrates captured with targets form the matrix, by using such as a membrane filter, [60] filter paper [61] and even commercial tap-based substrates [61]. Besides the mentioned traditional methods for sample concentration and separation, there are several other typical strategies that have been applied effectively, such as electrochemical concentration, hydrophobic concentration, paper-based substrate for separation and hydrogel-based structure for target gathering. The integrated SERS detecting, preconcentrating and separating make the whole SERS method have the promoted ability for fast and facile application.

3.1. Electrochemical and hydrophobic concentration

Electrochemical techniques such as electrostatic concentration offer a reliable and convenient way of concentration target form the matrix. It is an effective way to draw charged analytes toward the substrates through electrostatic forces and hence increase the concentration of the analytes to the required levels. Dan et al. proposed silver-electrode-posited screen-printed electrodes for concentrating aniline and phenol derivatives (as shown in **Figure 3a**, and realized both the qualification and quantification of these pollutants in the concentration range

http://dx.doi.org/10.5772/64813

of 1 nM–1 μM [62]. Li and co-workers reported a disposable Ag-graphene sensor for concentrating antibiotics, and found that under optimized conditions (applied potential and preconcentration time), their proposed SERS detection method displayed a significant performance for rapid and sensitive analysis of low concentration polar antibiotics without preseparation step [63]. Another promising way is to use superhydrophobic surfaces to concentrate the analytes. For commonly used hydrophilic surface, the samples randomly spread over the substrate when they are dipped, but the surface with superhydrophobic activity can overcome the "diffusion limit" of analytes in highly diluted aqueous solutions by concentrating analytes into a small area arising from the small superhydrophobic substrate–water interface, thereby further improving SERS detection sensitivity (typical illustration of such phenomenon is shown in **Figure 3b**). Xu et al. fabricated a superhydrophobic Ag-coated ZnO array SERS platform for the highly diluted and small volume target detection [64]. This emphasized the synergistic effect of both intense electromagnetic field and superhydrophobic surface with target concentrating effect, which were also used for the ultrasensitive trace detection of rhodamine 6G with a LOD as low as to 10^{-16} M by employing superhydrophobic Ag nanocubes as substrate [65]. Recently, a universal SERS substrate called "slippery liquid-infused porous substrate" that enables the enrichment and delivery of targets originating from various phases into the SERS-active sites was proposed with using superhydrophobic surface. By the aid of this universal substrate, the detection of various chemicals, biologicals and environmental contaminates was obtained with sensitivity down to subfemtomolar level [66].

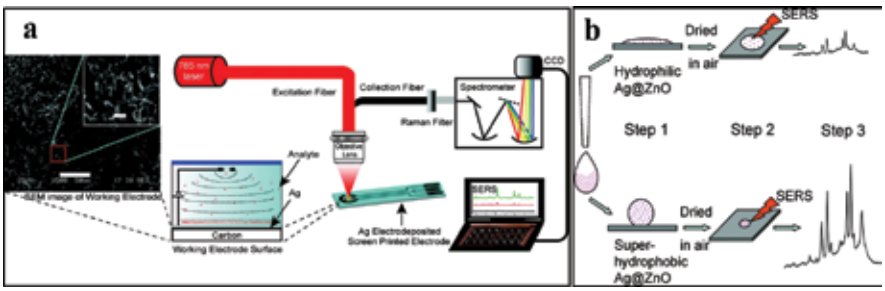

Figure 3. (a) Schematic representation of the portable SERS sensor used for detection of polar molecules in solution with the contribution from electronic concentration. Reproduced with the permission from Ref. [62]. (b) Principle of Superhydrophobic condensation for amplifying SERS Signal. Reproduced with the permission from Ref. [64].

3.2. Paper-based substrate for both concentrating and separating

Paper has been widely used as a flexible supporting material in electronic devices and also in the SERS substrate. There is growing interest in fabricating of low-cost flexible substrates by making use of cellulose paper impregnated with SERS-active structures for SERS application [67]. Besides the advantages of flexible and low cost, paper-based substrates also hold the ability for concentrating and separating analytes, which is rather useful for environmental application. For example, a starlike shape paper-based SERS device was fabricated for the subattomolar detection [68]. The complex samples are separated by a surface chemical gradient

created by polyelectrolyte coated paper, and the designed starlike shape generates a rapid capillary driven flow capable of dragging targets and SERS-active nanoparticles into a single cellulose microfiber, providing an concentrated and optically active observation spot. An important but often overlooked consideration for the developed substrates for real application is the efficiency of the target collection. Conventional designs based on rigid materials such as silicon and alumina resist effective contact to the interested surface, leading to inefficient target collection. However, the paper-based structure is flexible and allows conformal contact to real-world surfaces, which dramatically enhances the sample collection efficiency. The successfully detection of trace analytes (140 pg spread over 4 cm^2) was realized by simply swabbing the surface with the paper-based substrate [69]. The hierarchical structure of the paper contributes to easy uptake and concentration the target into the SERS hot spots and leads to excellent performance. Similarly, Ag NPs-decorated filter paper was synthesized as a "dynamic SERS" substrate for the rapid and accurate identification of pesticide residues at various peels [70].

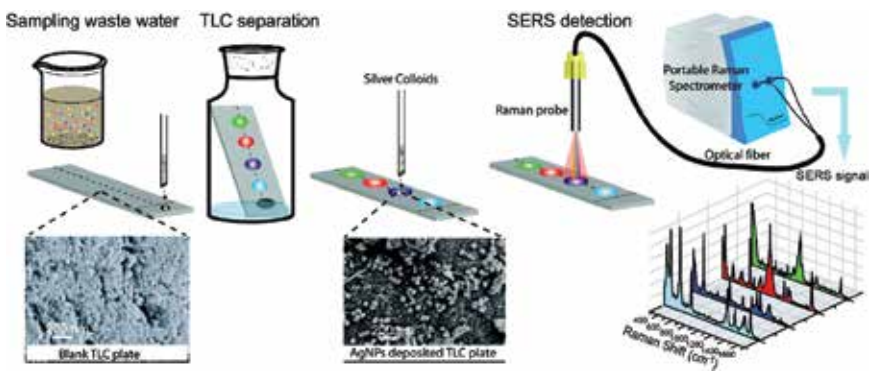

Figure 4. Schematic illustration of TLC-SERS for on-site detection of substitute aromatic pollutants in waste water. Reproduced with the permission from Ref. [77].

By using the separation ability of paper-based strip, the paper-based substrate is possibly applied for trace detection from the complex sample containing multiple components. Lateral flow assay (LFA) strip biosensor has been extensively used in point-of-care (POC) test, infectious disease diagnosis and field detection for hazardous materials in environmental samples [71]. In a typical detection procedure, the mobile phase is first pulled through the stationary phase capillary action, then passes through capture zone, and the labeled probes are then captured and detected. When combined with SERS technique, the sensitivity and quantification capability are enhanced. From the view point of SERS methods, the selectivity and anti-interference ability are also improved. Such a SERS-based LFA strip was proposed for the sensitive quantitative evaluation of staphylococcal enterotoxin B (SEB) down to 0.001 ng mL^{-1} [72]. Concerning to environmental real-life samples with complex constituents, the multiple rendering detection of each component is a challenge, even for finger-print spectrum-based SERS method. Accordingly, separation techniques such as thin-layer chromatography (TLC) and capillary electrophoresis (CE) could be combined with SERS to realize separation and detection of multiple analytes [73, 74]. TLC as a traditional separation techni-

que is very suitable to be combined with SERS because of the facile operation, no need of special instruments, and effective target concentration and separation ability. It has been successfully applied into SERS detection of various analytes, such as carotenoids, medicinal herbs and dyes in textiles [75, 76]. Recently, the TLC-SERS technique has also be used for the on-site detection of substituted aromatic pollutants in water (the whole detection process is shown in **Figure 4**) [77]. Various pollutants in the water were separated by a convenient TLC platform and detected by a portable Raman spectrometer, which was successfully applied to the detection of aniline <0.1 ppm [77]. These results reveal the ability of the proposed method for effective separation and concentration of substituted pollutants in site from environmental samples, and the shorted overall analysis time is appreciated for both emergency and routing detection of pollutants.

3.3. Hydrogel-based substrate for target gathering

As mentioned above, paper-based substrates can collect sample effectively from different surfaces by simply wiping or dipping. Hydrogel with a flexible polymer structure also holds such ability for facile target collection, which has been used as SERS substrate for the nondestructive identification of organic colorants from an ancient painting [78]. The self-standing hydrogel-based substrate also shows good prospects with advantages of fast target gathering and easy to recycle from the matrix for detection [79]. Because of the fast mass transfer between the matrix and the hydrogel network, the hydrogel substrate can act as a scaffold for target capture and concentration [80]. Le et al. prepared a gold NPs-embedded alginate gel for the detection of PAHs and found that the targets were captured by the three-dimensional network and brought close to the hot spots generated by the nanoparticles embedded in the gel, leading to significant SERS enhancement [80]. Using this substrate, quantitative analysis of four PAHs such as benzo(a)pyrene was realized with LODs as low as to 0.365 nmol L^{-1} [81]. By making use of the collapse and recover ability of the hydrogel upon drying and rehydrated, the hydrogel-based substrate can also act as excellent mechanical molecular trap for the SERS detection. More importantly, when the hydrogel is loaded with SERS-active nanoparticles, the network volume decrease will give rise to dynamic hot spots because the particles are driven close to each other, thereby generating promoted enhancing effect. This method was successfully applied to the detection of dichlorodiphenyltrichloroethane and pesticides down to $10^{-8}$and 10^{-9} mol L^{-1}, respectively [82, 83].

Besides the gathering and trapping effect for targets, the hydrogel is a bulk structure with three-dimensional network. When loaded with nanoparticles, the nanoparticles are distributed in a three-dimensional manner, and hence, the formed hot spots were not only limited on a plane but also in three-dimensional volumes which would give rise to better enhancement. In our earlier work, a polyvinyl alcohol (PVA) hydrogel substrate decorated with Ag nanoparticles was fabricated for trace SERS detection [84]. The in situ reducing process offered the hydrogel substrate with tunable, easily-operational properties with extremely homogeneous hot spot distribution. Due to its good light penetration, more than 100 mm of effective depth was confirmed by both slice observation and depth scanning techniques (the illustration for the structure and the effective depth is shown in **Figure 5**). The effective harvesting plasmonic

effects between active Ag particle couplings in all the x, y and z directions lead to a great average field within the whole substrate region, which results in excellent SERS performance [84]. Because of the large effective depth, the substrate is more tolerant toward an out-of-focus laser position, being favorable to the analysis operation on portable Raman instrument. After modified with specific capture scaffold, the hydrogel-based substrate has been successfully applied for the identification and trace detection of pollutants (such as sulfonamides, and 2,2-dipydyl) in real-world samples [45, 84].

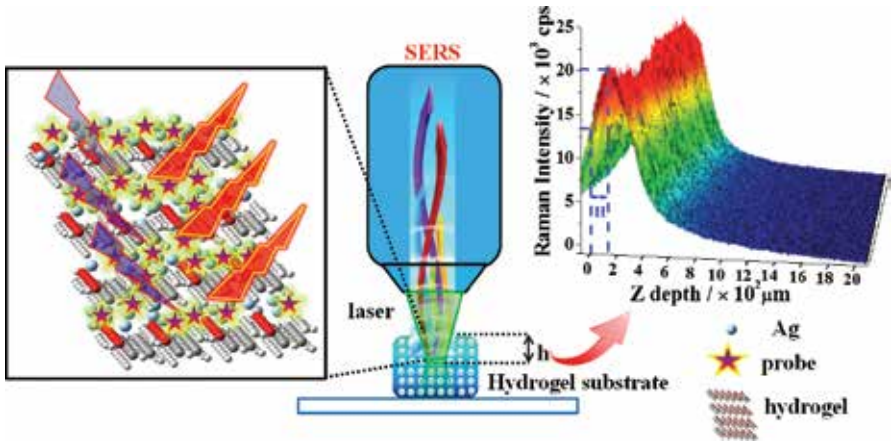

Figure 5. PVA-Ag hydrogel substrate with macroscale effective depth for trace detection. Reproduced with the permission from Ref. [84].

4. Strategies for multiple phase detection

Environmental samples frequently contain multiple analytes dispersed in various phases including aqueous phase, gaseous phase and even that dissolved in organic solvents at the same time. Therefore, the demands of multiple phases (or states) detection and identification are still a great challenge for the analytical methods. It is easy to fabricate substrate that suitable for SERS detection in a single phase such as aqueous and even organic phase, but the substrate or system that could be applied for the multiple phase detection is rather rare. Recently, a SERS sensor assembled at the liquid–liquid interface capable of multiple-phase, multiple-analyte detection was proposed, and such a liquid/liquid system allows the SERS-active particles to access either hydrophilic, hydrophobic or amphiphilic molecules at the same time [85]. The method for airborne analyte detection was also realized by simple conversion of a liquid–liquid interface to liquid–air interface. The interface assembled structure was further modified for the trace detection of Hg^{2+}. The functional polyaromatic ligands are soluble in organic phase, while the Hg^{2+} ion is soluble in aqueous phase. The interface self-assembly realizes the effective interaction between them and enables the sensitive detection down to 10 p mol level, and the airborne mercury detection was proved to be possible within 5 min of exposure [86]. Such

http://dx.doi.org/10.5772/64813

interface assembly strategy provides us a facile way to build a structure that has the access of multiple phases, but for such assembled film, the interacted surface is limited and the mass transfer is rather slow. Other surface assembled structure such as Pickering emulsion can further overcome these limits. Pickering emulsion is a promising way of producing ordered NP assemblies in three-dimensions that building blocks (such as nanoparticles) were assembled on the interface of different phases. It has been proven to be versatile immobilization techniques that provide efficient encapsulation in structures, which shows promising application in biphasic reactions [87]. By employing SERS-active particles with suitable wettability as the building block, it is possible to fabricate plasmonic Pickering emulsions as the SERS observation platform for multiphase detection. For example, surface-modified Ag nanocubes were used for constructing plasmonic colloidsomes as three-dimensional multiplex sensing platforms for ultratrace detection of both aqueous and organic soluble toxins low to sub-femtomole level [88]. Because of the emulsion-based structure, only sub-microliter sample volume is needed.

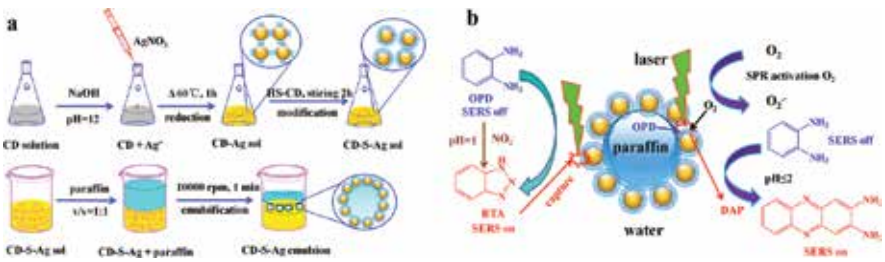

Figure 6. (a) Schematic illustration of the preparation of CD–S–Ag NPs and its emulsions. (b) The application of the proposed plasmonic Pickering emulsion system for the multiple phase pollutant detection. Reproduced with the permission from Ref. [89].

In our earlier work, we applied mercapto-β-cyclodextrin (HS-CD) as both emulsifier and functional host molecule to fabricate a Pickering emulsion-based SERS sensing system to selective detection of targets from both aqueous and organic phases (the synthesis process and the basic principle for quantify detection are shown in **Figure 6**) [89]. The HS-CD-modified Ag NPs were emulsified to assemble stable Pickering emulsion with paraffin, which shows much promoted SERS performance with dense hot spots and enables them accessible for multiple targets at the same time. Two special interface reactions on the emulsion surface were investigated and then used for detection of common pollutants NO_2^- and o-phenylenediamine (OPD). For water-soluble ionic pollutant NO_2^-, it was emulsified and reacted with the CD-captured SERS-inactive OPD to form SERS-active benzotriazole, and then, the indirect quantification of its concentration was realized with the LOD down to 1 μmol L^{-1}. For the oil-soluble OPD, its trace detection was also achieved by using the surface catalyzed oxidation to form a SERS-active 2,3-diaminophenazine (DAP) under acidic conditions. The detection limit was as low as 1 nmol L^{-1}. From the *in situ* SERS monitoring, the kinetic data of the reaction(s) were obtained and the reaction mechanism was also proposed.

5. Special measures for practical on-site application

SERS is a promising trace analytical technique. However, we have noted that among thousands of the reported SERS researches, most are limited on conceptual or laboratorial uses. The outroom or on-site SERS analysis that required special instruments such as portable SERS device is also important to make such ideas into real application. In this part, we mainly focus on special measures for real application, including specially designed SERS substrates and the newly reported SERS-based devices that are designed with the goal of real application with facile sample preparation, fast signal readout and also ability for online sensitive quantification.

5.1. Special SERS substrates matching with miniaturized (portable) Raman instrument

Concerning to infield detection or fast signal readout, portable Raman instrument is no doubt more favorable, but unfortunately, most commonly used nanoparticle-based substrates are not suitable on portable Raman instrument because of the high demands of focus position (partly due to low reproducibility from Brownian movement and uncontrollable aggregation). The assembled or encapsulated substrates have been successfully applied in developing SERS detection system combined with portable instruments. For example, the PVA hydrogel-based substrate was applied into the trace antibiotics detection form the real polluted water with portable Raman spectrometer [45]. Recently, a portable SERS kit was demonstrated for rapid and reliable detection of trace drugs from environmental samples [90]. The whole detection procedure included a 3-min pretreatment for target extraction and a handheld Raman detection with highly reproducible assembled gold nanorod array as substrate (the sample preparation and detection process are shown in **Figure 7a**). The portable kit was successfully used for detecting methamphetamine, 3,4-methylenedioxymethamphetamine and methcathinone from real urine samples, showing great prospective toward public safety and healthcare [90].

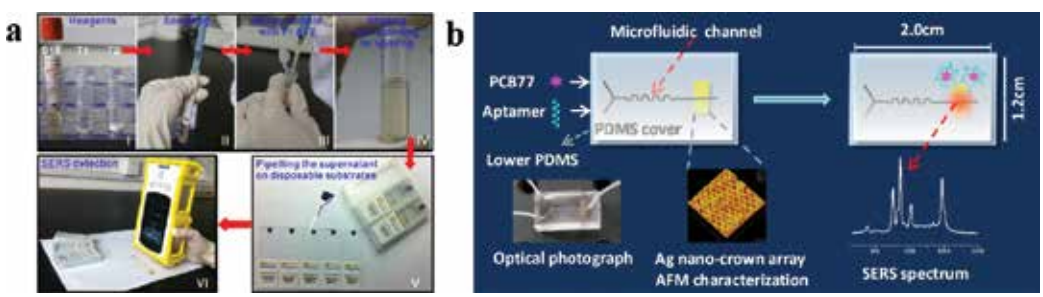

Figure 7. (a) Illustration of a portable kit for rapid SERS detection of drugs in real human urine. Reproduced with the permission from Ref. [90]. (b) Schematic diagram of the fabrication of the aptamer-based SERS microfluidic sensor for the detection of PCB77. Reproduced with the permission from Ref. [52].

5.2. Microfluidic SERS device

In recent years, applications of microfluidic system (or lab-on-a-chip) to environmental analysis have attracted much attention because of the notable advantages such as low sample consumption, rapid analysis, online analysis and incorporation of separation, concentration and quantification process [6]. The combination of microfluidic device with SERS technique not only makes use of these advantages, but also benefits a lot for the sensitive and fast online or infield detection. A microfluidic chip was developed for the trace detection of polychlorinated biphenyls [52]. The targets were selectively captured into the detection zone in the channel with aptamer functionalization, and then detected with Ag nanocrown array as enhancing substrate (illustration for the microchip is shown in **Figure 7b**). The detection concentration down to 1.0×10^{-8} mol L^{-1} demonstrates such smart chip can be utilized for sensitive detection of pollutants in the environment [52]. Similarly, by mixing the confluent streams of Ag colloids and trace analytes in the channel through triangular structure, the trace detection of cyanide was accomplished in an alligator teeth-shaped microfluidic channel [91]. An integrated real-time sensing system by making use of a portable Raman spectrometer and a micropillar array chip was developed for the field analysis of two pollutants dipicolinic acid and malachite green, and the observed LOD was estimated to be 200 and 500 ppb, respectively, and further exhibited the capability of microfluidic-SERS ship for environmental detection in the field [92].

6. Challenges and outlook

As a promising advanced analytical technique, SERS has illustrated its potential for a wide range of applications due to its capability of achieving high sensitivity and providing molecular information. In this review, we mainly summarized the achievements in the selective target trace detection for the environmental application. For a given target, an appropriate strategy should be chosen according to the nature of the target and the sample matrix. Even though a great achievement has been made in this area, there still are some challenges for the real implementation in environmental analysis.

Surface functionalization strategies may be applied to enhance the detection sensitivity and selectivity, but the high cost of the capture element such as antibody and their low stability under harsh analysis conditions are not favorable in the large-scale practical applications, which need to be improved by further studying. In addition to the sensitivity, for the developing of SERS-based methods for environmental detection, the attention should also be paid to the guarantee of good accuracy and reproducibility. The highly sensitive SERS response can lead to signal deviation, while reliable quantification becomes difficult due to the relatively poorer reproducibility. Fabrication of substrates with high selectivity, enough sensitivity and reliable reproducibility are the basic demands for real application. On the other hand, advanced data analysis technique such as chemometrics methods can also be applied to further get into the abundant spectrum information for

multiplex component analysis. By the way, most of the reported SERS substrates are still based on results obtained in laboratory, and commercial products are still rare. Therefore, more concerning should be paid onto developing substrate that can be manufactured on large scale and used easily during the on-site analysis. Concerning to large batch production, the cheap, robust and stable substrate such as hydrogel or paper-based substrate would find more applications.

Detection systems that can be directly applied for infield SERS detection are still rare. For the practical application, the followings are required: (1) the preoperation for the sample preparation should be easy and fast. (2) the target capture, concentration and separation should also be accomplished without additional complex procedures. (3) the detection system should be portable and can be easily extended to the infield detection. In order to meet the demands for real sample which also contains complex matrix, we believe that the future development of SERS-based detection strategy will be combined with advanced separation or concentration techniques such as fluidic chip devices and test strip techniques. This trend will continue through the future designing of portable integrated systems.

Author details

Lei Ouyang[1,2], Dingyi Li[1], Lihua Zhu[1*] and Heqing Tang[2*]

*Address all correspondence to: lhzhu63@hust.edu.cn and tangheqing@mail.scuec.edu.cn

1 School of Chemistry and Chemical Engineering, Huazhong University of Science and Technology, Wuhan, China

2 Key Laboratory of Catalysis and Materials Science of the State Ethnic Affairs Commission and Ministry of Education, College of Resources and Environmental Science, South Central University for Nationalities, Wuhan, China

References

[1] Zhang, L., Fang, M. Nanomaterials in pollution trace detection and environmental improvement. Nano Today, 2010, 5 (2): 128–142.

[2] Alvarez-Puebla, R., Liz-Marzan, L. Environmental applications of plasmon assisted Raman scattering. Energy and Environmental Science, 2010, 3 (8): 1011–1017.

[3] Steinberg, S. M., Poziomek, E. J., Engelmann, W. H., et al. A review of environmental applications of bioluminescence measurements. Chemosphere, 1995, 30 (11): 2155–2197.

[4] Wilson, A. D. Review of electronic-nose technologies and algorithms to detect hazardous chemicals in the environment. Procedia Technology, 2012, 1: 453–463.

[5] Wang, C., Yu, C. Detection of chemical pollutants in water using gold nanoparticles as sensors: a review. Reviews in Analytical Chemistry, 2013, 32 (1): 1–14.

[6] Li, H.-F., Lin, J.-M. Applications of microfluidic systems in environmental analysis. Analytical and Bioanalytical Chemistry, 2009, 393 (2): 555–567.

[7] Liu, Y., Su, G., Zhang, B., et al. Nanoparticle-based strategies for detection and remediation of environmental pollutants. Analyst, 2011, 136 (5): 872–877.

[8] Smichowski, P. Antimony in the environment as a global pollutant: a review on analytical methodologies for its determination in atmospheric aerosols. Talanta, 2008, 75 (1): 2–14.

[9] Haynes, C. L., McFarland, A. D., Duyne, R. P. V. Surface-enhanced Raman spectroscopy. Analytical Chemistry, 2005, 77 (17): 338 A–346 A.

[10] Schlücker, S. Surface-enhanced Raman spectroscopy: concepts and chemical applications. Angewandte Chemie International Edition, 2014, 53 (19): 4756–4795.

[11] Li, D.-W., Zhai, W.-L., Li, Y.-T., et al. Recent progress in surface enhanced Raman spectroscopy for the detection of environmental pollutants. Microchimica Acta, 2014, 181 (1–2): 23–43.

[12] Wei, H., Abtahi, S. M. H., Vikesland, P. J. Plasmonic colorimetric and SERS sensors for environmental analysis. Environmental Science: Nano, 2015, 2 (2): 120–135.

[13] Alvarez-Puebla, R. A., Liz-Marzán, L. M. SERS detection of small inorganic molecules and ions. Angewandte Chemie International Edition, 2012, 51 (45): 11214–11223.

[14] Craig, A. P., Franca, A. S., Irudayaraj, J. Surface-enhanced Raman spectroscopy applied to food safety. Annual Review of Food Science and Technology, 2013, 4: 369–380.

[15] Alvarez-Puebla, R. A., Liz-Marzan, L. M. Traps and cages for universal SERS detection. Chemical Society Reviews, 2012, 41 (1): 43–51.

[16] Zhao, Y., Newton, J. N., Liu, J., et al. Dithiocarbamate-coated SERS substrates: sensitivity gain by partial surface passivation. Langmuir, 2009, 25 (24): 13833–13839.

[17] Ouyang, L., Zhu, L., Jiang, J., et al. A surface-enhanced Raman scattering method for detection of trace glutathione on the basis of immobilized silver nanoparticles and crystal violet probe. Analytica Chimica Acta, 2014, 816: 41–49.

[18] Alvarez-Puebla, R. A., Aroca, R. F. Synthesis of silver nanoparticles with controllable surface charge and their application to surface-enhanced Raman scattering. Analytical Chemistry, 2009, 81 (6): 2280–2285.

[19] Du, J., Jing, C. Preparation of thiol modified Fe_3O_4@ Ag magnetic SERS probe for PAHs detection and identification. The Journal of Physical Chemistry C, 2011, 115 (36): 17829–17835.

[20] Kubackova, J., Fabriciova, G., Miskovsky, P., et al. Sensitive surface-enhanced raman spectroscopy (SERS) detection of organochlorine pesticides by alkyl dithiol-functionalized metal nanoparticles-induced plasmonic hot spots. Analytical Chemistry, 2014, 87 (1): 663–669.

[21] Yuan, Y., Yu, X., Zhang, Q., et al. Sensitive detection of polycyclic aromatic molecules: surface enhanced Raman scattering via π–π stacking. Analytical Chemistry, 2016, 88 (8): 4328–4335.

[22] Dai, P., Xue, Y., Wang, X., et al. Pollutant capturing SERS substrate: porous boron nitride microfibers with uniform silver nanoparticle decoration. Nanoscale, 2015, 7 (45): 18992–18997.

[23] Senapati, T., Senapati, D., Singh, A. K., et al. Highly selective SERS probe for Hg (II) detection using tryptophan-protected popcorn shaped gold nanoparticles. Chemical Communications, 2011, 47 (37): 10326–10328.

[24] Sun, B., Jiang, X., Wang, H., et al. Surface-enhancement Raman scattering sensing strategy for discriminating trace mercuric Ion (II) from real water samples in sensitive, specific, recyclable, and reproducible manners. Analytical Chemistry, 2015, 87 (2): 1250–1256.

[25] Wang, Y., Irudayaraj, J. A SERS DNAzyme biosensor for lead ion detection. Chemical Communications, 2011, 47 (15): 4394–4396.

[26] Dasary, S. S., Singh, A. K., Senapati, D., et al. Gold nanoparticle based label-free SERS probe for ultrasensitive and selective detection of trinitrotoluene. Journal of the American Chemical Society, 2009, 131 (38): 13806–13812.

[27] Ruan, C., Luo, W., Wang, W., et al. Surface-enhanced Raman spectroscopy for uranium detection and analysis in environmental samples. Analytica Chimica Acta, 2007, 605 (1): 80–86.

[28] Guerrini, L., Garcia-Ramos, J. V., Domingo, C., et al. Self-assembly of a dithiocarbamate calix [4] arene on Ag nanoparticles and its application in the fabrication of surface-enhanced Raman scattering based nanosensors. Physical Chemistry Chemical Physics, 2009, 11 (11): 1787–1793.

[29] Aswathy, B., Avadhani, G., Suji, S., et al. Synthesis of β-cyclodextrin functionalized gold nanoparticles for the selective detection of Pb^{2+} ions from aqueous solution. Frontiers of Materials Science, 2012, 6 (2): 168–175.

[30] Shen, X., Zhu, L., Wang, N., et al. Molecular imprinting for removing highly toxic organic pollutants. Chemical Communications, 2012, 48 (6): 788–798.

[31] Xu, S., Yuan, H., Chen, S., et al. Selection of DNA aptamers against polychlorinated biphenyls as potential biorecognition elements for environmental analysis. Analytical Biochemistry, 2012, 423 (2): 195–201.

[32] Piñeiro, Á., Banquy, X., Perez-Casas, S., et al. On the characterization of host-guest complexes: surface tension, calorimetry, and molecular dynamics of cyclodextrins with a non-ionic surfactant. The Journal of Physical Chemistry B, 2007, 111 (17): 4383–4392.

[33] De Silva, A. P., McCaughan, B., McKinney, B. O., et al. Newer optical-based molecular devices from older coordination chemistry. Dalton Transactions, 2003, (10): 1902–1913. DOI: 10.1039/B212447P.

[34] Guerrini, L., Aliaga, A., Carcamo, J., et al. Functionalization of Ag nanoparticles with the bis-acridinium lucigenin as a chemical assembler in the detection of persistent organic pollutants by surface-enhanced Raman scattering. Analytica Chimica Acta, 2008, 624 (2): 286–293.

[35] López-Tocón, I., Otero, J., Arenas, J., et al. Multicomponent direct detection of polycyclic aromatic hydrocarbons by surface-enhanced Raman spectroscopy using silver nanoparticles functionalized with the viologen host lucigenin. Analytical Chemistry, 2011, 83 (7): 2518–2525.

[36] Guerrini, L., Garcia-Ramos, J. V., Domingo, C., et al. Building highly selective hot spots in Ag nanoparticles using bifunctional viologens: application to the SERS detection of PAHs. The Journal of Physical Chemistry C, 2008, 112 (20): 7527–7530.

[37] Guerrini, L., Garcia-Ramos, J. V., Domingo, C., et al. Functionalization of Ag nanoparticles with dithiocarbamate calix [4] arene as an effective supramolecular host for the surface-enhanced Raman scattering detection of polycyclic aromatic hydrocarbons. Langmuir, 2006, 22 (26): 10924–10926.

[38] Taylor, R. W., Coulston, R. J., Biedermann, F., et al. *In situ* SERS monitoring of photochemistry within a nanojunction reactor. Nano Letters, 2013, 13 (12): 5985–5990.

[39] Xie, Y., Wang, X., Han, X., et al. Sensing of polycyclic aromatic hydrocarbons with cyclodextrin inclusion complexes on silver nanoparticles by surface-enhanced Raman scattering. Analyst, 2010, 135 (6): 1389–1394.

[40] Zhu, C., Meng, G., Huang, Q., et al. Large-scale well-separated Ag nanosheet-assembled micro-hemispheres modified with HS-β-CD as effective SERS substrates for trace detection of PCBs. Journal of Materials Chemistry, 2012, 22 (5): 2271–2278.

[41] Wang, J., Kong, L., Guo, Z., et al. Synthesis of novel decorated one-dimensional gold nanoparticle and its application in ultrasensitive detection of insecticide. Journal of Materials Chemistry, 2010, 20 (25): 5271–5279.

[42] Xie, Y., Wang, X., Han, X., et al. Selective SERS detection of each polycyclic aromatic hydrocarbon (PAH) in a mixture of five kinds of PAHs. Journal of Raman Spectroscopy, 2011, 42 (5): 945–950.

[43] Premkumar, T., Geckeler, K. E. Facile synthesis of silver nanoparticles using unmodified cyclodextrin and their surface-enhanced Raman scattering activity. New Journal of Chemistry, 2014, 38 (7): 2847–2855.

[44] Kochkar, H., Aouine, M., Ghorbel, A., et al. Shape-controlled synthesis of silver and palladium nanoparticles using β-cyclodextrin. The Journal of Physical Chemistry C, 2011, 115 (23): 11364–11373.

[45] Ouyang, L., Zhu, L., Ruan, Y., et al. Preparation of a native β-cyclodextrin modified plasmonic hydrogel substrate and its use as a surface-enhanced Raman scattering scaffold for antibiotics identification. Journal of Materials Chemistry C, 2015, 3 (29): 7575–7582.

[46] Goldberg, R. J. A theory of antibody—antigen reactions. I. Theory for reactions of multivalent antigen with bivalent and univalent antibody. Journal of the American Chemical Society, 1952, 74 (22): 5715–5725.

[47] Guven, B., Basaran-Akgul, N., Temur, E., et al. SERS-based sandwich immunoassay using antibody coated magnetic nanoparticles for *Escherichia coli* enumeration. Analyst, 2011, 136 (4): 740–748.

[48] Wang, Y., Ravindranath, S., Irudayaraj, J. Separation and detection of multiple pathogens in a food matrix by magnetic SERS nanoprobes. Analytical and Bioanalytical Chemistry, 2011, 399 (3): 1271–1278.

[49] Cho, I.-H., Radadia, A. D., Farrokhzad, K., et al. Nano/micro and spectroscopic approaches to food pathogen detection. Annual Review of Analytical Chemistry, 2014, 7: 65–88.

[50] Granger, J. H., Schlotter, N. E., Crawford, A. C., et al. Prospects for point-of-care pathogen diagnostics using surface-enhanced Raman scattering (SERS). Chemical Society Reviews, 2016, 45(14):3865–3882.

[51] Vikesland, P. J., Wigginton, K. R. Nanomaterial enabled biosensors for pathogen monitoring—a review. Environmental Science and Technology, 2010, 44 (10): 3656–3669.

[52] Fu, C., Wang, Y., Chen, G., et al. Aptamer-based surface-enhanced Raman scattering-microfluidic sensor for sensitive and selective polychlorinated biphenyls detection. Analytical Chemistry, 2015, 87 (19): 9555–9558.

http://dx.doi.org/10.5772/64813

[53] Feng, J., Xu, L., Cui, G., et al. Building SERS-active heteroassemblies for ultrasensitive bisphenol A detection. Biosensors and Bioelectronics, 2016, 81: 138–142.

[54] Wang, G. Q., Chen, L. X. Aptameric SERS sensor for Hg^{2+} analysis using silver nanoparticles. Chinese Chemical Letters, 2009, 20 (12): 1475–1477.

[55] Luo, W., Zhu, L., Yu, C., et al. Synthesis of surface molecularly imprinted silica microparticles in aqueous solution and the usage for selective off-line solid-phase extraction of 2,4-dinitrophenol from water matrixes. Analytica Chimica Acta, 2008, 618 (2): 147–156.

[56] Zhang, L., Jin, Y., Huang, X., et al. Ligand replacement approach to Raman-responded molecularly imprinted monolayer for rapid determination of penicilloic acid in penicillin. Analytical Chemistry, 2015, 87 (23): 11763–11770.

[57] Kamra, T., Zhou, T., Montelius, L., et al. Implementation of molecularly imprinted polymer beads for surface enhanced Raman detection. Analytical Chemistry, 2015, 87 (10): 5056–5061.

[58] Saha, A., Jana, N. R. Detection of cellular glutathione and oxidized glutathione using magnetic–plasmonic nanocomposite-based "turn-off" surface enhanced Raman scattering. Analytical Chemistry, 2013, 85 (19): 9221–9228.

[59] Yang, D., Pang, X., He, Y., et al. Precisely size-tunable magnetic/plasmonic core/shell nanoparticles with controlled optical properties. Angewandte Chemie, 2015, 127 (41): 12259–12264.

[60] Cho, I.-H., Bhandari, P., Patel, P., et al. Membrane filter-assisted surface enhanced Raman spectroscopy for the rapid detection of *E. coli* O157: H7 in ground beef. Biosensors and Bioelectronics, 2015, 64: 171–176.

[61] Zheng, G., Polavarapu, L., Liz-Marzán, L. M., et al. Gold nanoparticle-loaded filter paper: a recyclable dip-catalyst for real-time reaction monitoring by surface enhanced Raman scattering. Chemical Communications, 2015, 51 (22): 4572–4575.

[62] Li, D., Li, D.-W., Fossey, J. S., et al. Portable surface-enhanced Raman scattering sensor for rapid detection of aniline and phenol derivatives by on-site electrostatic preconcentration. Analytical Chemistry, 2010, 82 (22): 9299–9305.

[63] Li, Y.-T., Qu, L.-L., Li, D.-W., et al. Rapid and sensitive in-situ detection of polar antibiotics in water using a disposable Ag–graphene sensor based on electrophoretic preconcentration and surface-enhanced Raman spectroscopy. Biosensors and Bioelectronics, 2013, 43: 94–100.

[64] Xu, F., Zhang, Y., Sun, Y., et al. Silver nanoparticles coated zinc oxide nanorods array as superhydrophobic substrate for the amplified SERS effect. The Journal of Physical Chemistry C, 2011, 115 (20): 9977–9983.

[65] Lee, H. K., Lee, Y. H., Zhang, Q., et al. Superhydrophobic surface-enhanced Raman scattering platform fabricated by assembly of Ag nanocubes for trace molecular sensing. ACS Applied Materials and Interfaces, 2013, 5 (21): 11409–11418.

[66] Yang, S., Dai, X., Stogin, B. B., et al. Ultrasensitive surface-enhanced Raman scattering detection in common fluids. Proceedings of the National Academy of Sciences, 2016, 113 (2): 268–273.

[67] Polavarapu, L., Liz-Marzán, L. M. Towards low-cost flexible substrates for nanoplasmonic sensing. Physical Chemistry Chemical Physics, 2013, 15 (15): 5288–5300.

[68] Abbas, A., Brimer, A., Slocik, J. M., et al. Multifunctional analytical platform on a paper strip: separation, preconcentration, and subattomolar detection. Analytical Chemistry, 2013, 85 (8): 3977–3983.

[69] Lee, C. H., Tian, L., Singamaneni, S. Paper-based SERS swab for rapid trace detection on real-world surfaces. ACS Applied Materials and Interfaces, 2010, 2 (12): 3429–3435.

[70] Zhu, Y., Li, M., Yu, D., et al. A novel paper rag as 'D-SERS'substrate for detection of pesticide residues at various peels. Talanta, 2014, 128: 117–124.

[71] Song, S., Liu, N., Zhao, Z., et al. Multiplex lateral flow immunoassay for mycotoxin determination. Analytical Chemistry, 2014, 86 (10): 4995–5001.

[72] Hwang, J., Lee, S., Choo, J. Application of a SERS-based lateral flow immunoassay strip for the rapid and sensitive detection of staphylococcal enterotoxin B. Nanoscale, 2016, 8(22):11418–11425.

[73] Oriňák, A., Talian, I., Efremov, E. V., et al. Diterpenoic acids analysis using a coupled TLC-surface-enhanced Raman spectroscopy system. Chromatographia, 2008, 67 (3–4): 315–319.

[74] Dijkstra, R. J., Gerssen, A., Efremov, E. V., et al. Substrates for the at-line coupling of capillary electrophoresis and surface-enhanced Raman spectroscopy. Analytica Chimica Acta, 2004, 508 (2): 127–134.

[75] Caudin, J., Beljebbar, A., Sockalingum, G., et al. Coupling FT Raman and FT SERS microscopy with TLC plates for *in situ* identification of chemical compounds. Spectrochimica Acta Part A: Molecular and Biomolecular Spectroscopy, 1995, 51 (12): 1977–1983.

[76] Brosseau, C. L., Gambardella, A., Casadio, F., et al. Ad-hoc surface-enhanced Raman spectroscopy methodologies for the detection of artist dyestuffs: thin layer chromatography-surface enhanced Raman spectroscopy and *in situ* on the fiber analysis. Analytical Chemistry, 2009, 81 (8): 3056–3062.

[77] Li, D., Qu, L., Zhai, W., et al. Facile on-site detection of substituted aromatic pollutants in water using thin layer chromatography combined with surface-enhanced Raman spectroscopy. Environmental Science and Technology, 2011, 45 (9): 4046–4052.

[78] Leona, M., Decuzzi, P., Kubic, T. A., et al. Nondestructive identification of natural and synthetic organic colorants in works of art by surface enhanced Raman scattering. Analytical Chemistry, 2011, 83 (11): 3990–3993.

[79] Lin, X., Lou, X.-T., Lin, D.-Y., et al. Fabrication of transparent SERS platform via interface self-assembly of gold nanorods and gel trapping technique for on-site real time detection. Physical Chemistry Chemical Physics, 2015, 17 (46): 31324–31331.

[80] Contreras-Cáceres, R., Abalde-Cela, S., Guardia-Girós, P., et al. Multifunctional microgel magnetic/optical traps for SERS ultradetection. Langmuir, 2011, 27 (8): 4520–4525.

[81] Bao, L., Sheng, P., Li, J., et al. Surface enhanced Raman spectroscopic detection of polycyclic aromatic hydrocarbons (PAHs) using a gold nanoparticles-modified alginate gel network. Analyst, 2012, 137 (17): 4010–4015.

[82] Aldeanueva-Potel, P., Faoucher, E., Alvarez-Puebla, R.A., et al. Recyclable molecular trapping and SERS detection in silver-loaded agarose gels with dynamic hot spots. Analytical Chemistry, 2009, 81 (22): 9233–9238.

[83] Wu, Y., Li, P., Yang, L., et al. Individual SERS substrate with core–satellite structure decorated in shrinkable hydrogel template for pesticide detection. Journal of Raman Spectroscopy, 2014, 45 (1): 68–74.

[84] Ouyang, L., Zhu, L., Jiang, J., et al. Three-dimensional plasmonic hydrogel architecture: facile synthesis and its macroscale effective space. RSC Advances, 2015, 5 (3): 2231–2238.

[85] Cecchini, M. P., Turek, V. A., Paget, J., et al. Self-assembled nanoparticle arrays for multiphase trace analyte detection. Nature Materials, 2013, 12 (2): 165–171.

[86] Cecchini, M. P., Turek, V. A., Demetriadou, A., et al. Heavy metal sensing using self-assembled nanoparticles at a liquid–liquid interface. Advanced Optical Materials, 2014, 2 (10): 966–977.

[87] Chen, Z., Zhou, L., Bing, W., et al. Light controlled reversible inversion of nanophosphor-stabilized pickering emulsions for biphasic enantioselective biocatalysis. Journal of the American Chemical Society, 2014, 136 (20): 7498–7504.

[88] Phan-Quang, G. C., Lee, H. K., Phang, I. Y., et al. Plasmonic colloidosomes as three-dimensional SERS platforms with enhanced surface area for multiphase sub-microliter toxin sensing. Angewandte Chemie, 2015, 127 (33): 9827–9831.

[89] Ouyang, L., Li, D., Zhu, L., et al. A new plasmonic Pickering emulsion based SERS sensor for *in situ* reaction monitoring and kinetic study. Journal of Materials Chemistry C, 2016, 4 (4): 736–744.

[90] Han, Z., Liu, H., Meng, J., et al. Portable kit for identification and detection of drugs in human urine using surface-enhanced Raman spectroscopy. Analytical Chemistry, 2015, 87 (18): 9500–9506.

[91] BurmáKyong, J., KyuáLee, E. Ultra-sensitive trace analysis of cyanide water pollutant in a PDMS microfluidic channel using surface-enhanced Raman spectroscopy. Analyst, 2005, 130 (7): 1009–1011.

[92] XuanáQuang, L., HunáSeong, G., JunáDo, K. A portable surface-enhanced Raman scattering sensor integrated with a lab-on-a-chip for field analysis. Lab on a Chip, 2008, 8 (12): 2214–2219.

Edited by Khan Maaz

Raman spectroscopy has a number of applications in various fields including material science, physics, chemistry, biology, geology, and medicine. This book illustrates necessary insight and guidance in the field of Raman spectroscopy with detailed figures and explanations. This presents deep understanding of new techniques from basic introduction to the advance level for scientists and engineers. The chapters cover all major aspects of Raman spectroscopy and its application in material characterization with special emphasis on both the theoretical and experimental aspects. This book is aimed to provide solid foundation of Raman spectroscopy to the students, scientists, and engineers working in various fields as mentioned above.

ISBN 978-953-51-4112-9

Photo by yuyanga / iStock

IntechOpen